Second Edition

Advanced Nanomaterials and Their Applications in Renewable Energy

Edited by
Jingbo Louise Liu • Tian-Hao Yan • Sajid Bashir

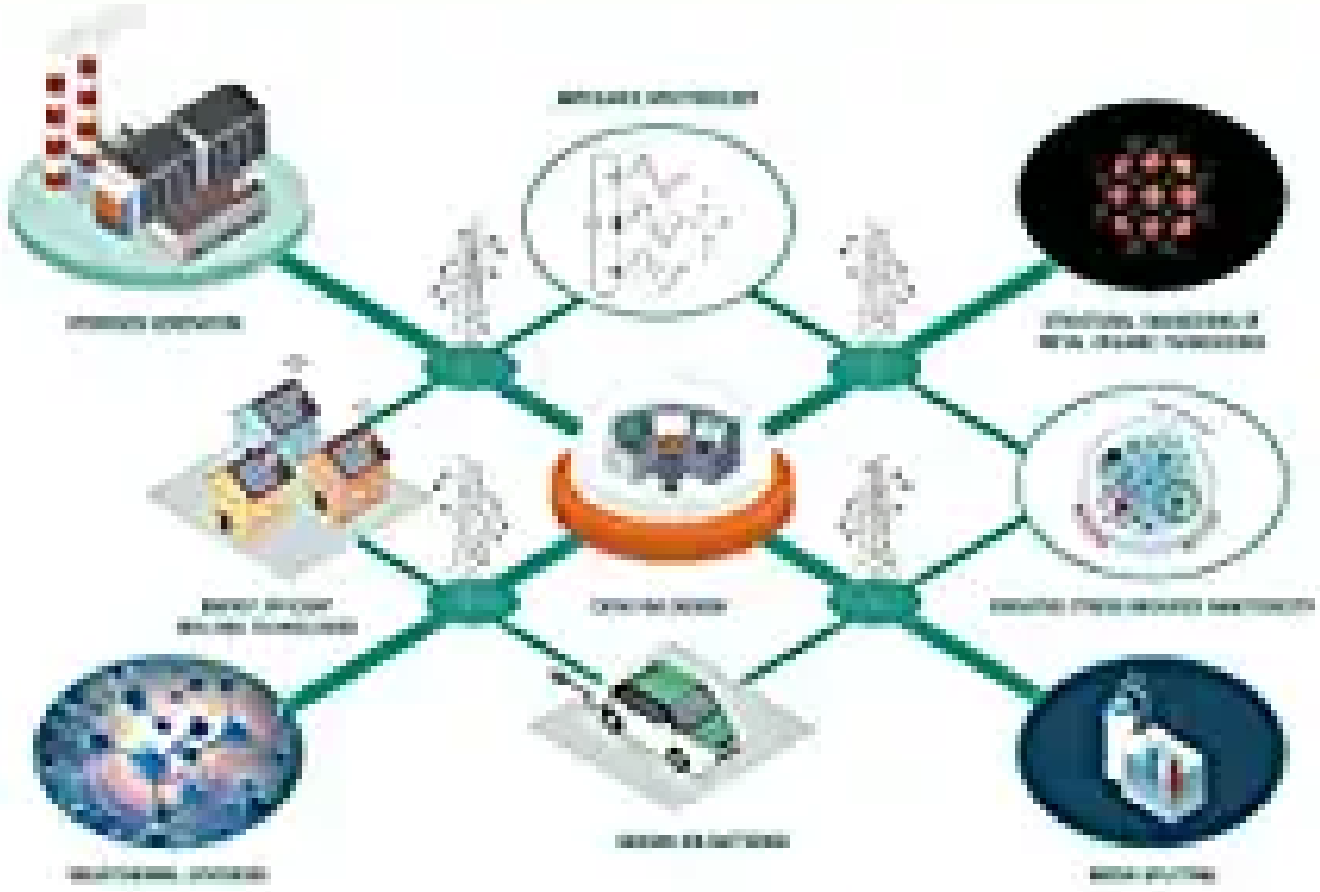

Advanced Nanomaterials and Their Applications in Renewable Energy

Second Edition

Edited by

Jingbo Louise Liu
The Department of Chemistry, Texas A&M University, Kingsville, TX, United States; Texas A&M Energy Institute, College Station, TX, United States

Tian-Hao Yan
The Department of Chemistry, Texas A&M University, College Station, TX, United States

Sajid Bashir
The Department of Chemistry, Texas A&M University, Kingsville, TX, United States

ELSEVIER

Elsevier
Radarweg 29, PO Box 211, 1000 AE Amsterdam, Netherlands
The Boulevard, Langford Lane, Kidlington, Oxford OX5 1GB, United Kingdom
50 Hampshire Street, 5th Floor, Cambridge, MA 02139, United States

Notices

Knowledge and best practice in this field are constantly changing. As new research and experience broaden our understanding, changes in research methods, professional practices, or medical treatment may become necessary.

Practitioners and researchers must always rely on their own experience and knowledge in evaluating and using any information, methods, compounds, or experiments described herein. In using such information or methods they should be mindful of their own safety and the safety of others, including parties for whom they have a professional responsibility.

To the fullest extent of the law, neither the Publisher nor the authors, contributors, or editors, assume any liability for any injury and/or damage to persons or property as a matter of products liability, negligence or otherwise, or from any use or operation of any methods, products, instructions, or ideas contained in the material herein.

ISBN: 978-0-323-99877-2

Publisher: Susan Dennis
Editorial Project Manager: Catherine Costello
Production Project Manager: Bharatwaj Varatharajan
Cover Designer: Mark Rogers

Typeset by TNQ Technologies

Contributors

Sajid Bashir The Department of Chemistry, Texas A&M University, Kingsville, TX, United States

Diego Cazorla-Amorós University Materials Institute of Alicante (IUMA), University of Alicante, Alicante, Spain

Sai Raghuveer Chava Texas A&M University-Kingsville, TAMUK, The Department of Chemistry, Kingsville, TX, United States

Praveen Kumar Cheekatamarla Buildings and Transportation Science Division, Oak Ridge National Laboratory, Oak Ridge, TN, United States

Fan Chen The Department of Chemistry, Texas A&M University, College Station, TX, United States

Kazunari Domen Research Initiative for Supra-Materials, Interdisciplinary Cluster for Cutting Edge Research, Shinshu University, Nagano, Japan; Office of University Professors, The University of Tokyo, Tokyo, Japan

Yu-Chuan Hsu The Department of Chemistry, Texas A&M University, College Station, TX, United States

Shumaila Ibraheem Institute for Advanced Study, Shenzhen University, Shenzhen, Guangdong, China; College of Physics and Optoelectronic Engineering, Shenzhen University, Shenzhen, Guangdong, China

Sehrish Ibrahim College of Life Science and Technology, Beijing University of Chemical Technology, Beijing, China

Demetrios Kouretas Department of Biochemistry and Biotechnology, University of Thessaly, Larissa, Greece

Maria Kourti Department of Biochemistry and Biotechnology, University of Thessaly, Larissa, Greece

Andrei Kulikovsky Forschungszentrum Jülich GmbH, Theory and Computation of Energy Materials (IEK-13), Institute of Energy and Climate Research, Jülich, Germany

Anuj Kumar Nano-Technology Research Laboratory, Department of Chemistry, GLA University, Mathura, Uttar Pradesh, India

Yasutaka Kuwahara School of Engineering, Osaka University Division of Materials and Manufacturing Science, Japan

Ioannis D. Kyriazis Department of Biochemistry and Biotechnology, University of Thessaly, Larissa, Greece

Hengyu Kengsley Lin The Department of Chemistry, Texas A&M University, College Station, TX, United States

Lihua Lin Research Initiative for Supra-Materials, Interdisciplinary Cluster for Cutting Edge Research, Shinshu University, Nagano, Japan

Jingbo Louise Liu The Department of Chemistry, Texas A&M University, Kingsville, TX, United States; Texas A&M Energy Institute, College Station, TX, United States

Kohsuke Mori Japan Units of Elements Strategy Initiative for Catalysts and Batteries, Kyoto University, Kyoto, Japan; Division of Materials and Manufacturing Science, Osaka University, Suita, Osaka, Japan

Muhammad Asim Mushtaq Institute for Advanced Study, Shenzhen University, Shenzhen, Guangdong, China

Swarnava Nandy Research Initiative for Supra-Materials, Interdisciplinary Cluster for Cutting Edge Research, Shinshu University, Nagano, Japan

Miriam Navlani-García University Materials Institute of Alicante (IUMA), University of Alicante, Alicante, Spain

Rajesh Pathak Applied Materials Division, Argonne National Laboratory, Lemont, IL, United States

Tatyana Reshetenko Hawaii Natural Energy Institute, University of Hawaii, Honolulu, HI, United States

David Salinas-Torres Department of Chemical and Environmental Engineering, Technical University of Cartagena, Cartagena, Spain; University Materials Institute of Alicante (IUMA), University of Alicante, Alicante, Spain

Vishal Sharma Buildings and Transportation Science Division, Oak Ridge National Laboratory, Oak Ridge, TN, United States

Som Shrestha Buildings and Transportation Science Division, Oak Ridge National Laboratory, Oak Ridge, TN, United States

Zoi Skaperda Department of Biochemistry and Biotechnology, University of Thessaly, Larissa, Greece

Fotios Tekos Department of Biochemistry and Biotechnology, University of Thessaly, Larissa, Greece

Periklis Vardakas Department of Biochemistry and Biotechnology, University of Thessaly, Larissa, Greece

Kun-Yu Wang The Department of Chemistry, Texas A&M University, College Station, TX, United States

Hiromi Yamashita Japan Units of Elements Strategy Initiative for Catalysts and Batteries, Kyoto University, Kyoto, Japan; Division of Materials and Manufacturing Science, Osaka University, Suita, Osaka, Japan

Tian-Hao Yan The Department of Chemistry, Texas A&M University, College Station, TX, United States; Department of Chemistry, Hong-Cai Zhou Research Group, Texas A&M University, College Station, TX, United States

Zhentao Yang The Department of Chemistry, Texas A&M University, College Station, TX, United States

Ghulam Yasin Institute for Advanced Study, Shenzhen University, Shenzhen, Guangdong, China; College of Physics and Optoelectronic Engineering, Shenzhen University, Shenzhen, Guangdong, China

Jiaqi Zhang The Department of Chemistry, Texas A&M University, College Station, TX, United States

Preface: Opportunities and challenges for a sustainable energy future

Advanced nanomaterials and their applications in renewable energy present new areas of focus related to nanomaterials' facile synthesis, characterization, and application in sustainable energy. The monograph with the leading subject matter experts provides insights and scientific discoveries in sustainable energy, with technical content that the layperson easily understands. Advanced energy materials are important in energy generation and storage with greater physical, electronic, and optical properties. This book delivers the fundamental physics and chemistry underpinning the techniques to develop materials with high charge densities and energy conversion efficiencies. New analytical techniques (synchronous X-ray), which probe the interactions of particles and radiation with matter are also explored, making this book an invaluable reference for practitioners and those interested in the science.

The requirement for the survival of any form of life is the generation of chemical energy. This monograph covers aspects of sustainable energy from synthesis, characterization, and applications, and herein lies the policy question. What is the best manner to meet energy demand? What are the likely trends in energy over the next 25 years, and which areas not discussed in this monograph will be necessary should this book gestate to a third edition in 2027. We will address the first obvious question and review global energy demand from 1950 onward. We start with the accepted premise that all life requires chemical energy for survival. This mechanism by which this chemical energy is obtained may be by photosynthesis, redox-based respiration/combustion, or mechanical. For humans, survival is more than access to molecules that lend to the biosynthesis of chemical energy. For humans, it is access to raw materials for clothing, shelter, and production of essential foodstuffs. This energy is to grow and consume foods, heat/air conditioning, transport, housing, fabrication of clothing, consumer and industrial goods, and commerce. Throughout human evolution, the population has increased from half a billion individuals to over 7, summarized in Figure 1.

In the same period, the global energy demand has increased from 6 TWh (1870) to 173 TWh (2019). A brief break extracted from the graph shows that in 2019, the total global energy demand was from various energy resources was: Biomass (11 TWh), coal (44 TWh),

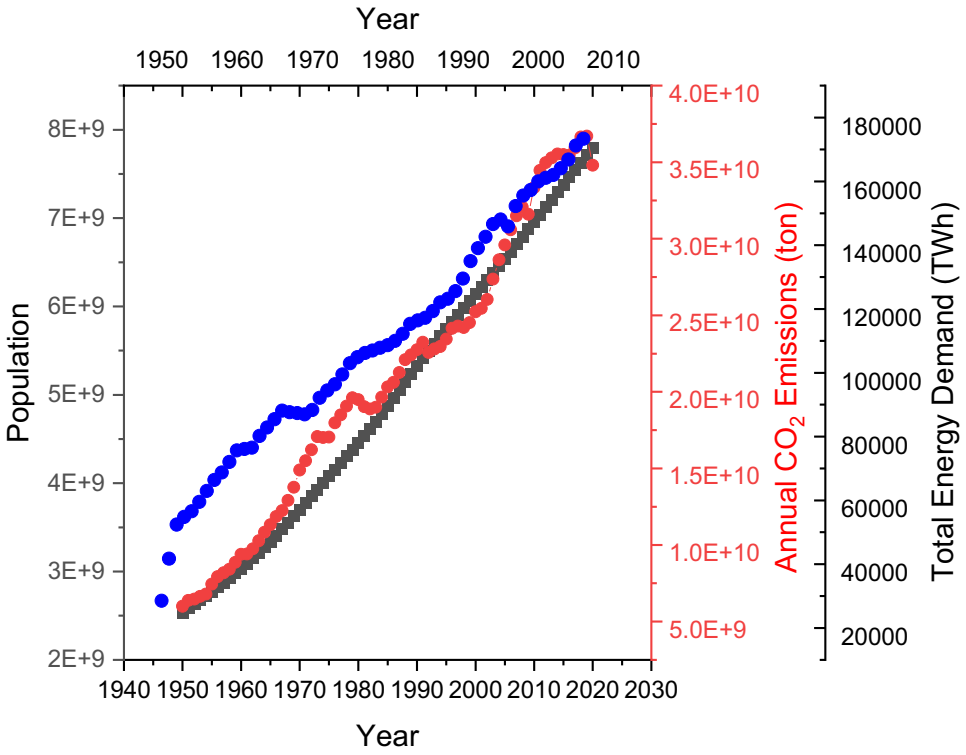

Figure 1

A plot of increase in global population with CO_2 emissions (ton). *Adapted from https://ourworldindata.org/energy-overview.*

oil (53.6 TWh), gas (39 TWh), nuclear 7 (TWh), hydropower (10.5 TWh), wind (3.5 TWh), solar (<2 TWh), and other (<2 TWh).

A brief analysis of the above plot yields a positive causative relationship between population, carbon emissions, and energy demand. It suggests the energy demand may be maintained without a related increase in carbon emissions if different carbon and noncarbon sources can be utilized with lesser CO_2 equivalence, summarized in Table 1 and shown in Figure 2.

The energy security model can be considered transport with canals, rivers being central to power. In a world war, I and II, access and exploitation of oil drive the war machine. This was illustrated during the first Gulf embargo, where oil prices increased sharply and are often credited to President Carter losing his bid for a second term. This shaped US Policy and the contained theory by limiting access to potential adversaries to an open transport system to the sea and, if possible limited access to oil and, recently, uranium ore. Today, the security concept revolves around the security square, where each corner represents availability, access, affordability, and acceptability in supply and environmental footprint.

Table 1: Summary of CO_2 emission potential of different energy resources.

Type	Fuel	CO_2 (kG/kWh)
Steam	From fossil fuels	0.83–1.16
Gas	From coal	0.79
Thermal heat	From oil	0.76
Gas-driven turbine	Natural gas	0.58
Nuclear	Pressurized water	0.025
Thermal	Uranium	0.45
Thermal	Sun	0.1–0.15
Light	Photovoltaic	0.1–0.2
Wind	Air pressure difference	0.02
Hydroelectric	Momentum energy of water	0.004

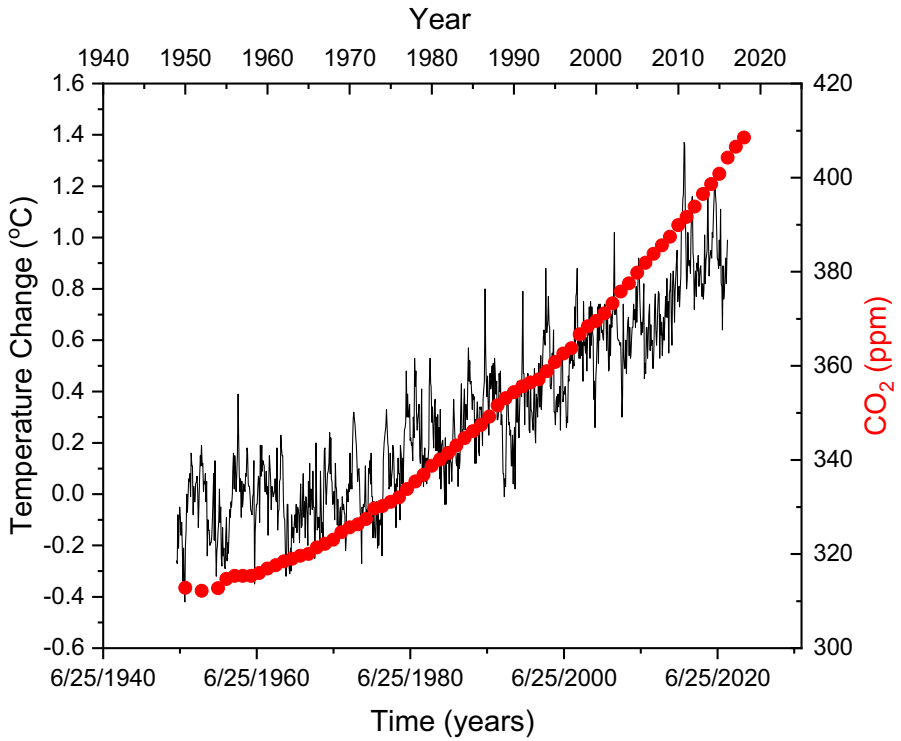

Figure 2

A plot of increase in global temperature (oC) with CO_2 emissions (ppm). *Adapted from https://ourworldindata.org/.*

This translates to countries not being dependent upon other countries for water or energy to the degree they cannot function if these supplies were cut. The oil embargo transitioned the US toward natural gas and renewables to offset the economic and political drag caused by the embargo. Today security is also dimensioned by elements related to the generation of

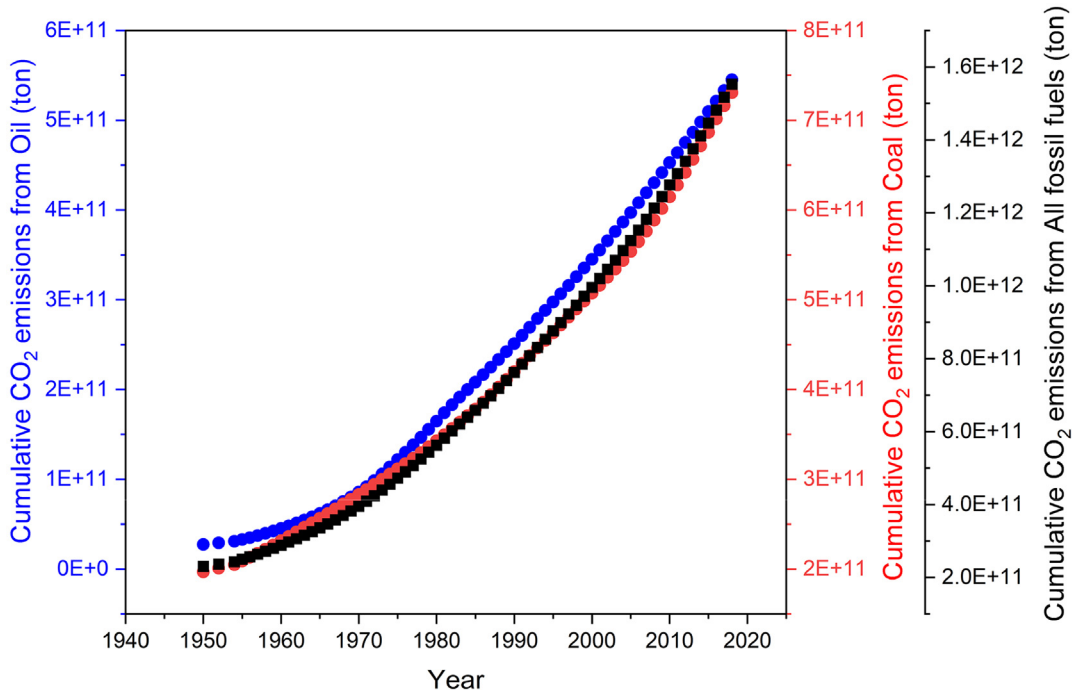

Figure 3

A plot of increase in CO_2 emissions (ton) by fossil fuel. *Adapted from https://ourworldindata.org/.*

greenhouses acids, particulate matter, acid rain capacity, in addition to the security square concept enshrined in 17 United Nations (Figure 3).

The 2008 energy and 2018 COVID crisis have focused attention on the food-water-energy nexus. They suggest that the green new deal concept is subtly different from the primary sustainable goals or transition to energy security model from the 1970s for the United States. The big difference is that the European Union, China, and Japan have the significant economic and technical capability as a counterweight to the United States, with newer capacities in Brazil and India. There is a general Paris Agreement and the extension of the SDGs toward 2030. COVID-19 has highlighted the importance of sustainability in terms of water, food, and energy security. The data in Figure 3 confirm that most of the energy production is allied to coal and oil. It is unlikely to diminish as total carbon emissions mirror emissions from coal, with a small divergence points to that some countries have implemented SDGs. This is a counterpoint for economics governed by access to fossil fuels, and those who have no strategic transition plan might be a stress point in the future. The consensus is that governments need to transition to sustainable energy goals faster to lower carbon emissions and create viable employment, lesser environmental stress, and healthier lives.

The big three in terms of growth appear to be increased capacity due to wind, solar, and cogeneration of hydrogen from nuclear energy. There appears to be the likely transition

cross-over points to the adoption of SDGs toward a more secure water-food-energy highway and are briefly discussed.

1. Wind energy

The target to restrict global temperature increase to below 2°C is a challenge for the modern world, and it would be achievable only with lower overall energy demand [1]. The need to reduce energy-related CO_2 emissions is important to limit the temperature increase between the range of 1.5−2°C, which requires significant changes in global lifestyle and energy usage policy [2]. One of the cleaner energy options is wind energy, known as the fastest-growing electrical energy source globally. Due to its availability, environmental reliability, and flexibility in energy capture and storage, wind power has received attention from all across the globe, even though it is a novel energy source of consideration. From small-scale turbines to supersized offshore plants, additional wind energy innovations are necessary to power our future electricity systems to reach their full potential. Onshore and offshore wind can generate 35% of global electricity needs and become a key energy resource by 2050 [3].

According to NREL and IRENA reports, within the last few years, the wind energy industry in the United States, Asia, and Europe has grown at a rate of 20%−40% per year. Despite such rapid growth, wind currently supports only 1% of overall electricity consumption in the United States [4]. As nature has blessed us with an abundance of wind energy potential, on and offshore wind resource has been estimated to be sufficient to supply the electrical energy needs of the entire world if we can harness this energy efficiently. The vision of the wind industry across the United States and Europe is to improve this wind energy efficiency to over 20% within the next 2 decades [5]). Recently, the US Department of Energy, in collaboration with the American Wind Energy Association (AWEA) and the National Renewable Energy Laboratory (NREL) studied the possibility of producing as much as 20% of the nation's electricity via wind energy if it is possible to address the topics that are vital for wind energy sustenance, such as the wind resource assessment, materials and manufacturing resources, environmental and siting issues, transmission, system integration, etc [6].

Sustainable wind energy will reduce massive energy-related carbon emissions (as much as 6.3 GT of CO_2), over one-quarter of the total emissions reduction potential from the renewable energy sector [7]. Wind power contributes to major emissions reduction potential by 2050, higher than any other renewable energy source. This is mostly because of the possibility of large deployments of wind energy, which can replace conventional power generation sources by using a vast supply of resources at various locations, along with benefits from cost reductions, significant end-use electrification of transport and heat applications, shifting energy demand to electricity, and rising a greener future.

Escalating concerns about climate change, air pollution−related health effects, energy security and access, and ever-increasing oil price, all of these have led to the necessity of

alternative, low-carbon renewable technology options. In recent days, in terms of total installed capacity, wind power is the leading renewable energy technology after hydropower, with 500 GW installed globally till 2018. Only next to solar, wind-dominated total renewable capacity additions, with around 43 GW of wind capacity added globally in 2018 [8].

Since wind energy's evolution, several milestones have been achieved within the last few decades in installations, technology advancements, and cost reductions, along with the establishment of key wind energy associations. By the end of 2020, onshore wind offered a less expensive source of new electricity than the least-cost fossil fuel alternative in most regions [9].

Europe was a crucial enabler for global wind power deployment throughout the early years of the industry. In 2010, the region accounted for 47% of all onshore installations globally [10]. Other regions, particularly China, have had fast wind deployment since 2010, with a CAGR of over 27% [11]. By 2018, China had surpassed Europe as the world's largest onshore wind market, accounting for about a third of all installed capacity [12]. Regarding financing new wind capacity, the European Union (EU) experienced a record year in 2018, with about 16.7 GW of potential wind power projects reaching the Final Investment Decision [13]. In 2018, about USD 29.4 billion was spent on new wind farms, with onshore wind averaging USD 1.54 million per megawatt (MW) and offshore wind averaging USD 2.57 million per MW [14].

The onshore wind market would grow substantially over the next 3 decades with increasing technological improvements and cost reductions and the correct policies and supportive measures in place. Along with the expansion of net wind capacity over the next 3 decades, another important issue is the replacement of wind turbines that are approaching the end of their technical lives and repowering existing projects to extend their commercial lives. Maintenance and updates at the system level, such as replacing outdated components with advanced technology, can help extend the socioeconomic benefits of the initial installations. By 2018, wind turbines accounted for nearly a quarter of the market for wind energy system equipment (USD 50.3 billion), followed by rotor blades with a 15% share, gearboxes at 7%, and generators covering the remainder according to GlobalData [15]. Globally, the European producers occupy a major share of the supply side of wind turbine technologies. In 2018, some 37 wind turbine manufacturers installed an estimated 20 641 individual wind turbines globally [16].

Job prospects are an important factor to consider while preparing for low-carbon economic growth. Many countries have made renewable energy production a top priority, largely cutting emissions and achieving international climate objectives and broader socioeconomic advantages. In 2018, the onshore and offshore wind industry employed 1.16 million people throughout the world. The majority of wind jobs are concentrated in a limited number of nations; however, this is less true than in the solar PV industry. Asia employed over half of the world's wind workers (620 000), followed by Europe (28%) and North America (12%) [17]. On a national basis, China dominates the world in wind installations, accounting for

44% of worldwide wind employment (510 000 jobs) in 2018. Germany came in second with 140 800 wind jobs, followed by the United States, where wind employment increased by 8% to a record high of 114 000 jobs at the end of 2018 [18].

Combining wind systems with other renewable generation sources such as solar PV, hydro, or storage technologies, or emerging technologies such as hydrogen, would be a solution to overcome the intermittency issue arising from the variable nature of wind energy and to maintain the reliability and continuous operation of the power system in times of low resource availability. Build Your Dreams (BYD), and the State Grid Corporation of China constructed the world's first hybrid project at Zhangbei, Hebei Province, in 2012. It integrated 100 MW of wind and 40 MW of solar PV power with a 36 MW lithium-ion energy storage capacity unit [19]. Vestas, a wind energy company, launched a large-scale hybrid project in 2017 that included 43.2 MW of wind and 15 MW of solar power and a 2 MW battery storage unit [20]. According to Zion Market, the worldwide hybrid solar-wind industry is predicted to grow rapidly, i.e., USD 0.89 billion in 2018 to over USD 1.5 billion by 2025, reflecting a CAGR of nearly 8.5% over the 7 years of research in 2019. In 2018, China was the largest market for solar-wind hybrid systems, and it is anticipated to continue to do so in the next decades.

Despite their increasing pace, wind power projects continue to encounter significant challenges that impede their development and commercialization. Renewable energy sources are often harmed to variable degrees due to various project requirements, regional settings, and maturity levels. No substantial technological advances in land-based technologies are required for a significant geographic penetration of wind power on the electric grid. Advancement necessitates a systems development and integration strategy that reflects the high degree of engineering in today's machines. Existing impediments to wind power deployment at many scales (technology, economics, socio-politics, and the environment) might stymie wind capacity deployment in the next 3 decades. Immediate mitigation of these hurdles through various support policies and implementation strategies is critical for future wind deployment as a sustainable energy source.

2. Solar energy

The Sun is a major source of unlimited free energy for Earth, commonly known as solar energy. New methods are now being used to create power from the solar energy gathered. These systems have previously been proved and are extensively used as renewable alternatives to nonhydro technology worldwide. Solar photovoltaics have been installed in large capacity throughout the last decade, which is more than any other power-generation technology, with a total capacity of more than 600 GW at the end of 2019 [21]. Many future low-carbon energy scenarios, however, have failed to recognize this technology's promise.

The ongoing campaign to reduce global carbon emissions, a major worldwide environmental, social, and economic challenge in recent years, is a huge promise for solar research. The installation of 113,533 residential solar systems in California, for example, resulted in the reduction or avoidance of 696,544 metric tons of CO_2 emissions [22]. As a

result, solar technology adoption would considerably minimize and relieve difficulties such as energy security, climate change, unemployment, etc. It is also expected to play a significant role in the transportation industry because it does not need gasoline.

On the African continent, the sunniest spots on the Earth may be found. The potential for concentrated solar power (CSP) and photovoltaic (PV) energy in Africa is projected to be roughly 470 and 660 petawatt hours (PWh), respectively [23]. However, in regions other than Africa (such as the southwest United States, Central, and South America, North and Southern Africa, the Middle East, India, Pakistan, Australia, and the desert plains of India, Pakistan, and Australia), such potential is limited to 125 gigawatt-hours (GWh) per sq. km of land [24]. Roughly 6300 sq. km of wasteland in China's northern and western areas (where solar radiation is among the greatest in the country) has around 1300 GW energy generating capacity [25]. The National Renewable Energy Laboratory (NREL) in the United States, on the other hand, estimates that the solar energy potential in the United States is capable of providing 400 zettawatt-hours (ZWh) every year much beyond the existing electricity generating capacity (22,813 TWh). Also, Morocco, a northern African nation with around 3000 hours of sunlight per year, has just initiated one of the world's largest solar energy projects—combining PV and CSP technologies, intending to generate 2000 megawatts (MW) by 2020 [22]. Due to the favorable weather circumstances, such a strategy is appropriate (high altitudes, low fugitive dust, high transparency, and low humidity).

The collection and usage of light and/or heat energy created by the Sun and the technologies (passive and active) involved in attaining such goals are considered the entirety of the solar energy concept. Passive technology, by definition, is the collection of solar energy without converting thermal or light energy into another form, i.e., power generation [26]. Passive solar technology collects, stores, and distributes solar energy in the form of heat for the heating of dwellings (particularly during the winter season). On the other hand, active solar systems absorb solar radiation and convert it to heat and electricity using mechanical and electrical equipment (pumps or fans). The solar water heater system is the most well-known use of this system.

In general, active solar energy technology is divided into two categories: photovoltaic and solar thermal. Photovoltaic technology, which uses semiconductors to convert sunlight directly into electrical energy, has been a popular choice in recent years [27]. The intensive study efforts of energy specialists in solar alternatives have resulted in increased photovoltaic technology efficiency. Solar thermal technology converts solar energy into thermal energy for use in residential and/or commercial applications, including drying, heating, cooling, cooking, and so on [28]. On a larger scale, however, concentrated solar thermal (CST) and concentrated solar power (CSP) technologies meet such heating needs, while CSP technologies generate energy. The latter involves concentrating solar energy with high-magnification mirrors before converting it to heat energy to power a steam turbine.

Solar energy is a steady power source that can provide everyone with energy security and independence. This proclivity is critical for people and the socioeconomic prosperity of businesses, society, governments, and countries. Nonetheless, solar power is currently being

used to meet energy demands in many developed and developing countries as a natural and significant aspect of electricity generation. Solar power technologies are considered more labor-intensive than fossil fuel technologies, which are predominantly automated and capital heavy. Solar technology should increase work prospects, which is a favorable component of this concept. Solar energy, on average, can produce more employment per unit of power output than fossil fuels. Solar power systems require an initial investment for installation, but they function at a relatively cheap cost after that. Unlike the price of fossil fuels, which fluctuates dramatically, the financial demand for solar energy is rather consistent over time. Furthermore, solar panels include no (mechanically) moving components, making them noise-free and long-lasting (no wear and tear), with little maintenance requirements. Solar panels may also be put on rooftops and fixed on building walls, indicating their versatility in installation.

However, there are several flaws in the solar energy system. One of the major problems is the high initial installation cost; for example, in early 2016, the average price per watt for solar energy in the United States was $3.70 [22]. When the Federal solar tax credit is considered, a typical solar energy system of 5 kW per dwelling would cost $13,000, reducing costs up 30%. However, long payback periods and limited revenue sources lower the value of credits for such systems [29]. Furthermore, most household solar panels have an efficiency of roughly 10%−20%, which is another drawback of solar technology [23]. Solar panels that are more efficient (about 20%) are available at a greater cost. Other components' performance constraints, like batteries and inverters, are also areas where development is necessary.

Another obvious flaw is that solar energy can only be harnessed during the day and is most effective when sunny. As a result, solar energy is unlikely to be the most reliable energy source in areas where the weather or climate is unsustainable. Furthermore, the performance of solar cells might be influenced by air pollution levels in the installation location [30]. The current of silicon solar cells was shown to be reduced by 10% and 7%, respectively, when exposed to exhaust fumes and aerosols.

Solar energy is one of the greatest possibilities for meeting future energy demand since it outperforms other renewable energy sources regarding availability, cost-effectiveness, accessibility, capacity, and efficiency [31]. Researchers have successfully monitored the flow of solar energy in and between distinct regions of a photosynthetic organism for the first time [32]. The result is the first step in research that might lead to the creation of solar energy systems that are significantly more efficient than what is now available. According to researchers from the Graphene Flagship, the lifespan of perovskite solar cells may be greatly increased by utilizing few-layer MoS2 flakes as an active buffer interface layer, according to researchers from the Graphene Flagship [33].

Furthermore, scientists in Hong Kong announced that they had constructed perovskite-silicon tandem solar cells with a 25.5 percent power conversion efficiency, which is the greatest in the world [34]. It is worth noting that when perovskite solar cells were originally introduced in 2009, their efficiency was only 3.8 percent [31], and since then, it has come a

long way. Se mi-transparent perovskite solar cells with excellent power conversion efficiency and visible light transmission while blocking infrared light have recently been developed, making them ideal candidates for solar windows [35]. The polymer poly (3,4-ethylene dioxythiophene) has been shown to offer significant potential as a material for cost-effective and highly efficient perovskite solar cells [36].

Despite recent dramatic decreases in solar technology costs, the overall costs of producing solar electricity remain high. Incentives and rebates critical for the growth of the solar energy sector highlight the need for new techniques to lower the budgetary burden of various governmental incentives. On the other hand, the solar business should emphasize the quality and advancement of its technologies. Researchers should also concentrate on enhancing solar power's competitiveness versus both conventional and renewable energy sources. Appropriate regulations are required to guarantee that high installation rates are sustained in the near term, and that solar PV's potential environmental, social, and economic advantages are realized.

3. Nuclear energy for hydrogen production

In present days around the globe, the hydrogen economy is gaining more awareness and political momentum. Within the framework of sustainable energy technologies, hydrogen is seen as a vital energy transporter and fuel. While increasing the usage of hydrogen in energy applications, it is critical to identify techniques to create hydrogen in a more environmentally responsible manner. Nuclear hydrogen production methods offer a lot of promise and benefits over other options for increasing hydrogen's part of the global energy economy in the future [37]. In the United States, nuclear power produces 20% of total electricity. This much-misunderstood energy source emits no carbon dioxide and has the greatest capacity factor of any generating station, providing electricity over 92 % [38].

Today, most hydrogen is produced by steam reforming natural gas or coal gasification, both of which emit carbon dioxide [39]. The majority of future hydrogen demand will be for zero-carbon hydrogen. Electrolysis using power from intermittent renewable sources is the basis for enhanced hydrogen production plans [40]. It is also possible to exploit the off-peak capacity of conventional nuclear reactors or other power sources. Decomposition of water by direct use of heat from nuclear energy, employing a thermochemical process facilitated by high-temperature reactors, is a key prospect for zero-carbon hydrogen synthesis in the future [41].

Nuclear energy is being considered primarily to maintain energy supply security and reduce reliance on fossil fuel imports. In most nations, one of the key goals of the energy strategy is to develop indigenous energy sources. Nuclear energy nonelectric goods can boost a country's energy independence [42]. Exploring the possibilities and benefits of nuclear hydrogen generation is gaining popularity and support. High-temperature electrolysis can make low-cost hydrogen using energy and heat supplied by nuclear power reactors (HTE).

The heat and steam generated by nuclear power stations are used in these electrolysis devices, which require far less electricity than regular electrolysis [43].

The first option is to simply generate energy from nuclear power, which can electrolyze water. Under the Office of Nuclear Energy Advanced Reactor Development Project, the US DOE granted $15.2 million in financing for advanced nuclear technology initiatives in the US in September 2019 [44]. As increasingly affordable natural gas and renewable energy supplies flood power markets, three financing channels have been defined to strengthen the nuclear sector's long-term competitiveness. The generation of hydrogen at three nuclear facilities owned by FirstEnergy Solutions (FES), Xcel Energy, and Arizona Public Service is one option (APS). The demonstrations will be held at FES′ Davis-Besse facility in Ohio, APS′ Palo Verde plant in Arizona, and an Xcel nuclear reactor in Minnesota, thanks to DOE financing. The programs aim to enhance hydrogen generation from nuclear activities in order to provide "green" products for both domestic and international markets [45].

International interest in nuclear hydrogen generation is also developing. In the United Kingdom, EDF, a French electric utility corporation, is interested in widespread hydrogen generation utilizing nuclear power stations (UK). In order to meet the increased demand for hydrogen, EDF plans to use nuclear-generated electricity to power electrolyzers that manufacture hydrogen. EDF showed the technological feasibility of creating clean hydrogen using electrolysis facilities at a nuclear plant in Lancashire, UK, through the Hydrogen to Heysham (H2H) collaboration [46].

Hydrogen supply to industrial users is currently a big industry all over the world. Hydrogen demand has increased by more than thrice since 1975. It is nearly exclusively met by fossil fuels, with 6% of world natural gas and 2% of global coal going toward hydrogen generation [47]. As a result, the generation of hydrogen results in CO_2 emissions of roughly 830 million tons per year, which is equal to the combined CO_2 emissions of the United Kingdom and Indonesia [48].

Conventional low-temperature electrolysis utilizing inexpensive off-peak electricity from existing nuclear power stations is a near-term alternative for nuclear hydrogen generation that is widely available [49]. This, however, is only possible if nuclear power plays a significant role in electricity generation. However, as the cost of fossil fuels rises, the utilization of nuclear power as a backup power source becomes increasingly appealing. Since fundamental technologies have been developed, nuclear steam reforming is another major near-term alternative for the industrial and transportation sectors, potentially saving up to 35% of methane feedstock [50]. The rising cost of natural gas will help to boost competitiveness.

Linking a nuclear reactor with a hydrogen production plant in a chemical complex necessitates extra caution regarding safety, regulatory considerations, and licensing. There is a need for nuclear process heat reactors to have a unified approach to safety concerns connected to hydrogen, such as explosions and fires, containment and limitations of pollutants (e.g., tritium), and dependable isolation of both nuclear and chemical facilities within the EU and the GIF, respectively [51].

For nuclear power to become a viable alternative to traditional fossil fuels in the future, more effort must be made to integrate nuclear technology with varied industrial demands. Ambitious initiatives have been launched in China, France, Japan, Korea, and the United States with the primary goal of bringing nuclear hydrogen production to the energy market [52]. Several institutes prove the viability of nuclear hydrogen generation, followed by performance testing and demonstration of the technology in question. For example, the United States has pledged $20 million in financing to showcase technologies for producing clean hydrogen energy from nuclear power [48]. This novel technology will enable clean hydrogen to be used as a source of zero-carbon electricity and a valuable commercial commodity for nuclear power plants. This is encouraging news for moving the global energy cycle toward a greener direction.

While there is currently a burgeoning hydrogen economy tied to the global chemical and refining industries, as well as the possibility for steelmaking, a far larger one is on the horizon [53]. The advantages of nuclear hydrogen over other sources are substantial, and hydrogen generation may become a larger part of the global energy system in the future. Nuclear hydrogen processes, on the other hand, are technically unclear and require extensive study and development. Safety concerns and hydrogen storage and distribution are essential areas for research to support a flourishing hydrogen economy. Apart from establishing the economics of production and end-use, prerequisites regarding customer perceptions of availability and convenience and social approval by both the public and the industry must be addressed. Only then can we consider nuclear energy as a viable option for producing clean hydrogen, which could be used to power our future generations.

The monograph is broken down into three general parts, where each chapter has a singular focus with fine examples from a leading practitioner in the field. Where appropriate, keywords and a glossary are given for quick reference lookup. The monograph connects theory and practice related to synthesis. Here the concept and best practices are outlined. The purpose is to understand a hypothesis-based approach rather than trial-and-error or a recipe that can become outdated. The focus is on symmetry and dimensionality, where an appreciation is developed to understand better the nature of surfaces and how these surfaces can give rise to surface catalysis. The characterization is a large aspect of materials design, and new advances on electrochemical and spectroscopic techniques are discussed in terms of an electrode to devise integration and optimization. The porosity, heterogeneity, and nanostructure all play a critical role in the ultimate catalytic or Faraday efficiency where appropriate. This often means understanding the boundaries between doped surfaces, internal defects or grain boundaries, surface composites' tendency to segregate during sintering or annealing, and the concept behind metal atom or single-atom catalysis. The last part is related to specific applications. It includes using artificial intelligence algorithms or density functional theory tools to better understand the nanoproperties of surfaces prior to actual synthesis. Here, the intent is to understand how chemical and physical processes in material design and execution impact device performance in terms of interior grain boundaries, defects, surface-to-volume ratio, and geometry of the surface.

All the hard work is collaborative, and appreciation is given to Kostas Marinakis, Joshua Bayliss, and Catherine Costello. Their vision and attention to detail allow a pain-free gestation to birth. The invaluable assistance of Catherine, Susan, and their colleagues on the Editorial Staff at Elsevier is not forgotten or underestimated, with one exception that any errors, omissions, or failings are mine as lead and not of the editorial staff or subject matter experts or for that matter my fellow co-editors.

Lastly, but not least, I am humbled by the support of our colleagues at Texas A&M University, Kingsville, Department of Chemistry, and that Department of Chemistry at Texas A&M University, as well as the Materials Characterisation Facility and Microscopy & Imaging Center, also at TAMU and the TAMU Energy Institute. I also acknowledge and thanks to the contributions of the corresponding authors, their co-authors, contributors, collaborators, students, postdoctoral research associates, and colleagues, as well as the leadership of the Departments, Colleges, and Universities from which they belong, including our Department, College of Arts & Sciences, and the University for their faith and unwavering support in this boom project.

Lastly, two individuals deserve special citation of merit. Dr. Rajesh Pathak [ANL] and Dr. Dan Kong [UCL] as individuals of extraordinary ability in the sciences, and whose sustained international acclaim has resulted in the recruitment of top-notch authors and reviews to be associated with this project. Their unfailing dedication, expertise, and field of who have risen to the very top of the field of endeavor have allowed us to craft the best handbook on sustainable energy that is currently possible.

I, on behalf of the editors and indebted and eternally grateful.

Sajid Bashir

Texas A&M University-Kingsville, TAMUK, The Department of Chemistry, Kingsville, TX, United States

Special Contributors:

Ashraf Abedin

Cain Department of Chemical Engineering, Louisiana State University, Baton Rouge, LA, United States

Sai Raghuveer Chava

TAMUK, The Department of Chemistry, Kingsville, TX, United States

Co-editors:

Jingbo Louise Liu

TAMUK, The Department of Chemistry, TAMU Energy Institute, Frederick E. Giesecke Engineering Research Building, TX, United States

Tianhao Yan

TAMU, Hong-Cai Zhou Research Group, Department of Chemistry, Texas A&M University, TX, United States

Author contributions and acknowledgments

The bulk of the preface was written by A. A and the last section by SB. SRC collated the data, and TY and JLL edited the sections. This work is partially supported by the Welch Foundation (AC 0006).

References

[1] J. Rogelj, A. Popp, K.V. Calvin, G. Luderer, J. Emmerling, D. Gernaat, et al., Scenarios towards limiting global mean temperature increase below 1.5 C, Nat. Clim. Change 8 (4) (2018) 325−332.
[2] A. Grubler, C. Wilson, N. Bento, B. Boza-Kiss, V. Krey, D.L. McCollum, et al., A low energy demand scenario for meeting the 1.5 C and sustainable development goals without negative emission technologies, Nat. Energy 3 (6) (2018) 515−527.
[3] R.J. Lowe, P. Drummond, Solar, wind and logistic substitution in global energy supply to 2050−Barriers and implications, Renew. Sustain. Energy Rev. 153 (2022) 111720.
[4] M. DeCastro, S. Salvador, M. Gómez-Gesteira, X. Costoya, D. Carvalho, F.J. Sanz-Larruga, L. Gimeno, Europe, China, and the United States: Three different approaches to developing offshore wind energy, Renew. Sustain. Energy Rev. 109 (2019) 55−70.
[5] V. Igwemezie, A. Mehmanparast, A. Kolios, A review of the current offshore wind energy sector trend and material requirements for fatigue resistance improvement in large wind turbine support structures, Renew. Sustain. Energy Rev. 101 (2019) 181−196.
[6] I. Kumar, W.E. Tyner, S. Labi, K.C. Sinha, "The Answer, My Friend, is Blowin' in the Wind": A stochastic assessment of financial feasibility and economic efficiency of wind farms, Energy Policy 159 (2021) 112598.
[7] A.M. Oliveira, R.R. Beswick, Y. Yan, A green hydrogen economy for a renewable energy society, Curr. Opin. Chem. Eng. 33 (2021) 100701.
[8] J. Zhang, A. Daniela, Y. Fang, A. Desmonda, E.O. Antwi, Review on China's renewable energy and future projections, Int. J. Smart Grid Clean Energy 7 (3) (2018) 218−224.
[9] X. Yue, N. Patankar, J. Decarolis, A. Chiodi, F. Rogan, J.P. Deane, B. O'Gallachoir, Least cost energy system pathways towards 100% renewable energy in Ireland by 2050, Energy 207 (2020) 118264.
[10] R. Lacal-Arántegui, Globalization in the wind energy industry: contribution and economic impact of European companies, Renew. Energy 134 (2019) 612−628.
[11] B.K. Sahu, Wind energy developments and policies in China: A short review, Renew. Sustain. Energy Rev. 81 (2018) 1393−1405.
[12] D. Gielen, F. Boshell, D. Saygin, M.D. Bazilian, N. Wagner, R. Gorini, The role of renewable energy in the global energy transformation, Energy Strategy Rev. 24 (2019) 38−50.
[13] M. Ozcan, The role of renewables in increasing Turkey's self-sufficiency in electrical energy, Renew. Sustain. Energy Rev. 82 (2018) 2629−2639.
[14] R. Lacal-Arántegui, J.M. Yusta, J.A. Domínguez-Navarro, Offshore wind installation: analysing the evidence behind improvements in installation time, Renew. Sustain. Energy Rev. 92 (2018) 133−145.
[15] Global Data, Wind Energy Infrastructure Providers, 2019. https://www.globaldata.com/esg/companies/wind-energy-infrastructure-providers/ (Accessed Feb 10, 2021).

[16] E. Artigao, S. Martín-Martínez, A. Honrubia-Escribano, E. Gómez-Lázaro, Wind turbine reliability: A comprehensive review towards effective condition monitoring development, Appl. Energy 228 (2018) 1569−1583.
[17] W. Gostomczyk, Trends in the Development of the Global Renewable Energy Market, Roczniki Ekonomiczne Kujawsko-Pomorskiej Szkoły Wyższej w Bydgoszczy 11 (2018) 39−52.
[18] R.H. Wiser, M. Bolinger, 2018 Wind Technologies Market Report, 2019.
[19] A. Jager-Waldau, European Commission Joint Research Center. Institute for Energy and Transport. PV Status Report, 2014.
[20] C. Hudson, MLPs & the Commercial Wind Energy Industry: Fighting the Tax Laws in the Fight to Stay Afloat, Tex. J. Oil Gas Energy L. 14 (2019) 129.
[21] A. Louwen, W. van Sark, Photovoltaic solar energy. Technological Learning in the Transition to a Low-Carbon Energy System, Academic Press, 2020, pp. 65−86.
[22] E. Kabir, P. Kumar, S. Kumar, A.A. Adelodun, K.H. Kim, Solar energy: Potential and prospects, Renew. Sustain. Energy Rev. 82 (2018) 894−900.
[23] B. Resch, G. Sagl, T. Törnros, A. Bachmaier, J.B. Eggers, S. Herkel, et al., GIS-based planning and modeling for renewable energy: Challenges and future research avenues, ISPRS Int. J. Geo-Inf. 3 (2) (2014) 662−692.
[24] M. Adaramola, Solar Energy: Application, Economics, and Public Perception, CRC Press, 2014.
[25] Q. Hang, Z. Jun, Y. Xiao, C. Junkui, Prospect of concentrating solar power in China—the sustainable future, Renew. Sustain. Energy Rev. 12 (9) (2008) 2505−2514.
[26] D. Sun, L. Wang, Research on heat transfer performance of passive solar collector-storage wall system with phase change materials, Energy Build. 119 (2016) 183−188.
[27] M. Herrando, C.N. Markides, Hybrid PV and solar-thermal systems for domestic heat and power provision in the UK: Techno-economic considerations, Appl. Energy 161 (2016) 512−532.
[28] S. Seddegh, X. Wang, A.D. Henderson, Z. Xing, Solar domestic hot water systems using latent heat energy storage medium: a review, Renew. Sustain. Energy Rev. 49 (2015) 517−533.
[29] M.B. Jebli, S.B. Youssef, The environmental Kuznets curve, economic growth, renewable and non-renewable energy, and trade in Tunisia, Renew. Sustain. Energy Rev. 47 (2015) 173−185.
[30] A.R. Radivojević, T.M. Pavlović, D.D. Milosavljević, A.V. Đorđević, M.A. Pavlović, I.M. Filipović, et al., Influence of climate and air pollution on solar energy development in Serbia, Thermal Sci. 19 (suppl. 2) (2015) 311−322.
[31] N. Kannan, D. Vakeesan, Solar energy for future world:-A review, Renew. Sustain. Energy Rev. 62 (2016) 1092−1105.
[32] J. Dostál, J. Pšenčík, D. Zigmantas, In situ mapping of the energy flow through the entire photosynthetic apparatus, Nat. Chem. 8 (7) (2016) 705−710.
[33] A. Capasso, F. Matteocci, L. Najafi, M. Prato, J. Buha, L. Ciná, F. Bonaccorso, Few-layer MoS_2 flakes as active buffer layer for stable perovskite solar cells, Adv. Energy Mater. 6 (16) (2016) 1600920.
[34] F.E. Cherif, H. Sammouda, Strategies for high-performance perovskite/c-Si tandem solar cells: Effects of bandgap engineering, solar concentration, and device temperature, Optical Mater. 106 (2020) 109935.
[35] H. Kim, H.S. Kim, J. Ha, N.G. Park, S. Yoo, Empowering semi-transparent solar cells with thermal-mirror functionality, Adv. Energy Mater. 6 (14) (2016) 1502466.
[36] X. Jiang, Z. Yu, Y. Zhang, J. Lai, J. Li, G.G. Gurzadyan, et al., High-performance regular perovskite solar cells employing low-cost poly (ethylene dioxythiophene) as a hole-transporting material, Scientific Rep. 7 (1) (2017) 1−9.
[37] M. Balat, The potential importance of hydrogen as a future solution to environmental and transportation problems, Int. J. Hydrogen Energy 33 (15) (2008) 4013−4029.
[38] L. Davis, C. Hausman, Market impacts of a nuclear power plant closure, Am. Econ. J. Appl. Econ. 8 (2) (2016) 92−122.
[39] S. Li, Q. Kang, J. Baeyens, H.L. Zhang, Y.M. Deng, Hydrogen production: state of technology, IOP Conf. Ser. Earth Environ. Sci. 544 (1) (2020, July) 012011. IOP Publishing.

[40] Y.A. Alhamdani, M.H. Hassim, R.T. Ng, M. Hurme, The estimation of fugitive gas emissions from hydrogen production by natural gas steam reforming, Int. J. Hydrogen Energy 42 (14) (2017) 9342−9351.
[41] A. Pareek, R. Dom, J. Gupta, J. Chandran, V. Adepu, P.H. Borse, Insights into renewable hydrogen energy: Recent advances and prospects, Mater. Sci. Energy Technol. 3 (2020) 319−327.
[42] M.A. Fütterer, L. Fu, C. Sink, S. de Groot, M. Pouchon, Y.W. Kim, et al., Status of the very high-temperature reactor system, Prog. Nuclear Energy 77 (2014) 266−281.
[43] D. Parigi, E. Giglio, A. Soto, M. Santarelli, Power-to-fuels through carbon dioxide Re-Utilization and high-temperature electrolysis: a technical and economic comparison between synthetic methanol and methane, J. Clean. Prod. 226 (2019) 679−691.
[44] M. Bowen, Strengthening Nuclear Energy Cooperation between the United States and Its Allies, 2020.
[45] K. Verfondern, X. Yan, T. Nishihara, H.J. Allelein, The safety concept of nuclear cogeneration of hydrogen and electricity, Int. J. Hydrogen Energy 42 (11) (2017) 7551−7559.
[46] E. Barbour, I.G. Wilson, J. Radcliffe, Y. Ding, Y. Li, A review of pumped hydro energy storage development in significant international electricity markets, Renew. Sustain. Energy Rev. 61 (2016) 421−432.
[47] A. Demirbas, Future hydrogen economy and policy, Energy Sources Part B Econ. Plan. Policy 12 (2) (2017) 172−181.
[48] S.Z. Zhiznin, V.M. Timokhov, A.L. Gusev, Economic aspects of nuclear and hydrogen energy in the world and Russia, Int. J. Hydrogen Energy 45 (56) (2020) 31353−31366.
[49] Y. Li, S. Kimura, Economic competitiveness and environmental implications of hydrogen energy and fuel cell electric vehicles in ASEAN countries: The current and future scenarios, Energy Policy 148 (2021) 111980.
[50] P. Nikolaidis, A. Poullikkas, A comparative overview of hydrogen production processes, Renew. Sustain. Energy Rev. 67 (2017) 597−611.
[51] R.O.A. Rahman, R.Z. Rakhimov, N.R. Rakhimova, M.I. Ojovan, Cementitious materials for nuclear waste immobilization, John Wiley & Sons, 2014.
[52] H. Nazir, C. Louis, S. Jose, J. Prakash, N. Muthuswamy, M.E. Buan, et al., Is the H_2 economy realizable in the foreseeable future? Part I: H_2 production methods, Int. J. Hydrogen Energy 45 (27) (2020) 13777−13788.
[53] A. Finkel, The hydrogen economy: When the old is new-and doable, Griffith Rev. 64 (2019) 134−142.

Biography of the editors

Professor Sajid Bashir received his Ph.D. training in matrix-assisted laser desorption/ionization time-of-flight mass spectrometry from the University of Warwick (UK) in 2001 and previously graduate training in Fourier transform ion cyclotron resonance mass spectrometry from the University of New York at Buffalo (USA). He was a postgraduate research associate at Cornell University (USA) in the field of plant proteomics. Currently, he is a Full Professor at Texas A&M University-Kingsville (TAMUK) and a past Faculty Fellow at the US Air Force. He has directed and participated in more than 20 projects supported by the Welch Foundation, TAMUK, Texas Workforce Commission, and US National Institute of Health. He has co-authored $>$ 80 book chapters and peer-reviewed journal articles. He is a fellow of the Royal Society of Chemistry and also holds Chartered Chemist and separately Chartered Scientists from the Science Council (UK). He is also the American Chemical Society, Energy and Fuels Division Technical Secretary (2018−2022). During his service at TAMUK, he trained more than 3000 students on both undergraduate and graduate levels. He created online courses and established safety training protocols in conjunction with Risk Management. Currently, he collaborated with local law enforcement as a consultant in forensic chemistry.

Professor Jingbo (Louise) Liu received her Ph.D. in Materials Science and Engineering from the University of Science and Technology Beijing (China) in 2001. She completed her postgraduate training at the University of Calgary in Alberta (Canada) in electrochemistry analysis of nanomaterials. She is at present a full professor at Texas A&M University-Kingsville (TAMUK, USA) and focused on materials preparation, characterization, and applications. She is a fellow of the Royal Society of Chemistry, and

Separately the American Chemical Society, a Vebleo Fellow, and a Fellow of the International Association of Advanced Materials Society. She also holds Chartered Chemist status and separately Chartered Scientists status from the Science Council, UK. She also holds DEBI Faculty Fellow status at the US Air Force Research Laboratory and is a past JSPS IF (Japan) and FFSI in Israel awardee recipient, respectively. She has authored and co-authored, books, book chapters, and peer-reviewed journal articles (>100). During her 12.5-year services at TAMUK, in chemistry, she has taught >8700 students and trained about 150 students and scholars to conduct leading-edge research. She directed and/or participated in the projects (>40) supported by the NSF (US and China), NSERC (CANADA), ACS Petroleum Research Funds, and Department of Education as PI, Co-PI, and senior personnel. She was recently elected as the Division Program Chair, Chair-Elect, and Chair of Energy and Fuels of the American Chemical Society.

Tian-Hao Yan is a Ph.D. candidate in Chemistry at Texas A&M University. He received his B.S. in Chemistry from Fudan University, Shanghai, China, in 2018. He worked as an undergraduate researcher at Yong Cao's lab in Fudan, where his research focused on designing novel supported Au nanocatalysts for biomass upgrading. He joined Dr. Hong-Cai Zhou's lab at Texas A&M in 2018 and being co-advised by Dr. Ya Wang from Department of Mechanical Engineering. His current research focuses on developing stimuli-responsive nanocarriers (Au NPs combined with porous coordination cages or metal-organic frameworks) for high-capacity drug loading and on-demand drug release.

Special Review and Subject Matter Expert Team

Dr. Ashraf Abedin received his PhD from the Cain Department of Chemical Engineering at Louisiana State University, under the supervision of Professor James J. Spivey in December 2021. He completed his bachelor's in 2016 from the Department of Chemical Engineering at Bangladesh University of Engineering & Technology. Toward the end of his PhD, Dr. Abedin worked as a researcher for Novelis Global Research and Technology Center in Kennesaw, Georgia. He currently works at the National Energy Technology Laboratory, Morgantown, West Virginia as a Leidos Research Scientist. His research focuses on catalytic conversion of fossil fuel to produce clean energy and value-added chemicals. He authored and coauthored numerous book chapters and peer-reviewed journal articles and worked as a Guest Editor and Reviewer for prestigious scientific journals including *Catalysis Today.*

Mr. Sai Raghuveer Chava has received his M.S. in Chemistry from Texas A&M University-Kingsville in 2010. He was a graduate research assistant at NNTRC, Kingsville, who researched snake venoms. Currently, he is working as a scientist on vaccine research, focusing on the analytical method development, formulation, and process-related problems using the analytical data. He has also worked on ophthalmic formulations, process characterization, method developments, and method validations. He has co-authored five journal articles and a book chapter and peer-reviewed journal articles. He is an elected member of the Royal Society of Chemistry and Sigma Xi.

Dr. Rajesh Pathak received his MSc. in Physics from the GoldenGate International College, Tribhuvan University, Nepal (2009–2011), and received his Ph.D. from South Dakota State University (2016–2020). He is a postdoctoral appointee in the Applied Materials Division at Argonne National Laboratory, Lemont, USA. Currently, his research focuses on the development of atomic layer processing methods to tailor the surface properties of next-generation lithium-ion battery electrodes using nanoscale thin films and

surface treatments. He has co-authored more than 60 peer-reviewed journal articles including the leading journals, such as Nature Communications, 11(1), 1−10, and Advanced Energy Materials, 9(36), 1,901,486.

Biography of the Authors

Professor Diego Cazorla-Amorós received PhD Degree from the University of Alicante in 1991. He spent pre- and postdoctoral stays at the Université Claude Bernard (France), Tohoku University (Japan), Amsterdam University, and Brown University (USA). He became an associate professor in 1994 at the University of Alicante and got promoted as a full professor in 2002. His research interests include the design of a wide range of materials, including carbon materials, zeolites, mesoporous materials, and metal-containing nanoparticles and their use in energy storage and production and pollutant removal. He is also very much interested in the development and improvement of chemical technologies. For this reason, he pays strong attention to the preparation of nanostructured thin films applied in microreactors and electrodes.

Praveen Cheekatamarla received his Ph.D. in Chemical Engineering from the University of Alabama, in 2004. He is a senior researcher at Oak Ridge National Laboratory, focusing on developing energy-efficient building equipment such as dryers, boilers, water heaters, space heating furnaces, and combined heat and power systems. He has over 16 years of industrial experience in energy efficient product development and served as a technical leader and principal engineer. He was the Director of Research and Product Development at Atrex Energy and was the principal developer of the fuel cell technologies enabling Atrex Energy to commercially deploy more than 800 fuel cell remote power generators in North America. His primary areas of expertise include fuel processing, fuel cells, heterogeneous catalysis, combustion, thermo-chemical processes, cogeneration technologies, energy modeling, systems analysis, fuels, systems integration, reaction engineering, and energy efficient process/product development. He has more than 60 publications and presentations, and a patent to his name. He is an active peer reviewer, editorial board member, and guest editor for technical Journals.

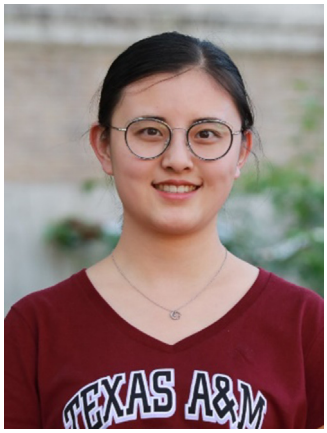

Fan Chen is a graduate student researcher at Texas A&M University. She received her BSc degree in chemistry from the Beijing Institute of Technology, China, in 2018. Her research includes the fabrication of metal-organic framework-based devices for pollutant filtration. She then joined Zhou group in Texas A&M University in 2018 fall to continue her investigation of porous materials. Her current research focuses on the manufacture of porous polymer network (PPN)-based mixed-matrix membranes for CO_2/N_2 separation and hollow fibers for direct carbon capture (DAC) from air.

Professor Kazunari Domen received his Ph.D. (1982) in chemistry from the University of Tokyo, Japan. He is currently a university professor at the University of Tokyo and a Special Contracted Professor at Shinshu University since 2017 and the team leader of Japan Technological Research Association of Artificial Photosynthetic Chemical Process (ARPChem). His research focuses on the development of photocatalysts for efficient solar hydrogen production by water splitting.

Dr. Miriam Navlani-García received her PhD degree in Material Science from Alicante University (Spain) in 2014 under the supervision of Professor Diego Cazorla-Amorós. In 2015, she moved to Osaka University, where she worked as a specially appointed assistant professor within the research group of Professor Hiromi Yamashita. In 2017, she was a recipient of a JSPS Postdoctoral Fellowship for Overseas Researchers (Standard) awarded by the Japan Society for the Promotion of Science. After that, she was awarded a Postdoctoral Fellowship for researchers with international experience (Plan GenT, Generalitat Valenciana), and she is currently a distinguished researcher at Alicante University. Her research interests are focused on the development of nanocatalysts and photocatalysts for environmental applications, mainly hydrogen purification and production.

Yu-Chuan Hsu received his BS degree in 2019 and MS degree in 2021 from National Taiwan University, where he worked on reactivity and catalytic performance of strong Lewis acidic borane species. In the fall of 2021, he joined Dr Hong-Cai Zhou's group as a PhD student at Texas A&M University in the Department of Chemistry. His research interest now focuses on the development of metal−organic framework for catalysis and gas storage.

Dr. Shumaila Ibraheem received her Master in Chemistry from the University of Agriculture Faisalabad, Faisalabad, Pakistan. She accomplished her Ph.D. in Chemical Engineering and Technology from Chongqing University, Chongqing, China with a specialization in New Energy Materials. Dr. Shumaila is presently working as a Senior Research Fellow in the Institute for Advanced Study, College of Physics and Optoelectronic Engineering, Shenzhen University, Shenzhen, Guangdong, China. She has published more than 40 scientific contributions in the form of Research and Review articles in peer-reviewed prestigious journals, as well as Book Chapters. She has won several honors and awards, including the Outstanding International Graduate Student Award of Chongqing University and the Academic Progress Award from Chongqing University. She is currently a regular reviewer for many SCI journals from ACS, Elsevier, RSC, and Springer-Nature. Her research interests include nanostructures and nanomaterials for electrochemical energy conversion and storage devices, particularly oxygen reduction reactions, oxygen evolution reactions, hydrogen evolution reactions, water electrolyzers, fuel cells, supercapacitors, metal-air batteries, as well as metal-ion batteries.

Sehrish Ibrahim received her Master in Zoology from the University of Education, Lahore, Pakistan. She is currently a Ph.D. student in Biological Engineering in the College of Life Science and Technology, Beijing University of Chemical Technology, Beijing, China. She has published several research articles in peer-reviewed journals and also authored many book chapters in the area of Microtechnology and Nanotechnology. Her research involves advanced nanomaterials and nanosystems for biomedical and energy-related applications.

Demetrios Kouretas received his Ph.D. in Biochemistry from the Department of Chemistry, Aristotle University of Thessaloniki, Greece, in 1989. He completed postdoctoral studies at the Department of Pediatrics at Harvard Medical School, USA (1990–1992). At present, he is a professor of Animal Physiology—Toxicology at the University of Thessaly, Larissa, Greece, and the President of the Hellenic Society of Toxicology. Furthermore, he is a member of the European Commission Council of Experts (risk assessment of chemical threats). He is an associate editor in "Food and Chemical Toxicology" and "Toxicology Reports" and academic editor in "Oxidative Medicine and Cellular Longevity" and "Antioxidants." Professor Kouretas has an h-index 57 and around 10,600 citations in his scientific publications. His research interests focus on the molecular mechanisms of antioxidant activity of plant phenolics, the adaptations in human exercise and, in particular, the study of redox and molecular mechanisms involved, and the functional food development and action in humans. He is the founder of the spin-off company of the University of Thessaly, FoodOxys.

Maria Kourti is a research scientist in the field of Redox Biology at the laboratory of Animal Physiology in the Department of Biochemistry and Biotechnology, University of Thessaly, Larissa, Greece. She received her BSc in Biology and her Master degree in Neurobiology at National and Kapodistrian University of Athens, Greece. Then, she earned her Ph.D. in Biochemistry from the Department of Medicine, the University of Thessaly, Greece, in 2016, where she investigated the regulation of transcription factor HIF-1 and its role in cellular metabolism. She earned a postdoctoral fellowship for studying the role of specific microRNAs in systemic lupus erythematosus (SLE), a project in cooperation with the Clinical Rheumatology and Clinical Immunology of the Department of Medicine of the University of Thessaly, Greece.

Andrei Kulikovsky received his PhD from the Institute for High Temperatures of the USSR Academy of Sciences. In 1998, he received the Doctor of Sciences (Research Professor) degree in Physics and Mathematics from the M.V. Lomonosov Moscow State University. While working in Russia, his main research interests were in the field of modeling of gas discharge plasmas. In 1998, Andrei moved to the Forschungszentrum Juelich (Research Centre Juelich), Germany, where Alexei Kornyshev engaged him into modeling of fuel cells, cell components, and stacks. Over the past 20 years, Andrei has published more than 100

research articles in high-ranked electrochemical journals; most of these articles have a sole author. In 2010, he published a book "*Analytical Modeling of Fuel Cells*" (Elsevier), which was the first monograph on theory and modeling of fuel cells. In 2014, together with Michael Eikerling, he published a book "*Polymer Electrolyte Fuel cells*: *Physical Principles of Materials and Operation*" (Taylor & Francis). In 2013, Andrei has been awarded with the Alexander Kuznetsov Prize for Theoretical Electrochemistry and in 2015, with the Schoenbein's medal of honor in recognition of the distinguished contributions to the science and technology of fuel cells.

Dr. Anuj Kumar is an Assistant Professor at GLA University, Mathura, India. His research focus is on molecular as well M-N-C electrocatalysts for H_2, O_2, and CO_2 involving electrocatalysis, nanomaterials, nanocomposites, fuel cells, water electrolyzers, nanosensors, bio-inorganic chemistry, and macrocyclic chemistry. He has published more than 45 articles in reputed peer-reviewed international journals. He has also contributed more than 12 book chapters in Elsevier, Springer, CRC Press and Bentham Science book series. For outstanding contribution in his research field, he has been awarded with "Best Young Scientist Award 2021" from the Tamil Nadu association of Intellectuals and Faculty (TAIF) and GRBS Educational Charitable Trust, India. "Young Researcher Award 2020," by Central Education Growth and Research (CEGR), India. He is serving as a section editor, guest editor, and editorial board member for various journals.

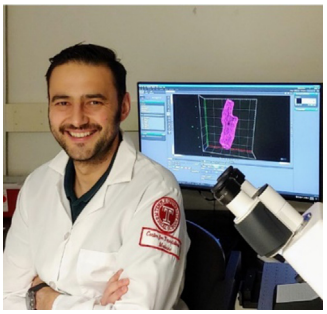

Ioannis Kyriazis is a research scientist at the University of Thessaly, Greece, under the supervision of Dr. Demetrios Kouretas. He earned his BSc in Biology from the Aristotle University of Thessaloniki and his Ph.D. in cellular immunology at Hellenic Pasteur Institute under the mentorship of Dr Eleni Dotsika. His studies in transcriptional factors regulation pushed him to join Dr Drosatos' lab, at Temple University, Philadelphia, USA, in 2017. He earned two postdoctoral fellowships from AHA and ADA for studying cardiac aging and skeletal muscle biology, respectively. He also continued his mentor project where he discovered a complex mechanism of transcriptional factor regulation that contributes to the development of diabetic cardiomyopathy, earning him a finalist spot for the prestigious BCVS Melvin L. Marcus Early Career Investigator Award in 2020. He also has three kids (Sofia, Eleni, Dimitris) with his beloved wife Maria.

Hengyu (Kingsley) Lin received his B.S. in Chemical Biology from Peking University in Beijing, 2019. He then joined Dr. Hong-Cai Zhou's group as a graduate assistant. Currently, he is a PhD candidate in Dr. Hong-Cai Zhou's group. His research focuses on light-responsive metal-organic frameworks (MOFs), MOF-derived 2-D nanosheets, and porous coordination cages (PCCs). He is interested in creating stable, environmentally friendly, and highly efficient photocatalysts for carbon−carbon and carbon−boron bond formation based on these materials.

Lihua Lin received his Ph.D. from Fuzhou University, China, in 2017. He is currently a postdoctoral research fellow at Shinshu University. His research interest is the utilization of solar energy and photocatalyst to split water into hydrogen.

Dr. Kohsuke Mori received his PhD degree from the Graduate School of Engineering Science at Osaka University in 2003. He has been as a postdoctoral fellow at the University of California, Berkeley, in 2004. He moved to current faculty in 2005 and then became an associate professor in 2009. His current research interests focus on metal and alloy nanoparticle catalysts to establish clean and environmentally friendly chemical processes, hybrid photocatalysts based on visible-light-responsible metal complexes, and automobile catalysts.

Dr. Yasutaka Kuwahara received his PhD degree in engineering from Osaka University in 2011. He joined Prof. C. W. Jones' group at Georgia Institute of Technology, USA, as a postdoctoral fellow in 2011. After the fellowship, Dr. Kuwahara was a researcher at the National Institute of Advanced Industrial Science and Technology (AIST), Japan in 2012−2014. He advanced to the current faculty position in 2014, became a lecturer in 2019, and became a associate professor in 2021. His current research interests include the design of nanostructured catalysts with multi-functionalities using porous materials, and their applications to green chemical reactions and the conversion of energy and resources.

Dr. Muhammad Asim Mushtaq received his Master in Polymer Engineering in 2015 from the University of Engineering and Technology Lahore, Pakistan. He obtained a Ph.D. degree in Chemical Engineering and Technology (2021) from Beijing University of Chemical Technology (BUCT), Beijing, China. Recently, he is a postdoc fellow at Shenzhen University, Guangdong, China. He worked under the supervision of Professor Dongpeng Yan and Professor Shengfu Ji at the Beijing Key Laboratory of Energy Conversion and Storage Materials, Beijing Normal University (BNU), and the State Key Laboratory of Chemical Resource Engineering, BUCT, China. His research focuses on the design and synthesis of catalytic materials for photo/electrochemical catalysis.

Swarnava Nandy received his Ph.D. in chemical system engineering from the University of Tokyo, Japan, in 2017. After postdoctoral stay at EPFL (Switzerland) and UESTC (China), currently, he is working for Japan Technological Research Association of Artificial Photosynthetic Chemical Process (ARPChem) at Shinshu University under the supervision of Professor Kazunari Domen. His current research interest includes materials development for overall water splitting under visible light.

Tatyana V. Reshetenko received her PhD in catalysis from Novosibirsk State University and Boreskov Institute of Catalysis (Russia) in 2003. Subsequently, she worked at Samsung SDI (South Korea) where her research shifted to fuel cell development and design of membrane electrode assemblies (MEAs) for direct methanol fuel cells (DMFCs) and proton exchange membrane fuel cells (PEMFCs). She has been with Hawaii Natural Energy Institute (USA) since 2007. Dr. Reshetenko's principal areas of interest are in the field of materials science, electrochemistry, and fuel cells with more than 25 years of R&D and project management. Her current work involves evaluation of electrochemical conversion and storage systems (DMFCs, PEMFCs, AEMFCs, and batteries) using novel and sophisticated methods such as segmented cell systems and impedance spectroscopy. Tatyana is PI and co-PI in projects sponsored by DOE, ARO, and ONR. She is an inventor on several patents, co-authored 70 technical articles, book chapters, and over 50 presentations at international conferences.

Vishal Sharma received his MS in Mechanical Engineering from Portland State University. He is a researcher in the Building Equipment Research Group at Oak Ridge National Laboratory (ORNL). At ORNL, he has been involved in the assessment and evaluation of low global warming potential (GWP) refrigerants and refrigeration systems. He has authored and co-authored over 60 peer-reviewed journal articles, conference articles, and reports.

Som Shrestha earned Ph.D. in Mechanical Engineering from Iowa State University in 2009. He is R&D Staff at Building Envelope Materials Research Group within Building Technologies Research and Integration center at Oak Ridge National Laboratory. His research focuses on experimental and analytical studies to improve the energy performance of building envelope components, equipment, and systems, including developing innovative materials and technologies, laboratory and field evaluation of energy efficiency enhancement technologies, and energy savings calculation from such technologies through modeling and simulations. Some of his recent works at ORNL include the development of thermally anisotropic building

envelopes to redirect heat and coolness from walls and roofs, new high-performance insulation materials, phase-change materials for thermal energy storage, modeling tool to guide the development of low thermal conductivity materials, and the development of an online energy savings and moisture transfer calculator for building envelope airtightness.

Zoi Skaperda was born in Larissa in 1994. She obtained her BSc from the Department of Biochemistry and Biotechnology, University of Thessaly, Larissa, Greece, and completed her postgraduate studies in the Postgraduate Program "Toxicology" of the same Department, where she is currently a PhD candidate in the laboratory of Animal Physiology. She received a Ph.D. scholarship that is co-financed by the European Regional Development Fund of the European Union and Greek national funds through the Operational Program Competitiveness, Entrepreneurship and Innovation, under the call RESEARCH–CREATE–INNOVATE. Her research interests are focused on the study of the effects of foods and food components, as well as xenobiotics on the redox profile, using both in vivo and in vitro models. She co-authored 20 articles in peer-reviewed journals.

Fotios Tekos was born in Thessaloniki, in 1995. He holds a degree in Biochemistry and Biotechnology from the University of Thessaly and graduated getting the highest degree in his year with distinction. He also earned an MSc in "Toxicology." At present, he is a Ph.D. candidate at laboratory of Animal Physiology at the Department of Biochemistry and Biotechnology, University of Thessaly, Larissa. His research interests are related to the study of the effects of several herbs, natural or synthetic extracts, and products on the redox profile in vitro and in vivo. He co-authored 20 articles in peer-reviewed journals. He is CEO in a spin off company of University of Thessaly, namely FoodOxys.

Dr. David Salinas-Torres obtained his PhD degree in Material Science from Alicante University (Spain) in 2014 under the supervision of Professor Cazorla-Amorós and Professor Morallón. He moved to the Université de Liège (Belgium) for 2 years. Then, he was a specially appointed assistant professor at Osaka University (Japan) in 2017. After that, he was granted a JSPS Postdoctoral Fellowship for Research in Japan. He was a recipient of a "Juan de la Cierva-Incorporación" contract (2019–2021) at the University

Materials Institute of Alicante. Currently, he works as an assistant professor at the Polytechnic University of Cartagena (Spain). His research interests are about the design of carbon-based materials for their use in energy storage (supercapacitors and fuel cells) and catalysis for hydrogen generation.

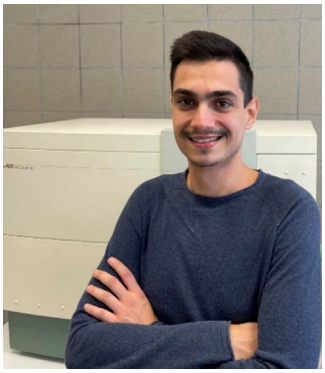

Periklis Vardakas was born in Thessaloniki, Greece, in 1994. He earned his BSc in Biology from the University of Patras, Greece, and his MSc in Toxicology from University of Thessaly, Greece. At present, he is a Ph.D. candidate at the laboratory of Animal Physiology at the Department of Biochemistry and Biotechnology, the University of Thessaly, Greece, under the supervision of Professor Demetrios Kouretas. His research interests focus on nanotoxicity and, more elaborately, the effects of engineered nanomaterials on redox status at cellular and organism levels. He co-authored four articles in peer-reviewed journals.

Kun-yu Wang is a PhD candidate at Texas A&M University. He received B.Sc. in Chemistry (Po-Ling class) from Nankai University in 2018. In 2017, he went to Northwestern University as an undergraduate researcher. In 2018, Kunyu joined Professor Hong-Cai Zhou's research group at Texas A&M University. His research interest now focuses on novel strategies to design multicomponent and hierarchically porous materials. During his study, Kunyu has published >30 peer-reviewed articles, including seven first/co-first author articles on top-notch journals, such as *Angew. Chem. Int. Ed.*, *ACS Materials Lett.*, *ACS Cent. Sci.*, and *Chem. Soc. Rev.* His research has been presented in RSC Faraday Discussion, Gordon Research Conference, and ACS National Meeting. Moreover, he was awarded the Dow Chemical Company Charlene Black Miller '79 Endowed Memorial Fellowship in Chemistry and Foresight Fellowship.

Professor Hiromi Yamashita has been a professor of Osaka University since 2004. He received his PhD degree from Kyoto University in 1987. He was an assistant professor of Tohoku University and an associate professor of Osaka Prefecture University. He was also a visiting research fellow at California Institute of Technology and Invited Professor of University Pierre and Marie Curie. He has been the president of Asia and Pacific Association of Catalysis Societies (2019), the president of Catalysis Society of Japan (2019-2020), the member of Academia Europea (2019), and the editor of Applied Catalysis B (2012). He received awards from several societies such as Catalysis Society of Japan, the Japan Petroleum Institute, Japanese Photochemistry Association, the Japan Institute of Metals and Materials, and Japan Society of Coordination Chemistry. His research interests include the design of single-site photocatalysts and nanostructured catalysts.

Zhentao Yang was born in Sichuan, China. He is expected to receive BS in chemistry from Nankai University and BE from Tianjin University in 2022. Now, he is a visiting student in Dr. Hong-Cai Zhou's group, focusing on the synthesizing MOFs and cages with new topology.

Dr. Ghulam Yasin received his Bachelor in Metallurgy and Materials Engineering from the Institute of Advanced Materials, Bahauddin Zakariya University, Multan, Pakistan. He did his Master and Ph.D. in Materials Science and Engineering from the College of Materials Science and Engineering, Beijing University of Chemical Technology, Beijing, China. He was working as Research Assistant in the Institute of Nuclear & New Energy Technology, Tsinghua University, Beijing, China, in 2020. Currently, he is working as a research fellow (faculty member) in the Institute for Advanced Study, and College of Physics and Optoelectronic Engineering, Shenzhen

University, Shenzhen, Guangdong, China. Dr. Yasin has over 100 publications in well-reputed peer-reviewed international journals. He is the author of several book chapters and editor of 17 Elsevier books in the Micro & Nano Technologies Series. He has h-index = 23 along with more than 2000 citations. Dr. Yasin has ranked in the world's top 2 % scientists (published by Elsevier BV, and Standford University, USA). He has been awarded various national and international awards. He is currently a regular reviewer for over 40 journals from ACS, Elsevier, RSC, Springer-Nature, and Wiley. Dr. Yasin is serving as an associate editor, section editor, guest editor, and editorial board member for several journals. His research focuses on the design and development of nanoscale advanced functional materials for energy conversion and storage hybrid devices/technologies, as well as nanostructures and nanomaterials for various functional applications.

Jiaqi Zhang received his B.S. in chemical biology and B.Ec. in economics from the Tsinghua University, Beijing, China, in 2021. He is a currently a first-year Ph.D. student in Professor Hong-Cai Zhou's research group at Texas A&M University. His main research interest is pore engineering in metal-organic framework and porous coordination cages.

CHAPTER 1

Energy-efficient building technologies

Praveen Kumar Cheekatamarla[a], **Vishal Sharma, Som Shrestha**
Buildings and Transportation Science Division, Oak Ridge National Laboratory, Oak Ridge, TN, United States

Abstract

Buildings consume one-third of the total final energy produced on the globe and are responsible for almost 40 percent of total carbon dioxide generation annually. The latest carbon dioxide burden of buildings approached 10 Gigatons in the year 2019. Energy-efficient building technologies are necessary to address the climate change induced by greenhouse gases and fulfill the growth in demand and continuously depleting energy reserves. To meet the net-zero carbon footprint goals, sustainable, renewable energy resources, efficient building technologies, and demand management strategies are needed. Achieving zero emissions will require buildings to be equipped with energy-efficient technologies while completely avoiding on-site fossil fuel consumption and being only powered by renewable energy. In this context, this chapter provides an overview of various building technologies, including envelopes, materials, equipment, appliances, and integration concepts, which will play a significant role in lowering the overall energy consumption in both existing building stock and new buildings. Specifically, the following areas are discussed in detail: emerging building envelope designs, thermal comfort and refrigeration equipment, bridging technologies for improved energy efficiency in the ongoing energy transition, hybrid renewable (photovoltaic) configurations, energy storage technologies, miscellaneous appliances, refrigerants, and renewable fuels. The influence of key design and operating characteristics on annual carbon footprint is presented.

Keywords: Appliances; Building equipment; Carbon dioxide; Carbon intensity; Cogeneration; Cooling; Decarbonization; Dehumidification; Envelope; Heating; Hydrogen; Refrigerants; Refrigeration; Thermal load.

1. Introduction

Energy plays a vital role in modern society; however, it is also responsible for greenhouse gas emissions. Global energy consumption is on the rise, driven by economic and

[a] This manuscript has been authored by UT-Battelle, LLC, under contract DE-AC05-00OR22725 with the US Department of Energy (DOE). The US government retains and the publisher, by accepting the article for publication, acknowledges that the US government retains a nonexclusive, paid-up, irrevocable, worldwide license to publish or reproduce the published form of this manuscript, or allow others to do so, for US government purposes. DOE will provide public access to these results of federally sponsored research in accordance with the DOE Public Access Plan (http://energy.gov/downloads/doe-public-access-plan).

Advanced Nanomaterials and Their Applications in Renewable Energy. https://doi.org/10.1016/B978-0-323-99877-2.00019-9

population growth. As shown in Fig. 1.1, although renewables are expected to become the primary resource, fossil fuels continue to increase, given the global demand increase [1].

By 2050, energy information administration (EIA) projects a 50% increase in global energy demand driven by a 65% increase in building energy consumption, a 79% increase in electrical power generation, and a 40% increase in natural gas consumption [2,3]. Among all energy consumers globally, buildings consume a third of total final energy consumption leading to greater than 40% of total direct and indirect carbon dioxide emissions [4]. In 2019 alone, $\sim 10\ GtCO_2$ was emitted due to electricity and heat consumption, the highest level ever recorded [4].

According to energy information administration statistics [5], residential and commercial buildings in the United States consumed 39 quadrillion Btus of energy in 2019, accounting for almost 39% of total primary energy. Electricity supply to the end consumer comes at a premium value since $\sim$65% of the primary energy is lost in production and distribution [6]. Given this high premium, the energy supplied to buildings must utilize it to its full potential at the highest possible conversion and utilization efficiency. From an energy efficiency perspective, heating and cooling equipment in a residential or commercial building consume up to 50% of the total energy supply [7,8]. Heating systems, for instance, utilize $\sim$60% of fossil fuels as the primary energy resource [9]. Globally, cooling demand is rising, driven by population and income growth, accounting for $\sim$20% of the total electricity used in buildings today [10].

As a result, building energy usage accounts for $\sim$40% of total annual carbon dioxide emissions globally [11,12]. Given these energy and environmental impacts and projected

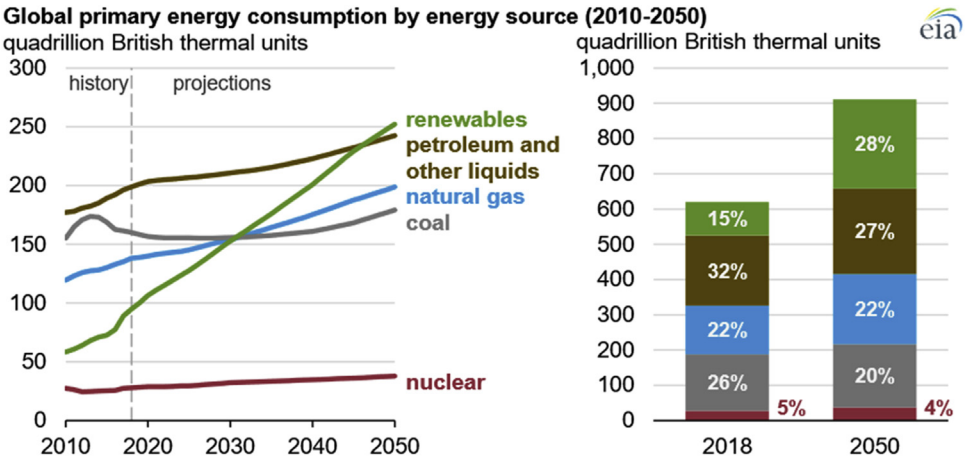

Figure 1.1

Global primary energy consumption by energy source, quadrillion Btu. *Source: https://www.eia.gov/todayinenergy/detail.php?id=41433.*

statistics, technology improvements to address high energy demand, carbon footprint, and emissions associated with building energy consumption are of enormous value for a sustainable energy future without negatively impacting the environment.

2. Building technologies

Buildings are a great resource and offer significant untapped potential in lowering the global energy demand and environmental footprint. Buildings can lower direct energy consumption via efficiency improvements and act as prosumers in grid stabilization and demand management via grid-interactive technologies, facilitating the integration of intermittent renewable energy within the grid infrastructure. Primary strategies to realize this potential include architectural improvements, envelope material and design innovations, energy management, and building equipment.

The following sections highlight the significance of each area in the context of building energy, efficiency, and carbon footprint, followed by an overview of the state-of-the-art and future direction. Economic aspects are not discussed in this chapter since the key focus is on energy efficiency and its environmental implications.

2.1 Building envelope

Building architecture and the way we build buildings have evolved with human civilization. The building envelope, which consists of the walls, windows, and foundation, encloses the structure between the exterior and interior environments. In addition, shading elements are also used to control solar heat gain. The building envelope comprises multiple components and systems that serve various functions, such as structural support, control of the water penetration, air leakage, heat transfer between the interior and exterior of the building, sound barrier, and aesthetic purposes.

Energy losses through building envelopes, which is the primary contributor to HVAC loads, significantly attribute energy use in buildings. As an example, Fig. 1.2 shows the primary energy consumption attributable to energy losses through building envelope components in the United States in 2010. To put the numbers in perspective, the energy losses through building envelopes were responsible for over 15% of United States primary energy consumption (98 quadrillions Btu) and over 38% of energy consumptions in residential and commercial buildings (40 quadrillions Btu).

Building energy efficiency standards, such as the International Energy Conservation Code (IECC), ANSI/ASHRAE/IES Standard 90.1—Energy Standard for Buildings Except for Low-Rise Residential Buildings, and ANSI/ASHRAE/IES Standard 90.2—Energy Efficient Design of Low-Rise Residential Buildings set minimum efficiency requirements for new

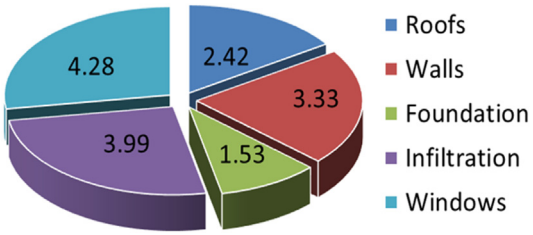

Figure 1.2
Primary energy consumption (quadrillion Btu) attributable to building envelope components in the United States in 2010. *Source: US Department of Energy Windows and Building Envelope Research and development: Roadmap for Emerging Technologies [13], Note: 1 quadrillion Btu = 293,071 GWh.*

and renovated buildings, assuring reductions in energy use and emissions over the life of the building. The minimum efficiency requirements vary based on the building applications and locations (climate zones). The efficiency requirements are becoming more rigorous to minimize energy use in buildings and their environmental impacts. The insulation and fenestration requirements for residential and commercial buildings have been prescribed by the 2018 IECC [14–16].

In addition to the requirements to minimize energy losses by the heat transfer through building envelopes, these standards also require building airtightness. 2018 IECC requires air leakage through residential building envelopes to be $\leq$5 air change per hour (ACH) at 50 Pa pressure differentials for climate zones 1 and 2 and $\leq$3 ACH for climate zones 3 to 8. Similarly, for commercial buildings, the measured air-leakage rate should not exceed 0.25 cfm/ft^2 under a pressure differential of 0.3 inches water column (75 Pa), with a calculated surface area the sum of the above-and below-grade building envelope. The air infiltration is verified by a whole-building pressurization test per ASTM E779 or ASTM E1827. The 2018 IECC requires continuous air barriers in commercial buildings in all climate zones to minimize air leakage, except climate zone 2B. Similarly, the 2018 ICEE code also prescribes maximum U-factor and solar heat gain coefficient (SHGC) requirements for commercial building envelope fenestration [17].

Various insulation materials reduce energy losses through building envelopes and meet the energy efficiency code requirements. However, the application of traditional thermal insulation materials requires thicker building envelopes to satisfy the requirements of the emerging zero energy and zero-emission buildings. As very thick building envelopes are not desirable for several reasons, for example, considering space issues concerning the economy, floor area, transport volumes, architectural restrictions and other limitations, material usage, and existing building techniques, there is a demand for developing high-performance thermal insulation [18]. To fulfill this requirement, high-performance thermal insulation materials are emerging. In addition, a new building envelope design that can

redirect the thermal energy (heat and coolness) from the building envelope is also being developed. Some of the high-performance thermal insulation materials, dynamic insulation materials, new building envelope design to redirect the thermal energy, and high thermal mass building envelope to reduce heating and cooling load associated with heat flow through building envelope are discussed below.

2.1.1 Vacuum insulation panels

Vacuum insulation panels (VIPs) typically consist of an open porous core of fumed silica or fibrous material enveloped on barrier material consisting of multilayered metalized polymer laminate films. VIPs represent today's state-of-the-art thermal insulation with thermal conductivities ranging from 3 to 4 mW/(mK) in pristine (nonaged) condition to typically 8 mW/(mK) after 25 years of aging due to water vapor and air diffusion through the VIP envelope and into the VIP core material, which has an open pore structure [19].

2.1.2 Aerogels

Aerogel is a synthetic porous ultralight material derived from a gel. The liquid component for the gel has been replaced with gas without significant collapse of the gel structure. The result is a solid with extremely low density and extremely low thermal conductivity [20]. Aerogels were discovered in the early 1930s by Samuel Kistler. Aerogels have a large specific surface area, a very low apparent density, and low thermal conductivity. Suppose one can be able to manufacture aerogel for a fraction of the current economic and environmental cost. In that case, aerogel insulation may become a decent alternative to current traditional building insulation materials combining the benefit of most traditional building insulation materials—that is, a robust bulk material—with a thermal conductivity 2 to 2.5 times lower than that of conventional mineral wool [21].

2.1.3 Active insulation materials and systems

Controllable active insulation systems (AISs), in which the thermal resistance of the insulation material can be dynamically controlled within a certain range, can expand the capabilities of the building envelope. With AISs, the building envelope is no longer a passive barrier between indoors and outdoors; instead, heat transfer can be controlled. Moreover, when AISs are combined with the thermal mass in the envelope system, these can act as thermal batteries that can be loaded and unloaded on demand [22]. Various options have been explored to control the thermal resistance on demand. Antretter et al. provided an overview of some of the proposed materials and technologies [22].

2.1.4 Thermally anisotropic building envelope

Traditional building envelopes, such as roofs and walls, use insulation to reduce heat flow. However, thermally anisotropic building envelope (TABE), a novel application of thermal anisotropy for improving the energy efficiency of building envelopes, adds thin conductive

layers between the insulation (Fig. 1.3). The conductive layers connect to a thermal loop that redirects the thermal energy (heat or coolness) to an energy storage system or can be used for other applications [23]. Stored energy is then used to heat or cool the indoor space. Sensors and controls determine when to transfer energy between the envelope and the loop to maximize energy savings or peak load reductions. Thus, TABEs allow harvesting natural thermal energy from the building envelope to offset the building's heating or cooling demand. Biswas et al. showed that a TABE coupled with a heat sink/source is more effective in reducing cooling and heating loads and peak cooling loads than foam insulation of the same thickness, as shown in Fig. 1.3.

2.1.5 Phase change materials

Phase change materials (PCMs) are a class of thermal storage materials that are commercially available and can be concentrated or integrated into the building structure or envelope and HVAC equipment. Existing PCMs charge and discharge passively in response to temperature changes. Depending on the PCM formulation, they can shift either peak heating or cool to off-peak hours, but they cannot control the timing of charging or discharging [24]. The ability to control the transition temperature of PCMs could also increase the value of such storage media. A recent study shows the results of an analysis of the effect of transition temperature tunability on energy storage in United States buildings [25]. These results show that regardless of whether the PCM is primarily intended for use during heating or cooling season, the addition of tunability to the transition temperature of the medium significantly increases the annual energy storage potential.

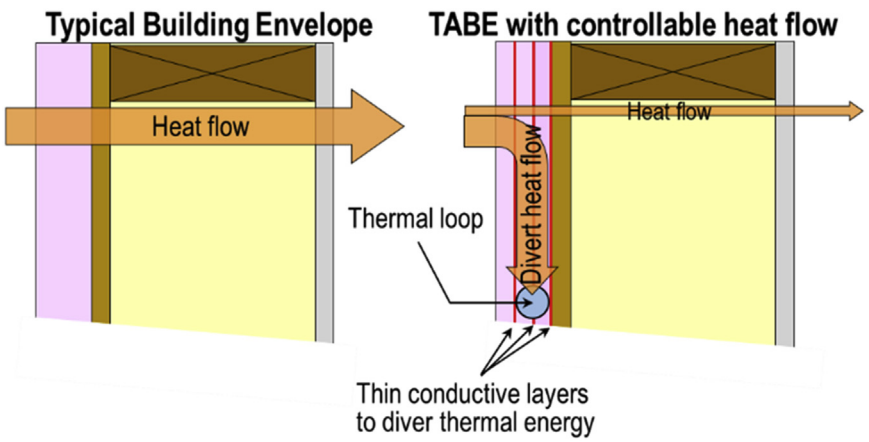

Figure 1.3
Schematic of a thermally anisotropic building envelope (TABE).

2.2 Building equipment

Decarbonization of buildings requires efficient utilization of the supplied energy. Fig. 1.4 displays a snapshot of the energy consumption in residential and commercial buildings. As shown, 40%−50% of the energy supply goes toward heating and cooling demand in the building. In contrast, the rest of the energy is consumed by numerous devices, including lighting, small appliances, washers, dryers, cooking, etc. Most of these needs are typically met by electricity, while fossil fuels or electricity serves heating loads. Given the energy impact of thermal load in a building, the following sections focus on numerous pieces of equipment with significant energy consumption and their desired performance characteristics. The following sections present individual building equipment and their associated carbon footprint under different operational and configurational aspects. Given CO_2's impact on climate change, it is the key metric evaluated in this work since it is a direct reflection of energy efficiency variation.

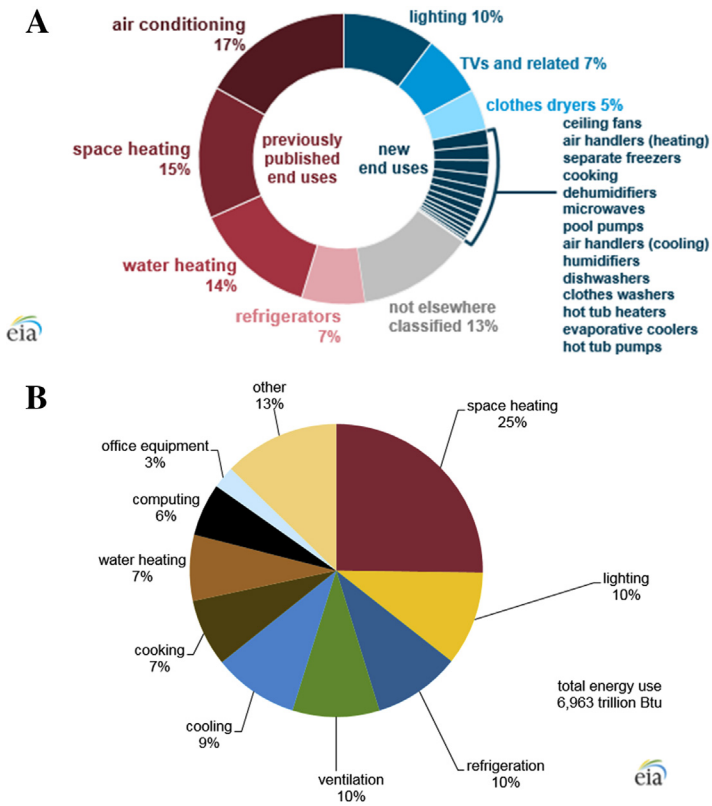

Figure 1.4
(A) Residential and (B) commercial building energy consumption [7,26].

2.2.1 Heat pumps

Heat pump technology (HPT) is highly effective in lowering the carbon footprint associated with the thermal load (heating and cooling). They are energy-efficient substitutes to fossil fuel–based heating systems, capable of achieving a coefficient of performance (COP) above three via the utilization of ambient heat energy. In simple terms, heat pumps extract heat from ambient air or renewable sources and transfer it to the refrigerant in a closed-loop system. Continuous evaporation and condensation of the refrigerant transfer the heat from the source to the sink. Although geothermal heat pumps are also gaining ground in some applications, air-source heat pumps are the most commonly used.

On the other hand, absorption heat pumps utilize heat energy to enable the heat pumping cycle, working on the same air source heat pump principles. Gas-fired sorption technologies offer lower COP than their electrical counterparts but offer resiliency at higher energy efficiency than conventional combustion-based heating systems. A generic representation of heat pump configuration is shown in Fig. 1.5.

Chua et al. recently reviewed advances in heat pumps where a comprehensive overview of the technology progress in the past decade was provided [27]. The influence of building heating equipment design configuration and the electric grid's efficiency factor was recently modeled and reported [28]. In this study, the authors showed the impact of the heat pump's COP and electrical grid's energy efficiency on primary energy consumed utility bill savings, and annual carbon dioxide emissions associated with supporting 12 kWh per day of thermal energy, representative of hot water demand in residential buildings. A detailed description of the modeling methodology utilized along with assumptions and calculations employed was provided. The present study extended this approach to evaluate the influence of COP and electric grid's carbon intensity at the higher thermal loads representative of space conditioning (heating or cooling) demand, in the

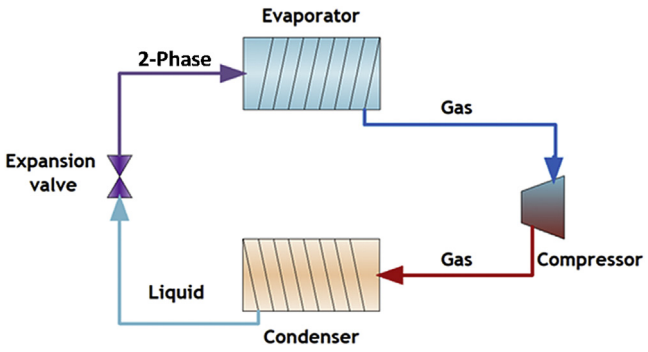

Figure 1.5
Schematic of a heat pump system.

range of 50–200 kWh per day. Fig. 1.6 displays the annual carbon dioxide emissions associated with heat pumps with COPs in the range of one–six serving a building with a thermal load of 100 kWh. A COP value of one represents an electrical system with joule heating (heating only), while higher COP values represent high efficient heat pump system. It can be noticed that heat pumps can lower the carbon footprint significantly at all carbon intensities of the grid. For instance, at a grid carbon intensity of 0.5 kg carbon dioxide (equivalent) per kWh of electricity produced, a heat pump system with a COP value of three produces 6 metric tons of carbon dioxide annually. This value further decreases with increased COP value and can significantly impact buildings served by a grid with higher carbon intensities.

Fig. 1.7 compares the annual carbon dioxide emissions using a heat pump system with a COP value of three in regions with different grid carbon intensities and thermal loads. The emissions trend demonstrates the positive influence of heat pump systems across all grid intensities. A COP value of three is possible across all climate zones in the continental United States. This figure provides a clear value proposition of the heat pump across regions with different carbon intensities.

Hybrid configurations consisting of heat pumps with solar thermal collectors are highly effective technologies in lowering the carbon footprint associated with water heating thermal load and providing resiliency and reliability. Several studies investigated the hybrid solar-heat pump configurations for performance, economic impact, and primary energy efficiency [29–31]. Poppi et al. for instance, concluded that residential-scale

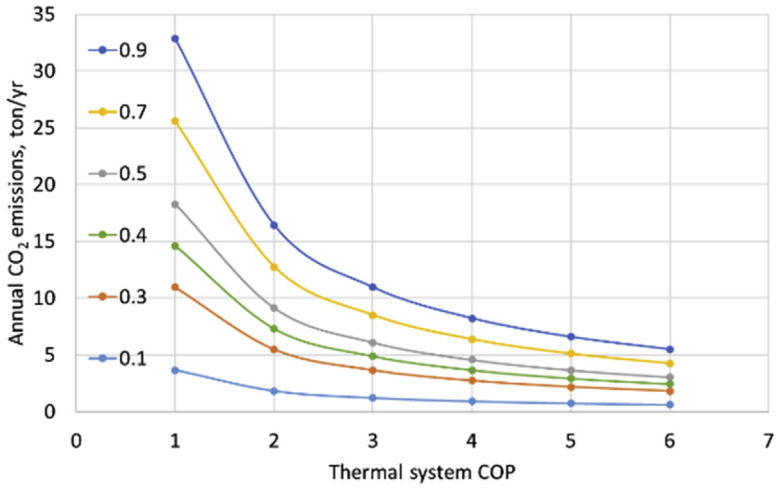

Figure 1.6

Impact of heat pump's coefficient of performance (COP) and electric grid's carbon intensity on annual carbon dioxide emissions in a building consuming 100 kWh/day of thermal energy.

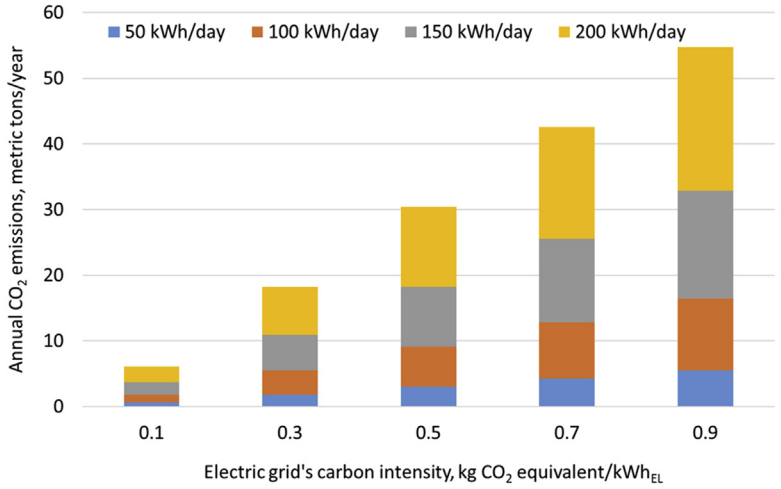

Figure 1.7
Impact of thermal load on annual carbon dioxide emissions and utility savings in a building served by a heat pump operating at an average coefficient of performance (COP) of 3.0.

photovoltaic-heat pump hybrid systems offer the highest COP of 3.75. In contrast, solar thermal-heat pump hybrid configurations offer the highest ROI at a lower COP of 2.9. Similarly, a more recent study investigated the influence of variance in renewable solar thermal energy input to the hybrid heat pump configuration on annual carbon footprint, primary energy, and utility costs [28]. For commercial buildings, heat pump-based system configurations primarily include single-split, multisplit, and variable refrigerant flow (VRF). The basic working principle remains the same as discussed above. However, the system configuration varies depending on the unique needs of commercial buildings where the thermal load varies zonally (mixed-use with simultaneous heating and cooling) irrespective of the season. Additionally, VRF systems can recover and transfer heat between different zones, further enhancing energy efficiency.

2.2.2 Combined heat and power/cogeneration

Balancing resiliency and decarbonization will be one of the most critical challenges of the ongoing energy transition. The electric grid's transformation with deep penetration of intermittent renewable power technologies requires the support of many ancillary technologies, including energy storage, on-site polygeneration, flexible grid-interactive technologies to address growing energy demand, and the evolution of new energy consumers (e.g., electric vehicles). Several researchers investigated the utilization of chemical energy to sustain current and future building energy requirements to simultaneously lower electrical demand and primary energy consumption while improving energy efficiency, grid resiliency, and carbon footprint of buildings [32–38]. The

sustainable, successful energy transition toward net-zero energy buildings is targeted by 2040 and beyond [39,40]. Significant reduction in existing building stock's energy consumption is the first step in this transition while simultaneously adopting clean, renewable technologies. In this regard, cogeneration and trigeneration systems capable of utilizing available fuels, including renewable fuels (biogas, Hydrogen, power-to-gas fuels, etc.), and energy-efficient on-site power and thermal sources have a significant role in fulfilling in certain regions and climate zones across the globe. The cogeneration approach consumes less energy and avoids transmission and distribution losses (of conventional separate heat and electric supply) while improving resiliency [33]. Hybridization of such technologies with on-site renewable energy and low carbon fuels (e.g., biogas, hydrogen) further decreases the effective carbon footprint of the building.

The biggest environmental impact of cogeneration in conjunction with PV is already presented in the above section. However, marginal emissions are inevitable in the near to midterm due to the rapid transition of the energy landscape toward clean, zero-carbon technologies. The growing population's energy needs to be combined with new energy consumers (transportation, electrical heating) will burden the existing grid infrastructure, leading to peaker power plants emitting higher emissions during the peak demand period. Cogeneration and energy storage technologies are hence necessary for addressing these marginal emissions. Fig. 1.8 demonstrates that on-site cogeneration can produce excess energy storage and utilization during the peak demand. One of the unique advantages of a cogeneration system is its ability to modulate the power output and thermal output depending on the energy needs of the building. The prime mover can modulate the power to heat ratio generation by changing critical operating parameters [33], for example, the fuel utilization value in a fuel cell-based cogeneration system. It has been shown that customized energy management strategies can be implemented to manage peak demand.

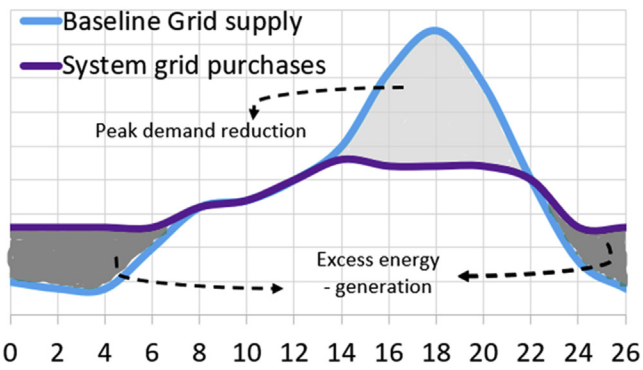

Figure 1.8
Peak demand management strategy to avoid marginal emissions burden (24h).

Sizing a cogeneration system to satisfy the energy needs is difficult since the daily and seasonal modulation of energy demand change substantially. Building loads are primarily driven by the climate zone where the ratio of electrical versus thermal demand can vary from 0.5 to 3.5 [41], due to a wide shift in the thermal demand from 30 Btu/ft^2 to 60 Btu/ft^2 [41]. Affordability and return on investment are other key factors and technical viability that can propel the deep penetration of such technologies. One way to address the economics is to optimize the size of the electrical output. The overall capital cost is minimized without generating excess thermal and electrical energy beyond what will be required in a complete 24-hour cycle. Given the significance of this aspect, the impact of the electrical power rating of the cogeneration system on carbon dioxide reduction in a residential building application is shown below, calculated according to the procedure utilized in a recent study [35]. The previous study established that excess thermal and electrical energy increases significantly as the cogeneration's power rating increases beyond 0.4 kW. Hence, the analysis was further extended to study the influence of this power rating at different electrical grid carbon intensities in the range of 0.2–0.63 kg of carbon dioxide per kilowatt-hour of electricity produced. The impact of a small-scale cogeneration system in a residential building with an average electrical energy demand of 15 kWh/day and 10 kWh/day of thermal energy while installed in locations with different electrical grid carbon intensities is shown in Fig. 1.9 (25% electrical efficiency). The gas-

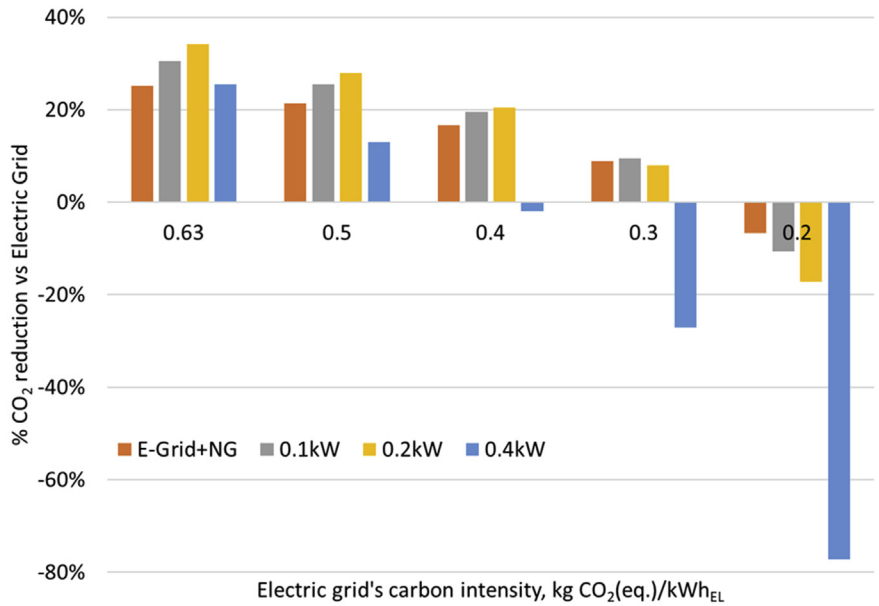

Figure 1.9

Influence of electric grid's carbon intensity on carbon dioxide reduction capability of a microcogeneration system (at different power ratings) in a residential building consuming 15 kWh/day of electrical energy and 10 kWh/day of thermal energy.

based systems offer carbon reduction until the grid's carbon intensity drops below 0.3 kg per kWh of electricity.

The analysis was further extended to investigate the performance of a 400 W cogeneration system operating at an electrical efficiency of 40% with an 85% heat recovery efficiency. Table 1.1 below shows the carbon reduction potential of such a system in comparison with (i) electric grid, (ii) electric grid plus natural gas for heat, and (iii) electric grid plus heat pump with a COP of 3. The carbon intensity of the electrical grid is crucial to realizing the benefits of each of these energy solutions. Regions with lower carbon intensities farewell with heat pump systems. In contrast, regions with moderate to high grid carbon intensities provide environmental benefits when utilizing a cogeneration system and improved resiliency.

2.2.3 Hybrid PV systems

Given the potential of heat pumps and cogeneration systems in improving energy efficiency, it is important to consider potential renewable energy sources to further lower the carbon footprint of buildings. Hybrid configurations consisting of heat pumps and cogeneration systems discussed in the above sections were analyzed to identify the impact of on-site photovoltaic (PV) on carbon dioxide reduction. Limited PV capacity was considered to lower the capital cost burden. Additionally, a 3 kWh capacity electrical energy storage was included in these configurations. These systems were analyzed according to the process outlined in previous work [33,35]. A schematic of the hybrid PV-energy storage-cogeneration configuration is shown in Fig. 1.10.

The impact of combining renewable PV with the cogeneration system was also analyzed by assuming the solar PV utilization. Case studies with heat pump (COP of 3) and cogeneration systems (electrical efficiency of 40% and heat recovery efficiency of 85%) were conducted in a building consuming 25 kWh/day of total energy, including 10 kWh/day of thermal energy [42]. PV power output was varied between 0 and 1 kW in cogeneration systems and fixed at 0.5 kW for the heat pump case. However, as noticed in Fig. 1.9, the carbon intensity

Table 1.1: Carbon dioxide emissions of different residential-scale energy solutions powered by an electric grid with different carbon intensities. 0.4 kW cogeneration system with 40% electrical efficiency and 85% heat recovery efficiency, natural gas fuel.

Grid C Intensity, kg/kWh	versus Grid	versus Grid + NG	versus Grid + HP (COP3)
200	−10%	−8%	−49%
300	18%	6%	−12%
400	32%	16%	7%
500	40%	22%	18%
630	47%	27%	28%

Source: Ref. [42].

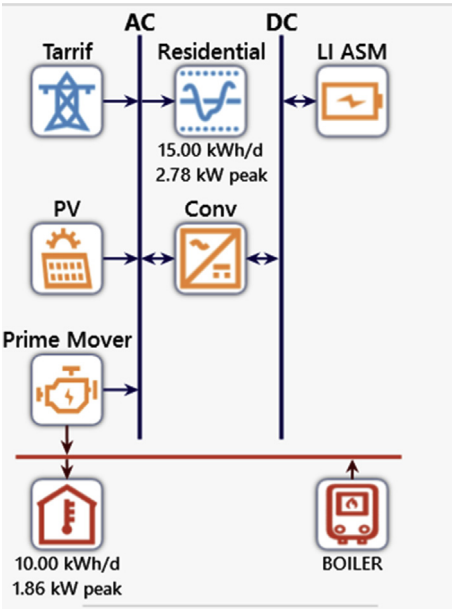

Figure 1.10
Hybrid energy configuration, taken with permission from HOMER Energy.

of the electrical grid is a key variable in such an analysis. Transformation of the electrical grid with higher contributions from renewable energy sources is continuously lowering the effective carbon intensity of the grid. Hence, the carbon footprint analysis was conducted with carbon dioxide intensities in the range of 0.1−0.63 kg CO_2 per kWh of electricity produced by the grid. Fig. 1.11 displays the annual carbon dioxide emissions generated from such a building while serving an electrical grid with different carbon dioxide intensities. The prime mover was allowed to modulate its power output by up to 50% due to PV generation. The solid lines displayed in the figure represent cogeneration configurations with different PV power ratings. As can be seen, the CO_2 emissions vary between 1.6 and 3.0 metric tons, gradually increasing with decreasing PV capacity and increasing grid carbo intensity. The dotted lines represent electrical/heat pump systems with and without 0.5 kW PV. It can be noticed that an all-electric grid-based system (COP one for heating) has a significantly higher carbon footprint than all the configurations analyzed.

Utilization of a heat pump with COP of 3 decreases the CO_2, varying between 1.3 and 4.2 metric tons per year, decreasing with a decrease in grid carbon intensity. Adding a 0.5 kW PV to this configuration further decreases the annual emissions to 3.8vmetric tons on the high end and 1.2 metric tons on the low end with a relatively clean grid (0.2 kg CO_2/kWh_{EL}). One key outcome from this figure is the cross-over point between electrical and

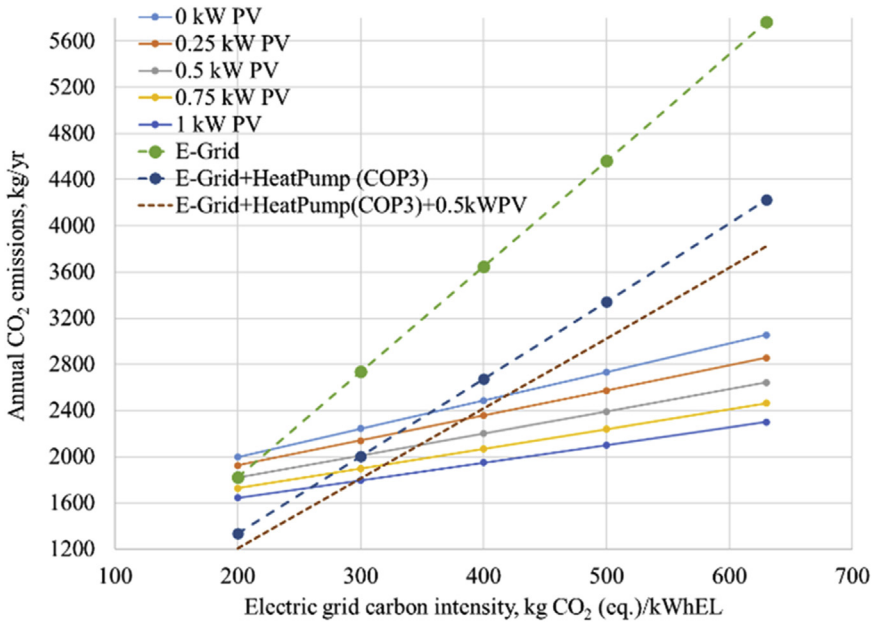

Figure 1.11

Comparison of cogeneration and heat pump systems with photovoltaic and 3 kW energy storage serving a building consuming an average of 15 kWh/day of electrical energy and 10 kWh of thermal energy. Cogeneration system's electrical efficiency of 40% and heat pump COP of 3. *Source: Ref. [42].*

gas-based cogeneration systems. Heat pump systems offer the best environmental benefits as the grid's carbon intensity decreases below 0.3 kg/kWh. For instance, the hybrid PV-heat pump system has higher CO_2 emissions compared to the hybrid cogeneration system up to carbon intensities of 0.35 kg/kWh, below which the heat pumps perform better.

2.2.4 Systems comparison

It is important to consider the energy supply and demand transformation when considering energy-efficient technological solutions for building applications. Some of the factors which are bound to evolve during this transition include: (i) increased electrical loads due to the adoption of new energy consumers within a building (e.g., electric vehicles, electrical heating), (ii) adoption of low carbon fuels (e.g., renewable hydrogen), (iii) seasonal, geographical, and time-of-day variance in electric grid's carbon intensity, and (iv) regional infrastructure limitations.

In light of these aspects, the analysis presented in the above three sub-sections was updated by considering the higher daily energy demand of 30 kWh of electrical energy and 60 kWh of thermal energy in a building. Primary energy providers considered were:

electrical, gas, and cogeneration systems. A heat pump with a COP value of 3, gas-based heating with both natural gas and 30% renewable hydrogen blended natural gas, and a cogeneration system with an electrical efficiency of 30%. The methodology utilized in the above sections [43] was also adopted in this analysis, while the electric grid's carbon intensity varied from 200 gCO_2/kWh_{EL} to 800 gCO_2/kWh_{EL}.

Fig. 1.12 displays the annual carbon dioxide emissions associated with each of these energy solutions. It can be noticed that the heat pump–based configuration is the most energy-efficient solution if the grid's carbon intensity is low, in line with conclusions drawn in Fig. 1.11. However, blending the natural gas with 30% renewable hydrogen (with zero carbon footprint) lowers the net annual carbon footprint significantly compared to heat pump-based solution at all grid carbon intensities examined, except at 0.2 kg/kWh. Similarly, gas-based 0.5 kW cogeneration systems perform better than heat pump systems at higher grid carbon intensities. A higher power rating of the cogeneration system at 1.5 kW, on the other hand, performs better at higher grid carbon intensities due to excess electricity production and export back to the grid at a relatively lower net carbon footprint of 0.183 kg/kWh (compared to the higher value of electrical grid).

Another important factor to consider in applying efficient building energy solutions is the true carbon footprint of the electrical grid rather than the average value. All the above analysis assumes an average carbon intensity rather than this marginal emissions factor, which can be higher due to inefficient and fossil fuel-based grid-scale power generation during the peak demand periods, both daily and seasonally. Hence the analysis was

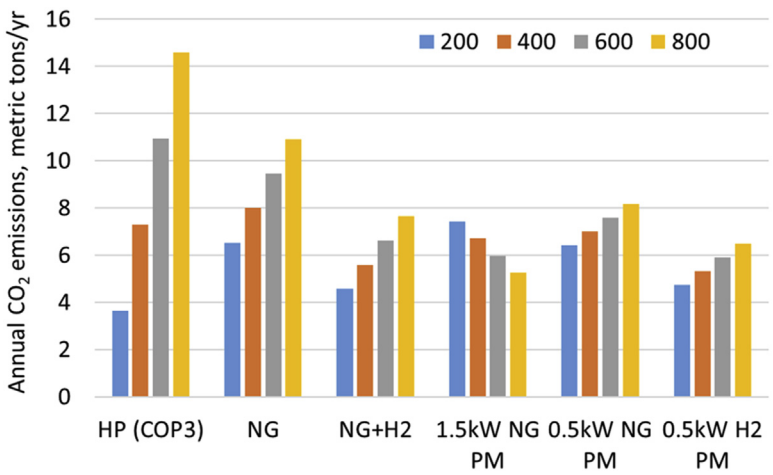

Figure 1.12
Impact of design configuration on annual carbon dioxide emissions in a building consuming 30 kWh of electrical energy and 60 kWh of thermal energy.

repeated by assuming 20% grid-scale power production at a carbon intensity of 0.6 kg/kWh and 80% production at 0.2 kg/kWh. This scale of marginal emissions is quite possible since the transition to lower carbon intensities and eventually net-zero is anticipated to happen gradually over the next 2 decades. As shown in Fig. 1.13, hydrogen-based systems (both combustion and cogeneration based) perform at the same level as a heat pump system even when considering the low grid carbon intensity of 0.2 kg/kWh. The trends and observations noticed so far with different energy-efficient systems are generally applicable for commercial-scale buildings. However, system configurations will have to be optimized to account for specific needs in commercial buildings where the heat to power ratio varies significantly based on building class and geographical region.

2.2.5 Energy storage

The significance of energy storage is rapidly growing due to the critical nature of renewable energy, energy security, energy resiliency, and energy efficiency. Integrating intermittent renewable energy sources with the grid (in both centralized and decentralized architectures) requires storing energy for usage during peak demand. Energy storage is needed for a renewable-based generation to stabilize production and ensure support during peak demand periods. A wide array of storage technologies is available for use in the entire energy supply chain, both at a grid and distributed scale. Broad technology categories include (1) Electrochemical-based batteries—with a range of chemistries

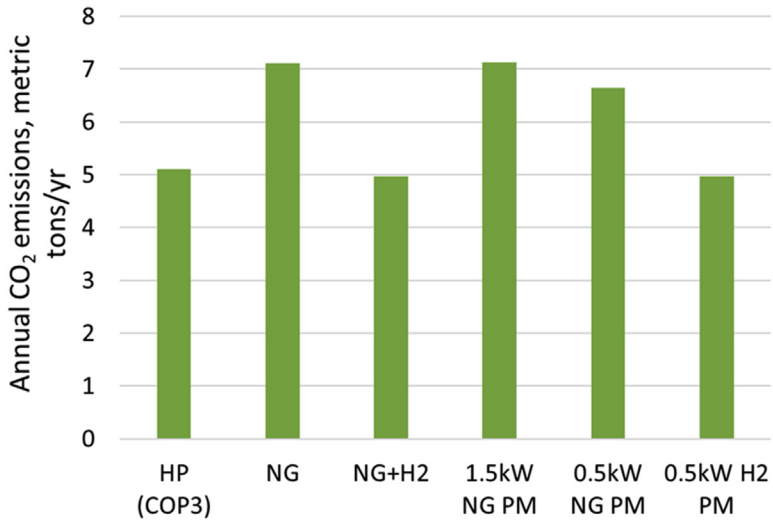

Figure 1.13
Annual carbon dioxide emissions from different building energy solutions corrected for higher marginal emissions by the electrical grid.

involving liquid and solid electrolytes, (2) mechanical—kinetic and gravitational energy storage via flywheels, compression-based systems, and hydraulic potential energy at large capacities, (3) Thermal—using the sensible, latent, and reaction heat associated with different materials and temperature ranges, (4) Hydrogen—via water electrolysis to fulfill energy demand associated with transportation, primary industrial energy, building energy via combustion, or electric power production via fuel cells, and (5) pumped hydro—proven utility-scale storage via large water reservoirs.

Residential scale application of different energy storage technologies was investigated for a tariff structure comprising time-of-use (TOU) demand charges [44]. The authors considered a full range of energy storage technologies analyzed at the utility-scale [45] and flow batteries, demonstrating economic viability with the compressed air energy storage (CAES) module. The scalability of CAES technology, combined with its long service life and relatively low cost, has been critical factors in the reemergence of CAES in commercial building applications. Key factors impacting the overall value proposition of energy storage for various residential and commercial-scale buildings were reported [46]. This study showed the significance of energy storage capacity on resilience, and the role incentive programs and tariff structures plays in the overall economics of the energy system configuration.

The transformation of the electricity sector must, and will, rely to a great degree on buildings to deliver demand flexibility. Energy storage solutions with high capacity are central to scaling demand flexibility in buildings and optimizing the transformation of our energy system. Electrochemical-based battery technologies for building applications are well established and commercially available for integration and deployment and renewable resources like photovoltaics. However, the need for thermal energy storage is growing rapidly due to the energy transition. Given the scale of the thermal load in a residential building Fig. 1.4 and its strain on the electric grid during peak demand, thermal energy storage technologies are necessary for sustainable energy infrastructure. Storing thermal energy utilization is a highly attractive option to reduce the grid peak demand burden for achieving an energy-efficient and resilient grid.

Thermal energy storage technology has recently gained renewed interest, with the majority of the focus on latent heat energy capture rather than thermochemical energy. To recognize this problem and its significance in the energy value chain, DOE's Research and Technology Investment Committee recently announced an Energy Storage Grand Challenge [47]. Several important metrics need consideration for a successful deployment of thermal energy storage systems associated with both materials and system, for instance, lifetime performance degradation. Table 1.2 outlines some of the critical considerations for thermal energy storage systems. PCMs have been extensively researched and applied [48,49].

Table 1.2: Critical thermal energy storage considerations.

Key metrics of performance	Example units	Material property	System/Reactor property
Storage energy density	MJ/kg, MJ/m^3	✓	✓
Transfer power density	MJ/kg.hr, MJ/L.hr	✓	✓
Operating temperature	°C	✓	✓
Cycle life	# Cycles	✓	✓
Self-discharge rate	%/hour		✓
Roundtrip efficiency	%		✓
Cost	$/MJ	✓	✓

2.2.6 Dehumidification

Humidity control in buildings has direct implications for energy efficiency, occupant comfort, process and product quality control, and indoor air quality. Relative humidity (RH) in a building environment plays a significant role in the health of occupants, building performance, and energy efficiency. The built environment can be severely impacted by high humidity. For instance, high humidity levels beyond 65% can lead to condensation, mold/mildew growth, corrosion, equipment damage, building fabric deterioration, loss of insulation properties, discoloration, and potentially slip hazards [50]. For instance, RH below 20% in a dry environment can create atmospheres suitable for viruses and infection [51]. The temperature, of course, plays a role in compounding the above issues further. Building energy performance, occupant comfort, and health impact are well documented in several research studies. Vellei et al. studied the influence of relative humidity on thermal comfort [52], where the authors analyzed and summarized a designer-friendly RH inclusive, adaptive model to extend the range of indoor conditions for low energy naturally conditioned buildings globally. The impact of RH and temperature on the structural properties of buildings was also reported [53].

In the Annual Energy Outlook 2021, the U.S. Energy Information Administration (EIA) estimated that in 2020, electricity usage for cooling the interior of buildings (space cooling) by the U.S. residential and commercial sectors was about 392 billion kilowatt-hours (kWh), which was equal to about 10% of total U.S. electricity consumption in 2020. The significance of relative humidity can be seen in the figure below. As shown, the amount of available energy to achieve the desired comfort temperature in a cooling system drops significantly as the relative humidity of the air being conditioned increases. The sensible load of the cooling system represents the energy to lower the temperature of the dry, warm air stream. In contrast, the latent load represents the energy necessary to condense the water vapor concentration by dropping the temperature below the dew point of the conditioned stream. As shown in Fig. 1.14, at an RH value of 80%, the latent load can be as high as 70%, significantly decreasing the capacity to achieve the desired setpoint.

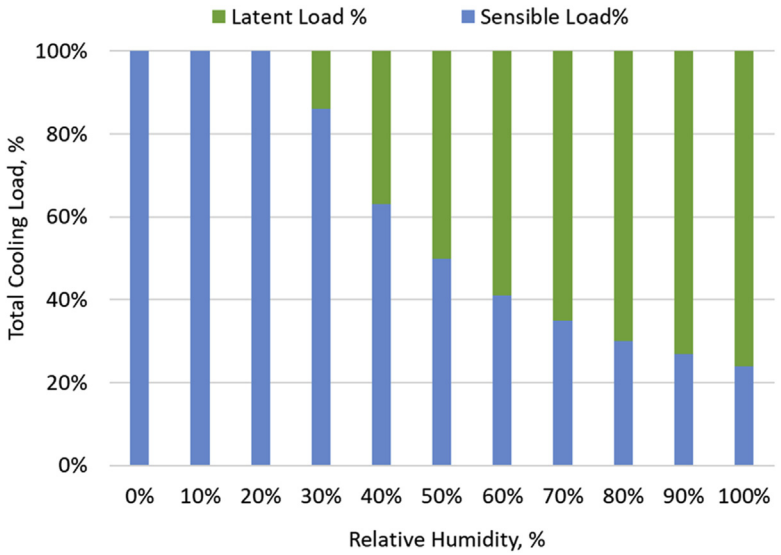

Figure 1.14
Energy split between sensible and latent cooling loads as a function of relative humidity.

In vapor compression systems (e.g., HVAC), the latent cooling load could be as high as 50% of the total cooling load, typically accomplished via cooling the process air below its dew point and then reheating to a comfortable temperature [54]. Hence, dehumidification of the air supply has significant potential in lowering the energy consumption during the space cooling process. Reducing latent cooling load via dehumidification before conditioning the temperature helps decrease the total energy consumption and enhance the cooling comfort temperature range. Dehumidification can certainly lower or eliminate this parasitic load if it can be efficiently accomplished via physisorption [55], chemisorption [56], or electrolytic processes [57].

2.2.7 Cooking

Global deployment of clean cooking technologies is necessary to address public health, local environment, and climate impact. Recent Energy Progress Report [58]identified approximately 2.8 billion people lacking clean, efficient, and affordable technologies. As a result, the economic burden is estimated to be USD 2.4 trillion each year [59], along with significant environmental impact [60]. The utilization of solid fuels emits significant GHG and health-related pollutants, leading to unsustainable deforestation. Clean and efficient stoves are known to decrease 1−2 metric tons of CO_2 per stove per year [61]. In the United States, ∼ 2.8% of the gas supply to residential buildings goes toward cooking applications [62], accounting for ∼ 33% of residential buildings leading to 930 trillion Btus (TBtu) of energy consumption. On the other hand, commercial buildings consume ∼800 TBtu [26] of gas with a combined CO_2 footprint of 97 million tons per year [63].

Primary energy sources for building cooking needs include natural gas, LPG, kerosene, coal, biomass, and electricity. Affordability, accessibility, and the electric grid's carbon intensity are key to adopting electricity as the primary energy for cooking applications. Traditional fuels (such as natural gas, LPG) and biomass have varying degrees of carbon footprint when consumed in a building. The stove's design has not changed much in the past century; however, the application of infrared gas stoves is 20%−30% efficient compared to flame-based burners [64]. Switching to renewable and sustainable fuels such as hydrogen and biogas, respectively, can further lower the carbon footprint associated with cooking. Utilization of waste heat from the cooking process in cogenerating electricity can further increase the overall efficiency; however, economic viability is still a major concern [65]. Reliance on renewable solar energy for cooking can be a much cleaner solution, although integration with thermal storage is necessary to increase reliability and resiliency [66].

2.2.8 Drying

Six percent of electricity and 2% of total gas consumed in the residential sector in the United States is used for drying clothes [67]. This leads to 40 million metric tons of CO_2 emissions from power consumption. Depending on the air circulation in the system, drying technologies could be divided into open and closed-loop drying. The major drying technologies are:

(1) Standard electric: The standard electric resistance dryer is an open-loop dryer. The ambient air from the surrounding is heated with the help of a resistance heating element before passing through the cloths in the dryer drum. The hot moist air exiting the drum is then vented outside the machine with the help of a blower. About 80% of the residential dryer in the United States use this technology [68]. The second open loop dryer is the standard gas dryer. It is similar to a standard electric resistance dryer with the only difference of heat source. In a standard gas dryer, the air is heated with the help of natural gas.
(2) Vapor compression heat pump: As the name signifies, the vapor compression HPT is based vapor compression system. It is a closed-loop system where the air is heated with the help of condenser heat for absorbing moisture from the wet cloths. The humid air is dehumidified by cooling it below the dew point with the help of an evaporator. It is the most energy-efficient dryer technology but takes longer than a standard electric dryer to dry cloths. This technology is extensively used in Australia and Europe [69].
(3) Condenser: A condenser drier is a closed-loop electric resistance dryer with an additional heat exchanger. In this technology, the inlet air to the dryer drum is heated with the help of an electric resistance heater. However, unlike a standard electric resistance dryer, the hot moist air exiting the drum is dehumidified by condensing moisture out with the help of a heat exchanger.

The drying, as mentioned above, technologies are commercialized and are well established. However, emerging technologies with good potential in further decreasing energy consumption include ultrasonic-based drying. In this new technology, piezoelectric transducers are used for drying laundry. In this system, the plurality of piezoelectric transducers is in electrical communication with a high-frequency piezoelectric oscillation generator. The piezoelectric oscillation generator resonant frequency source signal drives the plurality of piezoelectric transducers noncontinuously and helps remove water from wet clothes without adding heat. This is projected to be a more efficient technology with lesser drying time than traditional electric dryers [70].

Thermoelectric heat pump drying: This is another recently proposed drying technology. In this system, thermoelectric modules, a setup in which two semiconductors are coupled together to generate temperature gradient with the passage of DC, heat the air before passing it through the drum. The wet air exiting the drum is dehumidified by passing it over the cold side of thermoelectric modules. This technology could be designed as an open, as well as a closed-loop system [69].

2.2.9 Refrigeration

The refrigeration sector is one of the most energy-intensive sectors. It consumes over 17% of the total global electricity. Based upon the application, the refrigeration sector could be split into two major groups, commercial refrigeration and domestic refrigeration.

2.2.9.1 Commercial refrigeration

This sector consists of refrigeration systems for supermarkets, grocery stores, convenience stores, restaurants, cafeterias, and other food service establishments. There are over 38,000 supermarkets, 14,000 grocery stores, and 154,000 convenience stores [71,72]. The electrical energy consumption of the refrigeration systems in these retail food outlets is responsible for approximately 11% of the total electrical energy consumption in the US commercial building sector [73]. Commercial refrigeration accounts for 90 million units worldwide, including condensing units, stand-alone equipment, and centralized systems [74]. Commercial refrigeration systems store frozen foods, beverages, deli, and dairy products and produce at temperatures maintaining food safety and quality. The products are typically stored within two temperature ranges: the low-temperature (LT) range of −40 to −18°C (−40–0°F) and the medium-temperature (MT) range of −18 to 5°C (0–41°F) [75].

Commercial refrigeration encompasses various system configurations and sizes, ranging from small, self-contained refrigerated cabinets for foodservice applications to large, field-assembled centralized refrigeration systems for supermarket applications. A brief description of the different refrigeration systems is given below:

2.2.9.2 Direct expansion systems

In the centralized direct expansion (DX) refrigeration system, shown in Fig. 1.15, liquid refrigerant is distributed to all refrigerated display cabinets in the store's sales area. An expansion valve, either thermostatic or electronic, is used at each evaporator in the display cabinets to meter the flow of refrigerant through the evaporator. Refrigerant vapor from each evaporator then returns to the compressor rack to be compressed and condensed. The numerous display cabinets and walk-in coolers/freezers and the long lengths of refrigerant piping require a large refrigerant charge, typically on the order of 1000 kilograms or more.

The common refrigerant currently used in centralized DX systems is R-404A, with a relatively high GWP value of 3943 [27]. Older systems may use R-22 or R-507A. Newly developed lower GWP alternatives to R-404A are now commercially available, including the nonflammable and nontoxic blends R-448A and R-449A. These refrigerant blends are intended to be drop-in replacements for R-404A and have GWP values on the order of 1300. In addition, transcritical carbon dioxide (R-744) booster refrigeration systems are becoming increasingly more popular in commercial refrigeration applications due to the very low GWP of CO_2

2.2.9.2.1 Secondary loop systems Secondary loop systems consist of a primary refrigeration system used to chill a secondary heat transfer fluid. This heat transfer fluid, in turn, is circulated via a pump to the refrigerated display cabinets and walk-in coolers/freezers. Thus, the refrigerant and refrigerant piping is confined to the machine room, and the

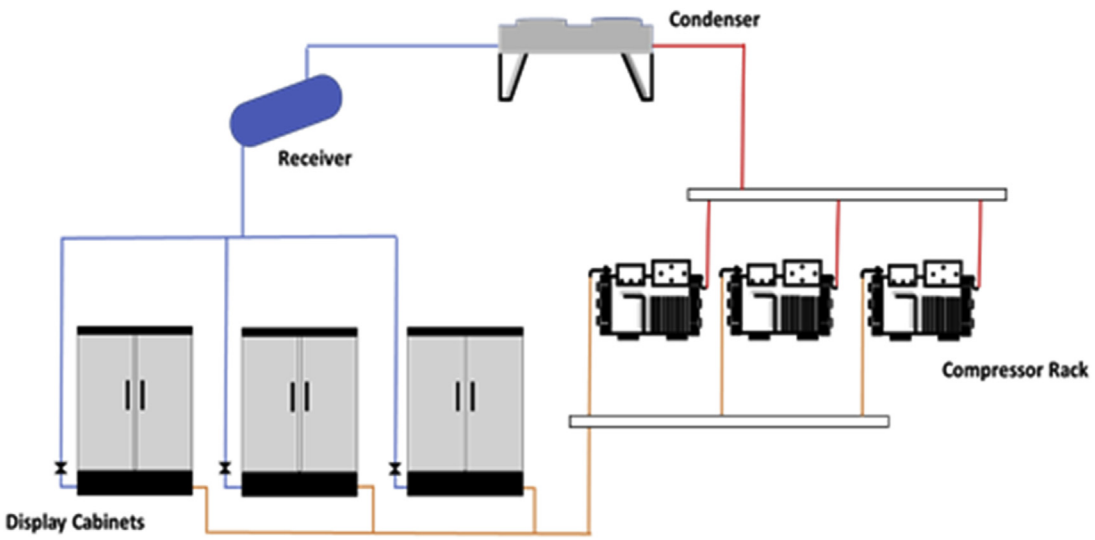

Figure 1.15
Centralized direct expansion system.

required refrigerant charge is much smaller than that of the centralized DX system. Lower cost nonmetallic piping can be used to distribute the secondary heat transfer fluid to the refrigerated fixtures. As with the centralized DX system, commonly used refrigerants in the primary refrigeration system include R-404A, R-22, and R-507A. The lower GWP alternatives, R-448A or R-449A, and ammonia (R-717) could also be used in the primary refrigeration system. The secondary heat transfer fluid is typically a single-phase fluid such as an inhibited propylene glycol mixture or a volatile fluid such as CO_2.

2.2.9.2.2 Distributed refrigeration systems In order to reduce the amount of refrigerant piping and refrigerant charge that is typically associated with centralized DX refrigeration systems, a distributed system can be used in which numerous parallel compressor cabinets are distributed around the store, located close to the refrigerated display cabinets and walk-in coolers/freezers [76]. Compared to the centralized DX system, the compressors and refrigerated fixtures are then close coupled via shorter liquid and suction refrigerant lines. The multiple compressor cabinets can be cooled with a closed-loop water system. Refrigerants used in distributed systems include those traditionally found in centralized DX systems, including R-404A, R-448A, R-449A, and flammable refrigerants such as prop iso-butane.

Stand-alone or self-contained commercial refrigeration cabinets: The systems include small vertical open, vertical reach-in, and tub-type cabinets as well as service deli cabinets, ice-cream cabinets, ice makers, and food and beverage vending machines. These systems have an integrated direct expansion refrigeration system that includes an evaporator located in an insulated compartment and a compressor and condenser. Since the refrigeration system in a stand-alone cabinet is sealed at the factory, no additional refrigerant piping is required. The energy absorbed from the stored product is typically rejected to the occupied retail space via an air-cooled condenser, thus adding to the HVAC load; however, in some instances, a fluid loop may be utilized to transport the condenser heat to an outdoor fluid cooler.

2.2.9.3 Domestic refrigeration

Domestic refrigeration includes residential refrigerators and freezers. It is estimated that over 1.5 billion domestic refrigeration units are functional worldwide, resulting in 4% of global electricity consumption. A traditional domestic refrigeration system is a direct expansion system with a requirement of about 0.5 pounds [77]. The traditional refrigerants used in domestic refrigerators include R-134a, R-404A, R−407C, and R−407F. However, due to low refrigerant charge need, low global warming potential flammable refrigerants, such as propane and isobutane, are permitted in domestic refrigerators.

2.2.10 Air-conditioning

The residential and commercial air-conditioning (AC) and heat pump (HP) sectors consist of small self-contained window air-conditioners for residential applications, small

packaged and split AC/HP units for residential and commercial use, and large packaged AC/HP units for commercial applications. Air conditioning constitutes 4% of building site energy consumption across the globe [10]. Over 600 million air conditioners and 160 million heat pumps operate in the residential, commercial, and industrial sectors [74]. As a result of rising global temperatures and the increasing purchasing power worldwide, the annual demand for air-conditioning is increasing at an average rate of 6%, resulting in 100 million AC units per year across the globe [78]. Air-conditioners and heat pumps can broadly be categorized based on the room's load, size, and design. Window and Small Packaged Units. Window and small packaged air-conditioners are single units with all 365 system components, including the evaporator, compressor, condenser, and expansion valve, packaged together. The room air is cooled by circulating the air around the evaporator and blowing it directly into the room with a blower fan. Window units are mounted through the building windows and commonly cool small domestic and office spaces. These units have a cooling capacity of 2−7 kW, and the typical refrigerants used in these systems include R-22, R-410A, and R-407C, with refrigerant charges ranging 370 from 0.2 to 2 kg [18]. Split Units. Split air-conditioners and heat pumps are two-unit systems, with an outdoor unit consisting of a compressor, condenser, and a fan, connected through refrigerant suction and liquid piping to an indoor unit, consisting of an evaporator and a fan. The remote location of the compressor, condenser, and condenser fan makes the indoor unit less noisy and more compact than a window air-conditioner or a small, packaged unit. However, the amount of refrigerant required increases in a split system compared to a window air-conditioner due to the extended refrigerant piping. Depending upon the application, the cooling capacity of split systems can vary from 2 to 12 kW for residential systems and from 10 to 40 kW for commercial systems. In addition, VRF systems for commercial cooling, which consist of several outdoor units connected to many indoor units, may range in capacity from 12 to 150 kW. The most widely used refrigerants in these systems include R-32, R-407C, and R-410A. Older systems may use R-22. Refrigerant charge size ranges from 0.5 kg for small split systems to 100 kg for the largest VRF systems [19,20]. Large Packaged Units. Large, packaged units for commercial heating and cooling applications, called rooftop units (RTUs), are combined direct expansion units that heat or cool ventilating air supplied to the space. Compared to VRF systems, packaged systems have a higher cooling capacity for the same amount of refrigerant charge. The cooling capacity ranges from 12 to 200 kW, and the refrigerant charge ranges from 5 to 100 kg.

2.2.11 Refrigerants

The selection of a good refrigerant, also known as working fluid, is critical for the proper functioning of a refrigeration or air-conditioning system. The first generation of vapor compression systems was manufactured in the latter half of the 19th century and the first quarter of the 20th century. These systems utilized refrigerants that were both readily

available and found to produce the desired cooling effect. The refrigerants of that time included chemicals such as sulfur dioxide (R-764), ethyl chloride (R-160), methyl chloride (R-40), and ammonia (R-717) among others. However, these refrigerants posed safety hazards due to their toxicity and/or flammability. Beginning in the 1930s, chlorofluorocarbon (CFC) and hydrochlorofluorocarbon (HCFC) refrigerants were developed as safe, nontoxic, and nonflammable alternatives for the early refrigerants [79]. In the ensuing years, the application of CFCs and HCFCs expanded to include uses such as aerosol propellants, cleaning agents for the microelectronics industry, and blowing agents for foam insulation. As a result, the quantities of CFCs and HCFCs produced increased rapidly during the 1950 and 1960s. Subsequently, in the 1970s, scientists discovered that CFC and HCFC refrigerants contributed to the ozone depletion in the Earth's stratosphere [80,81]. It was found that the stability of the CFC and HCFC molecules causes them to remain in the atmosphere for a significant time. Once these molecules migrate into the stratosphere, they dissociate and release chlorine atoms. The chlorine atoms then react with ozone (O_3) to produce diatomic oxygen (O_2), depleting the stratosphere's ozone. In 1987, an international treaty, the Montreal Protocol on Substances that Deplete the Ozone Layer, was ratified to protect the ozone layer by requiring the phase-out of numerous substances believed to be responsible for ozone depletion. The Protocol sets a mandatory timetable for the phase-out of ozone-depleting substances, including CFCs and HCFCs. In the United States, production and import of CFCs were banned completely in 1996, HCFCs are being phased down, with a complete phase-out set for 2030 [75]. Following the proposed phase-out of ozone-depleting refrigerants per the Montreal Protocol, hydrofluorocarbon (HFC) refrigerants were introduced, which are in common use today. HFC refrigerants contain no chlorine atoms, and thus, they have no ozone-depleting potential (ODP). However, HFC refrigerants typically have a high global warming potential, and thus, release of HFCs into the atmosphere represents a notable source of greenhouse gases. Since HFCs have a high GWP, there is strong interest to minimize the introduction and emissions of HFCs. Alternative refrigerants with lower or near zero GWP are available, including hydrocarbons such as propane (R-290) and isobutane (R-600a) [82], ammonia (R-717), carbon dioxide (R-744) [83], and new hydro fluoro-olefin (HFO) refrigerants such as R-1234yf and R-1234ze(E) and their blends [84].

2.2.12 Hydrogen based building technologies

Renewable hydrogen is considered a major part of the future energy infrastructure, playing the role of long-term renewable energy storage medium while fulfilling various energy needs, including buildings. Department of Energy (DOE) recently launched HyBlend [85], a research effort focused on enabling hydrogen blending in pipelines by addressing materials and economic challenges. Six national laboratories and 20 partner organizations are working toward achieving hydrogen blends for different end-use applications, including buildings.

The advantage of hydrogen as a renewable energy storage medium is well understood [86,87]. Hydrogen's usage in residential and commercial buildings using existing gas infrastructure is a highly effective approach in addressing growing energy demand at a reduced carbon footprint by utilizing the legacy gas infrastructure as a bridging resource to offset carbon footprint, while the grid transitions toward 100% renewables. Hydrogen blended natural gas (30%) utilization in buildings can lower the associated CO_2 emissions (due to renewable hydrogen with low/zero carbon footprint) by 150 MT annually (the year 2030 calculation; per DOE's Scout baseline energy calculator [63]). The impact of energy consumption on the environment is leading to a significant shift in the way the energy needs of an average consumer are going to be met. Thermal needs of a residence today include hot water and space heating, ranging from ~5 kWh/day to 400 kWh/day depending on the season, climate zone, and residential building size [https://openei.org]. Regions with high electric grid carbon intensities can lower their carbon footprint by adopting hydrogen-based fuels, as shown in Sections 2.2.2–2.2.4. For instance, approximately 50% of the hot water needs in the USA (approximately 15%–20% of residential energy consumption) are met via gas as the primary energy source [88]. In meeting the domestic hot water demand, gas utilization is expected to increase despite the push toward low/zero-carbon technologies. U.S. Energy information administration's (EIA) Annual Energy Outlook 2021 projects are growing oil, natural gas, and renewables production [89].

3. Summary

The role of different technologies in addressing the carbon footprint of buildings is presented in this chapter. Buildings consume one-third of total final energy and are responsible for almost 40% of carbon dioxide emissions. In order to achieve net-zero carbon goals, building technologies must utilize available energy efficiently and reliably. This chapter gives an overview of different enabling technologies, including energy-efficient heat pumps, hybrid cogeneration, novel building envelope materials, emerging technological solutions for energy storage, integration, dispatch, and bridging solutions for the successful and sustainable energy transition. The impact of primary energy consumers in buildings, including heating, cooling, and electricity, is discussed along with design and integration strategies associated with building materials, equipment, and energy management.

Acknowledgments

This work was supported by the DOE Office of Energy Efficiency and Renewable Energy (EERE), Building Technologies Office, and used resources at the Building Technologies Research and Integration Center, a DOE-EERE User Facility at Oak Ridge National Laboratory.

Author contribution

Praveen Cheekatamarla: Conceptualization, methodology, analysis, visualization, writing—original draft preparation, Introduction, Sections 1, 2, 2.2.1–2.2.7, 2.2.12. **Som Shrestha:** writing—Section 2.2.1, Review, analysis. **Vishaldeep Sharma:** review, analysis, writing—Sections 2.2.8–2.2.11.
The authors further acknowledges that there is no financial relationship with the editors or publisher and have contributed original work in this chapter, other than what was acknowledged or appropriately cited with copyright permission.

References

[1] EIA, EIA Projects a Nearly 50% Increase in World Energy Use by 2050, Led by Growth in Renewables, 2021. Available from: https://www.eia.gov/todayinenergy/detail.php?id=49876.
[2] Our World in Data–Primary Energy Consumption by World Region, 2021. Available from: https://ourworldindata.org/grapher/primary-energy-consumption-by-region.
[3] IEA, World Total Final Consumption (TFC), 2021. Available from: https://www.iea.org/reports/key-world-energy-statistics-2020/final-consumption.
[4] Programme, U.E. Building Sector Emissions Hit a Record High, but Low-Carbon Pandemic Recovery Can Help Transform Sector – UN Report, 2021. Available from: https://www.unep.org/news-and-stories/press-release/building-sector-emissions-hit-record-high-low-carbon-pandemic.
[5] EIA, Consumption & Efficiency, 2021. Available from: https://www.eia.gov/consumption/.
[6] EIA, EIA Updates its U.S. Energy Consumption by Source and Sector Chart, 2020. Available from: https://www.eia.gov/todayinenergy/detail.php?id=41093.
[7] EIA, Residential Energy Consumption Survey (RECS), 2020. Available from: https://www.eia.gov/consumption/residential/.
[8] Commercial Buildings Energy Consumption Survey (CBECS), 2020. Available from: https://www.eia.gov/consumption/commercial/.
[9] Energy. Gov. U.S. Households' Heating Equipment Choices Are Diverse and Vary by Climate Region, 2020. Available from: https://www.eia.gov/todayinenergy/detail.php?id=30672https://www.energy.gov/energysaver/heat-and-cool/home-heating-systems.
[10] Agency, I.E., the Future of Cooling, 2021. Available from: https://www.iea.org/reports/the-future-of-cooling.
[11] C2ES, Decarbonizing U.S. Buildings, 2021. Available from: https://www.c2es.org/document/decarbonizing-u-s-buildings/.
[12] IEA, Buildings, A Source of Enormous Untapped Efficiency Potential, 2021. Available from: https://www.iea.org/topics/buildings.
[13] EERE. Windows and Building Envelope R&D: Roadmap for Emerging Technologies, 2014. Available from: https://www.energy.gov/sites/prod/files/2014/02/f8/BTO_windows_and_envelope_report_3.pdf.
[14] EERE. Building Energy Codes Program: Residential Provisions of the 2018 IECC, 2018. Available from: https://www.energycodes.gov/technical-assistance/training/courses/residential-provisions-2018-iecc.
[15] ICC. ICC Digital Codes, International Energy Conservation Code (IECC). 2018, 2018. Available from: https://codes.iccsafe.org/content/iecc2018.
[16] EERE. Building Energy Codes Program: Commercial Scope and Envelope Requirements, 2018. Available from: https://www.energycodes.gov/sites/default/files/2019-09/2018_IECC_commercial_requirements_envelope.pdf.
[17] ICC. ICC Digital Codes–Chapter 4: Commercial Energy Efficiency, 2018. Available from: https://codes.iccsafe.org/content/iecc2018/chapter-4-ce-commercial-energy-efficiency.

[18] B.P. Jelle, et al., Thermal Superinsulation for Building Applications-From Concepts to Experimental Investigations, 2014.
[19] Y. Wang, J. Yang, Z. Chen, Insulation performance analysis of novel high-temperature vacuum insulated panels with 2D and 2.5 D braided structures, Mater. Res. Express 7 (1) (2020) 015616.
[20] U. Berardi, Aerogel-enhanced insulation for building applications, in: Nanotechnology in Eco-Efficient Construction, Elsevier, 2019, pp. 395−416.
[21] L. Melita, C. Croitoru, Aerogel, a high-performance material for thermal insulation-A brief overview of the building applications, in: E3S Web of Conferences, EDP Sciences, 2019.
[22] F. Antretter, et al., Assessing the Potential of Active Insulation Systems to Reduce Energy Consumption and Enhance Electrical Grid Services, Oak Ridge National Lab (ORNL), Oak Ridge, TN (United States), 2019.
[23] K. Biswas, et al., Thermally anisotropic composites for improving the energy efficiency of building envelopes, Energies 12 (19) (2019) 3783.
[24] C. Harris, et al., Grid-interactive Efficient Buildings Technical Report Series: Windows and Opaque Envelope, National Renewable Energy Lab (NREL), Golden, CO (United States), 2019.
[25] S. Mumme, et al., Smart and Efficient Building Envelopes: Thermal Switches and Thermal Storage for Energy Savings and Load Flexibility, Oak Ridge National Lab (ORNL), Oak Ridge, TN (United States), 2020.
[26] EIA, 2012 Commercial Buildings Energy Consumption Survey: Energy Usage Summary, 2020. Available from: https://www.eia.gov/consumption/commercial/reports/2012/energyusage/.
[27] K.J. Chua, S.K. Chou, W. Yang, Advances in heat pump systems: a review, Appl. Energy 87 (12) (2010) 3611−3624.
[28] P. Cheekatamarla, V. Sharma, B. Shen, Sustainable energy solutions for thermal load in buildings—role of heat pumps, solar thermal, and hydrogen-based cogeneration systems, J. Eng. Sustain. Bldgs. Cities 2 (3) (2021) 034501.
[29] H. Chen, S.B. Riffat, Y. Fu, Experimental study on a hybrid photovoltaic/heat pump system, Appl. Therm. Eng. 31 (17−18) (2011) 4132−4138.
[30] S. Ran, et al., A solar-air hybrid source heat pump for space heating and domestic hot water, Sol. Energy 199 (2020) 347−359.
[31] S. Poppi, et al., Techno-economic review of solar heat pump systems for residential heating applications, Renew. Sustain. Energy Rev. 81 (2018) 22−32.
[32] S. Martinez, et al., Micro-combined heat and power systems (micro-CHP) based on renewable energy sources, Energy Convers. Manag. 154 (2017) 262−285.
[33] P. Cheekatamarla, Performance analysis of hybrid power configurations: impact on primary energy intensity, carbon dioxide emissions, and life cycle costs, Int. J. Hydrog. Energy 45 (58) (2020) 34089−34098.
[34] A. Arsalis, A comprehensive review of fuel cell-based micro-combined-heat-and-power systems, Renew. Sustain. Energy Rev. 105 (2019) 391−414.
[35] P.K. Cheekatamarla, Decarbonization of residential building energy supply: impact of cogeneration system performance on energy, environment, and economics, Energies 14 (9) (2021) 2538.
[36] P. Cheekatamarla, et al., Reliable, Energy Efficient, Cost-Effective Power and Co-generation Technologies, Techno-Economic-Environmental Analysis, 2021.
[37] Y. Budak, Y. Devrim, Investigation of micro-combined heat and power application of PEM fuel cell systems, Energy Convers. Manag. 160 (2018) 486−494.
[38] P. Cheekatamarla, et al., Energy Efficient, Cost-Effective Power and Co-generation Technologies: Techno-Environmental Analysis, Oak Ridge National Lab (ORNL), Oak Ridge, TN (United States), 2021.
[39] Energy.Gov, Net Zero Buildings Week: Commercial Buildings, 2021 [cited 2021 June 2021]; Available from: Net Zero Buildings Week: Commercial Buildings.
[40] Agency, I.E., Pathway to Critical and Formidable Goal of Net-Zero Emissions by 2050 Is Narrow but Brings Huge Benefits, According to IEA Special Report, IEA, Editor, 2021.

[41] F. Calise, et al., Thermo-economic Analysis of hybrid solar-geothermal polygeneration plants in different configurations, Energies 13 (9) (2020) 2391.
[42] P. Cheekatamarla, Role of on-site generation in carbon emissions and utility bill savings under different electric grid scenarios, Energies 15 (2022) 3477, https://doi.org/10.3390/en15103477.
[43] P. Cheekatamarla, A. Abu-Heiba, A comprehensive review and qualitative analysis of micro-combined heat and power modeling approaches, Energies 13 (14) (2020) 3581.
[44] M. Zheng, C.J. Meinrenken, K.S. Lackner, Smart households: dispatch strategies and economic analysis of distributed energy storage for residential peak shaving, Appl. Energy 147 (2015) 246–257.
[45] S.R. Salkuti, Energy storage technologies for smart grid: a comprehensive review, Majlesi J. Electr. Eng. 14 (1) (2020) 39–48.
[46] A.-H. Ahmad, K. Saiid, P. Cheekatamarla, A. Momen, Novel GLIDES Technology for Grid Resiliency: Final Report, U.S. Department of Energy's Office of Electricity Office of Science and Technology. Information, Editor, OSTI.GOV, 2020.
[47] Energy.Gov, Energy Storage Grand Challenge, 2020. Available from: https://www.energy.gov/energy-storage-grand-challenge/energy-storage-grand-challenge.
[48] A. Mallow, S. Graham, O. Abdelaziz, Design of Compressed Graphite/PCM Thermal Batteries, Oak Ridge National Lab (ORNL), Oak Ridge, TN (United States), 2016.
[49] A. Sharma, et al., Review on thermal energy storage with phase change materials and applications, Renew. Sustain. Energy Rev. 13 (2) (2009) 318–345.
[50] U.S. Environmental Protection Agency. Why and where Mold Grows. Mold Course (Chapter 2) 2020 [cited 2021 March 31]; Available from: Mold Course (Chapter 2).
[51] W. Yang, L.C. Marr, Mechanisms by which ambient humidity may affect viruses in aerosols, Appl. Environ. Microbiol. 78 (19) (2012) 6781–6788.
[52] M. Vellei, et al., The influence of relative humidity on adaptive thermal comfort, Build. Environ. 124 (2017) 171–185.
[53] G. Zonno, et al., Analysis of the long and short-term effects of temperature and humidity on the structural properties of adobe buildings using continuous monitoring, Eng. Struct. 196 (2019) 109299.
[54] K. Nawaz, K. Gluesenkamp, Separate Sensible and Latent Cooling Systems: A Critical Review of the State-of-the-art and Future Prospects, 2018.
[55] W. Wang, et al., An overview of adsorbents in the rotary desiccant dehumidifier for air dehumidification, Dry. Technol. 31 (12) (2013) 1334–1345.
[56] M. Sultan, et al., An overview of solid desiccant dehumidification and air conditioning systems, Renew. Sustain. Energy Rev. 46 (2015) 16–29.
[57] H. Liu, H. Yang, R. Qi, A review of electrically driven dehumidification technology for air-conditioning systems, Appl. Energy 279 (2020) 115863.
[58] Energy, AAC. The Energy Progress Report. Tracking SDG 7 2021; Available from: https://trackingsdg7.esmap.org/.
[59] T.W. Bank, Nearly Half the World's Population Still Lacks Access to Modern Energy Cooking Services, 2020.
[60] H.R. Ayub, et al., A review of cooking systems and energy efficiencies, Am. J. Energy Eng. 9 (1) (2021) 1–7.
[61] USAID Clean and Efficient Cooking Technologies and Fuels. Climate Impact 2021. Available from: https://www.usaid.gov/sites/default/files/documents/1865/cookstoves-toolkit-2017-mod3-climate-impacts.pdf.
[62] Agency, U.S.E.I, Residential Energy Consumption Survey (RECS), 2015. Available from: https://www.eia.gov/consumption/residential/data/2015/.
[63] Office of Energy Efficiency & Renewable Energy, Baseline Energy Calculator, 2020. Available from: https://scout.energy.gov/baseline-energy-calculator.html.
[64] K. Krishnamurthy, et al., Infrared heating in food processing: an overview, Compr. Rev. Food Sci. Food Saf. 7 (1) (2008) 2–13.

[65] H. Gao, et al., Development of stove-powered thermoelectric generators: a review, Appl. Therm. Eng. 96 (2016) 297−310.
[66] M. Aramesh, et al., A review of recent advances in solar cooking technology, Renew. Energy 140 (2019) 419−435.
[67] NRDC, Residential Clothes Dryers: A Closer Look at Energy Efficiency Test Procedures and Savings Opportunities, 2018. Available from: https://www.nrdc.org/sites/default/files/ene_14060901a.pdf.
[68] B. Shen, et al., Heat Pump Clothes Dryer Model Development, 2016.
[69] D. Goodman, V.K. Patel, K.R. Gluesenkamp, Thermoelectric Heat Pump Clothes Dryer Design Optimization, Oak Ridge National Lab. (ORNL), Oak Ridge, TN, United States, 2017.
[70] A.M. Momen, K.R. Gluesenkamp, E.A. Vineyard, R.A. Kisner, Dryer Using High-Frequency Vibration, 2019.
[71] FMI, Supermarket Facts, 2021. Available from: www.fmi.org/research-resources/supermarket-facts.
[72] NACS, U.S. Convenience Store Count, 2021. Available from: https://www.convenience.org/Research/FactSheets/IndustryStoreCount.
[73] Research, I.F.E, EIA Releases Annual Energy Outlook 2021, 2021. Available from: https://www.instituteforenergyresearch.org/fossil-fuels/eia-releases-annual-energy-outlook-2021/.
[74] IIFIIR, The Role of Refrigeration in the Global Economy (2015), 29th Note on Refrigeration Technologies, 2016. Available from: https://iifir.org/en/fridoc/the-role-of-refrigeration-in-the-global-economy-2015-138763.
[75] Fundamentals, A.H., American Society of Heating, Refrigerating and Air-Conditioning Engineers, 2005.
[76] EPA, Refrigeration Technologies, 2020. Available from: https://www.epa.gov/greenchill/refrigeration-technologies#distro.
[77] EPA, Transitioning To Low-GWP Alternatives in Domestic Refrigeration, 2020. Available from: https://www.epa.gov/sites/default/files/2016-12/documents/transitioning_to_low-gwp_alternatives_in_domestic_refrigeration.pdf.
[78] Energy.Gov, The Future of Air Conditioning for Buildings, 2016. Available from: https://www.energy.gov/sites/prod/files/2016/07/f33/The%20Future%20of%20AC%20Report%20-%20Full%20Report_0.pdf.
[79] T. Midgley Jr., A.L. Henne, Organic fluorides as Refrigerants1, Ind. Eng. Chem. 22 (5) (1930) 542−545.
[80] M.J. Molina, F. Rowland, Predicted present stratospheric abundances of chlorine species from photodissociation of carbon tetrachloride, Geophys. Res. Lett. 1 (7) (1974) 309−312.
[81] M.J. Molina, F.S. Rowland, Stratospheric sink for chlorofluoromethanes: chlorine atom-catalyzed destruction of ozone, Nature 249 (5460) (1974) 810−812.
[82] K. Nawaz, et al., R290 (propane) and R600a (isobutane) as natural refrigerants for residential heat pump water heaters, Appl. Therm. Eng. 127 (2017) 870−883.
[83] K. Nawaz, et al., Performance optimization of CO2 heat pump water heater, Int. J. Refrig. 85 (2018) 213−228.
[84] Programme, U.N.E, Alternatives to HCFCs in the Refrigeration and Air Conditioning Sector, 2020. Available from: http://www.ammonia21.com/files/pdf_679.pdf.
[85] DOE, DOE Hydrogen and Fuel Cell Technologies Office and Global Perspectives, 2020. Available from: https://www.energy.gov/sites/default/files/2021/01/f82/hfto-satyapal-PIME-dec11.pdf.
[86] B. Widera, Renewable hydrogen implementations for combined energy storage, transportation, and stationary applications, Therm. Sci. Eng. Prog. 16 (2020) 100460.
[87] S. Kharel, B. Shabani, Hydrogen as a long-term, large-scale energy storage solution to support renewables, Energies 11 (10) (2018) 2825.
[88] Research, G. Water Heater Market Size, Share & Trends Analysis Report by Product (Electric, Solar, Gas), by Technology, by Capacity, by Application (Residential, Commercial), by Region, and Segment Forecasts, 2020−2027, 2020. Available from: https://www.grandviewresearch.com/industry-analysis/water-heaters-market.
[89] Research, IOE, EIA Releases Annual Energy Outlook 2021, 2021. Available from: https://www.instituteforenergyresearch.org/fossil-fuels/eia-releases-annual-energy-outlook-2021/.

CHAPTER 2

Synthesis of nanomaterials using top-down methods

Fan Chen[1], **Tian-Hao Yan**[1], **Sajid Bashir**[2], **Jingbo Louise Liu**[2]
[1]*The Department of Chemistry, Texas A&M University, College Station, TX, United States;* [2]*The Department of Chemistry, Texas A&M University, Kingsville, TX, United States*

Abstract

Nanomaterial synthesis procedures that are scalable, cheap, and green are not common. Several synthesis strategies are discussed with a focus on top-down syntheses. Here, ball milling for nanoalloys, composites, grains, and semicrystalline materials is discussed. The mechanical alloying processes are used to generate amorphous and crystalline alloys as well as metal and nonmetal nanocomposites by doping, metal insertion, and co-alloying are also discussed. The nonequilibrium processes whereby alloying is achieved are discussed in the thermodynamics of mixing different elemental powders, milling types, and inert atmosphere to generate stable mixed powder materials with the same composition stoichiometrically required. Under higher energies, deformation and fracture of the materials occur, and these deformations define particle shape and porosity. Cold-welding approaches also lead to material fracture and smaller powders for different alloying particles in grain-refined matrices. The application of mechanical milling of different alumina materials can lead to the synthesis of a wide variety of materials for specific applications, which can be further modified using postannealing or activation processes to generate activated materials. This chapter reviews the basic concepts, energetics, and considerations of synthesis of different nanomaterials for catalysis and energy applications.

Keywords
Fabrication
Synthesis
Top-down method

1. Introduction

Top-down approaches divide bulk materials into smaller particles, usually nanoparticles (NPs), by applying external force. The concept of the bottom-up method can be expressed in Fig. 2.1. The top-down process normally involves grinding, including both wet and dry systems. Typical examples for dry systems are ball milling, jet milling, and roller milling. Along with the breakdown process, condensation of particles also happens, which hinders the particles from being less than 3 mm. Wet systems include centrifugal fluid milling,

Advanced Nanomaterials and Their Applications in Renewable Energy. https://doi.org/10.1016/B978-0-323-99877-2.00007-2

Figure 2.1
Scheme of the top-down method to synthesize nanomaterials.

vibratory ball milling, flow conduit bead milling, and wet jet milling. Wet condition is usually considered an advantageous method compared with the dry condition since it hinders the agglomeration of particles and can achieve desirable sizes. Several classic bottom-up methods will be briefly introduced in this chapter, including ball mailing, etching, machining, sputtering, arc discharge method, and electrospinning.

2. Ball milling

Ball milling is an operation to grind materials into extremely fine powders, even in the nanoscale (Fig. 2.2) [1]. High-energy ball milling, also known as mechanical attrition or mechanical alloying, is an important industrial nanofabrication process. Ball milling mechanically ground coarse-grained powder materials (such as metals, ceramics, and

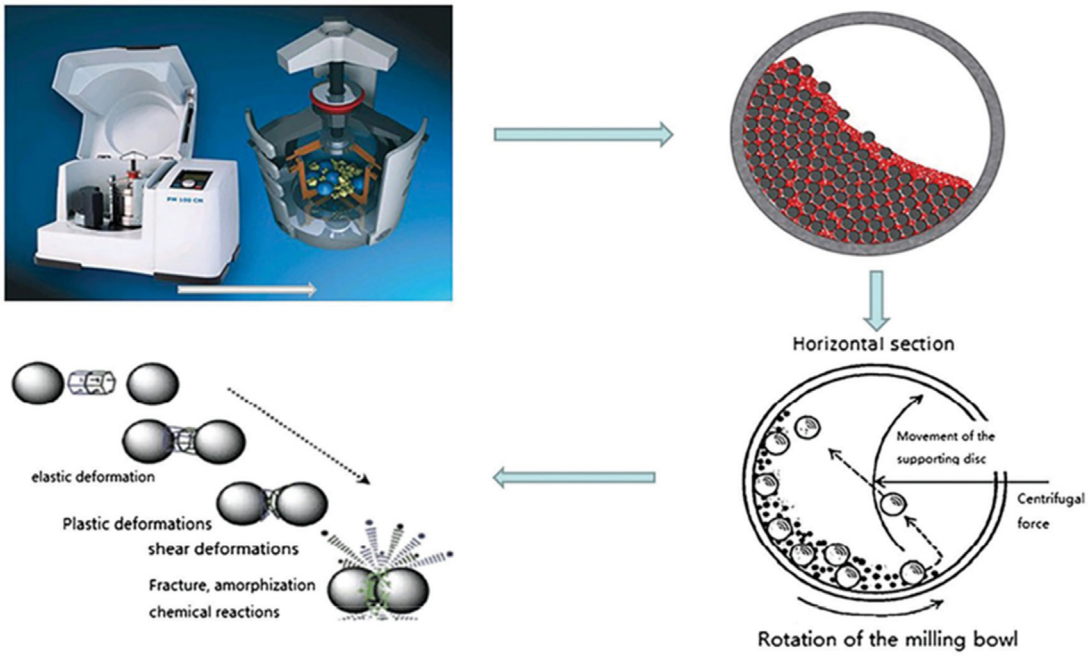

Figure 2.2
The principle of the ball milling method.

polymers) into fine powders. The entire process occurs in rotating drums composed of hard steel or tungsten carbide (WC) balls. Like the introduction of Ar gas, controlled atmospheric conditions can be applied to prevent unexpected reactions. Grain size can be reduced via the formation and organization of grain boundaries within particles. Ball milling can mechanically alloy different components together. It achieves nanosized dispersion of one phase into another, though the so-produced microstructures and phases can be thermodynamically metastable and transient. The milling technique can be operated on a large scale so that it has been widely utilized in mineral, ceramic processing, and powder metallurgy industries. Their objectives of milling include particle size reduction, mixing or blending of materials, and particle shape adjustment.

Tumble ball milling is a typical method used for the prementioned purposes—a cylindrical container rotated along its axis, and balls in the container impact the powders. The balls may roll down the surface of the chamber in a series of parallel layers, or they may fall freely and impact the powder and balls beneath them [2,3]. Milling occurs by an agitator's stirring action with a vertical rotating shaft with horizontal arms. This motion can introduce a differential movement between the balls and the powder. Therefore, a high degree of surface contact can be achieved in tumbler ball mills. The rotation speed of the tumbler mill cylinder and the attritor shaft are key factors determining the kinetic energy imparted to the milling media [3]. Tumbler mills can provide high energy if a large shaft diameter is used, and milling operates at critical speed for a short period to "pin" balls to the chamber wall. Another milling method, attrition mills, has been replaced by the large tumbler ball milling to achieve large-scale production of commercial alloys. Another type of mill, the vibratory tube mill, has been used for pilot-size production [4]. The motion of the balls and particles in a vibratory mill was complicated. The cylindrical container is vibrated, and the impact forces on the powders in the milling chamber highly depend on the rate of milling, the amplitude of vibration, and the mass of the milling medium [5].

High-energy milling forces can be obtained by using high vibrational frequencies and small vibration amplitudes. The energy of the milling media depends on the internal mechanics of the specific mill, the power supply that drives the milling chamber, and the composition, size, and size distribution of the balls. Since the balls' kinetic energy is a function of their mass and velocity, dense materials (steel or tungsten carbide) are preferable to ceramic balls. The size and size distribution should be optimized for the given mill [5]. Too dense packing of balls reduces the mean free path of the ball motion, while a dilute distribution minimizes the collision frequency.

Empirically, a mass ratio between ball and powder of 5−10 is typically used and is effective. One important process variable is the temperature of the mill and that induced in the powders by the kinetic energy of the milling media. This temperature may be critical for the reactions or transformations in the powders during milling. However, the precision

of milling temperatures induced by the powder surfaces remains improved. The milling of materials has been a major component of the ceramic processing and powder metallurgy industries.

Through milling, particle size can be reduced; mixing or blending can be improved, and particle shape can be changed. High-energy milling is often used to fabricate solid-state alloy mechanically. This process was developed by Benjamin and his colleagues at the international nickel company, and they provided a detailed description of this high-energy milling method [6]. This dry, high-energy ball milling process has been used to produce composite metal alloy powders, and the structure and size of the powders can be controlled well. Mechanical alloying is usually carried out in milling equipment capable of high-energy compressive impact forces such as attrition mills, vibrating ball mills, and shaker mills [7]. During comminution, the milling machine will stress the maximum number of individual powders. The starting fracture of materials will be initiated with minimum energy. The motion of milling medium and charge can be varying depending on the types of mills. The movement and trajectories of individual balls, movement and the mass of balls, and the degree of energy applied will highly influence shear, attrition, and compression forces acting on powder particles [8].

Tumbler ball mills: In the tumbler mill (Fig. 2.3A), the rotation speed of the milling chamber will determine the motion of balls or rods, which can roll or "cascade" down the surface of the changes in a series of parallel layers. These balls or rods can also project or "cataract" into the space and fall. The powder milling rate depends on the quantity of powder in the total volume between the balls and attains a maximum value when the powder fill is 100%. The 100% fill is defined as the space between the balls filled with powder [9]. To ensure operation with the required proportions of balls for "cascading" or "cataracting," the speed of the milling system can be adjusted. The above proportion of balls highly depends on the speed of rotation and the coefficient of friction of the charge material. The increase of the size of milling balls and the rate of milling

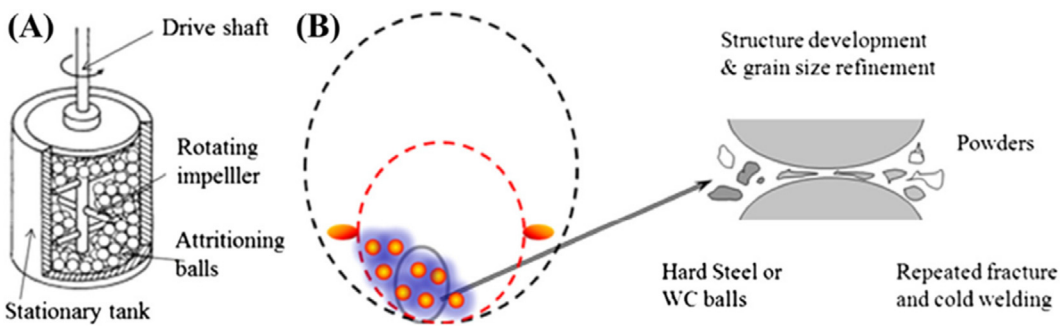

Figure 2.3
Schemes of (A) an attrition mill. (B) Cross-section of a tumbler ball mill.

are helpful to crush the fed particles to the maximum. Usually, tumbler ball mills are used for production runs of over 135−180 kg (300−400 lbs.) per day. The critical rotational speed of the mill may be calculated by Eq. (2.1) (assume the slip of the charge against the mill chamber wall is negligible).

$$N_C = 77.6\sqrt{{}^{1}/_{D}} \tag{2.1}$$

Where D is the mill diameter (ft with ball diameter in mm or), and N_C is the critical speed of the mill (rpm).

These parameters are approximate and may be inappropriate to calculate the mill speed for metal particles due to the agglomeration by welding. The tumbler mills are used to produce large-scale superalloy instead of attrition mills. Milling times in tumbler mills are prolonged to achieve the same blending level achieved in the attrition or vibratory mill. However, overall productivity in tumbler mills is not as high as other mill-type processes. Usually, metals can be flaked or comminuted using tumbler mills. In this process, a grinding aid or lubricant can prevent cold welding agglomeration and minimize oxidation [10].

Vibratory tube mill: In the laboratory vibratory tube mill, the oscillatory motion of the balls is complicated. There are many factors to determine the path of the balls and particles. These determining factors include "vibrational speed, amplitude, and curvature of the sides of the mill chamber wall, horizontal motion of the mill, and charge contact with the upper surface of the mill chamber." The milling balls gyrate around the chamber wall and sometimes travel horizontally in a spiral path [11]. Deformation and/or wear grooves in the inner chamber walls occasionally occur due to this gyration in cylindrical chambers. These grooves may extend 360 degrees, which depends on the contact of milling balls with the upper surface of the chamber wall. Balls also revolve at different rates and directions, leading to substantial shearing action. In general, additional shearing is desirable during the mixing and blending operation. The milling rate, the amplitude of vibration, and mass of milling media are important factors determining the impact forces on the powder to produce ultrafine products [12].

It was found that the high-energy milling forces can be achieved when high vibrational frequencies and small amplitudes of vibration are applied. The milling operation shown in Fig. 2.3B occurs at 3300 rpm, with about 2 mm (0.08 in) amplitude. Under this condition, maximum gravitational (g) acceleration can be reached (acceleration rate of 12.2 g). The gravitational acceleration is denoted as g at 9.81 m/s^2 (32.3 ft/s^2). Large production mills operate at relatively low vibrational frequencies (1000−1500 rpm) and high amplitude (up to 12 mm, or 0.48 in). A vibratory ball mill is an effective approach for producing solid-state alloy and dispersion-strengthened metals. The amounts of product can be up to 4.5 kg (10 lbs) or more, depending on the apparent density of the powder [13].

In the vibratory mill, the grinding medium receives rapid impulses at a rate proportional to the vibrational frequency of the mill. Impact forces acting on the powder exceed shearing and friction forces. The entire charge slowly revolves counterclockwise to the oscillatory vibrations. Therefore, the grinding and intense mixing occur simultaneously. Usually, the vibratory mills utilize smaller mediums because of higher impact forces, frequencies, and acceleration. Herein, a higher specific surface is available for milling. The factors (Table 2.1) that affect the rate of processing in a vibratory mill are listed as follows [14]:

1. Rate of processing is proportional to the density of balls (diameter constant);
2. Rate of processing is proportional to the diameter of the balls (density constant);
3. Rate of processing is proportional to the cube of the frequency of vibration;
4. Negligible for speeds less than 900−1000 rpm;
5. Rate of processing is proportional to the square root of ball diameter/mean particle diameter ratio;
6. Not significantly affected by chamber diameter;
7. Increased as the amount of powder in mill decreases; and
8. Greater with balls than cylinders or other shapes.

Attrition mill: An attrition mill is an operation to mechanically reduce the particle size of solid material by an intense agitation. This operation is highly affected by the stirring action of an agitator. The rotating shaft is vertical to their horizontal arms in the attrition chamber. The shaft rotation causes a differential movement between the balls and the starting materials being milled. The attrition mill provides a substantially higher degree of surface contact between milling balls and milled materials than is provided by either tumbler or vibratory mills. Machining a slurry of solid substances is mainly accomplished by impact and shear forces. A vortex will be formed between the rotating balls and milling product at the upper end of the stirring shaft, into which the milling products and balls are drawn [15].

Table 2.1: Number of impacts for various balls and kinetic energy values.

Mill operation for 0.5 s kinetic energy of impact (J)					
No. of balls (2 g each)	10^{-7} to 10^{-4}	10^{-4} to 10^{-3}	10^{-3} to 10^{-2}	10^{-2} to 10^{-1}	10^{-1} to 10^{-0}
5	0	43	297	1	0
10	0	78	505	13	1
15	4	124	928	24	0
Mill operation for 1.0 s					
5	0	78	612	3	0
10	0	148	1201	13	2
15	4	229	1873	24	0

In the attrition mill, larger mediums, normally bigger than 12.7 mm (0.5 in) balls, were used, which run at low rotational speeds of 10−50 rpm. The attrition mill agitator rotates at speeds ranging from 60 rpm for production units to 300 rpm for laboratory units and uses mediums that range from 3 to 6 mm (0.125−0.25 in). The medium of attrition mills can be agitated by externally applied power output. The attrition mills are more efficient in mixing and blending hard materials (for example, hard metals, metal carbides, and ceramics) than conventional tumbler and vibratory ball mills. The major advantages of attrition mills to mill tungsten carbide (WC)/cobalt (Co) are short milling time, ultrafine particle products (submicron-sized), and enhanced smearing of cobalt onto carbide particles. In an inert atmosphere, attrition mills effectively mill metals. However, the drawbacks of this method lie in high cost and low product output, compared to the large tumbler and vibratory ball mills [16].

The attrition mills' central rotating shaft of an attrition mill is equipped with several horizontal arms. It was found that this shaft exerts sufficient stirring action to tumble the grinding medium randomly through the entire chamber volume. The irregular movement was initiated and affected by the following factors [17]:

- Impact action on the medium.
- Rotational force on the medium and
- Tumbling force as medium fills the void left by the shaft.

Both impact and shearing forces must be collectively present to produce fine particles. In attrition mills, impaction is caused by constant impinging of the grinding medium due to irregular movement. Shearing action is generated by random movement of the milling balls in different rotational directions, which exerts shearing forces on the adjacent slurry of materials. The strongest agitation of the milling medium occurs at a location two-thirds away from the center. Grinding does not occur against the chamber walls, which serve as a container instead of a grinding surface. Minimal wear of chamber walls ensures the long service life of the attrition mills. In attrition grinding, the grinding time (t, s) required to reach a certain median particle size is related to medium diameter and agitator speeds within given limits. The t can be calculated by Eq. (2.2) [18]:

$$t = kd/\sqrt{n} \tag{2.2}$$

Where t is grinding time, k is a constant that varies according to the slurry of materials being milled, the type of medium, and the mill being used (cm^3/mol); d is the diameter of the medium (m), and n is shaft movement (rpm).

Attrition mills are classified into three types: batch, continuous, and circulation type. In the batch mill, the material to be processed is fed into the jacketed chamber and is ground to obtain the desired dispersion and particle size. In the grinding chamber, premixing can be accomplished. Chamber walls are jacketed to allow circulation of either hot or cold

water to control and maintain the temperature of the batch. Materials with high density can be ground by batch attrition, like tungsten carbide and viscous materials, suitable for dry grinding and processing dispersion-strengthened metals [19].

The second type, continuous attrition mills, is best suited for large production output. It consists of a tall, narrow, jacketed chamber. The well-remixed slurry is pumped in at the bottom of this chamber and discharged at the top. Grids located at the bottom and top retain the grinding medium. The circulation grinding system consists of an attrition mill and a large holding tank, which is generally about 10 times the volume of the grinding unit. This circulation attrition mill is filled with medium and contains grids that restrain the medium, while the slurry passes through. Attrition mills generally have high pumping rates. Usually, the holding tank contents are passed through the system 10 times per hour. One advantage of the circulation attrition mill is that large quantities of material can be processed with a minimum investment in grinding medium and equipment. The slurry can be monitored continuously, and processing can be stopped when the desired particle size dispersion is achieved [20].

3. Etching

The etching (or lithographic) process is printing using a plate or stone with a completely smooth surface. Nanoimprint lithography is a novel method to fabricate nanosized materials or patterns. Lithography uses visible or ultraviolet (UV) light, X-rays, electrons, or ions to project an image containing the desired pattern onto a surface [21]. These different techniques are generally termed photolithography, X-ray lithography, electron beam lithography, or ion beam lithography, depending on the radiation employed. The pattern-transferring processes include four key steps: (1) solution-based wet chemical etching procedures, (2) dry etching in a reactive plasma, (3) doping using ion implantation techniques, and (4) thin-film deposition [22]. Fig. 2.4 shows a generic procedure of lithographic processes to produce nanomaterials or nanoscaled patterns.

Lithography is a commonly used technique to transfer a computer-generated pattern onto a substrate (such as silicon (Si), semiconductor (GaAs), glass). This pattern is subsequently used to etch an underlying thin film (oxide and nitride) for various purposes (doping or etching). Photolithography, that is, lithography using an ultraviolet (UV) light source, is one of the most widely used techniques in microelectronic fabrication. The electron beam (Ce-beam) and X-ray lithography are two other alternatives, which have attracted considerable attention in the MEMS and nanofabrication areas [23]. We will briefly discuss photolithography, Ce-beam, and X-ray techniques in this section.

The starting point is the generation of a photomask, followed by creating the computer layout for a specific fabrication sequence. This involves a sequence of photographic

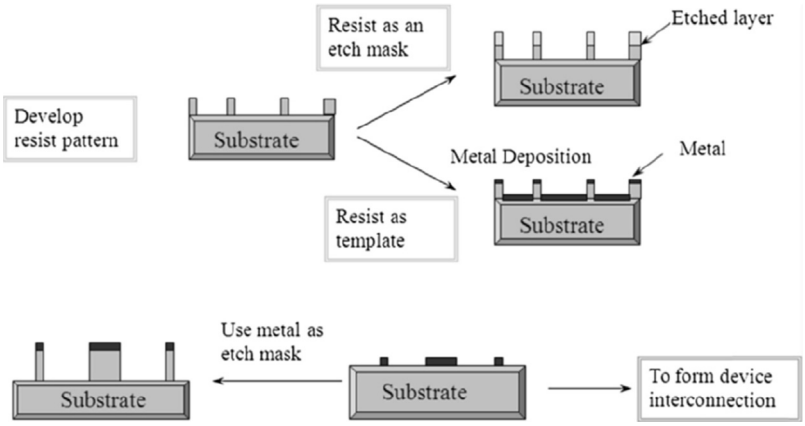

Figure 2.4
Scheme of the lithographic process produces various materials with controllable structures.

processes (using optical or "e-beam pattern generators"), which results in the desired pattern on the surface of a glass plate, which has a thin chromium layer (around 100 nm). Upon the photomask is generated, the lithography process can proceed, as shown in Fig. 2.3. Although this sequence demonstrates the pattern transfer onto a substrate coated with silicon dioxide (SiO_2), the same technique applies to other materials [24].

After the desired material is deposited on the substrate, the photolithography process starts with spin coating the substrate with a photoresist [25]. Prior to the application of the resist, a polymeric photosensitive material can be spun onto the wafer in liquid from an adhesion promoter (such as hexamethyldisilazane, $Si(CH_3)_3NHSi(CH_3)_3$, HMDS). The final resist thickness can be controlled in the typical 0.5−2.5 mm range by adjusting spinning speed and photoresist viscosity. Two different kinds of photoresists are available, in the form of positive and negative. UV-exposed areas will be dissolved in the subsequent development stage with positive resistance.

On the other hand, the exposed areas will remain intact after UV development with negative photoresist. Due to its better performance concerning process control in small geometries, a positive resist is most extensively used in the very-large-scale integration processes [26]. In one typical example, after spinning, the photoresist onto the wafer, the substrate is treated under moderate conditions (such as soft-baked for 5−30 min at 60−100°C) to remove the solvents from the resist and improve adhesion. As a result, the mask is aligned to the wafer, and the photoresist is exposed to a UV source. Different exposure systems are available, depending on the separation between the mask and the wafer [27]. Selected examples of its advantages and drawbacks are listed below:

1. A technique to fabricate dimensionally confined materials such as quantum wires or dots is to start with a quantum well, which provides confinement along one direction,

and selectively remove material to leave ridges or mesas, forming wires or dots, respectively. Material removal is achieved by the use of electron-beam lithography followed by etching.
2. Since the electron beam is rasterized over the required surface in sequence, specific geometries or shapes can be fabricated, which is an advantage to the fabrication of custom surfaces. Since the beams scan the surface, writing over a wide area would take a long time, a disadvantage.
3. Another potential disadvantage is that the adjoining areas can be damaged during the etching. One method to mitigate this situation can be the Formation of an optically inactive surface region, within which the dominant carrier recombination is nonradiative. The importance of this method increases as the size of the nanostructure decreases. A suitable choice of semiconductors can minimize this problem (the GaInAs-GaAs system is a common one), but it can never be eliminated.
4. The dimensional size limit of this approach would limit to 50 nm or more.

Combined lithography: A combination of micro- or nanoimprinting and solid-state forming of thin films on a microscale was reported by Truckenmüller et al. This process led to sophisticated overlaid surface textures [28]. Due to a direct-lithographic process, self-supporting thermoplastic polymer films can be formed, such as polymethylmethacrylate (PMMA). This method differentiates from usually employed layers of UV- or X-ray-sensitive resists. Here, the most critical step is lithographic exposure, performed on a planar flexible polymer film that can be easily planarized on a flat surface [29]. This planarization allows for a lateral resolution as good as conventional lithography by working with standard lithographic processes and equipment.

Additionally, working with self-supporting films opens up the possibility to set up continuous high-throughput processes. The rationale behind this combined lithography is to form the softened polymeric membrane after exposure but before development. In this case, the stored latent lithographic image can be generated under conditions of temporal coherence to adapt to the shape of a 3D micro mold (Fig. 2.5) [30].

Films were preirradiated through a mask with deep-UV light or X-rays to generate a lithographic image with high resolution. The previously treated films were clamped between two heatable metal plates of a press. The bottom plate was equipped with sealing, lines, and ports for evacuation and pressurization, and the upper one with an array of micro molds as reported [31]. These irradiated polymer films were then heated until they were stretched into the micro molds when a differential gas pressure of a few mPa was applied. The material coherence was maintained throughout the formation process to transform the planar lithographic images into spatially warped ones successfully. This microscale solid-state formation results in 3D structures with thin curved walls and warped latent images. This structure was still conserved after cooling down and demolding

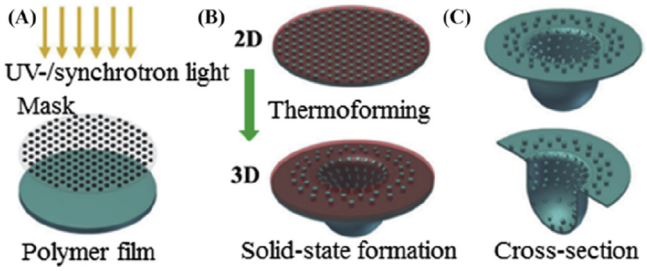

Figure 2.5

Diagram shows the process of fabricating hierarchically patterned films by combining solid-state forming and lithography. First, a thin and flat polymeric film is irradiated through a mask. Secondly, formation is carried out in the softened but still solid state of the polymer resulting in maintenance of the latent lithographic image (blue: pristine polymer; red: Exposed polymer). Thirdly, wet chemical development of the irradiated and formed structures leads to overlaid thermoformed and lithographic patterns. *Images were adapted from Ref. [30].*

[32–35]. The last step involves developing the exposed patterns by immersing them into a developer. Examples of multiscale structures created by this combined ultraviolet or X-ray lithography with solid-state film-forming are shown in Figs. 2.6 and 2.7.

Scanning tunneling E-beam lithography: To successfully explore the lithographic patterning, for example, in patterned graphene or CNTs, two conditions are required: (1) the width of the graphene nanoribbons (GNRs) has to be controlled down to a few nanometers in order to be able to achieve gap values under room temperature operation and (2) the crystallographic orientation of the GNRs has to be controlled equally precisely because the gap can be ruined due to the minor misorientation (a few degrees). A recently developed lithographic procedure (such as scanning tunneling microscopy (STM) lithography) [36] allows for the simultaneous control of width in the nanometer scale and the precise control of crystallographic orientation. The sheet-like geometry allows the cutting of desired, even complex interlinked patterns, and devices [37]. Both size and crystallographic orientation can be tuned after the orientation of the sheet is precisely established by STM imaging with atomic resolution. This procedure eliminates or mitigates the tedious steps to select a suitable type of CNTs from various tubes grown. Three major advantages of the STM approach are (1) to provide structural information from the atomic level; (2) to modify the sample surface with atomic resolution; (3) to provide insight on the atomic structure of the patterned materials; and (4) the ability to probe the electronic structure of the realized nano-object. The STM lithography has been studied recently [38], particularly surface modification of highly oriented pyrolytic graphite by STM [39]. Electron beam lithography was the first high-resolution lithographic technique used to produce GNRs. However, the smallest GNR width seems to be limited in the range of 10–20 nm [40], which is beyond the room temperature operation of GNR-

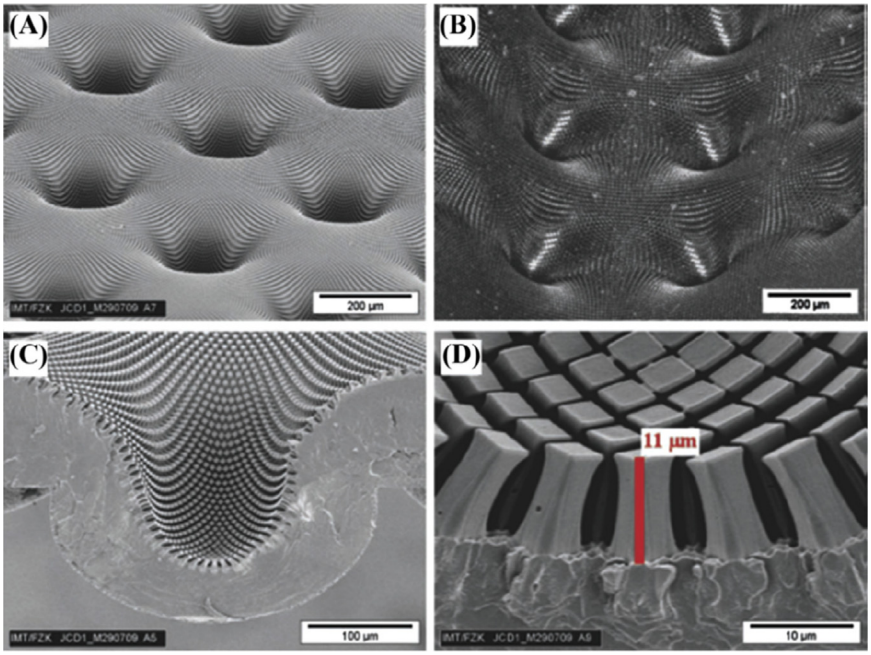

Figure 2.6

Combined UV lithograph and solid-state forming used to produce hierarchically patterned polymer films. The employed angle of irradiation allows for the overlaid lithographic patterns to be oriented perpendicular to the local surface of the 3D-shaped film. A regular deflection of the pillars occurs at the bottom of the cavities toward the cavity center. (A) Inclined view of a microwell array with depths of 100 mm with overlaid lithographic patterns (scanning electron microscopy image); and (B) The same array was lining the inner surface of a tube with a radius of curvature of 1 mm (confocal LASER scanning microscopy). (C, D) The cross-sections show the lithographic patterns with a height of 11 mm even on the nearly vertical sidewalls and at the bottom of a single microwell.

based nanoelectronics (Fig. 2.8). Moreover, the crystallographic orientation control cannot be achieved straightforwardly by e-beam lithography.

Recently several groups reported experiments on NP-based lithography of graphene and few-layer graphene systems [41–43]. The Fe, Ni, or Ag NPs catalyzed to promote local chemical reactions in the reported experiments. This procedure will extend one or a few graphene layers in-depth, which shows the crystallographic orientation in propelling the above NPs. Further work can improve a lithographic technique to allow more precise crystallographic control. However, the current techniques set the platform for future refinements. Biro group has reported that layer thickness of graphene nanolithography can be controlled within a single and few layers using STM. This technique provides "simultaneous crystallographic orientation control, single graphene layer manipulation,

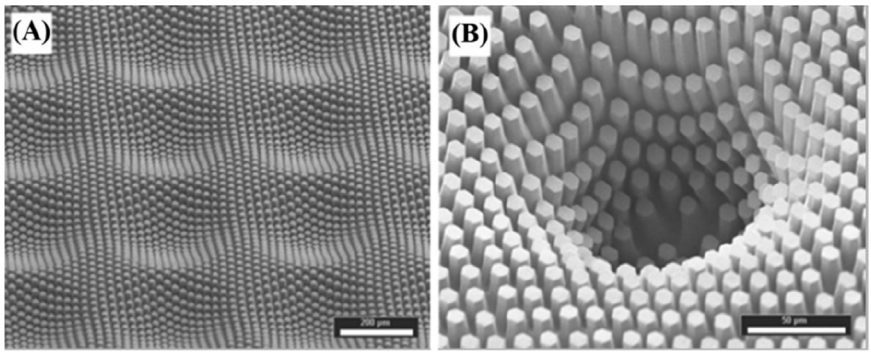

Figure 2.7

Thermoformed structures with overlaid patterns produced by X-ray lithography. (A) Angular view of a microwell array with the wells having a depth of approximately 40 mm. After irradiation, the polymer film was thermoformed at 99°C and 2 MPa. (B) Single cavity with a depth of approximately 290 mm (thermoforming parameters: 105°C, 2.5 MPa). Unlike the combination with UV lithography where only a smaller depth of the overlaid patterns with up to approximately 10 mm can be created, the combination of micro thermoforming and X-ray lithography allows creating noticeably deeper patterns, e.g., with a depth of 20–30 mm.

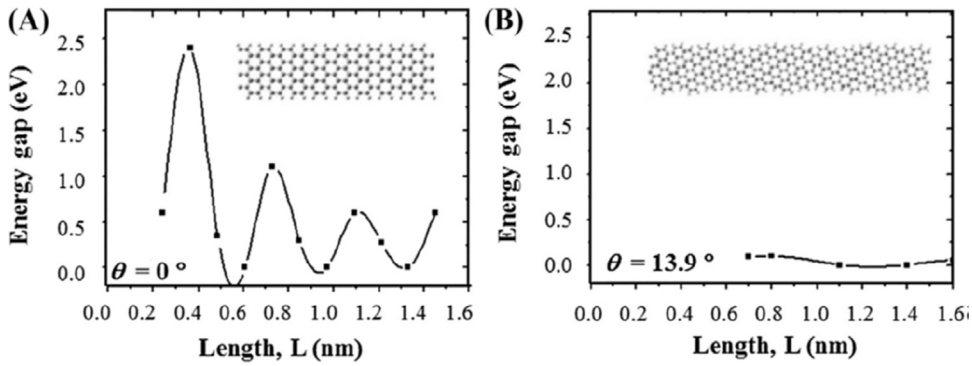

Figure 2.8

Tight-binding calculation showing the influence of deviation from the armchair direction on the magnitude of the energy gap of the GNR, (A) crystallographic orientation, $\theta = 0°$, and (B) $\theta = 13.9$ degrees. *Graphs were adapted from Ref. [36].*

layer removal, patterning few nm wide GNRs, and atomic resolution STM images" on the lithographic prepared nanoribbons.

The width of GNRs can be controlled within a few nanometers by placing two parallel trenches close to each other. Due to the reduction of the length over which the graphene layer is extended, a confinement-induced gap will open for graphene in certain "armchair" orientations GNRs (Fig. 2.9) [44]. This orientation is equivalent to "slicing" the graphene

through the first Brillouin zone (K point), similar to a technique applied with CNTs. The distance between the edges of the "armchair" GNR will define the position of the planes, noting that the edges will cross in the vicinity of the cone at the K point in the Brillouin zone. GNRs cut by the STM lithography are shown in Fig. 2.9, including a straight GNR and an etched one to join an armchair GNR with a "zig-zag" GNR. The 30 degrees "knee" (Fig. 2.9B) was found to constitute a nanoscale diode. The "zig-zag" GNR usually shows the metallic property, while the armchair GNR may have a confinement-induced gap.

After being cut, the GNRs were evaluated to determine their atomic structure in their central region and at the edges. In most experiments, the same STM tip was used in the lithographic process to collect atomic resolution images (shown in Fig. 2.10A). The image found that electronic interference occurs in the edge region, and superstructures appear due to scattering processes, as discussed by Biro in recent articles [45,46]. It was reported that the oxidation of the edges upon proper design and control might be used to smooth down such irregular edges to more desirable configurations. Milder processes than STM lithography can further control the GNR width. It was also found that the STM lithography can produce GNRs with widths down to 2.5 nm, even without combined lithographic and oxidative procedures (Fig. 2.10B). The scanning tunneling spectroscopy (STS) measurements reveal that the fabricated GNR displays a low bandgap at 0.5 eV. This bandgap allows the room temperature operation of circuitry constructed from GNRs, including flexible components such as curved cell phones and televisions. However, the

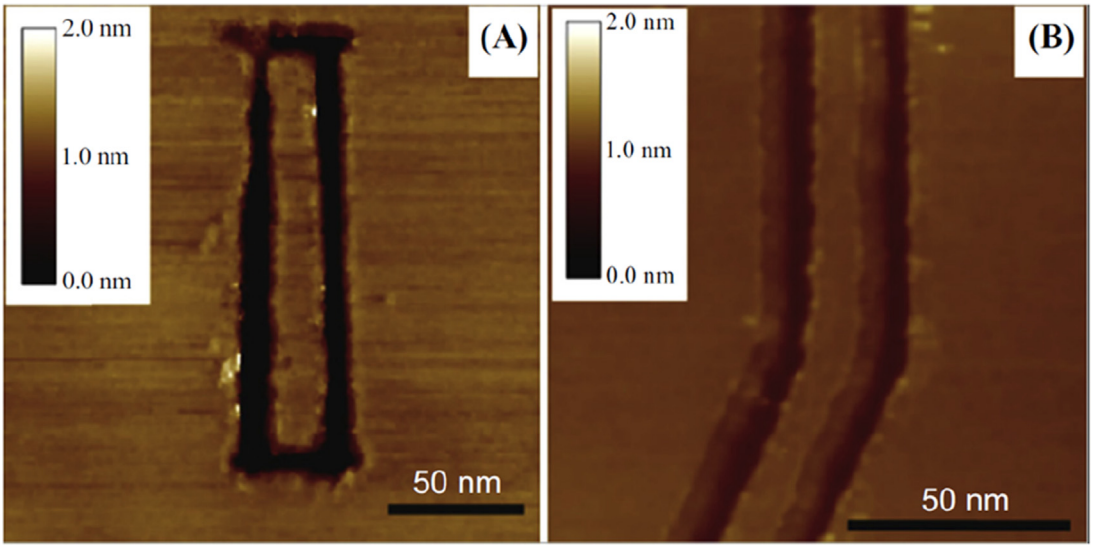

Figure 2.9

Graphene nanoribbons (GNRs) cut by scanning tunneling microscopy (STM) lithography. (A) 10 nm wide straight GNR. (B) 8 nm wide GNR "knee." *The images were adapted from Ref. [36].*

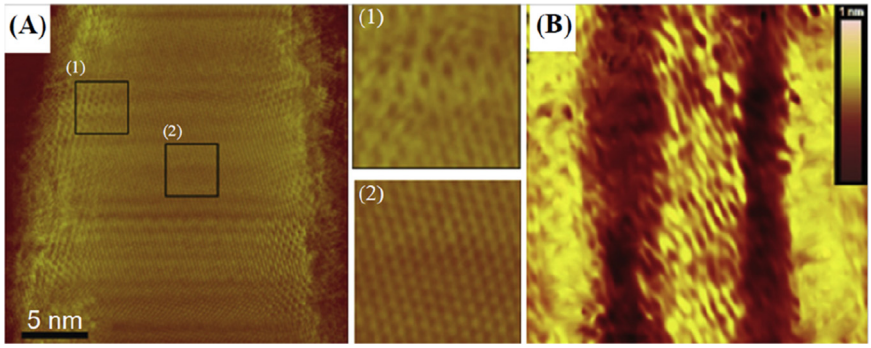

Figure 2.10

(A) Scanning tunneling microscopy (STM) image with an atomic resolution of a 20 nm wide "zig-zag" graphene nanoribbon (GNR): (1) resolution of the GNR and the electronic interference effects arising due to the irregularity of the edges and (2) the good atomic resolution in the central region; (B) the narrowest GNR produced by lithography patterning of 2.5 nm width. STS shows a confinement-induced gap of the order of 0.5 eV. *Images were adapted from Ref. [36].*

sequential lithography approach is too expensive for practical wide-scale applications. This bottleneck can be easily overcome by similar solutions like the millipede concept developed by the international business machine (IBM) to overcome this bottleneck [47]. To overcome the above disadvantage, massively parallel multitip arrays can be used in dip-pen nanolithography [48], with over 50,000 independent tips operating simultaneously.

4. Machining

A machining procedure is necessary to produce patterned and topographically constrained surfaces to produce materials in three dimensions. Focused ion beams (FIBs) and high-intensity LASERs are two common machining techniques. They have been used to fabricate and pattern materials at less than micron dimensions. FIB is an early technique used in the semiconductor industry from the 1970s for depth and surface analysis, patterning through deposition, and ablation originated from research intended for developing space thrusters. While developing thrusters that used charged metal droplets, Krohn first documented ion emission from a liquid metal source in 1961 [49]. His research on liquid metal ion sources (LMISs) for applications in outer space [50] quickly proved to be useful for many other areas, especially semiconductors and materials science. Commercialization of the FIB was not far behind in the 1980s, mainly oriented toward the rapidly growing semiconductor industry. The modern FIB system utilizes an LMIS at the top of its column to produce ions (Fig. 2.11). Gallium (Ga) is usually used for its low melting point (30°C), high mass, low volatility, and low vapor pressure and because it is easily distinguished from other elements. The Ga source is heated to near evaporation, allowing liquefying and flowing down the tungsten needle to remain in a liquid state for

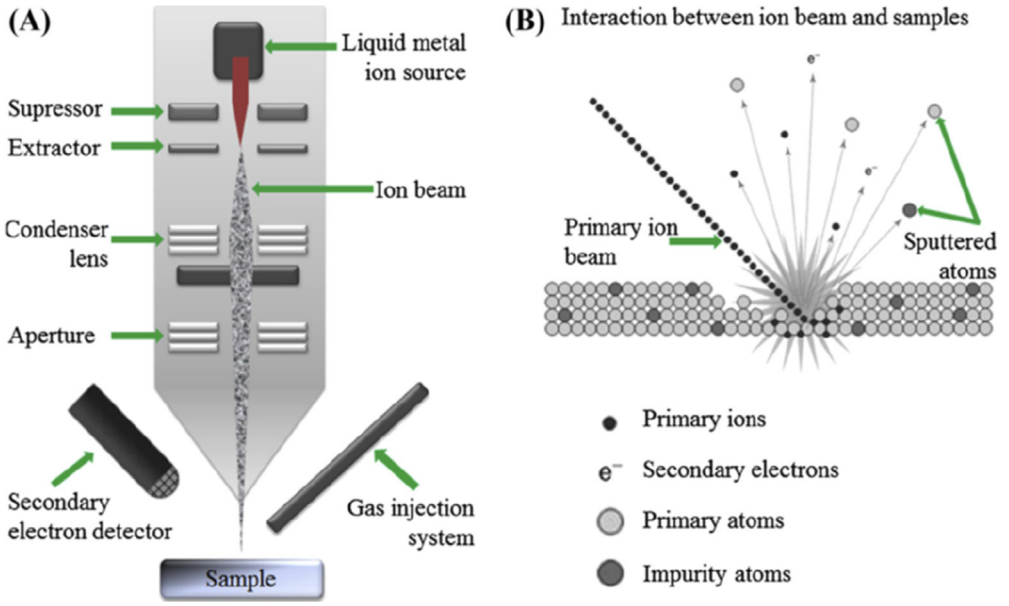

Figure 2.11
A schematic diagram of focused ion beams (FIBs), (A) the generic steps of FIB to produce nanomaterials and (B) interaction between ion beams and samples.

weeks without further heating, owing to its supercooling properties [51]. The extractor, an annular electrode centered just below the tip of the needle, is held at a voltage on the order of −6 kV relative to the source, drawing liquid Ga into a Taylor cone. An electric field on 10^{10} V/m between the tip and aperture induces field evaporation, causing ion emission and acceleration down the column. The source is typically operated at low emission currents of 1−3 μA to produce a stable beam [52]. Another suppressor electrode works alongside the extractor at around +2 kV to maintain a constant beam current. The suppressor and extractor act as the "fine" and "coarse" controls regulating the ion extraction current.

As a result of the creation of ions and ion−ion in the beam and ion−surface interactions are important considerations to ensure consistency and intricate patterning. The beam flux can be varied by changing the voltage between the electrodes. The rate of liquefying, the second parameter of ion−surface interaction, is more variable since the final pattern depends on ion energy, ion flux, and ion−surface interaction angle. Upon collisions, the ions are refracted (slow down within the solid), while some are reflected (backscattered). Since the ions are charged atoms, they have a larger radius than electrons (as in an electron beam), a lower probability of transmission than electrons, but the increased probability of interaction with atoms at the surface. In the collision process between ion

and surface, energy is lost in elastic collisions rather than inelastic collisions commonly seen between electron and surface collisions due to the larger size of ions [53].

In an elastic collision, kinetic energy and momentum are conserved. When the incident ions strike the target atoms, the energy and momentum are transferred to the atoms on the material's surface, causing a sufficient disturbance to remove them from their aligned positions. This sputtering effect, which does not occur when an electron beam is used, allows the FIB to precisely remove atoms from the material's surface in a controlled manner. The incident ions are also scattered, some becoming implanted in the material and others getting backscattered. Furthermore, collisions that result from ion beam bombardment induce many secondary processes such as recoil and sputtering of constituent atoms, electron excitation and emission, defect formation, and photon emission (Fig. 2.11) [54]. These collisions lead to thermal and radiation-induced diffusion, which contribute to various phenomena involving the constituent elements, including phase transformations, crystallization, amorphization, track formation, and so forth. Also, processes such as ion implantation and sputtering alter the surface morphology of the sample, resulting in the formation of craters, facets, pyramids, grooves, ridges, "blisters," or the formation of a porous surface. Electronic collisions produce secondary electrons and X-rays, apart from sputtering effects from elastic collisions. In the inelastic ion-electron collisions, the electrons are excited and ionized. Additionally, the incident ions transfer energy to the surface atoms and electrons, producing secondary electrons, ions, and electron ejection. If the incident ion has insufficient energy to penetrate deep inside the atom, the inner-shell electrons screen the nuclear charge; this screening effect by electrons must be taken into account for these nuclear collisions [50,55].

FIBs can deliver tens of nanoamps of current to a sample and image the sample with a spot size on a nanometer. FIB is an inherently destructive technique since the specimen upon rasterization is transformed. Due to the spattering capability of FIB, it is used as a micromachining tool [56]. Machining is an operation to achieve intricate three-dimensional patterning of a material. FIB and high-intensity LASERs have been used to directly pattern or shape materials at micron and submicron levels. FIB is a semiconductor and materials science technique for site-specific analysis, deposition, and ablation. The focused beam of gallium (Ga) can easily build an LMIS. Ga metal is placed in contact with a tungsten needle and heated. Gallium wets tungsten and high electric field ($>$108 V/cm) cause ionization and field emission of Ga atoms. FIB can be incorporated into a system with electron and ion beam columns [57,58].

LASER ablation synthesis is an emerging method in the machining field, generating NPs by hitting the target material with a powerful LASER. The high energy caused by LASER irradiation leads to source material vaporization. It has been widely utilized in producing NPs of metal, carbon, oxide composites, and ceramics. Specifically, its usage in the

preparation of noble metal NPs has attracted great interest due to the green process without stabilizing chemicals. Kim et al. deposited ultra-small Pd NPs on CdS nanorods with the technique of pulsed LASER ablation in liquid for photocatalytic hydrogen production (Fig. 2.12). The LASER wavelengths, fluences, and LASER salt addition were adjusted to generate monodisperse colloidal NP solutions without using other agents [59].

5. Sputtering

Sputtering is a process to prepare nanomaterials, especially nano-films, assisted by high-energy plasma or gas in an evacuated chamber. It involves the ionization of gas atoms by electrons emitted from a heated filament, and the gas ions in the plasma are accelerated to produce a directly guided ion beam. The ion beam strike or, to say, bombard the target material and generate the ejection of neutral small atom clusters which deposit on the substrate (Fig. 2.13). Meng et al. reported the formation of metal NPs by sputtering with a very short target-substrate distance. Their results proved that increased distance (several microns to 510 μm) had a higher possibility to produce a continuous film. Despite the distance, the ion concentration and sputtering time also affected the distribution and morphology of the product [60].

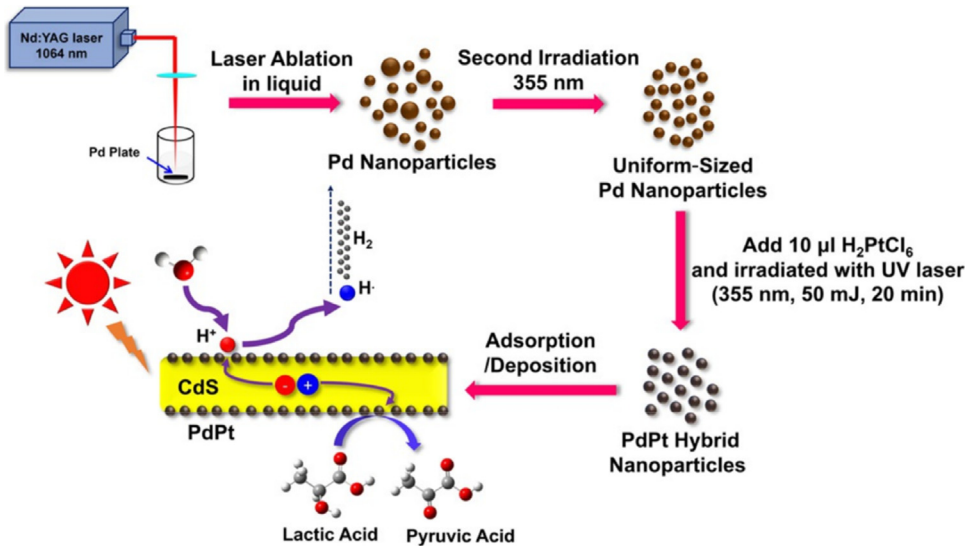

Figure 2.12

Scheme of the schematic of the synthesis of CdS—PdPt nanocomposites and photogenerated hydrogen evolution using CdS—PdPt nanocomposites under simulated solar light irradiation. *Images were adapted from Ref. [59].*

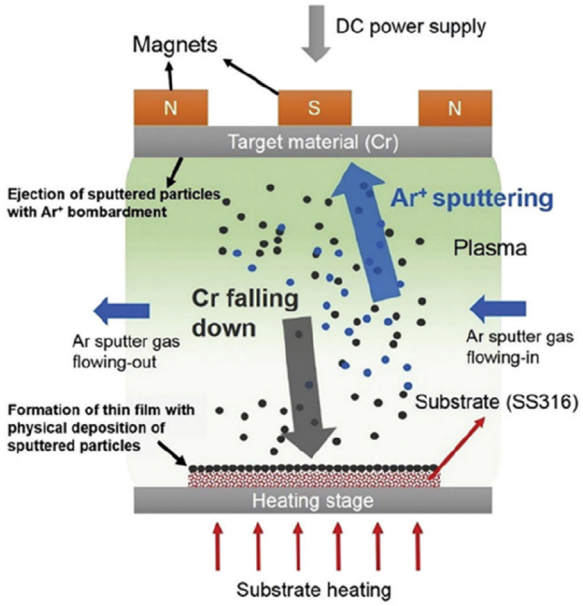

Figure 2.13
A schematic diagram of the DC magnetron sputtering process. *Images were adapted from Ref. [60].*

6. Arc discharge method

The arc discharge method is one of the oldest and the best techniques for preparing diverse nanosized materials, especially for generating carbon-based nanostructured materials, like carbon nanotubes (CNTs) and fullerenes [61]. It was first utilized in the production of CNTs by Iijima in 1991, and the general setup for arc discharge is shown in Fig. 2.14 [62,63]. To obtain CNTs, two electrodes are located in a chamber either filled with a gas or immersed in a liquid to avoid the negative effects of moisture or oxygen. The anode end contains the powdered carbon precursor, and the cathode end is usually a pure graphite rod. Upon the power supply, the two ends are placed at a distance of around 1−2 mm to keep a steady discharge. The very high temperature generated by this discharge process allows for the sublimation of carbon precursors. The carbon vapors aggregate and deposit onto the cool anode end, forming CNTs.

7. Electro-spinning

Electro-spinning is one of the most important ways to fabricate polymer nanofibers. In an electrospinning process, sufficiently high voltage is applied to draw charged threads of

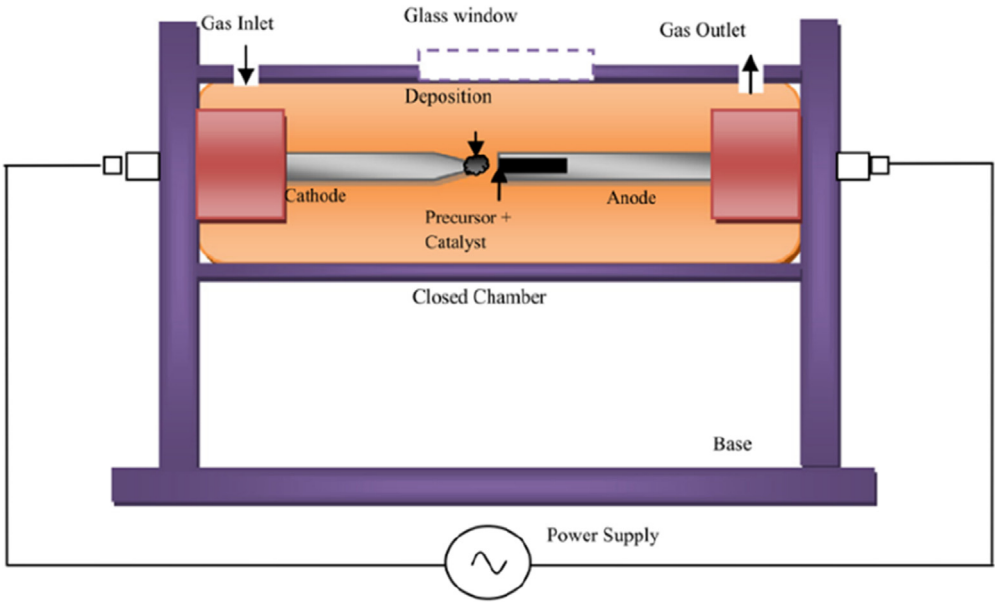

Figure 2.14
Scheme of an arc discharge setup. *Images were adapted from Ref. [62].*

polymer liquids (solutions or melts). The surface tension is overcome to give a stretched stream of liquid. The liquid jet dries in flight and deposits on the surface of the substrate to form thin films composed of nanofibers (Fig. 2.15) [64]. Electro-spinning is facile and easy but was limited to applying a single kind of polymer and the Formation of a single

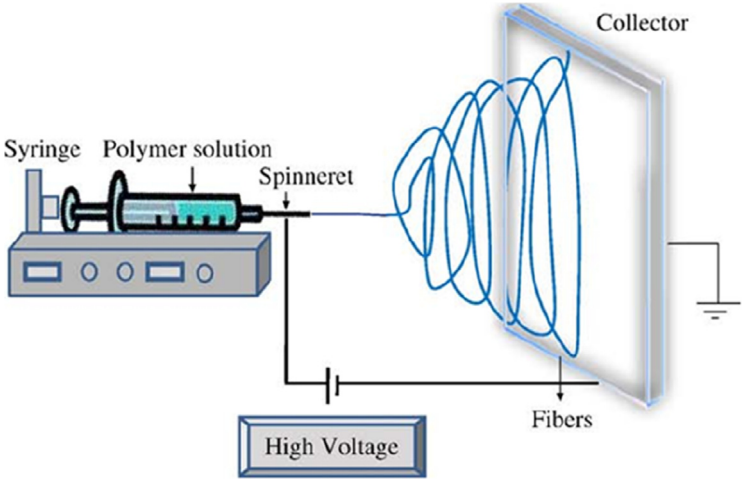

Figure 2.15
Scheme of electrospinning setup. *Images were adapted from Ref. [64].*

component nanofiber. Coaxial electrospinning improved forming core-shell nanofibers on large scales with two coaxial capillaries containing two different liquids [65].

Acknowledgments

This work is partially supported by Welch Foundation (AC 0006). The authors also gratefully acknowledge the helpful comments and suggestions of the reviewers, which have improved the presentation.

Author contribution

Fan Chen wrote the manuscript using the outline and preliminary results from Jingbo Liu. Tian-Hao Yan revised the manuscript, and Sajid Bashir edited it. All authors reviewed prior to submission. A summary of the contributions of each author and an ethics statement. The authors further acknowledge that there is no financial relationship with the editors or publisher and have contributed original work in this chapter, other than what was acknowledged or appropriately cited with copyright permission.

References

[1] S. Zhuang, E.S. Lee, L. Lei, B.B. Nunna, L. Kuang, W. Zhang, Synthesis of nitrogen-doped graphene catalyst by high-energy wet ball milling for electrochemical systems, Int. J. Energy Res. 40 (2016) 2136–2149.
[2] C.C. Koch, Materials synthesis by mechanical alloying, Annu. Rev. Mater. Sci. 19 (1989) 121–143.
[3] A. Acharya, A distinct element approach to ball mill mechanics, Commun. Numer. Methods Eng. 16 (2000) 743–753.
[4] A.M. Belenguer, G.I. Lampronti, D.J. Wales, J. Sanders, Direct observation of intermediates in a thermodynamically controlled solid-state dynamic covalent reaction, J. Am. Chem. Soc. 136 (2014) 16156–16166.
[5] M. Weiße, M. Zille, K. Jacob, R. Schmidt, A. Stolle, Hydroamination reactions of alkynes with ortho-substituted anilines in ball mills: synthesis of benzannulated N-heterocycles by a cascade reaction, Chem. Eur J. 21 (2015) 6511–6522.
[6] F. Boey, Z. Yuan, K.A. Khor, Mechanical alloying for the effective dispersion of sub-micron SiC pre-enforcement in Al–Li alloy composite, Mater. Sci. Eng. A 252 (1998) 276–287.
[7] C.C. Koch, The synthesis and structure of nanocrystalline materials produced by mechanical attrition: a review, Nanostruct. Mater. 2 (1993) 109–129.
[8] P. Balaz, E. Dutkova, Fine milling is applied mechanochemistry, Miner. Eng. 22 (2009) 681–694.
[9] R. Thorwirth, F. Bernhardt, A. Stolle, B. Ondruschka, J. Asghari, Switchable selectivity during oxidation of anilines in a ball mill, Chem. Eur J. 16 (2010) 13236–13242.
[10] L. Konnert, F. Lamaty, J. Martinez, E. Colacino, Solventless mechanosynthesis of N-protected amino esters, J. Org. Chem. 79 (2014) 4008–4017.
[11] M.K. Sureshan, R. Vedaraman, M. Ramanujam, Effects of grinding aids vibration milling of aluminum, Part. Sci. Technol. 1 (1983) 55–65.
[12] K. Zhuravleva, A. Chivu, A. Teresiak, S. Scudino, M. Calin, L. Schultz, J. Eckert, A. Gebert, Porous low modulus Ti40Nb compacts with electrodeposited hydroxyapatite coating for biomedical applications, Mater. Sci. Eng. C 33 (2013) 2280–2287.
[13] P.W. Furcht, H. Silla, Comparison of simultaneous wet milling and enzymatic hydrolysis of cellulose in ball mill and attrition mill reactors, Biotechnol. Bioeng. 35 (1990) 630–645.
[14] Q. Zhao, Z. Shao, C. Liu, M. Jiang, X. Li, R. Zevenhoven, H. Saxe'n, Preparation of Cu–Cr alloy powder by mechanical alloying, J. Alloys Compd. 607 (2014) 118–124.
[15] A.G. Hernandez-Torres, F. Mares-Briones, J.R. Romero-Romero, G. Rosas, CuAl2 intermetallic alloy subjected to the hydrogen embrittlement reaction using mechanical attrition in water, Mater. Sci. Forum 793 (2014) 29–35.

[16] J. Eckert, J.C. Holzer, M. Li, W.L. Johnson, Effects of chemistry on the grain size refinement in nanocrystalline Ru and Ru80C20 powders prepared by mechanical attrition, Nanostruct. Mater. 2 (1993) 433−439.
[17] B. Arifvianto, M. Mahardika, Effects of surface mechanical attrition treatment (SMAT) on a rough surface of AISI 316L stainless steel, Appl. Surf. Sci. 258 (2012) 4538−4543.
[18] B. Arifvianto, M. Mahardika, P. Dewo, P.T. Iswanto, U.A. Salim, Effect of surface mechanical attrition treatment (SMAT) on microhardness, surface roughness and wettability of AISI 316L, Mater. Chem. Phys. 125 (2011) 418−426.
[19] G. Ressel, S. Primig, H. Leitner, The Effect of Zr incorporation caused by ball abrasion in a milled Fe-Y2O3 model alloy, Metall. Mater. Trans. A 45 (2014) 1552−1558.
[20] A. Shrivastava, S. Sakthivel, B. Pitchumani, A.S. Rathore, A statistical approach for estimating significant variables in wet attrition milling, Powder Technol. 211 (2011) 46−53.
[21] B. Wong, F. Zach, V. Moroz, A. Mittal, G. Starr, A. Kahng, Lithography-Related Aspects of DFM. Nano-CMOS Design for Manufacturability: Robust Circuit and Physical Design for Sub-65 nm Technology Nodes, John Wiley & Sons, 2008, pp. 19−125.
[22] C. Mack, Lithographic Control in Semiconductor Manufacturing, Fundamental Principles of Optical Lithography: The Science of Microfabrication, John Wiley & Sons, Ltd, Chichester, UK, 2007, pp. 297−368 (Chapter 8).
[23] D. Iankov, V. Zuerbig, W. Pletschen, C. Giese, R. Iannucci, O. Ambacher, V. Lebedev, Processing of nanoscale gaps for boron-doped nanocrystalline diamond-based MEMS, Procedia Eng. 87 (2014) 903−906.
[24] V. Abramova, A.S. Slesarev, J.M. Tour, Meniscus-Mask lithography for fabrication of narrow nanowires, Nano Lett. 15 (2015) 2933−2937.
[25] V. Karitans, K. Kundzins, E. Laizane, M. Ozolinsh, L. Ekimane, Applicability of a binary amplitude mask for creating correctors of higher-order ocular aberrations in a photo resistive layer, Opt. Eng. 51 (2012), 078001-1.
[26] K. Nagahara, B.N. Trinh, E. Tokumitsu, S. Inoue, T. Shimoda, Fabrication of 120-nm-channel-length ferroelectric-gate thin-film transistor by nanoimprint lithography, Jpn. J. Appl. Phys. 53 (2014) 02BC14.
[27] N. Li, W. Wu, S.Y. Chou, Sub-20-nm alignment in nanoimprint lithography using Moire fringe, Nano Lett. 6 (2006) 2626−2629.
[28] S. Giselbrecht, M. Reinhardt, T. Mappes, M. Börner, E. Gottwald, C. van Blitterswijk, V. Saile, R. Truckenmüller, Closer to nature−bio-inspired patterns by transforming latent lithographic images, Adv. Mater. 23 (2011) 4873−4879.
[29] A. Verma, S. Sekhar, P. Sachan, P. Reddy, A. Sharma, Control of morphologies and length scales in intensified dewetting of electron beam modified polymer thin films under a liquid solvent mixture, Macromolecules 48 (2015) 3318−3326.
[30] R. Truckenmuller, S. Giselbrecht, C. Van Blitterswijk, N. Dambrowsky, E. Gottwald, T. Mappes, A. Rolletschek, Flexible fluidic microchips based on thermoformed and locally modified thin polymer films, Lab Chip 8 (2008) 1570−1579.
[31] M. Heilig, S. Giselbrecht, A. Guber, M. Worgull, Microthermoforming nanostructured polymer films: a new bonding method for integrating nanostructures in 3-dimensional cavities, Microsyst. Technol. 16 (2010) 1221−1231.
[32] R. Truckenmuller, S. Giselbrecht, N. Rivron, E. Gottwald, V. Saile, A. Berg, M. Wessling, C. Van Blitterswijk, Thermoforming of film-based biomedical microdevices, Adv. Mater. 23 (2011) 1311−1329.
[33] M. Focke, D. Kosse, D. Al-Bamerni, S. Lutz, C. Müller, H. Reinecke, R. Zengerle, F. von Stetten, Microthermoforming of microfluidic substrates by soft lithography (mTSL): optimization using design of experiments, J. Micromech. Microeng. 21 (2011) 115002.
[34] B. Lin, Deep UV lithography, J. Vac. Sci. Technol. 12 (1975) 1317−1320.
[35] T. Velten, H. Schuck, M. Richter, G. Klink, K. Bock, C. Khan Malek, S. Roth, H. Schoo, P.J. Bolt, Microfluidics on foil: state of the art and new developments, Proc. Inst. Mech. Eng. Part B J. Eng. Manuf. 222 (2008) 107−116.

[36] R. Truckenmuller, Z. Rummler, T.H. Schaller, W.K. Schomburg, Low-cost thermoforming of micro fluidic analysis chips, J. Micromech. Microeng. 12 (2002) 375.
[37] G. Dobrik, L. Tapaszto', P. Nemes-Incze, P. Lambin, L.P. Biro, Crystallographically oriented high-resolution lithography of graphene nanoribbons by STM lithography, Phys. Status Solidi 247 (2010) 896–902.
[38] L. Tapaszto, G. Dobrik, P. Lambin, L.P. Biro, Tailoring the atomic structure of graphene nanoribbons by scanning tunneling microscope lithography, Nat. Nanotechnol. 3 (2008) 397–401.
[39] D.A. Areshkin, C.T. White, Building blocks for integrated graphene circuits, Nano Lett. 7 (2007) 3253–3259.
[40] A.A. Tseng, A. Notargiacomo, T.P. Chen, Nanofabrication by scanning probe microscope lithography: a review, J. Vac. Sci. Technol. B 23 (2005) 877–894.
[41] S. Neubeck, F. Freitag, R. Yang, K.S. Novoselov, Scanning probe lithography on graphene, Phys. Status Solidi 247 (2010) 2904–2908.
[42] M.Y. Han, B. Ozyilmaz, Y. Zhang, P. Kim, Energy bandgap engineering of graphene nanoribbons, Phys. Rev. Lett. 98 (2007) 206805.
[43] S.S. Datta, D.R. Strachan, S.M. Khamis, A. Johnson, Crystallographic etching of few-layer graphene, Nano Lett. 8 (2008) 1912–1915.
[44] L. Ci, Z. Xu, L. Wang, W. Gao, F. Ding, K.F. Kelly, B.I. Yakobson, P.M. Ajayan, Controlled nano cutting of graphene, Nano Res. 1 (2008) 116–122.
[45] G. Lee, R.C. Cooper, S.J. An, S. Lee, A. Zande, N. Petrone, A.G. Hammerberg, High-strength chemical-vapor-deposited graphene and grain boundaries, Science 340 (2013) 1073–1076.
[46] V. Barone, O. Hod, G.E. Scuseria, Electronic structure and stability of semiconducting graphene nanoribbons, Nano Lett. 6 (2006) 2748–2754.
[47] L. Tapaszto, P. Nemes-Incze, Z. Osvath, Al Darabont, P. Lambin, L.P. Biro, Electron scattering in a multiwall carbon nanotube bend junction studied by scanning tunneling microscopy, Phys. Rev. B 74 (2006) 235422.
[48] G.M. Rutter, J.N. Crain, N.P. Guisinger, T. Li, P.N. First, J.A. Stroscio, Scattering and interference in epitaxial graphene, Science 317 (2007) 219–222.
[49] A. Knoll, P. Bachtold, J. Bonan, G. Cherubini, M. Despont, U. Drechsler, U. Durig, B. Gotsmann, W. Häberle, C. Hagleitner, D. Jubin, M.A. Lantz, A. Pantazi, H. Pozidis, H. Rothuizen, A. Sebastian, R. Stutz, P. Vettiger, D. Wiesmann, E.S. Eleftheriou, Probe-based ultrahigh-density storage technology, Microelectron. Eng. 83 (2006) 1692.
[50] J. Haaheim, O.A. Nafday, Dip pen nanolithography: a "Desktop Nanofab" approach using high-throughput flexible nanopatterning, Scanning 30 (2008) 137–150.
[51] D.J. Paulo (Ed.), Machining: Fundamentals and Recent Advances, Springer Science & Business Media, 2008.
[52] M.J. Madou, Fundamentals of Microfabrication: The Science of Miniaturization, CRC Press, 2002.
[53] H. Plank, Focused particle beam nano-machining: the next evolution step towards simulation aided process prediction, Nanotechnology 265 (2015), 050501-1-1.
[54] L. Repetto, G. Firpo, U. Valbusa, Applications of the focused ion beam in materials science, Mater. Technol. 42 (2008) 143–149.
[55] H.L. Simmons, Construction: Principles, Materials, and Methods, John Wiley and Sons, 2001.
[56] H. El-Hofy, Advanced Machining Processes: Nontraditional and Hybrid Machining Processes, McGraw Hill Professional, 2005.
[57] A.J. Kubis, T.E. Vandervelde, J.C. Bean, D.N. Dunn, R. Hull, Analysis of the three-dimensional ordering of epitaxial Ge quantum dots using focused ion beam tomography, Appl. Phys. Lett. 88 (2006), 263103-1-3.
[58] K.M. Lee, A. Neogi, J.M. Perez, T.Y. Choi, Focused-ion-beam-assisted selective control of graphene layers: acquisition of clean-cut ultrathin graphitic film, Nanotechnology 21 (2010) 205303.
[59] H. Park, D.A. Reddy, Y. Kim, S. Lee, R. Ma, T.K. Kim, Synthesis of ultra-small palladium nanoparticles deposited on CdS nanorods by pulsed laser ablation in liquid: role of metal nanocrystal size in the photocatalytic hydrogen production, Chem. Eur J. 23 (2017) 13112–13119.

[60] M. Nie, K. Sun, D.D. Meng, Formation of metal nanoparticles by short-distance sputter deposition in a reactive ion etching chamber, J. Appl. Phys. 106 (2009) 054314.
[61] N. Baig, I. Kammakakam, W. Falath, Nanomaterials: a review of synthesis methods, properties, recent progress, and challenges, Adv. Mater. 2 (2021) 1821−1871.
[62] S. Iijima, Helical microtubules of graphitic carbon, Nature 354 (1991) 56−58.
[63] N. Arora, N. Sharma, Arc discharge of carbon nanotubes: comprehensive review, Diam. Relat. Mater. 50 (2014) 135−150.
[64] N. Bhardwaj, S.C. Kundu, Electrospinning: a fascination fiber fabrication technique, Biotechnol. Adv. 28 (2010) 325−347.
[65] P.S. Kumar, J. Sundaramurthy, S. Sundarrajan, V.J. Babu, G. Singh, S.I. Allakhverdiev, S. Ramakrishna, Hierarchical electrospun nanofibers for energy harvesting, production and environmental remediation, Energy Environ. Sci. 7 (2014) 3192−3222.

CHAPTER 3

Synthesis of nanomaterials using bottom-up methods

Hengyu Kengsley Lin[1], Tian-Hao Yan[1], Sajid Bashir[2], Jingbo Louise Liu[2,3]
[1]The Department of Chemistry, Texas A&M University, College Station, TX, United States; [2]The Department of Chemistry, Texas A&M University, Kingsville, TX, United States; [3]Texas A&M Energy Institute, College Station, TX, United States

Abstract

Nanomaterials, due to their dimensions, enable most if not all atoms to be involved catalytically. Due to this, nanomaterials exhibit optoelectronic properties, which are absent in their bulk material counterparts. The synthesis of nanomaterials with high porosity and small grain size is a challenge addressed in this review. Unlike bulk material synthesis, bottom-up synthesis is preferred. The review covers aspects related to elemental selection, the effect of surface area, thermal properties, and diffusion in generating materials with appropriate chemical and mechanical properties. This has enabled the generation of materials that were not previously possible, such as nanocages using organic or peptides to synthesize nobel metals for biological or catalytic applications, which is not possible in bulk.

Keywords: Bottom-up method; Sol-gel; Synthesis; Top-down.

1. Introduction

The bottom-up method is widely used to construct desired structures from atom to atom. This synthetic approach involves the assembly of atoms or molecules into nano-structured arrays through attractive forces. In the "bottom-up" method (Fig. 3.1), starting materials can be in gas, liquid, and solid phases [1].

The bottom-up synthetic process (Fig. 3.1) essentially encompasses material synthesis to control deposition and material growth. The synthetic process can be achieved through reactions between solid, liquid, or gaseous states. Solid precursors/reactants are mixed at different temperatures in the solid-state synthesis. The diffusion of reactants occurs when the reaction temperature increases. An elevated temperature results in grain growth, normally as particles. The final product can have different grain sizes depending on dispersing agents or inhibitors. However, it is difficult to produce nanoscale materials from solid-state reactions because of the uncontrollable reactivities of substrates [2]. In general,

Advanced Nanomaterials and Their Applications in Renewable Energy. https://doi.org/10.1016/B978-0-323-99877-2.00003-5

Figure 3.1
Scheme of a bottom-up method to build nanomaterials.

the bottom-up method includes two categories: chaotic process and controlled process [3]. In the chaotic process, the constituent atoms/molecules are elevated to a chaotic state and then converted to an unstable or pseudo-stable state by a sudden change of reaction conditions. The synthetic parameters can be modified to produce desirable products. If the variables cannot be managed, the size of the final products will be randomly distributed. Therefore, nanoparticles (NPs) formation can be tuned by manipulating the end state of final products [4]. Chaotic processes include colloidal chemistry, combustion, exploding wire, flame pyrolysis, laser ablation, and precipitation techniques. Colloidal chemistry will be discussed as an example to produce different materials with high cost-effectiveness and homogeneity [5]. Controlled synthesis normally corresponds to a controllable delivery and diffusion of the constituent atoms or molecules to the reactive sites, where the NPs can form in a controllable approach. Accordingly, NPs can form via controlling the state of different reactants [6]. This method includes chemical vapor precipitation, self-limiting growth solution, MBE, and shaped pulse femtosecond laser techniques. In this chapter, MBE will be discussed briefly [7].

2. Colloidal methods

The colloidal method involves the formation of nano-sized particles within a continuous fluid solvent matrix. Ultrafine particles (from 10^{-7} to 10^{-9} m) are suspended in the dispersing medium to form a colloidal sol. In this method, the mono-dispersed system is found with a high energy state, which is equivalent to the free energy required to fabricate the increased surface area due to the attractive intermolecular forces (also known as van der Waals interaction). Dispersing agents or surfactants will be introduced to the colloidal systems to prevent particle aggregation. The energy barrier to agglomeration is highly dependent on the balance of attraction (van der Waals forces) and repulsion between the particles. The colloidal solution displays properties such as Brownian motion, and the kinetic energy can be expressed as K_BT. Table 3.1 lists various types of colloids [8].

The ultrafine particles were used as semiconductors, such as quantum dots. This material can be produced by impregnating suitable semiconductors into a glass matrix followed by

Table 3.1: Summary of different types of colloids.

Colloid type	Dispersed substance	Dispersing medium	Example
Aerosol	Liquid	Gas	Fog
Aerosol	Solid	Gas	Smoke
Foam	Gas	Liquid	Whipped cream
Solid foam	Gas	Solid	Marshmallow
Emulsion	Liquid	Liquid	Milk
Solid emulsion	Liquid	Solid	Butter
Sol	Solid	Liquid	Paint; cell fluid
Solid sol	Solid	Solid	Opal

heating. This approach allows the size of quantum dots to be controlled between 1 and 40 nm, depending on temperature and heating time. As a result, the electrical injection of carriers can be prevented due to an insulating glass matrix [9]. Recent research indicated that the injection of organometallic compounds allows for the formation of II-VI semiconductor quantum dots [10]. Our research indicated that the crystalline metal and metal oxide nanomaterials could be easily formed from an aqueous solution. The size can be tuned within 1−10 nm based on the addition of different dispersing agents, such as traditional Indian medicinal natural compounds [11]. Due to the steric hindrance effect, the NPs displayed high uniformity and tunable functionality. It was also found that polymeric grafting and functionalization of nanoscale metal oxides change the bandgap and magnetic properties [12]. Their surface area, reactive sites, and optical efficiency can be accordingly modified. The colloidal suspension of nanoscale noble metals and core-shell alloys exhibited excellent optical properties and long-term stability even in "stand-alone" (without functionalization) formulations. These colloids can be incorporated into or deposited onto substances by spin casting or screening printing to form thin films with different thicknesses, which may bring high ionic conductivity [13].

2.1 Coprecipitation

Coprecipitation (Fig. 3.2) is considered one of the most feasible liquid phase methods. Its advantages include cost-effectiveness, high yields, and ease to use. For example, the magnetic NPs (MNPs) can be prepared by coprecipitation, utilizing an aqueous solution and other solvents. NPs with sizes ranging from 30 to 100 nm can be synthesized using ferrous (Fe^{2+}) and ferric cation (Fe^{3+}) inorganic ionic compounds under a basic condition. Fe^{3+} and Fe^{2+} compounds, dissolved in aqueous solutions, are mixed stoichiometrically with a suspending agent, gum Arabic (GA), to yield spherical homogenous NPs [14].

The size and shape of these depend NPs highly on the counter ions, cation concentration, acidity (pH), and ionic intensity of the solution. Nevertheless, suspensions of MNPs, which are settled by electrostatic repulsion, are very delicate to external factors. pH and ionic strength can contribute to the adaptability in exterior properties of MNPs. Ultrafine

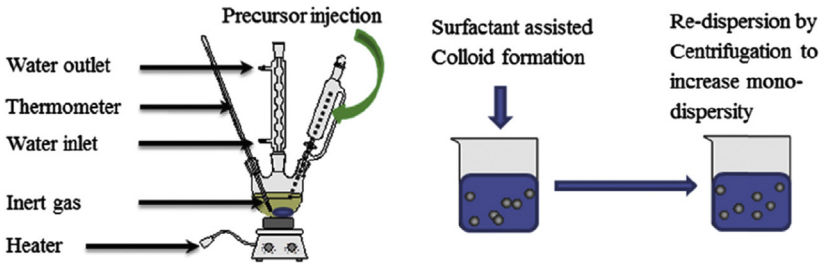

Figure 3.2
A simplified diagram of the synthesis of core-shelled magnetic nanoparticles (MNPs).

NPs generally display high surface tension and energy due to their large surface area. To decrease the surface energy and prevent particle agglomeration, dispensing agents can create steric hindrance or add ions to generate electrostatic repulsion. Additionally, NPs can be stabilized using different coating materials like starches (based on helical amylose and the branched amylopectin connectivity), polysaccharides (such as amylase, amylopectin, low mass cellulose or chitin, GA a complex mixture of polysaccharides of arabinose and ribose and arabinogalactan glycoproteins). These substances will be adsorbed on the NPs, preventing aggregation [15,16].

Preventing colloidal dispersions from aggregation is important in many fields, such as sustainable energy, the food industry, or personal care products. The aggregation includes coagulation when irreversible particle growth and flocculation when reversible. Often the system is an oil/water dispersion that can be stabilized by adding surfactants such as amphiphiles or proteins [15]. They segregate to the oil−water interface and stabilize emulsions by reducing surface tension, and the enhanced rigidity and elasticity of the membrane that forms also help prevent coalescence. Colloidal sols utilized in paints and pastes also need to be stabilized for long shelf life; this can be achieved in several ways [16]. First, for charged colloidal particles in an electrolyte medium, the balance between the repulsive electrostatic and attractive van der Waals contribution to the total potential energy can be adjusted (shown in Fig. 3.3) so that a barrier for aggregation is created.

The phenomenon of charge stabilization can be analyzed using the Derjaguin-Landau-Verwey-Overbeek (DLVO) theory [17]. The second method to prevent aggregation is steric stabilization. Long-chain molecules (for example, fatty acid) are chemically attached or physically attracted to colloidal particles, creating a repulsive force because of steric hindrance. The chains interpenetrate when the particles approach one another. Steric stabilization is highly applicable in nonaqueous media, different from charge stabilization. A wide range of particles can be produced with controllable sizes and uniformity. The concentration and characteristics of surfactants need to be selected carefully to achieve

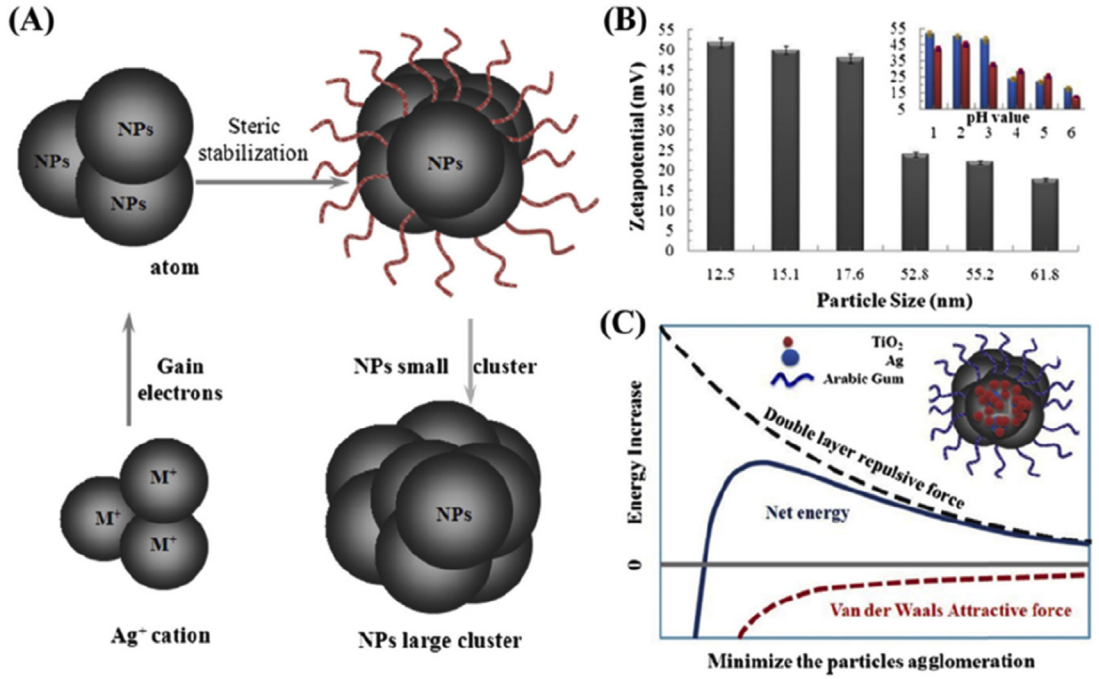

Figure 3.3

Diagram of stabilizing colloidal dispersions against aggregation by adding interracially active components. (A) A simplified diagram of nanoparticle synthesis using colloidal chemistry; (B) zeta potential analysis to demonstrate the formation of nanoparticles and their dependence on the pH value changes; (C) two forces (attractive forces, also called van der Waals forces; and repulsive forces), which determine the particle size depending on the net free energy to influence the effective interaction between particles (note: the insert in C shows that the choice dispensing agent is critical in steric stabilization).

steric stabilization. Polymeric surfactant chains can be attached to two (or more) particles at low concentrations, resulting in bridging flocculation.

At higher polymer concentrations, the nonadsorbed polymeric molecules can lead to depletion flocculation, recognized by Asakura and Oosawa [18]. Their mechanism stated that the polymers cannot penetrate the particles and are excluded from a depletion zone around them. When the particles approach each other, an overlap of depletion zones occurs. In this case, the polymers will be distributed into the bulk solution due to increased entropy. An effective attraction between particles will be generated due to the osmotic pressure of solvent from the gap between particles. Therefore, flocculation of particles occurs. If the concentrations of the colloids are on average, the colloidal particles depart from the polymer coil radius. If the concentration of the surfactant polymer is high, depletion stabilization may occur. Agglomeration of the particles would require the redistribution or "demixing" of polymer from the bulk solution. This process increases the

Gibbs' free energy. Therefore, the effective interaction between colloidal suspensions is repulsive [19].

2.2 Sol–gel method

Sol–gel method (Fig. 3.4) is a feasible wet chemical technique to fabricate materials starting from metal alkoxides (M-O-M) or metallic inorganic compound (M-H-M) solutions, which react to produce colloidal particles (known as a sol) [20]. The sol precursors dispersed in solvent are subject to hydrolysis and poly-condensation reactions to form a xero gel containing a continuous lattice, such as M-O-M or M-H-M [21].

The sol–gel method is used to create "an oxide matrix through poly-condensation of a subatomic precedent in a liquid" [22]. Sol is a mixture of steadily scattered colloidal polymers or colloidal particles in a solvent. Sol is composed of particles in a liquid, whereas an aerosol is composed of particles in a gas, and the particles can be either crystalline or amorphous [23]. A gel comprises a three-dimensional steady network, which encases a liquid stage. The system is fabricated from an agglomeration of colloidal particles in a colloidal gel. The idea behind sol–gel union is to "break down" the compound in a fluid and recombine as solid in a controlled way [24]. Multiconstituent compounds may be synthesized with controlled stoichiometry by combining sols of various precursors. The sol–gel technique's issues lie in coprecipitation, which may be a nonhomogeneous gelation response. If blending at the nuclear level is enabled, stabilized NPs will yield smaller particles. Sol–gel strategies mostly refer to the hydrolysis and

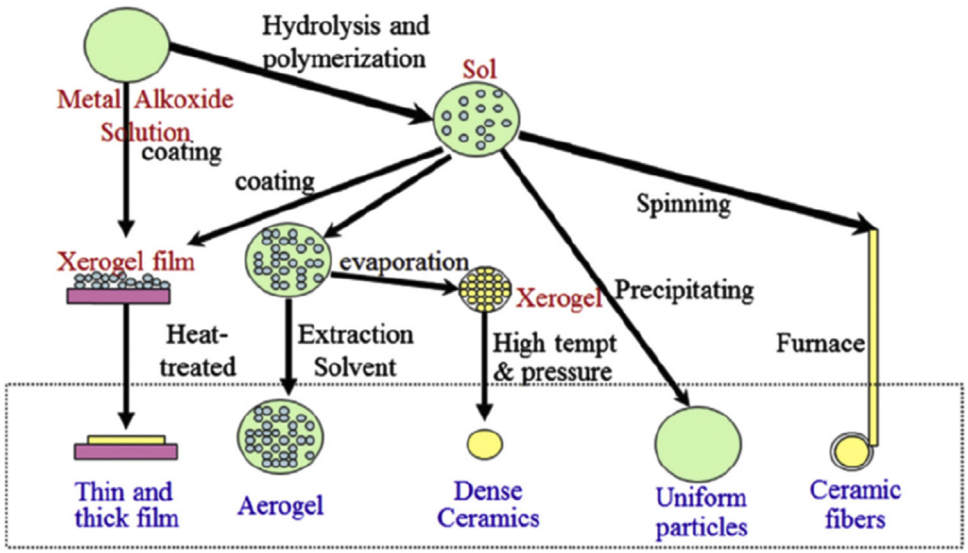

Figure 3.4
Diagram of a sol–gel method to form different types of nanomaterials.

buildup of metal alkoxides or alkoxide antecedents, prompting scattering of oxide particles in a "sol." Obtained sol is dried or gelatinized by chemical reaction or solvent removal [25].

The most popular solvent utilized is water, but acid or base can likewise hydrolyze the precursors. Appropriate catalysts affect the establishment of a colloidal gel, while acid yields a polymeric gel [26]. The rate of condensation and hydrolysis plays a major role in the properties of the final products. Smaller molecular size is acquired at a slower and highly controlled hydrolytic speed [27]. The molecular size likewise relies on the pH, temperature, and solution composition.

Magnetic oxides sequence in the sol–gel framework relies on the phases formed and the particle volume and is extremely delicate to the size dissemination and scattering of the particles. Because of nanocomposites inferred from gels, material porosity and structural parameters are controlled by the rate of hydrolysis and condensation of the gel precursors. Furthermore, other oxidation-reduction reactions happen while gelling and following heat treatment. There are three key steps, hydrolysis of alkoxides, condensation, and gelation, shown below [28].

2.2.1 Hydrolysis

During hydrolysis, hydroxide becomes attached to metal atoms. The hydrolysis can be simplified as a general reaction: $M^{+} + nH_2O = M(OH)_n + nH^{+}$. The metal cations from different groups (such as Sr^{2+}, La^{3+}, Ti^{4+}) are hydrated when dissolved in water. Furthermore, hydrolysis can be initiated by adding a base, which will cause the hydrolysis to proceed further to the forward direction of the above equation based on Le Chatelier's principle. When the metal alkoxide precursors are used, the sol is formed by the subsequent hydrolysis: $M(OR)_4 + nH_2O = M(OR)_{(4-n)}(OH)_n + nROH$ [29].

2.2.2 Condensation

Condensation is catalyzed by the addition of an acid or base above water. The reaction is shown as: $2M(OR)_{(4-n)}(OH)_n = (M(OR)_{(4-n)}(OH)_{(n-1)})_2O + H_2O$. This process liberates small molecules (water or alcohol), building larger molecules. The polymers' formation is accomplished in three steps: formation of dimer, chain, and ring (as shown in Eqs. (3.1)–(3.3)) [30].

Dimer formation:

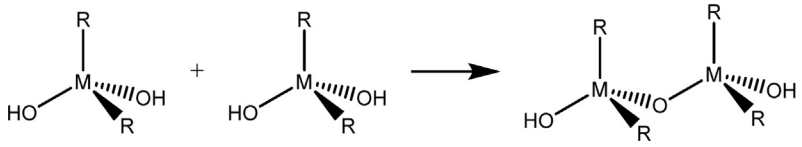

(3.1)

Chain formation:

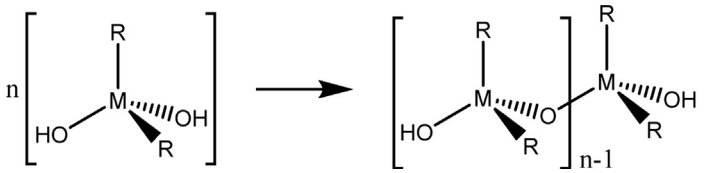

(3.2)

Ring formation:

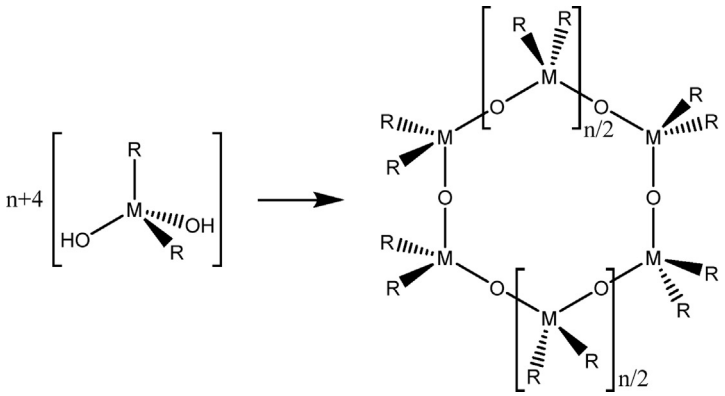

(3.3)

2.2.3 Gelation

The sol precursors will spontaneously coagulate to form a gel when the pH increases. In alkaline gelation, water is removed via dehydration. This process forms a gel that in macroscopic dimensions extends in the solution. At this point, the last bond will be formed to complete giant molecules. A continuous skeleton is enclosed in a continuous liquid phase within a gel molecule. This continuity of solid gel structure provides elasticity of the final products [31]. In the overall hydrolysis/condensation reaction of the metal alkoxide (Eq. 3.4):

Condensation reaction to form gel:

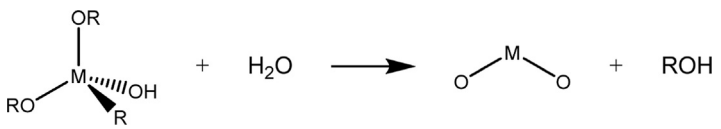

(3.4)

The formation of the M-O-M oxo bridges (as shown above) within the gel network begins and proceeds in three dimensions. The gel can be formed through covalent bonding or van der Waals forces. Therefore, the bonding in the gel skeleton can be either reversible or irreversible. During gel formation, it was found that the viscosity increases dramatically, and the solid structure begins to form. For example, among $La_xSr_{1-x}MnO_3$ (LSM)

materials, the homogeneity of Sr^{2+} and La^{3+} unit cells is crucial for the efficient conduction of electrons inside the cathode. Our study on fuel cell catalysts indicated that the formation of these M-O-M oxo bridges provides an even distribution between these two cations [32].

In general, the sol-gel process involves the transition of a system from a liquid "sol" (mostly colloidal) into a solid "gel" phase. Applying the sol−gel process, it is possible to fabricate ceramic or glass materials in a wide variety of forms, including ultrafine or spherical powders, thin-film coatings, ceramic fibers, microporous inorganic membranes, monolithic ceramics, glasses, and extremely porous aerogel materials [33]. The starting materials used to prepare the "sol" are usually inorganic metal salts or metal-organic compounds such as alkoxides. In a typical sol−gel process, the precursor is subjected to a series of hydrolysis and condensation/polymerization reactions to form a colloidal suspension or a "sol." Further processing of the "sol" enables the formation of ceramic materials in different forms [34]. Thin films can be produced on a substrate by spin coating or dip coating. When the "sol" is cast into a mold, a wet "gel" forms. After further drying and heating, the "wet gel" is converted into dense ceramics or glass. If the liquid in a wet "gel" is removed under supercritical conditions, a highly porous and extremely low-density material (known as aerogel) is obtained. As the viscosity of a "sol" is adjusted into a proper viscosity range, ceramic fibers can be drawn from the "sol." Ultrafine and uniform ceramic powders are formed by precipitation, spray pyrolysis, or emulsion techniques.

The sol−gel method is a versatile solution-phase process to produce ceramic and glass materials [35]. The product has several advantages: ultrasmall particle size; high specific surface area; long triple-phase boundary; control of composition at molecular scale; homogeneity; low cost; and ease of preparation. The sol−gel method can produce diversified materials and will be discussed below: (1) nanoporous oxide gels; (2) nano organic−inorganic hybrids (dyes, proteins, and polymers) in gels; (3) nano-crystallites obtained via controlled crystallization of gels; (4) semiconducting NP s; (5) metallic NP s; and (6) colloidal oxide particles.

2.2.3.1 Nanoporous oxide gels

A gel can be formed when the hydrolysis and condensation proceed. During condensation, the viscosity of the sol precursor was found to increase. Typically, the oxide M-O-M (Si−O−Si) bonds are formed. As a result, a network can be produced (as shown in Eq. 3.3), where the final products are trapped. The nanoporous structure can be generated when the products are extracted via evaporation. Pore size, size distribution, and interconnectivity are affected by processing parameters, such as the type and amount of solvent, catalyst, and temperature. In some cases, the presence and arrangement of templating molecules and acidity are also critical for forming nanoporous materials,

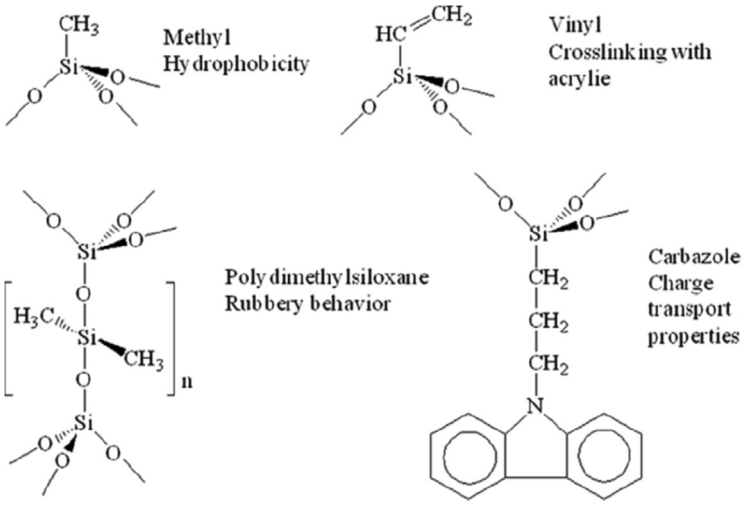

Figure 3.5
Network formation and grading organic entities into the oxide backbones.

constituting diversified nanomaterials. The nanoporous architecture (Fig. 3.5) may be tuned and tailored for connectivity, orientation, arrangement, and size by adjusting the fabrication variables.

Metal oxide sol-gel-derived NP s have been widely studied. TiO_2, ZnO, SnO_2, and WO_3 are four of the most commonly used NPs made from sol−gel synthetic routes. Several groups have reported the formation of TiO_2 NPs via the sol−gel method. Vijayalakshmi et al. prepared TiO_2 NPs by mixing titanium IV isopropoxide (TTIP) and ethanol, with nitric acid added to assist the hydrolysis process. The obtained NPs were around 9 nm. Jaroenworaluck et al. used a mixture of tetraisopropylorthotitanate (TIPT), methanol, and ethanol in different molar ratios to prepare TiO_2 NPs. The obtained NPs had a size of around 10 nm. A summary of reported syntheses of TiO_2 NPs via the sol−gel method is provided below in (Table 3.2).

The other reported syntheses of SnO_2, ZnO, and WO_3 are summarized in a recent review by Singh et al. [44]. The materials derived from the sol−gel method can be used in different fields, such as chromatography columns, sensors, actuators, catalyst support, low dielectric constant materials, and controlled reactant release [47]. The pores can be impregnated and functionalized through a postmodification. This procedure can produce a dye or organic molecule if they are interconnected. This type of organic material is used as the “backbone” of the packing in chromatography.

Table 3.2: Summary of nanomaterials synthesized by sol-gel methods.

Precursors	Synthesis conditions	Properties
TTIP, ethanol, nitric acid [36]	Drying: 2 h, 120°C Calcination: 2 h, 450°C	Highly crystalline NPs with the size of around 7 nm
TIPT, methanol, and ethanol [37]	Stirring: 3 h, 55°C Drying: 5 h, vacuum Calcination: 3–9 h, 400–800°C	Anatase at lower calcination temperatures (~10 nm) and rutile at higher calcination temperatures
$Ti(O\text{-}Bu)_4$, propanol, acetic acid, sulfuric acid, $Cu(NO_3)_2 \cdot 3H_2O$, $Ni(NO_3)_2 \cdot 6H_2O$, $Co(NO_3)_2 \cdot 6H_2O$, $Cr(NO_3)_3 \cdot 9H_2O$, $Mn(NO_3)_2 \cdot 5H_2O$, and Fe $(NO_3)_3 \cdot 9H_2O$ [38]	Drying: 15 h, 120°C Calcination: 2 h, 500°C Doping: 0.3% M/TiO_2, M(Cu, Ni, Co, Fe, Mn, Cr) added to the initial solution	Particles with different crystallite sizes were obtained ranging from 37 to 124 nm for doped and undoped samples, Cu/TiO_2 showed the highest photocatalytic activity for MB and MO dye
$Ti(O\text{-}Bu)_4$, ethanol, and hydrochloric acid [39]	Drying: 60–80°C Calcination: 2 h, 200–800°C	Anatase nano TiO_2 particles with negligible agglomeration and narrow particle size distribution were synthesized
Titanium (IV) *n*-butoxide, $AgNO_3$, ethanol, nitric acid, acetylacetone [40,41]	Mixing TiO_2 solution and $AgNO_3$ solution at 80°C for 8 h	A thin film of TiO_2 and Ag/TiO_2 on PET substrate with a film thickness of 85 and 87 nm
$Ti(O\text{-}Bu)_4$, dehydrated ethanol, glacial acetic acid, WD-11 [42]	Stirring: 8 h, at r.t. Drying: 48 h, 80°C Washed with ethanol and distilled water three times	TiO_2 NPs encapsulated by octadecyltrimethoxysilane were prepared for application in multifunctional lubricating oil additive and fabrication of inorganic/organic nanocomposites used in optical fields
TTIP, isopropanol, deionized water, and glacial acetic acid [43]	Stirring: 2 h, pH 1 Drying:1h, 80°C Calcination: 2 h, 450–700°C	Slightly agglomerated anatase and rutile phase TiO_2 NPs size of approximately 13 and 100 nm
TTIP, hydrochloric acid, ethanol, and water [44]	Stirring: 2 h, at r.t., pH 3–8 Drying: 100°C, 1 h Calcination: 350–750°C	Agglomerated particles confirming phase change from anatase to rutile as calcination temperature increased
TTIP, ethanol, hydrochloric acid, water [45]	Stirring: 60 s, under ice-bath Immersion of alumina template membrane in sol for 5–60 s Drying: 400°C, 6 h	TiO_2 tubules and fibrils were prepared with 200 nm diameter pores in the alumina membrane. Tubules were obtained if the membrane was immersed into the sol for a brief period, whereas solid TiO_2 fibrils were obtained after long immersion times

Continued

Table 3.2: Summary of nanomaterials synthesized by sol-gel methods.—cont'd

Precursors	Synthesis conditions	Properties
$Ti(O\text{-}Bu)_4$, TEOS, acetic acid, ethanol, nitric acid, and water [46]	Stirring: 5 h Add TEOS in sol and then dry: 70°C, 2 h Calcination: 450°C, 2 h Washing with HF solution 4%	Porous TiO_2 with BET as high as 118 $m^2\ g^{-1}$ for humidity sensing

Additionally, the nanoporosity of the gels can be exploited for many other purposes. For example, low dielectric constant materials can be made using tetramethyl ammonium silicate (TMAS). The role of TMAS is as a structuring agent and is often used in the synthesis of zeolite to control the porosity of the microporous system. It was found that the porosity at 50% and uniform pore size distribution (average pore size of 40 Å) silica films have been obtained, yielding a material with a dielectric constant of 2.5 as reported by Kim et al. [48]. A more recent development in the engineering of nanoporous materials is templating reagents [49]. Using surfactant micelles as pore-forming agents, 65 vol% nanoporous dielectric films with a uniform pore size can be obtained with a controllable size smaller than 5 nm. Bimbaum reports that the starting materials tetraethoxysilane ($Si(OC_2H_5)_4$, TEOS) as a surfactant when mixed in an acidic aqueous solution, a uniform sol precursor was formed. The solvent in the above precursor was rapidly removed through spin coating, and the surfactant molecules formed micellar aggregates. After removing the surfactant, a highly porous silica film formed with controlled porosity and pore sizes. Stable, low dielectric constants of 1.8—2.2 were obtained [50].

2.2.3.2 Nano-organic-inorganic hybrids (dyes, proteins, polymers) in gels

A gel derived from a sol—gel process can be controlled in particle size and pores within a nanoscale. In some cases, the porosity of the gel can be developed using a templating organic molecule. These templating molecules serve as surfactants to prevent particles from agglomeration and control network formation. Under other circumstances, porosity resulted from the evaporation of solvent during the reaction. The key advantage of the sol—gel method is the low processing temperature, which allows for the coexistence of organic and inorganic constituents within the same matrix. Traditionally, ceramic materials can be processed under low sintering temperatures. It was found that the organic entities that reside within the oxide gel, either chemically bonded or physically adsorbed, played a critical role in controlling the size and porosity of the final products. These organic substances can also provide functionality for the product at the nanoscale. As a result, these hybrid materials composed of organic—inorganic entities represent a type of nanocomposite, which is difficult to engineer [51].

2.2.3.3 Nano-crystallites obtained via controlled crystallization of gels

Traditional glass ceramics have been produced since the middle ages. They are typically obtained by forming a glass melt, quenching it, and heating it to grow a crystalline phase within the glass matrix. If the particle size is kept below the wavelength of visible light, the glass ceramic is transparent. Many materials, such as optical filters, zero thermal expansion coefficient materials for cooking ware, or telescopes, have been through this process. The crystallite size must be kept in the nanometer range to achieve the desired properties in many instances. The sol−gel process offers an elegant alternative to this high-temperature approach because many amorphous oxide gels can now be made at room temperature. This opens the possibility of growing a nano-crystallite within a matrix that contains organic entities. The low processing temperature of the sol−gel process opens the possibility of growing an oxide phase within an organically modified matrix by adding GA-based dispersing agents.

The sol−gel process has prepared many ferroelectric oxide materials [52]. Mackenzie's report indicated the growth of nano-crystallites of ferroelectric phases from gels. With increasing temperature, local ordering of the ferroelectric oxides has been observed, starting with the formation of nanosized clusters at low temperatures. Such clusters have been called "ferrons" and have been shown to exhibit ferroelectric properties despite their small size. A theoretical model explaining the behavior of these "ordered clusters" was developed [53].

Similarly, ferroelectric crystals of lithium niobium oxides ($LiNbO_3$) and barium titania ($BaTiO_3$) have been grown in an amorphous glass matrix of silicates (SiO_2) by the sol−gel technique. Such particles also grow in size and quantity with increasing temperature. Well-formed nano-crystallites of $BaTiO_3$ have been observed after heating for 2 h at 800°C. Our study also indicated that perovskite-based ceramic and rapid ion conductors could be formed through sol−gel methods with controllable size and porosity and high crystallinity (as shown in Fig. 3.6). By the sol−gel method, the uniformity of different elements can be controlled. These materials showed high electrochemical performance in fuel cells [54].

2.2.3.4 Semiconducting nanoparticles

For nonlinear optical applications, it is often desirable to grow NPs of semiconducting materials within optically transparent matrices. A summary in Table 3.3 lists the Bohr radii of several semiconductors that can substitute for perovskite La. To observe quantum confinement, particles must be smaller than the Bohr radius of the electron−hole pair, typically less than 200 Å. The sol−gel approach has been successfully used to synthesize such nanomaterials. Typically, a gel is obtained from the appropriate precursors, and the gel is subsequently heated in a sulfiding or reducing atmosphere to grow the semiconducting phase. We have synthesized and compared the properties of cadmium sulfide

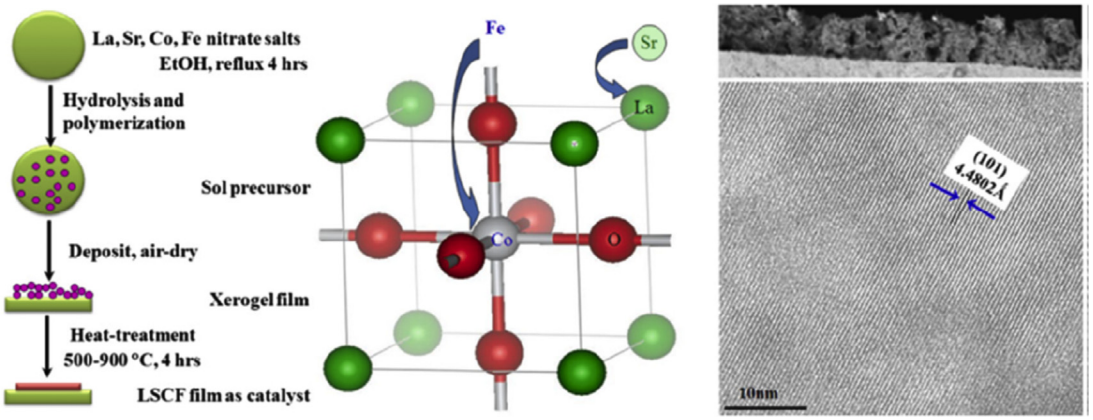

Figure 3.6
Sol-gel-derived $La_xSr_{1-x}Co_yFe_{1-y}O_{3-\delta}$-doped perovskite nanoparticles after high-temperature calcination.

Table 3.3: Summary of Bohr radii and band gap of selected semiconductors.

Semiconductor	Bohr radii (r_B, Å)	Band 1.7 gap (E_g, eV)
CdS	28	2.5
CdSe	53	1.7
CdTe	75	1.5
GaAs	124	1.4
PbS	1802.5	0.41

(CdS)-doped glasses, namely, a sodium borosilicate glass, obtained using TMOS, TEOS, boron ethoxide, and sodium acetate precursors, in ORMOSIL glass, obtained from a TEOS/polydimethylsiloxane (PDMS) system [55–57]. Cadmium was introduced into the two solutions as cadmium acetate and cadmium nitrate, respectively. After drying, the resulting film was exposed to hydrogen sulfide (H2S) gas and formed CdS crystals (up to 20 wt%).

As a further refinement of the approach, 3-aminopropyl-triethoxysilane (APTES) was also added to both solutions to provide enhanced control of the particle size and size distribution. Samples treated with APTES yielded smaller crystal particles with a narrower distribution (2.8 nm average size, with a 0.9 nm standard deviation).

APTES helped anchor the dopant ions to the silica network of the glass, thereby avoiding the precipitation of the salt during the sol–gel drying process. These materials observed chi ($\chi 3$) values around 10–6 to 10–8 electrostatic units. Channel waveguides were made by ion exchange in the sodium borosilicate glass, and propagation of 110 fs long pulses resulted in narrowing and spectral modulation of the input pulse [58,59].

2.2.3.5 Metallic nanoparticles

As in the case of semiconducting NPs, metallic NPs in oxide matrices can exhibit optical properties different from bulk materials. While NPs of metals in glass have been made using traditional glass processing for centuries, the sol−gel process offers an elegant and more versatile alternative. Typically, the technique in volves heating the gel in a reducing atmosphere. The host matrix may be an inorganic gel or an organic−inorganic hybrid. Many metallic NPs have precipitated in sol-gel-derived matrices. For example, silica sol−gel films were prepared by dipping starting from an acid-catalyzed solution of TEOS doped with gold (Au), silver (Ag), platinum (Pt), and palladium (Pd) metal colloids. The temperature at which the metal particles precipitate by heating in air depends upon the metallic species: 200°C for Au, 600°C for Ag, 800°C for Pt, and 1000°C for Pd [60]. Silver metal NPs were also produced in silica by introducing silver nitrate ($AgNO_3$) in the sol−gel precursor solution. The silver ions were thermally reduced in the air at 800°C, yielding an intense yellow coating film. Transmission electron microscopy (TEM) and X-ray diffraction observed the silver metal particles. The diameter of the silver particles was found to be about 10 nm. Thermochromic effects have been observed in such Ag colloid-doped gels, which usually are not observed in the bulk materials [61].

Series of noble metallic NPs with different metal cores were prepared from the sol−gel method, and the aggregation of the particles was prevented successfully during synthesis. Ag^{+}, Au^{3+}, and Pt^{4+} have been reduced to metals with reducing agents, respectively. The primary objectives of this work were to control the particle size and its structure, followed by nano-scale characterization. Particles' agglomeration was prevented by incorporating a surfactant capable of improving the dispersion of the final product. This process has the additional advantage of improving the wetting and dispersion of the surface of the engineering NPs. To maintain the stability of the colloidal system, the interlayer repulsive force must be dominant, relative to attractive van der Waals forces resulting from dipole moments between the noble metal ions and H_2O molecules (Fig. 3.7). Dispersing agents, such as GA polymers, are adsorbed onto the particle surface and weaken van der Waals forces. Significant steric repulsion prevents NPs from adhering, and the particle surface is separated as a result [62].

2.2.3.6 Colloidal oxide particles

A significant number of research on colloidal oxide materials used in abrasion-resistant coatings on polymeric ophthalmic lenses has been carried out. It was found that the coatings can be tintable and/or UV curable [63]. Colloidal particles other than silica (SiO_2), titania (TiO_2), zirconia (ZrO_2), and aluminum oxide (Al_2O_3) have also been doped into siloxane (with formula $H(OSiH_2)_nOH$ and $(OSiH_2)_n$) matrices [64]. Previous research indicates the presence of silica colloids in gels facilitates the deposition of thick coatings, and their thickness can be totaled at 300 μm [65]. The colloidal particles can prevent/

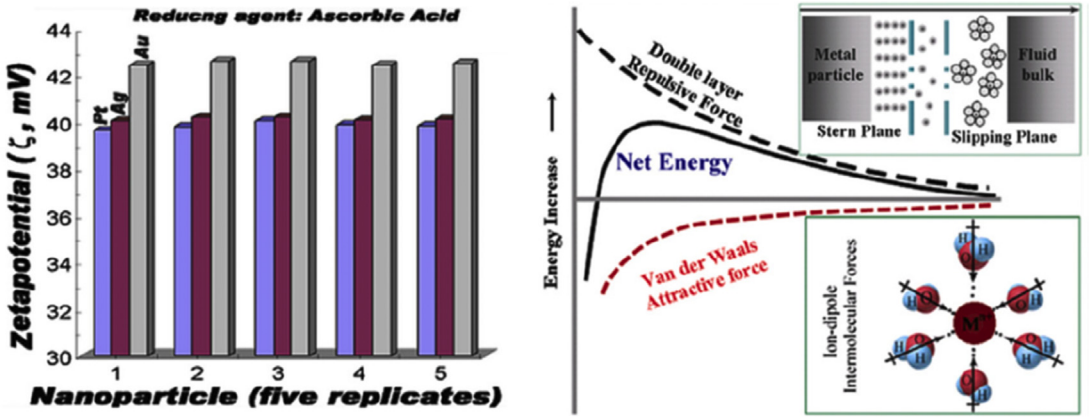

Figure 3.7

Sol-gel-derived noble metals using ascorbic acid, citric acid, coffee, and tea extract as reducing agent and gum Arabic as dispersing agents, left-hand panel: the zeta-potential of Ag, Au, and Pt; and right-hand panel: the stability of the colloidal system due to the double layer repulsive forces relative to attractive van der Waals forces.

mitigate the cracking observed during the drying phase of a SiO_2 gel synthesis. Large bulk oxide colloidal particles can be produced for different end applications [20]. The sol–gel process is also employed to produce glass monoliths by "alkoxide-oxide colloidal sol to form molded aerogels" [66].

A recent development in this area is the synthesis of core–shell structures, in which the core and shell of an NP consist of different materials. The core may be a semiconductor, and the shell may be a metal or vice versa. Alternatively, the core may be an oxide, a polymer, or a dye, and the shell may be a semiconductor, a polymer, a metal, or so on. There are many possible ways to tailor the structure of these NPs. The sol–gel method is suited for the synthesis of such architectures. For example, the particles can be prepared by reverse microemulsion methods.

In some cases, a passivation layer, e.g., an amino-silane amorphous layer, is in contact with the core [67]. The optical properties of such core–shell structures are of great interest. For example, luminescent nanocrystals were interesting applications as light-emitting transparent materials. The addition of polymeric molecules (such as extracts from natural products) can effectively prevent particle growth. Followed by low-temperature heat treatment, high crystallinity can be normally achieved. This method applies to a wide variety of materials.

3. Emulsion synthesis

Microemulsions (Fig. 3.8) are thermodynamically stable, fluid, optically clear dispersions of two immiscible liquids such as oil and water [68,69]. Microemulsions form when a

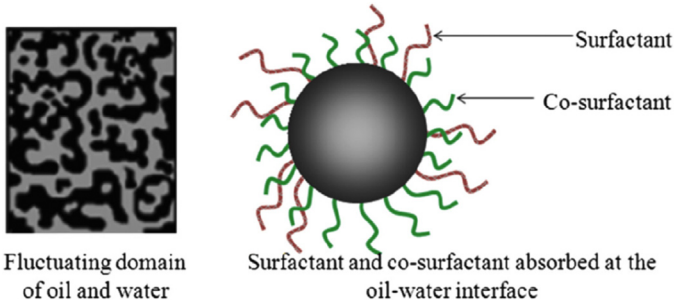

Figure 3.8

Represents a microemulsion processing, left-hand panel: fluctuating domains of oil and water, and right-hand panel: surfactant and cosurfactant molecules adsorbed at the oil/water interface.

surfactant, or more commonly a mixture of surfactants and co-surfactants, lowers the oil/water interfacial tension to less than 0.001 dyn/cm, allowing thermal motions to disperse the two immiscible phases [70] spontaneously. The term "microemulsion" has been defined by Danielsson and Lindmann [71,72] as "a system of water, oil, and amphiphile, which is a single-phase, optically isotropic and thermodynamically stable liquid solution." This definition is not universally accepted, and some researchers prefer to use the term microemulsion to refer to ultrasmall droplets in a medium. Since such droplets are usually in the nanometer size range, the term "nanodroplets" or nanoemulsion might be more appropriate. However, the Danielsson-Lindmann definition is helpful for systems where the structure of the medium is ill-defined or not known.

The main driving force for microemulsion formation arises from reducing the interfacial tension (interfacial free energy per unit area), which results from surfactant adsorption at the oil−water interface. However, unlike conventional emulsions, microemulsion domains fluctuate in size and shape and undergo spontaneous coalescence and split [73]. They exhibit aqueous continuous and bicontinuous structures, with typical equilibrium domain ("subphase") sizes ranging from 100 to 1000 Å [74]. Low surfactant concentrations produce microemulsions in equilibrium with excess dispersed phases, as shown in Fig. 3.9, while higher surfactant concentrations can microemulsify all dispersed phases. As a result, microemulsion systems may be represented as surfactant/oil/water mixtures, as were depicted in the pseudo-ternary phase diagram in Fig. 3.10 [75].

First described by Winsor [76], multiphase microemulsion systems are also important. These are in the "two-phase" region of the simplified phase diagram (shown in Fig. 3.9). As indicated in Fig. 3.9(2−4), there are three possibilities.

The affinity of the surfactant for oil or water at the interface is concentrated in a surfactant-rich middle phase (possibly bicontinuous), which coexists with oil and water phases containing low concentrations of droplets (w/o and o/w, respectively). The

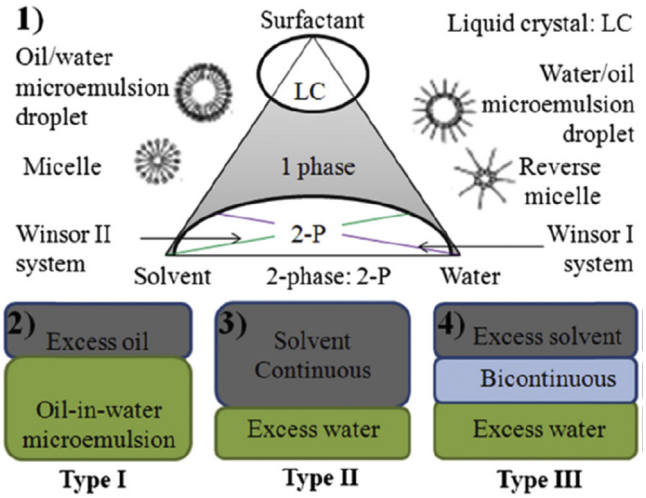

Figure 3.9

The triangle phase diagram and Winsor system, (1) hypothetical triangle phase diagram (at a constant concentration of cosurfactant) showing multiphase system at low concentrations (white), single-phase microemulsion (gray), and liquid crystal region at high surfactant concentrations (mottled), (2—4) summary of Winsor systems.

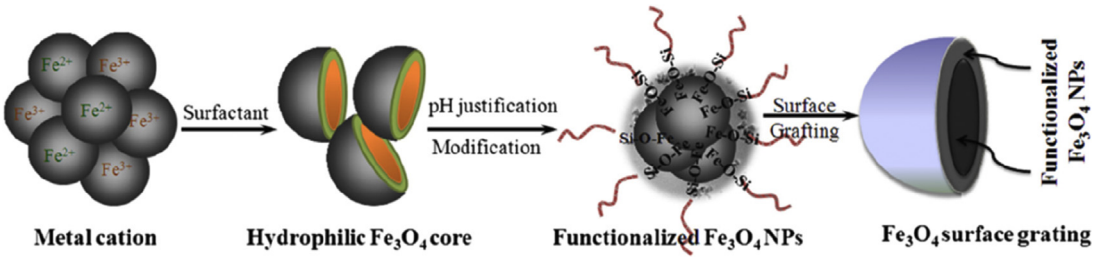

Figure 3.10

Microemulsion chemistry to produce mixed iron oxides. Restate: Inert gas (Ar) was introduced to prevent Fe^{2+} cation from being oxidized.

existence of this three-phase system is indicated by the presence of a triangle within the two-phase region (Fig. 3.9(1)). The technologically useful microemulsions often require high surfactant levels to provide sufficient interfacial coverage to completely microemulsify the required levels of ingredients and provide sufficient formulation stability to temperature and compositional changes to meet practical storage and use requirements [77,78]. However, high surfactant levels are often not acceptable for economic or performance reasons. For example, high surfactant levels in consumer product formulations may leave unacceptable residues on substrates. In chemical reaction media, high surfactant levels may constitute contaminants that need to be removed, resulting in unacceptable process costs.

There are two types of microemulsions, water-in-oil, and oil-in-water emulsion. In the water-in-oil microemulsion, NPs are scattered in the oil phase and stabilized by surfactants. This method has been widely used to prepare iron oxide (Fe_3O_4) MNPs. In the water-in-oil microemulsion, the liquid stage is scattered as microdroplets (ranging from 1 to 50 nm) encompassed by a monolayer of surfactant particles in the ceaseless hydrocarbon stage. The degree of molar ratio between water and surfactant is the factor to determine the size of the reverse micelle (shown in Fig. 3.9(1)). Two indistinguishable water-in-oil microemulsions can be mixed evenly to produce microdroplets. In the emulsion, the desired reactants are included.

Further, the microdroplets can be consistently combined and "deformed," leading to precipitations of final products in the micelles. If solvents (such as acetone or ethanol) were added to the microemulsions, the precipitate concentration could be elevated by centrifugation. In this case, a microemulsion can be used as a nanoreactor to prepare NPs. For example, if two reactants A and B are disintegrated in aqueous solutions of two similar water-in-oil microemulsions, an AB_x precipitate will be produced. The formed droplets will limit the size and shape of the precipitate. In our research, the synthesis of Fe_3O_4 MNPs (Fig. 3.10) was carried out using a dispersing agent to yield a microemulsion. The starting materials were primarily dispersed in an aqueous solution. The introduction of inert gas can prevent redox reactions, while gases like O2, NH3, and CO_2 can form metal oxides into the microemulsion [79].

The microemulsions show unique physical properties, allowing them to be used in applied sciences. In the microemulsion, universal solvents, three distinct domains are found: (1) a polar domain in which polar materials may be dissolved, (2) a nonpolar domain in which nonpolar materials may be dissolved, and (3) an interfacial domain where amphiphilic materials can be dissolved and where polar and nonpolar materials may be brought into proximity. Therefore, the microemulsions can dissolve materials of widely distributed polarities in the same solution. Microemulsion can be used to produce different systems: (1) superparamagnetic colloids, (2) nanocontainers, (3) cancer theragnostic materials, and (4) nanomagnets.

3.1 Superparamagnetic colloids

Du and coworkers reported the development of MNPs with core−shell structure, optimizing the feasible colloidal synthetic variables. The outstanding magnetic properties of grafted iron oxide (Fe_3O_4), restored close to the bulk value, have led to their use in cancer diagnosis and targeted drug delivery. The optimized synthetic pathways allow a controlled production of Fe_3O_4 with anticipated particle size, morphology, crystallinity, and chemical composition, which collectively result in desired magnetic properties. An improved preparation process of core−shell Fe_3O_4 MNPs through facile chemical

approach was reported, including major steps: (1) A complex between Fe^{3+} and Fe^{2+} cation and a ligand, that is the functional group of a surfactant as dispersing agent (octylphenol polyoxyethylene ether-ten OP-10), is formed in an aqueous solution; (2) the metal ions (Fe^{3+} and Fe^{2+}) were purged in inert argon gas to prevent Fe^{2+} from oxidation; (3) the hydrophilic Fe_3O_4 NPs were then converted to hydrophobic via introducing the active sites; and (4) methyl methacrylate (MMA) monomer was then grafted onto the hydrophobic Fe_3O_4 core with a radical initiator (2,20-Azobis(2-methyl propionitrile)). The experimental results found that the monodispersive and ultrafine Fe_3O_4/KH570/MMA NPs (7.5 nm) were obtained, whereas KH570 was the silane coupling agent (3-glycidoxypropyl trimethoxy silane). The oxidation of Fe^{2+} cations has been successfully prevented using an inert gas, while agglomeration of the Fe_3O_4 NPs using a dispersing agent (OP-10) as is shown in Fig. 3.10.

Fe3O4/KH570/MMA's major improvement lies in the colloidal synthetic atmosphere, achieving simplicity in experimental setup and efficiency in NPs preparation. This research aims to create ultrafine and homogeneous Fe_3O_4/KH570/MMA MNPs with mono-distributed and optimized composition to improve the paramagnetic properties of MNPs. Additionally, to allow for grafting polymerization, the surface of Fe_3O_4 NPs was required to be hydrophobic, which was accomplished via introducing active sites. Amphiphilic groups within silane coupling agent KH570 will introduce hydrophobic groups surrounding the Fe_3O_4 surface. This allows for easy grafting MMA monomer onto the surface of the Fe_3O_4 core. Furthermore, this leads to the functionalization of the MNPs surfaces via introducing the active sites for polymerization of MMA monomer. Consequently, the MMA monomers were grafted onto the hydrophobic Fe_3O_4 core using 2,2′-Azobis(2-methylpropionitrile) [80]. Transmission electron microscopic images of Fe_3O_4 (Fig. 3.11(1−4))) and grafted Fe_3O_4 NMPs indicated that near-spherical and monodispersive particles were formed. The ring pattern (Fig. 3.11(2)) and lattice fringe (Fig. 3.11(3)) of Fe_3O_4 NMPs collectively indicated the nanomagnetic particles are highly crystalline, which is well-indexed by X-ray powder diffraction (XRD) analyses. The above diffraction ring pattern confirmed the formation of highly crystalline Fe_3O_4 NMPs. These patterns result intrinsically from polycrystalline units. Its particle size averaged at 6.0 nm (determined from Fig. 3.11(4)), corresponding to the calculated results from XRD full width at half maximum.

Similarly, the TEM morphological analyses indicated that the grafted Fe_3O_4 NMPs (Fig. 3.12(1)) are also highly crystalline with a spherical appearance. This observation suggests that grafting maintains the morphology of the NMPs very well. Its particle size increased to 7.5 nm due to the surface attachment of the MMA polymer monomer onto the Fe_3O_4 NMPs (Fig. 3.12(2)).

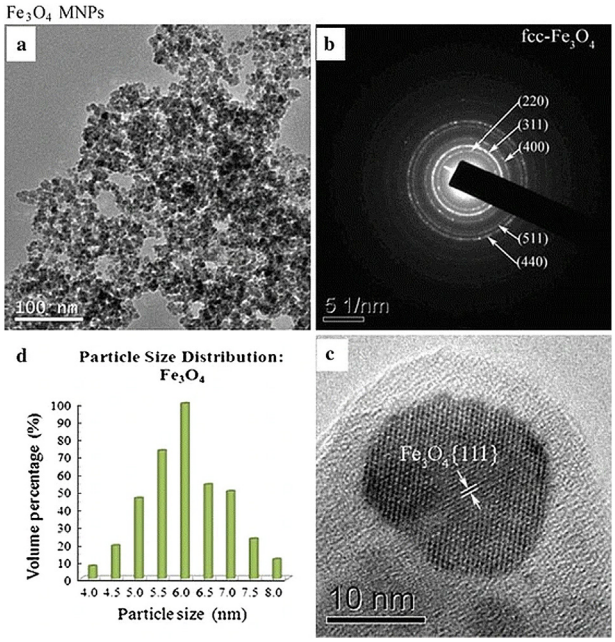

Figure 3.11

Morphological analyses and particle size distribution of Fe_3O_4 magnetic nanoparticles (MNPs), (1) TEM imaged, demonstrating the pseudo-spherical nanoparticles; (2) the ring pattern resulting from Fe_3O_4 polycrystals, indicating the high crystalline phase structure of the MNPs; (3) the lattice fringe of Fe_3O_4 MNPs, proving the high crystallinity; and (4) particle size averaged at 6.0 nm, with distribution ranging from 4.0 (8.7 vol%) to 8.0 nm (12.5 vol%) of the Fe_3O_4 MNPs. *Images were adapted from Ref. [80].*

3.2 Nanocontainers

Feldmann's research group recently reported that nanoscale hollow spheres are most prepared by precipitation of a shell representing the spherical wall later on a solid template. Accordingly, mono-dispersed, nonagglomerated, and nano-scaled templates, such as silica [82–84], elemental metals (e.g., Fe, Ag, Au, Pt) [81,85], quantum dots (e.g., CdSe) [86,87], or organic polymers (e.g., polymer lattices) [88–91] are prerequisite. Elemental Au, copper sulfide (CuS), aluminum oxyhydroxide (g-AlO(OH)), and tin oxide (SnO_2) are produced as nanoscale hollow spheres via the microemulsion approach. Although the synthesis differs in detail (use of water/oil (w/o) or o/w microemulsions, type and concentration of reactants, concrete duration, and temperature of reaction), the broad adaptability of the microemulsion approach resulting in metals, sulfides, and oxides is obvious. Since hollow spheres exhibit large specific surface, low specific weight, container-type morphology, and applications in catalysis, gas storage, low-weight building materials, or drug delivery, this synthetic approach can be upscaled to meet the anticipated demand of increased usage of hollow spheres [92].

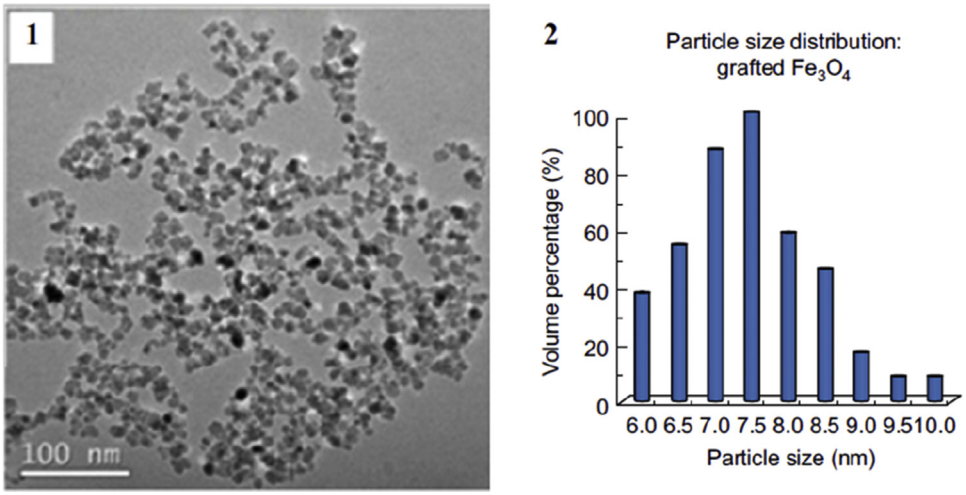

Figure 3.12

Transmission electron microscopy (TEM) morphological analyses and particle size distribution results of grafted Fe_3O_4@KH570-MMA, (1) TEM images of grafted Fe_3O_4 magnetic nanoparticles (MNP), suggesting pseudo-spherical morphology were maintained upon surface grafting and (2) the particle size distribution of the grafted Fe_3O_4 averaged at 7.5 nm. Particle distribution ranged from 6.0 (38.5 vol%) to 10.0 nm (10.2 vol%). The particle size increased from 6.0 to 7.5 on average due to the polymer layer formed on the Fe_3O_4 MNPs surface. *Images were adapted from Ref. [81].*

Electron microscopy images as an overview show a variety of nonagglomerated particles, exhibiting mean diameters of 25 ± 3 nm (Au), 25 ± 6 nm (CuS), 30 ± 5 nm (g-AlO(OH)), and 20 ± 3 nm (SnO_2) (Fig. 3.13(1)). These values are deduced based on a statistical evaluation of at least 100 particles. The presence of hollow spheres is evidenced by high-resolution TEM images (Fig. 3.13(2)), showing spherical to slightly ellipsoidal particles with outer diameters of about 21−23 nm (Au), 23−32 nm (CuS), 21−25 nm (g-AlO(OH)), 15−20 nm (SnO_2), and wall thicknesses of 2−3 nm (Au), 5−11 nm (CuS), 5−7 nm (g-AlO(OH)), and 3−5 nm (SnO_2).

3.3 Cancer theragnostic materials

This is a rapidly growing application in nanobiotechnology and nanomedicine of designing biocompatible mesoporous silica NP s (MSNs) for disease therapy and diagnosis [94]. As nanocarriers, MSNs with unique mesoporous structures have been explored as effective drug delivery systems for a variety of therapeutic agents to fight against various diseases, including bone/tendon tissue engineering [93−96], diabetes [97,98], inflammation [99], and cancer [100]. Through much effort, MSNs have been proven to possess unprecedented advantages by the US Food and Drug Administration (FDA) in 1995 for treatment of

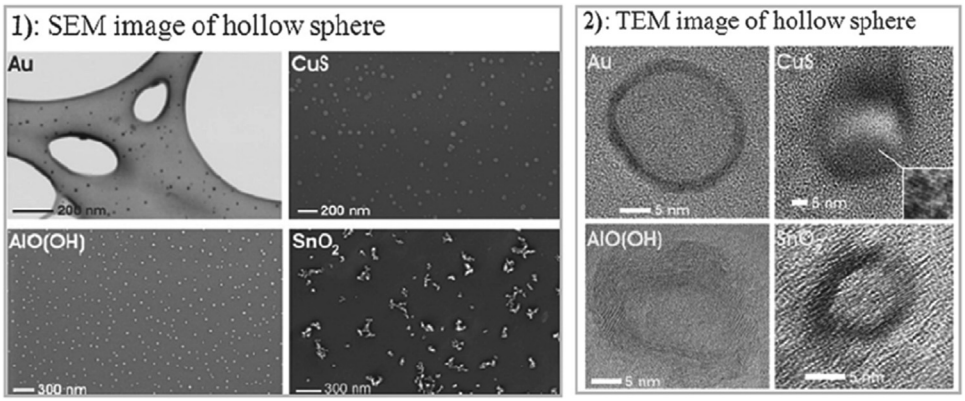

Figure 3.13

Electron microscopy overview of various nanoscale hollow spheres on holey carbon film copper grids (Au: transmission electron microscopy (TEM)) and silicon wafers (CuS, AlO(OH), SnO_2), (1) the scanning electron microscopy (SEM) image and (2) HRTEM image of the above hollow spheres. *Graphs were adapted from Ref. [93].*

refractory Kaposi's sarcoma (recurrent breast cancer and ovarian cancer) and Abraxane (albumin-bound paclitaxel) with a mean particle size of approximately 130 nm, which the FDA approved in 2005 for metastatic breast cancer. Here, key factors blocking the clinical translocation of laboratory-developed nanoformulations are the lack of long-term testing and appropriate animal models [101,102]. The first major hurdle is developing nanocarriers that encapsulate sufficient therapeutic agents with the activated release. Second, it is difficult to deliver the NPs efficiently to the desired location in the context of multiple in vivo physiological barriers. Third, the toxicity of engineered nanomaterials remains a pendant problem. Fourth, a prerequisite for industrial production and clinical translocation is the cost-effective and scalable fabrication of well-dispersed NPs, which is currently still a great challenge. To realize the clinical translocation of the developed nanoformulations [103].

Our study focuses on the MNPs used in the cancer theragnostic. It is commonly recognized that nanotechnology, a science to construct a small world, unlocks a new frontier in cancer research [104–106]. Magnetic nanomaterials will lead to a revolutionary opportunity to attack cancer cells at the cellular and genetic level with much greater precision and fewer side effects [107–109]. Encapsulating NPs with natural products extracted from traditional Chinese medicine (Cordyceps) will offer a creative approach to curing breast cancer. A long history of its medicinal use has proved that therapeutic applications of Cordyceps and their extracts are based on the key effects of increased oxygen utilization, increased adenosine triphosphate (ATP) production, and stabilization of blood sugar metabolism [110–113]. Synergistically, an anticancer camptothecin analog

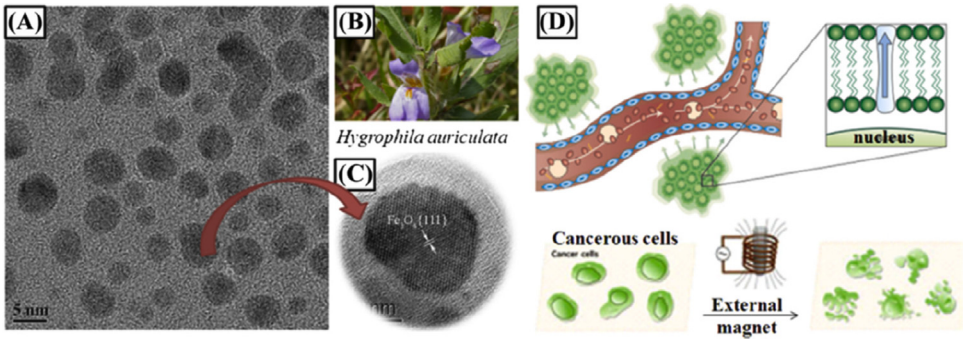

Figure 3.14

Magnetic nanoshells with controlled size at 6 nm will preferentially concentrate in cancer lesion sites, (A) the overview of core-shelled Fe_3O_4 magnetic nanoparticles coated by the *Hygrophila auriculata* extracts; (B) an image of *Hygrophila auriculata* Indian medicinal plant; (C) magnified core-shelled Fe_3O_4 magnetic nanoparticles; and (D) mechanistic study of nanocancer theragnostic (1) due to leaky endothelium, (2) when the magnetic field is applied.

(SN38) will be embedded onto the particle surfaces to advance the efficacy of targeted cancer treatment. However, the therapeutic action of NPs to reach their intended destinations is largely prevented due to several challenging biological barriers, such as the reticuloendothelial system, endothelial/epithelial membranes, complex networks of blood vessels, and interstitial pressure gradients [114,115]. We implement a strategy to treat drug-resistant tumors using combinatory therapeutic agents with different mechanisms for synergistic effect [116–118] to overcome these drawbacks.

In vitro cytotoxicity of chitosan-modified magnetic NPs (CS-MNPs) to various breast cancer cell lines will be determined by methyl thiazole tetrazolium (MTT) assay and compared with epithelial cells from the mammary gland (MCF-12A) cells. Briefly, the cells will be incubated with different concentrations of the CS-MNPs for a predetermined time. MTT (0.5 mg/mL) solution will be added and incubated for an optimized period. A known amount of dimethyl sulfoxide will be added to dissolve the formed formazan crystals. The optical density will be tested using a microplate reader with a 590 nm excitation wavelength and 650 nm background. The viability of cells exposed to the CS-MNPs will be presented as percentages of the viability of cells grown in a normal growth medium. The damaged cells will be characterized by TEM to visualize the mechanism of cancer cell damage (a hypothesized mode was shown in Fig. 3.14).

3.4 Nanomagnets

The core–shell nanostructures and magnetic properties could be tuned for unique end applications according to their desired physical properties. Our current research found that the magnetic Fe_3O_4 core shells are potentially applicable for cancer diagnosis and targeted

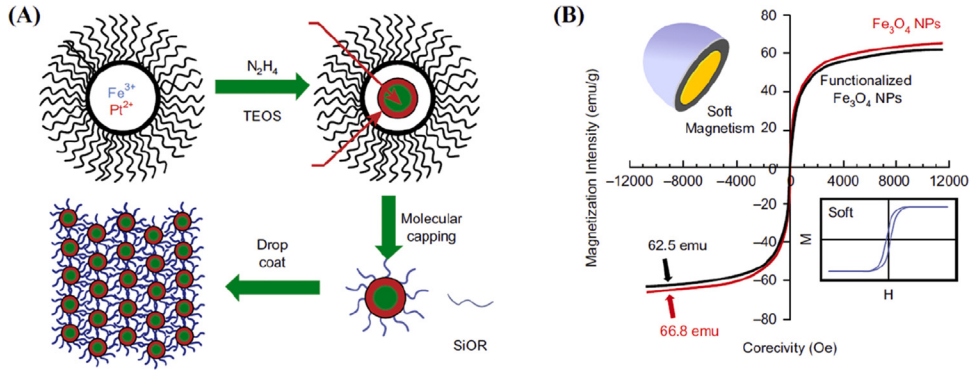

Figure 3.15

Functionalization of magnetic nanoparticles (MNPs) derived from a reverse microemulsion to adjust their magnetism, (A) synthesis, functionalization, and assembly of FePt-silica core/shell NP s from microemulsions. The core-shelled particles were formed through a redox reaction. Subsequent functionalization with dimethoxyorganosilanes facilitates the formation of ordered assemblies of nanoparticles; (B) soft magnetism of Fe_3O_4 MNPs and functionalized Fe_3O_4@KH570.

drug delivery, as mentioned above, which are generally carried out in the magnetic field to position the diseased region. The MNPs are needed for ferromagnetic behavior to ensure their conveying properties [119,120]. First, the ultrafine sizes allow Fe_3O_4 MNPs to interact with biological molecules and systems and to be moved under an external magnetic field gradient. It was found that the biological molecules or cells can be further isolated and moved under magnetic fields. Therefore, biomolecules of interest can be concentrated in solutions via specific binding with molecules, which were precoated on the surface of MNPs. Drugs can be delivered to the targeted region noninvasive to avoid damage to healthy cell lines [121,122]. The targeted delivery can be achieved by specific binding between the drug molecules and cancer cells or localizing the MNPs. The external magnetic forces must be strong enough to overcome viscous drag within the vascular tissue to achieve this goal. Upon functionalizing these MNPs, their nano-magnetism (shown in Fig. 3.15) has opened a new paradigm for novel cancer treatment utilizing magnetism and noninvasive and targeted therapy methods. Our study suggested that surface functionalization, particle size, and magnetic properties are critical factors to determine the performance of MNPs. This work lies in our ability to control the morphology of the particles, optimize the formulations, and tune their magnetism to meet the requirements for specific applications [123,124].

3.5 Solvothermal and hydrothermal methods

Solvothermal and hydrothermal methods are two of the most extensively used to produce nanostructured materials. In the hydrothermal method, heterogeneous reactions are carried

out in an aqueous medium in a sealed vessel at high pressure and temperature [125−127]. Similarly, the solvothermal method seals reactants in a vessel, fostering a high pressure and temperature for the reaction. However, a nonaqueous solvent is used in the solvothermal method.

The solvothermal and hydrothermal methods require the starting materials, including metal salts and dispersing agents, to be mixed in a solvent. Especially, acid is added in the synthesis of Pt NPs. The well-dispersed solution is transferred to an autoclave or a vessel, sealed later. The reaction container is then heated to initiate the reaction, and the temperature is usually above the solvent's boiling point. After the reaction, the container is cooled to room temperature. The precipitate is separated and washed with solvents to yield NPs.

The one-pot synthetic step makes solvothermal and hydrothermal methods easily applied in NP synthesis. Nevertheless, compared to other methods, there are fewer factors that can impact the properties of the synthesized NP s, that is, size distribution, surface functionalization, and nanostructure. Temperature, solvents, dispersing agents, and modulating agents are the major factors considered in a one-pot solvothermal and hydrothermal reaction. Solvents need to be compatible with the reaction temperature and be capable of dispersing the reactants. To avoid safety hazards, the reaction temperature is no more than 50°C higher than the boiling point of the solvents.

Platinum NPs are widely studied since they have extensive applications in catalysis, energy conversion, and fuel cells. Chen et al. summarized their hydrothermal and solvothermal syntheses. They are template-less and surfactant-free approaches to fabricate nanomaterials. The majority of Pt-based nanomaterials are synthesized from $H_2PtCl_6 \cdot xH_2O$ and $Pt(acac)_2$ via hydrothermal [128−144] and solvothermal [145,146] methods, respectively. Chen et al. [138] prepared nanoporous Pt networks by hydrothermal-assisted seed growth, where Pt NP s were synthesized onto a titanium substrate via the electrochemical deposition conditions: 20 mA cm^{-2} for 3 min. The solution contains 0.8 g L^{-1} H_2PtCl_6 and 0.3 g L^{-1} HCl. The NPs were later deposited onto a titanium substrate by placing the substrate inside the Teflon lined vessel with 0.8 g L^{-1} H_2PtCl_6 and 0.3 g L^{-1} HCl solution, and ethylene glycol, and heating the container to 100°C for 10 h. The as-synthesized Pt nanomaterials showed diameters ranging from ten to hundreds of nanometers and formed a nanoporous network on the Ti substrate. The nanoporous Pt networks possess a large electroactive surface, contributing to their enhanced electrocatalytic properties than polycrystalline Pt.

Recently, microwave-assisted solvothermal and hydrothermal reactions have seen a large development. Microwave is the electromagnetic wave between the infrared radiation and radio waves with the frequency at 300 MHz−300 GHz, and the wavelength range is 1 m−1 mm. Under electromagnetic fields, the particles of materials can generate

Table 3.4: Summary of different heating methods.

Methods	Temperature/°C	Time	Pressure/MPa	Reaction system
Hydrothermal	100–300	Hours-days	20–100	Close
Microwave	100–200	Min-hours	101.325 kPa	Open
MH methods	100–300	Min-hours	20–100	Close

polarization, such as electron polarization, atom polarization, orientation polarization, and space charge polarization. Unlike traditional methods, microwave heating is rapid volumetric heating without a heat conduction process, indicating uniform heating. Zhu and Chen have discussed the microwave-assisted preparation of inorganic nanostructures in aqueous solution polyols ionic liquids, mixed solvents, etc. [147]. The following Table 3.4 compares traditional heating methods and microwave heating characteristics. Lin et al. reported the microwave-assisted hydrothermal synthesis of functional nanomaterials from a spectrum of metal oxides [148]. Their applications are correspondingly introduced, including gas sensors, catalysis, electrochemistry, solar cells, and optics. Metal composite oxides were studied [148], with their applications in photocatalysis, electrochemistry, optics, and inorganic biomaterials discussed. The microwave-assisted synthesis proves a more efficient and energy-reserving synthetic method for NP s synthesis, which remains to be more deeply explored by other researchers.

4. Vapor phase deposition

The vapor deposition (shown in Fig. 3.16) process is used to produce solid materials with high purity and excellent performance, such as thin films, multilayers, nanotubes, nanofilaments, and NPs [149,150]. Generally, this technique can be classified into physical

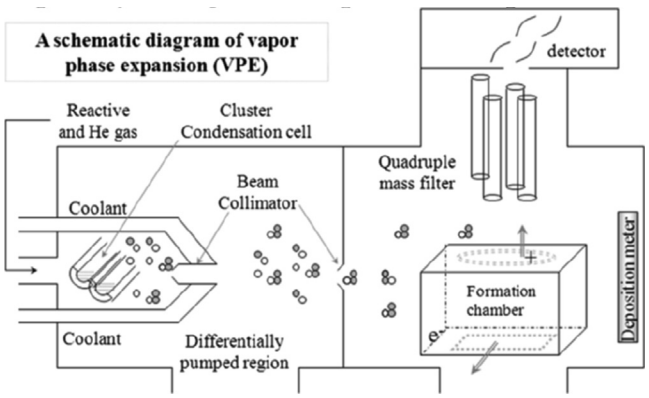

Figure 3.16
Scheme of vapor phase expansion (VPE).

vapor deposition (PVD) and chemical vapor deposition (CVD) [151]. The PVD converts solid materials into the gaseous phase through a physical process. These gaseous materials are then cooled down and deposited on a prepatterned substrate. The gaseous reaction can occur through thermal evaporation via resistive or electron beam heating or flame. Another approach is by LASER ablation or pulsed LASER deposition, where a short nanosecond pulse is focused on the surface of the target. Spark erosion and sputtering methods also remove target materials by bombardment with atoms/ions [152]. Subsequently, the gaseous species is deposited onto a substrate [153].

CVD is a chemical process used to produce high purity and higher performance substances. CVD involves thermal decomposition or other chemical reactions of gas-phase species, occurring at elevated temperatures, ranging from 500 to 1000°C. This CVD allows for deposition of target product using a substrate exposed into the volatile precursor, as indicated above. The CVD-deposited materials vary from monocrystalline, polycrystalline, amorphous, and epitaxial. Materials with different elemental compositions can be produced by CVD, such as silicon, carbon fiber, filament, silica (SiO_2), silicon-germanium (Si−Ge), tungsten (W), silicon carbide (SiC), titanium nitride (Ti_3N_4), various high-K dielectrics, and synthetic diamond [154].

In the conventional CVD technique, the whole substrate is heated, and the reactant gas or vapor is flown over the substrate surface, where chemical reactions occur and the film is deposited. This process is slow (the film growth rate is 100−1000 Å/min) and is not an energy-efficient process since the whole substrate is heated, but only the hot surface is used to carry out the film deposition. In this technique, the substrate temperature can be as high as 1500 K, depending on the chemical reaction temperature of the precursors and the properties of the film. Since the diffusion coefficients of the dopants become significant when the temperature exceeds 1100 K, such high temperatures affect the quality of semiconductor films because of the change in the impurity concentration profiles due to the diffusion of dopants into the film [155]. Also, contaminants may present inside the CVD chamber, or the wafer material can diffuse into the film grown at high temperatures.

The volatilities of various species used for deposition compound semiconductor films are different. Therefore, at high temperatures, the species will evaporate in different amounts during the film deposition process, which can affect the properties of the film. Physical damage to the wafers at high temperatures can also cause defects in the devices produced by the conventional CVD method. CVD deposit materials can be formed from monocrystalline, polycrystalline, amorphous, and epitaxial. Materials produced by CVD are highly diversified, including silicon, carbon nanotubes (CNTs) [156].

Liu and her collaborators employed the CVD (Fig. 3.17) method to synthesize the aligned CNTs (ACNTs). In this process, a two-compartment tube furnace was utilized. The reactants were vaporized at the first compartment and maintained at the second one to

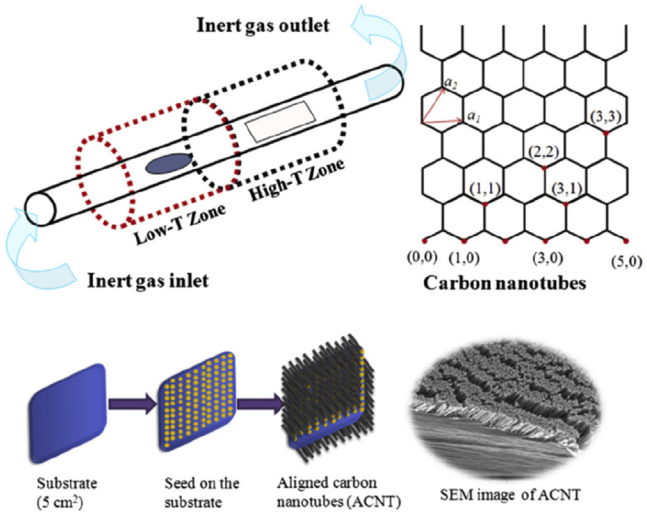

Figure 3.17
Preparation of aligned carbon nanotubes (ACNTs) using a chemical vapor deposition.

deposit the ACNT on the surface of the glass substrate. This process of two furnace steps is used to control the length and diameter of ACNTs. The length and diameter of ACNTs are critical to gas transport and water management in the fuel cell [157]. The precipitation of carbon leads to the formation of tubular carbon solids in an sp^2 structure, which provides the molecules with their unique strength. Our results show that the impurity of CNT can be controlled in a bifurcated furnace.

Moreover, in this study, ferrocene was used as ACNTs seeding material. Here, the product of oxygen partially reacted with the ferrocene, which decreased the efficiency of the fuel cell due to oxygen loss but maintained ACNT integrity. The ACNTs are synthesized using CVD with a xylene-ferrocene solution as the precursor. Xylene is the carbon source, while ferrocene provides the iron metal NPs, which function as the seed catalysts for the growth of the nanotubes. Three 5 cm^2 quartz substrates are placed inside the quartz reaction tube. The tube is placed in a two-stage furnace and tightly sealed from air. The first stage of the furnace is at a temperature of 225°C, which suffices to vaporize the solution. The second stage is held at 725°C and used to carbonize the vaporized solution, depositing the iron NPs on the quartz substrates and allowing the CNTs to grow along with the iron seeds [158]. The solution with the chemicals is injected into the reaction tube, on the low-temperature stage, using argon and hydrogen as the carrier gases, at flow rates of 100 and 50 mL/min, respectively. The chemicals injection rate is selected to be maintained at 0.225 and 0.250 mL/min, respectively [159].

Different catalysts can play greatly different roles in generating nanomaterials via the CVD method. The difference can result in different morphologies or even different types

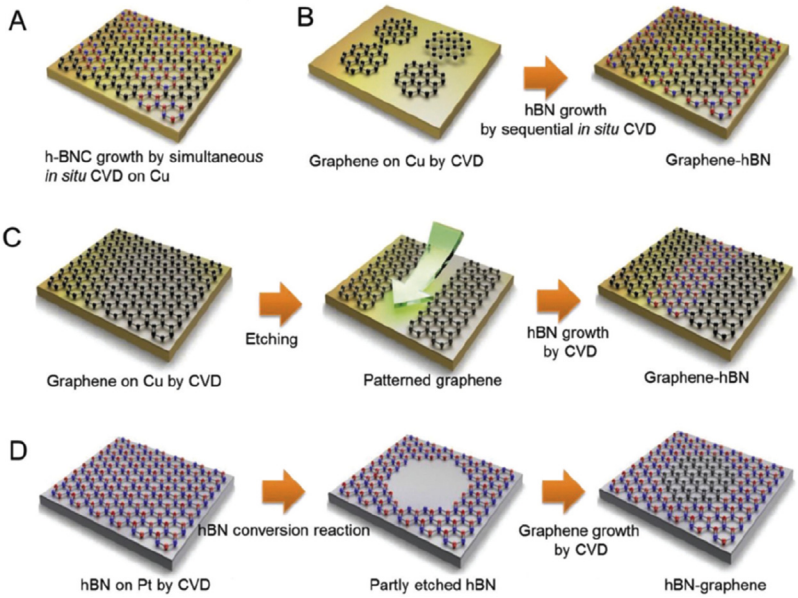

Figure 3.18

A schematic diagram of the growth of in-plane graphene and h-BN heterostructures via various techniques: (A) simultaneous in situ chemical vapor deposition (CVD) growth, (B) sequential in situ CVD growth, (C) lithography-assisted growth, and (D) conversion growth. *Adapted from Ref. [161].*

of nanomaterials. For example, Ni and Co can result in multilayer graphene to prepare graphene using a CVD method, while Cu will provide the monolayer product [160]. The materials that CVD can produce are not just limited to carbon materials. Other two-dimensional materials can be synthesized, as listed in Fig. 3.18 [161].

5. Molecular beam epitaxy

Several methods can be used to deposit single crystals on the substrate. One of them is using MBE. In this method, the thin film can grow epitaxially under the ultrahigh vacuum (for example, at 10^{-8} Pa) and with an ultraslow deposition rate (<1000 nm/h) [162]. The slow deposition rates require a proportionally ultrahigh vacuum to achieve impurity like other deposition techniques. Ultrapure elements (Ga and As) are heated in separate quasi-Knudsen effusion cells in a solid source MBE. These elements begin to sublimate into a gaseous state slowly. These gaseous elements then interact with the wafer for condensation by reacting with each other. For example, single-crystal gallium arsenide is formed when gaseous Ga and As react while condensed on the wafer. In the MBE technique (shown in Fig. 3.19), molecular and/or atomic "beams" of the precursors impinge on the surface of a single-crystal sample, which is heated suitably to facilitate the film growth process. In this

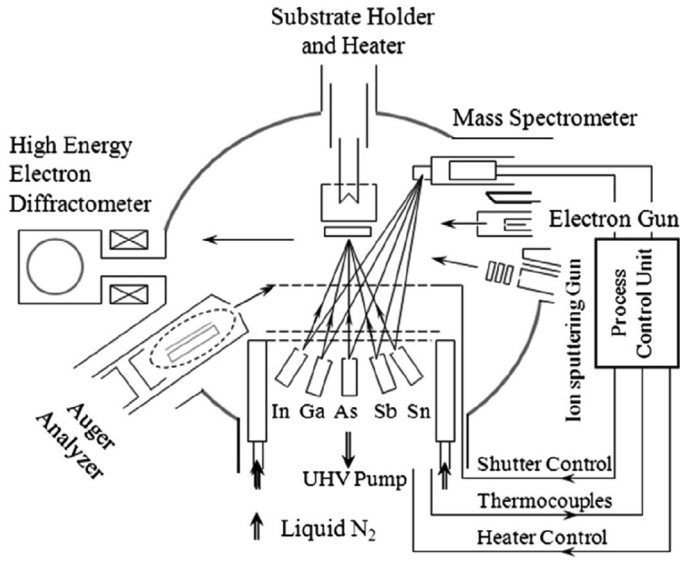

Figure 3.19
Scheme of a molecular beam epitaxy is commonly used to produce semiconductors under ultrahigh vacuum.

case, the "beam" means that evaporated atoms do not interact with each other or vacuum chamber gases until they reach the wafer due to the long mean free paths of the atoms [163]. The research data indicated that chemical reactions mainly occur on the surface of the substrate. The appropriate selection of a single crystal as the substrate provides a platform for the product film to grow epitaxially. As mentioned above, the pressure inside the growth chamber is very low (averaged about 10−11 torr). It is critical to control the MBE technique to grow epitaxial film, where their composition can be regulated to the monolayer level [164]. This MBE technique is beneficial to produce semiconductors composed of group III and V elements such as Ga, indium (In), As, phosphorous (P), and antimony (Sb).

Significant studies have been carried out to produce semiconductors and devices consisting of Si and Ge, II-VI, and IV-VI compounds using this MBE method. However, the prolonged growth (approximately 100−200 Å/min) has hindered the broad application of the MBE process [165].

The epitaxial techniques of MBE and MOVPE are briefly discussed. These techniques allow monoatomic layers to deposition from appropriate substrate feed materials and thin films of semiconductors. One example, quantum well structures have been fabricated with almost perfectly abrupt interfaces. It was also found that the doping can be modulated to control the doping of desired layers [166]. Both MBE and MOVPE are used extensively to fabricate highly responsive transistors and other rapid-speed electro-optical and electronic

switching devices or semiconductor-based lasers. The quantum wires and dots can also be developed by this MBE method.

During operation, reflection high energy electron diffraction is often used to monitor in situ growth of the crystal layers [167]. A computer-assisted control will be placed in front of each furnace, allowing precise control of the thickness of each layer at a level of a single layer of atoms. Additionally, this method can produce complicated and precisely controlled layers composed of different materials. Precise control has allowed the development of structures where the electrons can be confined in a different dimension, further yielding quantum wells or quantum dots. These intricately layered materials play a critical role in many modern semiconductor devices, for example, semiconductor lasers, and light-emitting diodes [166].

To restate, one of the important MBE involves organometallic vapor phase epitaxy, metalorganic chemical vapor deposition (MOCVD), and organometallic chemical vapor deposition [167]. The MOCVD technique relies on the pyrolysis of semiconductor materials' different organometallic compounds and hydrides. Its operational principle is similar to the conventional CVD process. In this MOCVD (Fig. 3.20), low-molecular-weight metal alkyls are used as the source for metals (Group II and III elements) to produce films of III−V and II-VI compounds and alloys. Examples include dimethyl cadmium ($(CH_3)_2Cd$) or trimethylgallium ($(CH_3)_3Ga$) [168]. Other types of organometallic compounds (such as trimethyl indium trimethyl phosphine $(CH_3)_3In- P(CH_3)_3$) can be used as metal sources.

Additionally, hydrides (AsH_3, PH_3, H_2Se, or H_2S) or alkyls (trimethyl antimony ($(CH_3)_3Sb$) or diethyl tellurium ($(C_2H_5)Te$) are usually used as a source for the nonmetal semiconductor materials, composed of Group V and VI elements [169]. In the

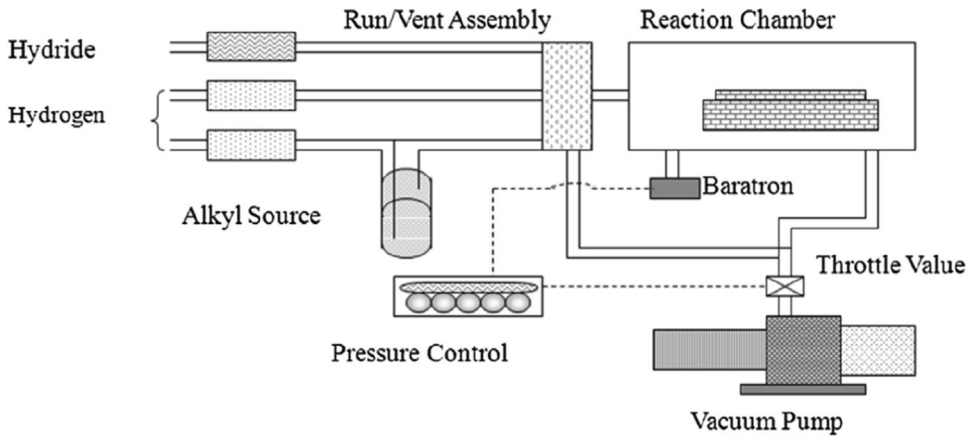

Figure 3.20
Scheme of a metal-organic chemical vapor deposition.

conventional CVD process, the vapor of the organometallic compounds is flown through a reaction chamber, where pyrolysis occurs at the surface of the hot substrate. The film deposition takes place on the substrate surface, which is heated. At the high temperature, the loss of film materials was detected due to evaporation and redistribution of dopants through diffusion. This loss of film elements affects the quality of the films fabricated using conventional MOCVD [170]. It is also important to point out that the deposition rate of the MOCVD process is very slow. The reproducibility of some of the properties remains to be improved. In addition, the difficulty of growing films with uniform layers over large areas raises other concerns related to the quality and uniformity of the as-is prepared surface [165,171]. These drawbacks hinder wide usage of the MOCVD application process in fabricating films and coated surfaces.

5.1 Metalorganic vapor phase epitaxy

Indium phosphide was found to grow in a reactor on a substrate by introducing trimethylindium ($(CH_3)_3In$) and phosphine (PH_3) by an MOVPE (as shown in Fig. 3.21) [172]. Formation of the epitaxial layer occurs by final pyrolysis of the constituent chemicals at the substrate surface. A vacuum is not needed, while the gas pressure must be controlled within a moderate range from 2 to 100 kPa. Thermodynamically, the formation of devices incorporates metastable alloys. This method becomes a dominant process for manufacturing laser diodes, solar cells, and light-emitting diodes [173].

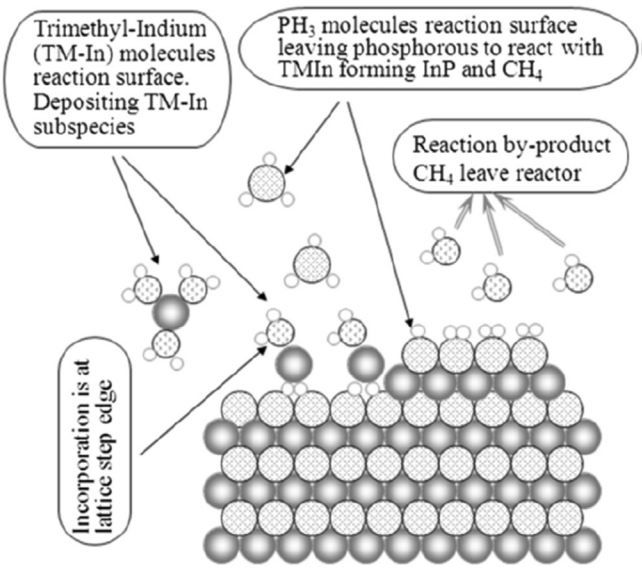

Figure 3.21
Scheme of a metalorganic vapor phase epitaxy.

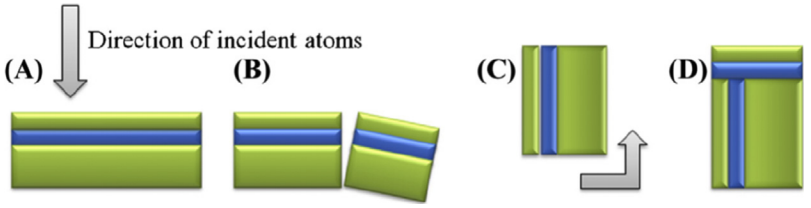

Figure 3.22
Cleaved-edge overgrowth in dimensionally confined structures, such as quantum wires, is through four general stages, (A) initialization of quantum well; (B) cleaving through in situ means; (C) structural reorientation; and (D) growth in the second dimension of additional well on the surface that has been cleaved.

Cleaved-edge overgrowth: Initiation with quantum well growth in an MBE reactor (Fig. 3.22). The wafer is then cleaved in situ along a plane normal to the well. The sample is rotated through 90 degrees, and a second quantum well and barrier are deposited on the cleaved surface. The two quantum wells form a T-shaped structure. At the intersection of the wells, the effective well width is increased slightly, resulting in a reduced potential, which traps both electrons and holes. As this potential minimum extends along the intersection of the wells, a quantum wire is formed. The initial growth of multiple wells followed by the overgrowth of the final well allows the formation of a linear array of wires. In addition, a second cleave followed by a further overgrowth step can be used to produce a quantum dot [174,175].

Growth on vicinal substrates: During the fabrication of crystalline nanosemiconductors, the orientation of flat surfaces occurs in a series of steps in either one or two dimensions. This step periodicity is influenced by the surface orientation ($<$20 nm). As stated earlier, epitaxial growth on vicinal or stepped surfaces results in the fabrication of spatially confined structures such as quantum wires (Fig. 3.23) [176], generated initially from the stepped surface deposition by MOVPE or MOVPE MBE fabrication techniques. Under suitable conditions, growth occurs preferentially at the step corners with the highest density of unterminated atomic bonds. Growth, consisting of a single atomic layer, proceeds laterally from the corner of the step. When half of the step has been covered, growth is switched to the barrier material used to cover the remainder of the step. Growth is then switched back to the initial semiconductor to increase the height of the wire. This growth cycle is repeated until the desired vertical thickness is obtained. Finally, the wire is overgrown with a thick layer of barrier material [177].

Strain-induced dots and wires: The material strain is where the uniform atomic spacing is distorted due to external stress to a material. With the correct sign, the strain reduces the bandgap. If the strain occurs over a small region, a local bandgap reduction occurs, resulting in a wire or dot formation. A strain can be produced by depositing a thin layer of

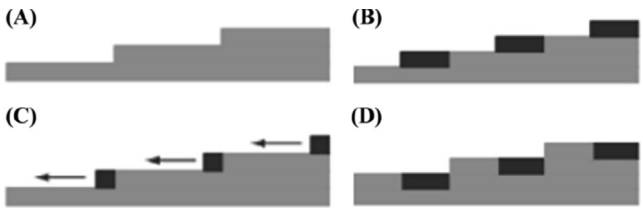

Figure 3.23
Orientation based growth on stepped or vicinal surfaces, (A) creation of initial periodic series of steps in one or two dimensions; (B) expansion of initial growth of confined structure such as a quantum wire in the step corner; (C) continuation of growth along the axial direction of the steps outward; and (D) growth in the second direction of step resulting on semiconductor barrier formation.

a different material (such as carbon) on the surface of a semiconductor. Because of their different lattice spacing, the materials distort near their interface to fit together. This distortion constitutes a strain, which extends a short distance into the bulk of the semiconductor [178]. If the carbon layer is patterned by lithography and then etched to leave only stripes or mesas, the resulting localized strain fields generate wires or dots in the underlying semiconductor. The remaining isolated regions of C are known as stressors. The strain only provides in-plane confinement, so it is necessary to place a quantum well near the surface to provide confinement along the third direction. Although this technique involves an etching step, it is only the optically inactive carbon layer that is etched, with the optically active quantum well spatially separated from any surface damaged region. Stressor-induced dots, therefore, exhibit high optical efficiency [179].

Electrostatically induced dots and wires: This technique of modulation doping results in two-dimensional sheets of electrons (or holes) that exhibit very high carrier mobilities at low temperatures (Fig. 3.24). The electron density of a two-dimensional electron sheet or gas (2DEG) can be modified by depositing a metal layer, known as a Schottky gate, on the surface of the semiconductor, and this gate can be patterned using electron-beam lithography followed by etching [180]. Applying a negative bias voltage to the gate repels the electrons of the 2DEG from the region immediately below the gate, forming a region depleted of free electrons. If two parallel but spatially separated metal gates (a split gate) are formed on the surface, biasing these gates depletes the regions below the gates but leaves a long, thin, underplated region directly below the gap between the gates. This underplated central region forms a quantum wire, consisting of a one-dimensional strip of free electrons [181].

When the gate voltage is increased, the area below the gates is depleted, extending outward in a horizontal direction. By adjusting the gate voltage, the dimension or width of the quantum wire can be controlled. If the width is made smaller in certain regions to alter

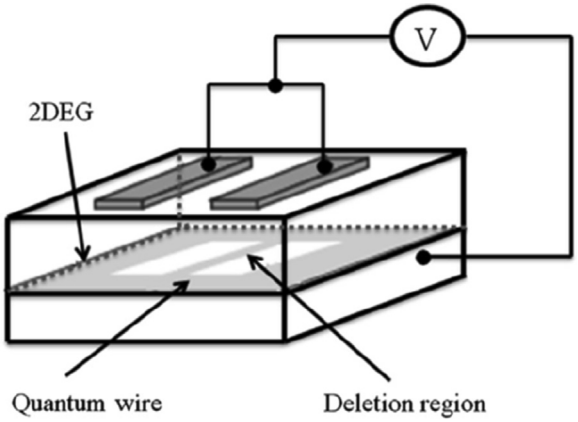

Figure 3.24
Illustration of split gate wire, where the quantum wire is formed due to electrons between the gates, with 2DEG remaining a distance from either gate.

the gap between the gates, quantum dots can be thus formed ("2DE"). Additional structural gating at both the bottom ("G") and at the top ("D") surface would enable the introduction of additional complexity into the material since both parallel surfaces can interact ("2DEG") through induction etching of the metal on the clean surface via the use of electrostatic forces. The advantage of this approach is that the semiconductor material is not etched, only the metal [182], allowing for low-temperature mobility of the carrier in confined or low-dimension systems. The low-temperature mobility is limited by their electronic properties, such as low spacing of the energy levels and shallow potential minima, to applications to cryogenic environments and is thus not used in optics.

6. Self-assembly techniques

The self-assembly technique is a process in which a disordered system of preexisting components forms an organized structure or pattern due to specific, local interactions among the components themselves, without external direction. Self-assembly (SA), in the classic sense, can be defined as the spontaneous and reversible organization of molecular units into ordered structures by noncovalent interactions. The first property of a self-assembled system is the spontaneity of the SA process: the interactions responsible for the formation of the self-assembled system act on a strictly local level; in other words, the nanostructure builds itself. An SA material can be generally classified into either static or dynamic methods. In static SA, the ordered arrangement of different particles will occur to reduce the system Gibbs free energy when the equilibrium is approached. At equilibrium, the static SA does not dissipate energy. Although the formation of a structure requires additional energy, it is stable after a structure is formed [183].

Principles of SA: SA, which is used to produce soft materials, relies on the fluctuations in the position and orientation of molecules or particles due to **Brownian motion** comparable to thermal energy. Thermal energy significantly influences the formation of soft materials at the nanoscale when the intermolecular forces are broken or reformed sometimes. This enables the system to reach thermodynamic equilibrium, often a nonuniform state. Because the intermolecular interactions between molecules are relatively weak (ranging from 10 to 600 kJ/mol), transitions from one structure to another can be carried out by changes in fabrication variables, such as temperature or pH. These external conditions can induce phase transitions, leading to "a host of responsive materials, or coupled with an appropriate source of energy to nanomechanical systems" [184]. It was found that the phase transitions between different structures in soft materials are highly diversified.

Derjaguin, Landau, Verwey, and Overbeek theory (DLVO theory): DLVO theory is widely used to evaluate the stability of a particle in solution. The particle stability is dependent upon its total potential energy function, VT. The DLVO theory indicates that VT is the sum of potential from solution, attraction, and repulsion (shown in Eq. 3.5) [185,186]:

$$V_T = V_A + V_R + V_S \tag{3.5}$$

V_A is the attraction potential, V_R is the repulsion potential, and V_S is the potential energy resulting from the solvent (in volts).

Notably, there exists a balance between V_A and V_R. These two contributions are potentially much larger and operate over a much larger distance in the system. On the other hand, the V_S contribution is marginal to the total potential energy and operates over the last few nanometers in the system. The attraction (van der Waals attractive forces) and repulsion (electrical double layer repulsive forces) potentials are described in Eqs. (3.6) and (3.7), respectively.

$$V_A = -\frac{A}{12\pi D^2} \tag{3.6}$$

A is the Hamaker constant (J), and D is the particle separation (m).

The repulsive potential, V_R, is a multicomponent function.

$$V_R = 2\pi\varepsilon_0 a_0 \xi^2 e^{-\kappa D} \tag{3.7}$$

where a is the particle radius (m), π is the solvent permeability (kg/m^{2}s) related to the double layer (ε, m), κ is a function of the ionic composition (mol/m^3), and ξ is the zeta potential (V). (Note: $\alpha_0/(4\pi\varepsilon_0)$ can be simplified to a volume (m^3) and a_0 (Jm^3) with other constants to cm^3/mol, unless otherwise defined.

DLVO theory indicates that the stability of a colloidal system is determined by the sum of these van der Waals attractive (V_A) and electrical double layer repulsive (V_R) forces. These

two forces exist between particles when they approach each other due to their Brownian motion. The DLVO theory proposes that the electrical repulsion as an energy barrier prevents particles from approaching each other and adhering together. This repulsion prevents particles from growth [187]. However, the particles will grow if they collide with sufficient energy to overcome the repulsive barrier. This attractive force resulting from van der Waals attraction will pull particles into contact. This attraction allows particles to adhere to each other firmly and irreversibly. In other words, particles will disperse if the repulsion is strong enough. This high repulsion allows for the dispersion to resist flocculation. Thus, the colloidal system will be stabilized due to high repulsion. On the contrary, the flocculation or coagulation will occur if the attraction is sufficiently high, resulting in particles growth [188].

The SA techniques can fabricate quantum dots or wires formed spontaneously under epitaxial growth conditions. It was found that the structures display high optical quality. The self-assembled quantum dots are suitable for a wide range of electro-optical applications [189]. The SA used to produce semiconductors involves growth on "prepatterned substrates." The flat semiconductor substrate is generally used as a starting material. An array of parallel stripes can be formed on the prepatterned substrate. The optical holography or electron beam irradiation can produce semiconductors with improved quality. An isotropically (influence in all directions) etch acid can attack different crystal surfaces at different rates.

By this method, arrays embedded with parallel V-shaped grooves were formed (Fig. 3.25A) [191]. The prepatterned substrate is then cleaned and transferred to a growth reactor to fabricate different materials. The SA has been widely used to produce soft materials. The formation of soft material indicates that the intermolecular forces between

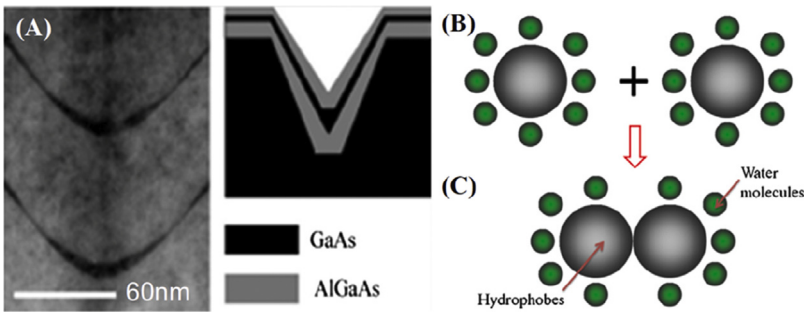

Figure 3.25

(A) Cartoon representing the cross-sectional area of a region of the quantum wire and actual transmission electron micrograph of twin stacked GaAs-AlGaAs V-grooved quantum wires. (B) A demonstration of hydrophobic effect and (C) hydrophobic interaction. *(A) The image was adapted from Ref. [190].*

molecules are evidentially weaker than the covalent bonds within the molecules [192]. However, the weak intermolecular interactions (van der Waals attraction) are responsible for the orderly arrangement of molecules in soft materials. These attractions, also known as van der Waals forces, include hydrogen bonds, ion-dipole forces, coordination covalent bonds between ligands and metal ions in the complexes, dipole—dipole interactions, and hydrophobic interactions.

The hydrophobic effect, "water-fearing," normally arises when a nonpolar solute is introduced into an aqueous solution. This hydrophobic effect (Fig. 3.25B) can be defined as the aggregation of nonpolar molecules in an aqueous solution, excluding water molecules. This hydrophobic effect needs to be distinguished from hydrophobic interaction, which is associated with water and hydrophobes (low water-soluble molecules) (Fig. 3.25C), which are mainly hydrocarbon systems. Traditionally, the hydrophobic effect is described as an alignment of water molecules surrounding the unassociated hydrophobes (shown in Fig. 3.25B). This effect leads to a reduction in entropy (**S**). This entropy reduction (**ΔS**) can be considered an offset when the hydrophobes are associated with micelles.

This association increased entropy as the "structured water" is broken up [193]. The entropy increase should also outweigh an enthalpy penalty for demixing water and solute to decrease Gibbs free energy for micellization (shown in Fig. 3.25C). The simplified model in Fig. 3.25 is based on an orientational arrangement of water molecules around the solute hydrophobic molecules [190,194]. However, there is an argument on the proposed models due to the nonpolar solutes' complexity, shape, and size.

7. Template-based synthesis

Other than automated methods, there is a method to build the desired materials (or the precursors) onto other materials that will be sacrificed or removed later. This synthetic method is called templating [195]. It can be summarized into three major pathways: soft, hard, and colloidal templates [196], see Fig. 3.26.

The templating method with hard templates is usually called "nano-casting." As described, solid materials with rigid structures are used as templates. Normally, the intrinsic pores or gaps of solid templates are filled with the precursor molecules to get these building ingredients prearranged [196]. To choose the right hard template, a wise selection is needed. First, the template should have well-organized pore structures (or regulated packing structures) to ensure the resulting structure can achieve some morphology. Secondly, the hard templates should tolerate the conditions when the synthesis of targeted materials is ongoing. Last but not least, the templates should be able to be removed in certain ways that will not disrupt the produced nanomaterials.

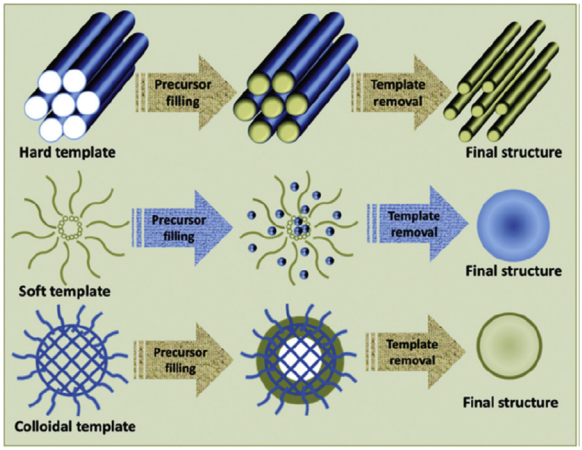

Figure 3.26
Scheme of synthesis of nanomaterials using different types of templates. *Adapted from Ref. [196].*

Various hard templates have been developed, including silica, carbon black, CNTs, colloidal crystals, solid polymers, and so on [197]. No matter which template is chosen, the overall protocol can be summarized as three major steps (Fig. 3.27): The template material is synthesized or obtained in the first step. Then, the precursor of the final product is filled into the template, whether into the pores of the template or onto the organized packing of templates. After that, the reaction of forming the materials goes through. In the last step, the template will finally be removed to achieve the nanostructure [198]. Different nanostructures, such as regulated NP s, nanorods, and nanowires, can be efficiently synthesized [199].

Another type of widely used template is a soft template. Compared to the hard templates, which usually have a certain shape or size, soft templates are usually still at the molecular

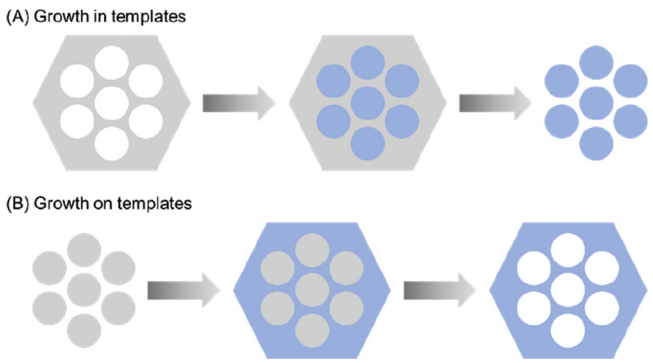

Figure 3.27
Two different pathways of templating: (A) Grow materials in templates; (B) grow materials on templates. Gray: templates; blue: synthesized materials.

level and thus have more flexibility [195]. For example, organic molecules, surfactants (which can be neutral, anionic, and cationic), and polymers with a lower degree of polymerization [200].

8. Conclusions

Unlike hard templates, where the templating is majorly caused by mechanical interaction, soft templates rely more on the intermolecular interactions, such as coulombic force, hydrogen bonds, and van der Waals force [196]. The results from soft templating are dependent on the type of surfactant, concentration of precursors, ratio of surfactants, and other experimental factors [195]. It is more likely to obtain nanomaterials with ordered porosity; the pore size can vary from micropores to mesopores, which can be easily tuned with the carbon chain length surfactants and type of micelles being formed. Overall, a wide range of nanomaterials can be synthesized through the templating method, which shows the importance of such a novel protocol.

Author contributions and acknowledgments

Hengyu Lin and Tian-Hao Yan wrote the manuscript using an outline generated by J. Liu and preliminary data and graphs. The manuscript was edited by S. Bashir and revised by all authors prior to submission. This work is partially supported by Welch Foundation (AC 0006).

References

[1] T.K. Sau, A.L. Rogach, Complex-Shaped Metal Nanoparticles: Bottom-Up Syntheses and Applications, Wiley-VCH, Weinheim, 2012.
[2] J.T. Polanams, Size Control in Nanoparticles Synthesis, Characterization and Photocatalysis, The University of New Mexico, 2006.
[3] N.J. Hoboken, K.J. Klabunde, R. Richards, Nanoscale Materials in Chemistry, Wiley, 2009.
[4] R.M. Richards, Introduction to nanoscale materials in chemistry, in: N.J. Hoboken, K.J. Klabunde, R. Richards (Eds.), Nanoscale Materials in Chemistry, second ed., Wiley, 2009, pp. 1−14.
[5] K.P. McKenna, Unique bonding in nanoparticles and powders, in: N.J. Hoboken, K.J. Klabunde, R. Richards (Eds.), Nanoscale Materials in Chemistry, second ed., Wiley, 2009, pp. 15−36.
[6] S.G. Kwon, T. Hyeon, Kinetics of colloidal chemical synthesis of monodisperse spherical nanocrystals, in: N.J. Hoboken, K.J. Klabunde, R. Richards (Eds.), Nanoscale Materials in Chemistry, second ed., Wiley, 2009, pp. 127−153.
[7] S. Franchi, Molecular beam epitaxy: fundamentals, historical background, and future prospects, in: M. Henini (Ed.), Molecular Beam Epitaxy: From Research to Mass Production, Elsevier, Amsterdam, 2013.
[8] M. Satake, Y. Hayashi, Y. Mido, S.A. Iqbal, M.S. Sethi, Colloidal & Surface Chemistry, Discovery Publishing House, New Delhi, India, 2003, pp. 17−47.
[9] M.J. Madou, Fundamentals of Microfabrication: The Science of Miniaturization, second ed., CRC Press, 2002.

[10] A. Tartakovskii, A.G. Tartakovski, Quantum Dots: Optics, Electron Transport, and Future Applications, Cambridge University Press, 2012.
[11] M.A. Lacaille-Dubois, Bioactive saponins with cancer-related and immunomodulatory activity: recent developments, Stud. Nat. Prod. Chem. 32 (2005) 209−246.
[12] P. Granitzer, K. Rumpf, M. Venkatesan, A.G. Roca, L. Cabrera, M.P. Morales, P. Poelt, M. Albud, Magnetic study of Fe3O4 nanoparticles incorporated within mesoporous silicon, J. Chem. Soc. 157 (2010) 145−151.
[13] S.A. Kulkarni, P.S. Sawadh, P.K. Palei, K.K. Kokate, Effect of synthesis route on the structural, optical, and magnetic properties of Fe3O4 nanoparticles, Ceram. Int. 40 (2014) 1945−1949.
[14] R.Y. Hong, J.H. Li, H.Z. Li, J. Ding, Y. Zheng, D.G. Wei, Synthesis of Fe3O4 nanoparticles without inert gas protection used as precursors of magnetic fluids, J. Magn. Mater. 320 (2008) 1605−1614.
[15] D. Yoo, J.-H. Lee, T.-H. Shin, J. Cheon, Theranostic magnetic nanoparticles, Acc. Chem. Res. 44 (2011) 863−874.
[16] A.M. Awwad, N.M. Salem, A green and facile approach for synthesizing magnetite nanoparticles, Nanosci. Nanotechnol. 2 (2012) 208−213.
[17] S. Bhattacharjee, M. Elimelech, M. Borkovec, DLVO interaction between colloidal particles: beyond Derjaguins approximation, Croat. Chem. Acta 71 (1998) 883−903.
[18] F. Oosawa, S. Asakura, Thermodynamics of the Polymerization of Protein, Academic Press, 1975.
[19] J. Mewis, N.J. Wagner, Colloidal Suspension Rheology, Cambridge University Press, 2012.
[20] J.D. Mackenzie, E.P. Bescher, Chemical routes in nanomaterials synthesis using the sol-gel process, Acc. Chem. Res. 40 (2007) 810−818.
[21] M. Tadic, M. Panjan, D. Markovic, I. Milosevic, V. Spasojevic, Unusual magnetic properties of NiO nanoparticles embedded in a silica matrix, J. Alloys Compd. 509 (2011) 7134−7138.
[22] V. Bounor-Legare, P. Cassagnau, In situ synthesis of organic-inorganic hybrids or nanocomposites from sol-gel chemistry in molten polymers, Prog. Polym. Sci. 39 (2014) 1473−1497.
[23] I. Lacatusu, N. Badea, R. Nita, A. Murariu, F. Miculescu, I. Iosub, A. Meghea, Encapsulation of fluorescence vegetable extracts within a templated sol-gel matrix, Opt. Mater. 32 (2010) 711−718.
[24] B. Menaa, F. Menaa, C. Aiolfi-Guimaraes, O. Sharts, Silica-based nanoporous sol-gel glasses: from bioencapsulation to protein folding studies, Int. J. Nanotechnol. 7 (2009) 1−45.
[25] L. Yang, X. Ning, Y. Bai, W. Jia, A scalable synthesis of non-agglomerated and low-aspect-ratio hydroxyapatite nanocrystals using a gelatinized starch matrix, Mater. Lett. 113 (2013) 142−145.
[26] J.P. Lewicki, C.A. Fox, M.A. Worsley, On the synthesis and structure of resorcinol-formaldehyde polymeric networks−precursors to 3d-carbon micro assemblies, Polymer 69 (2015) 45−51.
[27] M. Copuroglu, M. Sen, Identification of the relationship between the synthesis/process parameters and properties of a sol-gel derived polymer nanocomposite system, J. Appl. Polym. Sci. 129 (2013) 3704−3709.
[28] M. Chong, B. Jin, Sol-gel synthesis of inorganic mesostructured composite photocatalyst for water purification: an insight into the synthesis fundamentals, reaction, and binding mechanisms, Synth. React. Inorg. Metal-Org. Nano-Metal Chem. 42 (2012) 68−75.
[29] A. Suarez-Gomez, M. Sanchez-Tizapa, R. Castaneda-Valderrama, M.A. Carreon-Alvarez, Influence of chelation ratio of metal alkoxides on aging of PZT 53/47 sol-gel-based precursors, Bull. Mater. Sci. 37 (2014) 1123−1129.
[30] Z.S. Kalkan-Sevinc, L.A. Goettler, In situ polymerization of polyamide 66 nanocomposites utilizing interfacial polycondensation. III. Co-synthesis of silica nanocomposites via sol-gel chemistry, Polym. Eng. Sci. 52 (2012) 2410−2416.
[31] S. He, X. Cheng, Z. Li, X. Shi, K. Li, H. Zhang, Facile synthesis of sponge reinforced monolithic silica aerogels with improved mechanical property and excellent absorptivity, Mater. Lett. 154 (2015) 107−111.

[32] D.T. Hue, T.V. Manh, L.H. Anh, L.V. Hong, M.H. Phan, P.T. Huyen, H.D. Chinh, Sol-gel synthesis, characterization, and magnetic properties of double-layered perovskite manganite La1.25Sr1.75Mn2O7, Magn. IEEE Trans. 50 (2014) 1–4.
[33] S. Solgi, M. Shahrezaee, A. Zamanian, T.S. Jafarzadeh Kashi, M. Raz, K. Khoshroo, M. Tahriri, Sol-gel synthesis and characterization of SiO2-CaO-P2O5-SrO bioactive glass: in vitro study, Key Eng. Mater. 631 (2015) 30–35.
[34] F. Sevim, A. Kara, O. Aksakal, F. Demir, H. Eroglu, Synthesis and characterization of nanofibres of 2ZnO$3B2O3$5H2O ceramic composite using the sol-gel processing and the electrospinning techniques, Appl. Mech. Mater. 749 (2015) 169–173.
[35] M.R. Tohidifar, P. Alizadeh, A.R. Aghaei, Controlling the sol-gel process of nano-crystalline lithium mica glass-ceramic by its chemical composition and synthesis parameters, Mater. Char. 99 (2015) 61–67.
[36] R. Vijayalakshmi, V. Rajendran, Synthesis and characterization of nano-TiO2 via different methods, Arch. Appl. Sci. Res. 4 (2) (2012) 1183–1190.
[37] A. Jaroenworaluck, W. Sunsaneeyametha, N. Kosachan, R. Stevens, Characteristics of silica-coated TiO2 and its UV absorption for sunscreen cosmetic applications, Surf. Interface Anal. 38 (4) (2006) 473–477. An International Journal devoted to the development and application of techniques for the analysis of surfaces, interfaces, and thin films.
[38] O. Kerkez-Kuyumcu, E. Kibar, K. Dayıoğlu, F. Gedik, A.N. Akın, S. Özkara-Aydınoğlu, A comparative study for removal of different dyes over M/TiO2 (M= Cu, Ni, Co, Fe, Mn and Cr) photocatalysts under visible light irradiation, J. Photochem. Photobiol. Chem. 311 (2015) 176–185.
[39] Y. Li, T. White, S.H. Lim, Structure control and its influence on photoactivity and phase transformation of TiO, Rev. Adv. Mater. Sci. 5 (2003) 211–215.
[40] P. Peerakiatkhajohn, W. Onreabroy, C. Chawengkijwanich, S. Chiarakorn, Preparation of visible-light-responsive TiO2 doped Ag thin film on PET plastic for BTEX treatment, J. Sustain. Energy Environ. 2 (2011) 121–125.
[41] X.-G. Hou, M.-D. Huang, X.-L. Wu, A.-D. Liu, Preparation and studies of photocatalytic silver-loaded TiO2 films by hybrid sol-gel method, Chem. Eng. J. 146 (1) (2009) 42–48.
[42] H. Pan, X. Wang, S. Xiao, L. Yu, Z. Zhang, Preparation and Characterization of TiO 2 Nanoparticles Surface-Modified by Octadecyltrimethoxysilane, 2013.
[43] R.S. Dubey, Temperature-dependent phase transformation of TiO2 nanoparticles synthesized by sol-gel method, Mater. Lett. 215 (2018) 312–317.
[44] M. Parashar, V.K. Shukla, R. Singh, Metal oxides nanoparticles via sol-gel method: a review on synthesis, characterization, and applications, J. Mater. Sci. Mater. Electron. 31 (5) (2020) 3729–3749.
[45] B.B. Lakshmi, P.K. Dorhout, C.R. Martin, Sol-gel template synthesis of semiconductor nanostructures, Chem. Mater. 9 (3) (1997) 857–862.
[46] Z. Wang, L. Shi, F. Wu, S. Yuan, Y. Zhao, M. Zhang, The sol-gel template synthesis of porous TiO2 for a high-performance humidity sensor, Nanotechnology 22 (27) (2011) 275502.
[47] L. Klein, R.H. Woodman, Porous silica by the sol-gel process, Key Eng. Mater. 115 (1996) 109–124.
[48] D.Y. Kim, H. Du, S. Bhandarkar, D.W. Johnson Jr., Sol-gel processing of low dielectric constant nanoporous silica thin films, in: Nanophase Nanocompos. Mater. IV, Symp, 2002, pp. 147–152, vol. 703.
[49] Z.A. ALOthman, A review: fundamental aspects of silicate mesoporous materials, Materials 5 (2012) 2874–2902.
[50] S. Baskaran, J. Liu, X. Li, G.E. Fryxell, N. Kohler, C.A. Coyle, J.C. Bimbaum, G. Dunham, Molecular templated sol-gel synthesis of nanoporous dielectric films, Ceram. Trans. 123 (2001) 39–47.
[51] C. Sanchez, F. Ribot, Design of hybrid organic-inorganic materials synthesized via sol-gel chemistry, New J. Chem. 18 (1994) 1007–1047.
[52] J.D. Mackenzie, Y. Xu, Ferroelectric materials by the sol-gel method, J. Sol. Gel Sci. Technol. 8 (1997) 673–679.

[53] Y. Xu, J.D. Mackenzie, A theoretical explanation for ferroelectric-like properties of amorphous Pb(ZrxTi1x)O3 and BaTiO3, J. Non-Cryst. Solids 246 (1999) 136−149.
[54] J. Liu, A. Co, S. Paulson, V. Birss, Oxygen reduction reaction (ORR) studies at sol-gel derived La0.8Sr0.2Co0.8Fe0.2O3 (SG-LSCF) cathodes, Solid State Ion. 177 (2006) 277−287.
[55] C. Chia, Y.-H. Kao, Y. Xu, J.D. Mackenzie, Cadmium telluride quantum dot-doped glass by the sol-gel technique, Proc. SPIE-Int. Soc. Opt. Eng. 3136 (1997) 337−347.
[56] Y. Xu, F. Del Monte, J.D. Mackenzie, K. Namjoshi, P. Muggli, C. Joshi, Nanocomposite of semiconducting ferroelectric antimony sulphoiodide dots-doped glasses, Ferroelectrics 230 (1999) 313−322.
[57] F. Del Monte, Y. Xu, J.D. Mackenzie, Preparation and characterization of PbS quantum dots doped ormocers, J. Sol. Gel Sci. Technol. 17 (2000) 37−45.
[58] Y. Xu, Y.-H. Kao, C. Chia, J.D. Mackenzie, S. Honkanen, N. Peyghambarian, Optical waveguide based on CdS quantum dot doped sodium borosilicate glass fabricated by the sol-gel technique, Proc. SPIE Int. Soc. Opt. Eng. 3136 (1997) 326−336.
[59] F. Del Monte, Y. Xu, J.D. Mackenzie, Controlling the particle size of quantum dots incorporated in hybrid materials, Mater. Res. Soc. Symp. Proc. 519 (1998) 277−282.
[60] S. Sakka, H. Kozuka, Sol-gel preparation of coating films containing noble metal colloids, J. Sol. Gel Sci. Technol. 13 (1998) 701−705.
[61] V.M. Renteria, A. Campero, M.J. Garcia, Thermochromic properties of silver colloids embedded in SiO2 gels, J. Sol. Gel Sci. Technol. 13 (1998) 663−666.
[62] K. Onubogu, I. Medina-Ramirez, S. Bashir, Z. Luo, J. Liu, Colloidal synthesis and nanocharacterization of engineered noble metal nanoparticles, Int. J. Green Nanotechnol. Mater. Sci. Eng. 3 (2011) 140−151.
[63] J.R. January, Tintable Abrasion resistant coatings, U.S. Patent 4355135, issued October 19, 1982.
[64] A.M. Guest, M.W. Preus, W. Lewis, Highly Tintable Abrasion Resistant Coatings, U.S. Patent 5102695, issued April 07, 1992.
[65] M. Barrow, T. Olding, Colloidal composite sol-gel formulation with an expanded gel network for making thick inorganic coatings, U.S. Patent 20040258611 issued December 23, 2004.
[66] S. Weiss, M. Bruchez Jr, P. Alivisatos, Core with shell overcoating and linking agent for affinity molecule, U.S. Patent 6423551, issued July 23, 2002.
[67] A. Seifert, K. Ladewig, P. Schönherr, K. Hofmann, R. Lungwitz, I. Roth, A. Pohlers, Synthesis of dye functionalized xerogels via nucleophilic aromatic substitution of fluoro aromatic compounds with amino silanes, J. Sol. Gel Sci. Technol. 53 (2010) 328−341.
[68] J. Klier, C.J. Tucker, T.H. Kalantar, D.P. Green, Properties and applications of microemulsions, Adv. Mater. 12 (2000) 1751−1757.
[69] U. Jeong, X. Teng, Y. Wang, H. Yang, Y. Xia, Superparamagnetic colloids: controlled synthesis and niche applications, Adv. Mater. 19 (2007) 33−60.
[70] J. Biais, B. Clin, P. Laolanne, in: S.E. Friberg, P. Bothorel (Eds.), Microemulsions: Structure and Dynamics, CRC Press, Boca Raton, FL, 1987 (Chapter 4).
[71] M. Fanun, Physicochemistry of W/O Microemulsions: Formation, Stability, and Droplet Clustering, in: M. Fanun (Ed.), Microemulsions: Properties and Applications, 144, CRC Press, 2008, pp. 17−59.
[72] I. Danielsson, B. Lindmann, The definition of a microemulsion, Colloids Surf. A 3 (1981) 391.
[73] R. Zana, J. Lang, in: S.E. Friberg, P. Bothorel (Eds.), Microemulsions: Structure and Dynamics, CRC Press, Boca Raton, FL, 1987 (Chapter 6).
[74] S.E. Friberg, S.H. Friberg, Emulsion formation, in: Encyclopedia of Colloid and Interface Science, Springer, Berlin, Heidelberg, 2013, pp. 366−414.
[75] M. Penders, R. Strey, Phase behavior of the quaternary system H2O/n-octane/C8e5/n-octanol: role of the alcohol in microemulsions, J. Phys. Chem. 99 (1995) 10313−10318.
[76] R.H. Cole, G. Delbos, P. Winsor IV, T.K. Bose, J.M. Moreau, Study of dielectric properties of water/oil and oil/water microemulsions by time-domain and resonance cavity methods, J. Phys. Chem. 89 (1985) 3338−3343.

[77] W.A. de Morais, G.C. da Silva, A.L.P.F. Caroni, A.A. Dantas Neto, T.N.C. Dantas, J.L.C. Fonseca, Dynamic and static radiation scattering in a microemulsion as a function of dispersed phase concentration, Colloids Surf. A Physicochem. Eng. Aspects 465 (2015) 147−152.
[78] M. Bourrel, R.S. Schechter, Microemulsions and Related Systems: Formulation, Solvency, and Physical Properties, Editions Ophrys, 2010.
[79] M.J. Lawrence, G.D. Rees, Microemulsion-based media as novel drug delivery systems, Adv. Drug Deliv. Rev. 45 (1) (2000) 89−121.
[80] X. Du, Y. Ying, J. Liu, Structural architecture and magnetism control of metal oxides using surface grafting techniques, J. Nanoparticle Res. 15 (7) (2013) 1−8.
[81] J. Zhang, M.R. Langille, C.A. Mirkin, Synthesis of silver nanorods by low energy excitation of spherical plasmonic seeds, Nano Lett. 11 (2011) 2495−2498.
[82] R. Ras, M. Kemell, J. de Witt, M. Ritala, G. ten Brinke, M. Leskela, O. Ikkala, Adv. Mater. 19 (2007) 102.
[83] R. Liu, P. Dong, S.L. Chen, Monodisperse SiO2/TiO2 core-shell colloidal spheres: synthesis and ordered self-assembling, Chem. Lett. 34 (2005) 548−549.
[84] X. Wang, Y. Li, Fullerene-like rare-earth nanoparticles, Angew. Chem. Int. Ed. 42 (2003) 3497−3500.
[85] S. Peng, S. Sun, Synthesis and characterization of monodisperse hollow Fe3O4 nanoparticles, Angew. Chem. 119 (2007) 4233−4236.
[86] A. Cabot, R.K. Smith, Y. Yin, H. Zheng, B.M. Reinhard, H. Liu, A. Paul Alivisatos, Sulfidation of cadmium at the nanoscale, ACS Nano 2 (2008) 1452−1458.
[87] F. Teng, Z. Tian, G. Xiong, Z. Xu, Preparation of CdSeSiO2 core-shell particles and hollow SiO2 spheres ranging from nanometers to microns in the nonionic reverse microemulsions, Catal. Today 93 (2004) 651−657.
[88] J. Liu, A.I. Maaroof, L. Wieczorek, M.B. Cortie, Fabrication of hollow metal "nanocaps" and their redshifted optical absorption spectra, Adv. Mater. 17 (2005) 1276−1281.
[89] J. Han, G. Song, R. Guo, A facile solution route for polymeric hollow spheres with controllable size, Adv. Mater. 18 (2006) 3140−3144.
[90] J. Lu, P.H. Toy, Multifunctional organic polymeric catalysts and reagents, Pure Appl. Chem. 85 (2012) 543−556.
[91] X. Sun, Y. Li, Ga2O3 and GaN semiconductor hollow spheres, Angew. Chem. Int. Ed. 43 (2004) 3827−3831.
[92] J. Hainfeld, F.A. Dilmanian, D.N. Slatkin, H.M. Smilowitz, Radiotherapy enhancement with gold nanoparticles, J. Pharm. Pharmacol. 60 (2008) 977−986.
[93] A. Suwalski, H. Dabboue, A. Delalande, S.F. Bensamoun, F. Canon, P. Midoux, G. Saillant, D. Klatzmann, J.P. Salvetat, C. Pichon, Accelerated Achilles tendon healing by PDGF gene delivery with mesoporous silica nanoparticles, Biomaterials 31 (2010) 5237−5245.
[94] F. Tang, L. Li, D. Chen, Mesoporous silica nanoparticles: synthesis, biocompatibility, and drug, delivery, Adv. Mater. 24 (2012) 1504−1534.
[95] D. Lozano, C.G. Trejo, E. Gomez-Barrena, M. Manzano, J.C. Doadrio, A.J. Salinas, M. Vallet-Regí, N. García-Honduvilla, P. Esbrit, J. Bujań, Osteostatin-loaded onto mesoporous ceramics improves the early phase of bone regeneration in a rabbit osteopenia model, Acta Biomater. 8 (2012) 2317−2323.
[96] M. Vallet-Regí, Ordered mesoporous materials in the context of drug delivery systems and bone tissue engineering, Chem. Eur J. 12 (2006) 5934−5943.
[97] H.-J. Kim, H. Matsuda, H.S. Zhou, I. Honma, Ultrasound-triggered smart drug release from a poly (dimethylsiloxane)-mesoporous silica composite, Adv. Mater. 18 (2006) 3083−3088.
[98] Y. Zhao, B.G. Trewyn, I.I. Slowing, V.S.Y. Lin, Mesoporous silica nanoparticle-based double drug delivery system for glucose-responsive controlled release of insulin and cyclic AMP, J. Am. Chem. Soc. 131 (2009) 8398−8400.
[99] B. Moulari, D. Pertuit, Y. Pellequer, A. Lamprecht, The targeting of surface-modified silica nanoparticles to inflamed tissue in experimental colitis, Biomaterials 29 (2008) 4554.

[100] J. Lu, M. Liong, Z. Li, J. Zink, F. Tamanoi, Biocompatibility, biodistribution, and drug delivery efficiency of mesoporous silica nanoparticles for cancer therapy in animals, Small 6 (2010) 1794.
[101] R.K. Jain, T. Stylianopoulos, Delivering nanomedicine to solid tumors, Nat. Rev. Clin. Oncol. 7 (2010) 653.
[102] W.R. Sanhai, J.H. Sakamoto, R. Canady, M. Ferrari, Seven challenges for nanomedicine, Nat. Nanotechnol. 3 (2008) 242−244.
[103] E. Ruoslahti, S.N. Bhatia, M.J. Sailor, Targeting of drugs and nanoparticles to tumors, J. Cell Biol. 188 (2010) 759−768.
[104] M. Ferrari, Cancer nanotechnology: opportunities and challenges, Nat. Rev. Cancer 5 (2005) 161−171.
[105] C. Lok, Nanotechnology: small wonders, Nature 467 (2010) 18−21.
[106] L.H. Phillips, Nanotechnology: armed resistance, Nature 488 (2012) 576−579.
[107] R. Sengupta, R. Sasisekharan, Exploiting nanotechnology to target cancer, Br. J. Cancer 96 (2012) 1315−1319.
[108] A. Schroeder, D.A. Heller, M. Winslow, J.E. Dahlman, G.W. Pratt, Treating metastatic cancer with nanotechnology, Nat. Rev. Cancer 12 (2011) 39−50.
[109] C. Zandonella, Cell nanotechnology: the tiny toolkit, Nature 423 (2003) 10−12.
[110] M.J. van de Vijver, Y.D. He, L. Van't Veer, H. Dai, A. Hart, D.W. Voskuil, G.J. Schreiber, J.L. Peterse, C. Roberts, M.J. Marton, M. Parrish, D. Atsma, A gene-expression signature as a predictor of survival in breast cancer, N. Engl. J. Med. 347 (2002) 1999−2009.
[111] A. Lujambio, S.W. Lowe, The microcosmos of cancer, Nature 482 (2012) 347−355.
[112] L.J. Harper, D.E. Costea, L. Gammon, B. Fazil, A. Biddle, I.C. Mackenzie, Normal and malignant epithelial cells with stem-like properties have an extended G2 cell cycle phase associated with apoptotic resistance, BMC Cancer 10 (2010) 166.
[113] E.K. Chow, D. Ho, Cancer nanomedicine: from drug delivery to imaging, Sci. Transl. Med. 5 (2013) 216rv4.
[114] F. Al-Ejeh, C.E. Smart, B.J. Morrison, G. Chenevix-Trench, J.A. Lopez, S.R. Lakhani, M.P. Brown, K.K. Khanna, Breast cancer stem cells: treatment resistance and therapeutic opportunities, Carcinogenesis 32 (2011) 650−658.
[115] J. Qiu, Traditional medicine: a culture in the balance, Nature 448 (2007) 126−128.
[116] K.Y. Choi, K.H. Min, H.Y. Yoon, K. Kim, J.H. Park, I.C. Kwon, PEGylation of hyaluronic acid nanoparticles improves targetability in vivo, Biomaterials 32 (2011) 1880.
[117] A. Charlot, A. Heyraud, P. Guenot, M. Rinaudo, R. Auzely-velty, Controlled synthesis and inclusion ability of a hyaluronic acid derivative bearing b-cyclodextrin molecules, Biomacromolecules 7 (2006) 907−913.
[118] J. Motoyama, T. Hakata, R. Kato, N. Yamashita, T. Morino, T. Kobayashi, Size-dependent heat generation of magnetic nanoparticles under AC magnetic field for cancer therapy, in: Animal Cell Technology: Basic & Applied Aspects, Springer, Netherlands, 2010, pp. 415−421.
[119] L. Zhang, S.Z. Qiao, Y.G. Jin, Z.G. Chen, H.C. Gu, G.Q. Lu, Magnetic hollow spheres of periodic mesoporous organosilica and Fe3O4 nanocrystals: fabrication and structure control, Adv. Mater. 20 (2008) 805−809.
[120] S.-H. Noh, W. Na, J. Jang, J.H. Lee, E.J. Lee, S.H. Moon, Y. Lim, J.S. Shin, J. Cheon, Nanoscale magnetism control via surface and exchange anisotropy for optimized ferrimagnetic hysteresis, Nano Lett. 12 (2012) 3716−3721.
[121] A.H. Lu, E.L. Salabas, F. Schüth, Magnetic nanoparticles: synthesis, protection, functionalization, and application, Angew. Chem. Int. Ed. 46 (2007) 1222−1224.
[122] S. Laurent, D. Forge, M. Port, A. Roch, C. Robic, L.V. Elst, R.N. Muller, Magnetic iron oxide nanoparticles: synthesis, stabilization, vectorization, physicochemical characterizations, and biological applications, Chem. Rev. 108 (2008) 2064−2110.
[123] C. Wu, J. Chang, Y. Xiao (Eds.), Advanced Bioactive Inorganic Materials for Bone Regeneration and Drug Delivery, CRC Press, 2013.

[124] Y. Deng, D. Qi, C. Deng, X. Zhang, D. Zhao, Superparamagnetic high-magnetization microspheres with a Fe3O4@SiO2 core and perpendicularly aligned mesoporous SiO2 shell for removal of microcystins, J. Am. Chem. Soc. 130 (2008) 28−29.
[125] S. Cao, C. Zhao, T. Han, L. Peng, Hydrothermal synthesis, characterization and gas sensing properties of the WO3 nanofibers, Mater. Lett. 169 (2016) 17−20.
[126] X. Wu, G.Q. Lu, L. Wang, Shell-in-shell TiO2 hollow spheres synthesized by one-pot hydrothermal method for dye-sensitized solar cell application, Energy Environ. Sci. 4 (9) (2011) 3565−3572.
[127] J. Li, Q. Wu, J. Wu, Handbook of Nanoparticles, 2015.
[128] L. Chen, G. Lu, Hydrothermal synthesis of size-dependent Pt in Pt/MWCNTs nanocomposites for methanol electro-oxidation, Electrochim. Acta 53 (12) (2008) 4316−4323.
[129] J. Wang, P. Holt-Hindle, D. MacDonald, D.F. Thomas, A. Chen, Synthesis and electrochemical study of Pt-based nanoporous materials, Electrochim. Acta 53 (23) (2008) 6944−6952.
[130] Q. Yi, W. Huang, X. Liu, G. Xu, Z. Zhou, A. Chen, Electroactivity of titanium-supported nanoporous Pd−Pt catalysts towards formic acid oxidation, J. Electroanal. Chem. 619−620 (2008) 197−205.
[131] C.-H. Han, D.-W. Hong, I.-J. Kim, J. Gwak, S.-D. Han, K.C. Singh, Synthesis of Pd or Pt/titanate nanotube and its application to catalytic type hydrogen gas sensor, Sensor. Actuator. B Chem. 128 (1) (2007) 320−325.
[132] Q. Yi, L. Li, W. Yu, Z. Zhou, X. Liu, G. Xu, Hydrothermal synthesis of titanium-supported PtIrRu/Ti electrode and its electrocatalytic activity, J. Alloys Compd. 466 (1−2) (2008) 52−58.
[133] K. Byrappa, T. Adschiri, Hydrothermal technology for nanotechnology, Prog. Cryst. Growth Char. Mater. 53 (2) (2007) 117−166.
[134] Q. Yi, A. Chen, W. Huang, J. Zhang, X. Liu, G. Xu, Z. Zhou, Titanium-supported nanoporous bimetallic Pt−Ir electrocatalysts for formic acid oxidation, Electrochem. Commun. 9 (7) (2007) 1513−1518.
[135] P. Holt-Hindle, S. Nigro, M. Asmussen, A. Chen, Amperometric glucose sensor based on platinum-iridium nanomaterials, Electrochem. Commun. 10 (10) (2008) 1438−1441.
[136] L. Zheng, L. Xiong, J. Sun, J. Li, S. Yang, J. Xia, Capping agent-free synthesis of PtSn bimetallic nanoparticles with enhanced electrocatalytic activity and lifetime over methanol oxidation, Catal. Commun. 9 (5) (2008) 624−629.
[137] O. Masala, R. Seshadri, Synthesis routes for large volumes of nanoparticles, Annu. Rev. Mater. Res. 34 (1) (2004) 41−81.
[138] X. Peng, K. Koczkur, S. Nigro, A. Chen, Fabrication and electrochemical properties of novel nanoporous platinum network electrodes, Chem. Commun. (24) (2004) 2872−2873.
[139] J. Wang, D.F. Thomas, A. Chen, Direct growth of novel alloyed PtAu nanodendrites, Chem. Commun. (40) (2008) 5010−5012.
[140] G. Demazeau, Solvothermal reactions: an original route for synthesizing novel materials, J. Mater. Sci. 43 (7) (2007) 2104−2114.
[141] P. Holt-Hindle, Q. Yi, G. Wu, K. Koczkur, A. Chen, Electrocatalytic activity of nanoporous Pt−Ir materials toward methanol oxidation and oxygen reduction, J. Electrochem. Soc. 155 (1) (2008).
[142] Q. Yi, J. Zhang, A. Chen, X. Liu, G. Xu, Z. Zhou, Activity of a novel titanium-supported bimetallic PtSn/Ti electrode for electrocatalytic oxidation of formic acid and methanol, J. Appl. Electrochem. 38 (5) (2008) 695−701.
[143] H. Chen, Y. Wang, S. Dong, An effective hydrothermal route for the synthesis of multiple PDDA-protected noble-metal nanostructures, Inorg. Chem. 46 (25) (2007) 10587−10593.
[144] J. Wang, D.F. Thomas, A. Chen, Nonenzymatic electrochemical glucose sensor based on nanoporous PtPb networks, Anal. Chem. 80 (4) (2008) 997−1004.
[145] Y. Hou, H. Kondoh, R. Che, M. Takeguchi, T. Ohta, Ferromagnetic FePt nanowires: solvothermal reduction synthesis and characterization, Small 2 (2) (2006) 235−238.
[146] Z. Zhang, D.A. Blom, Z. Gai, J.R. Thompson, J. Shen, S. Dai, High-yield solvothermal formation of magnetic CoPt alloy nanowires, J. Am. Chem. Soc. 125 (25) (2003) 7528−7529.

[147] Y.-J. Zhu, F. Chen, Microwave-assisted preparation of inorganic nanostructures in liquid phase, Chem. Rev. 114 (12) (2014) 6462−6555.
[148] L.-Y. Meng, B. Wang, M.-G. Ma, K.-L. Lin, The progress of microwave-assisted hydrothermal method in the synthesis of functional nanomaterials, Mater. Today Chem. 1−2 (2016) 63−83.
[149] D.E. Deckman, S.M. Hsu, M. Stephen, E. Klaus, E. Erwin, Vapor Phase Deposition Studies of Phosphate Esters on Metal and Ceramic Surfaces, National Institute of Standards and Technology (U.S.), 1921.
[150] M. Baro, D. Gogoi, A.R. Pal, N.C. Adhikary, H. Bailung, J. Chutia, Pulsed PECVD for low-temperature growth of vertically aligned carbon nanotubes, Chem. Vap. Depos. 20 (2014) 161−169.
[151] R.R. Ismagilov, P.V. Shvets, A.A. Zolotukhin, A.N. Obraztsov, Growth of a carbon nanotube forest on silicon using remote plasma CVD, Chem. Vap. Depos. 19 (2013) 332−337.
[152] J.P. Espinó s, A. Fernańdez, A. Caballero, V.M. Jimeńez, J.C. Sańchez-López, L. Contreras, D. Leinen, A.R. Gonzaĺez-Elipe, Ion-beam-induced CVD: an alternative method of thin film preparation, Chem. Vap. Depos. 3 (1997) 219−226.
[153] S. Strehle, D. Schmidt, M. Albert, J.W. Bartha, Growth of the initial atomic layers of Ta-N films during atomic layer deposition on silicon-based substrates, Chem. Vap. Depos. 17 (2011) 37−44.
[154] D. Mohapatra, L. Jain, P. Rai, K. Hazra, I. Samajdar, D. Misra, Development of crystallographic texture and in-grain misorientation in CVD-produced single and polycrystalline diamond, Chem. Vap. Depos. 17 (2011) 107−113.
[155] S.-I. Nishizawa, M. Pons, Growth and doping modeling of SiC-CVD in a horizontal hot-wall reactor, Chem. Vap. Depos. 12 (2006) 516−522.
[156] J. Mazumder, A. Kar, Theory and Application of Laser Chemical Vapor Deposition, Springer, 1995.
[157] J. Smith, Y. Yuan, D.-J. Liu, J. Liu, Fabrication and characterization of platinum functionalized-carbon nanotubes for the proton exchange membrane fuel cells, J. Undergrad. Chem. Res. 10 (2011) 128−135.
[158] J. Liu, Y. Yuan, S. Bashir, Functionalization of aligned carbon nanotubes to enhance fuel cell performance, Energies 6 (2013) 6476−6486.
[159] D.-S. Jang, S.-H. Kwon, H.-Y. Lee, W.-K. Yang, J.-J. Lee, The effect of the H2 flow rate on the deposition of TiO2 film produced by inductively coupled plasma-assisted CVD, Chem. Vap. Depos. 15 (2009) 217−220.
[160] H. Ago, Frontiers of Graphene and Carbon Nanotubes, Springer, Japan, Tokyo, 2015, pp. 3−20.
[161] Q. Wu, W. Wongwiriyapan, J.-H. Park, S. Park, S.J. Jung, T. Jeong, S. Lee, Y.H. Lee, Y.J. Song, Curr. Appl. Phys. 16 (2016) 1175−1191.
[162] S. Franchi, Molecular beam epitaxy: fundamentals, historical background, and prospects, in: M. Henini (Ed.), Molecular Beam Epitaxy: From Research to Mass Production, Elsevier Science & Technology, 2012, pp. 1−31 (Chapter 1).
[163] S. Sanguinetti, N. Koguchi, Droplet epitaxy of nanostructures, in: M. Henini (Ed.), Molecular Beam Epitaxy: From Research to Mass Production, Elsevier Science & Technology, 2012, pp. 100−108 (Chapter 4).
[164] A. Coli, F. Martelli, S. Rubini, Growth of semiconductor nanowires by molecular beam epitaxy, in: M. Henini (Ed.), Molecular Beam Epitaxy: From Research to Mass Production, Elsevier Science & Technology, 2012, pp. 56−85 (Chapter 3).
[165] G. Springholz, Molecular beam epitaxy of IVeVI semiconductors: multilayers, quantum dots, and device applications, A. Coli, F. Martelli, S. Rubini, Growth of semiconductor nanowires by molecular beam epitaxy, in: M. Henini (Ed.), Molecular Beam Epitaxy: From Research to Mass Production, Elsevier Science & Technology, 2012, pp. 264−306 (Chapter 13).
[166] Y. Horishi, Migration-enhanced epitaxy for low-dimensional structures, in: M. Henini (Ed.), Molecular Beam Epitaxy: From Research to Mass Production, Elsevier Science & Technology, 2012, pp. 113−119 (Chapter 5).
[167] J. Mazumder, A. Kar, Theory and application of laser chemical vapor deposition, in: H. Kogelnik (Ed.), Lasers, Photonics, and Electro-Optics, Springer, 1995, pp. 2015−2284.

[168] H. Wang, Y. Zhao, X. Li, C. Wu, X. Dong, Y. Ma, B. Zhang, G. Du, Nickel flux induced effects on structural and optical properties of NiO films fabricated by PA-MOCVD, Vacuum 119 (2015) 77−80.
[169] J. Jiang, Y. Zhang, F. Yang, Z. Huang, L. Yan, P. Li, C. Chi, D. Zhao, B. Zhang, G. Du, Study of N-polar GaN growth with a high resistivity by metal-organic chemical vapor deposition, Vacuum 119 (2015) 63−67.
[170] H. Takuya, N. Kashio, H. Sugiyama, H. Yokoyama, K. Kurishima, M. Ida, H. Matsuzaki, M. Kohtoku, H. Gotoh, Corrigendum to "MOCVD-grown compressively strained C-doped InxGa1xAs1ySby with high-In/Sb content for very low turn-on-voltage InP-based DHBTs, J. Cryst. Growth 404 (2014) 172−176.
[171] X. Cui, J. Zhang, Effects of growth temperature on the valence, optical and magnetic properties of Mn-doped GaN films grown by metal-organic chemical vapor deposition, Opt. Mater. 46 (2015) 299−303.
[172] J. Zhang, M. Wei, D.M. Fryauf, J.J. Diaz Leon, K.J. Norris, H. Deng, N.P. Kobayashi, Single-crystal indium phosphide nanowires grown on polycrystalline copper foils with an aluminum-doped zinc oxide template, J. Mater. Sci. 50 (2015) 4926−4932.
[173] M. Aoukar, P.D. Szkutnik, D. Jourde, B. Pelissier, P. Michallon, P. Noé, C. Vallée, Control of carbon content in amorphous GeTe films deposited by plasma-enhanced chemical vapor deposition (PE-MOCVD) for phase-change random access memory applications, J. Phys. D Appl. Phys. 48 (2015) 265203.
[174] X.B. Niu, E. Uccelli, A. Fontcuberta I Morral, C. Ratsch, A level set simulation for ordering quantum dots via cleaved-edge overgrowth, Appl. Phys. Lett. 95 (2009) 023119.
[175] C.X. Cui, Y.H. Chen, C. Zhao, P. Jin, G.X. Shi, Y.L. Wang, B. Xu, Z.G. Wang, Cleaved-edge overgrowth of aligned InAs islands on GaAs (110), Nanotechnology 16 (2005) 2661−2664.
[176] L. Persichetti, A. Sgarlata, M. Fanfoni, A. Balzarotti, Heteroepitaxy of Ge on singular and vicinal Si surfaces: elastic field symmetry and nanostructure growth, J. Phys. Condens. Matter 27 (2015), 253001-1-13.
[177] F. Besahraoui, M. Bouslama, F. Saidi, L. Bouzaiene, M.H. Hadj Alouane, H. Maaref, N. Chauvin, M. Gendry, Z. Lounis, M. Ghaffour, Optical investigation of InAs quantum dashes grown on InP (001) vicinal substrate, Superlattice. Microst. 65 (2014) 264−270.
[178] Z. Ma, T. Holden, Z.M. Wang, G.J. Salamo, L. Malikova, S.S. Mao, Strain-induced electronic energy changes in multilayered InGaAs/GaAs quantum wire structures, J. Appl. Phys. 101 (2007) 0443051.
[179] N. Richard, T. Mano, Q. Gong, J.H. Wolter, Self-organized anisotropic strain engineering: a new concept for quantum dot ordering, Proc. IEEE 91 (2003) 1898−1906.
[180] M. Hagn, A. Zrenner, G. Bo̧hm, G. Weimann, Electric-field-induced exciton transport in coupled quantum well structures, Solid State Electron. 40 (1996) 429−431.
[181] J.A. Prieto, G.A. Reig, C. Priester, J.M. Garcia, L. Gonzalez, R. Garcia, Strain-induced optical anisotropy in self-organized quantum structures at the E1 transition, Appl. Phys. Lett. 76 (2000) 2197−2199.
[182] N.T. Bagraev, A.D. Buravlev, L.E. Klyachkin, A.M. Malyarenko, W. Gehlhoff, V.K. Ivanov, I.A. Shelykh, Quantized conductance in silicon quantum wires, Semiconductors 36 (2002) 439−460.
[183] A.I. Fajalia, M. Tsianou, Self-assembly control via molecular recognition: effect of cyclodextrins on surfactant micelle structure and interactions determined by SANS, Colloids Surf. A Physicochem. Eng. Aspects 480 (2015) 91−104.
[184] J. Hu, Adaptive and Functional Polymers, Textiles and Their Applications, Imperial College Press, London, 2011.
[185] R.J. Hunter, Zeta Potential in Colloid Science: Principles and Applications, vol. 2, Academic Press, 2013.
[186] R. Rajagopalan, P.C. Hiemenz, Principles of Colloid and Surface Chemistry, Marcel Dekker, New York, 1997, pp. 236−241, vol. 9397.

[187] D. Segets, R. Marczak, S. Schafer, C. Paula, J.-F. Gnichwitz, A. Hirsch, W. Peukert, Experimental and theoretical studies of the colloidal stability of nanoparticles general interpretation based on stability maps, ACS Nano 5 (6) (2011) 4658−4669.
[188] R. Guichard, A. Tanie‘re, E. Belut, N. Rimbert, Simulation of nanoparticle coagulation under Brownian motion and turbulence in a differential-algebraic framework: developments and applications, Int. J. Multiphas. Flow 64 (2014) 73−84.
[189] J.Y. Lee, B.H. Hong, W.Y. Kim, S.K. Min, Y. Kim, M.V. Jouravlev, R. Bose, Near-field focusing and magnification through self-assembled nanoscale spherical lenses, Nature 460 (2009) 498−501.
[190] R. Kelsall, I.W. Hamley, M. Geoghegan, Nanoscale Science and Technology, John Wiley & Sons, 2005.
[191] M. Takashiri, K. Imai, M. Uyama, H. Hagino, S. Tanaka, K. Miyazaki, Y. Nishi, Effects of homogeneous irradiation of electron beam on crystal growth and thermoelectric properties of nanocrystalline bismuth selenium telluride thin films, J. Alloys Compd. 612 (2014) 98−102.
[192] B. Lukanov, A. Firoozabadi, Specific ion effects on the self-assembly of ionic surfactants: a molecular thermodynamic theory of micellization with dispersion forces, Langmuir 30 (2014) 6373−6383.
[193] A.A. Steinschulte, B. Schulte, S. Rutten, T. Eckert, J. Okuda, M. Moller, S. Schneider, O.V. Borisov, F.A. Plamper, Effects of architecture on the stability of thermosensitive unimolecular micelles, Phys. Chem. Chem. Phys. 16 (2014) 4917−4932.
[194] Y. Li, K. Holmberg, R. Bordes, Micellization of true amphoteric surfactants, J. Colloid Interface Sci. 411 (2013) 47−52.
[195] Y. Liu, J. Goebl, Y. Yin, Templated synthesis of nanostructured materials, Chem. Soc. Rev. 42 (7) (2013) 2610−2653.
[196] R.R. Poolakkandy, M.M. Menamparambath, Soft-template-assisted synthesis: a promising approach for the fabrication of transition metal oxides, Nanoscale Adv. 2 (11) (2020) 5015−5045.
[197] B. Szczęśniak, J. Choma, M. Jaroniec, Major advances in the development of ordered mesoporous materials, Chem. Commun. 56 (57) (2020) 7836−7848.
[198] Y. Yamauchi, K. Kuroda, Rational design of mesoporous metals and related nanomaterials by a soft-template approach, Chem. Asian J. 3 (4) (2008) 664−676.
[199] S.J. Hurst, E.K. Payne, L. Qin, C.A. Mirkin, Multisegmented one-dimensional nanorods prepared by hard-template synthetic methods, Angew. Chem. Int. Ed. 45 (17) (2006) 2672−2692.
[200] W. Li, D. Zhao, An overview of the synthesis of ordered mesoporous materials, Chem. Commun. 49 (10) (2013) 943−946.

CHAPTER 4

Physics-based impedance spectroscopy characterization of operating PEM fuel cells

Tatyana Reshetenko[1], **Andrei Kulikovsky**[2]
[1]*Hawaii Natural Energy Institute, University of Hawaii, Honolulu, HI, United States;*
[2]*Forschungszentrum Jülich GmbH, Theory and Computation of Energy Materials (IEK-13), Institute of Energy and Climate Research, Jülich, Germany*

Abstract
Polymer electrolyte membrane fuel cell impedance models based on transient mass and charge conservation equations are developed. The models are fitted to experimental impedance spectra of the segmented high- and low-Pt cells operating in the range of current densities between 0.1 and 1.0 A cm^{-2}. The functional cell layers' fitting oxygen and proton transport parameters are discussed. We show how the models help to identify the peaks in the distribution of relaxation times spectra.

Keywords: Experiment; Impedance; Modeling; PEM fuel cell.

1. Introduction

Electrochemical impedance spectroscopy (EIS) has proven to be a powerful and efficient fuel cell characterization tool [1,2]. Like tomography, EIS is a nondestructive and noninvasive technique allowing in operando measuring of fuel cell transport and kinetic parameters. Not surprisingly, interest in EIS techniques has been growing exponentially [3].

However, understanding measured impedance spectra is a nontrivial task. Due to its simplicity, the most popular approach to spectra processing is the equivalent electric circuit (EEC) method. The method implies heuristic construction of EEC with impedance spectrum close to the spectrum of a fuel cell of interest. The EEC is usually assembled out of resistivities, capacitances, inductances, constant phase elements, and elements

Advanced Nanomaterials and Their Applications in Renewable Energy. https://doi.org/10.1016/B978-0-323-99877-2.00006-0

representing classic impedances of electrochemical systems. Two well-known examples are the Warburg element, which describes the impedance of a transport layer attached to a planar electrode and the Gerischer element representing the impedance of a transport layer with the distributed chemical reaction. The EEC has been widely used in fuel cell studies; however, the validity of this approach cannot be rigorously proved. First, there is no guarantee that the selected equivalent circuit is unique. Second, the classic solutions for the impedance of a system with the planar electrode are generally not applicable to a porous catalyst layer with the distributed electrochemical reaction. In addition, the determination of the physical cell transport and kinetic parameters from the equivalent circuit elements is usually beyond the scope of the approach [4].

Much more reliable is constructing an impedance model based on the fuel cell's mass and charge conservation equations [5–26]. Generally, any system of transient conservation equations can be linearized and Fourier-transformed to yield a system of linear equations for the AC perturbation amplitudes. Solution of this system leads to the cell impedance, either numerical or analytical (see a recent review of analytical solutions in Ref. [27] and a general review of EIS applications in fuel cells in Ref. [28]). However, the application of analytical solutions for the PEMFC impedance [17,18,21,22,24,29–31] is limited by low cell currents, typically below 100 mA cm^{-2}.

The linearization step can be omitted in numerical modeling, and impedance can be calculated by applying a small-amplitude potential or voltage step to the model equations [32]. The numerical Fourier transform of the solution allows calculating impedance in the whole frequency range, as the Fourier spectrum of a step function includes all frequencies. This method is invaluable for calculating impedance from large-scale computational fluid dynamics (CFD) cell models. However, CFD models are time-consuming, and the technique is hardly suitable for fitting experimental spectra.

This chapter summarizes key results of our group on development impedance models for characterization of high- and low-Pt proton exchange membrane fuel cells (PEMFCs) in real operating conditions, that is, in the range of current cell densities between 0.1 and 1 A cm^{-2}. It has been shown that in low-Pt cells, an important role is the transport of oxygen through a thin ionomer (Nafion) film covering Pt/C agglomerates [33–38]. In contrast, in high-Pt cells, the contribution of this process to the total cell impedance is marginal. We developed two basic impedance models for the high- and low-Pt cells: the high-Pt model is based on standard macro-homogeneous (MH) transient model for the cell performance [39], while the low-Pt model employs mass and charge transport equations in a single cylindrical pore surrounded by a thin Nafion film separating the pore volume from the Pt surface [40,41]. In the limit of zero Nafion film thickness, the single-pore, low-Pt model transforms into the standard MH model. As shown below, another advantage of the

single-pore model is that it can easily be generalized to take pore size distribution in the cathode catalyst layer.

Another useful technique of spectra analysis is the distribution of relaxation times (DRTs). This technique makes it possible to retrieve information on characteristic frequencies and partial resistivities of the cell's separate transport and kinetic processes. Due to its simplicity, this technique has a large potential in PEMFC studies; below, we describe the basics of DRT analysis and provide an informative example.

The models discussed in this Chapter aim to assist PEMFC designers in cell characterization, particularly in studying the cathode catalyst layers (CCLs). Furthermore, the authors believe that PEMFC would be one of the leading automotive and stationary applications technologies. As with any other mass product, PEMFCs would require a fast and reliable method of testing. For example, owners of fuel cell-based cars would need to make a standard checkup of the PEMFC stack; we have no doubts that EIS is best suited to accomplish this task. Another goal of the studies below is, thus, to support the replacement of EEC models by physics-based impedance models in standard software for industrial EIS meters.

2. Experimental

During PEM fuel cell operation, spatial performance inhomogeneities exist due to continuous depletion of oxygen, localized water accumulation, and build-up impurities along the flow field. Evaluation of fuel cell performance with a single, lumped cell does not reveal spatial behavior. In contrast, a segmented cell system provides locally resolved voltage, current, and impedance. To detect and measure localized PEMFC characteristics, we employed a segmented cell system developed in Hawaii Natural Energy Institute (HNEI) and presented in Fig. 4.1A [42–44]. The segmented cell setup consisted of the cell hardware, the current transducer system, the data acquisition device (DAQ), and a single cell test station (Fig. 4.1B). The current transducer system was custom designed using a closed-loop Hall sensor (Honeywell CSNN 191). The overall segmented system allowed the investigation of 10 current channels in high (standard) and low current modes. The standard current mode enabled the measurement of current segment densities up to 2 A cm^{-2}. The low current mode of the system yielded current measurement up to 50 mA cm^{-2}, which was typical for spatially distributed electrochemical diagnostics (cyclic voltammetry and linear sweep voltammetry). Voltage and current signal data were collected using a National Instrument PXI data acquisition instrument on HNEI-developed LabView software.

The segmented cell hardware was built using a 100 cm^2 cell and had segmented and nonsegmented flow fields. The segmented flow field was divided into 10 segments with an

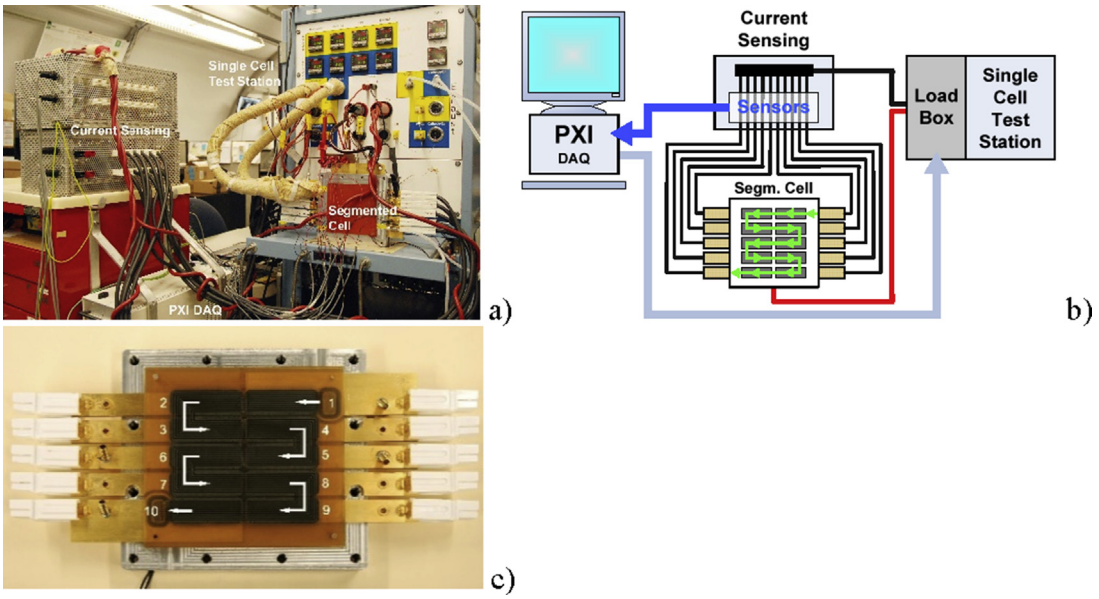

Figure 4.1

View of the tests station and the segmented cell (A), schematic of the segmented cell system (B), and segmented flow field (C). *(A) and (C) are reprinted from Ref. [44]; (B) is reprinted from Ref. [42].*

area of 7.6 cm^2 and manufactured of 10 graphite blocks embedded in an Ultem (polyetherimide) frame using two-component epoxy for sealing and attachment. The segments were connected in sequential order from segment 1 (cell inlet) to segment 10 (cell outlet) (Fig. 4.1C). The segmented flow field was equipped with segmented current collector plates aligned using another Ultem framework, ensuring electric isolation of the current collectors and an endplate. The segmented cell hardware and the data acquisition system were designed so that segmentation can be applied for anode or cathode, depending on the requirements of the experimental work. The same 10-channel serpentine design was used for the segmented and the standard flow fields, and the reactant streams were arranged in a co-flow configuration. The segments' voltage and cell voltage responses were the same for the current hardware design due to the relatively small electrode area.

The segmented cell was operated with commercially available 100 cm^2 Gore PRIMEA catalyst coated membranes (CCMs). The anode and cathode electrodes were made with Pt/C catalyst loading 0.4 mg_{Pt} cm^{-2} and 0.1 mg_{Pt} cm^{-2} for high- and low-Pt loaded CCMs, respectively (Fig. 4.2). Scanning electron microscopy (SEM) studies showed that the catalyst layer thickness was 11–15 and 3–4 μm for high- and low-Pt samples. For the production of membrane electrode assemblies (MEAs), Sigracet 25 BC with a thickness of 220–230 μm was used as the anode and cathode gas diffusion layers (GDLs). The cathode

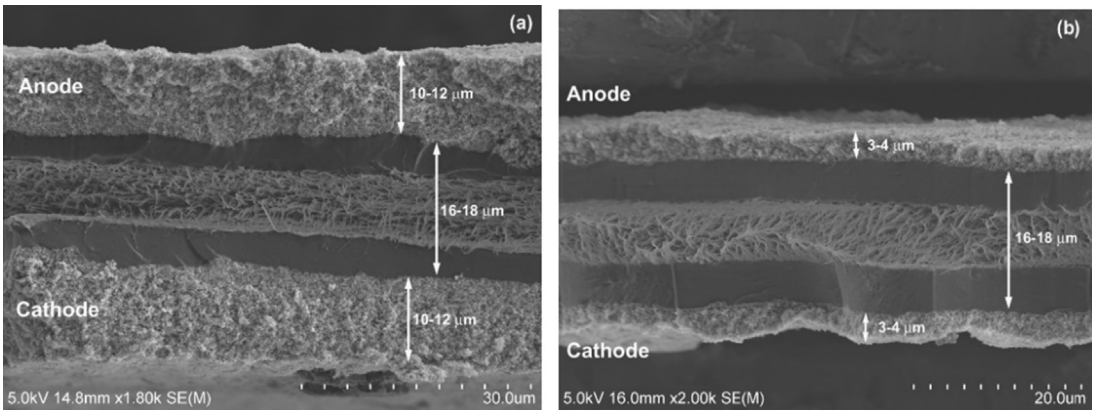

Figure 4.2
Scanning electron microscopy images of high-Pt (A) and low-Pt (B) catalyst coated membranes. *Reprinted from Ref. [24].*

used a segmented GDL and gasket configuration, whereas a single GDL was applied at the anode. Since the cathode electrode employed a segmented flow field, GDL, and gasket, the MEA active area was reduced from 100 to 76 cm^2. The gasket material was made of Teflon with varied thicknesses, ensuring a 25%−30% compression ratio for the studied MEAs.

The segmented cell was assembled, conditioned, and tested. The anode/cathode conditions were H_2/air and 100/50% relative humidity. Back pressure varied from ambient (101 kPa) to 150 kPa for both electrode compartments. The cell temperature varied from 60 to 80°C. The anode stoichiometry was two for all tests, while cathode stoichiometry was changed from 2 to 10 depending on the requirements of the experiment. The detailed conditions are presented in the corresponding tables in the text. The local or spatial EIS measurements were performed under galvanostatic control of the electronic load. The selected frequency range for the EIS experiments was 0.1 Hz−10 kHz, and the sinusoidal current signal perturbation amplitude was chosen to ensure a cell voltage response of 10 mV or lower.

The segmented cell system enabled the collection of spatially distributed information during a standard fuel cell experiment. It was operated as a single fuel cell using the custom-made test station and standardized testing protocols. During PEM fuel cell evaluation, the test station controlled reagents' flow rates, back pressure, cell temperature, and overall cell current/voltage. Such operation minimized any impact from the segmented cell system and facilitated distributions measurements without interference on the segments' performance. The operation of the segmented cell system represents operating conditions that are identical to real because only the overall current or voltage is controlled, whereas segments current and voltage are floating. It should be noted that the

segmented cell system allows us to obtain electrochemical characteristics not only for individual segments but also for the overall cell.

3. Model for high-Pt cell impedance

3.1 High stoichiometry of the air flow

At infinite air flow stoichiometry, we can ignore variations of the oxygen concentration and local current density along the active cell area. The cell performance model simplifies to a true one-dimensional one. The core of the impedance model form oxygen mass-transport and proton charge conservation equations through the CCL depth

$$\frac{\partial c}{\partial t} - D_{ox}\frac{\partial^2 c}{\partial x^2} = -\frac{i_*}{4F}\left(\frac{c}{c_h^{in}}\right)\exp\left(\frac{\eta}{b}\right) \tag{4.1}$$

$$C_{dl}\frac{\partial \eta}{\partial t} + \frac{\partial j}{\partial x} = -i_*\left(\frac{c}{c_h^{in}}\right)\exp\left(\frac{\eta}{b}\right) \tag{4.2}$$

For notations, please see the Nomenclature list at the end of the Chapter. Substituting Ohm's law

$$j = -\sigma_p\frac{\partial \eta}{\partial x} \tag{4.3}$$

into Eq. (4.2), we get a diffusion type equation for the positive by convention ORR overpotential η

$$C_{dl}\frac{\partial \eta}{\partial t} - \sigma_p\frac{\partial^2 \eta}{\partial x^2} = -i_*\left(\frac{c}{c_h^{in}}\right)\exp\left(\frac{\eta}{b}\right) \tag{4.4}$$

The system of Eqs. (4.1) and (4.4) describes the CCL performance. It is important to emphasize that the CCL oxygen diffusivity D_{ox} in Eq. (4.1) is a lumped parameter, which does not describe details of the oxygen transport in the CCL. Numerous scanning and transmission electron microscopy studies show that in CCLs, Pt/C particles are partially or completely covered by a thin Nafion film. To reach the Pt surface, oxygen must be dissolved in the film first. A definitive account of oxygen dissolution in Nafion and transport through the film will be done in Section 4, where the impedance model for a low-Pt cell is discussed. However, in standard high-Pt cells, the oxygen transport model of Eq. (4.1) is quite a reasonable approximation.

The diffusion equation describes oxygen transport in the gas diffusion layer

$$\frac{\partial c_b}{\partial t} - D_b\frac{\partial^2 c_b}{\partial x^2} = 0 \tag{4.5}$$

To simplify calculations, we introduce dimensionless variables

$$\widetilde{t}=\frac{t}{t_*},\ \widetilde{x}=\frac{x}{l_t},\ \widetilde{c}=\frac{c}{c_h^{in}},\ \widetilde{j}=\frac{j}{j_*},\ \widetilde{\eta}=\frac{\eta}{b},\ \widetilde{D}_{ox}=\frac{4FD_{ox}c_h^{in}}{\sigma_p b},\ \widetilde{D}_b=\frac{4FD_b c_h^{in}}{\sigma_p b}$$
$$\widetilde{\omega}=\omega t_*,\ \widetilde{Z}=\frac{Z\sigma_p}{l_t} \tag{4.6}$$

where

$$t_*=\frac{C_{dl}b}{i_*}\ \text{and}\ j_*=\frac{\sigma_p b}{l_t} \tag{4.7}$$

are the characteristic time of double-layer charging and the characteristic current density for proton transport, respectively. With these variables, Eqs. (4.1), (4.4), and (4.5) take the form

$$\mu^2\frac{\partial\widetilde{c}}{\partial\widetilde{t}}-\varepsilon_*^2\widetilde{D}_{ox}\frac{\partial^2\widetilde{c}}{\partial\widetilde{x}^2}=\widetilde{c}\exp\widetilde{\eta},\ \left.\frac{\partial\widetilde{c}}{\partial\widetilde{x}}\right|_{\widetilde{x}=0}=0,\ \widetilde{c}(1)=\widetilde{c}_b(1) \tag{4.8}$$

$$\frac{\partial\widetilde{\eta}}{\partial\widetilde{t}}-\varepsilon_*^2\frac{\partial^2\widetilde{\eta}}{\partial\widetilde{x}^2}=-\widetilde{c}\exp\widetilde{\eta},\ \widetilde{\eta}(0)=\widetilde{\eta}_0,\ \left.\frac{\partial\widetilde{\eta}}{\partial\widetilde{x}}\right|_{\widetilde{x}=1}=0 \tag{4.9}$$

$$\mu^2\frac{\partial\widetilde{c}_b}{\partial\widetilde{t}}-\varepsilon_*^2\widetilde{D}_b\frac{\partial^2\widetilde{c}_b}{\partial\widetilde{x}^2}=0,\ \left.\widetilde{D}_b\frac{\partial\widetilde{c}_b}{\partial\widetilde{x}}\right|_{\widetilde{x}=1+}=\left.\widetilde{D}_{ox}\frac{\partial\widetilde{c}}{\partial\widetilde{x}}\right|_{\widetilde{x}=1-},\quad \widetilde{c}_b\left(1+\widetilde{l}_b\right)=\widetilde{c}_h \tag{4.10}$$

where $\widetilde{c}_h$ is the oxygen concentration in the channel, and the dimensionless parameters are given by

$$\mu=\sqrt{\frac{4Fc_h^{in}}{C_{dl}b}},\ \varepsilon_*=\sqrt{\frac{\sigma_p b}{i_* l_t^2}} \tag{4.11}$$

Note the boundary conditions for Eqs. (4.8) and (4.10) at the CCL/GDL interface (at $\widetilde{x}=1$), prescribing continuity of the oxygen concentration and flux. The left boundary condition for Eq. (4.8) means zero oxygen flux through the membrane, and the right boundary condition for Eq. (4.10) establishes channel (reference) oxygen concentration at the GDL/channel interface. Eqs. (4.8)–(4.10) form the basis for the impedance model of the cell.

3.2 Impedance

The procedure for derivation of equations for small AC perturbation amplitudes consists of the following steps. First, we apply small-amplitude perturbations of $\widetilde{c}$, $\widetilde{\eta}$, and $\widetilde{c}_b$ of the form

$$\begin{aligned} \widetilde{c} &= \widetilde{c}^0(\widetilde{x}) + \widetilde{c}^1(\widetilde{t},\ \widetilde{x}), \quad \widetilde{c}^1 \ll \widetilde{c}^0 \\ \widetilde{\eta} &= \widetilde{\eta}^0(\widetilde{x}) + \widetilde{\eta}^1(\widetilde{t},\ \widetilde{x}), \quad \widetilde{\eta}^1 \ll \widetilde{\eta}^0 \\ \widetilde{c}_b &= \widetilde{c}_b^0(\widetilde{x}) + \widetilde{c}_b^1(\widetilde{t},\ \widetilde{x}), \quad \widetilde{c}_b^1 \ll \widetilde{c}_b^0 \end{aligned} \tag{4.12}$$

where the subscripts 0 and 1 mark the static variables and the small perturbation amplitudes, respectively. Substituting Eq. (4.12) into Eqs. (4.8)−(4.10), expanding exponent in Taylor series $\exp\left(\widetilde{\eta}^0 + \widetilde{\eta}^1\right) = \exp\left(\widetilde{\eta}^0\right)\left(1 + \widetilde{\eta}^1\right)$, neglecting terms with the product of perturbations and subtracting equations for the static variables, we get a system of transient equations for $\widetilde{c}^1$, $\widetilde{\eta}^1$, and $\widetilde{c}_b^1$. Making Fourier-transform

$$\widetilde{y}^1(t,\ \widetilde{x}) = \widetilde{y}^1\ (\widetilde{\omega},\ \widetilde{x})\exp(\mathrm{i}\widetilde{\omega}\widetilde{t}) \tag{4.13}$$

where $\widetilde{y}^1$ stands for $\widetilde{c}^1$, $\widetilde{\eta}^1$, and $\widetilde{c}_b^1$, we finally come to the system of linear equations for the perturbation amplitudes in the $\widetilde{\omega}$ - space:

$$\varepsilon_*^2 \widetilde{D}_{ox}\frac{\partial^2 \widetilde{c}^1}{\partial \widetilde{x}^2} = \left(\exp\left(\widetilde{\eta}^0\right) + \mathrm{i}\widetilde{\omega}\mu^2\right)\widetilde{c}^1 + \widetilde{c}^{\,0}\exp\left(\widetilde{\eta}^0\right)\widetilde{\eta}^1$$

$$\left.\frac{\partial \widetilde{c}^1}{\partial \widetilde{x}}\right|_{\widetilde{x}=0} = 0, \quad \widetilde{c}^1(1) = \widetilde{c}_b^1(1) \tag{4.14}$$

$$\varepsilon_*^2\frac{\partial^2 \widetilde{\eta}^1}{\partial \widetilde{x}^2} = \exp\left(\widetilde{\eta}^0\right)\widetilde{c}^1 + \left(\widetilde{c}^0\exp\left(\widetilde{\eta}^0\right) + \mathrm{i}\widetilde{\omega}\right)\widetilde{\eta}^1, \quad \widetilde{\eta}^1(1) = \widetilde{\eta}_1^1,$$

$$\left.\frac{\partial \widetilde{\eta}^1}{\partial \widetilde{x}}\right|_{\widetilde{x}=1} = 0 \tag{4.15}$$

$$\varepsilon_*^2 \widetilde{D}_b\frac{\partial^2 \widetilde{c}_b^1}{\partial \widetilde{x}^2} = \mathrm{i}\widetilde{\omega}\mu^2\widetilde{c}_b^1, \quad \widetilde{D}_b\left.\frac{\partial \widetilde{c}_b^1}{\partial \widetilde{x}}\right|_{\widetilde{x}=1+} = \widetilde{D}_{ox}\left.\frac{\partial \widetilde{c}^1}{\partial \widetilde{x}}\right|_{\widetilde{x}=1-},$$

$$\widetilde{c}_b\left(1 + \widetilde{l}_b\right) = \widetilde{c}_h^1 \tag{4.16}$$

where $\widetilde{c}_h^1$ is the oxygen perturbation in the channel (see below). Linearity of system Eqs. (4.14)−(4.16) guarantees that impedance is independent of the applied small potential perturbation $\widetilde{\eta}_1^1$, and it is convenient to apply this perturbation at $\widetilde{x} = 1$, as the boundary condition for Eq. (4.15) shows.

System Eq. (4.14)–(4.16) can be further simplified. Eq. (4.16) decouples from this system, and it can be solved:

$$\widetilde{c}_b^1 = -\frac{\sinh\left(\sqrt{\mathrm{i}\widetilde{\omega}/\left(\varepsilon_*^2\widetilde{D}_b\right)}\,\mu\left(1+\widetilde{l}_b-\widetilde{x}\right)\right)}{\mu\sqrt{\mathrm{i}\widetilde{\omega}\widetilde{D}_b/\varepsilon_*^2}\,\cosh\left(\sqrt{\mathrm{i}\widetilde{\omega}/\left(\varepsilon_*^2\widetilde{D}_b\right)}\,\mu\widetilde{l}_b\right)}\widetilde{D}_{ox}\frac{\partial\widetilde{c}^1}{\partial\widetilde{x}}\Big|_{\widetilde{x}=1} + \frac{\widetilde{c}_h^1\cosh\left(\sqrt{\mathrm{i}\widetilde{\omega}/\left(\varepsilon_*^2\widetilde{D}_b\right)}\,\mu(1-\widetilde{x})\right)}{\cosh\left(\sqrt{\mathrm{i}\widetilde{\omega}/\left(\varepsilon_*^2\widetilde{D}_b\right)}\,\mu\widetilde{l}_b\right)} \tag{4.17}$$

In this section, we consider the case of large air flow stoichiometry, and hence, the perturbation of oxygen concentration in the channel can be set to zero: $\widetilde{c}_h^1 = 0$. Substituting $\widetilde{c}_h^1 = 0$, $\widetilde{x} = 1$ into Eq. (4.17), we find

$$\widetilde{c}_b^1(1) = -\frac{\tanh\left(\mu\widetilde{l}_b\sqrt{\mathrm{i}\widetilde{\omega}/\left(\varepsilon_*^2\widetilde{D}_b\right)}\right)}{\mu\sqrt{\mathrm{i}\widetilde{\omega}\widetilde{D}_b/\varepsilon_*^2}}\widetilde{D}_{ox}\frac{\partial\widetilde{c}^1}{\partial\widetilde{x}}\Big|_{\widetilde{x}=1} \tag{4.18}$$

With Eq. (4.18), the system of equations for the CCL + GDL reduces to the CCL problem, Eqs. (4.14) and (4.15), with the Robin-type right boundary condition for Eq. (4.14):

$$\widetilde{c}^1(1) + \frac{\tanh\left(\mu\widetilde{l}_b\sqrt{\mathrm{i}\widetilde{\omega}/\left(\varepsilon_*^2\widetilde{D}_b\right)}\right)}{\mu\sqrt{\mathrm{i}\widetilde{\omega}\widetilde{D}_b/\varepsilon_*^2}}\widetilde{D}_{ox}\frac{\partial\widetilde{c}^1}{\partial\widetilde{x}}\Big|_{\widetilde{x}=1} = 0 \tag{4.19}$$

Physically, this means that information on the GDL impedance comes to the CCL impedance through the CCL/GDL boundary. Solution of the system Eqs. (4.14) and (4.15) gives $\widetilde{\eta}^1$, which determines the system impedance

$$\widetilde{Z} = -\frac{\widetilde{\eta}^1}{\partial\widetilde{\eta}^1/\partial\widetilde{x}}\Big|_{\widetilde{x}=0} \tag{4.20}$$

3.3 Static shapes

Static shapes $\widetilde{c}^0(\widetilde{x})$ and $\widetilde{\eta}^0(\widetilde{x})$ play a role of coefficient functions in system Eqs. (4.14), (4.15). These shapes have to be found from the system of static equations, which are derived by chalking out the time derivatives in Eqs. (4.8), (4.9):

$$\varepsilon_*^2\widetilde{D}_{ox}\frac{\partial^2\widetilde{c}^0}{\partial\widetilde{x}^2} = \widetilde{c}^0\exp(\widetilde{\eta}^0), \quad \frac{\partial\widetilde{c}}{\partial\widetilde{x}}\Big|_{\widetilde{x}=0} = 0, \quad \widetilde{c}^0(1) = 1 - \frac{\widetilde{j}_0\widetilde{l}_b}{\widetilde{D}_b} \tag{4.21}$$

$$\varepsilon_*^2 \frac{\partial^2 \widetilde{\eta}^0}{\partial \widetilde{x}^2} = \widetilde{c}^0 \exp(\widetilde{\eta}^0), \quad \widetilde{\eta}^0(0) = \widetilde{\eta}_0, \quad \left.\frac{\partial \widetilde{\eta}^0}{\partial \widetilde{x}}\right|_{\widetilde{x}=1} = 0, \tag{4.22}$$

Integrating the static proton charge conservation equation

$$\varepsilon_*^2 \frac{\partial \widetilde{j}^0}{\partial \widetilde{x}} = -\widetilde{c}^0 \exp(\widetilde{\eta}^0) \tag{4.23}$$

we get the total current density $\widetilde{j}_0$ in the system

$$\widetilde{j}_0 = \frac{1}{\varepsilon_*^2} \int_0^1 \widetilde{c}^0 \exp(\widetilde{\eta}^0)\, dx \tag{4.24}$$

Suppose that the static cell current $\widetilde{j}_0$ density is fixed. To find the corresponding $\widetilde{\eta}^0$ (polarization curve), we have two options. The first is the iterative solution of system Eqs. (4.21), (4.22) until Eq. (4.24) is met. The other, more attractive option arises if we eliminate $\widetilde{\eta}^0$ from the system of Eqs. (4.21)−(4.23), leading to the following problem (Ref. [3], page 123)

$$\frac{\partial^2 \widetilde{j}^0}{\partial \widetilde{x}^2} + \left(\widetilde{j}^0 - \frac{\partial \ln \widetilde{c}^0}{\partial \widetilde{x}}\right) \frac{\partial \widetilde{j}^0}{\partial \widetilde{x}} = 0, \quad \widetilde{j}^0(0) = \widetilde{j}_0, \quad \widetilde{j}^0(1) = 0 \tag{4.25}$$

$$\widetilde{D}_{ox} \frac{\partial \widetilde{c}^0}{\partial \widetilde{x}} = \widetilde{j}_0 - \widetilde{j}^0, \quad \widetilde{c}^0(1) = 1 - \frac{\widetilde{j}_0 \widetilde{l}_b}{\widetilde{D}_{ox}} \tag{4.26}$$

Solution of the system of Eqs. (4.25), (4.26) does not require iterations. Once $\widetilde{j}^0(\widetilde{x})$ is calculated, the static overpotential can be found from Eq. (4.23):

$$\widetilde{\eta}^0 = \ln\left(-\frac{\varepsilon_*^2}{\widetilde{c}^0} \frac{\partial \widetilde{j}^0}{\partial \widetilde{x}}\right) \tag{4.27}$$

3.4 Fitting spectra

The previous section's model has been used for fitting experimental spectra of the high-Pt cell operated at 50 mA cm^{-2} (Table 4.1). The results in this section have been obtained using the fitting procedure *NonlinearFit* in Maple environment. An example of experimental and fitted Nyquist curves is shown in Fig. 4.3 [45]. Mean over the cell active area fitting parameters are listed in Table 4.2. As can be seen, the model returns quite reasonable values of the ORR Tafel slope, CCL proton conductivity, and double-layer capacitance. The latter value is close to C_{dl} measured by cyclic voltammetry for the same

Table 4.1: The high-Pt cell geometrical and operating parameters.

GDL thickness l_b, cm	0.022 (220 μm)
Catalyst layer thickness l_t, cm	$15 \cdot 10^{-4}$ (15 μm)
Cell current density j_0, A cm^{-2}	0.05
Air flow stoichiometry λ	10
Back pressure P, kPa	101
Cell temperature T, K	273 + 70

cell. There is no literature data to compare the CCL oxygen diffusivity D_{ox} of $0.45 \cdot 10^{-4}$ cm^2 s^{-1} resulted from fitting. We need to keep in mind that D_{ox} is a lumped parameter, which represents oxygen transport in a void pore, oxygen dissolution in Nafion film, and, perhaps, oxygen adsorption on the Pt surface, a last potential-independent transport barrier of O_2 molecule on the way to the reaction site. In Section 4, we will discuss a more detailed model for oxygen diffusion in the CCL.

The GDL oxygen diffusivity varies along the channel from quite the expected value of 0.018 cm^2 s^{-1} at the inlet down to an unrealistically low 0.002 cm^2 s^{-1} close to the outlet (Table 4.2). Low D_b at the outlet is caused by elongation of spectra (Fig. 4.3, segments 9, 10). This elongation is caused by the channel impedance, which is ignored in the model discussed. Account of this impedance leads to the quite constant value of parameter D_b along the cell surface.

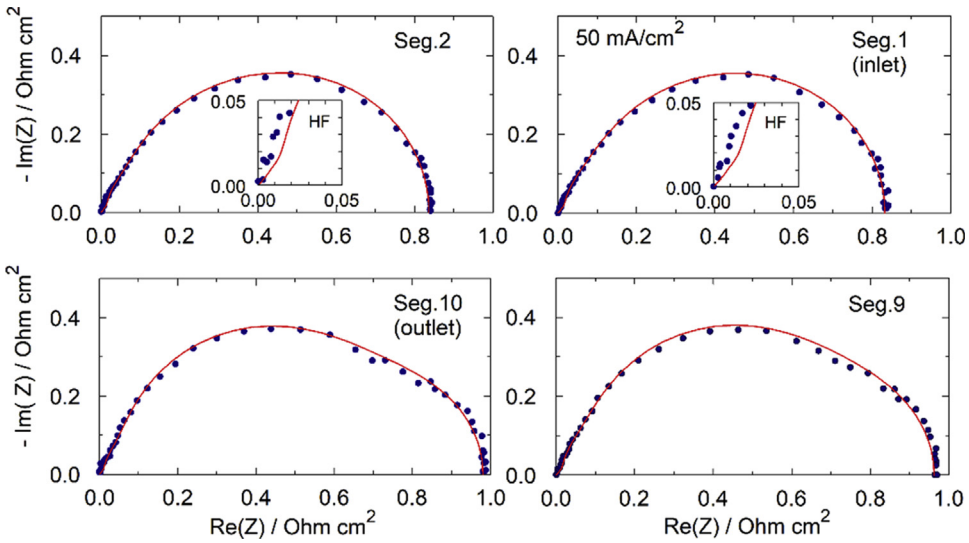

Figure 4.3

Experimental (points) and fitted model (line) local impedance spectra of a segmented proton-exchange membrane (PEM) fuel cell. Two spectra are shown at the inlet (segments 1, 2) and two at the outlet (segments 9, 10). Cell operating parameters are listed in Table 4.1.

Table 4.2: Mean over the cell active area fitting parameters from the spectra in Fig. 4.3 [45]. Parameter D_b varies along the channel; indicated are the values at the inlet and outlet.

ORR tafel slope b, mV/exp	32.7
CCL proton conductivity σ_p, mS cm^{-1}	11
Double layer capacitance C_{dl}, F cm^{-3}	20
CCL oxygen diffusivity D_{ox}, cm^2 s^{-1}	$0.45 \cdot 10^{-4}$
GDL oxygen diffusivity D_b, cm^2 s^{-1}	0.016 → 0.002

The other problem with this simple model is the poor fitting quality of the high-frequency (HF) part of the spectra (insets in Fig. 4.3). This puts into question the value of CCL proton conductivity indicated in Table 4.2. The problem of the HF part of the impedance spectra will be discussed in the next Section 3.5.

3.5 High-frequency part of the spectra

The high-frequency impedance of a PEMFC can be derived from the following arguments. Large $\widetilde{\omega}$ means that on the right side of Eq. (4.15), all terms except $\mathrm{i}\widetilde{\omega}\widetilde{\eta}^1$ can be neglected, and this equation simplifies

$$\varepsilon_*^2 \frac{\partial^2 \widetilde{\eta}^1}{\partial \widetilde{x}^2} = \mathrm{i}\widetilde{\omega}\widetilde{\eta}^1, \quad \widetilde{\eta}^1(1) = \widetilde{\eta}_1^1, \quad \left.\frac{\partial \widetilde{\eta}^1}{\partial \widetilde{x}}\right|_{\widetilde{x}=1} = 0 \tag{4.28}$$

Solving Eq. (4.28) and calculating impedance according to Eq. (4.20), we get the high-frequency CCL impedance

$$\widetilde{Z}_{HF} = \frac{1}{\sqrt{\mathrm{i}\widetilde{\omega}/\varepsilon_*^2}\tanh\sqrt{\mathrm{i}\widetilde{\omega}/\varepsilon_*^2}} \tag{4.29}$$

Note that Eq. (4.29) is independent of the cell current density. Separating the real and imaginary part of Eq. (4.29), it can be shown that the following relation holds:

$$\mathrm{Re}\left(\widetilde{Z}_{HF}\right) = -\mathrm{Im}\left(\widetilde{Z}_{HF}\right), \quad \widetilde{\omega} \to \infty \tag{4.30}$$

Thus, the high-frequency part of the spectra in the Nyquist coordinates is a straight line with a slope of 45 degrees [46]. In the dimension form, Eq. (4.29) reads

$$Z_{HF} = \frac{l_t}{\sigma_p\sqrt{\mathrm{i}\omega C_{dl} l_t^2/\sigma_p}\tanh\sqrt{\mathrm{i}\omega C_{dl} l_t^2/\sigma_p}} \tag{4.31}$$

Clearly, Eq. (4.31) describes the charging/discharging of the double layer due to the oscillation of protons in electrolyte around their equilibrium position. It follows that Eq. (4.31) also describes a spectrum of the cell operating in the H_2/N_2 regime [47]. Projection of the straight line Eq. (4.30) onto the real axis is a good estimate of the CCL proton resistivity $R_p = l_t/(3\sigma_p)$. The spectrum of Eq. (4.31) is shown in Fig. 4.4. Thus, in the high-frequency limit, the model predicts 45 degrees straight line in the Nyquist coordinates. However, the HF part of the real spectra exhibits a much higher slope (inset in Fig. 4.3). A possible origin of this effect is discussed below.

3.6 What is the origin of a high-frequency slope?

Using the transmission line approach, Lefebvre, Martin, Pickup [48] and later Li, and Pickup [49] explained the large slope of the PEMFC Nyquist spectrum in the HF domain by nonuniform distribution of proton conductivity through the electrode depth. This idea has further been studied by Gerteisen [20], who also modeled the effect of the nonuniform distribution of double-layer capacitance in the CCL. We employed this idea by incorporating the exponential decay of proton conductivity with the distance from the membrane [22,50]:

$$\sigma_p(\tilde{x}) = \sigma_o \exp(-\beta\tilde{x}) \equiv \sigma_o s(\tilde{x}) \tag{4.32}$$

where σ_o is the CCL proton conductivity at the membrane interface and β is the rate of the σ_p decay along $\tilde{x}$. Note that $\beta = 0$ describes CCL with uniform conductivity.

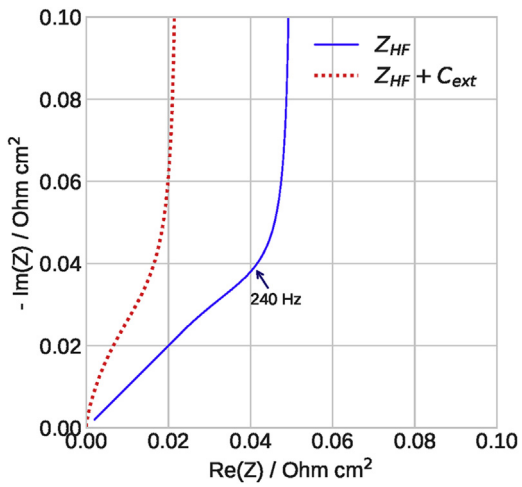

Figure 4.4

Solid line, the Nyquist spectrum of Eq. (4.31) for the parameters in Tables 4.1 and 4.2. Dotted line, the spectrum of Z_{HF}, Eq. (4.31), with the external capacitance $C_{ext,} = 10\ \mathrm{F\ cm^{-3}}$ connected in parallel (Fig. 4.5B).

With Eq. (4.32), the left side of Eq. (4.15) transforms to $\varepsilon_*^2 \frac{\partial}{\partial \widetilde{x}} \left(s(\widetilde{x}) \frac{\partial \widetilde{\eta}}{\partial \widetilde{x}} \right)$ with ε^* and other relevant parameters scaled using σ_o instead of σ_p. The fitting of the modified model greatly improves the quality of spectra fitting in the HF domain [22,50]. However, it leads to the unrealistically large value of the parameter β in Eq. (4.32). For example, fitting of spectra of an MEA with the Pt loading of 0.4 mg_{Pt} cm^{-2} gives $\beta = 7.3$, meaning that the electrode proton conductivity drops by three orders of magnitude through the CCL depth [22]. This decay seems to be unrealistic, as numerous SEM pictures show uniform structure of the CCL.

It looks like there is something else in PEM fuel cells, which increases the HF slope of the Nyquist spectra. Taking into account that in the frequency domain between $\simeq 10^3$ and 10^4 Hz impedance of the high-Pt cells is determined by proton transport for charging/discharging double layer, a possible source of high slope could be the capacitance of a double layer, connected in parallel to the "working" double layer in a cell. Due to impurities, water in the cell cathode is a weak electrolyte, leading to a system of double layers not participating directly in the ORR. This system is illustrated in Fig. 4.5A [51]; it includes a double layer at the carbon/water interface and double layers at either side of the water/ionomer interface. As the electron conductivity of the carbon phase is typically large, the total capacitance of the double layers in Fig. 4.5A is connected in parallel to the Pt/ionomer interface, where the ORR occurs. We incorporated the "external" (concerning Pt/ionomer) DLs as capacitance C_{ext} connected in parallel to the model CCL impedance, as shown in Fig. 4.5B. The spectrum of the system in Fig. 4.5B with Z_{mod} given by Eq. (4.31) and $C_{ext} = 10$ F cm^{-3} is shown in Fig. 4.4 (dotted line). Thus, the introduction of C_{ext} leads to a higher slope of the impedance curve in the HF domain.

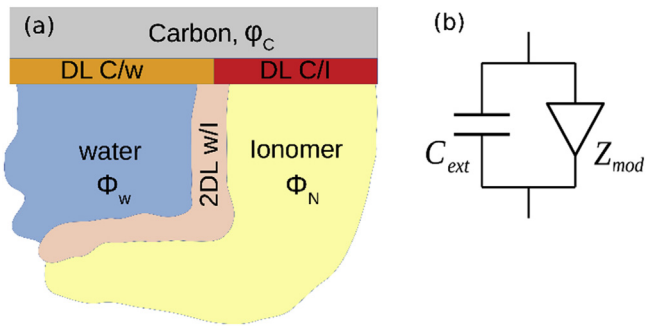

Figure 4.5

Schematic of the double layers in operating proton-exchange membrane (PEM) fuel cell (A) [51]. Schematic of the parallel connection of model impedance Z_{mod} and external capacitance C_{ext} (B).

Experimental and fitted spectra of a normal high-Pt cell operated at oxygen stoichiometry $\lambda = 9.5$ at 50 and 400 mA cm^{-2} are shown in Fig. 4.6. The cell operating parameters are gathered in Table 4.3. As can be seen, the incorporation of C_{ext} greatly improves the quality of spectra fitting in the HF domain (Fig. 4.6B and E). Parameters resulting from spectra fitting are shown in Fig. 4.7. The ORR Tafel slope exhibits a small variation in the range of 27−35 mV/exp, which agrees with the literature data [52,53] (Fig. 4.7A). The CCL oxygen diffusivity increases by order of magnitude as the current grows from 50 to 400 mA cm^{-2} (Fig. 4.7B). This growth could be caused by improving the oxygen transport in the void pores or the Nafion film covering Pt/C agglomerates. Model Eq. (4.1) does not allow us to distinguish these processes; however, more detailed model helps clarify this issue (Section 3.8). The oxygen diffusion coefficient in the GDL is about 0.02 cm^2 s^{-1} (Fig. 4.7B). This value seems to be quite reasonable, considering that the MEA contains a microporous layer, which the model does not explicitly describe. The double-layer capacitance decreases with the cell current, while the CCL proton conductivity increases (Fig. 4.7C and D). Both the trends could be explained by increasing the amount of liquid water in the CCL, which improves Nafion proton conductivity and covers Pt surface, thereby lowering C_{dl}.

Interestingly, the external capacitance C_{ext} is about three times less than the "working" DL capacitance, and it exhibits the same trend with the cell current (Fig. 4.7C). In the following examples, C_{ext} has been added as a fitting parameter to the model. If the slope

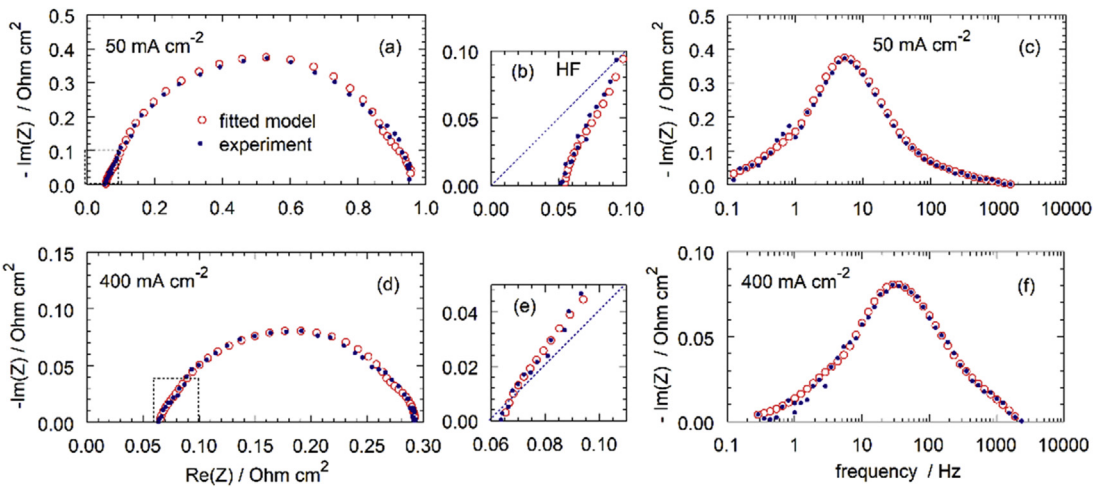

Figure 4.6

Experimental (points) and fitted model (open circles) Nyquist spectra of the cell. The frames (B) and (E) show the high-frequency part of the spectra; the dotted lines depict 45 degrees slope. Frequency dependence of imaginary part of the impedance (C), (F).

Table 4.3: The geometrical and operating parameters of the high-Pt MEA.

GDL thickness l_b, cm	0.023 (230 μm)
Catalyst layer thickness l_t, cm	$12 \cdot 10^{-4}$ (12 μm)
Air flow stoichiometry λ	9.5
Back pressure P, kPa	150
Cell temperature T, K	273 + 80

of experimental spectra is 45 degrees, the fitting procedure automatically reduces C_{ext} to negligible values.

3.7 Low air flow stoichiometry

3.7.1 Oxygen transport in the channel

Typically, PEM fuel cells operate at the stoichiometry of air flow around 2. This means that the oxygen concentration at the channel outlet is twice less than at the inlet. At these conditions, the impedance of oxygen transport in the channel cannot be neglected. To incorporate channel impedance into the model Eqs. (4.14)–(4.18), we note that the perturbation of oxygen concentration at the GDL/channel interface is not zero, meaning that in Eqs. (4.16), (4.17), we cannot neglect $\widetilde{c}_h^1$. Equation for $\widetilde{c}_h^1$ can be derived from the following arguments.

To a good approximation, oxygen mass transport in the channel can be described by the 1d + 1d plug flow equation:

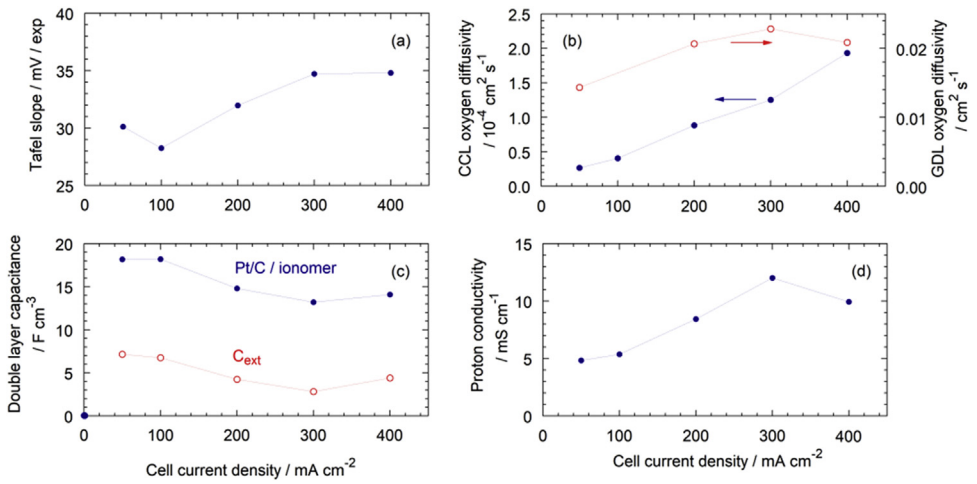

Figure 4.7

The ORR Tafel slope (A), the CCL oxygen diffusivity (B), the double layer capacitance (C), and the CCL proton condictivity (D) resulted from spectra fitting.

$$\frac{\partial c_h}{\partial t}+v\frac{\partial c_h}{\partial z}=-\frac{D_b}{h}\frac{\partial c_b}{\partial x}\bigg|_{x=l_t+l_b} \tag{4.33}$$

where c_h is the oxygen concentration in the channel, v is the air flow rate, z is the coordinate along the channel counted from the inlet, and h is the channel depth. The right side of Eq. (4.33) is the diffusive oxygen flux in the GDL at the channel/GDL interface, which represents the oxygen "sink."

With the dimensionless variables Eq. (4.6), Eq. (4.33) reads

$$\xi^2\frac{\partial\widetilde{c}_h}{\partial\widetilde{t}}+\lambda\widetilde{J}\frac{\partial\widetilde{c}_h}{\partial\widetilde{z}}=-\widetilde{D}_b\frac{\partial\widetilde{c}_b}{\partial\widetilde{x}}\bigg|_{\widetilde{x}=1+\widetilde{l}_b} \tag{4.34}$$

where

$$\widetilde{z}=\frac{z}{L} \tag{4.35}$$

L is the channel length, $\widetilde{J}$ is the mean current density in the cell

$$\widetilde{J}=\int_0^1\widetilde{j}_0\,d\widetilde{z} \tag{4.36}$$

ξ is the dimensionless parameter, and λ is the stoichiometry of air flow

$$\xi=\sqrt{\frac{4Fhc_h^{in}l_t i_*}{C_{dl}\sigma_p b^2}},\quad \lambda=\frac{4Fhvc_h^{in}}{LJ} \tag{4.37}$$

Eq. (4.34) is linear, and we can immediately write down the equation for the perturbation amplitude $\widetilde{c}_h^1$:

$$\lambda\widetilde{J}\frac{\partial\widetilde{c}_h^1}{\partial\widetilde{z}}=-\mathrm{i}\widetilde{\omega}\xi^2\widetilde{c}_h^1-\widetilde{D}_b\frac{\partial\widetilde{c}_b^1}{\partial\widetilde{x}}\bigg|_{\widetilde{x}=1+\widetilde{l}_b} \tag{4.38}$$

Differentiating Eq. (4.17), we find the flux $\widetilde{D}_b\frac{\partial\widetilde{c}_b^1}{\partial\widetilde{x}}\Big|_{\widetilde{x}=1+\widetilde{l}_b}$ and Eq. (4.38) takes the form

$$\begin{aligned}\lambda\widetilde{J}\frac{\partial\widetilde{c}_h^1}{\partial\widetilde{z}}=&-\mathrm{i}\widetilde{\omega}\xi^2\widetilde{c}_h^1-\cosh\left(\mu\widetilde{l}_b\sqrt{\mathrm{i}\widetilde{\omega}/\left(\varepsilon_*^2\widetilde{D}_b\right)}\right)^{-1}\widetilde{D}_{ox}\frac{\partial\widetilde{c}^1}{\partial\widetilde{x}}\bigg|_{\widetilde{x}=1}\\&-\widetilde{c}_h^1\mu\sqrt{\mathrm{i}\widetilde{\omega}\widetilde{D}_b/\varepsilon_*^2}\tanh\left(\mu\widetilde{l}_b\sqrt{\mathrm{i}\widetilde{\omega}/\left(\varepsilon_*^2\widetilde{D}_b\right)}\right),\quad\widetilde{c}_h^1(0)=0\end{aligned} \tag{4.39}$$

The impedance problem thus reduces to the system of Eqs. (4.14), (4.15), with the new Robin-type right boundary condition for Eq. (4.14):

$$\widetilde{c}^1(1)+\frac{\tanh\left(\mu\widetilde{l}_b\sqrt{\mathrm{i}\widetilde{\omega}/\left(\varepsilon_*^2\widetilde{D}_b\right)}\right)}{\mu\sqrt{\mathrm{i}\widetilde{\omega}\widetilde{D}_b/\varepsilon_*^2}}\widetilde{D}_{ox}\frac{\partial\widetilde{c}^1}{\partial\widetilde{x}}\bigg|_{\widetilde{x}=1}=\widetilde{c}_h^1\cosh\left(\mu\widetilde{l}_b\sqrt{\mathrm{i}\widetilde{\omega}/\left(\varepsilon_*^2\widetilde{D}_b\right)}\right)^{-1} \tag{4.40}$$

where $\widetilde{c}_h^1$ is obtained from Eq. (4.39). Note that Eq. (4.39), in turn, contains the flux $\widetilde{D}_{ox}\frac{\partial\widetilde{c}^1}{\partial\widetilde{x}}\Big|_{\widetilde{x}=1}$ and hence iterations are unavoidable. This flux is a function of coordinate $\widetilde{z}$.

3.7.2 Static local current density and oxygen concentration along the channel

Eqs. (4.14), (4.15) contain the cell local current density j_0, which varies along the channel. In our experiments with segmented cells, the shape $j_0(z)$ is measured, and we used these data in calculations. Alternatively, if $j_0(z)$ is unknown, it can be calculated as discussed in Ref. [54]. Once $\widetilde{j}_0(z)$ is known, the static shape of the oxygen concentration along the channel can be calculated from the static version of Eq. (4.34):

$$\lambda\widetilde{J}\frac{\partial\widetilde{c}_h^0}{\partial\widetilde{z}}=-\widetilde{j}_0(\widetilde{z}),\quad \widetilde{c}_h^0(0)=1 \tag{4.41}$$

3.7.3 Cell segmentation, solution strategy, and results

To solve the problem, Eqs. (4.14), (4.15) with the boundary condition (4.40), and Eq. (4.39), we consider segmented cell with the straight channel (Fig. 4.8). The iteration procedure for the cell impedance calculation is as follows.

1. Solve the static through-plane problem (4.25), (4.26) to find the local current density $\widetilde{j}^0(\widetilde{x})$ and concentration $\widetilde{c}^0(\widetilde{x})$.
2. Guess some initial non-zero shape of $\widetilde{c}_h^1(\widetilde{z})$. Perform the loop indicated by bullets until convergence is achieved:
   - Solve the problem (4.14), (4.15), (4.40) for every segment.

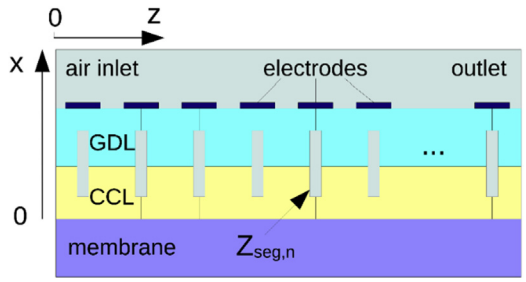

Figure 4.8
Sketch of the segmented cell.

- Calculate the oxygen flux at the CCL/GDL interface in every segment:
  $\widetilde{N}_1 = \widetilde{D}_{ox}\frac{\partial \widetilde{c}}{\partial \widetilde{x}}\Big|_{\widetilde{x}=1}$.
- Interpolate the fluxes $\widetilde{N}_1$ to get a smooth function of $\widetilde{z}$.
- Assuming $\widetilde{D}_b$ and other parameters are constant along $\widetilde{z}$, solve the problem for $\widetilde{c}_h$Eq. (4.39).
- Go to the beginning of the loop.

3. Calculate the segment impedances $\widetilde{Z}_{seg,\,n}$ according to Eq. (4.20).
4. Calculate the whole-cell impedance $\widetilde{Z}_{cell}$ from

$$\frac{1}{\widetilde{Z}_{cell}} = \frac{1}{N}\sum_{n=1}^{N}\frac{1}{\widetilde{Z}_{seg,n}} \tag{4.42}$$

where N is the number of segments.

Experimental and fitted spectra of the cell with high-Pt MEA operated at the air flow stoichiometry of $\lambda = 4$ are shown in Fig. 4.9. The other operating parameters are listed in Table 4.3. Formation of the low-frequency arc was observed (Fig. 4.9A), which is due to the finite rate of oxygen transport in the channel (cf. Fig. 4.6A, the spectrum measured at $\lambda = 9.5$). Overall, the model captures this process; however, the quality of spectra fitting is significantly lower than in Fig. 4.6. At low λ, the experimental spectra are rather noisy, especially in the low-frequency region, and the quality of spectra fitting progressively

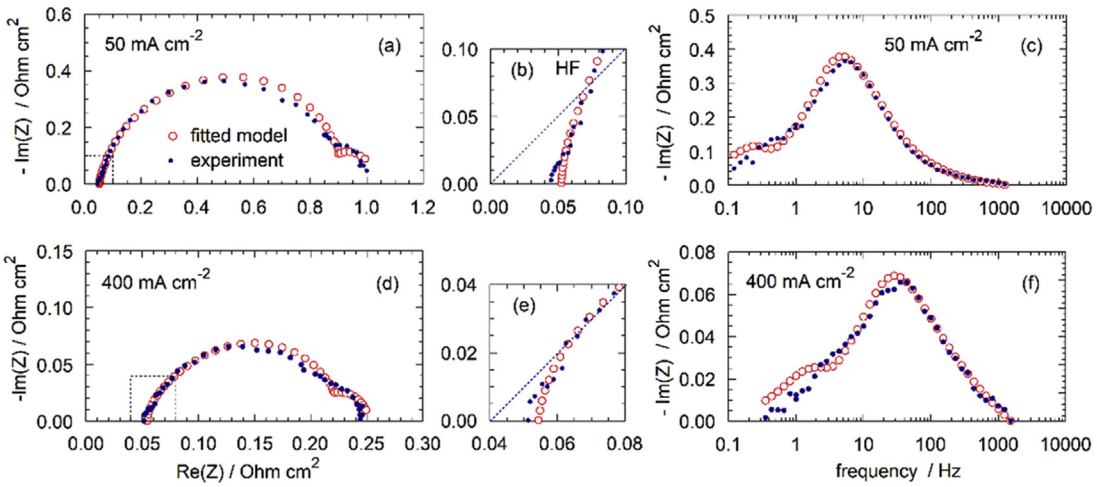

Figure 4.9

Experimental (points) and fitted model (open circles) Nyquist spectra of the cell. The frames (B) and (E) show the high-frequency part of the spectra. Here, the dotted lines depict 45 degrees slope. Frequency dependence of imaginary part of the impedance (C), (F).

worsens as the current cell increases (Fig. 4.9). Lower stoichiometry may lead to the formation of nonuniform distribution of CCL liquid water content along the channel, and a more accurate approach would be to fit local spectra (Section 3). The fitting parameters versus current cell density are shown in Fig. 4.10.

Between 200 and 400 mA cm^{-2}, the ORR Tafel slope exhibits variation between 22 and 27 mV (Fig. 4.10A). This value is somewhat lower than the standard 30 mV for this type of catalyst; the deviation presumably is due to insufficient quality of spectra fitting. The CCL oxygen diffusivity increases linearly with j_0 (Fig. 4.10B). The effect could be caused by the formation of temperature/pressure gradients in the CCL, which pushes out liquid water from the electrode. The double-layer capacitance of 15 F cm^{-3} is independent of cell current (Fig. 4.10C), while the external capacitance decreases linearly with j_0. The CCL proton conductivity increases from 2 to 8 mS cm^{-1}, seemingly due to growing liquid water content in the CCL. Overall, the trends and the range of parameters variation agrees with the results obtained with $\lambda = 9.5$ (Fig. 4.7). Unfortunately, the model could not capture the contribution of oxygen transport in the GDL to cell impedance. The GDL oxygen diffusivity returned by the fitting is unrealistically high, meaning that the fitting procedure has ignored the GDL impedance. Useful data on D_b can be obtained as discussed in the next section.

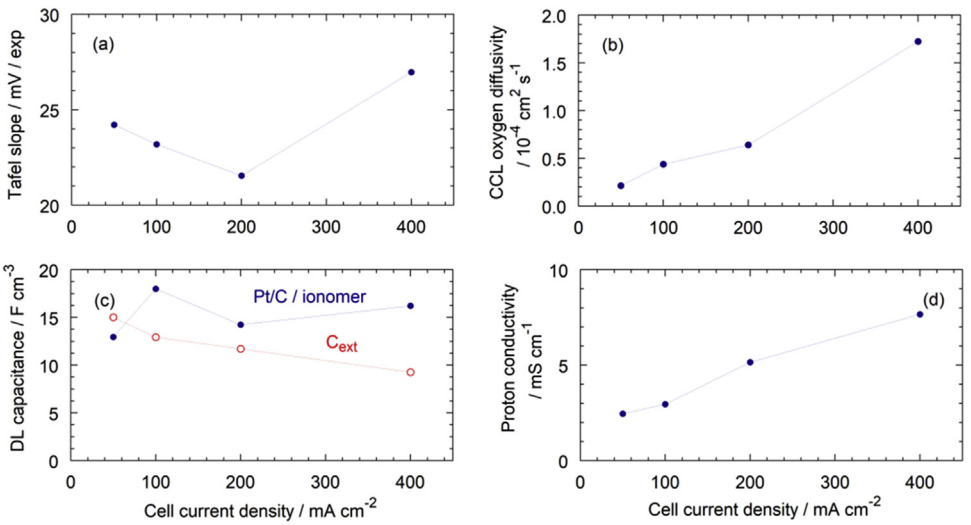

Figure 4.10

The ORR Tafel slope (A), the CCL oxygen diffusivity (B), the double layer capacitance (C), and the CCL proton condictivity (D) resulted from spectra fitting (Fig. 4.9).

3.8 Fitting high-Pt spectra using low-Pt model

It is insightful to compare the results in Fig. 4.10 with the parameters of the same cell obtained from quite different impedance models. The local impedance spectra of the high-Pt MEA operated at $\lambda = 4$ have been fitted using the "low-Pt" impedance model (Section 4). The detailed model description is given in the next section; here, we only mention that the model includes oxygen transport through the cylindrical void pores separated by a thin ionomer film from the Pt surface. The model includes two oxygen diffusion coefficients: D_p in the void pore and D_N in the Nafion film.

Mean over the cell surface parameters are shown in Fig. 4.11. Fig. 4.11A and B represent oxygen transport parameters of ionomer film, which will be discussed in the next section. Fig. 4.11C shows oxygen diffusivities of the void pore D_p and the GDL D_b. The diffusivity D_p exhibits the same linear growth with the cell current as D_{ox} in Fig. 4.10B, though the absolute value of D_p in Fig. 4.11C is about twice higher than of D_{ox} in Fig. 4.10B. This is not surprising, as D_{ox} in Fig. 4.10B is a lumped parameter, which implicitly includes oxygen transport in the Nafion film.

The double-layer capacitances in Figs. 4.11D and 4.10C are close, as well as the proton conductivities in Figs. 4.11E and 4.10D. A quite noticeable difference is found for the ORR Tafel slopes in Figs. 4.11F and 4.10A. The results from local spectra fitting in Fig. 4.11F are more accurate and hence trustworthy. The mean value of the ORR Tafel slope in Fig. 4.11F of 29 mV is close to the literature value of 30 mV [55]. We used Tafel slope b per exponential basis; to obtain the value in units of mV/dec, the numbers should be multiplied by 2.3. The low-Pt model also nicely extracts the GDL oxygen diffusivity from the local spectra; quite a reasonable value of $D_b \simeq 0.025\ \mathrm{cm}^2\ \mathrm{s}^{-1}$ is nearly independent of the cell current (Fig. 4.11C).

4. Impedance model for low-Pt cells

4.1 Model

As discussed in the Introduction, the feature of low-Pt cells is quite significant oxygen transport loss in the Nafion film covering Pt/C agglomerates in the CCL. The description of oxygen transport through the CCL by simple diffusion Eq. (4.1) is insufficient, and an impedance model with a detailed account of oxygen transport through the Nafion film is necessary.

To construct such a model, consider a single cylindrical straight pore penetrating through the CCL depth (Fig. 4.12). Let the pore side surface be separated from the Pt/C surface by a thing coaxial ionomer film. This system is the simplest way to incorporate both the through-plane and through-the-film oxygen transport pathways into the impedance model.

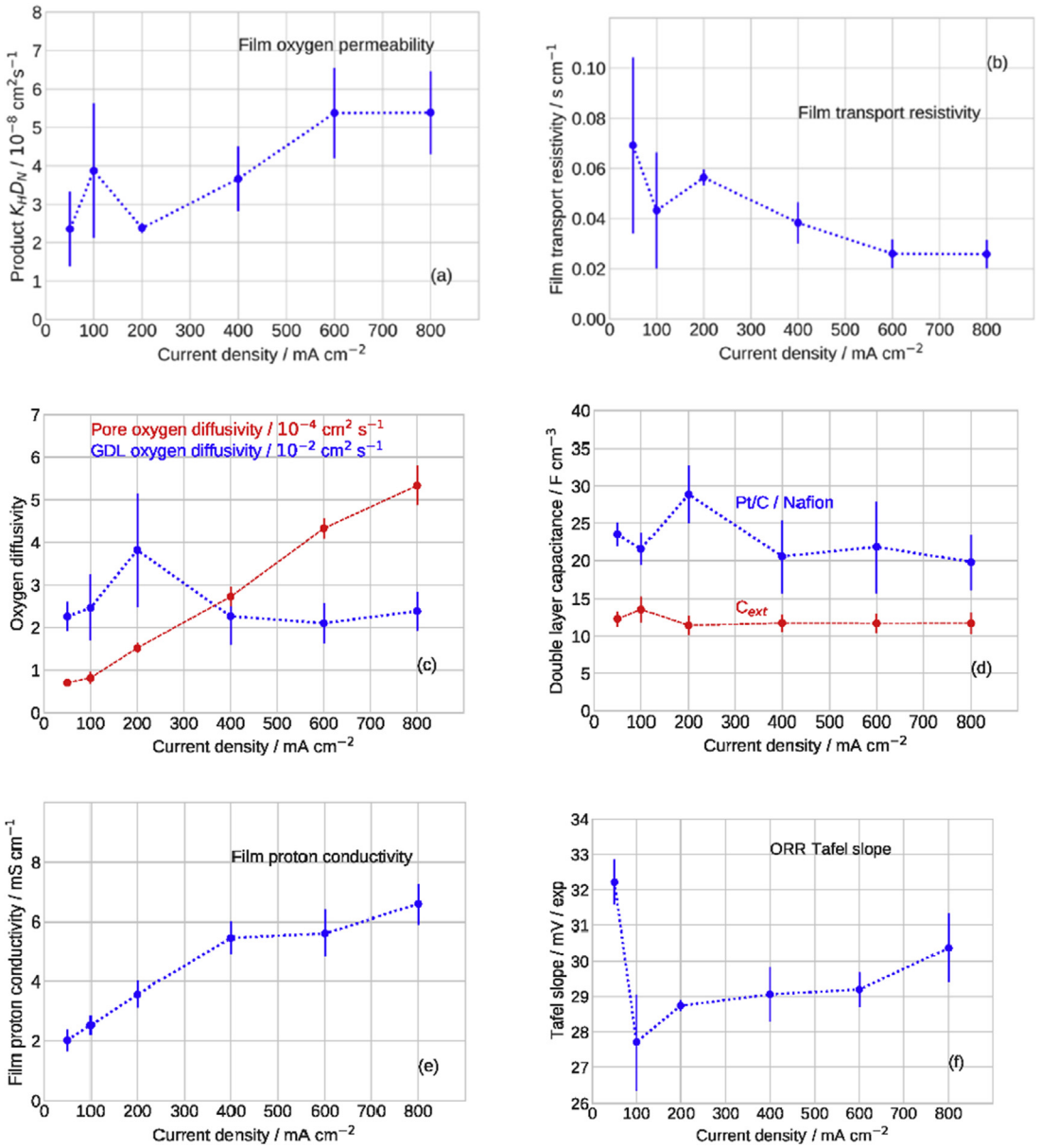

Figure 4.11

Mean over the cell surface parameters versus current cell density.

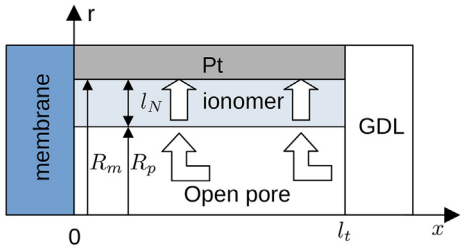

Figure 4.12

Schematic of a single pore for the description of cathose catalyst layer (CCL) impedance. Oxygen is transported along the pore axis x and radial direction through the ionomer film to the Pt surface, where the ORR occurs.

As before, we start with the transient performance model of the pore. The 1d + 1d oxygen diffusion equation along the pore axis is

$$\frac{\partial c}{\partial t} - D_p \frac{\partial^2 c}{\partial x^2} = -\frac{2}{R_p} N_{N,p}, \quad \left.\frac{\partial c}{\partial x}\right|_{x=0} = 0, \quad c(l_t) = c_1 \tag{4.43}$$

where c_1 is the oxygen concentration at the CCL/GDL interface and

$$N_{N,p} = -D_N \left.\frac{\partial c_N}{\partial r}\right|_{r=R_p+} \tag{4.44}$$

is the radial oxygen flux in the Nafion film at the pore/film interface.

Oxygen transport through the Nafion film along the radial direction is described by

$$\begin{gathered} \frac{\partial c_N}{\partial t} - \frac{D_N}{r}\frac{\partial}{\partial r}\left(r\frac{\partial c_N}{\partial r}\right) = 0, \quad c_N(R_p) = K_H c(x), \\ D_N \left.\frac{\partial c_N}{\partial r}\right|_{r=R_m} = -\frac{R_p i_*}{2(4F)}\left(\frac{c_{N,m}}{c_h^{in}}\right)\exp\left(\frac{\eta}{b}\right) \end{gathered} \tag{4.45}$$

Here, K_H is the dimensionless Henry constant (mol/mol) for oxygen solubility in Nafion, $c_{N,m} \equiv c_N(R_m)$

The second boundary condition for Eq. (4.45) means that the oxygen flux at the Nafion film/metal interface equals the Tafel rate of the oxygen consumption in the ORR multiplied by the factor $R_p/2$ having a dimension of length. This factor provides the correct transformation of the model into a standard MH model at the limit of zero film

thickness. Indeed, with $R_m \to R_p$, we have *please*, *delete*, $c_{N,m} \to c_{N,p}$ and the boundary condition at $r = R_m$ in Eq. (4.45) takes the form

$$-D_N \frac{\partial c_N}{\partial r}\bigg|_{r=R_p+} = \left(\frac{R_p}{2}\right)\frac{i_*}{4F}\left(\frac{c_{N,p}}{c_h^{in}}\right)\exp\left(\frac{\eta}{b}\right) \tag{4.46}$$

With Eq. (4.46) and $K_H = 1$, Eq. (4.43) transforms to the standard macro-homogeneous model equation for oxygen transport in the porous CCL, Eq. (4.1).

The proton current conservation equation completes the model

$$C_{dl}\frac{\partial \eta}{\partial t} - \sigma_p \frac{\partial^2 \eta}{\partial x^2} = -i_*\left(\frac{c_{N,m}}{c_h^{in}}\right)\exp\left(\frac{\eta}{b}\right) \tag{4.47}$$

which is quite analogous to Eq. (4.4) with the obvious replacement of c by $c_{N,m}$ in the Tafel ORR rate on the right side.

In addition to dimensionless variables Eq. (4.6), we introduce dimensionless radius

$$\widetilde{r} = \frac{r}{l_t} \tag{4.48}$$

With Eqs. (4.6), (4.43)–(4.48) take the form

$$\mu^2 \frac{\partial \widetilde{c}}{\partial \widetilde{t}} - \varepsilon_*^2 \widetilde{D}_{ox}\frac{\partial^2 \widetilde{c}}{\partial \widetilde{x}^2} = \gamma_p \varepsilon_*^2 \widetilde{N}_{N,p}, \quad \frac{\partial \widetilde{c}}{\partial \widetilde{x}}\bigg|_{\widetilde{x}=0} = 0, \quad \widetilde{c}(1) = \widetilde{c}_1 \tag{4.49}$$

$$\begin{gathered}\mu^2 \frac{\partial \widetilde{c}_N}{\partial \widetilde{t}} - \varepsilon_*^2 \widetilde{D}_N \frac{1}{\widetilde{r}}\frac{\partial}{\partial \widetilde{r}}\left(\widetilde{r}\frac{\partial \widetilde{c}_N}{\partial \widetilde{r}}\right) = 0, \quad \widetilde{c}_{N,p} = K_H \widetilde{c}(\widetilde{x}), \\ \gamma_p \varepsilon_*^2 \widetilde{D}_N \frac{\partial \widetilde{c}_N}{\partial \widetilde{r}}\bigg|_{\widetilde{r}=\widetilde{R}_m} = -\widetilde{c}_{N,m}\exp\widetilde{\eta}\end{gathered} \tag{4.50}$$

$$\frac{\partial \widetilde{\eta}}{\partial \widetilde{t}} - \varepsilon_*^2 \frac{\partial^2 \widetilde{\eta}}{\partial \widetilde{x}^2} = -\widetilde{c}_{N,m}\exp\widetilde{\eta}, \tag{4.51}$$

where $\widetilde{c}_{N,m} \equiv \widetilde{c}_N\left(\widetilde{R}_p\right)$. In Eq. (4.49), the dimensionless flux $\widetilde{N}_{N,m}$ is given by

$$\widetilde{N}_{N,p} = \frac{4Fl_t N_{N,p}}{\sigma_p b} = -\widetilde{D}_N \frac{\partial \widetilde{c}_N}{\partial \widetilde{r}}\bigg|_{\widetilde{r}=\widetilde{R}_p+}, \tag{4.52}$$

and γ_p is the dimensionless parameter

$$\gamma_p = \frac{2}{\widetilde{R}_p} \tag{4.53}$$

4.2 Static equations

The procedure of the derivation of the static equation is described in Ref. [40]; the resulting system of equations for $\widetilde{j}^0$ and $\widetilde{c}^0$ is

$$\frac{\partial^2\widetilde{j}^0}{\partial\widetilde{x}^2}-\left\{\frac{\partial\ln\left(\widetilde{c}^0\right)}{\partial\widetilde{x}}-\left(1+\frac{\alpha\varepsilon_*^2}{K_H\widetilde{c}^0}\frac{\partial\widetilde{j}^0}{\partial\widetilde{x}}\right)\widetilde{j}^0\right\}\frac{\partial\widetilde{j}^0}{\partial\widetilde{x}}=0,\ \widetilde{j}^0(0)=\widetilde{j}_0,\quad \widetilde{j}^0(1)=0 \tag{4.54}$$

and Eq. (4.26) for $\widetilde{c}^0$. Here, $\alpha>0$ is a constant parameter:

$$\alpha=\frac{\widetilde{R}_p\widetilde{R}_m}{2\varepsilon_*^2\widetilde{D}_N}\ln\left(\frac{\widetilde{R}_m}{\widetilde{R}_p}\right) \tag{4.55}$$

With $\widetilde{c}^0(\widetilde{x})$ and $\widetilde{j}^0(\widetilde{x})$ at hand, the static overpotential $\widetilde{\eta}^0(\widetilde{x})$ is obtained from

$$\widetilde{\eta}^0=\ln\left(-\frac{\varepsilon_*^2\partial\widetilde{j}^0/\partial\widetilde{x}}{K_H\widetilde{c}^0+\alpha\varepsilon_*^2\partial\widetilde{j}^0/\partial\widetilde{x}}\right). \tag{4.56}$$

Static oxygen concentration at the film/metal interface is given by [40]

$$\widetilde{c}_{N,m}^0=\frac{K_H\widetilde{c}^0}{1+\alpha\exp\widetilde{\eta}^0} \tag{4.57}$$

4.3 Equations for perturbation amplitudes

Now we can excite the system with small-amplitude harmonic perturbations of the form

$$\widetilde{c}(\widetilde{x},\widetilde{t})=\widetilde{c}^0(\widetilde{x})+\widetilde{c}^1(\widetilde{x},\widetilde{\omega})\exp(\mathrm{i}\widetilde{\omega}\widetilde{t}),\quad \widetilde{c}^1\ll\widetilde{c}^0 \tag{4.58}$$

and similar for $\widetilde{c}_N$ and $\widetilde{\eta}$. Substituting these Fourier-transforms into Eqs. (4.49), (4.50), and (4.51), subtracting the respective static equations, expanding exponent in Eq. (4.51) over small $\widetilde{\eta}^1$ and neglecting the term with perturbations product, we get a system of linear equations for the perturbation amplitudes

$$\begin{gathered}\varepsilon_*^2\widetilde{D}_{ox}\frac{\partial^2\widetilde{c}^1}{\partial\widetilde{x}^2}=-\gamma_p\varepsilon_*^2\widetilde{D}_N\frac{\partial\widetilde{c}_N^1}{\partial\widetilde{r}}\bigg|_{\widetilde{r}=\widetilde{R}_p}+\mathrm{i}\widetilde{\omega}\mu^2\widetilde{c}^1,\quad \frac{\partial\widetilde{c}^1}{\partial\widetilde{x}}\bigg|_{\widetilde{x}=0}=0,\\ \widetilde{c}^1(1)=\widetilde{c}_b^1(1)\end{gathered} \tag{4.59}$$

$$\varepsilon_*^2\widetilde{D}_N\frac{\partial}{\partial\widetilde{r}}\left(\widetilde{r}\frac{\partial\widetilde{c}_N^1}{\partial\widetilde{r}}\right)=\mathrm{i}\widetilde{\omega}\mu^2\widetilde{c}_N^1,\quad \widetilde{c}_N^1\left(\widetilde{R}_p\right)=K_H\widetilde{c}^1(\widetilde{x}),$$
$$\gamma_p\varepsilon_*^2\widetilde{D}_N\left.\frac{\partial\widetilde{c}_N^1}{\partial\widetilde{r}}\right|_{\widetilde{r}=\widetilde{R}_m}=-\exp\left(\widetilde{\eta}^0\right)\left(\widetilde{c}_{N,m}^1+\widetilde{c}_{N,m}^0\widetilde{\eta}^1\right) \tag{4.60}$$

$$\varepsilon_*^2\frac{\partial^2\widetilde{\eta}^1}{\partial\widetilde{x}^2}=\exp\left(\widetilde{\eta}^0\right)\left(\widetilde{c}_{N,m}^1+\widetilde{c}_{N,m}^0\widetilde{\eta}^1\right)+\mathrm{i}\widetilde{\omega}\widetilde{\eta}^1,$$
$$\widetilde{\eta}^1(1)=\widetilde{\eta}_1^1,\quad \left.\frac{\partial\widetilde{\eta}^1}{\partial\widetilde{x}}\right|_{\widetilde{x}=1}=0 \tag{4.61}$$

The right boundary condition in Eq. (4.59) describes continuity of the oxygen concentration perturbation at the CCL/GDL interface. Here, $\widetilde{c}_b^1$ is the perturbation amplitude of the oxygen concentration in the GDL given by Eq. (4.17).

System Eq. (4.59)–(4.61) can be simplified. Solving Eq. (4.60) and setting $\widetilde{r}=\widetilde{R}_m$ in the solution, we get $\widetilde{c}_{N,m}^1$, which appears in Eq. (4.61):

$$\widetilde{c}_{N,m}^1=\frac{1}{B}\left(-qA_cK_H\widetilde{c}^1+A_\eta E\widetilde{c}_{N,m}^0\widetilde{\eta}^1\right) \tag{4.62}$$

where

$$A_c=\mathrm{i}J_0\left(q\widetilde{R}_m\right)K_1\left(-\mathrm{i}q\widetilde{R}_m\right)+J_1\left(q\widetilde{R}_m\right)K_0\left(-\mathrm{i}q\widetilde{R}_m\right) \tag{4.63}$$
$$A_\eta=J_0\left(q\widetilde{R}_p\right)K_0\left(-\mathrm{i}q\widetilde{R}_m\right)-J_0\left(q\widetilde{R}_m\right)K_0\left(-\mathrm{i}q\widetilde{R}_p\right) \tag{4.64}$$
$$B=\left(J_0\left(q\widetilde{R}_m\right)K_0\left(-\mathrm{i}q\widetilde{R}_p\right)-J_0\left(q\widetilde{R}_p\right)K_0\left(-\mathrm{i}q\widetilde{R}_m\right)\right)E$$
$$-\left(\mathrm{i}J_0\left(q\widetilde{R}_p\right)K_1\left(-\mathrm{i}q\widetilde{R}_m\right)+J_1\left(q\widetilde{R}_m\right)K_0\left(-\mathrm{i}q\widetilde{R}_p\right)\right)q \tag{4.65}$$

and

$$q=\sqrt{-\frac{\mathrm{i}\widetilde{\omega}\mu^2}{\varepsilon_*^2\widetilde{D}_N}},\quad E=\frac{\exp\widetilde{\eta}^0}{\gamma_p\varepsilon_*^2\widetilde{D}_N} \tag{4.66}$$

The flux $\widetilde{N}_{N,p}^1=-\left.\frac{\partial\widetilde{c}_N^1}{\partial\widetilde{r}}\right|_{\widetilde{r}=\widetilde{R}_p}$ for Eq. (4.59) is obtained from a solution of Eq. (4.60), resulting in [56]

$$\widetilde{N}_{N,p}^1=\frac{\mu\widetilde{D}_N}{B_N}\left(Q_\eta\widetilde{\eta}^1+Q_cK_H\widetilde{c}^1\right) \tag{4.67}$$

where

$$B_N = \sqrt{2\widetilde{\omega}}\gamma_p\varepsilon_*^2\mu\widetilde{D}_N\big((1+\mathrm{i})K_1\big(-\mathrm{i}q\widetilde{R}_m\big)J_0\big(q\widetilde{R}_p\big)+(1-\mathrm{i})J_1\big(q\widetilde{R}_m\big)K_0\big(-\mathrm{i}q\widetilde{R}_p\big)\big)$$
$$-2\varepsilon_*\sqrt{\widetilde{D}_N}\exp\big(\widetilde{\eta}^0\big)\big(J_0\big(q\widetilde{R}_m\big)K_0\big(-\mathrm{i}q\widetilde{R}_p\big)-J_0\big(q\widetilde{R}_p\big)K_0\big(-\mathrm{i}q\widetilde{R}_m\big)\big) \quad (4.68)$$

$$Q_\eta = \sqrt{2\widetilde{\omega}}\exp\big(\widetilde{\eta}^0\big)\widetilde{c}^0_{N,m}\big((1+\mathrm{i})K_1\big(-\mathrm{i}q\widetilde{R}_p\big)J_0\big(q\widetilde{R}_p\big)+(1-\mathrm{i})J_1\big(q\widetilde{R}_p\big)K_0\big(-\mathrm{i}q\widetilde{R}_p\big)\big) \quad (4.69)$$

$$Q_c = \sqrt{2\widetilde{\omega}}\exp\big(\widetilde{\eta}^0\big)\big((1-\mathrm{i})K_0\big(-\mathrm{i}q\widetilde{R}_m\big)J_1\big(q\widetilde{R}_p\big)+(1+\mathrm{i})J_0\big(q\widetilde{R}_m\big)K_1\big(-\mathrm{i}q\widetilde{R}_p\big)\big)$$
$$-2\widetilde{\omega}\gamma_p\varepsilon_*\mu\sqrt{\widetilde{D}_N}\big(J_1\big(q\widetilde{R}_m\big)K_1\big(-\mathrm{i}q\widetilde{R}_p\big)-J_1\big(q\widetilde{R}_p\big)K_1\big(-\mathrm{i}q\widetilde{R}_m\big)\big) \quad (4.70)$$

Here, J_0, J_1 are the Bessel functions of the first kind, and K_0, K_1 are the modified Bessel functions of the second kind. Therefore, the problem for perturbation amplitudes is reduced to the system of two Eqs. (4.59), (4.61) with the right Robin-type boundary condition Eq. (4.40) for Eq. (4.59).

4.4 Fitting low-Pt cell spectra

The low-Pt impedance model discussed above has been fitted to local experimental spectra of a cellbased on MEA with the Pt loading of 0.1 $mg_{Pt}\ cm^{-2}$. The CCL and GDL thickness and the cell operating parameters are listed in Table 4.4. Furthermore, the single-pore model has been generalized to take into account pore size distribution (PSD) in the electrode.

The total oxygen flux along the void pore is proportional to the square of the pore radius, while this flux through the ionomer film covering the side surface of the pore is proportional to the first power of the radius. The electrode oxygen transport properties strongly depend on the PSD [57,58,59]. To accelerate calculations, the experimental PSD of a Gore PRIMEA electrode measured in Ref. [60] has been approximated by the stepwise PSD with the nine characteristic radii (Fig. 4.13, Table 4.5).

The segment impedance $Z_{seg,\ n}$ of the n-th segment has been calculated as the impedance of nine parallel pores:

Table 4.4: Low-Pt MEA parameters and operating conditions.

GDL thickness l_b, cm	$230 \cdot 10^{-4}$ (230 μm)
CCL thickness l_t, cm	$3.0 \cdot 10^{-4}$ (3.0 μm)
Ionomer film thickness l_N, cm	$10 \cdot 10^{-7}$ (10 nm)
Air flow stoichiometry λ	4
Back pressure, kPa	150
Cell temperature, K	273 + 80

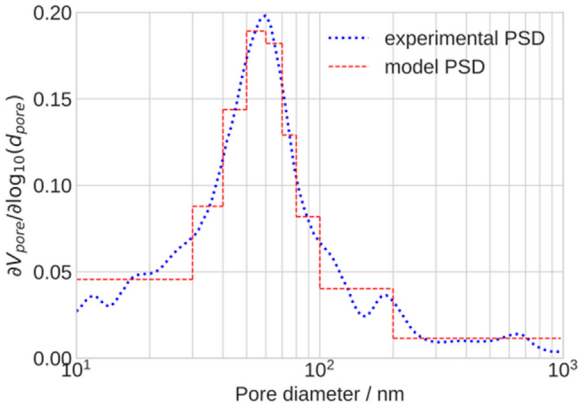

Figure 4.13
Experimental [52] (dotted line) and approximate model (dashed line) pore size distributions in the low-Pt cathode catalyst layer.

$$\frac{1}{Z_{seg,n}} = \sum_{k=1}^{9} \frac{w_k}{Z_{k,n}} \tag{4.71}$$

Where k enumerates pore size in the spectrum and w_k is the k-th pore volume fraction. The local impedance $Z_{k,n}$ of the k-th pore type in the n-th segment has been calculated from the numerical solution of Eq. (4.59) with (4.40), (4.61), and (4.39). The iteration procedure to solve the trough-plane and along-the-channel equations were discussed in Section 3. A parallel Python code has been developed using the message passing interface library. Calculated segment impedance $Z_{seg,n}$, Eq. (4.71) has been fitted to the respective local experimental spectrum using the least-squares procedure.

Local impedance spectra have been measured at the operating conditions listed in Table 4.4 for the current densities 50, 100, 200, 300, 400, 600, and 800 mA cm^{-2}. Local experimental and fitted model Nyquist spectra for the current density of 400 mA cm^{-2} are shown in Fig. 4.14. At the remote segments, 8 to 10, the low-frequency (LF) part of the spectra become noisy, and the quality of fitting of the LF arc decays (Fig. 4.14).

Code testing has shown that the fitting is more sensitive to the ratio l_N/D_N, rather than to l_N and D_N separately. Here, l_N and D_N are the ionomer film thickness and oxygen diffusivity, respectively. On the other hand, equations show that D_N appears in the model only as a product $K_H D_N$, where K_H is the dimensionless Henry's constant for oxygen solubility in ionomer film. To reliably obtain the parameter $K_H D_N$ from fitting, the ionomer film thickness has been fixed at $l_N = 10$ nm. This value agrees with our previous measurements [41] and with the literature sources [61–63]. For iterations, the starting value of $K_H D_N = 6.76 \cdot 10^{-9}$ cm^2 s^{-1} has been taken, which is the dimensionless Henry's

Table 4.5: Parameters of the stepwise PSD in Fig. 4.13.

	1	2	3	4	5	6	7	8	9
Pore radius, nm	16.5	35.4	45.0	54.3	65.1	75.1	88.8	130	152
Pore volume fraction	0.199	0.100	0.127	0.137	0.112	0.0685	0.0725	0.111	0.0727

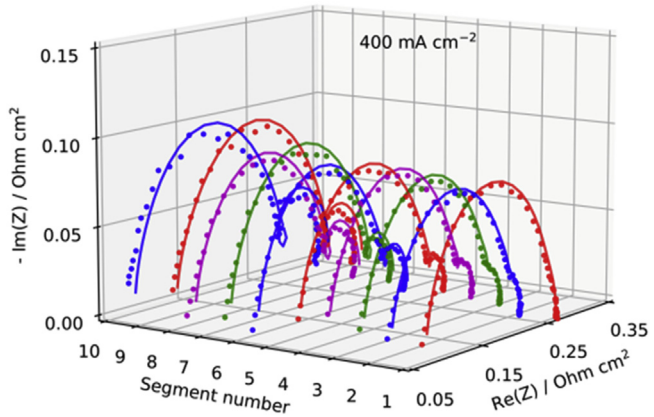

Figure 4.14
Experimental (points) and fitted model (lines) local Nyquist spectra from the individual segments. The air inlet is at segment 1. The outlet is at segment 10.

constant for oxygen solubility in water at 80°C multiplied by the oxygen diffusivity in bulk Nafion [64] of 10^{-6} cm^2 s^{-1}.

The product $K_H D_N$ resulting from fitting is nearly constant as the cell current density increases (Fig. 4.15A). The only imaginable difference between the low- and high-current cell operation is the amount of liquid water in the catalyst layer, which increases with j_0. Novitski and Holdcroft [65] measured the ionomer film oxygen diffusivity D_N using electrochemical cells and reported D_N growth with relative humidity. In our case, no significant variation of $K_H D_N$ with the current has been detected.

The ionomer film oxygen transport resistivity calculated as [66]

$$\mathcal{R}_N = \frac{R_p L_N}{2 D_N K_H l_t}, \quad R_p = \sum_{n=1}^{9} w_n R_{p,n} \tag{4.72}$$

is plotted in Fig. 4.15B. In the studied range of currents, the film resistivity is nearly constant at $\simeq$ 0.4 s cm^{-1} (Fig. 4.15B). This value is close to collected in Ref. [35] literature data of $\mathcal{R}_N \simeq$ 0.3 s cm^{-1} corresponding to Pt loading of 0.1 mg$_{Pt}$ cm^{-2}.

Surprisingly, the pore and GDL oxygen diffusivities are nearly constant in the studied range of currents (Fig. 4.15C). The pore oxygen diffusivity of 10^{-4} cm^2 s^{-1} and the GDL oxygen diffusivity of 0.025 cm^2 s^{-1} are quite realistic values. In this cell, no Tafel slope doubling up to 800 mA cm^{-2} is observed. The capacitance of the Pt/C/Nafion double layer decreases with the cell current by a factor of two, seemingly due to growing liquid water content in the electrode (Fig. 4.15D). For the same reason, the Nafion film proton conductivity σ_p exhibits linear growth with the cell current density followed by saturation

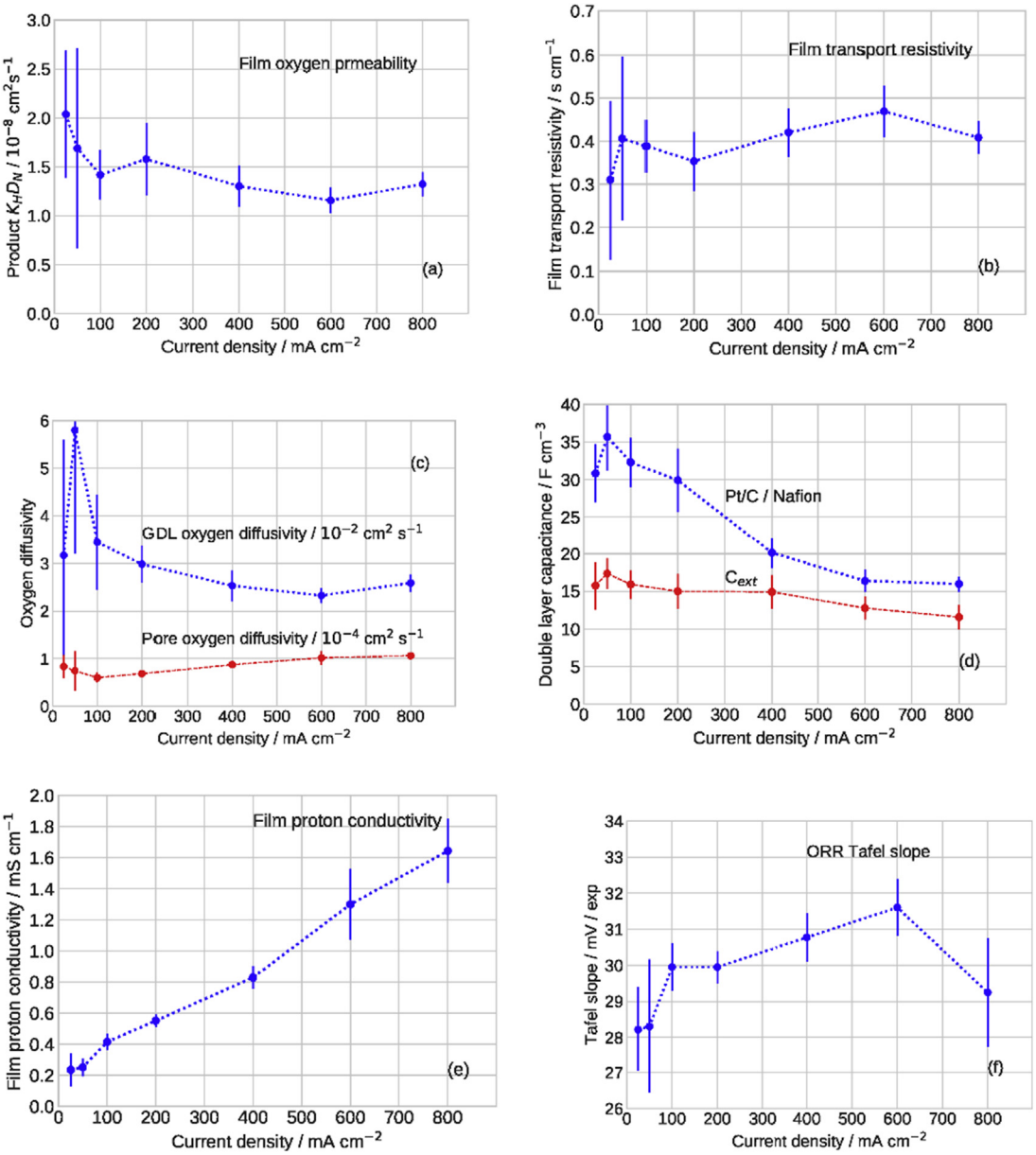

Figure 4.15

Mean over the cell surface parameters versus current cell density. Nafion film oxygen permeability (A), Nafion film transport resistivity (B), GDL and pore oxygen diffusivities (C), Double layer capacitance (D), Nafion film proton conductivity (E), and ORR Tafel slope (F).

at the level of $\sigma_p \simeq 0.8$ mS cm^{-1} (Fig. 4.15E). The conductivity σ_p is very small, indicating a low amount of ionomer in the CCL. The ORR Tafel slope is about 30 mV/exp, equivalent to about 70 mV/decade, a well-known from kinetic studies value (Fig. 4.15F).

5. Distribution of relaxation times

5.1 The idea of DRT

Physics-based modeling of cell impedance is a complicated task requiring substantial computing resources and time, while calculation of DRT is a simple and fast procedure. DRT function $\gamma(\tau)$ is a solution to equation [67,68–72]

$$Z(\omega) = R_\infty + R_{pol}\int_0^\infty \frac{\gamma(\tau)d\tau}{1+\mathrm{i}\omega\tau} \tag{4.73}$$

where Z is the fuel cell impedance, ω is the angular frequency, R_∞ is the high-frequency cell resistance, and R_{pol} is the total polarization resistance of the cell given by the total diameter of the Nyquist spectrum.

The impedance of a parallel RC circuit is $R/(1+\mathrm{i}\omega RC)$. Comparing this to Eq. (4.73), it is clear that Eq. (4.73) is an expansion of cell impedance over the infinite sum of parallel RC-circuit impedances, each one having the resistivity $R_{pol}\gamma d\tau$. From Eq. (4.73), it follows that the DRT spectrum of a single parallel RC-circuit is the Dirac δ-function positioned at $\tau_* = RC$.

The cell impedance is usually measured at equidistant on log-scale frequencies $\{f_i, i = 1, \ldots, N\}$, that is, for $\ln(f_{i+1}) - \ln(f_i)$ independent of i (this is seen in Fig. 4.16B). For numerical calculation of DRT, it is thus beneficial to consider function $G(\tau)$, which obeys the equation

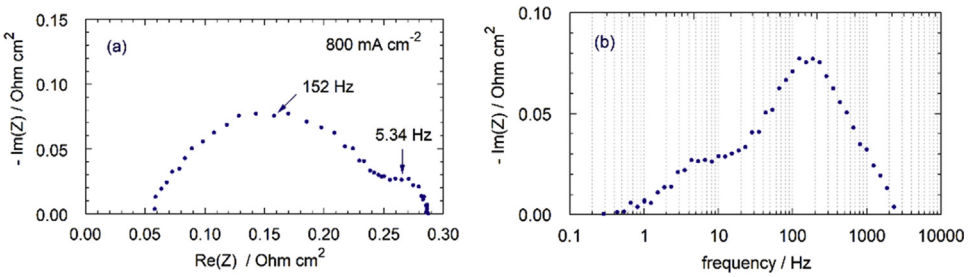

Figure 4.16

Experimental Nyquist spectrum of the low-Pt PEM fuel cell impedance at the cell current of 800 mA cm^{-2} (A). Frequency dependence of the imaginary part (B).

$$Z(\omega) = R_\infty + R_{pol} \int_{-\infty}^{\infty} \frac{G(\tau) d \ln(\tau)}{1 + i\omega\tau} \tag{4.74}$$

Since $\tau = 1/(2\pi f)$,

$$\gamma(\tau) = \frac{G(\tau)}{\tau}, \text{ or } G(f) = \frac{\gamma(f)}{2\pi f} \tag{4.75}$$

where f is the regular frequency (Hz). It follows that the dimension of γ is s^{-1}, while G is the dimensionless function. Setting in Eq. (4.73) $\omega = 0$ and taking into account that $Z(0) - R_\infty = R_{pol}$, we see that γ and G obey the respective normalization conditions

$$\int_0^\infty \gamma(\tau) d\tau = \int_{-\infty}^{\infty} G(\tau) d \ln(\tau) = 1 \tag{4.76}$$

A great advantage of DRT spectra over standard impedance is that the functions γ and G are extremely sensitive to *RC*-like components in the impedance spectrum. All kinetic and transport processes in a fuel cell eventually are linked to the charging/discharging of the double layer at the cathode catalyst/ionomer interface. One, therefore, may expect that the spectra of individual processes in the cell are close to the *RC*-circuit spectrum. If, in addition, the resonance frequencies of individual processes are well separated on the frequency scale, the spectrum of $\gamma(f)$ and/or $G(f)$ consists of a number of well-separated peaks. The peak frequency position f_n gives the characteristic frequency of the process, and the area under each peak on the τ-scale gives the contribution R_n of this process to the total R_{pol}:

$$R_n = R_{pol} \int_{\tau_n}^{\tau_{n+1}} \gamma(\tau) d\tau = R_{pol} \int_{\tau_n}^{\tau_{n+1}} G(\tau) d \ln(\tau) \tag{4.77}$$

where τ_n, τ_{n+1} are peak boundaries.

Analysis of DRT spectra of solid oxide fuel cells is a well-established field (see a review [73]), while in studies of low-temperature PEM fuel cells, DRT is a relatively new technique [72]. To the best of our knowledge, so far, DRT spectra of low-Pt PEMFC have been analyzed just in Ref. [74].

Eqs. (4.73), (4.74) belong to the class of Fredholm equations of the first kind. Direct numerical approximation of Eqs. (4.73), (4.74) leads to an ill-posed problem and numerical methods for the solution of Eqs. (4.73), (4.74) are usually based on variants of Tikhonov's regularization technique [70,75–77] (see also review [78]). In this work, Eq. (4.74) is solved numerically using our most recent scheme based on nonnegative least

squares (NNLS) [79] solution of Tikhonov's regularized system of equations [80]. This approach allows us to avoid projected gradient iterations suggested in Ref. [80], as the NNLS method does this job much faster. The Python code "DRT_Gfun_nnls_1.0.zip" for calculation of DRT $G(f)$ from fuel cell impedance can be downloaded from https://github.com/akulikovsky/DRT-python-code.

5.2 Impedance and DRT of high- and low-Pt cell

We processed spectra of two cells with the low- and high-Pt loading of 0.1 $mg_{Pt}\ cm^{-2}$ and 0.4 $mg_{Pt}\ cm^{-2}$, respectively, for both electrodes. The cell parameters and operating conditions are presented in Table 4.6. Impedance spectra have been collected for the overall cell current density in the range of 200−800 mA cm^{-2}.

The high-frequency part of impedance spectra (typically above 2 kHz) contains the points with positive imaginary parts. Fuel cell impedance is masked by the cable inductance in this frequency range, and the points with Im (Z) > 0 have been discarded. Prior to DRT calculation, the real part of the remaining high-frequency point has been subtracted from the cell impedance. This procedure eliminates R_∞ from Eq. (4.74), and the real part of this equation takes the form

$$Z_{re,*}(\omega) = R_{pol} \int_{-\infty}^{\infty} \frac{G(\tau) d \ln(\tau)}{1 + \omega^2 \tau^2} \tag{4.78}$$

where $Z_{re,*}(\omega) = Z_{re} - R_{pol}$ and the subscript "re" denotes the real part.

Fig. 4.16 shows an example of the whole low-Pt cell spectrum measured at the current density of 800 mA cm^{-2}. Fig. 4.17 shows DRT of the impedance spectrum from the first segment of the low-Pt cell, calculated from Eq. (4.78). The optimal regularization parameter λ for Tikhonov's regularization has been calculated using the L-curve method [81].

Table 4.6: Parameters and operating conditions of low-Pt and high-Pt cells.

Parameters	Low-Pt	High-Pt
Catalyst loading, $mg_{Pt}\ cm^{-2}$	0.1	0.4
CCL thickness l_t, cm	$3.0 \cdot 10^{-4}$	$11.0 \cdot 10^{-4}$
GDL thickness l_b, cm	0.023 (230 μb)	
Air channel depth h, cm	0.1	
Air flow stoichiometry λ	4	
Back pressure P, kPa	150	
Cell temperature, K	273 + 80	

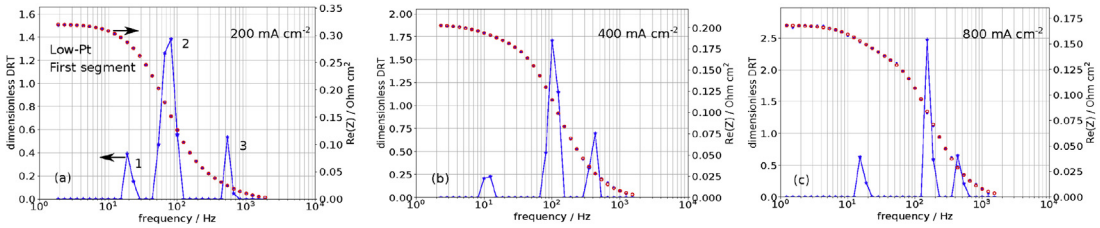

Figure 4.17

DRT $G(f)$ of impedance spectra from the first segment of a low-Pt PEMFC (solid blue line and stars) calculated using Eq. (4.74) and the real part of impedance (blue dots). Red open circles show the real part of impedance reconstructed from the calculated DRT using the real part of Eq. (4.78).

In most variants (48 out of 50), the local DRT spectrum consists of three peaks (Fig. 4.17). The leftmost peak in Fig. 4.17 can be attributed to oxygen transport in the gas diffusion layer (GDL) or rather in the GDL and channel. The middle peak in Fig. 4.17 represents the unresolved charge transfer and oxygen transport processes in the ionomer film. The rightmost peak in Fig. 4.17 manifests oxygen transport in void pores of the CCL. The remaining part of this section provides arguments supporting these statements.

5.3 Parameters of a low- and high-Pt MEAs

Ten local DRT spectra for every current density allowed us to calculate the mean over the segment's peak frequency position, peak resistance, and the corresponding standard

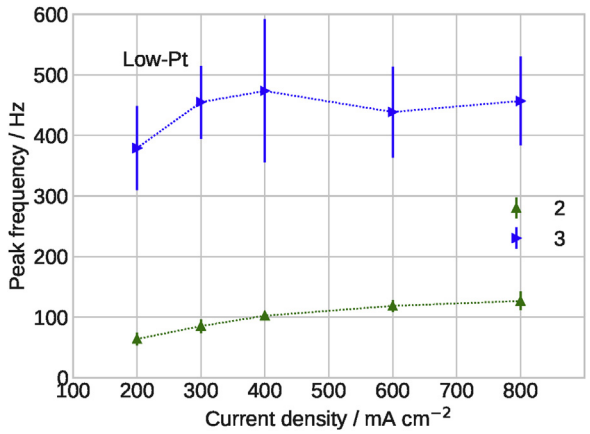

Figure 4.18

Mean over 10 segments frequency of distribution of relaxation time (DRT) peaks 2 and 3 of the low-Pt cell versus current cell density. Peak numbering is shown in Fig. 4.17A. The frequency position of the first peak strongly depends on the coordinate along the channel (Fig. 4.19A).

deviations. Let the peak characteristic frequencies numbered in the ascending order be $\{f_n, n = 1,\ 2, 3\}$ (Fig. 4.17A). Fig. 4.18 shows the dependence of frequency positions of peaks 2 and 3 on the cell current density. A quite small confidence interval for the curve f_2 in Fig. 4.18 means that the spread of f_2 between the segments is small. The frequencies of peak 3 (Fig. 4.18) exhibit a large statistical spread with no distinct dependence on segment location.

Position f_1 and resistivity R_1 of the first (leftmost) DRT peak exhibit distinct trends along the cathode channel: f_1 decreases while R_1 increases with the distance from the inlet (Fig. 4.19). Assuming that the first peak represents oxygen transport in the GDL, we may expect that f_1 obeys the Warburg finite-length formula

$$f_1 \simeq \frac{2.54 D_b}{2\pi l_b^2} \tag{4.79}$$

where D_b is the GDL oxygen diffusivity, and l_b is the GDL thickness. With l_b from Table 4.6 and f_1 decaying from 20 Hz at the channel inlet down to 2 Hz at the outlet (Fig. 4.19A), we get a range of D_b variation from $2.6 \cdot 10^{-2}$ cm^2 s^{-1} at the inlet to $2.6 \cdot 10^{-3}$ cm^2 s^{-1} at the outlet. The decay of GDL oxygen diffusivity along the channel is accompanied by the growth of the GDL oxygen transport resistivity toward the outlet (Fig. 4.19B). Strong decay of f_1 and the growth of the first peak resistivity along the cathode channel suggest higher liquid water content in the GDL of remote segments. With the growth of current cell density, the GDL water content becomes more uniform along the channel, and the f_1-shape in Fig. 4.19A becomes flatter. The growth of mean along the channel D_b with the cell current could be attributed to better water transport in the GDL at

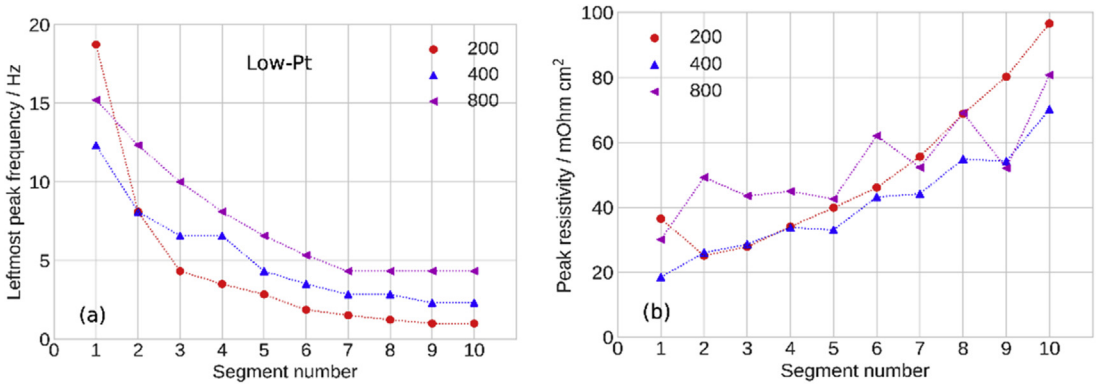

Figure 4.19

Frequency position (A) and resistivity of the first (leftmost) distribution of relaxation time (DRT) peak (B) of the low-Pt cell versus distance along the cathode channel for the indicated cell current densities (mA cm^{-2}).

higher currents. The mechanism of this effect presumably is due to higher air flow velocity in the channel at higher currents, which facilitates liquid water removal from the GDL.

Another possible explanation of the f_1 behavior is as follows. The first peak may represent merged peaks of oxygen transport in the GDL and the cathode channel. The characteristic frequency f_h of oxygen transport in the channel is [82].

$$f_h = \frac{3.3v}{2\pi L} \tag{4.80}$$

The flow oxygen stoichiometry λ is given by

$$\lambda = \frac{4Fhvc_h^{in}}{Lj_0} \tag{4.81}$$

Combining Eqs. (4.80) and (4.81), we get

$$f_h = \frac{0.825\lambda j_0}{2\pi Fhc_h^{in}} \tag{4.82}$$

With the data from Table 4.6, we get $f_h \simeq 2{-}6$ Hz, as j_0 increases from 0.2 to 0.8 A cm^{-2}. These values are close to the first peak frequency f_1 in the DRT spectra. We, thus, could assume that the first peak represents oxygen transport in a combined "GDL + channel" media. The growth of R_1 along the channel then correlates with the growth of the second, low-frequency arc in the local Nyquist spectra (Fig. 4.20). This effect was first demonstrated in experiments [83] and discussed in modeling studies [15,29,84]. Developing an analytical model for the "GDL + channel" impedance is still a field of ongoing research [26].

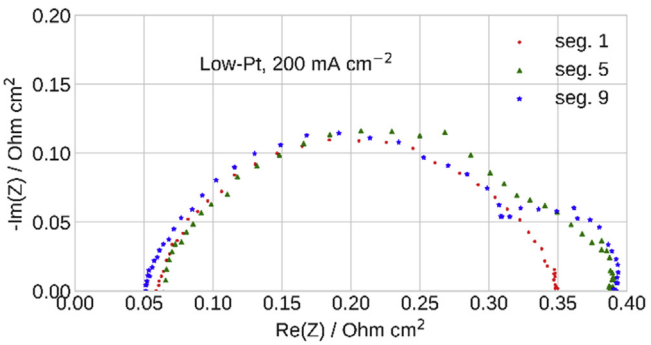

Figure 4.20
Local impedance spectra of a low-Pt cell at the current density of 200 mA cm^{-2}.

The growth of the second peak frequency f_2 with the cell current j_0 (Fig. 4.18) is explained by an increase in the frequency f_{ct} of the faradaic (charge transfer) process, which presumably gives the main contribution to this peak. At low cell currents, f_{ct} is proportional to j_0, as the charge-transfer resistivity R_{ct} is inversely proportional to j_0 [30]:

$$f_{ct} = \frac{1}{2\pi R_{ct} C_{dl} l_t} = \frac{j_0}{2\pi b C_{dl} l_t}, \quad R_{ct} = \frac{b}{j_0} \tag{4.83}$$

The average frequency position f_3 of the last third peak is nearly independent of the cell current density (Fig. 4.18).

To clarify the nature of the second and third peaks, we calculated DRT of local spectra of the high-Pt cell with the standard cathode Pt loading of 0.4 mg_{Pt} cm^{-2}. The spectra have been measured using the same segmented cell setup under the same operating conditions (Table 4.6) [19]. Quite similar to the low-Pt cell, the local DRT spectra of the high-Pt cell exhibit three peaks (Fig. 4.21). Fig. 4.22 shows a comparison of polarization resistivities of peaks 1 to 3 in the low-Pt and high-Pt cells. In the low-Pt cell, the second peak resistivity exhibits distinct decay with j_0, followed by flattening at higher currents (Fig. 4.22). In the high-Pt cell, the resistivity of peak 2 also decreases with the current density, suggesting that peak 2 exhibits the faradaic process in the cell. However, the gap between the low-Pt and high-Pt peak 2 curves (shaded area in Fig. 4.22) increases with the current. This indicates that peak 2 includes some additional resistivity in the low-Pt cell, which increases with the cell current. Analysis shows that the characteristic frequencies of charge-transfer and oxygen transport in ionomer film differ by the factor of $\sqrt{3}$ [66] and the respective DRT peaks could merge in one. The peak 2 representing practically pure charge-transfer resistivity in a high-Pt cell decreases with the cell current. In contrast, the significant contribution of ionomer-transport resistivity flattens the resistivity of peak 2 of the low-Pt cell at higher currents (Fig. 4.22). We presume that both the low-Pt and high-Pt MEAs employ the same Pt/C catalyst on the cathode side, and hence in the absence of ionomer film resistivity, the two upper curves in Fig. 4.22 should coincide or at least be

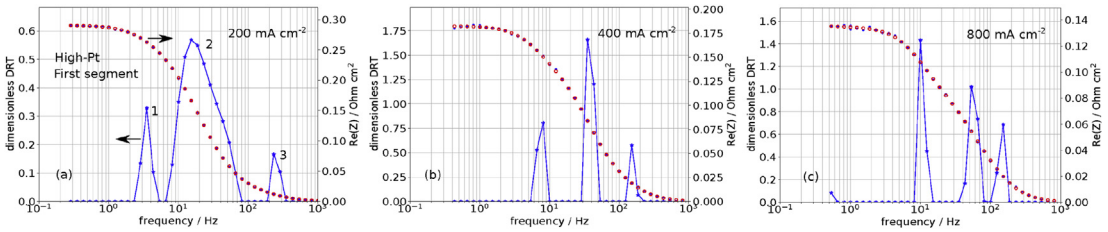

Figure 4.21
Distribution of relaxation time (DRT) of segment 1 in the high-Pt proton-exchange membrane fuel cell (PEMFC). Refer to Fig. 4.17 for curves meaning.

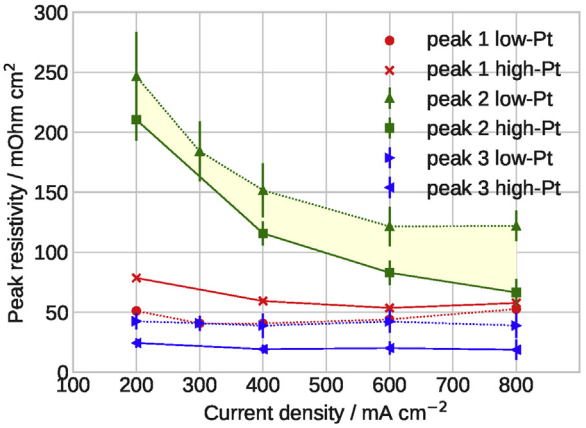

Figure 4.22

Mean over 10 segments polarization resistivities of peaks 1 to 3 of the low-Pt and high-Pt cells. For peak 1, the confidence intervals are not shown due to the smooth variation of peak resistivity along the channel (Fig. 4.19). The shaded area is the estimate of the ionomer film transport resistivity.

close to each other. Thus, the shaded area in Fig. 4.22 could be attributed to the oxygen transport resistivity of ionomer film [66].

In the low-Pt and high-Pt cells, the resistivity of peak 3 weakly depends on cell current density (Fig. 4.22). We assume that in both cells, the high-frequency peak 3 represents oxygen transport in void pores. In Ref. [74], we attributed the third DRT peak of the low-Pt cell to oxygen transport in the void pores and ionomer film. However, weak dependencies of f_3 and the third peak resistivity on cell current suggest that f_3-peak represents oxygen transport in void pores only. Taking again for the estimate Warburg finite-length formula $f_3 \simeq 2.54 D_p / \left(2\pi l_t^2\right)$, for the oxygen diffusivity in void pores of a low-Pt cell, we get $D_p \simeq 10^{-4}\ \mathrm{cm^2\ s^{-1}}$. Here, $l_t = 3 \cdot 10^{-4}$ cm and $f_3 \simeq 450$ Hz (Fig. 4.18). This value of D_p agrees well with the result obtained from fitting the physics-based model to the local impedance spectra (Fig. 4.15C). From Fig. 4.22, it follows that D_p practically does not change with the cell current density in the range of 200−800 mA $\mathrm{cm^{-2}}$, which correlates with the D_{ox} behavior in Fig. 4.15C [74].

The value of $D_p \simeq 10^{-4}\ \mathrm{cm^2\ s^{-1}}$ is an order of magnitude higher than the oxygen diffusivity in water and at least an order of magnitude lower than the oxygen diffusion coefficient in a free void space of a dry catalyst layer [85]. This finding suggests that the void pores of a low-Pt cell are partially flooded, as predicted in Ref. [86]. Further, a comparison of low- and high-Pt resistivity curves for the third peak shows that in the low-Pt cell, the resistivity R_{ox} of oxygen transport in void pores is about 1.5 times higher than

in the high-Pt cell (Fig. 4.22). This resistivity is proportional to l_t / D_p; for the estimates, we take the low-current formula [18].

$$R_{ox} = \frac{bl_t}{12FD_p c_1} \tag{4.84}$$

where c_1 is the oxygen concentration at the CCL/GDL interface. The low-Pt CCL is three to four times thinner than the high-Pt CCL, hence with the same Dp, Rox of the low-Pt CCL would have been three times lower than the high-Pt CCL, as it follows from Eq. (4.84). Thus, Fig. 4.22 shows that the oxygen diffusion coefficient in void pores of the low-Pt CCL is about five to six times less than in the high-Pt CCL. This is another indication that the low-Pt cathode is partially flooded.

The ratio $D_p^{high} \Big/ D_p^{low}$ can also be estimated from the peak frequencies. The characteristic frequency f_3^{high} in the high-Pt cell is about 200 Hz (Fig. 4.21). Taking into account that in the low-Pt cell $f_3^{low} \simeq 450$Hz and the ratio of CCL thicknesses in the high-Pt and low-Pt cells is about 3.5 (Table 4.6), from Warburg finite-length formula, it follows that the ratio

$$\frac{D_p^{high}}{D_p^{low}} = \frac{f_3^{high}}{f_3^{low}} \left(\frac{l_t^{high}}{l_t^{low}} \right)^2 \simeq 5.4 \tag{4.85}$$

which confirms the estimate from peak resistivities above.

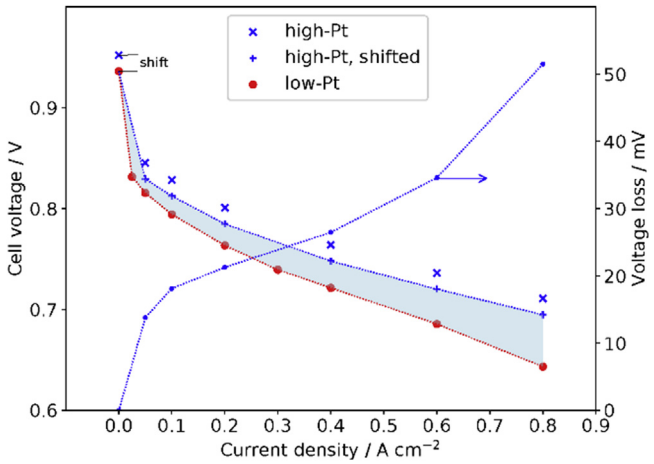

Figure 4.23

Polarization curves of the high- and low-Pt cells. Crosses indicate the high-Pt curve shifted down to combine the open-circuit point with the low-Pt one. The remaining voltage losses are given by the difference of curves indicated by the crosses and large points (shaded area). The shaded area width (mV) plot is shown by small dots (right axis).

It is advisable to compare the sum of potential losses calculated using the DRT technique with this sum resulting from polarization curves. Fig. 4.23 shows the polarization curves of the low- and high-Pt cells used in our experiments and the relative potential loss in the low-Pt cell. The "open circuit" points in Fig. 4.23 represent, in fact, the potential of the cells operating at the current density of about 3 mA cm^{-2} due to hydrogen crossover. The difference of cell potentials ΔV_0 at the highest point of the polarization curve is due to lower superficial exchange current density j^* in the low-Pt cell. Thus, by shifting the polarization curve of the high-Pt cell down by the value of ΔV_0, we compensate for the loss due to lower j^* in the low-Pt cell. In the absence of potential losses specific to low-Pt cells, the shifted IV curve of the high-Pt cell would overlap with the low-Pt cell curve. This, however, is not the case (Fig. 4.23), and the difference between the two curves can be attributed to the specific ionomer film transport losses in a low-Pt cell (shaded area in Fig. 4.23).

The accuracy of the low-current part of the peak 2 curves in Fig. 4.22 is low, and for comparison, we take the point 800 mA cm^{-2}. At this current, from Fig. 4.22, we get the potential losses in a low-Pt cell due to peaks 2 and 3 of 44 and 16 mV, respectively. The losses due to peak one in both the cells are almost equal, and hence they do not contribute to the resulting curve. The "losses" curve in Fig. 4.23 shows that the total voltage loss at 800 mA cm^{-2} is $\simeq$ 52 mV. Considering the relatively large standard deviation of the third peak resistivity, the value of 52 mV agrees reasonably well with the sum of $44 + 16 = 60$ mV following from Fig. 4.22.

6. Conclusion

High current and low stoichiometry impedance spectra of PEMFCs are typically noisy, especially in the low-frequency region. This is believed to be due to the transport of liquid water in the porous layers and membrane [87,88,89]. In addition, the accumulation of liquid water could lead to local CCL and/or GDL flooding. Segmented cell setup is an expensive and unique technique, while measuring the whole-cell spectra is routine. The goal of impedance theory is thus to develop models for the extraction of local transport parameters from the whole-cell spectra. The first attempt to construct such a model has been made in Ref. [90]; however, more experimental and theoretical studies are necessary to advance this technique.

From a numerical standpoint, the models discussed in this Chapter are not very time-consuming provided that the calculations are parallelized to take advantage of modern multicore processors. All the models have been parallelized in Python using a standard message passing interface (MPI). The high-Pt impedance model typically needs 10 to 40 cores for running; fitting a single spectrum takes 10−40 min on a cluster of modern 3−4 GHz PCs. The low-Pt model with nine pore types in Section 4 requires at least 90 cores, and it takes about 10−20 min to fit a set of 10 local spectra. The rapid development

of multicore processors gives hope that soon, the models could be run on a single standalone PC or even on a laptop.

Comparison of transport parameters obtained from the local and whole-cell impedance models shows that the accuracy of the latter models could be quite low, up to 100%. To improve the accuracy of fitting results, experimental spectra with 20 points per decade or more are needed. Measuring local spectra from the segmented cell is a more complicated task; however, this technique provides an opportunity to obtain statistically significant cell transport parameters with standard deviations, as discussed above.

Generally, fitting physics-based impedance models to spectra measured from the cell in a current production mode could give comprehensive information on cell parameters. Further advancement of models for cell impedance and comparing physics-based modeling with the DRT results seems to be the most promising way toward this goal.

Nomenclature

b	ORR Tafel slope, V
c	Oxygen molar concentration in the CCL/pore, mol cm^{-3}
c_b	Oxygen molar concentration in the GDL, mol cm^{-3}
C_{dl}	Double-layer volumetric capacitance, F cm^{-3}
c_h	Oxygen molar concentration in the channel, mol cm^{-3}
c_N	Oxygen molar concentration in the ionomer (Nafion) film, mol cm^{-3}
D_N	Oxygen diffusion coefficient in the Nafion film, cm^2 s^{-1}
D_{ox}	Effective oxygen diffusion coefficient in the CCL, cm^2 s^{-1}
D_p	Oxygen diffusion coefficient in the void pore, cm^2 s^{-1}
E	Auxiliary parameter, Eq. (4.66)
F	Faraday constant, C mol^{-1}
$\mathbf{i}$	Imaginary unit
j	Local proton current density along the CCL/pore, A cm^{-2}
K_H	Dimensionless Henry's constant for oxygen solubility in ionomer, mol/mol
l_N	Nafion film thickness, cm
l_t	CCL thickness/pore length, cm
N_N	Radial oxygen flux in the Nafion film, mol $cm^{-2}s^{-1}$
q	Auxiliary parameter, Eq. (4.66)
r	Radial coordinate, cm
R_{ccl}	Catalyst layer resistivity, Ohm cm^2
R_m	Radius of a Pt/C tube, cm
R_N	Nafion film transport resistivity, Ohm cm^2
R_p	Pore radius, cm
x	Coordinate along the pore, cm
c_h^{in}	Reference (inlet) oxygen concentration, mol cm^{-3}
i_*	ORR volumetric exchange current density, A cm^{-3}
j_N^{lim}	Limiting current density due to oxygen transport in Nafion film, A cm^{-2}
j_*	The characteristic current density of proton transport, A cm^{-2}, Eq. (4.7)
j_0	Local cell current density, A cm^{-2}
$\mathcal{R}_N$	Transport resistivity of Nafion _film, s cm^{-1}
t_*	Characteristic time, s, Eq. (4.7)

Z	Impedance, Ohm cm^2
Z_{ccl}	CCL impedance, Ohm cm^2
$\sim$	Marks dimensionless variables

Subscripts:

0	Membrane/CCL interface
1	CCL/GDL interface
b	In the GDL
ccl	Cathode catalyst layer
h	Air channel
m	Pt/C (metal) surface
N	Nafion film
p	Pore/Nafion _film interface

Superscripts:

0	Steady-state value
1	Small-amplitude perturbation
lim	Limiting
∞	Some parameter tends to be 1

Greek:

ε_*	Dimensionless Newman's reaction penetration depth, Eq. (4.11)
ω	Angular frequency of the AC signal, s^{-1}
η	ORR overpotential, positive by convention, V
μ	Dimensionless parameter, Eq. (4.11)
ξ	Dimensionless parameter, Eq. (4.37)
σ_p	Nafion film proton conductivity, S cm^{-1}

Acknowledgments

T. Reshetenko gratefully acknowledges funding from the US Office of Naval Research (N00014-19-1-2127, N00014-17-1-2206) and US Army Research Office (W911NF15-1-0188). The authors are thankful to Günter Randolf for their valuable help in the system operation.
Author contribution
T. Reshetenko: Investigation, writing—original draft, writing—review and editing; A. Kulikovsky: Conceptualization, investigation, writing—original draft, and writing—review and editing. The authors acknowledge that there is no financial relationship with the editors or publisher, and all the cited literature is acknowledged and appropriately cited with copyright permission.

References

[1] A. Lasia, Electrochemical Impedance Spectroscopy and its Applications, Springer, New York, 2014.
[2] M.E. Orazem, B. Tribollet, Electrochemical Impedance Spectroscopy, second ed., Wiley, New-York, 2017.

[3] A. Kulikovsky, Analytical Models for PEM Fuel Cell Impedance. Self-publishing, Eisma, 2018, ISBN 9781521470749. URL, https://www.amazon.com/Andrei-Kulikovsky/e/B00KBW7KVY.
[4] D. Macdonald, Reflections on the history of electrochemical impedance spectroscopy, Electrochim. Acta 51 (2006) 1376–1388.
[5] T.E. Springer, T.A. Zawodzinski, M.S. Wilson, S. Gottesfeld, Characterization of polymer electrolyte fuel cells using AC impedance spectroscopy, J. Electrochem. Soc. 143 (1996) 587–599.
[6] Y. Bultel, L. Genies, O. Antoine, P. Ozil, R. Durand, Modeling impedance diagrams of active layers in gas diffusion electrodes: diffusion, ohmic drop effects and multistep reactions, J. Electroanal. Chem. 527 (2002) 143–155.
[7] F. Jaouen, G. Lindbergh, Transient techniques for investigating mass-transport limitations in gas diffusion electrode, J. Electrochem. Soc. 150 (2003) A1699–A1710.
[8] Q. Guo, R.E. White, A steady-state impedance model for a PEMFC cathode, J. Electrochem. Soc. 151 (2004) E133–E149.
[9] Y. Bultel, K. Wiezell, F. Jaouen, P. Ozil, G. Lindbergh, Investigation of mass transport in gas diffusion layer at the air cathode of a PEMFC, Electrochim. Acta 51 (2005) 474–488.
[10] D. Gerteisen, A. Hakenjos, J.O. Schumacher, AC impedance modelling study on porous electrodes of proton exchange membrane fuel cells using an agglomerate model, J. Power Sources 173 (2007) 346–356.
[11] A.A. Franco, P. Schott, C. Jallut, B. Maschke, A multi-scale dynamic mechanistic model for the transient analysis of PEFCs, Fuel Cell. 7 (2007) 99–117.
[12] M. Cimenti, D. Bessarabov, M. Tam, J. Stumper, Investigation of proton transport in the catalyst layer of PEM fuel cells by electrochemical impedance spectroscopy, ECS Trans. 28 (23) (2010) 147–157.
[13] I.A. Schneider, M.H. Bayer, S. von Dahlen, Locally resolved electrochemical impedance spectroscopy in channel and land areas of a differential polymer electrolyte fuel cell, J. Electrochem. Soc. 158 (2011) B343–B348.
[14] J. Mainka, G. Maranzana, A. Thomas, J. Dillet, S. Didierjean, O. Lottin, One-dimensional model of oxygen transport impedance accounting for convection perpendicular to the electrode, Fuel Cell. 12 (2012) 848–861.
[15] G. Maranzana, J. Mainka, O. Lottin, J. Dillet, A. Lamibrac, A. Thomas, S. Didierjean, A proton exchange membrane fuel cell impedance model taking into account convection along the air channel: on the bias between the low frequency limit of the impedance and the slope of the polarization curve, Electrochim. Acta 83 (2012) 13–27.
[16] J.R. Vang, S.J. Andreasen, S.K. Kaer, A transient fuel cell model to simulate HTPEM fuel cell impedance spectra, J. Fuel Cell Sci. Technol. 9 (2012), 021005-1-021005-9.
[17] A.A. Kulikovsky, Exact low-current analytical solution for impedance of the cathode catalyst layer in a PEM fuel cell, Electrochim. Acta 147 (2014) 773–777.
[18] A.A. Kulikovsky, One-dimensional impedance of the cathode side of a PEM fuel cell: exact analytical solution, J. Electrochem. Soc. 162 (2015) F217–F222.
[19] T. Reshetenko, A. Kulikovsky, PEM fuel cell characterization by means of the physical model for impedance spectra, J. Electrochem. Soc. 162 (2015) F627–F633.
[20] D. Gerteisen, Impact of inhomogeneous catalyst layer properties on impedance spectra of polymer electrolyte membrane fuel cells, J. Electrochem. Soc. 162 (2015) F1431–F1438.
[21] A.A. Kulikovsky, A simple physics-based equation for low-current impedance of a PEM fuel cell cathode, Electrochim. Acta 196 (2016) 231–235.
[22] T. Reshetenko, A. Kulikovsky, Impedance spectroscopy study of the PEM fuel cell cathode with nonuniform nafion loading, J. Electrochem. Soc. 164 (2017) E3016–E3021.
[23] D. Vivona, A. Casalegno, A. Baricci, Validation of a pseudo 2D analytical model for high temperature PEM fuel cell impedance valid at typical operative conditions, Electrochim. Acta 310 (2019) 122–135.
[24] T. Reshetenko, A. Kulikovsky, Impedance spectroscopy characterization of oxygen transport in low- and high-Pt loaded PEM fuel cells, J. Electrochem. Soc. 164 (2017) F1633–F1640.

[25] A. Kosakian, M. Secanell, Estimating charge-transport properties of fuel cell and electrolyzer catalyst layers via electrochemical impedance spectroscopy, Electrochim. Acta 367 (2021) 137521.
[26] S. Cruz-Manzo, P. Greenwood, Analytical Warburg impedance model for EIS analysis of the gas diffusion layer with oxygen depletion in the air channel of a PEMFC, J. Electrochem. Soc. 168 (2021) 074502.
[27] J. Huang, Y. Gao, J. Luo, S. Wang, C. Li, S. Chen, J. Zhang, Editors' choice-review-impedance response of porous electrodes: theoretical framework, physical models and applications, J. Electrochem. Soc. 167 (2020) 166503.
[28] Z. Tang, Q.-A. Huang, Y.-J. Wang, F. Zhang, W. Li, A. Li, L. Zhang, J.J. Zhang, Recent progress in the use of electrochemical impedance spectroscopy for the measurement, monitoring, diagnosis and optimization of proton exchange membrane fuel cell performance, J. Power Sources 468 (2020) 228361.
[29] A.A. Kulikovsky, A model for local impedance of the cathode side of PEM fuel cell with segmented electrodes, J. Electrochem. Soc. 159 (2012) F294−F300.
[30] A.A. Kulikovsky, M. Eikerling, Analytical solutions for impedance of the cathode catalyst layer in PEM fuel cell: layer parameters from impedance spectrum without fitting, J. Electroanal. Chem. 691 (2013) 13−17.
[31] A.A. Kulikovsky, Analytical solutions for polarization curve and impedance of the cathode catalyst layer with fast oxygen transport in a PEM fuel cell, J. Electrochem. Soc. 161 (2014) E3171−E3179.
[32] C. Bao, W.G. Bessler, Two-dimensional modeling of a polymer electrolyte membrane fuel cell with long flow channel. Part II. Physics-based electrochemical impedance analysis, J. Power Sources 278 (2015) 675−682.
[33] T.A. Greszler, D. Caulk, P. Sinha, The impact of platinum loading on oxygen transport resistance, J. Electrochem. Soc. 159 (2012) F831−F840.
[34] J.P. Owejan, J.E. Owejan, W. Gu, Impact of platinum loading and catalyst layer structure on PEMFC performance, J. Electrochem. Soc. 160 (2013) F824−F833.
[35] A.Z. Weber, A. Kusoglu, Unexplained transport resistances for low-loaded fuel-cell catalyst layers, J. Mater. Chem. A 2 (2014) 17207−17211.
[36] A. Kongkanand, M.F. Mathias, The priority and challenge of high-power performance of low-platinum proton-exchange membrane fuel cells, Phys. Chem. Lett. 7 (2016) 1127−1137.
[37] K. Kudo, R. Jinnouchi, Y. Morimoto, Humidity and temperature dependences of oxygen transport resistance of Nafion thin film on platinum electrode, Electrochimica Acta 209 (2016) 682−690.
[38] A.T.S. Freiberg, M.C. Tucker, A.Z. Weber, Polarization loss correction derived from hydrogen local resistance measurement in low Pt-loaded polymer electrolyte fuel cells, Electrochem. Comm. 79 (2017) 14−17.
[39] M. Eikerling, A.A. Kulikovsky, Polymer Electrolyte Fuel Cells: Physical Principles of Materials and Operation, CRC Press, London, 2014.
[40] A. Kulikovsky, The effect of Nafion film on the cathode catalyst layer performance in a low-Pt PEM fuel cell, Electrochem. Commun. 103 (2019) 61−65.
[41] T. Reshetenko, A. Kulikovsky, A single-pore model for cathode catalyst layer impedance: the effect of Nafion film on PEM fuel cell performance, RSC Adv. 9 (2019) 38797−38806.
[42] T.V. Reshetenko, G. Bender, K. Bethune, R. Rocheleau, Systematic study of back pressure and anode stoichiometry effects on spatial PEMFC performance distribution, Electrochim. Acta 56 (2011) 8700−8710.
[43] T.V. Reshetenko, G. Bender, K. Bethune, R. Rocheleau, A segmented cell approach for studying the effects of serpentine flow field parameters on PEMFC current distribution, Electrochim. Acta 88 (2013) 571−579.
[44] T. Reshetenko, V. Laue, U. Krewer, K. Artyushkova, Study of degradation and spatial performance of low Pt-loaded proton exchange membrane fuel cells under exposure to sulfur dioxide in an oxidant stream, J. Power Sources 458 (2020) 228032.
[45] T. Reshetenko, A. Kulikovsky, Comparison of two physical models for fitting PEM fuel cell impedance spectra measured at a low air flow stoichiometry, J. Electrochem. Soc. 163 (2016) F238−F246.

[46] M. Eikerling, A.A. Kornyshev, Electrochemical impedance of the cathode catalyst layer in polymer electrolyte fuel cells, J. Electroanal. Chem. 475 (1999) 107−123.
[47] A. Kulikovsky, A model for impedance of a PEM fuel cell cathode with poor electron conductivity, J. Electroanal. Chem. 801 (2017) 122−128.
[48] M.C. Lefebvre, R.B. Martin, P.G. Pickup, Characterization of ionic conductivity profiles within proton exchange membrane fuel cell gas diffusion electrodes by impedance spectroscopy, Electrochem. Solid State Lett. 2 (1999) 259−261.
[49] G. Li, P.G. Pickup, Ionic conductivity of PEMFC electrodes. Effect of Nafion loading, J. Electrochem. Soc. 150 (2003) C754. C752.
[50] A.A. Kulikovsky, Impedance of a PEM fuel cell cathode with nonuniform ionomer loading: analytical and numerical study, J. Electroanal. Chem. 789 (2017) 174−180.
[51] T. Reshetenko, A. Kulikovsky, On the origin of high frequency impedance feature in a PEM fuel cell, J. Electrochem. Soc. 166 (2019) F1253−F1257.
[52] Y. Liu, M.W. Murphy, D.R. Baker, W. Gu, C. Ji, J. Jorne, H.A. Gasteiger, Proton conduction and oxygen reduction kinetics in PEM fuel cell cathodes: effects of ionomer-to-carbon ratio and relative humidity, J. Electrochem. Soc. 156 (2009) B970−B980.
[53] Y. Liu, C. Li, W. Gu, J. Jorne, H.A. Gasteiger, Effects of catalyst carbon support on proton conduction and cathode performance in PEM fuel cells, J. Electrochem. Soc. 158 (2011) B614−B621.
[54] T. Reshetenko, A. Kulikovsky, On the distribution of local current density along the PEM fuel cell cathode channel, Electrochem. Commun. 101 (2019) 35−38.
[55] M. Gattrell, B. MacDougall, Reaction mechanisms of the O_2 reduction/evolution reaction, in: W. Vielstich, H.A. Gasteiger, A. Lamm (Eds.), Handbook of Fuel Cells − Fundamentals, Technology and Applications, vol. 2, John Wiley & Sons, 2003. Electrocatalysis.
[56] A. Kulikovsky, T. Reshetenko, Correction: a single-pore model for cathode catalyst layer impedance: the effect of Nafion film on PEM fuel cell performance, RSC Adv. 9 (2019) 38797, https://doi.org/10.1039/c9ra07794d. RSC Adv., 11:6764-6765, 2021.
[57] J. Zhou, A. Putz, M. Secanell, A mixed wettability pore size distribution based mathematical model for analyzing two-phase flow in porous electrodes, J. Electrochem. Soc. 164 (2017) F530−F539.
[58] Z. Yu, R.N. Carter, J. Zhang, Measurements of pore size distribution, porosity, effective oxygen diffusivity, and tortuosity of PEM fuel cell electrodes, Fuel Cell. 12 (2012) 557−565.
[59] J. Liu, M. Eikerling, Model of cathode catalyst layers for polymer electrolyte fuel cells: the role of porous structure and water accumulation, Electrochim. Acta 53 (2008) 4435−4446.
[60] H. Yu, L. Bonville, R. Maric, Analysis of H2/Air polarization curves: the influence of low Pt loading and fabrication process, J. Electrochem. Soc. 165 (2018) F272−F284.
[61] M. Lopez-Haro, L. Guetaz, T. Printemps, A. Morin, S. Escribano, P.-H. Jouneau, P. Bayle-Guillemaud, F. Chandezon, G. Gebel, Three-dimensional analysis of Nafion layers in fuel cell electrodes, Nat. Commun. 5 (2013) 5229.
[62] F.C. Cetinbas, X. Wang, R.K. Ahluwalia, N.N. Kariuki, R. Winarski, Z. Yang, J. Sharman, D.J. Myers, Analysis and transport resistances of low-Platinum-loaded PEFC electrodes, J. Electrochem. Soc. 164 (2017) F1595−F1607.
[63] T. Suzuki, S. Okada, S. Tsushima, Analysis of ionomer distribution and Pt/C agglomerate size in catalyst layers by two-stage ion-beam processing, J. Electrochem. Soc. 167 (2020) 124513.
[64] V.A. Sethuraman, S. Khan, J.S. Jur, A.T. Haug, J. Weidner, Measuring oxygen, carbon monoxide and hydrogen sulfide diffusion coefficient and solubility in Nafion membranes, Electrochim. Acta 54 (2009) 6850−6860.
[65] D. Novitski, S. Holdcroft, Determination of O2 mass transport at the Pt/PFSA ionomer interface under reduced relative humidity, ACS Appl. Mater. Interfaces 7 (2015) 27314−27323.
[66] A. Kulikovsky, Impedance and resistivity of low-Pt cathode in a PEM fuel cell, J. Electrochem. Soc. 168 (2021) 044512.
[67] A.B. Tesler, D.R. Lewin, S. Baltianski, Y. Tsur, Analyzing results of impedance spectroscopy using novel evolutionary programming techniques, J. Electroceram. 24 (2010) 245−260.

[68] H. Schichlein, A.C. Müller, M. Voigts, A. Krügel, E. Ivers-Tiffée, Deconvolution of electrochemical impedance spectra for the identification of electrode reaction mechanisms in solid oxide fuel cells, J. Appl. Electrochem. 32 (2002) 875−882.
[69] D. Klotz, J.P. Schmidt, A. Kromp, A. Weber, E. Ivers-Tiffée, The distribution of relaxation times as beneficial tool for equivalent circuit modeling of fuel cells and batteries, ECS Trans 41 (2012) 25−33.
[70] Y. Zhang, Y. Chen, M. Yan, F. Chen, Reconstruction of relaxation time distribution from linear electrochemical impedance spectroscopy, J. Power Sources 283 (2015) 464−477.
[71] B.A. Boukamp, Derivation of a distribution function of relaxation times for the (fractal) finite length Warburg, Electrochim. Acta 252 (2017) 154−163.
[72] M. Heinzmann, A. Weber, E. Ivers-Tiffée, Impedance modelling of porous electrode structures in polymer electrolyte membrane fuel cells, J. Power Sources 444 (2019) 227279.
[73] E. Ivers-Tiffée, A. Weber, Evaluation of electrochemical impedance spectra by the distribution of relaxation times, J. Ceram. Soc. Jpn. 125 (2017) 193−201.
[74] T. Reshetenko, A. Kulikovsky, Distribution of relaxation times: a tool for measuring oxygen transport resistivity of a low-Pt PEM fuel cell cathode, J. Electrochem. Soc. 167 (2020) 144505.
[75] M. Saccoccio, T.H. Wan, C. Chen, F. Ciucci, Optimal regularization in distribution of relaxation times applied to electrochemical impedance spectroscopy: ridge and lasso regression methods−a theoretical and experimental study, Electrochim. Acta 147 (2014) 470−482.
[76] T.H. Wan, M. Saccoccio, C. Chen, F. Ciucci, Influence of the discretization methods on the distribution of relaxation times deconvolution: implementing radial basis functions with DRTtools, Electrochim. Acta 184 (2015) 483−499.
[77] J. Macutkevic, J. Banys, A. Matulis, Determination of the distribution of the relaxation times from dielectric spectra, Nonlinear Anal. Model Control 9 (2004) 75−88.
[78] S. Effendy, J. Song, M.Z. Bazant, Analysis, design, and generalization of electrochemical impedance spectroscopy (EIS) inversion algorithms, J. Electrochem. Soc. 167 (2020) 106508.
[79] C.L. Lawson, R.J. Hanson, Solving Least Squares Problems, Prentice-Hall, Englewood Cliffs, NJ, USA, 1974.
[80] A. Kulikovsky, PEM fuel cell distribution of relaxation times: a method for calculation and behavior of oxygen transport peak, Phys. Chem. Chem. Phys. 22 (2020) 19131−19138.
[81] T.M. Correia, A.P. Gibson, M. Schweiger, J.C. Hebden, Selection of regularization parameter for optical topography, J. Biomed. Opt. 14 (2009) 1−11.
[82] A. Kulikovsky, Analytical impedance of oxygen transport in a PEM fuel cell channel, J. Electrochem. Soc. 166 (2019) F306−F311.
[83] I.A. Schneider, S.A. Freunberger, D. Kramer, A. Wokaun, G.G. Scherer, Oscillations in gas channels. Part I. The forgotten player in impedance spectroscopy in PEFCs, J. Electrochem. Soc. 154 (2007) B383−B388.
[84] A. Kulikovsky, O. Shamardina, A model for PEM fuel cell impedance: oxygen flow in the channel triggers spatial and frequency oscillations of the local impedance, J. Electrochem. Soc. 162 (2015) F1068−F1077.
[85] J. Shen, J. Zhou, N.G.C. Astrath, T. Navessin, Z.-S. (Simon) Liu, C. Lei, J.H. Rohling, D. Bessarabov, S. Knights, S. Ye, Measurement of effective gas diffusion coefficients of catalyst layers of PEM fuel cells with a Loschmidt diffusion cell, J. Power Sources 96 (2011) 674−678.
[86] T. Muzaffar, T. Kadyk, M. Eikerling, Tipping water balance and the Pt loading effect in polymer electrolyte fuel cells: a model-based analysis, Sustain. Energy Fuels 2 (2018) 1189−1196.
[87] S.K. Roy, M.E. Orazem, Analysis of flooding as a stochastic process in polymer electrolyte membrane (PEM) fuel cells by impedance techniques, J. Power Sources 184 (2008) 212−219.
[88] S.K. Roy, M.E. Orazem, Stochastic analysis of flooding in PEM fuel cells by electrochemical impedance spectroscopy, ECS Trans. 11 (2007) 485−495.
[89] B.P. Setzler, T.F. Fuller, A physics-based impedance model of proton exchange membrane fuel cells exhibiting low-frequency inductive loops, J. Electrochem. Soc. 162 (2015) F519−F530.
[90] T. Reshetenko, A. Kulikovsky, A model for local impedance: validation of the model for local parameters recovery from a single spectrum of PEM fuel cell, J. Electrochem. Soc. 166 (2019) F431−F439.

CHAPTER 5

Structural engineering of metal-organic frameworks

Jiaqi Zhang, Zhentao Yang, Yu-Chuan Hsu, Kun-Yu Wang, Tian-Hao Yan
The Department of Chemistry, Texas A&M University, College Station, TX, United States

Abstract
Metal-organic frameworks (MOFs) are highly porous materials with metal coordinated with inorganic linkers as building blocks. The purpose of the synthetic pathway is to synthesize the metal coordinated topography without decomposition of the organic component. The crystallization kinetics must be fast enough to enable nucleation and growth. This review covers aspects for accelerated discovery by investigating various synthetic strategies for the optimized and stable synthesis of MOF materials.

Keywords: Metal-organic framework; Porous material; Postsynthetic modification.

1. Introduction

Metal-organic frameworks (MOFs) are advanced porous materials constructed with metal nodes and organic linkers. The assembly of the building blocks generates nanosized pores and infinite lattice. Inspired by the exceptional porosity of MOFs, extensive studies have been done to apply the MOFs in multiple applications, including gas storage/separation, catalysis, bio-medicine, and energy storage. Herein, it is imperative to customize MOFs' porosity and chemical compositions to meet the requirement of diverse applications. This chapter will introduce how to capitalize chemical or physical methods to manipulate MOF structures.

2. Engineering porosity of MOFs

2.1 Modulated synthesis

Modulated synthesis, which specifies using modulators, has been widely introduced into the crystallization process of hierarchically porous MOF (HP-MOF). The modulators can regulate fine-tuned structure during the one-pot synthesis by influencing the framework formation and dissolution equilibrium. Earlier examples include HP-MOF-5 reported by the Yaghi group, which used 4-(dodecyloxy)benzoic acid (DBA) as the modulator to

Advanced Nanomaterials and Their Applications in Renewable Energy. https://doi.org/10.1016/B978-0-323-99877-2.00014-X

synthesize sponge-MOF-5, showing macropores and mesopores permeating all crystals with well-preserved microporosity [1]. More stabilized HP-MOFs are also available. Jiang group introduced a modulator-induced defect-formation strategy to create mesopores in UiO-66 [2]. Later, various HP-MOFs were introduced, exerting this method, including HP-PCN-250, UiO-67, MIL-53, and DUT-5 [3]. Other methods and modifications related to modulating the synthesis of HP-MOFs are also present advantages for controlling uniform pores, such as acid-sensitive metal-organic assembly developed by the Li group [4]. To create more ordered frameworks for pores, the Goodwin group managed to correlate defects in hafnium terephthalate MOF [5]. The modulated approach is a powerful tool to introduce certain pores regarding previous research. Nonetheless, it shows some unwanted randomness universally, and the universality is constrained to specific linkers.

2.2 Templated synthesis

With the growing desire for hierarchical porous HP-MOFs with mesopores and macropores, template-based approaches have been developed. In the liquid phase, soft templates like micelles are formed from surfactant molecules spontaneously. Qiu's group reported that surfactant cetyltrimethylammonium bromide (CTAB) could be assembled into micelles, by which mesopores can be introduced naturally into HKUST-1 in synthesis [6]. Afterward, researchers, including the Kitagawa group and Zhou group, discovered other uses of surfactants, such as fabricating pore boundaries and chelating agents between the template and MOFs [7,8]. In addition to that, hard templates fulfill their goals in similar ways. Polyoxometalates can be incorporated into HKUST-1 to create a pore size of 5 nm, demonstrated by the Wee group [9]. From then on, similar top-down strategies are coming out. Many researchers, such as the Huo group and Lu group, have also applied other nanometer-sized materials [10,11]. Similarly, nanoparticles, nanotubes, and polystyrene spheres are typical and practical hard templates for controlling MOFs' shape, size, and distribution (Fig. 5.1) [12–15].

For MOFs with open architectures, other kinds of soft-template-based synthetic methods like continuous-flow microfluidics and spray-drying have been widely applied [16–18], regardless of their limitation to multiple morphologies. It usually requires hard templates such as polymers or crystalline materials to fabricate more diverse and ordered structures. Examples like core-shell PS@ZIF-8, ZIF-67@ZIF-8, yolk-shell nanoparticle@ZIF-8, and FeNi-MIL-88B, showing hierarchical structures can be fine-tuned by certain conditions [19–24]. In conclusion, utilizing sundry soft templates has offered unlimited possibilities for MOFs synthesis with various properties. However, MOFs with more complicated and ordered structures still rely on the more exact tuning of the template to be synthesized (Fig. 5.2) [24].

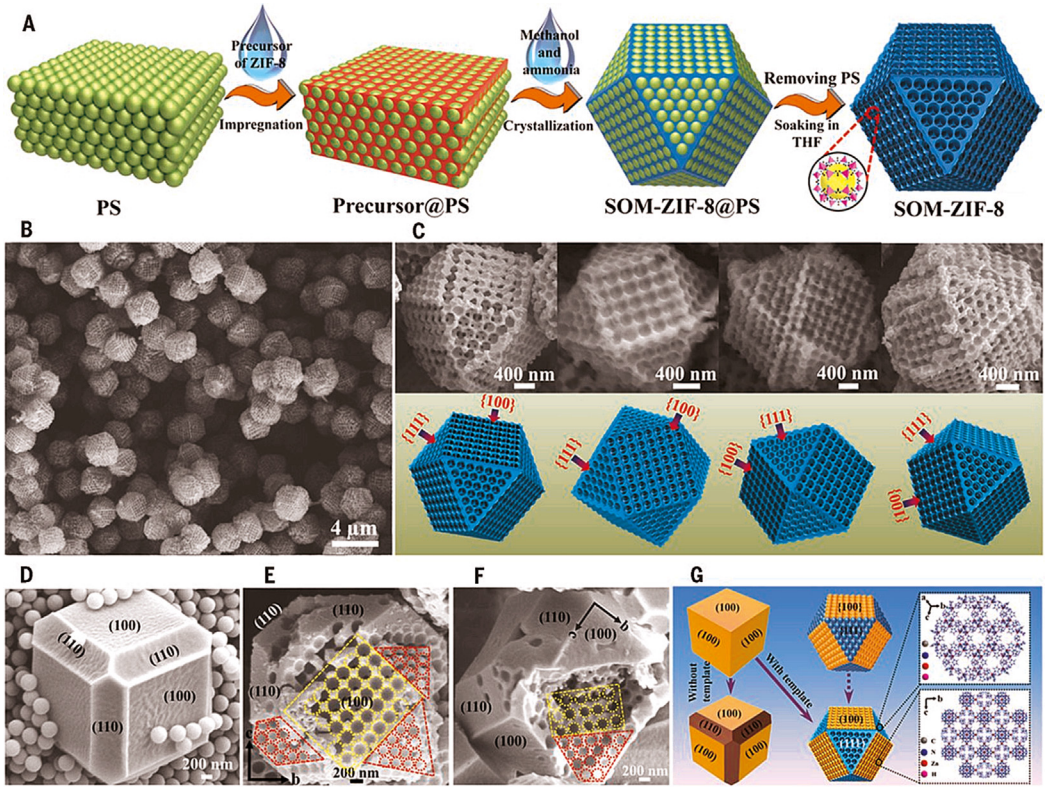

Figure 5.1
Template as polystyrene to fabricate ordered macro-microporous metal-organic framework (MOF) single crystals. *Images were adapted from Ref. [12].*

2.3 Template-free synthesis

Meanwhile, synthesis without a template can also be performed, categorized into bottom-up and top-down approaches. The bottom-up strategy controls the assembly of MOF nanoparticles by exact tunning synthetic conditions. For example, the Zaworotko group produced mesoporous nanocubic MOF-5 using solvothermal conditions to enhance uptake of hydrogen [25]. A similar work reported that the Zn-MOF-74 could be modified by changing solvents [26]. Also, the Li group used CO_2-expanded liquid to synthesize mesocellular HKUST-1 [27]; a 3D-printed method was used by the Lyu group to acquire self-standing MOFs [28].

On the contrary, postsynthesis using etchants, top-down synthesis features create mesopores or macropores. Earlier research from the Kim group utilized water to induce

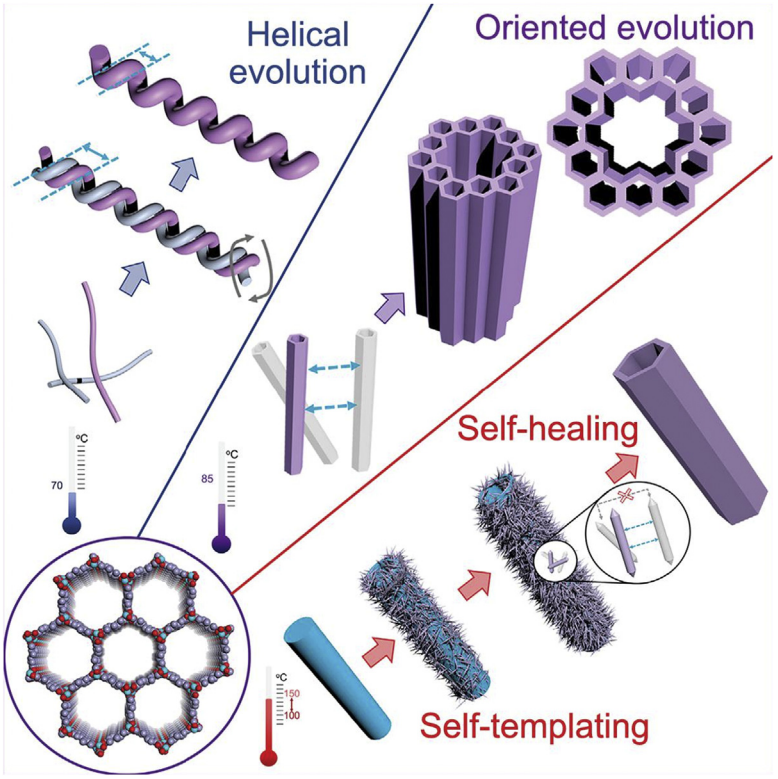

Figure 5.2
Examples of temperature-controlled evolution of hierarchically porous (HP)-metal-organic framework (MOF) superstructures. *Images were adapted from Ref. [24].*

hydrolyzation to form microporous POST-66(Y) [29]. Subsequent research applied acids made controllably distributed voids and specific patterns [30]. Hu group reported that phenolic acids etching the interior of MOFs selectively to afford hollow or tubular structures [31]. The Choe group also uses ions exchange with etching to create trigonal patterns on Zn-UMOM-10 to add Cu paddlewheels to MOFs [32].

Besides that, linker labilization in MOFs introduced by the Zhou group, which involved labile linkers and eliminated, has shown precisely tuned porosity [33]. Using labile 4-carboxybenzylidene-4-aminobenzoate (CBAB) and robust PCN-160, the linker thermolysis performed ended up generating mesopores as well as methods for temperature-dependent multivariate MOFs [34]. Linker labilization has shown its uniqueness and universality in controlling porosity to mesopores in robust MOFs [35,36], especially escalating from micropores. To summarize, considering limited linkers and conditions to regulate MOFs synthesis, template-free approaches are undoubtedly an essential method, showing its unique convenience and orderliness in controlling synthesis (Fig. 5.3).

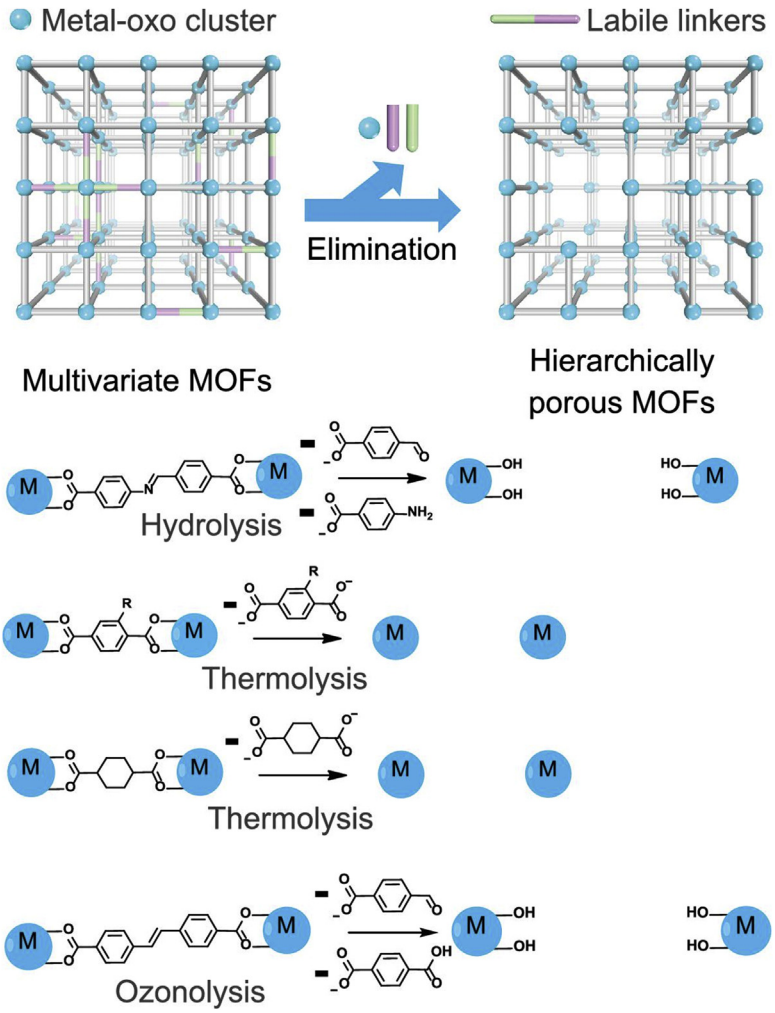

Figure 5.3
Introducing mesopores into microporous multivariate metal-organic frameworks (MOFs) by selectively removing labile linkers through hydrolysis, thermolysis, and ozonolysis. *Images were adapted from Ref. [24].*

3. Engineering chemical compositions of MOFs

3.1 Covalent postsynthetic modification

Robson first proposed the concept of postsynthetic modification in 1990 [37]. However, it took nearly a decade for the first successful case reported by Lobkovsky in 1999 with covalent postsynthetic modification [38]. The term "postsynthetic modification" was first used by Wang and Cohen in 2007 to describe the reaction of IRMOF-3 with acetic anhydride (Fig. 5.4) [39]. Covalent postsynthetic modification is described as introducing a

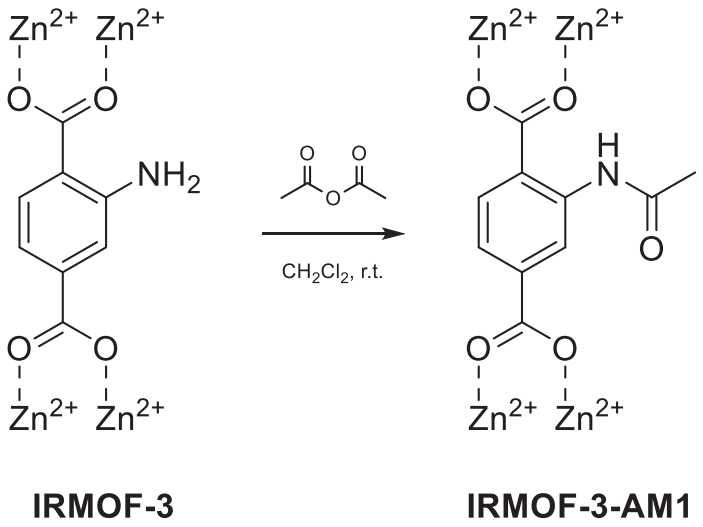

Figure 5.4
Covalent postsynthetic modification of IRMOF-3 with acetic anhydride.

new covalent bond on MOF structure postsynthetically. Most ligands used in this strategy contain functional groups that do not interact with metal clusters but further functionalize. The candidate reaction for postsynthetic modification should also be chemically compatible with the MOF backbone. Covalent postsynthetic modification has become more accessible with the development of much stable MOFs [40].

In addition to the amide formation performed by Wang and Cohen, another example is the introduction of the azide group for click reaction. In 2008, an azide-modified MOF (N_3-MOF-16) was reported by Sada, in which the azide group was able to undergo a click reaction with alkynes to form triazole groups postsynthetically (Fig. 5.5) [41]. Other strategies for covalent postsynthetic modification include but are not limited to imine formation [42,43], reduction of olefin [43], cyanation of aryl halides [44], and photochemical reactions [45].

3.2 Postsynthetic metalation modification

Another common postsynthetic modification technique is postsynthetic metalation, which refers to coordination modification, which incorporates another metal into the MOF structure. Early work for postsynthetic metalation can date back to 2005, which Lin and coworker construct an MOF structure with Cd(II) and (R)-6,6-dichloro-2,2-dihydroxy-1,1-binaphthyl-4,4-bipyridine [46]. The MOF was then treated with titanium isopropoxide to metalate the binaphthol and act as a catalyst for the asymmetric addition of aldehyde (Fig. 5.6).

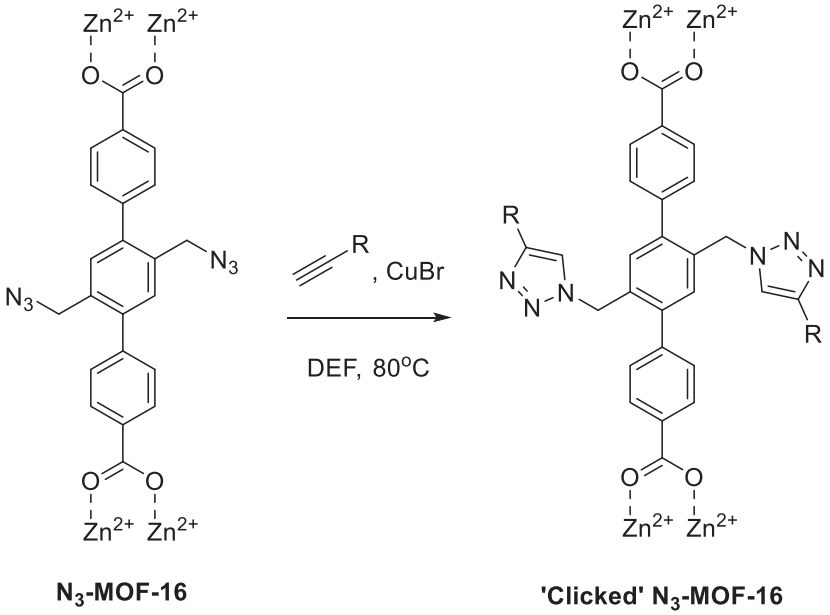

Figure 5.5
Click reaction performed on N_3-metal-organic framework-16.

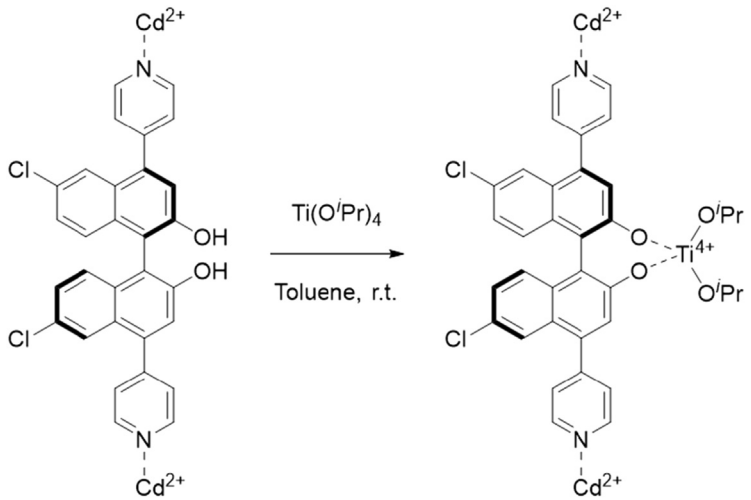

Figure 5.6
Postsynthetic metalation of binaphthol-containing metal-organic framework.

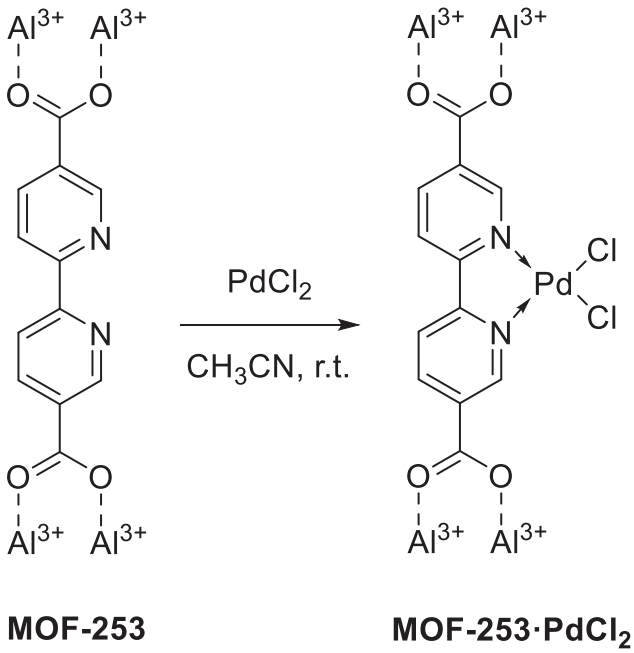

Figure 5.7
Postsynthetic metalation of metal-organic framework (MOF)-253 with $PdCl_2$.

One of the challenges for postsynthetic metalation is the potential coordination of metal cluster with secondary coordination site, which is modified for postsynthetic metalation, during the synthesis of MOF. In 2010, Yaghi and Long reported MOF-253, also known as UiO-67-bipy, which utilize 2,2-bipyridine-5,5-dicarboxylate as a linker for postsynthetic metalation [47]. Utilizing the hard-soft acid-base theory, carboxylate can coordinate with hard metal ions to construct MOF structure with bipyridine stays free to coordinate with soft metal ions (Fig. 5.7). This system has become one of the most widely used strategies for postsynthetic metalation. It has been used to coordinate various metal substrates to form the corresponding metallated frameworks. Other functional groups such as thiol [48], phosphine [49], porphyrin [50], and *N*-heterocyclic carbene have also been implanted in the MOF system as coordination sites for postsynthetic metalation [51].

3.3 Postsynthetic deprotection

Postsynthetic deprotection is similar to covalent postsynthetic modification. However, instead of generating a new covalent bond from a linker-based functional group, a preprotected functional group is premodified on the linker. Then, the protecting group is removed postsynthetically to reveal the desired functionality. This method can prevent the functional group from decomposing or interfering with the synthetic process. One of the

early reports of postsynthetic deprotection was published by Yamada and Kitagawa, referred to as the "protection-complexation-deprotection (PCD)" process [52]. Their study protected 2,5-di acetoxy terephthalic acid by acetylation with acetic anhydride prior to MOF synthesis. The complexation and deprotection of the linker with Zn(II) under DMF and bipyridine additive was observed in tandem (Fig. 5.8). The resulting free hydroxyl groups are involved in extensive intra- and intermolecular hydrogen bonding that is believed to help stabilize the MOF. Besides chemical deprotection, thermally deprotection has also been reported to remove the tert-butylcarbamate (Boc) group to generate primary amine [53].

3.4 Postsynthetic linker exchange

Postsynthetic exchange (PSE) is a special type of dative postsynthetic modification, also known as a bridging-linker replacement [54] or solvent-assisted linker exchange (SALE) [55]. It offers a new way to extend the structure of MOFs without changing the original topology [56]. It can also provide a powerful toolbox to synthesize some MOFs that are hard to obtain via direct solvothermal reaction [57]. We divide this strategy into two parts: Linker exchange and cation exchange in MOFs.

Although many groups have reported their linker exchange method in MOFs, the mechanisms of linker exchange have not been fully understood yet [58–60]. As a result, most works focus on a specific category, pillared-paddlewheel systems. The polycarboxylate paddlewheel building blocks in this system can generate 2D sheets. At the same time, the metal cluster is still open to ditopic nitrogen donor linkers, which can form pillars in this system. Because the metal-oxygen bonds are much stronger than the metal–nitrogen bonds, a new MOF structure can be obtained by replacing the pillar without changing the original 2D sheet. In a typical linker exchange procedure, a parent MOF will be immersed into the solution of a new ditopic nitrogen donor linker to undergo

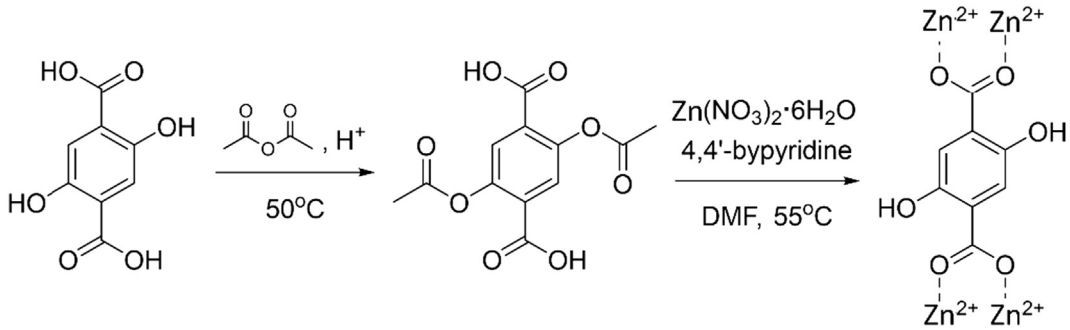

Figure 5.8
Protection-complexation-deprotection (PCD) process for generating metal-organic framework (MOF).

a heterogeneous reaction and generate a daughter MOF with the same topology as its parent MOF [54,61] (Fig. 5.9).

This strategy can be applied to control the porosity of an MOF by inhibiting or introducing catenation into an MOF. For example, Hupp and coworkers [62] (Fig. 5.10) reported that the structure of Zn_2(tcpb) (dped) (DO-MOF) could be transformed into a noncatenated framework via facile linker exchange with 4,4′-bipyridine, which was impossible under traditional solvent-thermal conditions.

What is more, linker exchange provides another way to generate larger pores and channels by replacing existing MOF linkers with longer linkers, which is similar to the isoreticular expansion in MOFs. However, this strategy can directly use the parent MOF as a template to generate the daughter MOF. Rosi and coworkers report the first example in 2013 [63]. They designed two MOFs from bio-MOF-101 and replaced its pillar 2,6-naphthalene dicarboxylate (NDC) with 4,4'-biphenyldicarboxylate (BPDC) and azobenzene-4,4'-dicarboxylate (ABDC), respectively, which generated larger pore volumes than the original parent MOF. Recently, there have also been reports on the SALEM MOF series [64] (Fig. 5.11)

3.5 Postsynthetic cation exchange

Cation exchange, also referred to as a metal exchange, has been widely used in nanocrystals and small molecules, which has a great potential in catalysis, gas storage, and other energy-related topics [65−67]. However, as an emerging field in MOFs, it is still challenging to elucidate the mechanism and the driving force of exchange in different MOF systems. Herein, we want to provide some examples of this strategy and list some essential questions to be answered in the future.

The rational design of cation exchange in MOFs has been heatedly discussed for many years, but no one can comprehensively explain that. To make this section easy to

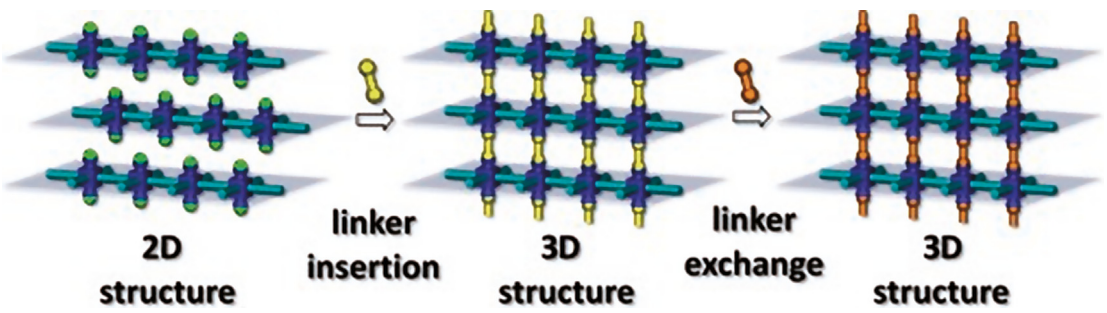

Figure 5.9
Representation of solvent-assisted linker exchange. *Images were adapted from Ref. [61].*

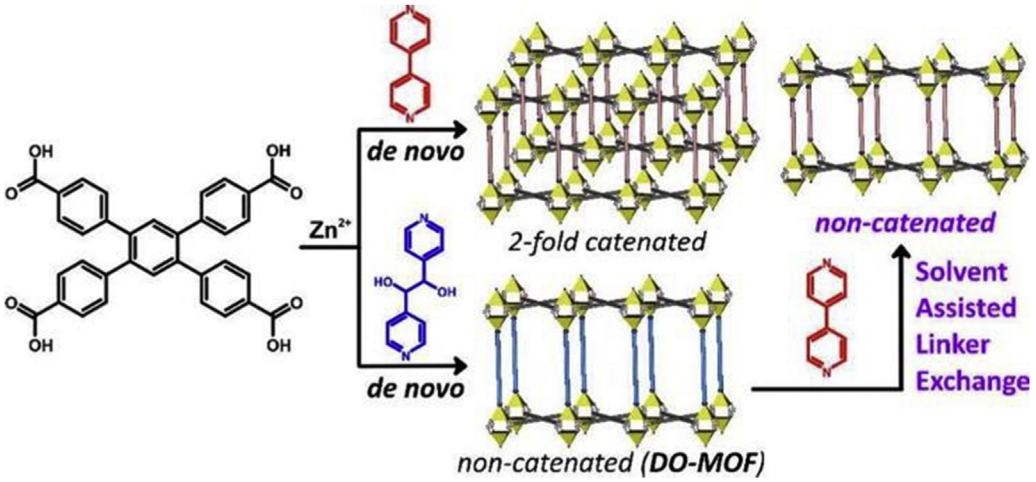

Figure 5.10
Illustration of step-wise linker exchange. *Images were adapted from Ref. [62].*

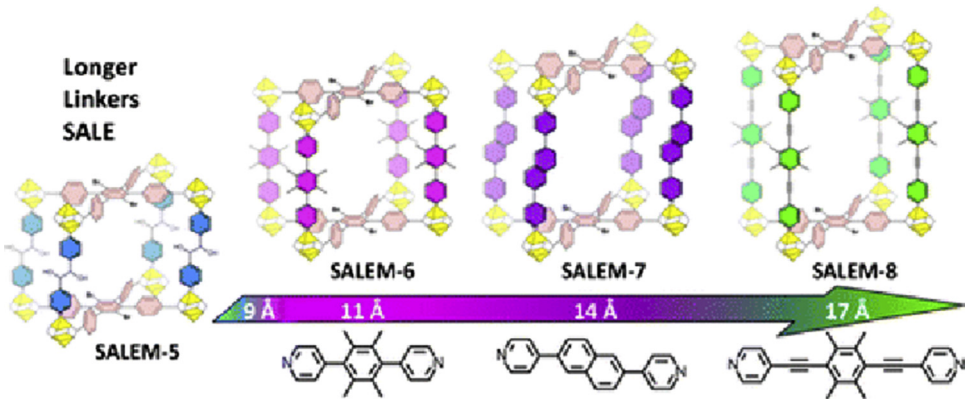

Figure 5.11
Illustration of SALEM metal-organic framework (MOF) series with different pillars. *Images were adapted from Ref. [64].*

understand, we supplement some important SBUs with reported examples of cation exchange below [68] (Fig. 5.12), which may assist researchers in designing new systems in cation exchange. With limited examples reported, we think it is crucial to answering the following questions.

The first issue is which ions can exchange into SBUs. Unlike the reactivity series of metals we are familiar with, the most examples of cation exchange at SBUs involve Cu^{2+} replacing Zn^{2+} or Cd^{2+}, but no attempts on other ions were reported [69–71]. Moreover, the reversibility of these processes has not been studied very well. For example, Zn^{2+} can

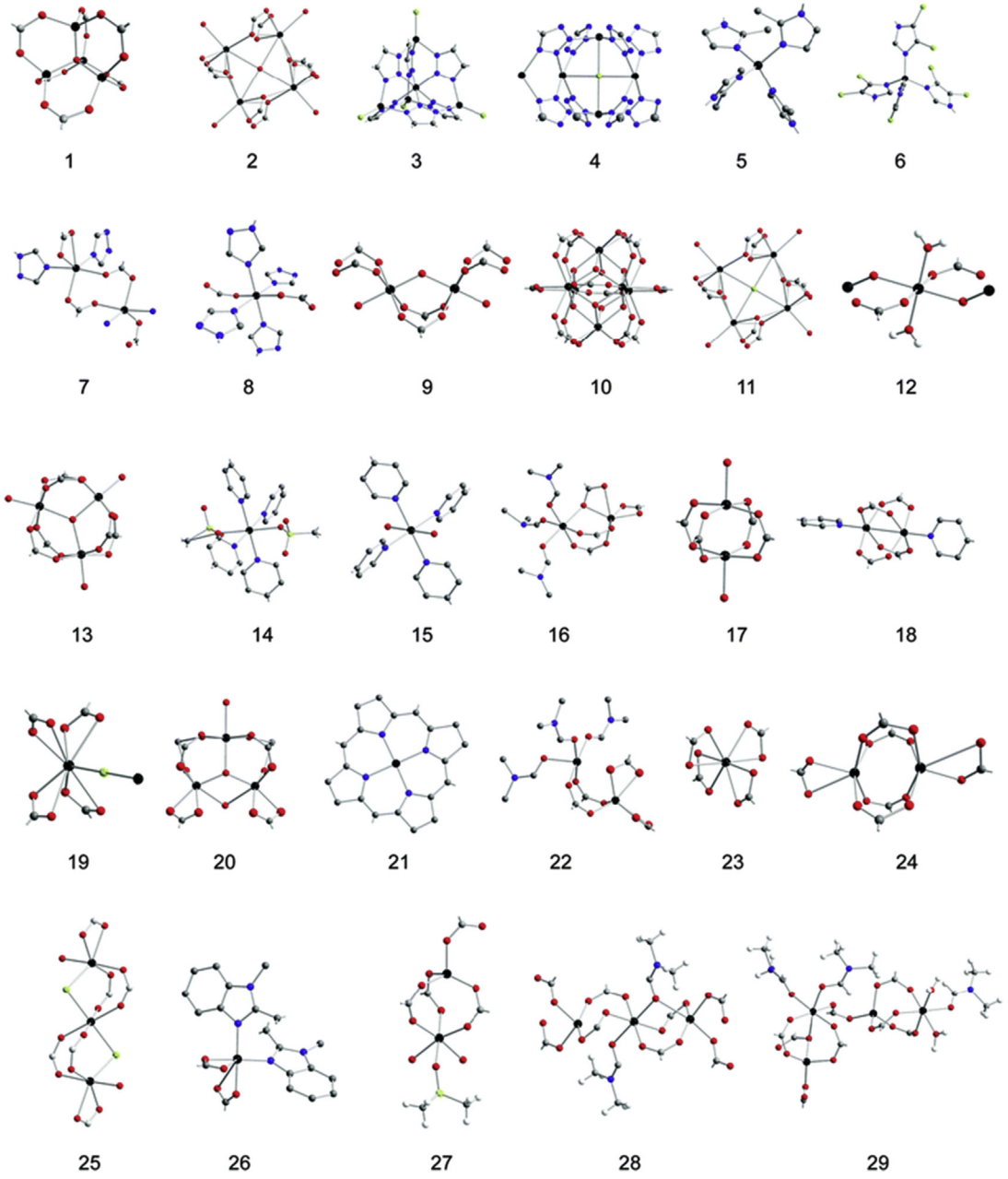

Figure 5.12
Secondary building units (SBUs) that can undergo cation exchange. *Images were adapted from Ref. [68].*

reversibly exchange into NTU-101-Cu or Cu-PMOF-222, while Zn^{2+} can partially replace Cu^{2+} in the framework of porph@MOM-11-Cu. Therefore, we propose that may be due to metal ions' inertness. Lincoln concluded the kinetic behavior of many metal ions, which may be enlightenment for us [72] (Fig. 5.13).

In addition to the metal ions, solvents and the structure of frameworks also affect the results. For example, the research on $\{[Zn_2(BDCPPI)\ (DMF)_3]\cdot 7DMF\cdot 5H_2O\}_n$ reveals that the radius of solvent molecules impacts the exchange rate. The exchange is fast in methanol, but it becomes slow in acetone and even does not occur in many solvents [73]. Since SBUs are part of the frameworks, it is reasonable to believe that frameworks influence the exchange, and we can tell that from the structural integrity of MOFs. For instance, after Co^{2+} replaces Cd^{2+} in MMPF-5(Cd), the surface area reduces significantly, caused by collapsed pores [74].

What is more, we could utilize cation exchange and linker exchange together to achieve the structures we pursue. In 2012, Cohen and coworkers first reported a route to combine

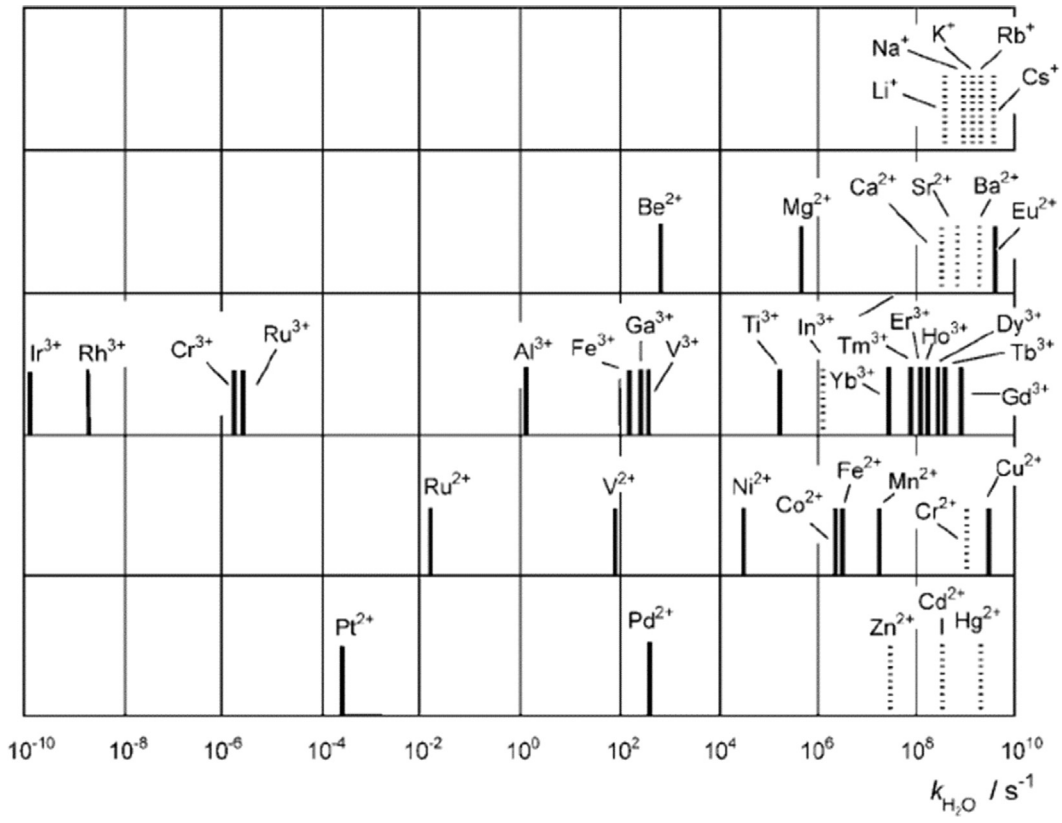

Figure 5.13
Water-exchange rate constants of common metal ions. *Images were adapted from Ref. [72].*

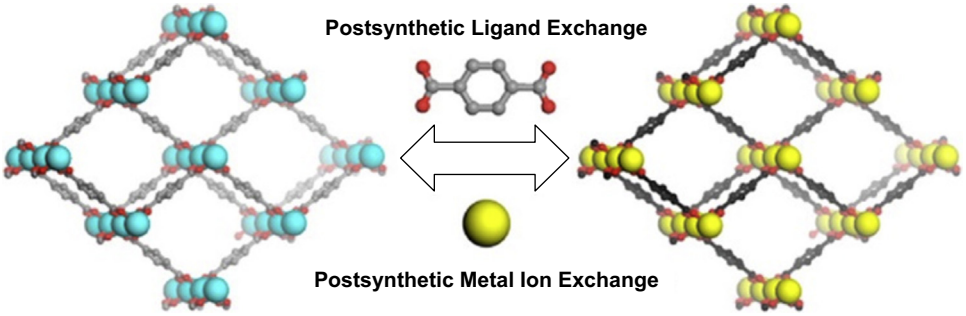

Figure 5.14
Illustration of combined linker exchange and cation exchange. *Images were adapted from Ref. [75].*

these two strategies [75] (Fig. 5.14). Instead of using the conventional MOFs with paddlewheel SBUs, they chose MIL-53 and MIL-68 as parent MOFs. Later, they developed this strategy and extended the substrate scope of PSE [76].

4. Conclusion

Porosity and chemical compositions are the two main facets of MOFs attracting the significant interest of researchers. Multiple applicable methods have been developed these years. The methods regarding engineering porosity in MOFs fall into three categories. The modulated synthesis could create mesopores and macropores, but it is limited to universal randomness and linker specialties. Templated synthesis utilizes soft or hard templates to modulate pores and hierarchical structures. Another method does not involve the template, instead of bottom-up and top-down approaches to place pores of uniqueness and order. These pore constructing methods undoubtedly bring new insights and opportunities to tune morphologies in MOFs. For chemical compositions, engineering usually focuses on postsynthetic modification. Covalent modifications incorporate new covalent linkages within stable MOFs to introduce diversities. Metalation modifications introduce extra metal ions forming a linkage with present linkers to perform complicated roles in MOFs. The deprotection method resembles covalent modification. However, it generates a covalent bond from the deprotection of functional groups. These minor modifications stress-specific groups within stable MOFs. Other types of postmodifications focus on components exchange. Linker exchange, yet its entire mechanism has not been illustrated completely, contributes a lot to introducing new linkers to develop new pore construction and modification. Another exchangeable component is the metal cation. Cation substitution greatly enlightens us to expand MOF functions with expected missions like catalysis and gas storage. The methods mentioned in this chapter have certainly inspired current research. Understanding multivariate MOFs may never be enough with different mechanisms to be probed into.

Acknowledgments

Foresight Institute partially supports this work. The authors acknowledge the cultivation of the Po-Ling Class Project and Molecular Science and Engineering of Nankai University and the Xuetang Talents Program of Tsinghua University. The authors also appreciate the helpful comments and suggestions of the reviewers, which have improved the presentation.

Author contribution

Jiaqi Zhang and wrote the first two sections. Zhentao Yang and Yu-Chuan Hsu, the last section. The entire chapter figures were obtained as cited with the assistance of Kun-Yu Wang, who also wrote the mini summaries. Tian-Hao Yan edited and reviewed the entire manuscript, which was reviewed by all.

References

[1] G. Cai, H.L. Jiang, A modulator-induced defect-formation strategy to hierarchically porous metal−organic frameworks with high stability, Angew. Chem. Int. Ed. 56 (2) (2017) 563−567.
[2] A. Kirchon, J. Li, F. Xia, G.S. Day, B. Becker, W. Chen, H.C. Zhou, Modulation versus templating: fine-tuning of hierarchally porous PCN-250 using fatty acids to engineer guest adsorption, Angew. Chem. Int. Ed. 58 (36) (2019) 12425−12430.
[3] H. Huang, J.R. Li, K. Wang, T. Han, M. Tong, L. Li, C. Zhong, An in situ self-assembly template strategy for the preparation of hierarchical-pore metal-organic frameworks, Nat. Commun. 6 (1) (2015) 1−8.
[4] M.J. Cliffe, W. Wan, X. Zou, P.A. Chater, A.K. Kleppe, M.G. Tucker, A.L. Goodwin, Correlated defect nanoregions in a metal−organic framework, Nat. Commun. 5 (1) (2014) 1−8.
[5] L.G. Qiu, T. Xu, Z.Q. Li, W. Wang, Y. Wu, X. Jiang, L.D. Zhang, Hierarchically micro-and mesoporous metal−organic frameworks with tunable porosity, Angew. Chem. Int. Ed. 47 (49) (2008) 9487−9491.
[6] S. Diring, S. Furukawa, Y. Takashima, T. Tsuruoka, S. Kitagawa, Controlled multiscale synthesis of porous coordination polymer in nano/micro regimes, Chem. Mater. 22 (16) (2010) 4531−4538.
[7] L.B. Sun, J.R. Li, J. Park, H.C. Zhou, Cooperative template-directed assembly of mesoporous metal−organic frameworks, J. Am. Chem. Soc. 134 (1) (2012) 126−129.
[8] L.H. Wee, C. Wiktor, S. Turner, W. Vanderlinden, N. Janssens, S.R. Bajpe, J.A. Martens, Copper benzene tricarboxylate metal−organic framework with wide permanent mesopores stabilized by keggin polyoxometallate ions, J. Am. Chem. Soc. 134 (26) (2012) 10911−10919.
[9] W. Zhang, Y. Liu, G. Lu, Y. Wang, S. Li, C. Cui, F. Huo, Mesoporous metal−organic frameworks with size-, shape-, and space-distribution-controlled pore structure, Adv. Mater. 27 (18) (2015) 2923−2929.
[10] F. Meng, S. Zhang, L. Ma, W. Zhang, M. Li, T. Wu, J. Lu, Construction of hierarchically porous frameworks composites by inherent defects for the enhancement of catalytic efficiency, Adv. Mater. 30 (2018) 1803263.
[11] K. Shen, L. Zhang, X. Chen, L. Liu, D. Zhang, Y. Han, B. Chen, Ordered macro-microporous metal-organic framework single crystals, Science 359 (6372) (2018) 206−210.
[12] Y. Zhao, J. Zhang, B. Han, J. Song, J. Li, Q. Wang, Metal−organic framework nanospheres with well-ordered mesopores synthesized in an ionic liquid/CO_2/surfactant system, Angew. Chem. Int. Ed. 50 (3) (2011) 636−639.
[13] S. Cao, G. Gody, W. Zhao, S. Perrier, X. Peng, C. Ducati, A.K. Cheetham, Hierarchical bicontinuous porosity in metal−organic frameworks templated from functional block co-oligomer micelles, Chem. Sci. 4 (9) (2013) 3573−3577.
[14] G. Zhan, H.C. Zeng, An alternative synthetic approach for macro−meso−microporous metal−organic frameworks via a “domain growth” mechanism, Chem. Commun. 52 (54) (2016) 8432−8435.

[15] G.Y. Jeong, R. Ricco, K. Liang, J. Ludwig, J.O. Kim, P. Falcaro, D.P. Kim, Bioactive MIL-88A framework hollow spheres via interfacial reaction in-droplet microfluidics for enzyme and nanoparticle encapsulation, Chem. Mater. 27 (23) (2015) 7903−7909.
[16] M. Pang, A.J. Cairns, Y. Liu, Y. Belmabkhout, H.C. Zeng, M. Eddaoudi, Synthesis and integration of Fe-soc-MOF cubes into colloidosomes via a single-step emulsion-based approach, J. Am. Chem. Soc. 135 (28) (2013) 10234−10237.
[17] A. Carné-Sánchez, I. Imaz, M. Cano-Sarabia, D. Maspoch, A spray-drying strategy for synthesis of nanoscale metal−organic frameworks and their assembly into hollow superstructures, Nat. Chem. 5 (3) (2013) 203−211.
[18] H.J. Lee, W. Cho, M. Oh, Advanced fabrication of metal−organic frameworks: template-directed formation of polystyrene@ ZIF-8 core−shell and hollow ZIF-8 microspheres, Chem. Commun. 48 (2) (2012) 221−223.
[19] J. Yang, F. Zhang, H. Lu, X. Hong, H. Jiang, Y. Wu, Y. Li, Hollow Zn/Co ZIF particles derived from core−shell ZIF-67@ ZIF-8 as selective catalyst for the semi-hydrogenation of acetylene, Angew. Chem. 127 (37) (2015) 11039−11043.
[20] C.H. Kuo, Y. Tang, L.Y. Chou, B.T. Sneed, C.N. Brodsky, Z. Zhao, C.K. Tsung, Yolk−shell nanocrystal@ ZIF-8 nanostructures for gas-phase heterogeneous catalysis with selectivity control, J. Am. Chem. Soc. 134 (35) (2012) 14345−14348.
[21] K. Li, S. Lin, Y. Li, Q. Zhuang, J. Gu, Aqueous-phase synthesis of mesoporous Zr-based MOFs templated by amphoteric surfactants, Angew. Chem. 130 (13) (2018) 3497−3501.
[22] Y.S. Wei, M. Zhang, M. Kitta, Z. Liu, S. Horike, Q. Xu, A single-crystal open-capsule metal−organic framework, J. Am. Chem. Soc. 141 (19) (2019) 7906−7916.
[23] L. Feng, K.Y. Wang, X.L. Lv, J.A. Powell, T.H. Yan, J. Willman, H.C. Zhou, Imprinted apportionment of functional groups in multivariate metal−organic frameworks, J. Am. Chem. Soc. 141 (37) (2019) 14524−14529.
[24] Z. Xin, J. Bai, Y. Pan, M.J. Zaworotko, Synthesis and enhanced H_2 adsorption properties of a mesoporous nanocrystal of MOF-5: controlling nano-/mesostructures of MOFs to improve their H_2 heat of adsorption, Chem. Eur. J. 16 (44) (2010) 13049−13052.
[25] Y. Yue, Z.A. Qiao, P.F. Fulvio, A.J. Binder, C. Tian, J. Chen, S. Dai, Template-free synthesis of hierarchical porous metal−organic frameworks, J. Am. Chem. Soc. 135 (26) (2013) 9572−9575.
[26] L. Peng, J. Zhang, Z. Xue, B. Han, X. Sang, C. Liu, G. Yang, Highly mesoporous metal−organic framework assembled in a switchable solvent, Nat. Commun. 5 (1) (2014) 1−7.
[27] Z. Lyu, G.J. Lim, R. Guo, Z. Kou, T. Wang, C. Guan, J. Wang, 3D-printed MOF-derived hierarchically porous frameworks for practical high-energy density Li−O_2 batteries, Adv. Funct. Mater. 29 (1) (2019) 1806658.
[28] J. Koo, I.C. Hwang, X. Yu, S. Saha, Y. Kim, K. Kim, Hollowing out MOFs: hierarchical micro-and mesoporous MOFs with tailorable porosity via selective acid etching, Chem. Sci. 8 (10) (2017) 6799−6803.
[29] P. Yang, F. Mao, Y. Li, Q. Zhuang, J. Gu, Hierarchical porous Zr-based MOFs synthesized by a facile monocarboxylic acid etching strategy, Chem. Eur. J. 24 (12) (2018) 2962−2970.
[30] M. Hu, Y. Ju, K. Liang, T. Suma, J. Cui, F. Caruso, Void engineering in metal−organic frameworks via synergistic etching and surface functionalization, Adv. Funct. Mater. 26 (32) (2016) 5827−5834, 6.
[31] J. Lee, J.S. Choi, N.C. Jeong, W. Choe, Formation of trigons in a metal−organic framework: the role of metal−organic polyhedron subunits as meta-atoms, Chem. Sci. 10 (24) (2019) 6157−6161.
[32] S. Yuan, L. Zou, J.S. Qin, J. Li, L. Huang, L. Feng, H.C. Zhou, Construction of hierarchically porous metal−organic frameworks through linker labilization, Nat. Commun. 8 (1) (2017) 1−10.
[33] L. Feng, S. Yuan, L.L. Zhang, K. Tan, J.L. Li, A. Kirchon, H.C. Zhou, Creating hierarchical pores by controlled linker thermolysis in multivariate metal−organic frameworks, J. Am. Chem. Soc. 140 (6) (2018) 2363−2372.

[34] B. Bueken, N. Van Velthoven, A. Krajnc, S. Smolders, F. Taulelle, C. Mellot-Draznieks, D. De Vos, Tackling the defect conundrum in UiO-66: a mixed-linker approach to engineering missing linker defects, Chem. Mater. 29 (24) (2017) 10478−10486.

[35] V. Guillerm, H. Xu, J. Albalad, I. Imaz, D. Maspoch, Postsynthetic selective ligand cleavage by solid−gas phase ozonolysis fuses micropores into mesopores in metal−organic frameworks, J. Am. Chem. Soc. 140 (44) (2018) 15022−15030.

[36] B.F. Hoskins, R. Robson, Design and construction of a new class of scaffolding-like materials comprising infinite polymeric frameworks of 3D-linked molecular rods. A reappraisal of the zinc cyanide and cadmium cyanide structures and the synthesis and structure of the diamond-related frameworks [N (CH3) 4][CuIZnII (CN) 4] and CuI [4, 4′, 4″, 4‴-tetracyanotetraphenylmethane] BF4. xC6H5NO2, J. Am. Chem. Soc. 112 (4) (1990) 1546−1554.

[37] Y.H. Kiang, G.B. Gardner, S. Lee, Z. Xu, E.B. Lobkovsky, Variable pore size, variable chemical functionality, and an example of reactivity within porous phenylacetylene silver salts, J. Am. Chem. Soc. 121 (36) (1999) 8204−8215.

[38] Z. Wang, S.M. Cohen, Postsynthetic covalent modification of a neutral metal− organic framework, J. Am. Chem. Soc. 129 (41) (2007) 12368−12369.

[39] J.H. Cavka, S. Jakobsen, U. Olsbye, N. Guillou, C. Lamberti, S. Bordiga, K.P. Lillerud, A new zirconium inorganic building brick forming metal organic frameworks with exceptional stability, J. Am. Chem. Soc. 130 (42) (2008) 13850−13851.

[40] Y. Goto, H. Sato, S. Shinkai, K. Sada, "Clickable" metal− organic framework, J. Am. Chem. Soc. 130 (44) (2008) 14354−14355.

[41] A.D. Burrows, C.G. Frost, M.F. Mahon, C. Richardson, Post-synthetic modification of tagged metal−organic frameworks, Angew. Chem. 120 (44) (2008) 8610−8614.

[42] K. Hindelang, A. Kronast, S.I. Vagin, B. Rieger, Functionalization of metal−organic frameworks through the postsynthetic transformation of olefin side groups, Chem. Eur. J. 19 (25) (2013) 8244−8252.

[43] M. Kim, S.J. Garibay, S.M. Cohen, Microwave-assisted cyanation of an aryl bromide directly on a metal − organic framework, Inorg. Chem. 50 (3) (2011) 729−731.

[44] M.H. Mir, L.L. Koh, G.K. Tan, J.J. Vittal, Single-crystal to single-crystal photochemical structural transformations of interpenetrated 3 D coordination polymers by [2+ 2] cycloaddition reactions, Angew. Chem. Int. Ed. 49 (2) (2010) 390−393.

[45] C.D. Wu, A. Hu, L. Zhang, W. Lin, A homochiral porous metal− organic framework for highly enantioselective heterogeneous asymmetric catalysis, J. Am. Chem. Soc. 127 (25) (2005) 8940−8941.

[46] E.D. Bloch, D. Britt, C. Lee, C.J. Doonan, F.J. Uribe-Romo, H. Furukawa, O.M. Yaghi, Metal insertion in a microporous metal− organic framework lined with 2, 2′-bipyridine, J. Am. Chem. Soc. 132 (41) (2010) 14382−14384.

[47] K.K. Yee, N. Reimer, J. Liu, S.Y. Cheng, S.M. Yiu, J. Weber, Z. Xu, Effective mercury sorption by thiol-laced metal−organic frameworks: in strong acid and the vapor phase, J. Am. Chem. Soc. 135 (21) (2013) 7795−7798.

[48] J.E. Reynolds, K.M. Walsh, B. Li, P. Kunal, B. Chen, S.M. Humphrey, Highly selective room temperature acetylene sorption by an unusual triacetylenic phosphine MOF, Chem. Commun. 54 (71) (2018) 9937−9940.

[49] W. Morris, B. Volosskiy, S. Demir, F. Gándara, P.L. McGrier, H. Furukawa, O.M. Yaghi, Synthesis, structure, and metalation of two new highly porous zirconium metal−organic frameworks, Inorg. Chem. 51 (12) (2012) 6443−6445.

[50] G.Q. Kong, S. Ou, C. Zou, C.D. Wu, Assembly and post-modification of a metal−organic nanotube for highly efficient catalysis, J. Am. Chem. Soc. 134 (48) (2012) 19851−19857.

[51] T. Yamada, H. Kitagawa, Protection and deprotection approach for the introduction of functional groups into metal− organic frameworks, J. Am. Chem. Soc. 131 (18) (2009) 6312−6313.

[52] R.K. Deshpande, G.I. Waterhouse, G.B. Jameson, S.G. Telfer, Photolabile protecting groups in metal−organic frameworks: preventing interpenetration and masking functional groups, Chem. Commun. 48 (10) (2012) 1574−1576.
[53] B.J. Burnett, P.M. Barron, C. Hu, W. Choe, Stepwise synthesis of metal−organic frameworks: replacement of structural organic linkers, J. Am. Chem. Soc. 133 (26) (2011) 9984−9987.
[54] Y. Lee, S. Kim, J.K. Kang, S.M. Cohen, Photocatalytic CO_2 reduction by a mixed metal (Zr/Ti), mixed ligand metal−organic framework under visible light irradiation, Chem. Commun. 51 (26) (2015) 5735−5738.
[55] M. Lanchas, D. Vallejo-Sanchez, G. Beobide, O. Castillo, A.T. Aguayo, A. Luque, P. Román, A direct reaction approach for the synthesis of zeolitic imidazolate frameworks: template and temperature mediated control on network topology and crystal size, Chem. Comm. 48 (79) (2012) 9930−9932.
[56] K.L. Mulfort, O.K. Farha, C.L. Stern, A.A. Sarjeant, J.T. Hupp, Post-synthesis alkoxide formation within metal− organic framework materials: a strategy for incorporating highly coordinatively unsaturated metal ions, J. Am. Chem. Soc. 131 (11) (2009) 3866−3868.
[57] M.H. Beyzavi, N.A. Vermeulen, K. Zhang, M. So, C.W. Kung, J.T. Hupp, O.K. Farha, Liquid-phase epitaxially grown metal−organic framework thin films for efficient tandem catalysis through site-isolation of catalytic centers, ChemPlusChem 81 (8) (2016) 708−713.
[58] Y. Xu, N.A. Vermeulen, Y. Liu, J.T. Hupp, O.K. Farha, SALE-Ing a MOF-based "ship of theseus." sequential building-block replacement for complete reformulation of a pillared-paddlewheel metal-organic framework, Eur. J. Inorg. Chem. 2016 (27) (2016) 4345−4348.
[59] T. Islamoglu, S. Goswami, Z. Li, A.J. Howarth, O.K. Farha, J.T. Hupp, Postsynthetic tuning of metal−organic frameworks for targeted applications, Acc. Chem. Res. 50 (4) (2017) 805−813.
[60] O. Karagiaridi, W. Bury, J.E. Mondloch, J.T. Hupp, O.K. Farha, Solvent-assisted linker exchange: an alternative to the de novo synthesis of unattainable metal−organic frameworks, Angew. Chem. Int. Ed. 53 (18) (2014) 4530−4540.
[61] W. Bury, D. Fairen-Jimenez, M.B. Lalonde, R.Q. Snurr, O.K. Farha, J.T. Hupp, Control over catenation in pillared paddlewheel metal−organic framework materials via solvent-assisted linker exchange, Chem. Mater. 25 (5) (2013) 739−744.
[62] T. Li, M.T. Kozlowski, E.A. Doud, M.N. Blakely, N.L. Rosi, Stepwise ligand exchange for the preparation of a family of mesoporous MOFs, J. Am. Chem. Soc. 135 (32) (2013) 11688−11691.
[63] O. Karagiaridi, W. Bury, E. Tylianakis, A.A. Sarjeant, J.T. Hupp, O.K. Farha, Opening metal−organic frameworks Vol. 2: inserting longer pillars into pillared-paddlewheel structures through solvent-assisted linker exchange, Chem. Mater. 25 (17) (2013) 3499−3503.
[64] J.H. Liao, W.T. Chen, C.S. Tsai, C.C. Wang, Characterization, adsorption properties, metal ion-exchange and crystal-to-crystal transformation of Cd 3 [(Cd 4 Cl) 3 (BTT) 8 (H 2 O) 12] 2 framework, where BTT 3−= 1, 3, 5-benzenetristetrazolate, CrystEngComm 15 (17) (2013) 3377−3384.
[65] J.A. Zhao, L. Mi, J. Hu, H. Hou, Y. Fan, Cation exchange induced tunable properties of a nanoporous octanuclear Cu (II) wheel with double-helical structure, J. Am. Chem. Soc. 130 (46) (2008) 15222−15223.
[66] M. Dinca, J.R. Long, High-enthalpy hydrogen adsorption in cation-exchanged variants of the microporous metal− organic framework Mn3 [(Mn4Cl) 3 (BTT) 8 (CH3OH) 10] 2, J. Am. Chem. Soc. 129 (36) (2007) 11172−11176.
[67] C.K. Brozek, M. Dincă, Cation exchange at the secondary building units of metal−organic frameworks, Chem. Soc. Rev. 43 (16) (2014) 5456−5467.
[68] X. Song, S. Jeong, D. Kim, M.S. Lah, Transmetalations in two metal−organic frameworks with different framework flexibilities: kinetics and core−shell heterostructure, CrystEngComm 14 (18) (2012) 5753−5756.
[69] Z. Wei, W. Lu, H.L. Jiang, H.C. Zhou, A route to metal−organic frameworks through framework templating, Inorg. Chem. 52 (3) (2013) 1164−1166.

[70] X.J. Wang, P.Z. Li, L. Liu, Q. Zhang, P. Borah, J.D. Wong, Y. Zhao, Significant gas uptake enhancement by post-exchange of zinc (ii) with copper (ii) within a metal−organic framework, Chem. Commun. 48 (83) (2012) 10286−10288.

[71] S.F. Lincoln, Mechanistic studies of metal aqua ions: a semi-historical perspective, Helv. Chim. Acta 88 (3) (2005) 523−545.

[72] T.K. Prasad, D.H. Hong, M.P. Suh, High gas sorption and metal-ion exchange of microporous metal−organic frameworks with incorporated Imide groups, Chem. Eur. J. 16 (47) (2010) 14043−14050.

[73] X.S. Wang, M. Chrzanowski, L. Wojtas, Y.S. Chen, S. Ma, Formation of a metalloporphyrin-based nanoreactor by postsynthetic metal−ion exchange of a polyhedral-cage containing a metal−metalloporphyrin framework, Chem. Eur. J. 19 (10) (2013) 3297−3301.

[74] M. Kim, J.F. Cahill, H. Fei, K.A. Prather, S.M. Cohen, Postsynthetic ligand and cation exchange in robust metal−organic frameworks, J. Am. Chem. Soc. 134 (43) (2012) 18082−18088.

[75] H. Fei, J.F. Cahill, K.A. Prather, S.M. Cohen, Tandem postsynthetic metal ion and ligand exchange in zeolitic imidazolate frameworks, Inorg. Chem. 52 (7) (2013) 4011−4016.

[76] S. Pullen, H. Fei, A. Orthaber, S.M. Cohen, S. Ott, Enhanced photochemical hydrogen production by a molecular diiron catalyst incorporated into a metal−organic framework, J. Am. Chem. Soc. 135 (45) (2013) 16997−17003.

CHAPTER 6

Oxidative stress–mediated nanotoxicity: mechanisms, adverse effects, and oxidative potential of engineered nanomaterials

Periklis Vardakas, Ioannis D. Kyriazis, Maria Kourti, Zoi Skaperda, Fotios Tekos, Demetrios Kouretas

Department of Biochemistry and Biotechnology, University of Thessaly, Larissa, Greece

Abstract

The current energy crisis constitutes a serious problem that humanity is called upon to manage. Engineered nanomaterials have emerged as promising candidates to overcome such challenges, subserving the gradual transition to more sustainable forms of energy. However, as we progressively approach the era of nanotechnology, nano-biosafety is a major concern that must be clarified. Toxicological investigations of several engineered nanomaterials have revealed their capability of disturbing redox homeostasis, bringing the concept of oxidative stress to the fore to evaluate the potential nanotoxicity. The competency of such nanoscale materials to promote the generation of reactive species is owed to specific physicochemical characteristics and may occur via direct and indirect mechanisms. Based on the above, the purpose of the present chapter is to elucidate the toxic effects of engineered nanomaterials mediated by oxidative stress and to promote the thorough evaluation of oxidative stress as a reliable endpoint for predicting the potential risks arising from real-life exposure.

Keywords: Engineered nanomaterials; Oxidative stress; Physicochemical characteristics; Redox biomarkers; Redox state; ROS generation.

1. Introduction

The global energy crisis and its implications are major intricacies that humanity faces and are projected to grow even more in the impending future. More specifically, the overpopulation of Earth, the high energy needs of modern lifestyle, and the heavy reliance on fossil fuels compose a mosaic of factors that continuously challenge the availability of nonrenewable energy sources. Additionally, the extended use of fossil

Advanced Nanomaterials and Their Applications in Renewable Energy. https://doi.org/10.1016/B978-0-323-99877-2.00012-6

fuels, such as petroleum, coal, natural gas, and lignite, is linked to environmental deterioration due to the hazardous emissions of their combustion and adverse effects upon human health, resulting from exposure to the produced air pollutants [1,2]. More elaborately, the byproducts of fossil fuels combustion include carbon dioxide (CO_2), oxides of nitrogen (NO_x) and sulfur (SO_x), particulate matter (PM), which are a greenhouse gas and the main contributor to progressive climate change [3], important air pollutants and key components of acid rain [4], and toxic agents for the respiratory and the cardiovascular system [5], respectively. Hence, the transition to more efficient and cleaner forms of energy is imperative, both for the sustainability of the natural environment and the protection of human welfare.

In recent decades, the breakthroughs in the scientific field of nanotechnology have directed to its close interrelation with numerous fields of research and industry. Engineered nanomaterials (ENMs) are materials of anthropogenic origin, manufactured with optative technical features, and at least one of their dimensions is at the nanoscale (1−100 nm). ENMs are characterized by their extremely small size and high surface area to mass ratio, which are the most prominent features of their unique set of physicochemical characteristics. The above render them improved or novel properties compared to their larger-scale counterparts [6]. In this light, their synthesis and utilization are expected to revolutionize most of science and industrial fields and critically improve the human life quality.

ENMs could be promising contenders to address the burning issues of nonrenewable resource depletion and fossil fuels' harmful emissions by moving to sustainable forms of energy. Noteworthy, ENM uses in energy sources is a major application area of nanotechnology. The quantum phenomena arising at this size scale offer significant energy generation, conversion, transportation, and storage [7]. As a result, the corresponding uses of ENMs occupy a prominent place in the global market of nanotechnology, the second behind the technical field of electronics [8].

A wide variety of ENMs are involved in the field of energy, with different uses, advantages, and expected results, among which carbon-based nanomaterials [9,10], metal or metal oxide nanoparticles [11] and nanocomposites [12,13]. For instance, the high electron mobility and conductivity of carbon based-nanostructures, such as carbon nanotubes and graphene, enable their utilization in photovoltaic technology and, in particular, in dye-sensitized solar cells [14]. Graphene is also implicated in manufacturing lithium-ion batteries and cathodes with high electron conductivity [15]. In addition, metal-based nanoparticles are also used in photovoltaics and other solar energy systems due to their enhanced absorbance in visible light [16]. Their photocatalytic activities can also be exploited in converting CO_2 into hydrocarbon fuels to limit greenhouse gas emissions [17].

Indisputably, the utilization of ENMs offers significant technical advantages. However, the ENMs production rate exceeds the available knowledge regarding their impact on humans and the environment, raising serious safety concerns. To date, we know that the physicochemical characteristics that provide ENMs with enhanced properties are also responsible for their high biological activity, associated with the elicitation of detrimental effects in living organisms [18]. Nevertheless, special emphasis must be placed on the biological outcome and the possible mechanisms to the exerted phenotypes.

A plethora of studies have indicated that a common toxicological mechanism recognized across the various types of ENMs is their ability to induce disturbances of the prevailing redox state via the increased generation of reactive oxygen species (ROS) [19,20,21]. The redox homeostasis is disrupted during oxidative stress either via the excessive formation of free radicals or reactive species or by the inability of the cellular defense mechanisms to restore the redox balance. Of particular interest for oxidative stress is detected in various pathophysiological conditions without knowing if it is also a risk factor [22]. In this light, the prooxidant capacity of ENMs, although it is not the only mechanism implicated in nanotoxicity, has been an item of extensive investigation in nanotoxicology to elucidate possible clinical implications of nano-bio interactions.

Based on the above, the purpose of the present chapter is to provide an insight into the oxidative stress-induced toxic effects of ENMs, commonly utilized in applications of sustainable energy. To this end, we provide a basic introduction into the oxygen dynamics, the generation of ROS and its sources, and the emergence of oxidative stress and its implications in human health. Particular emphasis is given not only to the physicochemical characteristics of ENMs, considered as the key factors for the formation of ROS, but also to the mechanisms implicated in such oxidative events. In addition, the impact of representative ENMs, broadly used in the sector of sustainable energy, on redox state is extensively discussed both at the cellular and organism levels. Conclusively, we strongly believe and promote the significance of evaluating the redox-related properties of ENMs, an investigation that could help us predict the potential risks arising for human health.

2. The paradox of aerobic life and the “dark side” of oxygen

About 2.4 billion years ago, Earth’s atmosphere began to be enriched with oxygen via the oxygenic photosynthesis of cyanobacteria, a geological episode characterized as the “Great Oxidation Event.” The significant changes in atmospheric composition boosted the transition of life to early aerobes and progressively to complex biological systems for which oxygen is crucial for their existence [23]. However, this is only the one side of the coin, since the concept of “Oxygen Paradox,” initially introduced by Davies and Ursini, describes the double-edged effects of oxygen on aerobic lifeforms [24]. According to this, multicellular eukaryotic organisms require the presence of oxygen in

order to survive, as it possesses a key role in cellular bioenergetics, particularly in the chemical energy production in the form of ATP via oxidative phosphorylation [25]. Nevertheless, contingently, it can be a toxic agent through its entrenchment in forming highly reactive derivatives, the so-called ROS, responsible for detrimental effects on cellular homeostasis [26].

3. A preface to ROS generation and oxidative stress emergence

ROS refers to oxygen-centered forms that are more reactive than molecular oxygen itself [27]. It encompasses both short-lived free radicals, such as superoxide ($O_2^{\bullet -}$), hydroxyl ($OH^{\bullet}$), peroxyl ($ROO^{\bullet}$), alkoxy ($RO^{\bullet}$), and hydroperoxyl ($HO_2^{\bullet}$) radicals, and the nonradical entities hydrogen peroxide (H_2O_2), ozone (O_3), and singlet oxygen ($^1O_2$) [28]. ROS are generated either as by-products of endogenous physiological processes or in response to an external stimulus. Regarding the internal sources, the mitochondrial electron transport chain is the main source that contributes decisively to the formation of $O_2^{\bullet -}$ via the direct interaction of leaked electrons with molecular oxygen [29] (Fig. 6.1). NADPH oxidases are important cellular sources mainly related to the immune system since they effectuate an oxidative burst of $O_2^{\bullet -}$ as a defensive strategy against pathogens [30]. Fig. 6.1 summarizes the main routes of ROS generation intracellularly. Additionally, cytochrome P450 and xanthine oxidase enzymes also contribute to a minor extent in the ROS formation inside the cell [31]. On the other hand, an imbalanced diet, smoking, irradiation, drug usage, exposure to environmental pollutants, and xenobiotics comprise external factors that trigger the intracellular ROS generation [32].

Intracellular ROS maintenance at basal, physiological levels requires numerous and heterogenic antioxidant defense mechanisms. With the term antioxidant the scientific community refers to "any substance that delays, prevents or removes oxidative damage to a target molecule" [33]. In a more precise manner, antioxidants can be divided into two major classes: the endogenous, consisting of important enzymatic mechanisms, such as catalase (CAT), superoxide dismutase (SOD), glutathione peroxidase (GPx), and glutathione reductase (GR), and low-molecular-weight compounds, such as the reduced form of glutathione (GSH) and the diet-obtained exogenous ones, such as vitamins and phytochemicals [34]. Antioxidants exert their protective activities by lessening the concentration of molecular oxygen, trapping reactive species, scavenging free radicals that initiate chain reactions or breaking the chain-reaction process, quenching singlet oxygen, and chelating transition-metal ions [35]. Interestingly, previous studies have indicated that specific types of ENMs exert antioxidant activities, mainly in vitro cell-free systems, either attributed to their intrinsic characteristics or stem from their functionalization with conventional antioxidant molecules [36].

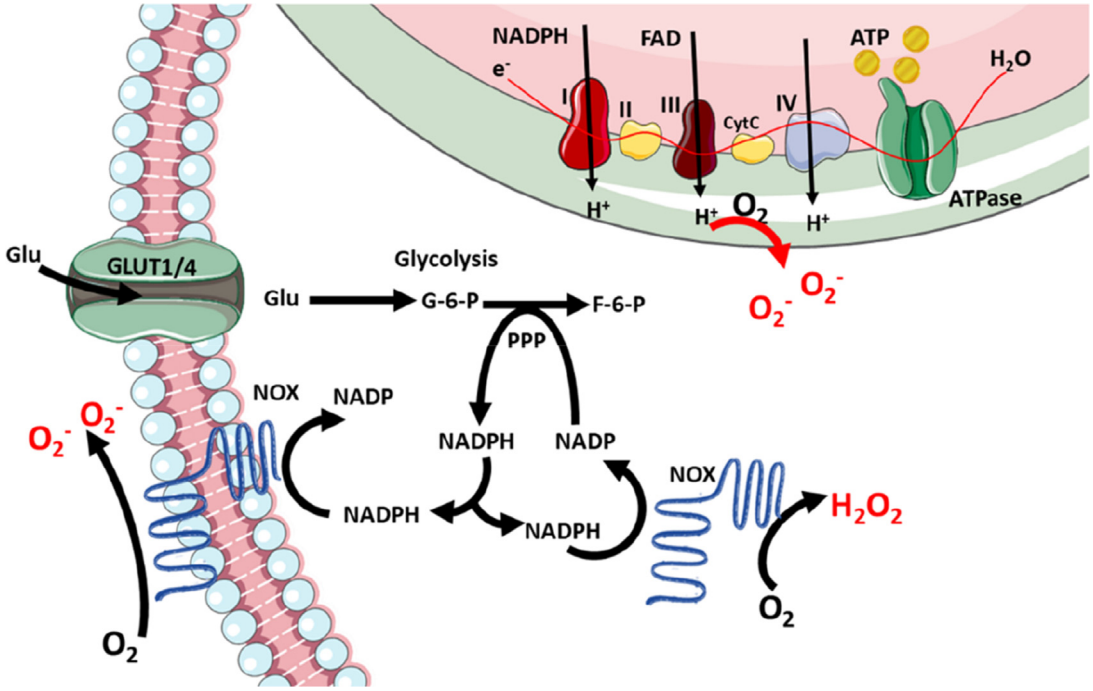

Figure 6.1

An illustrative summary of the main cellular routes of oxygen radicals formation. Glucose glycolysis supplies the pentose phosphate pathway (PPP) to regenerate nicotinamide adenine dinucleotide phosphate (NADPH). NADPH constitutes the substrate of NADPH oxidases to generate superoxide anion ($O_2^{\bullet -}$) or hydrogen peroxide (H_2O_2). NOXs are present in the cytoplasmic membrane or the membranes of intracellular organelles like mitochondria. In the inner membrane of the mitochondria, the electron transport chain (ETC) utilizes the substrates that the Krebs cycle generates and can create an electrochemical gradient. This is formed by the transfer of electrons via the different complexes of ETC that allows proton pumping into the intermembrane space. The mitochondrial membrane potential allows ATPase to produce energetic coins in ATP used for numerous metabolism processes. *Graph designed with "SMART—Servier medical art" image databank at https://smart.servier.com.*

The biological outcome of ROS deeply depends on their intracellular levels, and in consequence, on cell's capacity to regulate redox balance [22]. ROS are essential for cell survival at low to moderate concentrations. They contribute to some physiological processes, including maintaining cellular homeostasis and activating specific signaling pathways [37]. On the other hand, the high and long-lasting ROS generation and the inability or limitation of antioxidants to scavenge and counteract generated oxidants lead to oxidative stress, disruption of redox signaling, and/or molecular damage [38]. Under these circumstances, the elevated ROS levels beget oxidative modifications to biological macromolecules, principally lipids, proteins, and nucleic acids, leading to severe cell damage and potentially cell death [32].

Notably, oxidative stress represents a dynamic state within the cell with distinct gradation that depends on the stimulus intensity and continuation, resulting in different signaling pathways activation and biological outcomes [39] (Fig. 6.2). At mild levels of oxidative stress, controlled by the presence of xenobiotic agents and stressful conditions, the transcription factor nuclear factor erythroid 2-related factor (Nrf-2) is activated, coordinating the upregulation of antioxidant and detoxifying defense mechanisms [40]. In a more precise manner, under basal state, Nrf-2 is sequestered in the cytoplasm by its complexation with Kelch-like ECH-associated protein 1 (Keap1), a cysteine-rich protein that serves as a ubiquitin adaptor. The eventual result is the degradation of the ubiquitinated Nrf-2 by proteasomes [41]. Conversely, at the time that low levels of oxidative stress challenge the intracellular redox state, electrophiles and oxidants react with the cysteine residues of Keap1, and, accordingly, Nrf-2 is disassociated, stabilized, and translocated to the nucleus in order to upregulate the expression of a series of antioxidant response elements (AREs)-dependent genes [42].

Intermediate levels of oxidative stress promote inflammatory responses via the actuation of transcription factors nuclear factor-κB (NF-κB) and activator protein 1 (AP-1). Under physiological conditions, NF-kB remains inactive in the cytoplasm due to the tight binding with the inhibitory IkB proteins. Nevertheless, in the presence of harmful stimuli, the inhibitory proteins are phosphorylated and degraded by proteasomes, enabling NF-kB to

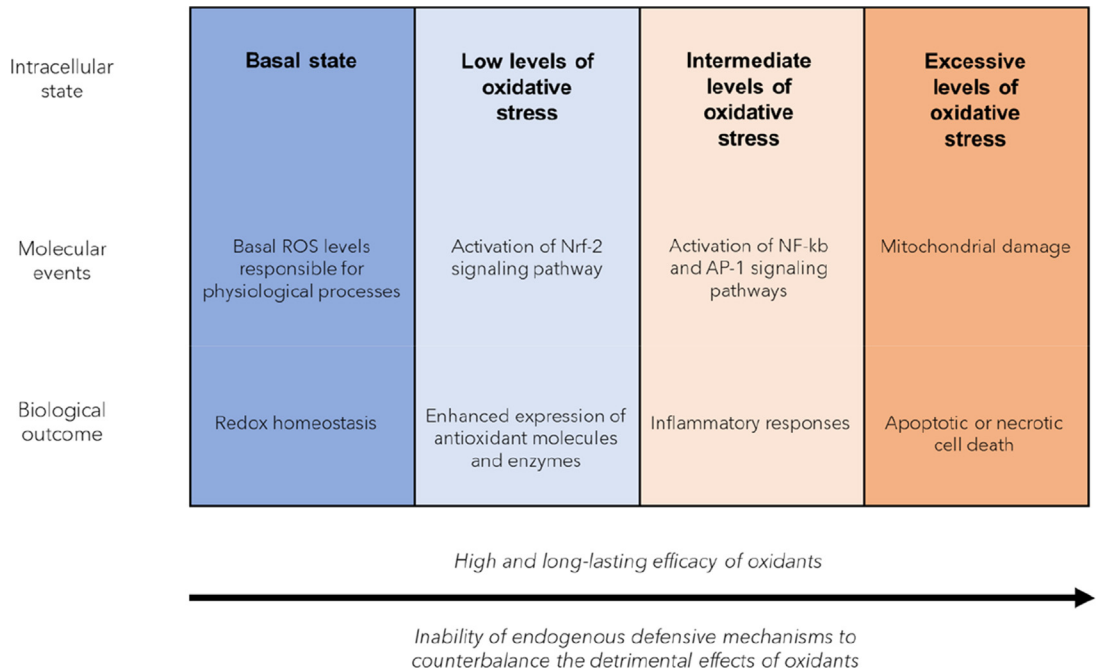

Figure 6.2
The distinct levels of oxidative stress.

translocate to the nucleus and upregulate proinflammatory gene expression, encoding cytokines chemokines [43]. Typical inducers of NF-kB activation are ROS and RNS, namely H_2O_2, $^1O_2$, $ONOO^-$, and HOCl, and proinflammatory cytokines, such as tumor necrosis factor-a (TNF-a) and interleukin 1 (IL-1) [44]. In addition, AP-1 is a heterodimeric transcription factor comprised of members of Jun and Fos protein families. Under the basal state, the intracellular Jun and Fos levels are extremely low, and in some cases, imperceptible, depending on the individual cell [45]. Nevertheless, Jun and Fos expression levels elevate upon stimulating conditions, and the protein subunits dimerize to regulate the expression of antioxidant enzymes and immunoreactive proteins [46]. Eventually, the excessive levels of oxidative stress cause severe mitochondrial damage and disruption of the electron transport chain, thereby promoting cell death via apoptosis or necrosis [47].

4. Specific physicochemical characteristics of engineered nanomaterials are responsible for ROS generation

As mentioned previously, the physicochemical characteristics of ENMs possess double-edged efficacies, providing technical advantages while inducing toxic effects in the biological systems. Accordingly, to assess the complex nano-bio interactions, characterization of the physicochemical properties and their biological impact is required. However, ENMs from the same category with different characteristics and the difficulty to elucidate whether the toxic effect is derived by a single or combination of characteristics constitute two parameters that render this task difficult. Size, surface properties, band gap, and chemical composition seem to highly contribute to ENMs-mediated redox homeostasis disturbance (Fig. 6.3).

The extremely small size of ENMs is a decisive factor for their toxic effects. Specifically, small size provides ENMs the ability to cross-biological barriers in the human body and exert secondary effects at sites beyond the route of exposure [48]. It should also be considered that the size of ENMs is inextricably linked to their surface reactivity and chemistry [49]. The smaller the ENMs size, the higher the surface area per mass unit becomes, as well as the reactivity of the surface. The high surface reactivity has been documented with the high capacity of ENMs to produce ROS via two distinct pathways. On the one hand, the concomitant presence of oxidizing agents and free radicals that can be bound to the surface of ENMs and lead to the formation of more reactive entities, which belong to ROS, such as harmful $O_2^{\bullet-}$ and $OH^{\bullet}$ [50]. For instance, silica nanoparticles can generate surface-bound radicals, such as $SiO_2^{\bullet}$ and Si^{+}-$O_2^{\bullet-}$ when they react with H_2O_2 to produce $OH^{\bullet}$ [51].

On the contrary, surface chemistry changes emerge from size alterations, conduce defects, and modifications of electronic properties that create reactive surface sites. The ENMs can

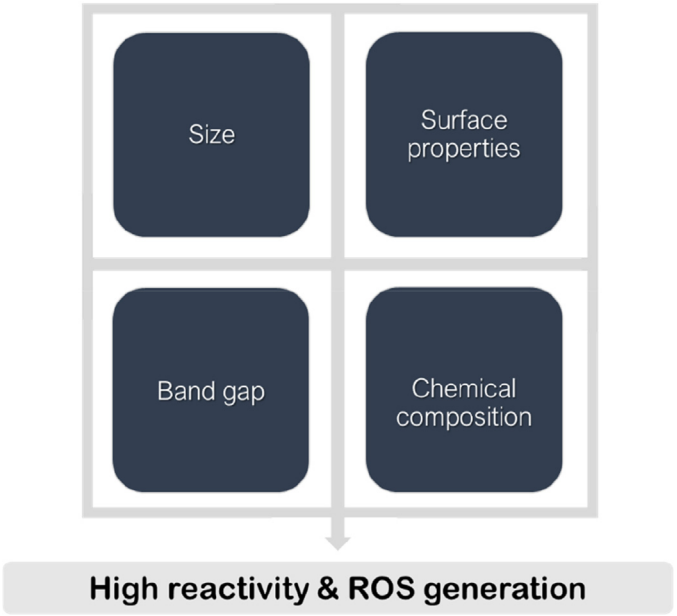

Figure 6.3
The main physicochemical characteristics of engineered nanomaterials yield high reactivity and contribute to reactive oxygen species (ROS) formation.

interact with O_2, exchange electrons, and generate $O_2^{\bullet -}$ [49]. In line with the above, Carlson et al. have reported that silver nanoparticles exert toxic effects in alveolar macrophages in a size-dependent manner, largely attributed to increased intracellular ROS levels [52]. Furthermore, silver nanoparticles of different sizes, that is, 4, 20, and 70 nm, trigger size-dependent inflammatory responses and ROS generation in human promonocytic cells. The smaller tested nanoparticles are the most effective [53].

Similarly, Zhou et al. have highlighted that different sizes of yttrium oxide nanoparticles (60, 100, and 300 nm) exhibit pernicious effects in primary osteoblasts in a size-dependent manner [54]. In this study, authors have found that the smaller nanoparticles tested are the most potent to induce ROS generation. Finally, Passagne et al. have established that silicon dioxide nanoparticles can induce size-dependent toxicity in human and porcine kidney cells, featuring elevated ROS and lipid peroxidation levels [55].

The bandgap is a parameter that must be considered when evaluating the ability of ENMs, especially those containing metal oxides, to induce redox perturbations. As band gap, we refer to the minimum amount of energy required to release an electron from the valence band and relocate it to the conduction band within any electron orbital of the respective material. Previously, Burello and Worth have proposed a theoretical model in which the redox potential of metal oxide nanoparticles could be predicted, by determining the energy

levels of the valence band, i.e., valence energy (E_V), and the conduction band, i.e., conduction energy (E_C) [56]. Determination of these energy levels allows scientists to calculate the energy required for the electron transfer between the respective bands and the surrounding environment [57]. Then, these energy levels are compared to the cellular redox potential, ranging from −4.12 to −4.84 eV [58]. Particular emphasis is placed on E_C, considering that the electron transfer from the conduction band is more likely to occur due to the less energy needed. The energy level alignment between the metal oxide nanoparticles and the intracellular environment can lead to electron exchange and, eventually, to the generation of free radicals and reactive species [59]. For instance, the band gap of zinc oxide (ZnO) nanoparticles strongly correlates with ROS generating capacity that induces apoptotic cell death in fibroblastic cells [60]. In addition, Co_3O_4, Cr_2O_3, Ni_2O_3, Mn_2O_3, and CoO nanoparticles have comparable Ec with the cellular redox potential, promoting oxidative stress both in in vitro cell-based and in vivo systems [58].

Following size and band gap, the chemical composition is a major contributing factor that affects the oxidative stress–mediated toxicity of ENMs. Hence, diverse materials, in terms of the specific characteristic, have been evaluated for their potential to trigger ROS formation. Indeed, several studies have incriminated carbon-based nanomaterials, such as fullerenes and fullerene derivatives [61,62], carbon nanotubes [63,64], and graphene [65], as well as metal and metal oxide nanoparticles [66,67] with their ability to stimulate ROS formation. As regards metal and metal oxide nanoparticles, those consisting of transition elements, such as iron (Fe), copper (Cu), cobalt (Co), chromium (Cr), and vanadium (Va), have attained particular interest since the Fenton and Haber-Weiss reactions can occur, playing a pivotal role in the formation of ROS. The classic Fenton chemistry describes the reaction of ferrous ions (Fe^{2+}), acting as catalysts, with H_2O_2, to yield the highly reactive $OH^{\bullet}$ and ferric ions (Fe^{3+}) [68]. When Fe^{3+} or other transition metal ions replace the catalyst, the occurring reactions are characterized as Fenton-like, leading to the generation of $OH^{\bullet}$. For instance, the similar redox potential of copper (Cu) enables its involvement in such reactions, wherein cuprous ions (Cu^{1+}) can react with H_2O_2 in order to produce $OH^{\bullet}$ and cupric ions (Cu^{2+}) (S [69]). On the other hand, the Haber-Weiss reaction describes the reaction of $O_2^{\bullet-}$ with H_2O_2, catalyzed by iron or other transition metal ions, to produce O_2 and $OH^{\bullet}$ [70]. Nanoparticles containing Fe and Cu catalyze Fenton and Fenton-like reactions, while nanoparticles comprised of Co, Cr, and Va can catalyze both Fenton and Haber-Weiss reactions [71].

5. Engineered nanomaterials stimulate ROS formation via direct and indirect mechanisms

Even though ENMs have been strongly associated with generating ROS, the mechanism is not always direct. The direct mechanism, as previously stated, stems predominantly but

not exclusively from their physicochemical characteristics. Contrariwise, the indirect mechanisms include the impairment of mitochondria function, since specific nanoparticles penetrate the mitochondrial membrane, militating structural and functional alterations that affect mitochondrial dynamics. Secondly, ENMs can indirectly activate the phagocytic NADPH oxidase system as a cellular defense mechanism toward the entry of ENMs, promoting the generation of both oxygen-centered and nitrogen-centered reactive species (reactive nitrogen species; RNS) [72].

Concerning the direct mechanism of ROS production, size, shape, surface chemistry and charge, chemical composition, and dissolution are strongly interrelated. Size has received the most attention due to the dynamics that it provides to the specific ENM, rendering it highly reactive, and more specifically, the size regulates diverse mechanisms of cellular internalization, the rate of cellular uptake, the kinetics, and the subcellular distribution [73]. The internalization pathway is not monadical since ENMs can enter the cells either by active endocytic or passive pathways. Nevertheless, endocytosis consists of the most common pathway that ENMs follow to enter the cells since the size of ENMs is comparable to endogenous biomacromolecules [74]. Additionally, their size range from a few nanometers to several hundred nanometers and enter cells via pinocytosis/macropinocytosis. In contrast, ENMs ranging from 120−150 to 200 nm can be internalized through clathrin- or caveolin-mediated endocytosis. Furthermore, for bigger ENMs (250 nm up to 3 μm), the internalization is mediated by phagocytosis. Finally, when the size exceeds the latter class, the cellular entrance is accomplished with great difficulty through the caveolae-mediated pathway [75]. The size of the ENM can also decisively determine the rate of cellular entry, with a size around 50 nm to be ideal to allow the optimal rate of cellular uptake [76]. ENMs of extremely small size can easily penetrate the epithelial and endothelial barriers and reach the lymphatic and circulatory systems, allowing their translocation to other tissues and organs, eliciting secondary effects on remote sites from the route of exposure [77]. The small size of ENMs also enables them to enter cellular organelles, such as mitochondria, and nucleus, leading to alterations in cell metabolism, genotoxicity, and cellular death. The ROS-mediated toxic effects, dependent on particle's size, have been well-established for a variety of ENMs, among which nanoparticles consisting of silver [78,79], silicon [80,81], iron [82], titanium [83], and quantum dots [84].

Nevertheless, the extremely small size is not the only incriminating parameter that has been shown to induce toxicity. For instance, titanium dioxide particles, ranging in the microscale, were more efficacious to induce genotoxicity than the corresponding nanoforms, a phenomenon that might be attributed to their crystallinity [85]. Alumina nanoparticles, with different external morphology, exerted significant cytotoxicity, inflammation, and ROS accumulation. However, a stronger response was observed in the case of nanorods than nanoflakes, indicating that the shape is also a parameter dictating

the toxicity-mediated by ENMs [86]. Moreover, chemical composition and dissolution are implicated in ROS-dependent toxicity of ENMs, considering that metal and metal oxide nanoparticles per se or ions released from their surface can act as catalysts in Fenton and Haber-Weiss reactions, as previously described. Finally, a few ENMs, predominantly belonging to metal-oxide and carbon-based nanomaterials can be activated upon exposure to photon energy (ultraviolet or visible irradiation) and produce electrons, that result in the generation of $O_2^{\bullet -}$, $OH^{\bullet}$, and $^1O_2$ in aqueous suspensions [87,88,89,90].

Mitochondria, regularly referred to as cell powerhouses, are vital, semi-autonomous organelles inextricably linked to energy production, ion homeostasis, ROS generation, cell metabolism, cell signaling, and regulation of cell death [91]. Their internal structure consists of two membrane systems, the outer, separating the intermembrane space from the cytosol, and the inner, wherein a series of protein complexes reside, comprising the electron transport chain (ETC) [92]. The electrochemical gradient created by these protein complexes across the inner membrane is the driving force for converting ADP to ATP from ATP synthase [93]. Electron leaking throughout the ETC can produce superoxide anion ($O_2^{\bullet -}$) and therefore ROS accumulation within mitochondria, which can further lead to mitochondrial DNA damage, membrane phospholipid damage, and loss of mitochondrial membrane potential. The severity of damage determines whether the dysfunctional mitochondrion will selectively disintegrate via mitophagy or the whole cell will be directed to apoptotic or necrotic death [94].

ENMs can impair mitochondria and affect their functions by direct ROS damage or chronic redox state alterations, leading to cellular reprogramming. Of note, following the penetration of mitochondrial membrane, ENMs can stimulate the formation of $O_2^{\bullet -}$ either by blocking ETC or by accelerating electron transfer to O_2 [95]. For instance, titanium dioxide nanoparticles alter the mitochondrial morphology, induce perturbations of mitochondrial dynamics, and promote ROS generation in primary rat astrocytes and isolated lung tissue mitochondria [96,97]. Silica nanoparticles penetrate the mitochondrial membrane, inducing reactive species within mitochondria, inflicting structural and functional alterations, including loss of membrane potential, defects in cell respiration, dysregulation in ATP synthesis, and mitochondrial biogenesis in endothelial cells [98]. Mitochondrial membrane damage is also observed during zinc oxide nanoparticles exposure, without affecting the redox state in human hepatocytes [99]. Furthermore, multiwalled carbon nanotubes cause upregulation of mitochondrial gene expression and decrease the number of intracellular mitochondria and oxygen consumption rate, driving mitophagy in human bronchial epithelial cells [100].

The second indirect mechanism through which ENMs can induce excessive ROS production is the activation of NADPH oxidase (NOX), predominantly, the phagocytic one, also called NOX2. NOX2 is a multisubunit, transmembrane enzyme complex situated

at professional phagocytes, such as monocytes, macrophages, neutrophils, and dendritic cells, representing a critical regulator of inflammatory responses [101]. Specifically, NOX2 is responsible for the oxidative burst of $O_2^{\bullet-}$ in the presence of pathogens, exerting tremendous microbicidal activity either directly or via the production of stronger oxidizing agents [102]. For several decades, the NOX-mediated $O_2^{\bullet-}$ generation was attributed only to phagocytes. Nevertheless, to date, seven NOX isoforms have been identified in mammals, differing at the molecular level but displaying functional similarities to NOX2 and collectively referred to as the NOX family [103]. The NOX genes encode the transmembrane proteins in charge of electrogenic processes across the biological membranes. Once the stressful stimulus causing NOX activation is eliminated, the excessive production of $O_2^{\bullet-}$ is limited.

Cells of the innate immune system, such as monocytes and macrophages, are the first responders to the invasion of xenobiotics, implicated in ROS production via NOX activity during phagocytosis, and in the emergence of an inflammatory response, procedures that enable the effective eradication of most foreign agents [104]. Contrariwise, ENMs, recognized as xenobiotics, cannot be cleared by the elevated ROS production and steadily activate the NOX system, thus creating a vicious cycle [57]. Masoud et al. have demonstrated the inefficiency of titanium dioxide nanoparticles to activate the NOX complex by themselves in a cell-free system. However, after the NOX activation, the concomitant presence of titanium dioxide nanoparticles can generate ROS [105]. Ye et al. have indicated the potency of multiwalled carbon nanotubes to activate the NOX system in human primary macrophages. In their presence, the NOX subunits are translocated to the membrane, an event that is associated with NOX activation. Simultaneously, the NOX-mediated ROS generation is boosted, triggering cell death [106]. Besides the direct activation of the NOX system, ENMs might also be NOX biomimetics. Wu et al. have reported that Fe-N-doped graphene nanomaterials can catalyze the conversion of NADPH to $NADP^+$, thus stimulating ROS formation in human leukemia monocytes. Finally, WO3/Pt nanoparticles, proposed as a potential tumoricidal tool [107], mimic the activities of leukocytes NOX system, especially the oxidation of NADPH and the generation of ROS in breast cancer cells [108].

6. Diverse engineered nanomaterials dictate to perturbations of redox homeostasis

6.1 Carbon-based nanomaterials

6.1.1 Fullerenes and fullerene derivatives

Fullerenes are carbon-caged nanostructures constituted of carbon atoms conjugated with single and double bonds to fabricate pentagonal and hexagonal rings [109]. In sustainable

energy, fullerenes are utilized to manufacture photovoltaic systems due to their exceptional optical properties [110]. Several studies have investigated the impact of fullerenes or fullerene derivatives on the redox state of cells and living organisms either as a clinical endpoint or as an underlying mechanism associated with other biological outcomes. Although controversial findings have been obtained in cytotoxicity, the redox milieu is affected by the presence of fullerenes or their derivatives in most in vitro cell-based studies. Accordingly, such ENMs possess the ability to elicit perturbations of redox homeostasis, which in cases of severe oxidative damage direct to oxidative stress-mediated cell death.

Wang et al. evaluated the toxicity of fullerene C_{60} nanoparticles on human lung adenocarcinoma A549 cells after a 6-h exposure. Although no decrease of cell viability was observed in all tested doses, the intracellular redox state was deteriorated, as denoted by the increase in ROS levels, despite cells' attempt to maintain the redox balance via the increase in reduced glutathione (GSH) levels [111]. Cell death was absent after human keratinocyte HaCaT cells, and A549 cells were exposed to fullerene C_{70} nanoparticles for 6 h or 24 h. Nevertheless, mild oxidative stress was induced in both cell lines, and the redox perturbations were constituted by elevation in ROS levels and lipid peroxidation products [112]. The same pattern was repeated in cerebral T98G cells and human cervical cancer HeLa cells exposed to fullerene C_{60} and fullerenol nanoparticles. No cell death was detected in all administered doses. In terms of ROS generation, an interesting feature was the ability of fullerenols to confine the maximum ROS production. In contrast, fullerene C_{60} nanoparticles induced a slight increase in ROS generation only in HeLa cells [113].

On the other hand, exposure of rat isolated hepatocytes to hydroxylated fullerenes resulted in a time-dependent and dose-dependent decrease of cell viability. The depletion of GSH levels and protein thiols, along with the increase in the oxidized form of glutathione, i.e., GSSG, and in lipid peroxidation products, indicated the presence of oxidative stress [114]. Ershova et al. highlighted the genotoxic effects of a water-soluble fullerene derivative in human embryonic lung fibroblasts. According to their results, the fullerene derivative caused time-dependent changes in ROS levels, accompanied by severe DNA damage, that further directed to necrotic cell death [115].

A feature of particular interest is the characterization of fullerenes as "free-radical sponges" due to their effectiveness in scavenging various free radicals [116]. However, whether this ability is maintained in biological systems and the parameters that affect the fine balance between antioxidant/prooxidant action are still under investigation. Indeed, the current literature is somewhat contradictory, provided that some in vivo studies have highlighted their prooxidant effects, thus disturbing redox balance and triggering oxidative stress. In contrast, others have demonstrated that they exert antioxidant properties, either by directly scavenging free radicals or triggering endogenous antioxidant mechanisms.

Oberdörster investigated the effects of fullerene C_{60} nanoparticles on the redox status of juvenile largemouth bass. Following a 48-h exposure to the corresponding ENM, tissue-dependent perturbations of redox state were observed at doses that simulated the potential concentrations in the aquatic ecosystems. The brain was the most susceptible tissue in terms of oxidative damage, as depicted by the increased oxidative modifications in lipids [117]. Usenko et al. assessed the oxidative potential of fullerene C_{60} nanoparticles in zebrafish embryos, an aquatic animal model. Toward this direction, the significance of light activation, GSH and vitamin C administration, and chemical supplementation with inhibitors of GSH production were evaluated. Of note, when inhibiting the synthesis of GSH with chemical agents, the concentrations of fullerenes required to elicit detrimental effects were significantly lower, demonstrating the vital importance of GSH in the prevention of fullerenes oxidative damage [118].

Furthermore, Park et al. highlighted the immunotoxicity, in the form of an inflammatory response, in male ICR mice, appearing after exposure to fullerene C_{60} nanoparticles. To be more accurate, the experimental animals were exposed intratracheally to a single dose of the ENM and sacrificed at different time points, i.e., 1, 7, 14, and 28 days, following the treatment. The results revealed mainly an elevated secretion of preinflammatory and inflammatory cytokines in bronchoalveolar lavage fluid. At the same time, the lung tissue gene expression showed, among others, an increase in superoxide dismutase (SOD) activity during the experimental period [119].

On the opposite side, Jiao et al. demonstrated that hydroxylated fullerene nanoparticles and metallofullerene nanoparticles attenuated the oxidative stress in the lungs of tumor implanted female C57/BL mice. More specifically, the evaluation of a panel of redox biomarkers in lung tissue homogenates revealed that the intraperitoneal injection with both nanoparticles not only reduced the oxidative stress levels, in comparison with the nonsupplemented, tumor-invaded group but also restored the redox milieu to the state of normal mice. Their results included changes in GSH reservoirs, GSH-related antioxidant enzymes' activity, and the formation of lipid peroxidation products [120]. Gonchar et al. established that an aqueous solution of C_{60} fullerenes protected against the detrimental oxidative events emerging from restraint stress in male Wistar rats. Toward this end, the experimental animals were pretreated for 1 week with the respective solution and then subjected to acute restrain stress for 6 h. According to their results, the presupplementation with the aqueous solution of C_{60} fullerenes prevented oxidative damage in the brain and heart compared to the group exposed to restrain stress alone. Their findings included a decrease in ROS generation, H_2O_2 formation, lipid peroxidation products, an increase in GSH content, and the activity of GSH-associated antioxidant enzymes in both tissues. Moreover, the administration of the aqueous solution prior to restraining stress-induced the nuclear translocation of Nrf2 and promoted the expression of important Nrf2-targeted antioxidant enzymes [121].

Moreover, Vani et al. evaluated the oxidative stress-preventive activity of polyhydroxylated fullerene nanoparticles in an ischemic stroke rat model. To be more specific, the respective ENM was intraperitoneally administered in male Wistar rats, either pre or post treatment, and suppressed the oxidative damage induced by brain ischemia/reperfusion, as depicted by the increase in SOD activity and the decrease in nitrate and lipid peroxidation products [122]. Finally, Halenova et al. highlighted that C_{60} fullerene nanoparticles protected from redox equilibrium disturbances induced by a high-fat diet in a rat model. The experimental animals, that is, male Wistar rats, were fed a high-fat diet for 28 days. Every second day was intraperitoneally injected the fullerene nanoparticles for the next 6 weeks. The exported results revealed a decrease in lipid peroxidation products and an increase in SOD activity in the serum of animals posttreated with the nanoparticles compared to the nontreated obese rats [123].

6.1.2 Carbon nanotubes

Carbon nanotubes are carbon allotropes with characteristic tubular structures that can be distinguished into single-walled or multi-walled, depending on the number of graphene layers they are composed of. Such carbon-based nanomaterials can be deployed to manufacture electrodes incorporated into Li-ion batteries and supercapacitors [10]. The oxidative stress-mediated toxicity exerted by carbon nanotubes, either single-walled (single-walled carbon nanotubes; SWCNTs) or multi-walled (multiwalled carbon nanotubes; MWCNTs), has been established in a vast number of research studies, utilizing both in vitro cell—based and in vivo systems [124,125]. Herein, we present some indicative studies, testing SWCNTs or MWCNTs either individually or comparatively, to identify potential differences in terms of their toxicity. In addition, we provide insight into the effects arising from their surface functionalization. This intervention modifies surface chemistry, which could potentially lead to distinct effects compared to the new materials.

To begin with the redox-related effects of SWCNTs in the cellular level, Cheng et al. demonstrated their ability to induce oxidative stress in primary rat aortic endothelial cells at the exposure of 72 and 96 h, as denoted by the dose-dependent and time-dependent negative effects on intracellular GSH levels and the enhancement of ROS levels. To reinforce this finding, lipid peroxidation was also promoted at 72 h in a dose-dependent manner [126]. Staying within this subject, SWCNTs were associated with severe lung damage after investigating their effects on human bronchial epithelial BEAS-2B cells, human lung adenocarcinoma A549 cells, and lung fibroblast WI38 cells. To be more accurate, the study results revealed dose-dependent and time-dependent toxic effects after exposure to SWCNTs for 1—6 days, depending on the cell line, and elevated ROS formation after 16-h exposure in all cell lines. Noteworthy, BEAS-2B cells were more susceptible to oxidative damage than the other cell lines tested [127].

Moreover, Rodríguez-Yáñez et al. assessed the oxidative potential of SWCNTs in human umbilical vein endothelial cells (HUVECs) exposed in various concentrations of the respective nanomaterial for 2 h. It was found that SWCNTs acted as prooxidants, thus affecting cellular redox state, as denoted by the dose-dependent increase in a redox index associated with ROS production [128]. In addition, exposure to SWCNTs induced oxidative stress in primary mice pancreatic islets after 24-h incubation. The decrease in the activity of important antioxidant enzymes, that is, CAT, SOD, and GPx, and in GSH levels, along with the increase in ROS generation and lipid peroxidation, were causative factors for the manifestation of oxidative events [129].

The deleterious effects of SWCNTs have been evaluated in many animal studies, with interesting findings from a tissue-centric point of view. Lungs are the main organs targeted after CNTs exposure through the inhalation route [130]. Inoue et al. evaluated the pulmonary effects of SWCNTs, either alone or in combination with an allergen, in male ICR mice, after repeated intratracheal administration for 6 weeks. Their results revealed the presence of oxidative stress in the lungs after exposure to SWCNTs individually, emerging from the increased activity of myeloperoxidase and the enhanced levels of nitric oxide and 8-hydroxy-2′-deoxyguanosine (8-OHdG), a well-established biomarker of oxidative DNA damage [131]. Skin is also a major tissue affected after the dermal deposition of SWCNTs. In that frame, the dermal toxicity of SWCNTs was studied in the research of Murray et al. using both in vitro and in vivo models. Exposure of hairless SKH-1 mice to SWCNTs resulted in redox perturbations, consisting of depletion of GSH levels and promotion of protein carbonylation [132]. A link between exposure to SWCNTs and impairment of the central nervous system has also been confirmed. On that note, Liu et al. assessed the neurotoxic effects of SWCNTs in male Kunming mice after a 9-d exposure. According to their results, the experimental animals displayed significant neurobehavioral changes, followed by alterations of the brain's redox state. The highest treated doses caused the depletion of GSH levels, whereas the enhanced generation of ROS contributed to the formation of lipid peroxidation products [133].

Concerning the prooxidant activities of MWCNTs, Srivastava et al. signified their implication in apoptotic events in A549 cells after a 72-h exposure, regulated by redox equilibrium disturbances. Specifically, the disruption of the intracellular redox state resulted from the depletion of GSH reservoirs and the decreased CAT activity, followed by an elevation in ROS generation and lipid peroxidation levels [134]. Furthermore, Chen et al. demonstrated that MWCNTs promoted cell death in a dose-dependent manner in murine macrophages RAW264.7 and A549 cells, following a 24-h exposure. The observed effect was mainly attributed to redox state alterations, characterized by a significant decrease in biomarkers of antioxidant capacity, that is, GSH levels and SOD activity, and an increase in free radicals and lipid peroxidation [135]. In addition, MWCNTs subserved

an apoptotic function in L929 mouse fibroblasts, after exposure for 24 and 48 h, due to the induction of oxidative stress. The increase in SOD activity could not counterbalance the detrimental effects in lipids caused by the enhanced ROS generation, while GSH concentration was diminished [136]. Finally, Lucas et al. indicated that a 72-h exposure of BEAS-2B cells to MWCNTs affected redox stability, as shown by the increased ROS levels, and led to cellular responses associated with inhibition of cell proliferation [137].

To continue with MWCNTs, their genotoxic effects, mediated by the prevalence of oxidative stress, have been established in many studies. For instance, oxidative stress—mediated genotoxicity was investigated in Kato et al. wherein ICR mice were intratracheally administered a single dose of MWCNTs. Their results suggested that lungs were particularly prone to DNA oxidative damage, as denoted by the increase in DNA adducts, further associated with the induction of oxidative stress and lipid peroxidation [138]. The interrelation between oxidative stress and DNA damage was also evaluated. However, it is a different animal model in the study of Saria et al. wherein *Xenopus laevis* tadpoles were exposed to MWCNTs over a short period. The results highlighted redox perturbations in the presence of MWCNTs as, although the antioxidant defense mechanisms were intensified, their strengthening was not sufficient to prevent H_2O_2 generation. In parallel, at the systemic level, oxidative DNA damage was observed [139].

Furthermore, the impact of MWCNTs functionalized with single-strand DNA was evaluated by Clichici et al. in Wistar rats, both at the systemic level and in the liver, a crucial detoxification tissue. The rats were intraperitoneally administered a single dose of the respective nanomaterial, and the assessment of a redox biomarkers network indicated the induction of oxidative stress in both tissues [140]. Moreover, Patllola et al. demonstrated the ability of carboxylated MWCNTs to provoke toxic effects in the liver of Swiss—Webster mice when intraperitoneally injected for 5 days. The underlying mechanism of hepatotoxicity, resulting in histopathological lesions, was attributed to oxidative stress, based on the elevated levels of ROS and lipid hydroperoxides in tissue homogenate, which followed a dose-dependent pattern [141].

From another perspective, Migliore et al. investigated, in a comparative way, the genotoxic effects of SWCNTs and MWCNTs in RAW264.7 cells after a 24 h exposure. To be more specific, they ascertained that the ensuing oxidative damage could induce DNA and chromosome damages in both cases [142]. Within the same logic, Khaliullin et al. evaluated the differences in the toxicity of SWCNTs and MWCNTs in RAW 264.7 cells and BEAS-2B cells, following exposure for 24 and 48 h. MWCNTs did not affect the viability of RAW264.7 cells in contrast to SWCNTs, wherein cell viability drastically decreased in all cases. However, redox-state alterations were observed after exposure in both materials, as shown by the decrease in GSH levels [143]. In addition, Ghanbari et al. conducted a comparative study of SWCNTs and MWCNTs toxicity using isolated

mitochondria derived from primary rat skin cells. Their results revealed dose-dependent toxicity for both materials after the 1-h exposure, resulting in structural and functional mitochondrial changes caused by ROS generation. However, the most intense mitochondrial damage was observed in the case of SWCNTs [144].

A feature of particular interest is the functionalization of carbon nanotubes to enhance the interplay with their environment and strengthen their biocompatibility [145]. However, the particular intervention modifies their surface chemistry, leading to distinct toxic effects compared to the raw ones. For instance, Kyriakidou et al. demonstrated a significant difference among pristine and carboxylated MWCNTs in cytotoxicity when incubated with A549 cells for 3 h. The rationale for selecting this exposure time was the simulation of an occupational scenario, particularly a workplace accident, finding out that the functionalized MWCNTs posed a greater threat to cell survival than the nonfunctionalized [146]. Contradictory, in the study of Shen et al. the pristine SWCNTs appeared to be more efficacious in oxidative potential. Specifically, the toxicity profile of pristine, carboxylated, and hydroxylated SWCNTs was assessed in human hepatocarcinoma cells HepG2 exposed to the corresponding nanomaterials for 24 h. The authors established that the mechanisms involved in the observed cytotoxicity were plasma membrane damage and the promotion of oxidative stress through ROS production [147].

On the other hand, pristine, hydroxylated, and carboxylated MWCNTs induced oxidative damage that further promoted apoptosis to HUVECs when incubated with them in various concentrations for 24 h. Indeed, the study results showed a decrease in intracellular GSH levels, along with an increase in ROS levels. However, in that case, no significant differences were observed between the nonfunctionalized and functionalized MWCNTs, in a frame of their oxidative potential [148].

Additionally, Sabido et al. evaluated the redox-related effects of pristine, acid-functionalized, and annealed MWCNTs in RAW264.7 macrophages, following exposure to 90 min and 24 h. The exported results indicated that the short-term exposure to all materials induced redox imbalance, as depicted by the increased ROS generation, which did not persist in the long run, as the antioxidant enzyme mechanisms could compensate for it. Nevertheless, the most thorough analysis of $O_2^{\bullet -}$ and $OH^{\bullet}$ revealed that acid functionalization and annealing strongly impacted their production [149].

6.2 Metal-based nanoparticles

6.2.1 Iron-based nanoparticles

In recent years, iron-based nanoparticles have gained significant ground in sustainable energy applications due to their distinctive optical, electrical, magnetic, and catalytic properties [150]. More elaborately, they are employed as catalysts in the production of

biofuels [151,152], as electrodes for sodium-ion [153] and lithium-ion [154] batteries, and as photoanodes for the conversion of solar energy into fuels [155]. Nevertheless, iron-based nanoparticles elicit severe adverse effects when interacting with biological systems, predominantly related to their high oxidative potential. The mechanisms through which iron-based nanoparticles trigger intracellular ROS generation, leading to the prevalence of oxidative stress, have been previously reported. Among them, Fenton, Fenton-like, and Haber-Weiss reactions stand out [156]. The following text presents various studies that differ in the nanomaterial of interest, the biological system under investigation, and the biological outcome. However, we collectively conclude that oxidative stress is the main mechanism of toxicity of such nanoparticles.

Zhu et al. reported the robustness of iron oxide nanoparticles, particularly ferric oxide (Fe_2O_3) and ferriferous oxide (Fe_3O_4) nanoparticles, to incite cell mortality in human umbilical vein endothelial ECV304 cells at various time points. The loss of mitochondrial membrane potential and the abnormal nuclear chromatin clumping, detected in the cellular presence of both nanoparticles, were interpreted as signs of apoptosis, stimulated by the excessive generation of ROS and RNS [157]. The toxicity profile of Fe_2O_3 nanoparticles has further been characterized by Alarifi et al. in human breast cancer MCF-7 cells with interesting findings from a redox perspective. In a more precise manner, after 24 and 48 h of exposure, the redox homeostasis was dreadfully disturbed, as denoted by the depletion of GSH content, the lessening in antioxidant enzymes activity, and the promotion of lipid peroxidation and ROS generation. The elevated ROS levels begot oxidative DNA damage, leading to apoptotic cell death [158]. On the same pattern, Gaharwar et al. highlighted the cytotoxic effects of Fe_2O_3 nanoparticles in rat primary splenic lymphocytes exploiting various endpoints. Their findings were supported by the loss of mitochondrial membrane potential, the severity of oxidative DNA damage, and apoptosis detection. The exerted phenotype was largely attributed to redox dysregulation, as depicted by the diminished content and activity of GSH and antioxidant enzymes, respectively, and the ascent ROS levels, further stimulating lipid peroxidation [159]. In addition, Fe_3O_4 nanoparticles elicited genotoxic actions, leading to apoptotic death, in skin epithelial A431 cells and A549 cells. After 24 h of exposure to the individual nanoparticles, the intracellular redox equilibrium was disrupted in both cell lines, as showed by the depletion of GSH reservoirs and the intensified ROS formation, which eventually promoted lipid peroxidation and severe oxidative DNA damage [160]. Apoptotic events have also been reported by Naqvi et al. In the case of super paramagnetic iron oxide nanoparticles (SPIONs). More specifically, exposure of murine macrophages J774 to the corresponding nanoparticles for 6 h directed to severe damage of cell membrane, mediated by the enhanced ROS levels [161].

It is well documented that exposure to iron oxide nanoparticles induces detrimental effects in vivo, resulting from sustained oxidative stress, both at the systemic and at the tissue level [162]. Nemmar et al. demonstrated the cardiotoxic effects of Fe_3O_4

nanoparticles in BALB/C mice. More elaborately, the intravenous administration resulted in severe DNA damage in the heart of the experimental animals, mediated by the emergence of oxidative stress. The oxidative alterations in the heart's redox state comprised ROS levels that promoted lipid peroxidation processes. Noteworthy, the activation of antioxidant enzyme mechanisms, that is, SOD activity, was insufficient to counterbalance the adverse effects caused by the excessive ROS formation [163]. The neurotoxicity of Fe_3O_4 nanoparticles has been established in the study of Wu et al. in SD rats, indicating the capacity of such nanoparticles to translocate from the site of nasal deposition to the brain and elicit deleterious effects. More specifically, 7 d after exposure, redox alterations were detected in the striatum and hippocampus, consisting of H_2O_2 elevation in both tissues. At the same time, depletion of GSH levels was also observed in the case of the striatum [164]. Pulmonary toxicity was an inevitable outcome in the acute toxicity study of Srinivas et al., wherein Wistar rats were exposed to Fe_3O_4 nanoparticles for 4 h via the inhalation route. Their findings suggested the induction of oxidative stress in the lungs 24 h postexposure, supported by the increase in malondialdehyde content, a well-established lipid peroxidation biomarker, and diminished GSH levels and antioxidant enzyme activities [165].

6.2.2 Gold nanoparticles

Gold (Au) nanoparticles that possess superior thermal, electrical, and optical properties are efficient absorbers of visible light, and, for that reason, they can be deployed in solar energy technologies, for example, in the improvement of photovoltaic systems [166,167]. In general terms, Au nanoparticles are considered safe because of their low toxicity levels compared to other metal-based nanoparticles [168]. Nevertheless, their biological impact has not yet been fully elucidated. In contrast, a series of in vitro cell—based and in vivo studies have attempted to clarify the competence of Au nanoparticles to disrupt intracellular redox homeostasis [169,170].

Li et al. investigated the pulmonary toxicity caused by Au nanoparticles in human lung fibroblasts MRC-5. According to their findings, after a 72-h exposure, oxidative stress was induced, as showcased by the emergence of lipid peroxidation. Simultaneously, autophagy was promoted, presumably as a defense mechanism to prevent perishing [171]. Enea et al. defined the toxicity profile of a broad spectrum of Au nanoparticles that diverged in size, shape, and surface coating in human proximal tubule HK-2 cells. Interestingly, all examined Au nanoparticles resulted in high cell mortality that followed a dose-dependent pattern; however, 13 nm nanospheres were the most fatal, reinforcing the significance of particle size. In their case, a decrease in the mitochondrial membrane potential along with an increase in ROS and RNS formation was detected [172]. In addition, Xia et al. demonstrated the capability of Au nanoparticles to provoke size-dependent genotoxic effects in HepG2 cells. More elaborately, following a 24-h exposure, the larger

nanoparticles showed no apparent cytotoxicity. In contrast, the lowest size nanoparticles, that is, 5 nm, displayed a high rate of cellular uptake, accompanied by increased DNA damage and ROS formation [173].

Concerning the redox potential of Au nanoparticles in vivo, Tedesco et al. evaluated their effects in an aquatic animal model, namely, *Mytilus edulis*, to clarify their toxicological and environmental aspects. After 24 h of exposure, the redox-thiol proteins in the digestive gland were significantly reduced, a finding accompanied by advanced lipid peroxidation product in the respective island in the gills and mantle. Collectively, their findings advocated the induction of oxidative stress as the main mechanism triggering toxicity [174]. The oxidative stress—mediated toxicity of Au nanoparticles has also been established in the study of Shrivastava et al. in Swiss albino mice. Brain, liver, kidney, and spleen were vulnerable to redox balance alterations, as denoted by the increase in ROS generation and the activity of antioxidant enzymes associated with GSH. Redox perturbations were also observed in the systemic level comprised of elevated ROS levels, depleted GSH content, and decreased activity of antioxidant enzymes [175]. In addition, Siddiqi et al. demonstrated that the brain is a tissue particularly susceptible to oxidative damage induced by Au nanoparticles in Wistar rats. The evaluation of the brain's redox state, after intraperitoneal administration for 3d, revealed the prevalence of adverse effects in the antioxidant defense system, accompanied by the promotion of lipid peroxidation and DNA damage [176].

6.2.3 Silicon-based nanoparticles

The exceptional optical and electrical properties of silicon-based nanoparticles render them prominent contenders for a multitude of sustainable energy applications, among which the manufacturing of anodes for lithium-ion batteries [177], their incorporation into high-performance photovoltaic systems [178], and their utilization as catalysts for the production of biodiesel [179]. Interestingly, the overly intense use of nanoscale forms of silicon dioxide (SiO_2), else known as silica, in industrial and, latterly, biomedical applications [55,180] has attracted considerable interest, raising serious concerns regarding human safety. Herein, we report some in vitro cell—based and in vivo studies that assess the capacity of SiO_2 nanoparticles to induce perturbations of the normal redox state as a reliable index toward the identification of their biological outcomes.

The harmful effects of SiO_2 nanoparticles were verified in the study of Ye et al. using myocardial H9c2(2-1) cells. Postexposure to the respective nanoparticles, dose-, size-, and time-dependent cell mortality was detected, predominantly attributed to the excessive levels of oxidative stress. The dysregulation of redox balance was supported by the increase in ROS levels, which further promoted oxidative modifications in lipids and the reduced levels of GSH [181]. Similar findings were also observed in HUVECs following exposure to SiO_2 nanoparticles of different particle sizes. Notwithstanding the activation of

the antioxidant mechanism to prevent cells from oxidative damage, the protection provided was not adequate, directing to the onset of lipid peroxidation and inflammation [182]. In addition, SiO_2 nanoparticles stimulated oxidative stress and inflammatory responses in human peripheral blood mononuclear cells. From a redox perspective, the diminished GSH levels, the elevated ROS levels, and the formation of protein radicals were the main findings [183].

Furthermore, exposure to SiO_2 nanoparticles led to mitochondrial-dependent apoptosis in HepG2 cells. The assessment of intracellular redox state revealed depletion of GSH reservoirs and augmentation in ROS levels, implying that oxidative stress is the potential underlying mechanism for the observed apoptotic death [184]. On the contrary, SiO_2 nanoparticles did not induce apoptosis in MRC-5 cells but promoted autophagy, presumably as a desperate attempt of the cells to ensure survival. Nevertheless, the redox balance was adversely affected, as showcased by the ascent in ROS levels, the decrease in GSH content, and the aggrandizement in the irreversible process of protein carbonylation [185].

In terms of the in vivo adverse effects, following exposure to SiO_2 nanoparticles, abnormal findings have been reported in blood and tissues. For instance, acute systemic exposure to amorphous SiO_2 nanoparticles induced oxidative stress, inflammatory responses, and oxidative DNA damage in vital organs of Tuck-Ordinary mice. It is of particular interest that the upregulation of the antioxidant mechanisms in all examined tissues, that is, brain, liver, kidney, and lung, was not sufficient to prevent the promotion of lipid peroxidation, except for the heart [186]. Hepatic and renal toxicity was also observed in the study of Azouz et al. in Sprague−Dawley rats. The prolonged exposure to amorphous SiO_2 nanoparticles decreased GSH content and CAT activity in both tissues, leading to oxidative occurrences in lipids. The resulting oxidative stress strongly affected liver and kidney normal functions, concomitantly inducing severe histopathological lesions [187].

Furthermore, pulmonary and cardiac toxicity emerged in Wistar rats after a 30-d exposure to mesoporous SiO_2 nanoparticles. The increased generation of reactive species belonging to ROS and RNS negatively affected the arsenal of endogenous antioxidants, further enhancing oxidative lipid damage. The ramifications in the redox state were accompanied by histopathological findings, while at the systemic level, inflammatory responses were induced [188].

6.2.4 Titanium-based nanoparticles

Titanium-based nanoparticles, particularly those composed of titanium dioxide (TiO_2), hold multiple semiconducting and photocatalytic properties [189]. Under them, they are leveraged in the manufacturing of anodes for sodium-ion batteries [190], in the engineering of thermoelectric materials [191], and the production of energy storage

devices [192] and photoanodes for dye-sensitized solar cells [193]. Of note, their utilization has been extended in products of everyday life, such as sunscreens, due to their ability to efficiently absorb UV irradiation [194], and in biomedical applications, as a prominent photodynamic therapy for various diseases, including cancer treatment [195]. Nevertheless, investigations of the toxicity profile of TiO_2 nanoparticles have revealed an interplay between their endogenous presence and redox dysregulation [196,197]. Accordingly, we mention a few studies in the cellular and organism levels to reinforce the notion that such nanoparticles might constitute a risk for human health.

In the study of Park et al. the intracellular presence of TiO_2 nanoparticles was associated with the promotion of apoptotic death in BEAS-2B cells. This phenomenon was ascribed to redox imbalance, caused by increased ROS levels, decreased GSH content, and the changes in important antioxidant and inflammation-related enzymes [198]. Apoptotic events were also observed in human neuroblastoma SH-SY5Y cells after exposure to TiO_2 nanoparticles. The exerted cytotoxicity was intervened by oxidative stress, as denoted by the elevated ROS generation and the nuclear translocation of Nrf-2 to promote the expression of antioxidant enzymes [199]. Furthermore, TiO_2 nanoparticles caused prejudicial effects on glial cells of both human and rat origin, including morphological alterations, mitochondrial damage, and depolarization of the mitochondrial membrane. The predominance of oxidative stress was evident by the significant peroxidation of lipids, which could not be prevented by activating enzymatic antioxidant mechanisms [200]. Supplementarily, the study of Santonastaso et al. revealed signs of reproductive toxicity following exposure of human sperm cells to TiO_2 nanoparticles. Increased intracellular ROS levels prompted oxidative DNA damage, and the genotoxic lesions affected sperm cell motility [201]. Finally, the interaction of TiO_2 nanoparticles with rat cardiomyoblasts H9c2 decreased the potential of mitochondrial membrane, altered the cell-cycle dynamics, and stimulated necrotic death, mediated by the excessive ROS generation [202].

In addition to in vitro studies, the oxidative potential of TiO_2 nanoparticles has also been confirmed in vivo, demonstrating their ability to disrupt the endogenous redox balance. The liver is prone to oxidative damage since TiO_2 nanoparticles. In a relevant study, the oral administration of the corresponding nanoparticles for 14 d elicited hepatotoxicity in Swiss albino mice. The evaluation of the liver's redox state revealed the depletion of GSH pools, along with an increase in ROS levels and advanced lipid peroxidation. Oxidative DNA damage was also detected, and apoptosis was promoted in hepatocytes. It is noteworthy that the findings at the molecular level were also associated with histopathological lesions [203].

Moreover, Chen et al. indicated the ability of TiO_2 nanoparticles to induce oxidative stress in the intestine of Sprague—Dawley rats after oral exposure for 30 d. According to their results, the antioxidant activity of SOD was significantly decreased, whereas the oxidative

deterioration of lipids was enhanced. Collectively, these oxidizing events provoked alterations in gut microbiota [204].

Furthermore, TiO_2 nanoparticles perturbed the spleen's redox homeostasis when administered by gavage for 14 d in Wistar rats. The evaluation of a redox biomarkers network disclosed depreciation in the activity of important antioxidant enzymes and total antioxidant capacity levels, along with an increase in biomarkers associated with oxidative status and damage. Notably, the simultaneous administration of vitamin A and E ameliorated the nanoparticles' effects, thus preventing tissue from oxidative stress [205]. Additionally, Sun et al. highlighted the pulmonary toxicity of TiO_2 nanoparticles in CD-1 (ICR) female mice after intratracheal administration for 90 d. More elaborately, the long-term, low-dose exposure induced oxidative stress in the lungs of laboratory animals, an assertion supported by the depletion of GSH reservoirs, the elevation of ROS levels, and the elevated lipid peroxidation [206].

6.2.5 Zinc-based nanoparticles

Zinc-based nanoparticles are characterized by outstanding optical, chemical, semiconducting, and catalytic properties, and, accordingly, they have attracted significant scientific and industrial interest in recent years [207]. In the field of sustainable energy, their usages encompass but are not limited to the production of biodiesel [207], the engineering of novel energy storage devices [208,209], and the conversion of solar energy into other energy forms [210]. Respectively, as the applications of zinc-based nanoparticles increase, so do human exposure, a cause of concern in their biosafety. As such, their potential toxicity has been the main research item of various studies, and among the most common findings are the disturbances in redox equilibrium that reveal their robust prooxidant nature [211,212].

Ng et al. reported the ability of ZnO nanoparticles to exert cytotoxic and genotoxic effects in human fetal lung fibroblasts MRC5, at various time points, mediated by the excessive generation of ROS, that begot oxidative DNA damage [213]. Dysregulation of redox balance was also observed in colorectal epithelial adenocarcinoma cells after 24 h of exposure to ZnO nanoparticles. The results were supported by the elevation in ROS levels, the decrease in SOD activity, and the increase in GSH content as a compensatory antioxidant mechanism, which, however, was not competent to prevent cell mortality [214]. In a comparative study, among a broad range of metal-based nanoparticles, ZnO nanoparticles were found to possess a higher potential to manifest toxic effects in rabbit cornea SIRC cells. Interestingly, significant ROS formation was detected only in the case of ZnO nanoparticles, indicating oxidative stress as the presumable underlying mechanism for the exerted cytotoxicity [215]. In addition, an interesting study by Annangi et al. attempted to evaluate the real-life risks arising from exposure to ZnO nanoparticles. In that frame, acute exposure to various concentrations of ZnO nanoparticles induced oxidative

stress and DNA damage in mouse embryonic fibroblasts and their knockout derivatives when administered in high, unrealistic doses. Contradictory, the long-term, low-dose administration was unable to exert perturbations of redox state and genotoxicity in both cell lines tested, highlighting the need for reassessment of nanoparticles toxicity profile in a more realistic way [216].

The detrimental effects of ZnO nanoparticles on redox states have been reported in many in vivo studies [217]. Herein, we review some representative studies with intriguing findings, depending on the route of exposure, the organ or tissue studied, and the animal model used. Repeated oral exposure to ZnO nanoparticles for 14 d resulted in significant accumulation of the individual nanoparticles in the liver of Swiss albino mice. In contrast, a slight but not significant increase was also observed in kidneys. As such, lipid peroxidation was promoted in both tissues, accompanied by histopathological lesions, while oxidative DNA damage was also observed in the case of the liver.

Additionally, the oxidative events in the liver led to apoptotic death in hepatocytes [218]. Exposure to ZnO nanoparticles through the inhalation route was associated with adverse effects on the central nervous system of Sprague—Dawley rats. After a single dose, the brain of the experimental animals succumbed to oxidative stress without any behavioral or cognitive changes in the neurobehavioral tests subjected [219]. In addition, ZnO nanoparticles induced renal toxicity in Wistar rats when administered via intraperitoneal injection for five consecutive days. The antioxidant enzyme activities, that is, SOD and CAT activity, in the renal cortex exacerbated, demonstrating the prooxidant action of such nanoparticles, followed by alterations in physiological parameters [220]. Concerning the effects of ZnO nanoparticles on the systemic level, the intraperitoneal injection in Wistar rats, for 10 d in a row, perturbed the redox state of the blood. Indeed, the levels of total antioxidant capacity were decreased, and as a result, total oxidant status elevated, promoting the production of lipid peroxidation byproducts [221].

7. The significance of evaluating the redox-related properties of engineered nanomaterials

The advantages proceeding from the utilization of ENMs are indisputably numerous, and, in broad terms, they encompass the provision of enhanced or even novel properties to conventional materials. Nevertheless, as we progressively enter the nano-era, we encounter two important issues that urgently require delineation, the potential of human exposure and the biological imprint. To date, the predominant and most intense exposure to ENMs is detected in the occupational environment via the inhalation of airborne nanoparticles [222]. To a minor extent, the general population is also exposed either directly via releases from nanotechnology products or indirectly through contact with contaminated

environmental matrices [223]. Toxicological investigations of such materials have revealed their strong interactions with the endogenous redox system, upgrading oxidative stress to a key mechanism for a better understanding of their biological effects [224,225].

Oxidative stress is inextricably linked to the pathophysiology of several diseases associated with redox equilibrium disturbances, including diabetes mellitus, neurodegenerative disorders, cardiovascular and respiratory diseases, and even cancer [226]. Indeed, high levels of reactive species in biological samples are considered a hallmark and reliable clinical outcome in such pathologies. Nevertheless, to date, there is no direct correlation between specific reactive species and the onset of redox-related diseases [22], placing oxidative stress presumably as causality or a cog in the transmission that drives the vicious cycle, aggravating the pathophysiologies above.

In recent years, diverse methodologies have been developed to assess the biological outcome of ENMs, placing the investigation of redox profile in a prominent position [227,228,229,223]. To this end, the adoption of reliable methods and tools is of paramount importance to avoid pitfalls and misleading results due to the complex nature of such materials [230]. Redox biomarkers that can efficiently serve this purpose encompass biomarkers of antioxidant capacity, biomarkers of severe oxidative damage, and, of course, reactive species per se [231]. In this light, in a previous study of our research group, we proposed a multilevel methodology to elucidate the impact of ENMs in the scientific field of Redox Biology. It is worth noting that the specific approach not only focuses on the ramifications of ENMs on the endogenous redox state but also provides an overview of the potential antioxidant capacity, that stems from their intrinsic physicochemical characteristics [223].

An interesting concept that is expected to attract even more scientific interest soon is the assessment of the effects caused by low doses of ENMs in the long run. Repeated low-dose exposures to such materials may reflect the risks arising in real life more adequately than the short-term administration of high and, as such, unrealistic doses that are typically toxic [57]. On that note, oxidative stress might be a reliable endpoint for unveiling the biological outcome of materials in the nanoscale. Such studies are expected to clarify whether there is a direct correlation between exposure to ENMs and the initiation or exacerbation of specific diseases and if oxidative stress is essential and capable of causing the prevalence of this phenotype.

Author contribution

Periklis Vardakas: Visualization and writing—original draft. Ioannis D. Kyriazis: Visualization and writing—review and editing. Maria Kourti: Visualization and writing—original draft. Zoi Skaperda: Visualization and writing—original draft. Fotios Tekos: Visualization and writing—original draft. Demetrios Kouretas: Conceptualization, project administration, and supervision. Authors declare that there is no financial relationship with the

editors or publisher. They have contributed to the original work in this chapter, other than what was acknowledged or appropriately cited with copyright permission.

References

[1] V.S. Arutyunov, G.V. Lisichkin, Energy Resources of the 21st century: problems and forecasts. Can renewable energy sources replace fossil fuels, Russ. Chem. Rev. 86 (8) (2017) 777, https://doi.org/10.1070/RCR4723.

[2] M.E. Munawer, Human health and environmental impacts of coal combustion and post-combustion wastes, J. Sustain. Min. 17 (2) (2018) 87–96, https://doi.org/10.1016/J.JSM.2017.12.007.

[3] T.M. Letcher, Why do we have global warming?, in: Managing Global Warming: An Interface of Technology and Human Issues 3–15, 2019, https://doi.org/10.1016/B978-0-12-814104-5.00001-6.

[4] I. Manisalidis, E. Stavropoulou, A. Stavropoulos, E. Bezirtzoglou, Environmental and health impacts of air pollution: a review, Front. Public Health 0 (2020) 14, https://doi.org/10.3389/FPUBH.2020.00014.

[5] A. Mukherjee, M. Agrawal, World air particulate matter: sources, distribution and health effects, Environ. Chem. Lett. 15 (2) (2017) 283–309, https://doi.org/10.1007/S10311-017-0611-9.

[6] J. Jeevanandam, A. Barhoum, Y.S. Chan, A. Dufresne, M.K. Danquah, Review on nanoparticles and nanostructured materials: history, sources, toxicity, and regulations, Beilstein J. Nanotechnol. 9 (Issue 1) (2018) 1050–1074, https://doi.org/10.3762/bjnano.9.98. Beilstein-Institut Zur Forderung der Chemischen Wissenschaften.

[7] Q. Zhang, E. Uchaker, S.L. Candelaria, G. Cao, Nanomaterials for energy conversion and storage, Chem. Soc. Rev. 42 (7) (2013) 3127–3171, https://doi.org/10.1039/C3CS00009E.

[8] E. Inshakova, A. Inshakova, A. Goncharov, Engineered nanomaterials for the energy sector: market trends, modern applications, and future prospects, IOP Conf. Ser. Mater. Sci. Eng. 971 (3) (2020), https://doi.org/10.1088/1757-899X/971/3/032031.

[9] S. Afreen, R.A. Omar, N. Talreja, D. Chauhan, M. Ashfaq, Carbon-based nanostructured materials for energy and environmental remediation applications, Nanotechnol. Life Sci. (2018) 369–392, https://doi.org/10.1007/978-3-030-02369-0_17.

[10] G. Centi, S. Perathoner, Carbon nanotubes for sustainable energy applications, ChemSusChem 4 (7) (2011) 913–925, https://doi.org/10.1002/CSSC.201100084.

[11] Z. Sun, T. Liao, L. Kou, Strategies for designing metal oxide nanostructures, Sci. China Mater. 60 (1) (2016) 1–24, https://doi.org/10.1007/S40843-016-5117-0.

[12] R. Leary, A. Westwood, Carbonaceous nanomaterials for the enhancement of TiO2 photocatalysis, Carbon 49 (3) (2011) 741–772, https://doi.org/10.1016/J.CARBON.2010.10.010.

[13] Z.B. Shifrina, V.G. Matveeva, L.M. Bronstein, Role of polymer structures in catalysis by transition metal and metal oxide nanoparticle composites, Chem. Rev. 120 (2) (2019) 1350–1396, https://doi.org/10.1021/ACS.CHEMREV.9B00137.

[14] M. Janani, P. Srikrishnarka, S.V. Nair, A.S. Nair, An in-depth review of the role of carbon nanostructures in dye-sensitized solar cells, J. Mater. Chem. 3 (35) (2015) 17914–17938, https://doi.org/10.1039/C5TA03644E.

[15] J.R. Siqueira, O.N. Oliveira, Carbon-based nanomaterials, Nanostructures (2017) 233–249, https://doi.org/10.1016/B978-0-323-49782-4.00009-7.

[16] C. Fei Guo, T. Sun, F. Cao, Q. Liu, Z. Ren, Metallic nanostructures for light trapping in energy-harvesting devices, Light Sci. Appl. 3 (4) (2014), https://doi.org/10.1038/lsa.2014.42 e161–e161.

[17] W. Tu, Y. Zhou, Z. Zou, Photocatalytic conversion of CO2 into renewable hydrocarbon fuels: state-of-the-art accomplishment, challenges, and prospects, Adv. Mater. 26 (27) (2014) 4607–4626, https://doi.org/10.1002/ADMA.201400087.

[18] A. Pietroiusti, Health implications of engineered nanomaterials, Nanoscale 4 (4) (2012) 1231–1247, https://doi.org/10.1039/C2NR11688J.

[19] A. Kermanizadeh, B.K. Gaiser, G.R. Hutchison, V. Stone, An in vitro liver model - assessing oxidative stress and genotoxicity following exposure of hepatocytes to a panel of engineered nanomaterials, Part. Fibre Toxicol. 9 (1) (2012) 1−13, https://doi.org/10.1186/1743-8977-9-28.
[20] V. Kodali, B.D. Thrall, Oxidative stress and nanomaterial-cellular interactions, in: Studies on Experimental Toxicology and Pharmacology, 2015, pp. 347−367, https://doi.org/10.1007/978-3-319-19096-9_18.
[21] Y. Teow, P.V. Asharani, M.P. Hande, S. Valiyaveettil, Health impact and safety of engineered nanomaterials, Chem. Commun. 47 (25) (2011) 7025−7038, https://doi.org/10.1039/c0cc05271j.
[22] A.S. Veskoukis, A. Tsatsakis, D. Kouretas, Approaching reactive species in the frame of their clinical significance: a toxicological appraisal, in: Food and Chemical Toxicology, Elsevier Ltd, 2020, https://doi.org/10.1016/j.fct.2020.111206 vol. 138.
[23] K. Stamati, V. Mudera, U. Cheema, Evolution of oxygen utilization in multicellular organisms and implications for cell signaling in tissue engineering, J. Tissue Eng. 2 (1) (2011) 1−12, https://doi.org/10.1177/2041731411432365.
[24] K.J.A. Davies, F. Ursini, The Oxygen Paradox, CLEUP University Press, 1995.
[25] M. Bonora, S. Patergnani, A. Rimessi, E. De Marchi, J.M. Suski, A. Bononi, C. Giorgi, S. Marchi, S. Missiroli, F. Poletti, M.R. Wieckowski, P. Pinton, ATP synthesis and storage, Purinergic Signal. 8 (3) (2012) 343, https://doi.org/10.1007/S11302-012-9305-8.
[26] V.I. Lushchak, Free radicals, reactive oxygen species, oxidative stress, and its classification, Chem. Biol. Interact. 224 (2014) 164−175, https://doi.org/10.1016/J.CBI.2014.10.016.
[27] B. Halliwell, Free radicals and other reactive species in disease, ELS 1−9 (2015), https://doi.org/10.1002/9780470015902.A0002269.PUB3.
[28] M. Herb, A. Gluschko, M. Schramm, Reactive oxygen species: not omnipresent but important in many locations, Front. Cell Dev. Biol. 0 (2021) 2503, https://doi.org/10.3389/FCELL.2021.716406.
[29] R. Zhao, S. Jiang, L. Zhang, Z. Yu, Mitochondrial electron transport chain, ROS generation, and uncoupling (Review), Int. J. Mol. Med. 44 (1) (2019) 3−15, https://doi.org/10.3892/IJMM.2019.4188.
[30] M. Canton, R. Sánchez-Rodríguez, I. Spera, F.C. Venegas, M. Favia, A. Viola, A. Castegna, Reactive oxygen species in macrophages: sources and targets, Front. Immunol. 0 (2021) 4077, https://doi.org/10.3389/FIMMU.2021.734229.
[31] K. Krumova, G. Cosa, Chapter 1 overview of reactive oxygen species, in: Singlet Oxygen: Applications in Biosciences and Nanosciences, Volume 1, 2016, pp. 1−21, https://doi.org/10.1039/9781782622208-00001.
[32] M. Sharifi-Rad, N.V. Anil Kumar, P. Zucca, E.M. Varoni, L. Dini, E. Panzarini, et al., Lifestyle, oxidative stress, and antioxidants: back and forth in the pathophysiology of chronic diseases, Front. Physiol. 0 (2020) 694. https://doi.org/10.3389/FPHYS.2020.00694.
[33] J.M.C. Gutteridge, B. Halliwell, Antioxidants: molecules, medicines, and myths, Biochem. Biophys. Res. Commun. 393 (Issue 4) (2010) 561−564, https://doi.org/10.1016/j.bbrc.2010.02.071.
[34] Z. Moussa, Z.M.A. Judeh, S.A. Ahmed, Nonenzymatic exogenous and endogenous antioxidants, Free Radic. Med. Biol. (2019), https://doi.org/10.5772/INTECHOPEN.87778.
[35] A.M. Pisoschi, A. Pop, The role of antioxidants in the chemistry of oxidative stress: a review, Eur. J. Med. Chem. 97 (2015) 55−74, https://doi.org/10.1016/j.ejmech.2015.04.040.
[36] V. Luca, A. Baschieri, R. Amorati, Antioxidant activity of nanomaterials, J. Mater. Chem. B 6 (14) (2018) 2036−2051, https://doi.org/10.1039/C8TB00107C.
[37] H. Sies, D.P. Jones, Reactive oxygen species (ROS) as pleiotropic physiological signaling agents, Nat. Rev. Mol. Cell Biol. 21 (7) (2020) 363−383, https://doi.org/10.1038/s41580-020-0230-3.
[38] H. Sies, Oxidative stress: a concept in redox biology and medicine, Redox Biol. 4 (2015) 180−183, https://doi.org/10.1016/J.REDOX.2015.01.002.
[39] G. Gloire, S. Legrand-Poels, J. Piette, NF-κB activation by reactive oxygen species: fifteen years later, Biochem. Pharmacol. 72 (11) (2006) 1493−1505, https://doi.org/10.1016/J.BCP.2006.04.011.
[40] C. Tonelli, I.I.C. Chio, D.A. Tuveson, Transcriptional regulation by Nrf2, Antioxid. Redox Signal. 29 (17) (2018) 1727, https://doi.org/10.1089/ARS.2017.7342.

[41] C.A. Silva-Islas, P.D. Maldonado, Canonical and non-canonical mechanisms of Nrf2 activation, Pharmacol. Res. 134 (2018) 92−99, https://doi.org/10.1016/J.PHRS.2018.06.013.
[42] E. Panieri, A. Buha, P. Telkoparan-akillilar, D. Cevik, D. Kouretas, A. Veskoukis, Z. Skaperda, A. Tsatsakis, D. Wallace, S. Suzen, L. Saso, Potential applications of NRF2 modulators in cancer therapy, Antioxidants 9 (Issue 3) (2020), https://doi.org/10.3390/antiox9030193. MDPI AG.
[43] T. Liu, L. Zhang, D. Joo, S.-C. Sun, NF-κB signaling in inflammation, Signal Transduct. Targeted Ther. 2 (2017) 17023, https://doi.org/10.1038/SIGTRANS.2017.23.
[44] K. Lingappan, NF-κB in oxidative stress, Curr. Opin. Toxicol. 7 (2018) 81−86, https://doi.org/10.1016/J.COTOX.2017.11.002.
[45] R.S. Duman, D.H. Adams, B.B. Simen, Transcription factors as modulators of stress responsivity, Tech. Behav. Neural Sci. 15 (PART 1) (2005) 679−698, https://doi.org/10.1016/S0921-0709(05)80036-7.
[46] S. Di Meo, G. Napolitano, P. Venditti, Mediators of physical activity protection against ROS-linked skeletal muscle damage, Int. J. Mol. Sci. 20 (12) (2019) 3024, https://doi.org/10.3390/IJMS20123024.
[47] A.C. Kent, K.B.Y. El Baradie, M.W. Hamrick, Targeting the mitochondrial permeability transition pore to prevent age-associated cell damage and neurodegeneration, Oxid. Med. Cell. Longev. 2021 (2021), https://doi.org/10.1155/2021/6626484.
[48] A. Pietroiusti, L. Campagnolo, B. Fadeel, Interactions of engineered nanoparticles with organs protected by internal biological barriers, Small 9 (9−10) (2013) 1557−1572, https://doi.org/10.1002/SMLL.201201463.
[49] A. Manke, L. Wang, Y. Rojanasakul, Mechanisms of nanoparticle-induced oxidative stress and toxicity, BioMed Res. Int. 2013 (2013), https://doi.org/10.1155/2013/942916.
[50] A.A. Dayem, M.K. Hossain, S.B. Lee, K. Kim, S.K. Saha, G.M. Yang, H.Y. Choi, S.G. Cho, The role of reactive oxygen species (ROS) in the biological activities of metallic nanoparticles, Int. J. Mol. Sci. 18 (Issue 1) (2017) 120, https://doi.org/10.3390/ijms18010120. MDPI AG.
[51] B. Fubini, A. Hubbard, Reactive oxygen species (ROS) and reactive nitrogen species (RNS) generation by silica in inflammation and fibrosis, Free Radic. Biol. Med. 34 (Issue 12) (2003) 1507−1516, https://doi.org/10.1016/S0891-5849(03)00149-7. Elsevier Inc.
[52] C. Carlson, S.M. Hussain, A.M. Schrand, L.K. Braydich-Stolle, K.L. Hess, R.L. Jones, J.J. Schlager, Unique cellular interaction of silver nanoparticles: size-dependent generation of reactive oxygen species, J. Phys. Chem. B 112 (43) (2008) 13608−13619, https://doi.org/10.1021/JP712087M.
[53] J. Park, D.-H. Lim, H.-J. Lim, T. Kwon, J. Choi, S. Jeong, I.-H. Choi, J. Cheon, Size-dependent macrophage responses and toxicological effects of Ag nanoparticles, Chem. Commun. 47 (15) (2011) 4382−4384, https://doi.org/10.1039/C1CC10357A.
[54] G. Zhou, Y. Li, Y. Ma, Z. Liu, L. Cao, D. Wang, S. Liu, W. Xu, W. Wang, G. Zhou, Y. Li, Y. Ma, Z. Liu, L. Cao, D. Wang, S. Liu, W. Xu, W. Wang, Size-dependent cytotoxicity of yttrium oxide nanoparticles on primary osteoblasts in vitro, J. Nurs. Res. 18 (5) (2016) 135, https://doi.org/10.1007/S11051-016-3447-5.
[55] I. Passagne, M. Morille, M. Rousset, I. Pujalté, B. L'Azou, The implication of oxidative stress in size-dependent toxicity of silica nanoparticles in kidney cells, Toxicology 299 (2−3) (2012) 112−124, https://doi.org/10.1016/J.TOX.2012.05.010.
[56] E. Burello, A.P. Worth, A theoretical framework for predicting the oxidative stress potential of oxide nanoparticles, Nanotoxicology 5 (2) (2011) 228−235, https://doi.org/10.3109/17435390.2010.502980.
[57] R.P. Mendoza, J.M. Brown, Engineered nanomaterials and oxidative stress: current understanding and future challenges, Curr. Opin. Toxicol. 13 (2019) 74−80, https://doi.org/10.1016/j.cotox.2018.09.001. Elsevier B.V.
[58] H. Zhang, Z. Ji, T. Xia, H. Meng, C. Low-Kam, R. Liu, S. Pokhrel, S. Lin, X. Wang, Y.-P. Liao, M. Wang, L. Li, R. Rallo, R. Damoiseaux, D. Telesca, L. Mädler, Y. Cohen, J.I. Zink, A.E. Nel, Use of metal oxide nanoparticle band gap to develop a predictive paradigm for oxidative stress and acute pulmonary inflammation, ACS Nano 6 (5) (2012) 4349−4368, https://doi.org/10.1021/NN3010087.

[59] E. Burello, A.P. Worth, A rule for designing safer nanomaterials: do not interfere with the cellular redox equilibrium, Nanotoxicology 1−2 (2013), https://doi.org/10.3109/17435390.2013.828109.
[60] M. Arakha, J. Roy, P.S. Nayak, B. Mallick, S. Jha, Zinc oxide nanoparticle energy bandgap reduction triggers oxidative stress resulting in autophagy-mediated apoptotic cell death, Free Radic. Biol. Med. 110 (2017) 42−53, https://doi.org/10.1016/J.FREERADBIOMED.2017.05.015.
[61] X. Lv, B. Huang, X. Zhu, Y. Jiang, B. Chen, Y. Tao, J. Zhou, Z. Cai, Mechanisms underlying the acute toxicity of fullerene to Daphnia magna: energy acquisition restriction and oxidative stress, Water Res. 123 (2017) 696−703, https://doi.org/10.1016/J.WATRES.2017.07.023.
[62] A. Trpkovic, B. Todorovic-Markovic, V. Trajkovic, Toxicity of pristine versus functionalized fullerenes: mechanisms of cell damage and the role of oxidative stress, Arch. Toxicol. 86 (12) (2012) 1809−1827, https://doi.org/10.1007/S00204-012-0859-6.
[63] S. Pichardo, D. Gutiérrez-Praena, M. Puerto, E. Sánchez, A. Grilo, A.M. Cameán, Á. Jos, Oxidative stress responses to carboxylic acid functionalized single wall carbon nanotubes on the human intestinal cell line Caco-2, Toxicol. Vitro 26 (5) (2012) 672−677, https://doi.org/10.1016/J.TIV.2012.03.007.
[64] A.R.N. Reddy, Y.N. Reddy, D.R. Krishna, V. Himabindu, Multiwall carbon nanotubes induce oxidative stress and cytotoxicity in human embryonic kidney (HEK293) cells, Toxicology 272 (1−3) (2010) 11−16, https://doi.org/10.1016/J.TOX.2010.03.017.
[65] A. Jarosz, M. Skoda, I. Dudek, D. Szukiewicz, Oxidative stress and mitochondrial activation as the main mechanisms underlying graphene toxicity against human cancer cells, Oxid. Med. Cell. Longev. 2016 (2016), https://doi.org/10.1155/2016/5851035.
[66] A. Sarkar, M. Ghosh, P.C. Sil, Nanotoxicity: oxidative stress-mediated toxicity of metal and metal oxide nanoparticles, J. Nanosci. Nanotechnol. 14 (1) (2014) 730−743, https://doi.org/10.1166/JNN.2014.8752.
[67] A.B. Sengul, E. Asmatulu, Toxicity of metal and metal oxide nanoparticles: a review, Environ. Chem. Lett. 18 (5) (2020) 1659−1683, https://doi.org/10.1007/S10311-020-01033-6.
[68] K. Jomova, S. Baros, M. Valko, Redox-active metal-induced oxidative stress in biological systems, Transit. Met. Chem. 37 (2) (2012) 127−134, https://doi.org/10.1007/S11243-012-9583-6.
[69] S. Hussain, E. Aneggi, D. Goi, The catalytic activity of metals in heterogeneous Fenton-like oxidation of wastewater contaminants: a review, Environ. Chem. Lett. 19 (3) (2021) 2405−2424, https://doi.org/10.1007/S10311-021-01185-Z.
[70] F. Collin, Chemical basis of reactive oxygen species reactivity and involvement in neurodegenerative diseases, Int. J. Mol. Sci. 20 (10) (2019), https://doi.org/10.3390/IJMS20102407.
[71] R. Ganguly, A.K. Singh, R. Kumar, A. Gupta, A.K. Pandey, A.K. Pandey, Nanoparticles as modulators of oxidative stress, in: Nanotechnology in Modern Animal Biotechnology: Concepts and Applications 29−35, 2019, https://doi.org/10.1016/B978-0-12-818823-1.00003-X.
[72] C. Buzea, I.I. Pacheco, K. Robbie, Nanomaterials and nanoparticles: sources and toxicity, Biointerphases 2 (4) (2007) MR17−MR71, https://doi.org/10.1116/1.2815690.
[73] L. Shang, K. Nienhaus, G.U. Nienhaus, Engineered nanoparticles are interacting with cells: size matters, J. Nanobiotechnol. 12 (1) (2014) 1−11, https://doi.org/10.1186/1477-3155-12-5.
[74] P. Sabourian, G. Yazdani, S.S. Ashraf, M. Frounchi, S. Mashayekhan, S. Kiani, A. Kakkar, Effect of physico-chemical properties of nanoparticles on their intracellular uptake, Int. J. Mol. Sci. 21 (21) (2020) 8019, https://doi.org/10.3390/IJMS21218019.
[75] M.R. Gedda, P.K. Babele, K. Zahra, P. Madhukar, Epigenetic aspects of engineered nanomaterials: is the collateral damage inevitable? Front. Bioeng. Biotechnol. 0 (SEP) (2019) 228, https://doi.org/10.3389/FBIOE.2019.00228.
[76] P. Foroozandeh, A.A. Aziz, Insight into cellular uptake and intracellular trafficking of nanoparticles, Nanoscale Res. Lett. 13 (1) (2018) 1−12, https://doi.org/10.1186/S11671-018-2728-6.
[77] A. Sukhanova, S. Bozrova, P. Sokolov, M. Berestovoy, A. Karaulov, I. Nabiev, Dependence of nanoparticle toxicity on their physical and chemical properties, Nanoscale Res. Lett. 13 (1) (2018) 1−21, https://doi.org/10.1186/S11671-018-2457-X.

[78] A.R. Gliga, S. Skoglund, I. Odnevall Wallinder, B. Fadeel, H.L. Karlsson, Size-dependent cytotoxicity of silver nanoparticles in human lung cells: the role of cellular uptake, agglomeration and Ag release, Part. Fibre Toxicol. 11 (1) (2014) 1−17, https://doi.org/10.1186/1743-8977-11-11.
[79] T.-H. Kim, M. Kim, H.-S. Park, U.S. Shin, M.-S. Gong, H.-W. Kim, Size-dependent cellular toxicity of silver nanoparticles, J. Biomed. Mater. Res. 100 (2012) 1033−1043, https://doi.org/10.1002/jbm.a.34053.
[80] Y. Li, L. Sun, M. Jin, Z. Du, X. Liu, C. Guo, Y. Li, P. Huang, Z. Sun, Size-dependent cytotoxicity of amorphous silica nanoparticles in human hepatoma HepG2 cells, Toxicol. Vitro 25 (7) (2011) 1343−1352, https://doi.org/10.1016/J.TIV.2011.05.003.
[81] X. Wan, X. Zhang, W. Pan, B. Liu, L. Yu, H. Wang, N. Li, B. Tang, Ratiometric fluorescent quantification of the size-dependent cellular toxicity of silica nanoparticles, Anal. Chem. 91 (9) (2019) 6088−6096, https://doi.org/10.1021/ACS.ANALCHEM.9B00633.
[82] Y. Xie, D. Liu, C. Cai, X. Chen, Y. Zhou, L. Wu, Y. Sun, H. Dai, X. Kong, P. Liu, Size-dependent cytotoxicity of Fe3O4 nanoparticles induced by biphasic regulation of oxidative stress in different human hepatoma cells, Int. J. Nanomed. 11 (2016) 3557, https://doi.org/10.2147/IJN.S105575.
[83] F. Liao, L. Chen, Y. Liu, D. Zhao, W. Peng, W. Wang, S. Feng, The size-dependent genotoxic potentials of titanium dioxide nanoparticles to endothelial cells, Environ. Toxicol. 34 (11) (2019) 1199−1207, https://doi.org/10.1002/TOX.22821.
[84] F.M. Winnik, D. Maysinger, Quantum dot cytotoxicity and ways to reduce it, Acc. Chem. Res. 46 (3) (2012) 672−680, https://doi.org/10.1021/AR3000585.
[85] H.L. Karlsson, J. Gustafsson, P. Cronholm, L. Möller, Size-dependent toxicity of metal oxide particles—a comparison between nano- and micrometer size, Toxicol. Lett. 188 (2) (2009) 112−118, https://doi.org/10.1016/J.TOXLET.2009.03.014.
[86] L. Dong, S. Tang, F. Deng, Y. Gong, K. Zhao, J. Zhou, D. Liang, J. Fang, M. Hecker, J.P. Giesy, X. Bai, H. Zhang, Shape-dependent toxicity of alumina nanoparticles in rat astrocytes, Sci. Total Environ. 690 (2019) 158−166, https://doi.org/10.1016/J.SCITOTENV.2019.06.532.
[87] C.Y. Chen, C.T. Jafvert, The role of surface functionalization in the solar light-induced production of reactive oxygen species by single-walled carbon nanotubes in water, Carbon 49 (15) (2011) 5099−5106, https://doi.org/10.1016/J.CARBON.2011.07.029.
[88] N.M. Idris, S.S. Lucky, Z. Li, K. Huang, Y. Zhang, Photoactivation of core-shell titania coated upconversion nanoparticles and their effect on cell death, J. Mater. Chem. B 2 (40) (2014) 7017−7026, https://doi.org/10.1039/C4TB01169D.
[89] P. Sivakumar, M. Lee, Y.-S. Kim, M.S. Shim, Photo-triggered antibacterial and anticancer activities of zinc oxide nanoparticles, J. Mater. Chem. B 6 (30) (2018) 4852−4871, https://doi.org/10.1039/C8TB00948A.
[90] S. Xiong, S. George, Z. Ji, S. Lin, H. Yu, R. Damoiseaux, B. France, K.W. Ng, S.C.J. Loo, Size of TiO2 nanoparticles influences their phototoxicity: an in vitro investigation, Arch. Toxicol. 87 (1) (2013) 99−109, https://doi.org/10.1007/S00204-012-0912-5.
[91] M.D. Brand, A.L. Orr, I.V. Perevoshchikova, C.L. Quinlan, The role of mitochondrial function and cellular bioenergetics in aging and disease, Br. J. Dermatol. 169 (0 2) (2013) 1, https://doi.org/10.1111/BJD.12208.
[92] W. Kühlbrandt, Structure and function of mitochondrial membrane protein complexes, BMC Biol. 13 (1) (2015) 1−11, https://doi.org/10.1186/S12915-015-0201-X.
[93] P.J. Burke, Mitochondria, bioenergetics, and apoptosis in cancer, Trends Cancer 3 (12) (2017) 857−870, https://doi.org/10.1016/J.TRECAN.2017.10.006.
[94] R. Scherz-Shouval, Z. Elazar, ROS, mitochondria, and the regulation of autophagy, Trends Cell Biol. 17 (9) (2007) 422−427, https://doi.org/10.1016/J.TCB.2007.07.009.
[95] R. Canaparo, F. Foglietta, T. Limongi, L. Serpe, Biomedical applications of reactive oxygen species generation by metal nanoparticles, Materials 14 (1) (2021) 1−14, https://doi.org/10.3390/MA14010053.
[96] V. Freyre-Fonseca, N.L. Delgado-Buenrostro, E.B. Gutiérrez-Cirlos, C.M. Calderón-Torres, T. Cabellos-Avelar, Y. Sánchez-Pérez, E. Pinzón, I. Torres, E. Molina-Jijón, C. Zazueta, J. Pedraza-Chaverri,

C.M. García-Cuéllar, Y.I. Chirino, Titanium dioxide nanoparticles impair lung mitochondrial function, Toxicol. Lett. 202 (2) (2011) 111−119, https://doi.org/10.1016/J.TOXLET.2011.01.025.
[97] C. Wilson, V. Natarajan, S. Hayward, O. Khalimonchuk, S. Kidambi, Mitochondrial dysfunction and loss of glutamate uptake in primary astrocytes exposed to titanium dioxide nanoparticles, Nanoscale 7 (44) (2015) 18477−18488, https://doi.org/10.1039/C5NR03646A.
[98] C. Guo, J. Wang, L. Jing, R. Ma, X. Liu, L. Gao, L. Cao, J. Duan, X. Zhou, Y. Li, Z. Sun, Mitochondrial dysfunction, perturbations of mitochondrial dynamics, and biogenesis involved in endothelial injury induced by silica nanoparticles, Environ. Pollut. 236 (2018) 926−936, https://doi.org/10.1016/J.ENVPOL.2017.10.060.
[99] M. Chevallet, B. Gallet, A. Fuchs, H. Jouneau, K. Um, E. Mintz, I. Michaud-Soret, Metal homeostasis disruption and mitochondrial dysfunction in hepatocytes exposed to sub-toxic doses of zinc oxide nanoparticles, Nanoscale 8 (43) (2016) 18495−18506, https://doi.org/10.1039/C6NR05306H.
[100] R.J. Snyder, K.C. Verhein, H.L. Vellers, A.B. Burkholder, S. Garantziotis, S.R. Kleeberger, Multi-walled carbon nanotubes upregulate mitochondrial gene expression and trigger mitochondrial dysfunction in primary human bronchial epithelial cells, Nanotoxicology 13 (10) (2019) 1344−1361, https://doi.org/10.1080/17435390.2019.1655107.
[101] K.L. Singel, B.H. Segal, NOX2-dependent regulation of inflammation, Clin. Sci. (Lond.) 130 (7) (2016) 479, https://doi.org/10.1042/CS20150660.
[102] G.Y. Lam, J. Huang, J.H. Brumell, The many roles of NOX2 NADPH oxidase-derived ROS in immunity, Semin. Immunopathol. 32 (4) (2010) 415−430, https://doi.org/10.1007/S00281-010-0221-0.
[103] A. Panday, M.K. Sahoo, D. Osorio, S. Batra, NADPH oxidases: an overview from structure to innate immunity-associated pathologies, Cell. Mol. Immunol. 12 (1) (2015) 5, https://doi.org/10.1038/CMI.2014.89.
[104] P. Italiani, D. Boraschi, Induction of innate immune memory by engineered nanoparticles: a hypothesis that may become true, Front. Immunol. 0 (JUN) (2017) 734, https://doi.org/10.3389/FIMMU.2017.00734.
[105] R. Masoud, T. Bizouarn, S. Trepout, F. Wien, L. Baciou, S. Marco, C.H. Levin, Titanium dioxide nanoparticles increase superoxide anion production by acting on NADPH oxidase, PLoS One 10 (12) (2015) e0144829, https://doi.org/10.1371/JOURNAL.PONE.0144829.
[106] S. Ye, Y. Wang, F. Jiao, H. Zhang, C. Lin, Y. Wu, Q. Zhang, The role of NADPH oxidase in multi-walled carbon nanotubes-induced oxidative stress and cytotoxicity in human macrophages, J. Nanosci. Nanotechnol. 11 (5) (2011) 3773−3781, https://doi.org/10.1166/JNN.2011.3862.
[107] H.R. Petty, Could nanoparticles that mimic the NADPH oxidase be used to kill tumor cells? Nanomedicine 11 (13) (2016) https://doi.org/10.2217/NNM-2016-0193/ASSET/IMAGES/LARGE/FIGURE1.JPEG.
[108] A.J. Clark, E.L. Coury, A.M. Meilhac, H.R. Petty, WO 3/Pt nanoparticles are NADPH oxidase biomimetics that mimics effector cells in vitro and in vivo, Nanotechnology 57 (2015) 06501, https://doi.org/10.1088/0957-4484/27/6/065101.
[109] B. Szefler, Nanotechnology, from quantum mechanical calculations up to drug delivery, Int. J. Nanomed. 13 (2018) 6143−6176, https://doi.org/10.2147/IJN.S172907.
[110] S. Collavini, J.L. Delgado, Fullerenes: the stars of photovoltaics, Sustain. Energy Fuels 2 (11) (2018) 2480−2493, https://doi.org/10.1039/C8SE00254A.
[111] F. Wang, C. Jin, H. Liang, Y. Tang, H. Zhang, Y. Yang, Effects of fullerene C60 nanoparticles on A549 cells, Environ. Toxicol. Pharmacol. 37 (2) (2014) 656−661, https://doi.org/10.1016/J.ETAP.2014.01.015.
[112] M. Horie, K. Nishio, H. Kato, N. Shinohara, A. Nakamura, K. Fujita, S. Kinugasa, S. Endoh, Y. Yoshida, Y. Hagihara, H. Iwahashi, In vitro evaluation of cellular influences induced by stable fullerene C70 medium dispersion: induction of cellular oxidative stress, Chemosphere 93 (6) (2013) 1182−1188, https://doi.org/10.1016/J.CHEMOSPHERE.2013.06.067.
[113] G.F. Schirinzi, I. Pérez-Pomeda, J. Sanchís, C. Rossini, M. Farré, D. Barceló, Cytotoxic effects of commonly used nanomaterials and microplastics on cerebral and epithelial human cells, Environ. Res. 159 (2017) 579−587, https://doi.org/10.1016/J.ENVRES.2017.08.043.

[114] Y. Nakagawa, T. Suzuki, H. Ishii, D. Nakae, A. Ogata, Cytotoxic effects of hydroxylated fullerenes on isolated rat hepatocytes via mitochondrial dysfunction, Arch. Toxicol. 85 (11) (2011) 1429—1440, https://doi.org/10.1007/S00204-011-0688-Z.

[115] E.S. Ershova, V.A. Sergeeva, A.I. Chausheva, D.G. Zheglo, V.A. Nikitina, T.D. Smirnova, L.V. Kameneva, L.N. Porokhovnik, S.I. Kutsev, P.A. Troshin, I.I. Voronov, E.A. Khakina, N.N. Veiko, S.V. Kostyuk, Toxic and DNA damaging effects of a functionalized fullerene in human embryonic lung fibroblasts, Mutat. Res. Genet. Toxicol. Environ. Mutagen 805 (2016) 46—57, https://doi.org/10.1016/J.MRGENTOX.2016.05.004.

[116] H.J. Johnston, G.R. Hutchison, F.M. Christensen, K. Aschberger, V. Stone, The biological mechanisms and physicochemical characteristics responsible for driving fullerene toxicity, Toxicol. Sci. 114 (2) (2010) 162—182, https://doi.org/10.1093/TOXSCI/KFP265.

[117] E. Oberdörster, Manufactured nanomaterials (fullerenes, C60) induce oxidative stress in the brain of juvenile largemouth bass, Environ. Health Perspect. 112 (10) (2004) 1058—1062, https://doi.org/10.1289/EHP.7021.

[118] C.Y. Usenko, S.L. Harper, R.L. Tanguay, Fullerene C60 exposure elicits an oxidative stress response in embryonic zebrafish, Toxicol. Appl. Pharmacol. 229 (1) (2008) 44—55, https://doi.org/10.1016/J.TAAP.2007.12.030.

[119] E.J. Park, H. Kim, Y. Kim, J. Yi, K. Choi, K. Park, Carbon fullerenes (C60s) can induce inflammatory responses in the lung of mice, Toxicol. Appl. Pharmacol. 244 (2) (2010) 226—233, https://doi.org/10.1016/J.TAAP.2009.12.036.

[120] F. Jiao, Y. Qu, G. Zhou, Y. Liu, W. Li, C. Ge, Y. Li, W. Hu, B. Li, Y. Gao, C. Chen, Modulation of oxidative stress by functionalized fullerene materials in the lung tissues of female C57/BL mice with a metastatic Lewis lung carcinoma, J. Nanosci. Nanotechnol. 10 (12) (2010) 8632—8637, https://doi.org/10.1166/JNN.2010.2489.

[121] O.O. Gonchar, A.V. Maznychenko, N.V. Bulgakova, I.V. Vereshchaka, T. Tomiak, U. Ritter, Y.I. Prylutskyy, I.M. Mankovska, A.I. Kostyukov, C 60 fullerene prevents restraint stress-induced oxidative disorders in rat tissues: possible involvement of the Nrf2/ARE-antioxidant pathway, Oxid. Med. Cell. Longev. 2018 (2018), https://doi.org/10.1155/2018/2518676.

[122] J.R. Vani, M.T. Mohammadi, M.S. Foroshani, M. Jafari, Polyhydroxylated fullerene nanoparticles attenuate brain infarction and oxidative stress in a rat model of ischemic stroke, EXCLI J. 15 (2016) 378, https://doi.org/10.17179/EXCLI2016-309.

[123] T. Halenova, N. Raksha, T. Vovk, O. Savchuk, L. Ostapchenko, Y. Prylutskyy, O. Kyzyma, U. Ritter, P. Scharff, Effect of C60 fullerene nanoparticles on diet-induced obesity in rats, Int. J. Obes. 42 (12) (2018) 1987—1998, https://doi.org/10.1038/s41366-018-0016-2.

[124] A.P. Francis, T. Devasena, Toxicity of carbon nanotubes: a review, Toxicol. Ind. Health 34 (3) (2018) 200—210, https://doi.org/10.1177/0748233717747472.

[125] M. Hussain, P. Khalid, M.A. Hussain, V.B. Suman, A.B. Arun, Toxicology of carbon nanotubes-A review, Int. J. Appl. Eng. Res. 11 (1) (2016) 159—168. http://www.ripublication.com.

[126] W.-W. Cheng, Z.-Q. Lin, Q. Ceng, B.-F. Wei, X.-J. Fan, H.-S. Zhang, W. Zhang, H.-L. Yang, H.-L. Liu, J. Yan, L. Tian, B.-C. Lin, S.-M. Ding, Z.-G. Xi, Single-wall carbon nanotubes induce oxidative stress in rat aortic endothelial cells, Toxicol. Mech. Methods 22 (4) (2012) 268—276, https://doi.org/10.3109/15376516.2011.647112.

[127] X. He, S.-H. Young, J.E. Fernback, Q. Ma, Single-walled carbon nanotubes induce fibrogenic effect by disturbing mitochondrial oxidative stress and activating NF-κB signaling, J. Clin. Toxicol. (2012), https://doi.org/10.4172/2161-0495.S5-005. Suppl 5(01).

[128] Y. Rodríguez-Yáñez, D. Bahena-Uribe, B. Chávez-Munguía, R. López-Marure, S. González-Monroy, B. Cisneros, A. Albores, Commercial single-walled carbon nanotubes effects in fibrinolysis of human umbilical vein endothelial cells, Toxicol. Vitro 29 (5) (2015) 1201—1214, https://doi.org/10.1016/J.TIV.2015.02.009.

[129] A. Ahangarpour, S. Alboghobeish, A. Oroojan, M. Dehghani, Mice pancreatic islets protection from oxidative stress induced by single-walled carbon nanotubes through naringin, Hum. Exp. Toxicol. 37 (12) (2018) 1268−1281, https://doi.org/10.1177/0960327118769704.
[130] S. Luanpitpong, L. Wang, Y. Rojanasakul, The effects of carbon nanotubes on lung and dermal cellular behaviors, Nanomedicine 9 (6) (2014) 895, https://doi.org/10.2217/NNM.14.42.
[131] K. ichiro Inoue, R. Yanagisawa, E. Koike, M. Nishikawa, H. Takano, Repeated pulmonary exposure to single-walled carbon nanotubes exacerbates allergic inflammation of the airway: possible role of oxidative stress, Free Radic. Biol. Med. 48 (7) (2010) 924−934, https://doi.org/10.1016/J.FREERADBIOMED.2010.01.013.
[132] A.R. Murray, E. Kisin, S.S. Leonard, S.H. Young, C. Kommineni, V.E. Kagan, V. Castranova, A.A. Shvedova, Oxidative stress and inflammatory response in dermal toxicity of single-walled carbon nanotubes, Toxicology 257 (3) (2009) 161−171, https://doi.org/10.1016/J.TOX.2008.12.023.
[133] X. Liu, Y. Zhang, J. Li, D. Wang, Y. Wu, Y. Li, Z. Lu, S.C. Yu, R. Li, X. Yang, Cognitive deficits and decreased locomotor activity induced by single-walled carbon nanotubes and neuroprotective effects of ascorbic acid, Int. J. Nanomed. 9 (1) (2014) 823, https://doi.org/10.2147/IJN.S56339.
[134] R.K. Srivastava, A.B. Pant, M.P. Kashyap, V. Kumar, M. Lohani, L. Jonas, Q. Rahman, Multi-walled carbon nanotubes induce oxidative stress and apoptosis in human lung cancer cell line-A549, Nanotoxicology 5 (2) (2011) 195−207, https://doi.org/10.3109/17435390.2010.503944.
[135] B. Chen, Y. Liu, W.M. Song, Y. Hayashi, X.C. Ding, W.H. Li, In vitro evaluation of cytotoxicity and oxidative stress induced by multiwalled carbon nanotubes in murine RAW 264.7 macrophages and human A549 lung cells, Biomed. Environ. Sci. 24 (6) (2011) 593−601, https://doi.org/10.3967/0895-3988.2011.06.002.
[136] S. Alarifi, D. Ali, Mechanisms of multi-walled carbon nanotubes−induced oxidative stress and genotoxicity in mouse fibroblast cells, Int. J. Toxicol. 34 (3) (2015) 258−265, https://doi.org/10.1177/1091581815584799.
[137] J.H. Lucas, Q. Wang, T. Muthumalage, I. Rahman, Multi-walled carbon nanotubes (MWCNTs) cause cellular senescence in TGF-β stimulated lung epithelial cells, Toxics 9 (6) (2021) 144, https://doi.org/10.3390/TOXICS9060144.
[138] T. Kato, Y. Totsuka, K. Ishino, Y. Matsumoto, Y. Tada, D. Nakae, S. Goto, S. Masuda, S. Ogo, M. Kawanishi, T. Yagi, T. Matsuda, M. Watanabe, K. Wakabayashi, Genotoxicity of multi-walled carbon nanotubes in both in vitro and in vivo assay systems, Nanotoxicology 7 (4) (2012) 452−461, https://doi.org/10.3109/17435390.2012.674571.
[139] R. Saria, F. Mouchet, A. Perrault, E. Flahaut, C. Laplanche, J.C. Boutonnet, E. Pinelli, L. Gauthier, Short-term exposure to multi-walled carbon nanotubes induces oxidative stress and DNA damage in *Xenopus laevis* tadpoles, Ecotoxicol. Environ. Saf. 107 (2014) 22−29, https://doi.org/10.1016/J.ECOENV.2014.05.010.
[140] S. Clichici, A.R. Biris, F. Tabaran, A. Filip, Transient oxidative stress and inflammation after intraperitoneal administration of multiwalled carbon nanotubes functionalized with single-strand DNA in rats, Toxicol. Appl. Pharmacol. 259 (3) (2012) 281−292, https://doi.org/10.1016/J.TAAP.2012.01.004.
[141] A.K. Patlolla, D. Hackett, P.B. Tchounwou, Genotoxicity study of silver nanoparticles in bone marrow cells of Sprague-Dawley rats, Food Chem. Toxicol. 85 (2015) 52−60, https://doi.org/10.1016/j.fct.2015.05.005.
[142] L. Migliore, D. Saracino, A. Bonelli, R. Colognato, M.R. D'Errico, A. Magrini, A. Bergamaschi, E. Bergamaschi, Carbon nanotubes induce oxidative DNA damage in RAW 264.7 cells, Environ. Mol. Mutagen. 51 (4) (2010) 294−303, https://doi.org/10.1002/EM.20545.
[143] T.O. Khaliullin, L.M. Fatkhutdinova, R.R. Zalyalov, E.R. Kisin, A.R. Murray, A.A. Shvedova, In vitro toxic effects of different types of carbon nanotubes, IOP Conf. Ser. Mater. Sci. Eng. 98 (1) (2015) 012021, https://doi.org/10.1088/1757-899X/98/1/012021.

[144] F. Ghanbari, P. Nasarzadeh, E. Seydi, A. Ghasemi, M.T. Joghataei, K. Ashtari, M. Akbari, Mitochondrial oxidative stress and dysfunction induced by single- and multiwall carbon nanotubes: a comparative study, J. Biomed. Mater. Res. 105 (7) (2017) 2047–2055, https://doi.org/10.1002/JBM.A.36063.
[145] W. Liu, G. Speranza, Functionalization of carbon nanomaterials for biomedical applications, C 5 (4) (2019) 72, https://doi.org/10.3390/C5040072.
[146] K. Kyriakidou, D. Brasinika, A.F.A. Trompeta, E. Bergamaschi, I.K. Karoussis, C.A. Charitidis, In vitro cytotoxicity assessment of pristine and carboxyl-functionalized MWCNTs, Food Chem. Toxicol. 141 (2020), https://doi.org/10.1016/j.fct.2020.111374.
[147] Z. Shen, J. Wu, Y. Yu, S. Liu, W. Jiang, H. Nurmamat, B. Wu, Comparison of cytotoxicity and membrane efflux pump inhibition in HepG2 cells induced by single-walled carbon nanotubes with different length and functional groups, Sci. Rep. 9 (1) (2019) 1–9, https://doi.org/10.1038/s41598-019-43900-5.
[148] Y. Sun, J. Gong, Y. Cao, Multi-walled carbon nanotubes (MWCNTs) activate apoptotic pathway through ER stress: does surface chemistry matter? Int. J. Nanomed. 14 (2019) 9285, https://doi.org/10.2147/IJN.S217977.
[149] O. Sabido, A. Figarol, J.-P. Klein, V. Bin, V. Forest, J. Pourchez, B. Fubini, M. Cottier, M. Tomatis, D. Boudard, Quantitative flow cytometric evaluation of oxidative stress and mitochondrial impairment in RAW 264.7 macrophages after exposure to pristine, acid functionalized, or annealed carbon nanotubes, Nanomaterials 10 (2) (2020) 319, https://doi.org/10.3390/NANO10020319.
[150] M. Ashraf, I. Khan, M. Usman, A. Khan, S.S. Shah, A.Z. Khan, K. Saeed, M. Yaseen, M.F. Ehsan, M.N. Tahir, N. Ullah, Hematite and magnetite nanostructures for green and sustainable energy harnessing and environmental pollution control: a review, Chem. Res. Toxicol. 33 (6) (2019) 1292–1311, https://doi.org/10.1021/ACS.CHEMRESTOX.9B00308.
[151] Du Hongbo, F. Deng, R.R. Kommalapati, A.S. Amarasekara, Iron-based catalysts in biomass processing, Renew. Sustain. Energy Rev. 134 (2020) 110292, https://doi.org/10.1016/J.RSER.2020.110292.
[152] M. Srivastava, N. Srivastava, M. Saeed, P.K. Mishra, A. Saeed, V.K. Gupta, B.D. Malhotra, Bioinspired synthesis of iron-based nanomaterials for application in biofuels production: a new insight, Renew. Sustain. Energy Rev. 147 (2021) 111206, https://doi.org/10.1016/J.RSER.2021.111206.
[153] Y. Fang, Z. Chen, L. Xiao, X. Ai, Y. Cao, H. Yang, Recent progress in iron-based electrode materials for grid-scale sodium-ion batteries, Small 14 (9) (2018) 1703116, https://doi.org/10.1002/SMLL.201703116.
[154] D.M. Valvo, D.A. Liivat, D.H. Eriksson, D.C. Tai, P.K. Edström, Iron-based electrodes meet water-based preparation, fluorine-free electrolyte, and binder: a chance for more sustainable lithium-ion batteries? ChemSusChem 10 (11) (2017) 2431, https://doi.org/10.1002/CSSC.201700070.
[155] P. Saurabh Bassi, L.H. Gurudayal, L. Helena Wong, J. Barber, Iron-based photoanodes for solar fuel production, Phys. Chem. Chem. Phys. 16 (24) (2014) 11834–11842, https://doi.org/10.1039/C3CP55174A.
[156] J. Paunovic, D. Vucevic, T. Radosavljevic, S. Mandić-Rajčević, I. Pantic, Iron-based nanoparticles and their potential toxicity: focus on oxidative stress and apoptosis, Chem. Biol. Interact. 316 (2020), https://doi.org/10.1016/J.CBI.2019.108935.
[157] M.T. Zhu, Y. Wang, W.Y. Feng, B. Wang, M. Wang, H. Ouyang, Z.F. Chai, Oxidative stress and apoptosis induced by iron oxide nanoparticles in cultured human umbilical endothelial cells, J. Nanosci. Nanotechnol. 10 (12) (2010) 8584–8590, https://doi.org/10.1166/JNN.2010.2488.
[158] S. Alarifi, D. Ali, S. Alkahtani, M.S. Alhader, Iron oxide nanoparticles induce oxidative stress, DNA damage, and caspase activation in the human breast cancer cell line, Biol. Trace Elem. Res. 159 (1) (2014) 416–424, https://doi.org/10.1007/S12011-014-9972-0.
[159] U.S. Gaharwar, R. Meena, P. Rajamani, Iron oxide nanoparticles induced cytotoxicity, oxidative stress, and DNA damage in lymphocytes, J. Appl. Toxicol. 37 (10) (2017) 1232–1244, https://doi.org/10.1002/JAT.3485.

[160] A. M, A. HA, A. J, K. MA, A. D, A. S, Iron oxide nanoparticle-induced oxidative stress and genotoxicity in human skin epithelial and lung epithelial cell lines, Curr. Pharmaceut. Des. 19 (37) (2013) 6681−6690, https://doi.org/10.2174/1381612811319370011.
[161] S. Naqvi, M. Samim, M. Abdin, F.J. Ahmed, A. Maitra, C. Prashant, A.K. Dinda, Concentration-dependent toxicity of iron oxide nanoparticles mediated by increased oxidative stress, Int. J. Nanomed. 5 (1) (2010) 983, https://doi.org/10.2147/IJN.S13244.
[162] R. Vakili-Ghartavol, A.A. Momtazi-Borojeni, Z. Vakili-Ghartavol, H.T. Aiyelabegan, M.R. Jaafari, S.M. Rezayat, S.A. Bidgoli, Toxicity assessment of superparamagnetic iron oxide nanoparticles in different tissues, Artif. Cells Nanomed. Biotechnol. 48 (1) (2020) 443−451, https://doi.org/10.1080/21691401.2019.1709855.
[163] A. Nemmar, S. Beegam, P. Yuvaraju, J. Yasin, S. Tariq, S. Attoub, B.H. Ali, Ultrasmall superparamagnetic iron oxide nanoparticles acutely promote thrombosis and cardiac oxidative stress, and DNA damage in mice, Part. Fibre Toxicol. 13 (1) (2016) 1−11, https://doi.org/10.1186/S12989-016-0132-X.
[164] J. Wu, T. Ding, J. Sun, The neurotoxic potential of iron oxide nanoparticles in the rat brain striatum and hippocampus, Neurotoxicology 34 (1) (2013) 243−253, https://doi.org/10.1016/J.NEURO.2012.09.006.
[165] A. Srinivas, P.J. Rao, G. Selvam, A. Goparaju, B.P. Murthy, N.P. Reddy, Oxidative stress and inflammatory responses of the rat following acute inhalation exposure to iron oxide nanoparticles, Hum. Exp. Toxicol. 31 (11) (2012) 1113−1131, https://doi.org/10.1177/0960327112446515.
[166] M. Notarianni, K. Vernon, A. Chou, M. Aljada, J. Liu, N. Motta, Plasmonic effect of gold nanoparticles in organic solar cells, Sol. Energy 106 (2014) 23−37, https://doi.org/10.1016/J.SOLENER.2013.09.026.
[167] C.C.D. Wang, W.C.H. Choy, C. Duan, D.D.S. Fung, W.E.I. Sha, F.-X. Xie, F. Huang, Y. Cao, Optical and electrical effects of gold nanoparticles in the active layer of polymer solar cells, J. Mater. Chem. 22 (3) (2011) 1206−1211, https://doi.org/10.1039/C1JM14150C.
[168] S. Shaikh, N. Nazam, S.M.D. Rizvi, K. Ahmad, M.H. Baig, E.J. Lee, I. Choi, Mechanistic insights into the antimicrobial actions of metallic nanoparticles and their implications for multidrug resistance, Int. J. Mol. Sci. 20 (10) (2019) 2468, https://doi.org/10.3390/IJMS20102468.
[169] Y.P. Jia, B.Y. Ma, X.W. Wei, Z.Y. Qian, The in vitro and in vivo toxicity of gold nanoparticles, Chin. Chem. Lett. 28 (4) (2017) 691−702, https://doi.org/10.1016/J.CCLET.2017.01.021.
[170] C. Lopez-Chaves, J. Soto-Alvaredo, M. Montes-Bayon, J. Bettmer, J. Llopis, C. Sanchez-Gonzalez, Gold nanoparticles: distribution, bioaccumulation, and toxicity. In vitro and in vivo studies, Nanomed. Nanotechnol. Biol. Med. 14 (1) (2018) 1−12, https://doi.org/10.1016/J.NANO.2017.08.011.
[171] J.J. Li, D. Hartono, C.N. Ong, B.H. Bay, L.Y.L. Yung, Autophagy and oxidative stress associated with gold nanoparticles, Biomaterials 31 (23) (2010) 5996−6003, https://doi.org/10.1016/j.biomaterials.2010.04.014.
[172] M. Enea, E. Pereira, M. P. de Almeida, A.M. Araújo, M. de L. Bastos, H. Carmo, Gold nanoparticles induce oxidative stress and apoptosis in human kidney cells, Nanomaterials 10 (5) (2020) 995, https://doi.org/10.3390/NANO10050995.
[173] Q. Xia, H. Li, Y. Liu, S. Zhang, Q. Feng, K. Xiao, The effect of particle size on the genotoxicity of gold nanoparticles, J. Biomed. Mater. Res. 105 (3) (2017) 710−719, https://doi.org/10.1002/JBM.A.35944.
[174] S. Tedesco, H. Doyle, J. Blasco, G. Redmond, D. Sheehan, Oxidative stress and toxicity of gold nanoparticles in *Mytilus edulis*, Aquat. Toxicol. 100 (2) (2010) 178−186, https://doi.org/10.1016/J.AQUATOX.2010.03.001.
[175] R. Shrivastava, P. Kushwaha, Y.C. Bhutia, S. Flora, Oxidative stress following exposure to silver and gold nanoparticles in mice, Toxicol. Ind. Health 32 (8) (2014) 1391−1404, https://doi.org/10.1177/0748233714562623.
[176] N.J. Siddiqi, M.A.K. Abdelhalim, A.K. El-Ansary, A.S. Alhomida, W.Y. Ong, Identification of potential biomarkers of gold nanoparticle toxicity in rat brains, J. Neuroinflammation 9 (1) (2012) 1−7, https://doi.org/10.1186/1742-2094-9-123.

[177] H. Tian, J. Liang, J. Liu, Nanoengineering carbon spheres as nanoreactors for sustainable energy applications, Adv. Mater. 31 (50) (2019) 1903886, https://doi.org/10.1002/ADMA.201903886.
[178] M.J. Carnie, C. Charbonneau, M.L. Davies, B.O. Regan, D.A. Worsley, T.M. Watson, Performance enhancement of solution-processed perovskite solar cells are incorporating functionalized silica nanoparticles, J. Mater. Chem. 2 (40) (2014) 17077−17084, https://doi.org/10.1039/C4TA03387F.
[179] N. Zou, X. Lin, M. Li, L. Li, C. Ye, J. Chen, T. Qiu, Ionic Liquid@Amphiphilic silica nanoparticles: novel catalysts for converting waste cooking oil to biodiesel, ACS Sustain. Chem. Eng. 8 (49) (2020) 18054−18061, https://doi.org/10.1021/ACSSUSCHEMENG.0C06139.
[180] Y. Yang, M. Zhang, H. Song, C. Yu, Silica-based nanoparticles for biomedical applications: from nanocarriers to biomodulators, Acc. Chem. Res. 53 (8) (2020) 1545−1556, https://doi.org/10.1021/ACS.ACCOUNTS.0C00280.
[181] Y. Ye, J. Liu, M. Chen, L. Sun, M. Lan, In vitro toxicity of silica nanoparticles in myocardial cells, Environ. Toxicol. Pharmacol. 29 (2) (2010) 131−137, https://doi.org/10.1016/J.ETAP.2009.12.002.
[182] C. Guo, Y. Xia, P. Niu, L. Jiang, J. Duan, Y. Yu, X. Zhou, Y. Li, Z. Sun, Silica nanoparticles induce oxidative stress, inflammation, and endothelial dysfunction in vitro via activation of the MAPK/Nrf2 pathway and nuclear factor-κB signaling, Int. J. Nanomed. 10 (2015) 1463, https://doi.org/10.2147/IJN.S76114.
[183] A. Mendoza, J.A. Torres-Hernandez, J.G. Ault, J.H. Pedersen-Lane, D. Gao, D.A. Lawrence, Silica nanoparticles induce oxidative stress and inflammation of human peripheral blood mononuclear cells, Cell Stress Chaperones 19 (6) (2014) 777−790, https://doi.org/10.1007/S12192-014-0502-Y.
[184] X. Lu, J. Qian, H. Zhou, Q. Gan, W. Tang, J. Lu, Y. Yuan, C. Liu, In vitro cytotoxicity and induction of apoptosis by silica nanoparticles in human HepG2 hepatoma cells, Int. J. Nanomed. 6 (2011) 1889, https://doi.org/10.2147/IJN.S24005.
[185] S.N.P. Voicu, D. Dinu, C. Sima, A. Hermenean, A. Ardelean, E. Codrici, M.S. Stan, O. Zărnescu, A. Dinischiotu, Silica nanoparticles induce oxidative stress and autophagy but not apoptosis in the MRC-5 cell line, Int. J. Mol. Sci. 16 (12) (2015) 29398−29416, https://doi.org/10.3390/IJMS161226171.
[186] A. Nemmar, P. Yuvaraju, S. Beegam, J. Yasin, E.E. Kazzam, B.H. Ali, Oxidative stress, inflammation, and DNA damage in multiple organs of mice acutely exposed to amorphous silica nanoparticles, Int. J. Nanomed. 11 (2016) 919, https://doi.org/10.2147/IJN.S92278.
[187] R.A. Azouz, R.M.S. Korany, Toxic impacts of amorphous silica nanoparticles on liver and kidney of male adult rats: an in vivo study, Biol. Trace Elem. Res. 199 (7) (2020) 2653−2662, https://doi.org/10.1007/S12011-020-02386-3.
[188] W.G. Hozayen, A.M. Mahmoud, E.M. Desouky, E.S. El-Nahass, H.A. Soliman, A.A. Farghali, Cardiac and pulmonary toxicity of mesoporous silica nanoparticles is associated with excessive ROS production and redox imbalance in Wistar rats, Biomed. Pharmacother. 109 (2019) 2527−2538, https://doi.org/10.1016/J.BIOPHA.2018.11.093.
[189] Ş. Sungur, Titanium dioxide nanoparticles, in: Handbook of Nanomaterials and Nanocomposites for Energy and Environmental Applications, 1−18, 2020, https://doi.org/10.1007/978-3-030-11155-7_9-1.
[190] Y. Mei, Y. Huang, X. Hu, Nanostructured Ti-based anode materials for Na-ion batteries, J. Mater. Chem. 4 (31) (2016) 12001−12013, https://doi.org/10.1039/C6TA04611H.
[191] Y.E. Putri, S.M. Said, M. Diantoro, Nanoarchitectured titanium complexes for thermal mitigation in thermoelectric materials, Renew. Sustain. Energy Rev. 101 (2019) 346−360, https://doi.org/10.1016/J.RSER.2018.10.006.
[192] Z. Su, J. Liu, M. Li, Y. Zhu, S. Qian, M. Weng, J. Zheng, Y. Zhong, F. Pan, S. Zhang, Defect engineering in titanium-based oxides for electrochemical energy storage devices, Electrochem. Energy Rev. 3 (2) (2020) 286−343, https://doi.org/10.1007/S41918-020-00064-5.
[193] R. Krishnapriya, C. Nizamudeen, B. Saini, M.S. Mozumder, R.K. Sharma, A.-H.I. Mourad, MOF-derived Co2+-doped TiO2 nanoparticles as photoanodes for dye-sensitized solar cells, Sci. Rep. 11 (1) (2021) 1−12, https://doi.org/10.1038/s41598-021-95844-4.

[194] M.A. Irshad, R. Nawaz, M.Z.U. Rehman, M. Adrees, M. Rizwan, S. Ali, S. Ahmad, S. Tasleem, Synthesis, characterization and advanced sustainable applications of titanium dioxide nanoparticles: a review, Ecotoxicol. Environ. Saf. 212 (2021) 111978, https://doi.org/10.1016/J.ECOENV.2021.111978.
[195] D. Ziental, B. Czarczynska-Goslinska, D.T. Mlynarczyk, A. Glowacka-Sobotta, B. Stanisz, T. Goslinski, L. Sobotta, Titanium dioxide nanoparticles: prospects and applications in medicine, Nanomaterials 10 (2) (2020), https://doi.org/10.3390/NANO10020387.
[196] E. Baranowska-Wójcik, D. Szwajgier, P. Oleszczuk, A. Winiarska-Mieczan, Effects of titanium dioxide nanoparticles exposure on human health—a review, Biol. Trace Elem. Res. 193 (1) (2019) 118−129, https://doi.org/10.1007/S12011-019-01706-6.
[197] D. Zhou, S. Han, T. Yan, C. Long, J. Xu, P. Zheng, Z. Chen, G. Jia, Toxicity of titanium dioxide nanoparticles induced by reactive oxygen species, ROS 8 (23) (2019) 267−275. https://rosj.org/index.php/ros/article/view/243.
[198] E.J. Park, J. Yi, K.H. Chung, D.Y. Ryu, J. Choi, K. Park, Oxidative stress and apoptosis induced by titanium dioxide nanoparticles in cultured BEAS-2B cells, Toxicol. Lett. 180 (3) (2008) 222−229, https://doi.org/10.1016/J.TOXLET.2008.06.869.
[199] S.A. Ferraro, M.G. Domingo, A. Etcheverrito, D.G. Olmedo, D.R. Tasat, Neurotoxicity mediated by oxidative stress caused by titanium dioxide nanoparticles in human neuroblastoma (SH-SY5Y) cells, J. Trace Elem. Med. Biol. 57 (2020) 126413, https://doi.org/10.1016/J.JTEMB.2019.126413.
[200] E. Gutiérrez Iglesias, J.A. Pérez-Arizti, S.G. Márquez-Ramírez, N.L. Delgado-Buenrostro, Y.I. Chirino, G.G. Iglesias, R. López-Marure, Titanium dioxide nanoparticles induce strong oxidative stress and mitochondrial damage in glial cells, Free Radic. Biol. Med. 73 (2014) 84−94, https://doi.org/10.1016/J.FREERADBIOMED.2014.04.026.
[201] M. Santonastaso, F. Mottola, N. Colacurci, C. Iovine, S. Pacifico, M. Cammarota, F. Cesaroni, L. Rocco, In vitro genotoxic effects of titanium dioxide nanoparticles (n-TiO2) in human sperm cells, Mol. Reprod. Dev. 86 (10) (2019) 1369−1377, https://doi.org/10.1002/MRD.23134.
[202] E. Huerta-García, I. Zepeda-Quiroz, H. Sánchez-Barrera, Z. Colín-Val, E. Alfaro-Moreno, M.D.P. Ramos-Godinez, R. López-Marure, Internalization of titanium dioxide nanoparticles is cytotoxic for H9c2 rat cardiomyoblasts, Molecules 23 (8) (2018) 1955, https://doi.org/10.3390/MOLECULES23081955.
[203] R.K. Shukla, A. Kumar, N.V.S. Vallabani, A.K. Pandey, A. Dhawan, Titanium dioxide nanoparticle-induced oxidative stress triggers DNA damage and hepatic injury in mice, Nanomedicine 9 (9) (2014) 1423−1434, https://doi.org/10.2217/NNM.13.100.
[204] C. Zhangjian, S. Han, D. Zhou, S. Zhou, G. Jia, Effects of oral exposure to titanium dioxide nanoparticles on gut microbiota and gut-associated metabolism in vivo, Nanoscale 11 (46) (2019) 22398−22412, https://doi.org/10.1039/C9NR07580A.
[205] M. Afshari-Kaveh, R. Abbasalipourkabir, A. Nourian, N. Ziamajidi, The protective effects of vitamins A and E on titanium dioxide nanoparticles (nTiO2)-Induced oxidative stress in the spleen tissues of male wistar rats, Biol. Trace Elem. Res. 199 (10) (2020) 3677−3687, https://doi.org/10.1007/S12011-020-02487-Z.
[206] Q. Sun, D. Tan, Y. Ze, X. Sang, X. Liu, S. Gui, Z. Cheng, J. Cheng, R. Hu, G. Gao, G. Liu, M. Zhu, X. Zhao, L. Sheng, L. Wang, M. Tang, F. Hong, Pulmotoxicological effects caused by long-term titanium dioxide nanoparticles exposure in mice, J. Hazard Mater. 235−236 (2012) 47−53, https://doi.org/10.1016/J.JHAZMAT.2012.05.072.
[207] I.B. Laskar, L. Rokhum, R. Gupta, S. Chatterjee, Zinc oxide supported silver nanoparticles as a heterogeneous catalyst for the production of biodiesel from palm oil, Environ. Prog. Sustain. Energy 39 (3) (2020) e13369, https://doi.org/10.1002/EP.13369.
[208] M.S. Yadav, N. Singh, A. Kumar, Synthesis and characterization of zinc oxide nanoparticles and activated charcoal-based nanocomposite for supercapacitor electrode application, J. Mater. Sci. Mater. Electron. 29 (8) (2018) 6853−6869, https://doi.org/10.1007/S10854-018-8672-5.

[209] J.W. Zhang, G.A. Xue, T.P. Yao, C.Y. Hu, P. Huang, Enhanced electron evacuation performance of zinc oxide nanocomposites for sustainable energy storage technology, J. Clean. Prod. 216 (2019) 167−171, https://doi.org/10.1016/J.JCLEPRO.2019.01.005.

[210] M.M. Ghafurian, F.T. Dastjerd, A. Afsharian, F.R. Esfahani, H. Niazmand, H. Behzadnia, S. Wongwises, O. Mahian, Low-cost zinc-oxide nanoparticles for solar-powered steam production: superficial and volumetric approaches, J. Clean. Prod. 280 (2021) 124261, https://doi.org/10.1016/J.JCLEPRO.2020.124261.

[211] M. Pandurangan, D.H. Kim, In vitro toxicity of zinc oxide nanoparticles: a review, J. Nanoparticle Res. 17 (3) (2015) 1−8, https://doi.org/10.1007/S11051-015-2958-9.

[212] S. Singh, Zinc oxide nanoparticles impacts: cytotoxicity, genotoxicity, developmental toxicity, and neurotoxicity, Toxicol. Mech. Methods 29 (4) (2019) 300−311, https://doi.org/10.1080/15376516.2018.1553221.

[213] C.T. Ng, L.Q. Yong, M.P. Hande, C.N. Ong, L.E. Yu, B.H. Bay, G.H. Baeg, Zinc oxide nanoparticles exhibit cytotoxicity and genotoxicity through oxidative stress responses in human lung fibroblasts and *Drosophila melanogaster*, Int. J. Nanomed. 12 (2017) 1621, https://doi.org/10.2147/IJN.S124403.

[214] Y. Song, R. Guan, F. Lyu, T. Kang, Y. Wu, X. Chen, In vitro cytotoxicity of silver nanoparticles and zinc oxide nanoparticles to human epithelial colorectal adenocarcinoma (Caco-2) cells, Mutat. Res. Fund Mol. Mech. Mutagen 769 (2014) 113−118, https://doi.org/10.1016/J.MRFMMM.2014.08.001.

[215] H. Lee, K. Park, In vitro cytotoxicity of zinc oxide nanoparticles in cultured statens seruminstitut rabbit cornea cells, Toxicol. Rese. 35 (3) (2019) 287−294, https://doi.org/10.5487/TR.2019.35.3.287.

[216] B. Annangi, L. Rubio, M. Alaraby, J. Bach, R. Marcos, A. Hernández, Acute and long-term in vitro effects of zinc oxide nanoparticles, Arch. Toxicol. 90 (9) (2015) 2201−2213, https://doi.org/10.1007/S00204-015-1613-7.

[217] S. Keerthana, A. Kumar, Potential risks and benefits of zinc oxide nanoparticles: a systematic review, Crit. Rev. Toxicol. 50 (1) (2020) 47−71, https://doi.org/10.1080/10408444.2020.1726282.

[218] V. Sharma, P. Singh, A.K. Pandey, A. Dhawan, Induction of oxidative stress, DNA damage, and apoptosis in mouse liver after sub-acute oral exposure to zinc oxide nanoparticles, Mutat. Res. Genet. Toxicol. Environ. Mutagen 745 (1−2) (2012) 84−91, https://doi.org/10.1016/J.MRGENTOX.2011.12.009.

[219] H.-C. Chuang, Y.-T. Yang, H.-C. Chen, Y.-H. Hwang, K.-Y. Wu, T.-F. Chen, C.-L. Chen, M.-K. Jhan, T.-J. Cheng, Acute effects of pulmonary exposure to zinc oxide nanoparticles on the brain in vivo, Aerosol Air Qual. Res. 20 (7) (2020) 1651−1664, https://doi.org/10.4209/AAQR.2019.10.0523.

[220] L. Xiao, C. Liu, X. Chen, Z. Yang, Zinc oxide nanoparticles induce renal toxicity through reactive oxygen species, Food Chem. Toxicol. 90 (2016) 76−83, https://doi.org/10.1016/J.FCT.2016.02.002.

[221] R. Abbasalipourkabir, H. Moradi, S. Zarei, S. Asadi, A. Salehzadeh, A. Ghafourikhosroshahi, M. Mortazavi, N. Ziamajidi, Toxicity of zinc oxide nanoparticles on adult male Wistar rats, Food Chem. Toxicol. 84 (2015) 154−160, https://doi.org/10.1016/J.FCT.2015.08.019.

[222] W.K. Boyes, C. Van Thriel, Neurotoxicology of nanomaterials, Chem. Res. Toxicol. 33 (5) (2020) 1121, https://doi.org/10.1021/ACS.CHEMRESTOX.0C00050.

[223] P. Vardakas, Z. Skaperda, F. Tekos, A.-F. Trompeta, A. Tsatsakis, C.A. Charitidis, D. Kouretas, An integrated approach for assessing the in vitro and in vivo redox-related effects of nanomaterials, Environ. Res. 197 (2021) 111083, https://doi.org/10.1016/j.envres.2021.111083.

[224] M. Horie, Y. Tabei, Role of oxidative stress in nanoparticles toxicity, Free Radic. Res. 55 (4) (2020) 331−342, https://doi.org/10.1080/10715762.2020.1859108.

[225] P. Khanna, C. Ong, B.H. Bay, G.H. Baeg, Nanotoxicity: an interplay of oxidative stress, inflammation, and cell death, Nanomaterials 5 (3) (2015) 1163−1180, https://doi.org/10.3390/NANO5031163.

[226] G. Pizzino, N. Irrera, M. Cucinotta, G. Pallio, F. Mannino, V. Arcoraci, F. Squadrito, D. Altavilla, A. Bitto, Oxidative Stress: Harms and Benefits for Human Health. Oxidative Medicine and Cellular Longevity, 2017, p. 2017, https://doi.org/10.1155/2017/8416763.

[227] R.N.R. Anreddy, N.R. Yellu, K.R. Devarakonda, Oxidative biomarkers to assess the nanoparticle-induced oxidative stress, Methods Mol. Biol. 1028 (2013) 205−219, https://doi.org/10.1007/978-1-62703-475-3_13.

[228] B. Hellack, C. Nickel, C. Albrecht, T.A.J. Kuhlbusch, S. Boland, A. Baeza-Squiban, W. Wohlleben, R.P.F. Schins, Analytical methods to assess the oxidative potential of nanoparticles: a review, Environ. Sci. J. Integr. Environ. Res.: Nano 4 (10) (2017) 1920−1934, https://doi.org/10.1039/C7EN00346C.

[229] A. Kumar, V. Sharma, A. Dhawan, Methods for detection of oxidative stress and genotoxicity of engineered nanoparticles, Methods Mol. Biol. 1028 (2013) 231−246, https://doi.org/10.1007/978-1-62703-475-3_15.

[230] J. Tournebize, A. Sapin-Minet, G. Bartosz, P. Leroy, A. Boudier, Pitfalls of assays devoted to the evaluation of oxidative stress induced by inorganic nanoparticles, Talanta 116 (2013) 753−763, https://doi.org/10.1016/J.TALANTA.2013.07.077.

[231] A. Veskoukis, E. Kerasioti, A. Priftis, P. Kouka, Y. Spanidis, S. Makri, D. Kouretas, The biomarker issue is a battery of translational biomarkers for assessing the in vitro and in vivo antioxidant action of plant polyphenolic compounds, Curr. Opin. Toxicol. 13 (2019) 99−109, https://doi.org/10.1016/J.COTOX.2018.10.001.

CHAPTER 7

Particulate photocatalysts for overall water splitting and implications regarding panel reactors for large-scale applications

Swarnava Nandy[1], **Lihua Lin**[1], **Kazunari Domen**[1,2]

[1]*Research Initiative for Supra-Materials, Interdisciplinary Cluster for Cutting Edge Research, Shinshu University, Nagano, Japan;* [2]*Office of University Professors, The University of Tokyo, Tokyo, Japan*

Abstract

Using particulate photocatalysts, solar-driven overall water splitting (OWS) can enable large-scale hydrogen production as an inexpensive, renewable, environmentally friendly, and carbon-neutral fuel. One of the most promising means of realizing OWS is to develop systems in which photocatalysts are embedded in large panel arrays. At present, the primary obstacle to the commercialization of this technology is the limited solar-to-hydrogen (STH) conversion efficiencies of available photocatalysts. Numerous visible-light-driven photocatalysts have been studied to obtain improved water splitting activity by suppressing surface defects or by loading co-catalysts with different functions to promote the kinetics of the water reduction and oxidation reactions. Recent studies of photocatalyst sheets incorporating two photocatalysts and a solid-state electron mediator have shown this technology to be readily scalable with no loss of activity. The best performing system comprising Rh, La co-doped $SrTiO_3$, and Mo-doped $BiVO_4$ embedded in a thin conductive Au layer achieved an STH of 1.0% at near-ambient pressure. Narrow bandgap nonoxide photocatalysts can provide better performance on a thermodynamic basis at present, but the activities of these materials are currently inferior to those of OWS systems composed of metal oxides. This chapter describes various strategies for developing highly active, narrow bandgap photocatalysts, and the working mechanisms of powder suspension and photocatalyst sheets with various surface modifications. Recent progress in photocatalyst panels is also discussed, focusing on the separation of gaseous products and safety issues.

Keywords: Nonoxide photocatalysts; Panel reactor; Photocatalyst sheet; Reaction pressure; Visible light.

1. Introduction

At present, the increasing worldwide demand for energy has resulted in serious concerns related to the depletion of fossil fuels and environmental degradation. The efficient utilization of renewable energy resources will be an indispensable aspect of addressing

Advanced Nanomaterials and Their Applications in Renewable Energy. https://doi.org/10.1016/B978-0-323-99877-2.00020-5

these challenges shortly [1]. One of the most promising approaches to renewable energy is to convert solar radiation into transportable, storable forms. The annual amount of solar energy reaching the Earth's surface is several orders of magnitude higher than global energy consumption [2]. The conversion of solar energy could potentially be achieved based on splitting water into hydrogen and oxygen over semiconductor photocatalysts driven by sunlight [3,4]. The hydrogen resulting from the water reduction reaction could then be used in fuel cells and serve as an important feedstock in chemical industries. Currently, hydrogen is mainly produced by reforming fossil fuels, which emit various pollutants and carbon dioxide. So, mass hydrogen production via an inexpensive process such as water splitting could mitigate climate change and energy shortages [5].

There are three main semiconductor-based water-splitting technologies at the moment: photocatalysis, photoelectrochemical (PEC) processes, and photovoltaic powered electrolysis (PV-E) [6]. Various PV-E systems have demonstrated higher solar-to-hydrogen (STH) conversion efficiencies compared with the other two methods, in the vicinity of 30% [7,8]. However, large PEC or PV-E reactors tend to suffer from pH gradients and high solution resistance because the reduction and oxidation reaction sites are far apart. In addition, these techniques require electrolyte solutions and vigorous stirring and so are not readily scaled up. In contrast, photocatalytic water splitting systems are much simpler because the reduction and oxidation reactions occur on the same individual particles, such that mass transfer limitations are removed. Even so, the vast majority of water splitting processes developed to date have various issues in terms of efficiency and stability, and none has been able to demonstrate an STH conversion efficiency above 1% at ambient pressure. Interestingly, a recent techno-economic study showed that an STH conversion efficiency in the range of 3%–5% is required to allow photocatalytic water splitting to compete with fossil fuels on an economic basis [9].

Water-splitting reactions over semiconductor photocatalysts in response to solar radiation as a means of renewable H_2 production have been studied extensively. This process involves an energetically uphill reaction with a standard Gibbs free energy change of +237 kJ/mol of water, requiring an external energy source [10]. As a consequence, only photons with energies greater than the bandgap of the semiconductor photocatalyst can be used to generate exciting electron–hole pairs. Up to the present, numerous photocatalysts exhibiting excellent gas evolution activity have been reported. However, most can only absorb ultraviolet (UV) light, accounting for just 5% of the solar spectrum. Therefore, increasing the energy conversion efficiency of overall water splitting (OWS) systems will require the synthesis of visible-light-driven photocatalysts. The present chapter explains the basic theory behind the OWS reaction. Also, it examines photocatalyst development, the associated reaction mechanisms, and the design of powder

suspension and sheet-based systems for OWS. In addition, key challenges associated with the fabrication of panel reactors using particulate photocatalysts for large-scale applications are also addressed.

2. Basic principles of photocatalytic water splitting

Photocatalytic OWS involves three fundamental steps: (i) the absorption of photons having energies greater than the photocatalyst bandgap such that electron–hole (e^--h^+) pairs are formed in the conduction and valence bands, respectively, (ii) the transportation of these excited charge carriers from the bulk to active sites on the surface, and (iii) surface chemical reactions in which electrons reduce H^+ to H_2 while holes oxidize H_2O to O_2. All three steps combine to determine the overall efficiency of a water-splitting system. The band edge potentials of the conduction band minimum (CBM) and valence band maximum (VBM) for a selected photocatalyst must be situated at more negative and more positive energy levels than the water reduction and oxidation potentials to enable H_2 and O_2 evolution reactions (OER), respectively [4,10]. These are crucial thermodynamic criteria for a photocatalyst to participate in OWS. Depending on the number of photoexcitation steps involved, the OWS reaction can be classified as either one step or two step, as shown in Fig. 7.1. One-step OWS proceeds via the process described immediately above, but it is rare for a single photocatalyst to have a suitable CBM and VBM simultaneously. Thus, very few OWS photocatalysts have been reported.

In contrast, in the case of two-step photoexcitation (Z-scheme) systems, a pair of photocatalysts are combined, with each promoting either the H_2 or O_2 evolution reaction.

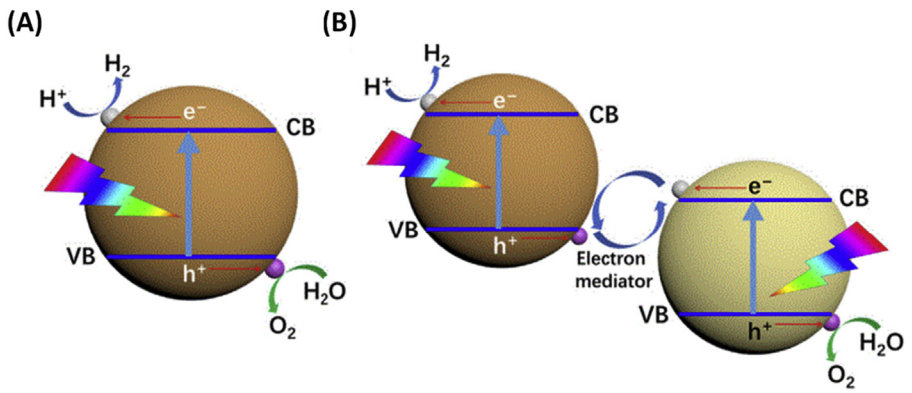

Figure 7.1
Diagrams showing photocatalytic OWS involving (A) one-step and (B) two-step (i.e., Z-scheme) photoexcitation. *Reprinted with permission from Ref. [3].*

Specifically, electrons in the CB of the hydrogen evolution photocatalyst (HEP) and holes in the VB of the oxygen evolution photocatalyst (OEP) participate in water reduction and oxidation reactions. In contrast, holes in the VB of the HEP and electrons in the CB of the OEP are oxidized and reduced, respectively, by a redox mediator. These mediators can be either water soluble or in a solid state. The CBM and VBM of the HEP and OEP photocatalysts, respectively, have to meet only one of the respective thermodynamic criteria. So a wider range of materials can be employed in Z-scheme systems.

The apparent quantum yield (AQY) and STH values for photocatalytic systems commonly compare performance. These two terms are both directly proportional to the H_2 evolution activity of the photocatalyst and can be expressed as follows.

$$\mathrm{AQY}(\%) = \frac{4 \times \mathrm{N}(\mathrm{H_2})}{\mathrm{N}(\mathrm{photons})} \times 100 \tag{7.1}$$

$$\mathrm{STH}(\%) = \frac{\mathrm{R}(\mathrm{H_2}) \times \Delta\mathrm{G}}{\mathrm{P} \times \mathrm{S}} \times 100 \tag{7.2}$$

In the definition of AQY, $N(H_2)$ and N(photons) are the numbers of H_2 molecules generated by the water-splitting reaction and the number of incident photons, respectively. In the definition of STH, $R(H_2)$, ΔG, P, and S are the rate of H_2 gas production, the Gibbs free energy change for the OWS reaction, the irradiation intensity, and the effective irradiation area, respectively. STH is typically determined using a solar simulator with an intensity, P, of 100 $\mathrm{mW \cdot cm^{-2}}$. AQY values can be obtained for the OWS reaction and the separate H_2 and O_2 evolution half-reactions at different wavelengths, whereas STH is measured only for the OWS reaction.

3. Metal oxide and nonoxide photocatalysts in one-step OWS using powder suspensions

3.1 $SrTiO_3$

$SrTiO_3$ (STO) is one of the most advanced photocatalysts for large-scale OWS applications, although the thermodynamic characteristics of this material are not ideal because it absorbs only UV light. STO has been studied for several decades in the form of powder suspensions. Our group has also reported the application of this oxide to Z-scheme OWS after being processed into photocatalyst sheets together with Mo-doped $BiVO_4$ (see Section 4). Despite having wide bandgap energy of 3.2 eV, STO has been extensively assessed due to its excellent photocatalytic activity. The first work using $SrTiO_3$ modified with NiO to split water into H_2 and O_2 was published in 1980 and represented one of the earliest reports of the OWS phenomenon [11]. Since then, various research projects have attempted to improve the photocatalytic activity of STO by applying different surface treatments and by the loading of co-catalysts. For example, the synthesis of STO assisted

by an $SrCl_2$ flux improved the material's crystallinity drastically. It generated particles 0.2−2 μm in size, in contrast to the irregular particle shapes in pristine STO [12]. The flux-treated STO primarily contained truncated cubic particles that exhibited a perovskite structure and had a low Brunauer, Emmett, and Teller (BET) surface area, in agreement with the change in particle size. In addition, controlled Al doping (0.1% at Ti sites) and the flux-mediated synthesis of STO modified with $Rh_{2-y}Cr_yO_3$ have been used to generate an H_2 evolution co-catalyst. The STO was loaded with $Rh_{2-y}Cr_yO_3$ by impregnation followed by calcination in the air to form $Rh_{2-y}Cr_yO_3$/STO: Al, which provided an AQY of 30% at 360 nm. It is worth mentioning that no significant morphological change was observed in the case of STO doped only with Al, indicating the necessity of applying a flux treatment to induce such changes.

The photocatalyst and co-catalyst must also be chemically stable to maintain their photocatalytic activity over a prolonged period. Deactivation of the photocatalyst can be prevented by adding protective layers made of materials such as amorphous TiO_2 or SiO_2. It is also vital to preserving the co-catalysts original chemical state so as not to lose activity over time. A detailed study showed that the dissolution of Cr from an unprotected $Rh_{2-y}Cr_yO_3$ mixed oxide co-catalyst led to the exposure of Rh, which in turn promoted oxygen reduction and water formation backward reactions. It so lowered the photocatalytic activity of the material [13]. This problem was addressed by the photo-reductive/oxidative deposition of additional co-catalysts, as discussed below.

In 2017, Chiang et al. attempted to improve the AQY of an $Rh_{2-y}Cr_yO_3$/STO: Al photocatalyst via the co-loading of MoO_y. MoO_y was photo-deposited at a level of 0.03 wt% (as confirmed by inductively coupled plasma optical emission spectroscopy), followed by calcination at 573 K. The resulting material exhibited an AQY of 69% at 365 nm [14]. The MoO_y did not act as a traditional co-catalyst by promoting H_2 or O_2 evolution but rather modified the chemical state of the $Rh_{2-y}Cr_yO_3$ during the OWS reaction. This work demonstrated that Mo^{6+} in MoO_4^{2-} deposited as MoO_3 upon calcination at 573 K. A portion of the Mo^{6+} in the photocatalyst was reduced to Mo^{5+} during the reaction owing to the formation of H_zMoO_3 based on the reaction $MoO_3 + ze^- + zH^+ \rightarrow H_zMoO_3$. This additional reaction involved photoexcited electrons and hydrogen atoms coordinated to oxygen atoms in the MoO_3 via a hydrogen-bonding network. Thus, the addition of MoO_3 maintained the original chemical states of the Rh and Cr, which in turn improved the OWS activity.

A long-term stability test of $Rh_{2-y}Cr_yO_3$-impregnated STO: Al synthesized by a flux-assisted method was performed over 168 h using a Hg lamp ($\lambda > 300$ nm) [13]. During this time, the H_2 and O_2 evolution rates were approximately 35.0 and 17.0 mmol/h, respectively. The activity of the material was found to decrease by 14% throughout the trial. However, this activity loss was greatly decreased after loading of

CoOOH (equivalent to 0.3 wt% Co), as shown in Fig. 7.2A. The CoOOH did not improve the OWS activity as such but instead is thought to have been deposited on the oxidation sites to promote the water oxidation reaction, which competed with the oxidation of Cr^{3+} in $Rh_{2-y}Cr_yO_3$ to Cr^{6+}. This unwanted oxidation to form water-soluble Cr^{6+} changed the local chemical environment of the co-catalyst and consequently destabilized the system to lower the OWS activity over time. CoOOH is known to extract h+ and promote the O_2 OER and is also believed to suppress Cr loss from the co-catalyst and consequently enhance water oxidation. Photodeposition of a TiO_2 layer (at a level of 3 wt%) onto the CoOOH/$Rh_{2-y}Cr_yO_3$/STO: Al further improved the activity and stability of the material when used in a 5 × 5 cm sheet in a panel reactor. This sheet exhibited an H_2 gas evolution rate of 5.7 μmol/h/cm^2 along with an initial STH of 0.4% at ambient pressure. Also, it maintained 80% of its initial activity after 1300 h while showing an STH of 0.3%, as shown in Fig. 7.2B. This work with the TiO_2/CoOOH/$Rh_{2-y}Cr_yO_3$/STO: Al system not only demonstrated an STO-based photocatalyst with moderately high performance over a prolonged period but also suggested potential approaches to the use of other narrow bandgap photocatalysts to promote OWS at near ambient pressure.

In previous studies, $Rh_{2-y}Cr_yO_3$ co-catalysts were loaded onto STO:Al using impregnation methods, leading to the homogeneous distributions of Rh and Cr species over the entire surface of the photocatalyst. However, the H_2 evolution co-catalyst was also deposited onto the oxidation sites and consequently shielded these sites. Our group recently studied the sequential photo-deposition of Rh (0.1 wt%)/Cr_2O_3 (0.05 wt%) and CoOOH (0.05 wt%) as H_2 and O_2 evolution co-catalysts, respectively, and observed 3.8 and 1.9 mmol/h H_2 and O_2 generation rates, respectively (Fig. 7.3A). These values were

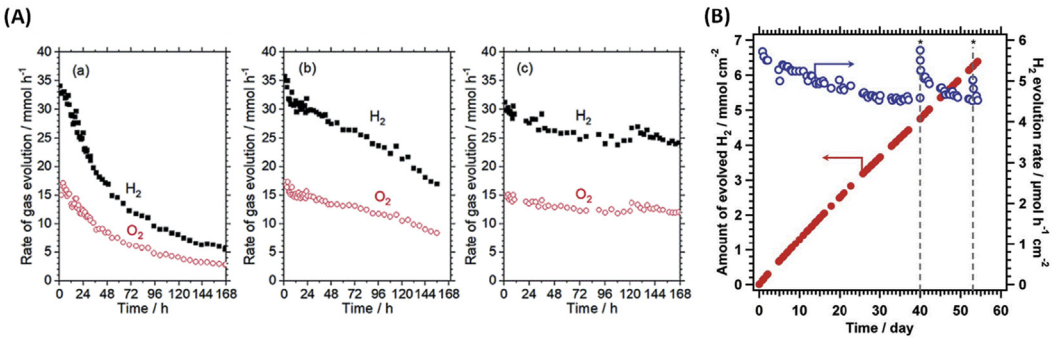

Figure 7.2

(A) Time courses of OWS reactions over $SrTiO_3$:Al loaded with (a) $RhCrO_x$, (b) $RhCrO_x$ and 0.3 wt% Co species, and (c) $RhCrO_x$, 0.3 wt% Co species and 3 wt% TiO_2. Each reaction was carried out at 291 K under a 450 W high-pressure Hg lamp (λ > 300 nm) as a light source. (B) Long-term H_2 gas evolution activity over a panel reactor is 5 × 5 cm TiO_2/CoOOH/RhCrOx/$SrTiO_3$:Al sheet. The reaction was carried out at 291 K under an AM1.5G solar simulator as a light source. *Reprinted with permission from Ref. [13].*

almost twice those obtained from the same STO:Al after the co-impregnation of $Rh_{2-y}Cr_yO_3$ (0.1 wt% of each metal) [15]. This high OWS activity was also retained for approximately 12.5 h. The two-step photo-deposition process allowed the formation of an Rh/Cr_2O_3 core/shell structure in which the Rh promoted the H_2 evolution and the backward oxygen reduction reaction (ORR). At the same time, the Cr_2O_3 suppressed the access of molecular O_2 to the Rh surface to inhibit the reverse reaction. This Rh/Cr_2O_3/CoOOH/STO material exhibited EQE values of 95.7%, 95.9%, and 91.6% at 350, 360, and 365 nm, respectively, as shown in Fig. 7.3B. These values were equivalent to an internal quantum efficiency (IQE) of approximately 100% based on the number of photons absorbed. However, the EQE was drastically lowered beyond 370 nm due to decreased light absorption. The STH value observed under a solar simulator was 0.65%, which was the highest value reported at the time for a one-step OWS system having an almost perfect IQE of nearly 100%.

The microstructure of STO modified with various co-catalysts was analyzed by scanning electron microscopy (SEM) while also acquiring the selected area electron diffraction (SAED) pattern of a single particle. The resulting SEM images (Fig. 7.4) indicated that the STO particles were not perfectly cubic but rather had some nonequivalent facets. The distributions of the co-catalysts Rh and Cr_2O_3 on the STO surface were very similar, implying that these materials were loaded onto the same crystal facets, providing evidence for forming a core/shell structure. The SAED pattern in Fig. 7.5 demonstrates that the Rh/Cr_2O_3 was preferentially deposited on the {100} crystal facets, whereas the CoOOH co-catalyst was primarily located on the {110} facets. This indicates that the photo-excited

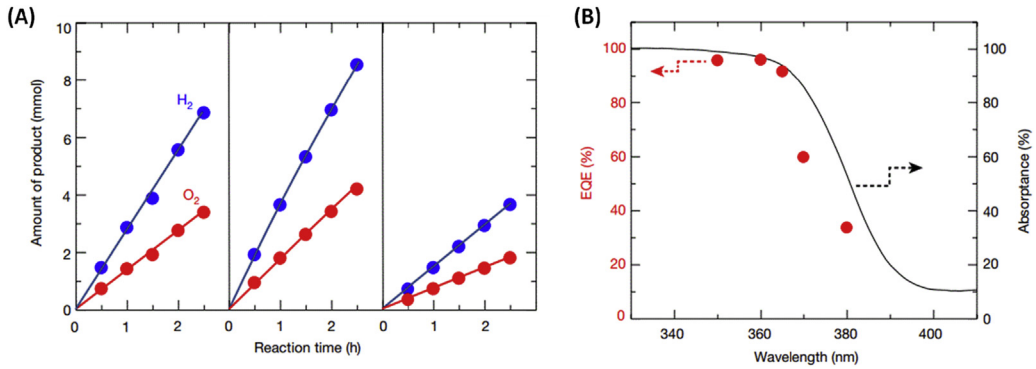

Figure 7.3

(A) OWS gas evolution data obtained using (left) Cr_2O_3(0.05 wt%)/Rh(0.1 wt%)/$SrTiO_3$:Al loaded via two-step photo-deposition, (middle) CoOOH(0.05 wt%)/Cr_2O_3(0.05 wt%)/Rh(0.1 wt%)/$SrTiO_3$:Al loaded via three-step photo-deposition, and (right) Rh (0.1 wt%)—Cr(0.1 wt%)/$SrTiO_3$:Al loaded by co-impregnation. (B) The external quantum efficiency (EQE) of CoOOH/Cr_2O_3/Rh/$SrTiO_3$:Al during the OWS as a function of wavelength. *Reprinted with permission from Ref. [15].*

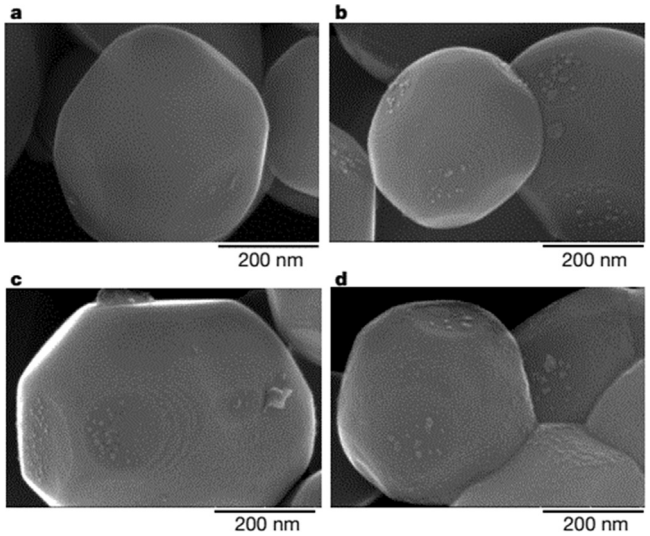

Figure 7.4

SEM images of $SrTiO_3$:Al (A) without co-catalysts and loaded with (B) Rh (0.1 wt%), (C) Cr_2O_3 (0.05 wt%)/Rh (0.1 wt%), and (D) CoOOH (0.05 wt%)/Cr_2O_3 (0.05 wt%)/Rh (0.1 wt%). *Reprinted with permission from Ref. [15].*

charge carriers traveled in different paths to participate in the water reduction and oxidation reactions, thus drastically reducing charge recombination in the bulk of the material. The observed anisotropic deposition of these co-catalysts is attributed to the charge rectification effect inside each STO particle induced by an internal electric field. This field, in turn, originated from the difference in the work functions of the {110} and {100} crystal facets, similar to the p-n junction of a solar cell resulting from different Fermi levels. A work function difference of 0.2 eV between the {100} and {110} facets is usually sufficient for anisotropic charge separation. It is, therefore, able to increase the local concentrations of e^- and h^+ at the respective facets.

3.2 (Oxy)nitrides

The VBMs of (oxy)nitride materials are composed of N 2p and O 2p orbitals located at more negative potentials than the corresponding oxides. In contrast, the CBMs are primarily composed of metal and orbitals and are not changed, such that (oxy)nitrides exhibit narrower bandgaps than metal oxides. Several Ta-based oxy(nitride) semiconductors are known to promote one-step OWS under visible light. These include TaON (bandgap energy, Eg = 2.5 eV) [16], Ta_3N_5 (Eg = 2.1 eV) [17] and $LaMg_{1/3}Ta_{2/3}O_2N$ (Eg = 2.1 eV) [18,19], all of which have d^0 electronic configurations. The latter compound is an n-type perovskite semiconductor, a solid solution of $LaMg_{1/3}Ta_{2/3}O_2N$

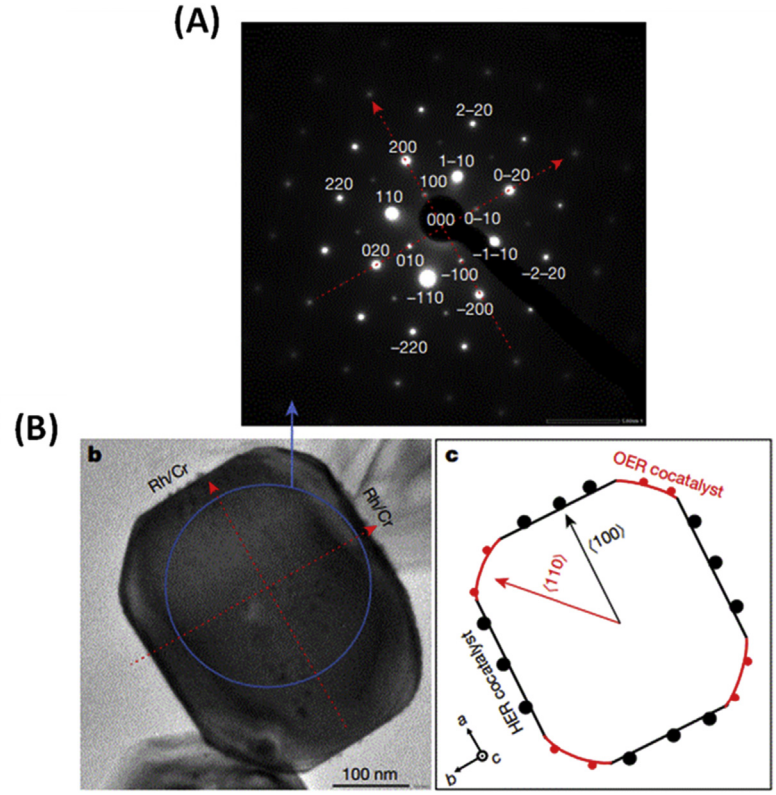

Figure 7.5

(A) SAED pattern obtained from a $CoOOH/Cr_2O_3/Rh/SrTiO_3$:Al particle and (B, C) particle morphology and crystal orientation. *Reprinted with permission from Ref. [15].*

and $LaTaON_2$ in which the CBM and VBM are located at −0.66 and + 1.40 V (vs. RHE), respectively. As such, this material is suitable for both water reduction and oxidation reactions.

Interestingly, $RhCrO_x$-modified $LaTaON_2$ evolves H_2 predominately, whereas $LaMg_{1/3}Ta_{2/3}O_2N$ generates hydrogen and oxygen from pure water. However, this material also undergoes rapid self-oxidation with the generation of nitrogen. Modification of the $RhCrO_x/LaMg_{1/3}Ta_{2/3}O_2N$ surface with an amorphous TiO_2 layer by photodeposition results in the stoichiometric evolution of H_2 and O_2. This coating also suppresses self-oxidation by inhibiting the diffusion of O_2 to the photocatalyst surface and so inhibits the ORR. The deposition of a SiO_2 layer further improved the activity of $LaMg_{1/3}Ta_{2/3}O_2N$ presumably because of suppression of the ORR owing to the formation of a more homogeneous and dense coating layer. Unfortunately, the activity of this material was only in the range of 5−6 μmol/h with an AQY of 0.18% [19]. This limited performance was

ascribed to the presence of surface defects and grain boundaries that resulted from nitridation.

In 2002, Ta_3N_5 was found to promote water reduction and oxidation reactions in the presence of sacrificial electron donors and acceptors, respectively, indicating that the CBM and VBM potentials for this material were suitable for a one-step OWS reaction [20]. Since then, various strategies have been investigated to achieve one-step OWS by suppressing surface defects. These have included morphological control and surface modifications that improve the activities of the H_2 and O_2 evolution half-reactions and PEC water oxidation. It has been reported that prolonged nitridation of various precursors to this compound at high temperature forms grain boundaries and defects that can subsequently act as charge recombination centers for e^-—h^+ pairs. In 2018, Zheng et al. studied the rapid growth of Ta_3N_5 nanorods from the edges of lattice-matched cubic $KTaO_3$ particles during a brief nitridation process. Volatilization of K species was promoted during this process, and the relatively brief nitridation period facilitated the growth of single crystals comprising discrete Ta_3N_5 nanorods free from grain boundaries. The resulting $Ta_3N_5/KTaO_3$ was found to promote the OWS following surface modification with Cr_2O_3/Rh and exhibited stoichiometric evolution of H_2 and O_2 at rates of 11.0 and 4.8 μmol/h, respectively, under a Xe lamp ($\lambda > 420$ nm) (Fig. 7.6). An AQY of 2.2% was achieved at 320 nm, although this value was reduced by order of magnitude between 420 and 560 nm. The higher AQY below 350 nm was attributed to the excitation of $KTaO_3$ by UV radiation, implying that the OWS primarily occurred on the $KTaO_3$ particles.

3.3 Oxysulfides

Oxysulfide materials have attracted increasing interest in recent years. Compared with sulfides, oxysulfides are more stable due to the co-existence of metal—oxygen and metal—sulfur bonds. This, in turn, enhances the interactions between the metal cations and anions. In addition, the bandgap energies of oxysulfides are comparable to those of metal sulfides, ensuring highly efficient absorption of solar energy [21].

Early studies primarily focused on preparing new oxysulfide materials and determining the crystal structures of these materials [22—25]. Other important studies examined the optical properties of oxysulfides, and a systematic investigation of the $Ln_2Ti_2O_5S_2$ series (Ln = Nd, Sm, Gd, Tb, Dy, Ho, Er, and Y) found that all these compounds showed a strong absorption band in the vicinity of 2 eV [26]. Oxysulfides can absorb at long wavelengths, and $Sm_2Ti_2O_5S_2$ was studied as a potential photocatalytic water-splitting catalyst [21]. This compound was synthesized by the solid-state reaction (SSR) method in a sealed quartz tube under vacuum at 1273 K, giving almost pure $Sm_2Ti_2O_5S_2$ with relatively large particle sizes of 2—4 μm after prolonged sintering. The bandgap of

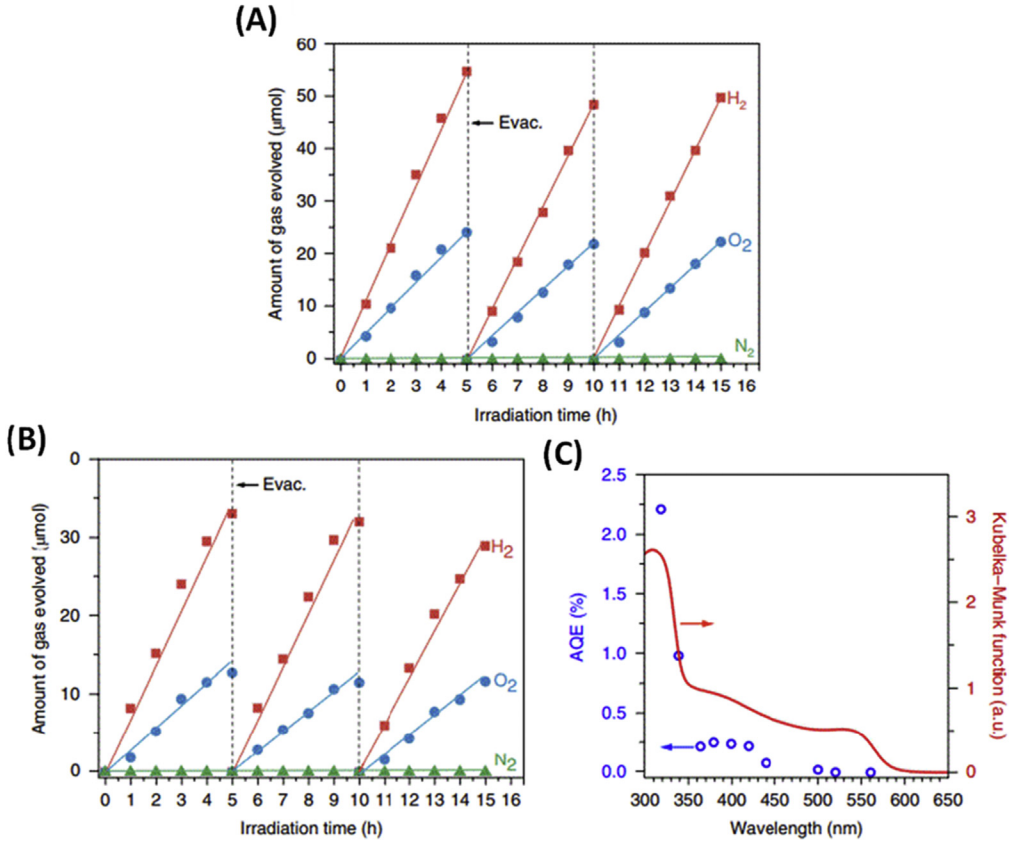

Figure 7.6

Time courses of gas evolution over Cr_2O_3/Rh-modified Ta_3N_5/$KTaO_3$ synthesized by 0.25 h nitridation under (A) a 300 W Xe lamp ($\lambda > 420$ nm) and (B) simulated sunlight. (C) AQY for this material as a function of wavelength. *Reprinted with permission from Ref. [17].*

$Sm_2Ti_2O_5S_2$ was estimated to be 2.1 eV based on UV-visible diffuse reflectance spectroscopy (DRS), and photocatalytic hydrogen and oxygen evolution half-reactions were achieved over this material in the presence of sacrificial agents. Although $Sm_2Ti_2O_5S_2$ has not yet been used to promote the one-step OWS reaction, it has been successfully employed in the two-step OWS reaction under visible light. Ma et al. reported a Z-scheme water splitting system in which $Sm_2Ti_2O_5S_2$ and H^+/Cs^+-modified WO_3 served as the HEP and OEP, respectively, along with the I^{3-}/I^- redox couple as a shuttle electron mediator [27]. A novel method of synthesizing $Sm_2Ti_2O_5S_2$ via H_2S-based sulfurization of $Sm_2Ti_2O_7$ has also been reported [28]. After subsequent heating in air, the performance of $Sm_2Ti_2O_5S_2$ prepared by this sulfurization method was comparable to that of a sample obtained using the SSR method but with a much shorter heating period.

A breakthrough in the study of oxysulfide photocatalysts for one-step OWS was achieved by the synthesis of $Y_2Ti_2O_5S_2$ (YTOS) in 2019 [29]. This material, which is similar to $Sm_2Ti_2O_5S_2$, was prepared using an SSR method in a sulfur-rich environment that gave almost pure YTOS with particle sizes of approximately 1−2 μm. The bandgap energy for YTOS was estimated to be 1.9 eV based on DRS analyses, the CBM was determined to lie between −1.1 and −1.0 V versus NHE, and the VBM was around 0.8−0.9 V versus NHE. Therefore, YTOS had the potential to promote OWS in mildly alkaline solutions on a thermodynamic basis. Stoichiometric evolution of H_2 and O_2 was observed over Cr_2O_3/Rh/IrO_2-loaded YTOS in the pH range of 8−9 (Fig. 7.7). Reducing the calcination temperature from 1073 to 973 K was also found to increase the performance of this catalyst by reducing the particle size. However, transmission electron microscopy (TEM)

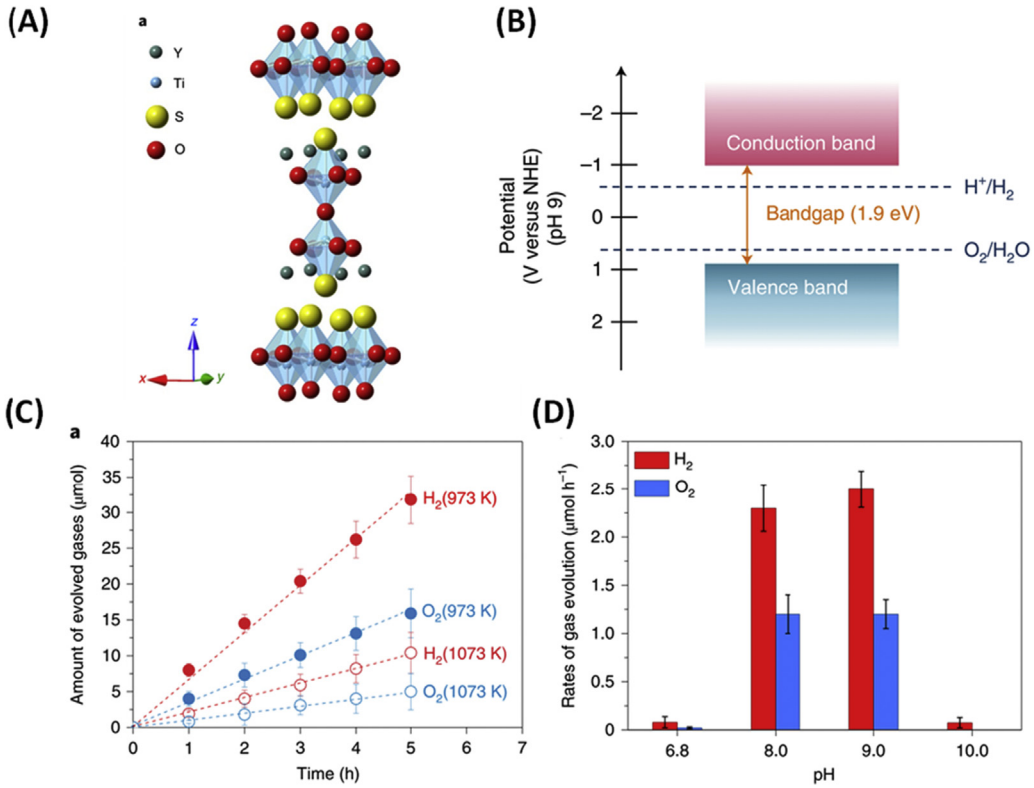

Figure 7.7

(A) Crystal structure of YTOS, (B) diagram of YTOS band structure, (C) time courses of water-splitting reaction over Cr_2O_3/Rh/IrO_2-modified YTOS synthesized at 1073 K (open symbols) and 973 K (filled symbols) in distilled water buffered with La_2O_3 (pH 8.5). (D) Gas evolution rates over Cr_2O_3/Rh/IrO_2-loaded YTOS at various reaction solution pH values. *It was reprinted with permission from Ref. [29].*

analysis confirmed that defects were still present in the bulk YTOS and acted as centers for recombining photo-generated charges. Therefore, there is still room for improvement in terms of the performance of YTOS based on controlling the particle morphology and reducing the defect concentration, as well as the loading of suitable co-catalysts.

3.4 Conjugated polymers

Conjugated polymers have emerged as a new branch of the photocatalyst family. The alternating double and single bonds along the backbone of a conjugated polymer allow the overlap of carbon p orbitals such that π electrons are delocalized, and these materials show semiconductor-like properties. For these reasons, conjugated polymers can possess a bandgap and absorb sunlight to create photo-generated electron−hole pairs that participate in the water-splitting reaction if the VBM and CBM are located at suitable potentials. In addition, the frameworks of conjugated polymers can be easily modified by standard organic synthesis methods to achieve specific properties.

Significant progress in applying conjugated polymers to photocatalytic water splitting was achieved in 2009 when Wang et al. reported the synthesis of polymeric carbon nitride (PCN) [30]. A DRS analysis of a yellow powder obtained after heating N-contained precursors at 823 K for 4 h yielded a bandgap of 2.9 eV. This PCN exhibited photocatalytic hydrogen evolution activity in the presence of a sacrificial agent without any metal-based co-catalyst, although Pt loading greatly enhanced its performance. After some years of research, a one-step OWS reaction was achieved using PCN nanosheets with suitable co-catalysts. When using urea as the precursor for PCN synthesis, large volumes of gases such as NH_3 and CO_2 were generated during polymerization. A product with a nanosheet morphology with a high surface area was obtained. This morphology would be expected to accelerate charge separation and migration and to expose more reactive sites. Photodeposition of Pt on the PCN nanosheets resulted in the stoichiometric production of H_2 and O_2 under a mixture of UV and visible light or pure visible light without any sacrificial reagents, as shown in Fig. 7.8B [31]. Loading with the OER co-catalyst CoO_x further enhanced the OWS performance. Other co-catalysts such as Rh, RhO_x, CoP, and single-site $Co1{-}P_4$ also provided improved OWS performance [32−34]. In 2008, Bojdys et al. reported the preparation of a crystalline PCN using a eutectic KCl/LiCl mixture, which they termed poly-triazine imide (PTI) [35]. The triazine subunits of this polymer were later determined to be connected by NH groups. The conjugated layers in the crystalline state were found to be stacked along the c-axis [36]. After photodeposition of Pt and CoO_x, this material demonstrated OWS activity with stoichiometric H_2 and O_2 evolution and showed a level of performance that was significantly enhanced compared with that of PCN nanosheets [37]. Analyses using aberration-corrected integrated differential phase-contrast imaging found that two

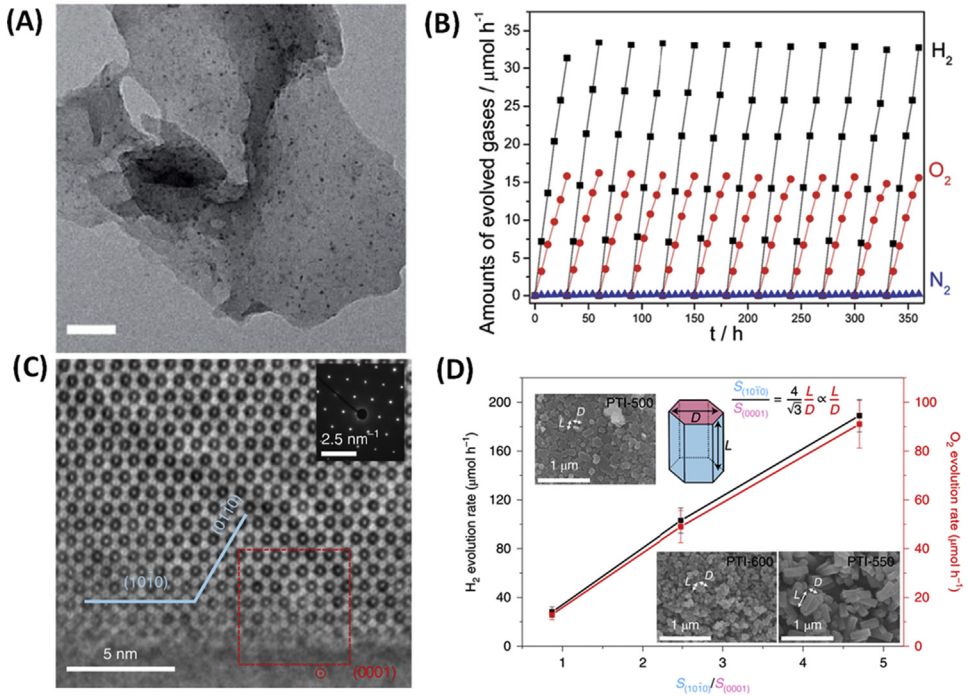

Figure 7.8

(A) TEM image of PCN with Pt photo deposited in situ and (B) time course of water splitting over PCN modified with 3 wt% Pt, PtO_x and 1 wt% CoO_x under visible light ($\lambda > 420$ nm). (C) AC-iDPC image of typical PTI/Li^+Cl^- crystal aligned along [0001] direction. The inset shows the corresponding diffraction pattern. (D) Maximum hydrogen and oxygen evolution rates as functions of the ratio of {1010} and {0001} mean surface areas. *Reprinted with permission from (B) Ref. [31]. (D) Ref. [38].*

hexagonal {0001} facets enclosed the PTI crystals as basal planes and six rectangular {10-10} facets as prismatic planes. The majority of the Pt and CoO_x was photo-deposited on the {10-10} facets rather than the {0001} facets (Fig. 7.8D). Therefore, the performance of PTI can be effectively increased by increasing the area of the side surfaces. By adjusting the preparation conditions, PTI specimens with different area ratios were obtained, and the OWS performance of these materials was directly correlated with the surface area ratio of the {10-10} and {0001} planes [38].

In recent years, some groups have reported the OWS activity of other conjugated polymers. Wang et al. prepared 1,3-diyne-linked conjugated microporous polymer nanosheets by oxidative coupling of terminal alkynes. This material was found to function as a visible-light-responsive photocatalyst for OWS [39]. The same group also reported the construction of polymer-based van der Waals heterostructures to provide a Z-scheme OWS system using aza-fused microporous polymers and ultrathin C_2N nanosheets as the HEP

and OEP, respectively [40]. By employing high-throughput screening of a library of components, Bai et al. identified conjugated polymers with the potential to act as the HEP in organic–inorganic Z-scheme water-splitting systems. One such material was P10 (a homopolymer of dibenzo[b,d]thiophene sulfone). $BiVO_4$, as the OEP showed OWS activity under visible light when using Fe^{2+}/Fe^{3+} as the redox mediator. Although the preliminary efficiency of this system was low, further optimization of the system could provide highly efficient OWS [41].

4. Photocatalyst sheets for Z-scheme overall water splitting

4.1 Structure and general properties of photocatalyst sheets composed of $SrTiO_3$:Rh, La, and $BiVO_4$:Mo

In prior work, $SrTiO_3$:Rh, La, and $BiVO_4$ (or the Mo-doped analog) intended for use as the HEP and OEP, respectively, were synthesized according to previously reported procedures [42]. These photocatalysts had particle sizes of several micrometers, exhibited a tendency to form aggregates, and were formed into sheets via a particle transfer method (Fig. 7.9) [42]. In this process, equivalent amounts of the two photocatalysts were suspended in 2-propanol by several minutes of sonication, after which the dispersion was

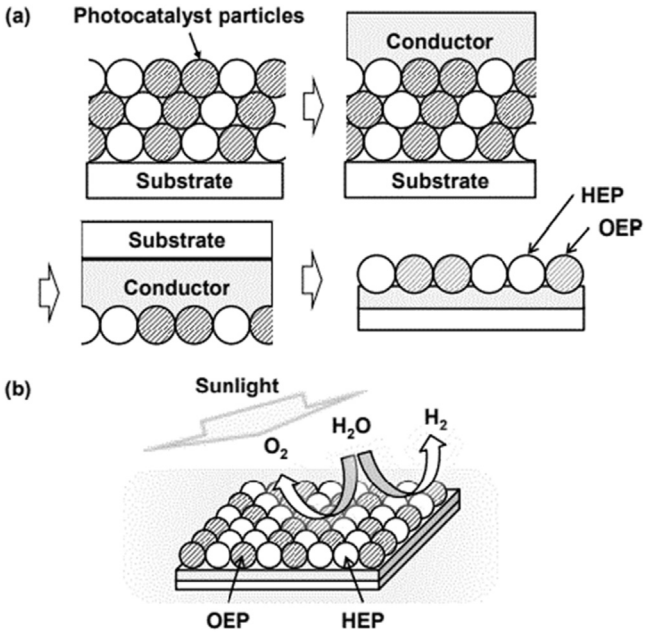

Figure 7.9
Diagrams show photocatalyst sheets' fabrication by the particle transfer method using two different photocatalysts as the HEP and OEP. *Reprinted with permission from Ref. [2].*

drop-cast onto a glass substrate. After the solvent evaporated, a thin, conductive Au or C layer with a thickness of approximately 300 nm was deposited by vacuum evaporation or magnetron sputtering, respectively. The assembly was peeled away from the glass plate and transferred to another plate, following which the loosely bound photocatalyst was removed by sonication. This method was used to produce $SrTiO_3$:Rh, La/Au/$BiVO_4$, $SrTiO_3$:Rh, La/Au/$BiVO_4$:Mo, and $SrTiO_3$:Rh, La/C/$BiVO_4$:Mo photocatalyst sheets. A top view image acquired using scanning electron microscopy-energy dispersive X-ray spectroscopy (SEM-EDS) demonstrated that the two photocatalysts covered more than 80% of the underlying Au layer. Both the HEP and OEP were in direct contact with the Au or C layer, and thus, electrons could be transferred between these particles.

The OWS activity of the sheets was evaluated using a closed gas circulation system similar to that employed in a powder suspension system. Ru and Cr_2O_3 were successfully photo deposited as co-catalysts onto the photocatalyst sheets. The OWS performance of the resulting $SrTiO_3$:Rh, La/Au/$BiVO_4$ sheet is compared with that of a powder suspension of the same materials in Table 7.1. The sheet system showed a more than five times higher gas evolution rate than the powder suspension [42]. However, in the case of a sheet without an Au layer, the gas evolution rate was negligible or even lower than that of the powder suspension system, indicating that electron transfer between the HEP and OEP occurred through the underlying Au layer and proceeded more efficiently than interparticle electron transfer in the powder suspension system.

To allow a detailed comparison of a powder suspension, photocatalyst sheet, and p/n PEC cell, the OWS activity of an STO: Rh, La/Au/BVO: Mo photocatalyst sheet was evaluated in pure water along with a powder suspension and parallel cells employing STO/Au and BVO/Au as the photocathode and photoanode, respectively [43]. The parallel cells were

Table 7.1: OWS activity under visible light from a 300 W Xe lamp (λ > 420 nm) using $SrTiO_3$:La, Rh, and $BiVO_4$ in various systems.

Sample[a]	STO: Rh, La (HEP)	BVO (OEP)	Au	H_2 ($\mu mol/h/cm^2$)	H_2 ($\mu mol/h/cm^2$)
[b]Suspension	O	O		0.8	0.4
[c]Sheet	O	O	O	4.5	2.2
	O	O		0.2	0.1
	O		O	<0.007	<0.02
		O	O	<0.007	<0.02

[a]Reactions were performed at 288 K and 5 kPa.
[b]Photocatalysts: 10 mg each; irradiation area: 13 cm^2.
[c]Sample area: 9 cm2 "O" indicates that the material was used in a given trial.

fabricated by drop-casting the photocatalysts onto separate glass plates, followed by Au layer deposition and particle transfer, and connected via a conductive wire. Following surface modification with Ru/Cr_2O_3 co-catalysts, the sheet exhibited a gas evolution rate an order of magnitude greater than those provided by the parallel PEC cells and powder suspension. This result demonstrated that the interparticle electron transfer rate in pure water is intrinsically low due to the generation of solution resistance and a pH gradient. Specifically, the pH increases and decreases in the vicinities of the photocathode and photoanode during the OWS, which generates a backward bias according to the Nernst equation due to insufficient mass transfer. The addition of sodium sulfate (Na_2SO_4) or potassium phosphate (KH_2PO_4) supporting electrolytes and buffering reagents lowered the solution resistance and pH gradient, thus improving the gas evolution activity over the parallel PEC cells. However, the activity of the sheet system was still far better than those of the other two systems because the two photocatalysts were directly fixed on a conductive film, and H_2 and O_2 were evolved near.

As a consequence, the OWS activity of the sheet system was essentially unaffected by the pH of the solution or by the formation of a pH gradient and solvent resistance. In contrast, selecting the optimal reaction solution pH is vital for a powder suspension because the two different photocatalysts have to be oppositely charged in response to electrostatic attraction to enable interparticle charge transfer. It should also be noted that the activity of a sheet system can be slightly improved by mild acidification of the reaction solution. Results such as these demonstrate that sheet systems are directly scalable without any loss of activity and any further consideration given to electron and mass transfer between HEP and OEP particles.

4.2 Influence of reaction conditions on OWS activity

The effect of the background pressure on the photocatalytic activity of a Ru photo deposited STO: Rh, La/Au/BVO: Mo sheet is presented in Fig. 7.10. At 10 kPa and 288 K, the H_2 and O_2 evolution rates were 11.0 and 6.0 μmol/h/cm^2, respectively. These rates were drastically decreased, to 0.6 and 0.3 μmol/h/cm^2, upon increasing the background pressure to 91 kPa, primarily because the unprotected Ru on the catalyst's surface promoted the ORR. High pressures also reduced the growth rate of bubbles and increased the bubble residence time on the sheet, both of which promoted the backward reaction. When using an aqueous methanol solution, the H_2 evolution rate was almost independent of the background pressure, further evidence that backward reactions were promoted in the presence of molecular oxygen generated on the sheet.

The ORR can be suppressed by using amorphous metal oxides such as Cr_2O_3 and TiO_2 as molecular sieves to inhibit the access of molecular oxygen to the catalyst. A trial using a Ru/STO: Rh, La/Au/BVO: Mo sheet showed that depositing a Cr_2O_3 layer significantly

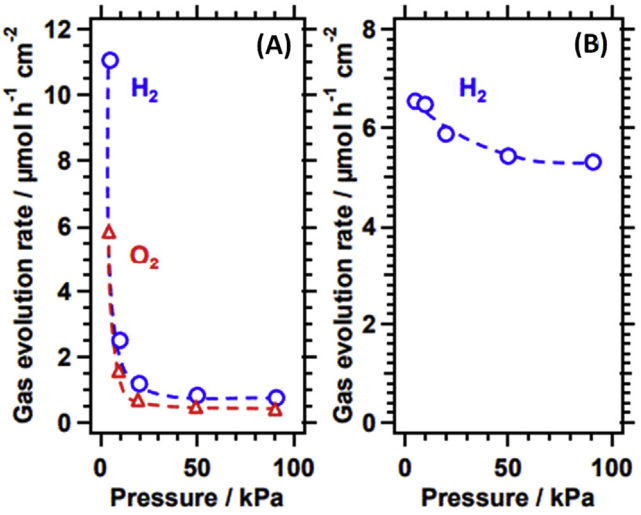

Figure 7.10

Gas evolution rate over $Ru/SrTiO_3$:La, $Rh/Au/BiVO_4$:Mo sheet under visible light ($\lambda > 420$ nm) as a function of background Ar pressure in (A) pure water and (B) aqueous methanol (10 vol%) at 288 K. *Reprinted with permission from Ref. [44].*

reduced the negative effect of high background pressure on the OWS activity. In contrast, the activity at low pressure remained largely unchanged. The subsequent application of a TiO_2 layer (Fig. 7.11) on the $Cr_2O_3/Ru/STO$: Rh, La/Au/BVO: Mo sheet further improved

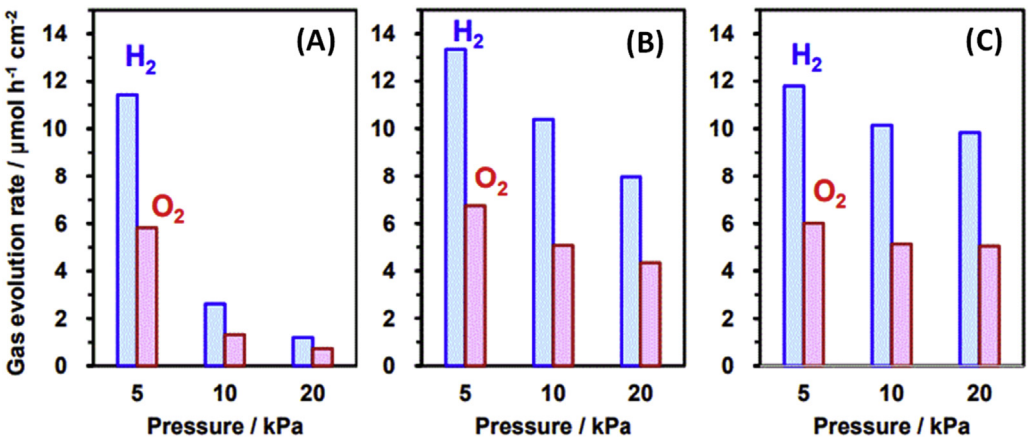

Figure 7.11

Gas evolution rate over $SrTiO_3$:La, $Rh/Au/BiVO_4$:Mo sheets modified with (A) Ru co-catalyst, (B) Cr_2O_3/Ru, and (C) $TiO_2/Cr_2O_3/Ru$ under visible light ($\lambda > 420$ nm) as a function of background Ar pressure at 288 K. *Reprinted with permission from Ref. [44].*

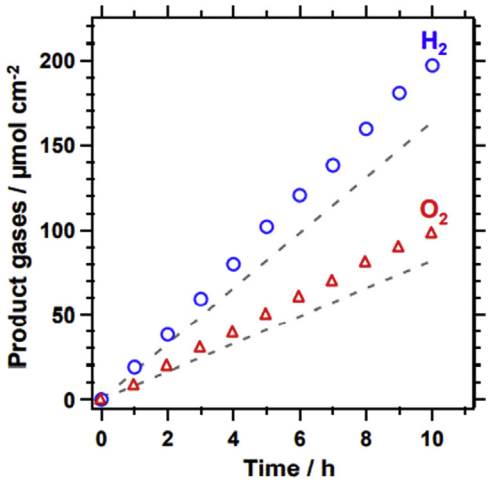

Figure 7.12

Gas evolution overtime during the OWS reaction using a Cr_2O_3/Ru/$SrTiO_3$:La, Rh/Au/$BiVO_4$:Mo sheet under simulated sunlight (AM1.5G) at 331 K and 10 kPa. The dashed lines show the gas evolution corresponding to an STH conversion efficiency of 1%.

the activity at near ambient pressure, giving rates of 10.0 and 5.0 μmol/h/cm^2 for H_2 and O_2, respectively, and also reduced the change in activity at a pressure of 10 kPa.

The activity of a Cr_2O_3/Ru/STO: Rh, La/Au/BVO: Mo sheet was also monitored under simulated sunlight at a 5 kPa background pressure and was found to increase monotonically with increasing temperature from 279 to 318 K. The apparent activation energy for the OWS was determined to be 18.0 kJ/mol from these data. Fig. 7.12 plots the gas evolution rates obtained from that sheet at 331 K and 10 kPa, for which an AQY of 33% was observed at 419 nm along with an STH of 1.1% [44]. Gas bubble formation spontaneously occurred on the sheet in response to simulated sunlight and ceased immediately after termination of the irradiation. This STH was the highest value reported as of 2016 for unassisted pure water splitting using particulate photocatalysts. However, gas evolution from this system decreased significantly upon increasing the background pressure, indicating that backward reactions were occurring.

A Ru/STO: Rh, La/C/BVO: Mo photocatalyst sheet with a conductive C layer was shown to retain 70% of its base performance at 5 kPa upon increasing the background pressure to 91 kPa without Cr_2O_3 or TiO_2 layers, as shown in Fig. 7.13. This was in contrast to the behavior of a TiO_2/Cr_2O_3/Ru/STO: Rh, La/Au/BVO: Mo sheet. A Cr_2O_3/Ru/STO: Rh, La/C/BVO: Mo sheet was also able to retain 80% of its base performance at near ambient pressure because C promoted the ORR to a lesser extent than Au. As a result, this system exhibited STH values of 1.2% and 1.0% at 10 and 91 kPa, respectively, at 331 K.

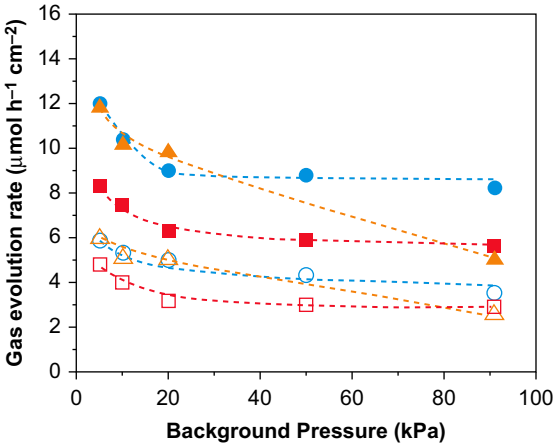

Figure 7.13

Gas generation rate during OWS over photocatalyst sheets under visible light ($\lambda > 420$ nm) as a function of background pressure. Squares (□), circles (○), and triangles (Δ) indicate Ru-loaded $SrTiO_3$:La, Rh/C/$BiVO_4$:Mo, Cr_2O_3/Ru-loaded $SrTiO_3$:La, Rh/C/$BiVO_4$:Mo, and a-TiO_2/Cr_2O_3/Ru-loaded $SrTiO_3$:La, Rh/Au/$BiVO_4$:Mo, respectively. Closed and open symbols represent hydrogen and oxygen, respectively. The reaction was carried out at 288 K. *Reprinted with permission from Ref. [45].*

4.3 Application of nonoxide photocatalysts to photocatalyst sheet systems

4.3.1 $LaMg_{2/3}Ta_{1/3}O_2N$

The CBM and VBM for $LaMg_{1/3}Ta_{2/3}O_2N$ are at −0.66 and + 1.40 V versus RHE, respectively. Considering the suitable CBM potential of this material, it has applications as the HEP in photocatalyst sheet–based systems. Photocatalyst sheets consisting of $LaMg_{1/3}Ta_{2/3}O_2N$ as the HEP and Mo-doped $BiVO_4$ (BVO: Mo) as the OEP with an underlying conductive Au layer (thickness: 300 nm) have been demonstrated to split water into hydrogen and oxygen under visible light [46,47]. Although this photocatalyst sheet also evolves N_2 due to the self-oxidation of the $LaMg_{1/3}Ta_{2/3}O_2N$. This can be effectively suppressed by applying an amorphous TiO_2 layer with an optimum thickness [46,48], similar to the case of one-step OWS using a powder suspension [18]. In addition, the incorporation of reduced graphene oxide (RGO) enhances the charge transfer within the particulate photocatalyst layer on the sheet (Fig. 7.14). A $LaMg_{1/3}Ta_{2/3}O_2N$/(Au, RGO)/$BiVO_4$:Mo sheet exhibited a maximum STH of 0.0035% [47], which is nearly three orders of magnitude lower than that obtained from sheets consisting of $SrTiO_3$:La, Rh, and $BiVO_4$:Mo. These results suggest that the performance of $LaMg_{1/3}Ta_{2/3}O_2N$ as the HEP is inferior to that of $SrTiO_3$:La, Rh, presumably because of the high concentration of anion defects and grain boundaries present in $LaMg_{1/3}Ta_{2/3}O_2N$ particles.

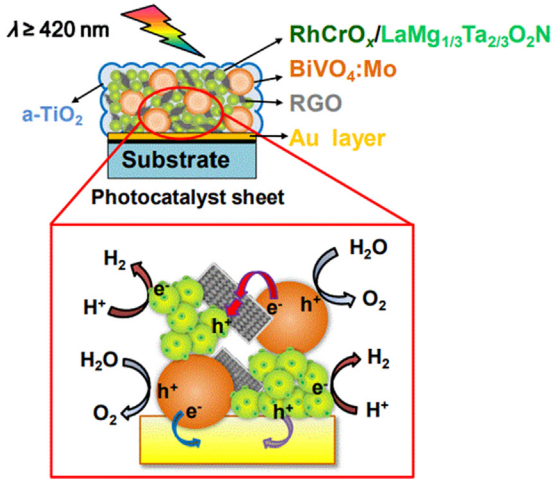

Figure 7.14
Diagram showing the functioning of amorphous TiO_2-coated $RhCrO_x$-modified $LaMg_{1/3}Ta_{2/3}O_2N$/(Au, RGO)/$BiVO_4$:Mo photocatalyst sheet during OWS. *Reprinted with permission from Ref. [47].*

4.3.2 $La_5Ti_2Cu_{0.9}Ag_{0.1}S_5O_7$

In 2004, Meignen et al. published the first report of two oxysulfides, $La_5Ti_2CuS_5O_7$ (LTC) and $La_5Ti_2AgS_5O_7$ (LTA), with bandgap energies of 1.9 and 2.2 eV, respectively [49]. In the case of LTC, the VBM is composed of Cu 3d orbitals and is situated at a more negative potential than that for LTA, whose VBM is mainly composed of O 2p and S 3p orbitals. LTC has been extensively studied concerning PEC H_2 evolution because it exhibits an onset potential of +0.88 V versus RHE, which is among the most positive values for existing photocathode materials. LTC has been shown to promote H_2 and O_2 evolution in a powder suspension in conjunction with sacrificial electron donors and acceptors [50]. Its PEC performance was also enhanced by p-type doping and by forming the solid solution $La_5Ti_2Cu_{0.9}Ag_{0.1}S_5O_7$ (LTCA) [51]. This narrow bandgap semiconductor has received attention as a potential photocathode material due to its excellent H_2 evolution activity. It has been combined with $BaTaO_2N$ and Ta_3N_5 (as photoanode) to construct a p/n PEC cell for unassisted OWS [52,53]. Based on this material's H_2 evolution photocatalytic and PEC activity, it has also been employed in a photocatalyst sheet system in combination with BVO, embedded in a thin conductive Au layer similar to other such systems [54]. A photocatalyst sheet composed of LTCA/Au/BVO showed significantly higher activity than an LTC/Au/BVO system after modifying both sheets with Cr_2O_3/Rh co-catalysts. Analysis by X-ray photoelectron spectroscopy (XPS) (Fig. 7.15A) indicated the presence of metallic and trivalent (Rh_2O_3) Rh species on the LTCA surface, which catalyzed the H_2 evolution reaction. In contrast, RhO_x deposited on BVO did not

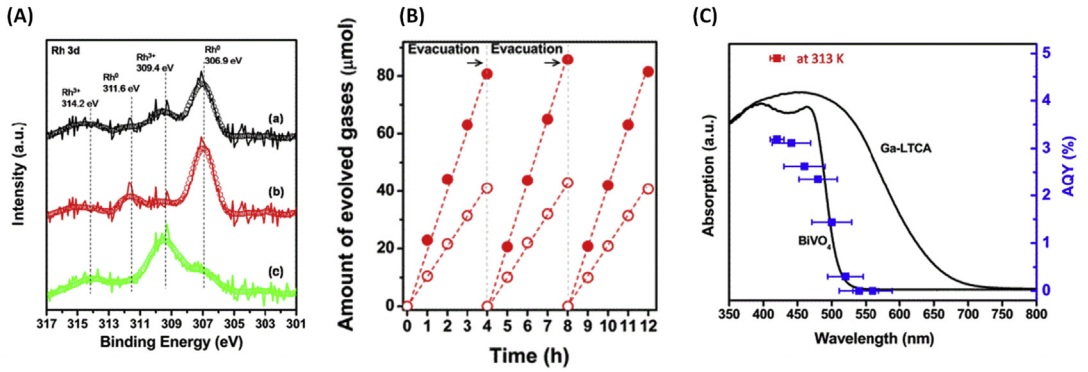

Figure 7.15

(A) Rh 3d XPS spectra obtained from (a) Cr_2O_3/Rh/LTC/Au/$BiVO_4$, (b) Rh/LTC/Au, and (c) Rh/$BiVO_4$/Au sheets, (B) time courses of gas evolution over Cr_2O_3/Rh/LTCA/Au/$BiVO_4$ photocatalyst sheet under visible light. Closed and open circles represent H_2 and O_2, respectively. Reaction conditions: distilled water (pH 6.9, 40 mL); light source, 300 W Xe lamp equipped with a visible light filter ($\lambda > 420$ nm); irradiation area, 8 cm^2. (C) AQY as a function of wavelength for the Cr_2O_3/Rh/LTCA/Au/$BiVO_4$ sheet. *Reprinted with permission from Ref. [54].*

catalyze the OER judging from the very low activity of a RhO_x/BVO/Au sheet. The effects of the p-type doping of LTCA (LTCA:*y*) with lower valence cations such as Ga^{3+}, Al^{3+}, and Mg^{2+} at Ti-sites were also investigated. A photocatalyst sheet having the structure Cr_2O_3/Rh/LTCA: Ga/Au/BVO exhibited the highest OWS activity, with H_2 and O_2 evolution rates of 22.0 and 11.0 μmol/h, respectively, under visible light (300 W Xe lamp, $\lambda > 420$ nm) at 288 K and 5 kPa. Under these conditions, an AQY of 3.2% was obtained at 420 nm [54]. Increasing the temperature to 313 K gave an AQY of 4.9% at 420 nm and an STH of 0.11% (Fig. 7.15B and C). The latter value was one of the highest ever achieved using a nonoxide photocatalytic OWS system absorbing visible light up to 710 nm. However, the maximum utilizable wavelength of this system was restricted to 520 nm owing to the low absorption edge of the BVO photocatalyst.

The replacement of S^{2-} anions with Se^{2-} anions in LTC was also studied by synthesizing a series of solid solution photocatalysts with the composition $La_5Ti_2Cu(S_{1-x}Se_x)_5O_7$ ($0 \geq x \geq 1$) via a solid-state reaction. The incorporation of Se^{2-} generated a VBM at a more negative potential than that for the S^{2-} formulation, such that the absorption edge was red-shifted beyond 700 nm [55]. However, the photocatalytic H_2 evolution activity of the as-synthesized oxysulfoselenides in the presence of sacrificial electron donors was found to decrease with increasing Se^{2-} incorporation due to a reduction in the driving force for water reduction. Co-loading of Pt and NiS as catalysts for water reduction and oxidation of S^{2-} and SO_3^{2-}, respectively, and lowering the calcination temperature to suppress the growth of rod-like particles were found to improve the photocatalytic activity [56,57]. Even so, the H_2 evolution activity of the Se^{2-} containing photocatalysts remained

inferior to that of the parent oxysulfide. Incorporation of Se via diffusion (x = 0.2) was also carried out to generate oxysulfoselenides from well-crystallized and highly active LTC, and the resulting LTC:Se showed an AQY of 0.9% at 420 nm during sacrificial H_2 evolution. This value was higher than that obtained for a material produced using one-step synthesis [58]. A photocatalyst sheet was fabricated using LTC:Se in combination with BVO as the OEP, and this sheet demonstrated stoichiometric evolution of H_2 and O_2, but with an activity that was about one order of magnitude lower than that of a photocatalyst sheet composed of LTCA:Ga/Au/BVO.

4.3.3 $(ZnSe)_{0.5}(CuGa_{2.5}Se_{4.25})_{0.5}$

Metal selenide photocatalysts have much narrower bandgaps than the corresponding metal (oxy)sulfides and oxides due to shallower bands formed by Se 4p orbitals, which are at more negative potentials than the S 3p and O 2p orbitals that generate the VBM [55]. These materials are not usually considered for one-step OWS applications because their VBMs are typically located close to the water oxidation potential, meaning that photo-generated holes oxidize the selenides (that is, photo corrosion proceeds) instead of participating in water oxidation. Selenide materials combined with sacrificial electron donors have been widely studied about H_2 evolution under visible light. Solid solutions of zinc selenide (ZnSe) and copper gallium selenide (CGSe), denoted as ZnSe: CGSe, were prepared by solid-state reactions and absorbed visible light in the range of 480−750 nm depending on the specific composition [59,60]. A recent study using $(ZnSe)_{0.5}(CuGa_{2.5}Se_{4.25})_{0.5}$ modified with a Ni−Ru composite co-catalyst achieved an AQY of 13.7% at 420 nm under visible light (300 W Xe lamp, $\lambda > 420$ nm) during a sacrificial H_2 evolution reaction [60]. $(ZnSe)_{0.5}(CuGa_{2.5}Se_{4.25})_{0.5}$ was subsequently employed as the HEP combined with BVO and Au as the OEP and a conductive layer, respectively. Surface modifications of the mixed photocatalyst sheet with Cr_2O_3/Pt and CoO_x as H_2 and O_2 evolution co-catalysts, respectively, gave an AQY of only 0.54% at 420 nm [59].

A comparison of the OWS activities of ZnSe:CGSe/Au/BVO and the highly efficient STO:Rh, La/Au/BVO:Mo sheet system indicated that H_2 evolution was the rate-determining step when a similar OEP and electron mediator were used for both systems. Therefore, improved charge separation in ZnSe:CGSe is necessary. Similar to PV and PEC cells based on p-type selenide materials, the formation of p-n junctions in sheet systems improves charge separation in the HEP photocatalyst [61]. These junctions can be formed by incorporating an n-type CdS layer (via an impregnation-thermal sulfurization method) on the top of ZnSe:CGSe. The OWS activity of the resulting Pt/CdS/ZnSe:CGSe/Au/BVO sheet was found to slightly decreasing after adding the CdS layer, most likely because the CdS promoted photo corrosion. The deposition of a TiO_2 layer over the CdS using a photo-deposition process suppressed this photo-corrosion effect and consequently

improved the separation of photo-excited charge carriers. Deposition of 5 wt% CdS and 3 mg TiO_2 was optimal and produced H_2 and O_2 at 12.0 and 6.0 μmol/h, respectively, under visible light (300 W Xe lamp) with a much improved AQY of 1.5% at 420 nm.

Detailed investigations of a ZnSe: CGSe/Au/BVO photocatalyst sheet modified with CdS or TiO_2/CdS were performed to clarify the role of these additives. CdS were loaded using an impregnation-thermal sulfurization method with cadmium acetate as the precursor. SEM images of the resulting CdS/ZnSe: CGSe/Au/BVO sheet showed that the CdS nanoparticles were dispersed on the ZnSe:CGSe surface as aggregates, while TiO_2 particles 10 nm in size covered the whole sample surface. Photoexcited electrons were expected to be spontaneously transferred from the CBM of the ZnSe:CGSe to the CdS upon surface modification. However, the sheet showed slightly lower than expected OWS activity due to the photo corrosion effect of CdS involving photoexcited holes. In the case of self-oxidative photo corrosion, h+ from the VBM of the ZnSe:CGSe were transferred to the CdS via the reactions $CdS + 2h+ \rightarrow Cd^{2+} + S$ and $CdS + 4h^{+} + 2H_2O + O_2 \rightarrow Cd^{2+} + SO_4^{2-} + 4H^{+}$. Both CdS/ZnSe: CGSe/Au/BVO and TiO_2/CdS/ZnSe: CGSe/Au/BVO sheets were photo-irradiated for 5 h. The reaction solutions were subsequently analyzed by inductively coupled plasma atomic emission spectroscopy to determine the Cd^{2+} ion concentrations. The results showed 0.014 and 0.002 mg/L concentrations for the CdS-modified and TiO_2/CdS-modified sheets, respectively. These results indicate that deposition of the TiO_2 layer suppressed the CdS photocorrosion effect by preventing the transfer of excited holes from the CdS to water due to the formation of a deep valence band.

5. Development of solar panel reactors for practical implementation

At present, most photocatalyst water splitting systems are based on powder suspensions, which can be readily assessed on a laboratory scale. However, there are several challenges related to the scale-up of these suspension systems for practical applications. For example, a large mechanical stirring process is necessary to maintain the suspension state of the photocatalyst, which results in the need for additional energy input. As well, collecting the H_2 that is produced requires a large gas-tight reactor and gas circulation system. Finally, it is difficult to recycle the suspended photocatalyst powder on a large scale. Those disadvantages significantly increase the cost of suspended powder photocatalyst water splitting systems when used on a large scale.

One alternative to suspensions is to immobilize the photocatalyst on a suitable panel, similar to the fixed bed morphologies used in conventional catalytic reactions. This configuration mitigates the major shortcomings of suspended powder systems. Schröder et al. reported a panel-type reactor for photocatalytic H_2 evolution in the presence of a sacrificial electron donor. The photocatalyst was immobilized on a stainless-steel plate

array in the reactor [62]. This prior work demonstrated that photocatalytic water splitting panels could be used on a large scale. However, compared with the H_2 evolution half-reaction, it is more challenging to perform OWS with a panel reactor since a suitable photocatalyst is required. As noted above, Al-doped STO has been found to function as a highly active photocatalyst for OWS. So this material may be a good candidate for the fabrication of water splitting panels. Goto et al. reported a water-splitting panel reactor based on fixed Al-doped STO as the photocatalyst. When filled with a 1 mm deep layer of water, this reactor rapidly released bubbles of the gaseous reaction products without forced convection (Fig. 7.16A). An STH efficiency of 0.4% was achieved under natural sunlight using a flat panel reactor with a 1 m^2 light-accepting area. The original activity level of the photocatalyst was found to be maintained for at least the initial 150 h of the trial [63]. Recently, these 1 m^2 panels have been extended to produce a 100 m^2 array of panel reactors (Fig. 7.16C) [64]. This system functioned safely over several months, during which hydrogen was automatically collected from the moist gaseous product

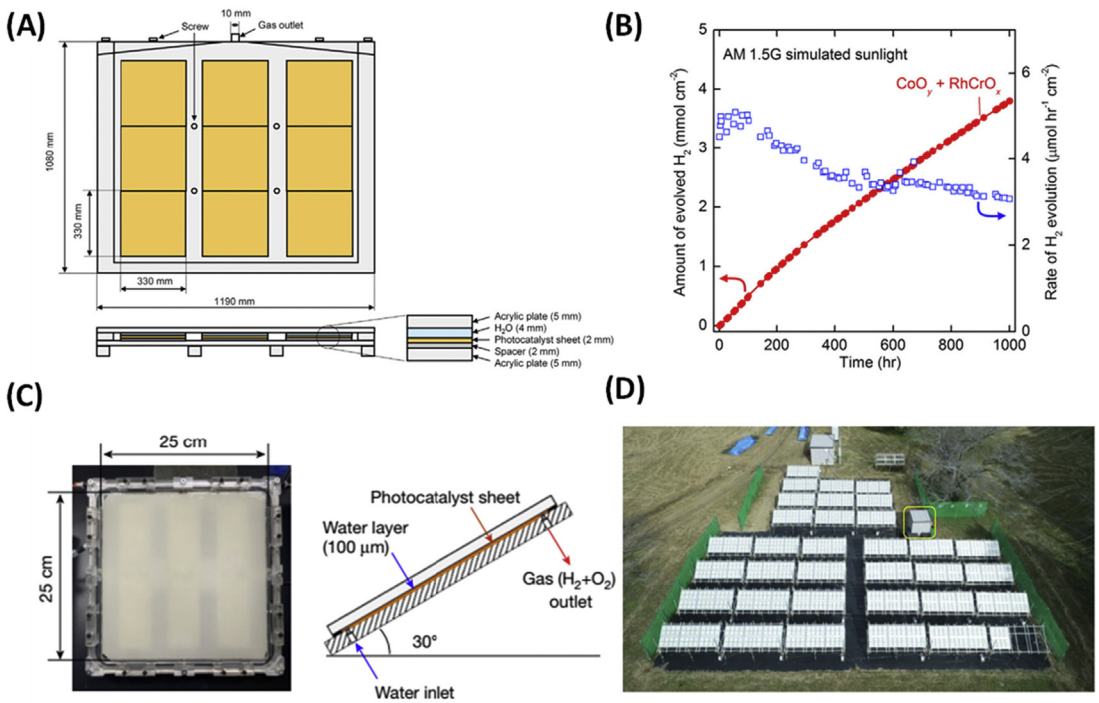

Figure 7.16

(A) Diagram of a 1 × 1 m water-splitting panel, (B) time courses of water splitting reaction over 5 × 5 cm panel containing $SrTiO_3$:Al loaded with $RhCrO_x$ and CoO_y under simulated sunlight (AM 1.5 G). (C) Photographic image and diagram of 625 cm^2 panel reactor unit. (D) Overhead view of 100 m^2 solar hydrogen production system consisting of 1600 panel reactor units. *Reprinted with permission from (B) Ref. [63] (D) Ref. [64].*

mixture via a gas separation membrane. A maximum STH of 0.76% was achieved in field tests. Although the present system cannot produce hydrogen with a net energy gain, it demonstrates the concept of safe, large-scale photocatalytic water splitting in conjunction with gas separation and collection.

6. Summary and prospects

This chapter summarizes the development of various prospective photocatalysts while also examining the associated reaction mechanisms and the design of state-of-the-art photocatalyst sheets for the OWS reaction. These units have exhibited significantly higher OWS activity than powder suspension and parallel cells based on STO:Rh, La, and BVO:Mo photocatalysts. This improved performance is obtained because the HEP and OEP are rigidly embedded in conductive layers so that surface chemical reactions are close to one another. This concept is readily scalable and permits efficient electron transfer between the HEP and OEP while reducing solution resistance and inhibiting the formation of the pH gradients that occur in PEC cells. Therefore, supporting electrolytes or pH adjustments are not required to drive the OWS reaction. This review shows that metal oxide photocatalysts with wide bandgaps have been assessed and have exhibited STH values as high as 1.2% and 1.0% under reduced and ambient pressure, respectively, in the case that backward reactions are suppressed by applying Cr_2O_3 and TiO_2 protecting layers. Among the various narrow bandgap nonoxide photocatalysts, $LaMg_{2/3}Ta_{1/3}O_2N$, $La_5Ti_2Cu_{0.9}Ag_{0.1}S_5O_7$, and $(ZnSe)_{0.5}(CuGa_{2.5}Se_{4.25})_{0.5}$ (as HEPs) and $LaTiO_2N$ (as an OEP) have been employed in sheet systems. However, the efficiency of such systems is several times lower than those of OWS systems composed of STO:Rh, La, and BVO:Mo. The highest efficiency achieved was only 0.11% under reduced pressure, using $La_5Ti_2Cu_{0.9}Ag_{0.1}S_5O_7$:Ga and BVO as the HEP and OEP, respectively. The properties of OWS systems involving narrow bandgap photocatalysts at elevated pressures have not yet been examined.

Another important obstacle to research in this field is the unavailability of efficient narrow bandgap OEPs. To date, BVO and WO_3 have been primarily used to construct visible-light-driven Z-scheme OWS systems in combination with various HEPs. However, the maximum useable wavelength of a Z-scheme OWS system depends on the particular wide bandgap energy photocatalyst employed as either HEP or OEP. For example, photocatalyst sheets composed of STO: Rh, La + BVO: Mo, and $La_5Ti_2Cu_{0.9}Ag_{0.1}S_5O_7$:Ga + BVO can utilize visible light up to 520 and 540 nm, respectively. Achieving STH values over 5% will require utilizing a large portion of the visible light spectrum. Several recently reported photocatalysts, such as YTOS and Ta_3N_5, can promote one-step OWS and should be considered potential OEPs employed in Z-schemes based on their VBM potentials.

Several crucial challenges remain concerning producing hydrogen as an energy source that can compete with traditional fossil fuels. Firstly, the highest STH efficiency obtained at ambient pressure thus far with an OWS panel is still lower than the threshold of 5%−10% necessary for practical applications. The primary reason for this low efficiency is that the bandgap of Al-doped STO is too wide to utilize a large portion of visible light wavelengths, which account for more than 50% of the total solar energy. Therefore, developing photocatalysts with narrow bandgaps will be indispensable for achieving high STH efficiency soon. Secondly, the stability of present-day photocatalysts is still insufficient for long-term operation. Although panels with deactivated photocatalysts can be replaced easily, enhanced stability would significantly reduce operating costs. Thirdly, the efficiency with which product gases are separated must be further improved to extract the most H_2 possible while also increasing the safety of H_2 gas storage and operation. Lastly, the material costs for constructing an entire OWS system must be reduced to maximize the benefits of such facilities. Considerable effort will be required to develop photocatalysts, gas separation membranes, gas storage units, and integrated systems before the commercialization of photocatalytic OWS panel systems is a viable approach to addressing environmental concerns.

Acknowledgments

This work was financially supported by the Artificial Photo-synthesis Project of the New Energy and Industrial Technology Development Organization (NEDO).

Authors contributions

SN, LL, and KD wrote the manuscript. KD directed the research.

References

[1] Q. Wang, K. Domen, Particulate photocatalysts for light-driven water splitting: mechanisms, challenges, and design strategies, Chem. Rev. 120 (2020) 919−985.
[2] T. Hisatomi, K. Domen, Introductory lecture: sunlight-driven water splitting and carbon dioxide reduction by heterogeneous semiconductor systems as key processes in artificial photosynthesis, Faraday Discuss. 198 (2017) 11−35.
[3] L. Lin, T. Hisatomi, S. Chen, T. Takata, K. Domen, Visible-light-driven photocatalytic water splitting: recent progress and challenges, Trends Chem. 2 (2020) 813−824.
[4] S. Nandy, S.A. Savant, S. Haussener, Prospects and challenges in designing photocatalytic particle suspension reactors for solar fuel processing, Chem. Sci. 12 (2021) 9866−9884.
[5] T. Hisatomi, J. Kubota, K. Domen, Recent advances in semiconductors for photocatalytic and photoelectrochemical water splitting, Chem. Soc. Rev. 43 (2014) 7520−7535.
[6] G.M. Walter, L.E. Warren, J.R. McKone, S.W. Bottcher, Q. Mi, E.A. Santori, N.S. Lewis, Solar water splitting cells, Chem. Rev. 110 (2010) 6446−6473.
[7] A. Nakamura, Y. Ota, K. Koike, Y. Hidaka, K. Nishioka, M. Sugiyama, K.A. Fujii, A 24.4% solar to hydrogen energy conversion efficiency by combining concentrator photovoltaic modules and electrochemical cells, Appl. Phys. Express 8 (2015) 107101−107104.

[8] J. Jia, L.C. Seitz, J.D. Benck, Y. Huo, Y. Chen, J.W.D. Ng, T. Bilir, J.S. Harris, T.F. Jaramillo, Solar water splitting by photovoltaic-electrolysis with a solar-to-hydrogen efficiency over 30%, Nat. Commun. 7 (2016) 13237.
[9] B.A. Pinaud, J.D. Benck, L.C. Seitz, A.J. Forman, Z. Chen, T.G. Deutsch, B.D. James, K.N. Baum, G.N. Baum, S. Ardo, H. Wang, E. Miller, T.F. Jaramillo, Technical and economic feasibility of centralized facilities for solar hydrogen production via photocatalysis and photoelectrochemistry, Energy Environ. Sci. 6 (2013) 1983−2002.
[10] T. Takata, K. Domen, Particulate photocatalysts for water splitting: recent advances and future prospects, ACS Energy Lett. 4 (2019) 542−549.
[11] K. Domen, S. Naito, M. Soma, T. Onishi, K. Tamaru, Photocatalytic decomposition of water vapour on an NiO-$SrTiO_3$ catalyst, J. Chem. Soc. Chem. Commun. (1980) 543−544.
[12] Y. Ham, T. Hisatomi, Y. Goto, Y. Moriya, Y. Sakata, A. Yamakata, J. Kubota, K. Domen, Flux-mediated doping of $SrTiO_3$ photocatalysts for efficient overall water splitting, J. Mater. Chem. 4 (2016) 3027−3033.
[13] H. Lyu, T. Hisatomi, Y. Goto, et al., An Al-doped $SrTiO_3$ photocatalyst maintaining sunlight-driven overall water splitting activity for over 1000 h of constant illumination, Chem. Sci. 10 (2019) 3196−3201.
[14] T.H. Chiang, H. Lyu, T. Hisatomi, Y. Goto, T. Takata, M. Katayama, T. Minegishi, K. Domen, Efficient photocatalytic water splitting using Al-doped $SrTiO_3$ coloaded with molybdenum oxide and rhodium−chromium oxide, ACS Catal. 8 (2018) 2782−2788.
[15] T. Takata, J. Jiang, Y. Sakata, M. Nakabayashi, N. Shibata, V. Nandal, K. Seki, T. Hisatomi, K. Domen, Photocatalytic water splitting with a quantum efficiency of almost unity, Nature 581 (2020) 411−414.
[16] S. Chen, T. Takata, K. Domen, Particulate photocatalysts for overall water splitting, Nat. Rev. Mater. 2 (2017) 17050.
[17] Z. Wang, Y. Inoue, T. Hisatomi, R. Ishikawa, Q. Wang, T. Takata, S. Chen, N. Shibata, Y. Ikuhara, K. Domen, Overall water splitting by Ta_3N_5 nanorod single crystals grown on the edges of $KTaO_3$ particles, Nat. Catal. 1 (2018) 756−763.
[18] C. Pan, T. Takata, M. Nakabayashi, T. Matsumoto, N. Shibata, Y. Ikuhara, K. Domen, A complex perovskite-type oxynitride: the first photocatalyst for water splitting operable at up to 600 nm, Angew. Chem. Int. Ed. 54 (2015) 2955−2959.
[19] C. Pan, T. Takata, K. Domen, Overall water splitting on the transition-metal oxynitride photocatalyst $LaMg_{1/3}Ta_{2/3}O_2N$ over a large portion of the visible-light spectrum, Chem. Eur. J. 22 (2016) 1854−1862.
[20] G. Hitoki, et al., Ta_3N_5 as anNovel visible light-driven photocatalyst (λ<600 nm), Chem. Lett. 31 (2002) 736−737.
[21] A. Ishikawa, T. Takata, J.N. Kondo, M. Hara, H. Kobayashi, K. Domen, Oxysulfide $Sm_2Ti_2S_2O_5$ as a stable photocatalyst for water oxidation and reduction under visible light irradiation ($\lambda \leq 650$ nm), J. Am. Chem. Soc. 124 (2002) 13547−13553.
[22] M. Goga, R. Seshadri, V. Ksenofontov, P. Gütlich, W. Tremel, $Ln_2Ti_2S_2O_5$ (Ln = Nd, Pr, Sm): a novel series of defective Ruddlesden−Popper phases, Chem. Commun. (1999) 979−980.
[23] S.G. Denis, S.J. Clarke, Two alternative products from the intercalation of alkali metals into cation-defective Ruddlesden−Popper oxysulfides, Chem. Commun. (2001) 2356−2357.
[24] O.J. Rutt, T.L. Hill, Z.A. Gál, M.A. Hayward, S.J. Clarke, The cation-deficient Ruddlesden−Popper oxysulfide $Y_2Ti_2O_5S_2$ as a layered sulfide: topotactic potassium intercalation to form $KY_2Ti_2O_5S_2$, Inorg. Chem. 42 (2003) 7906−7911.
[25] J.A. Cody, J.A. Ibers, Synthesis and characterization of the new rare-earth/transition-metal oxysulfides $La_6Ti_2S_8O_5$ and $La_4Ti_3S_4O_8$, J. Solid State Chem. 114 (1995) 406−412.
[26] C. Boyer-Candalen, J. Derouet, P. Porcher, Y. Moëlo, A. Meerschaut, The family of $Ln_2Ti_2S_2O_5$ cCompounds (Ln=Nd, Sm, Gd, Tb, Dy, Ho, Er, and Y): optical properties, J. Solid State Chem. 165 (2002) 228−237.

[27] G. Ma, S. Chen, Y. Kuang, S. Akiyama, T. Hisatomi, M. Nakabayashi, N. Shibata, M. Katayama, T. Minegishi, K. Domen, Visible light-driven Z-scheme water splitting using oxysulfide H_2 evolution photocatalysts, J. Phys. Chem. Lett. 7 (2016) 3892−3896.
[28] A. Ishikawa, Y. Yamada, T. Takata, J.N. Kondo, M. Hara, H. Kobayashi, K. Domen, Novel synthesis and photocatalytic activity of oxysulfide $Sm_2Ti_2S_2O_5$, Chem. Mater. 15 (2003) 4442−4446.
[29] Q. Wang, M. Nakabayashi, T. Hisatomi, S. Sun, S. Akiyama, Z. Wang, Z. Pan, X. Xiao, T. Watanabe, T. Yamada, N. Shibata, T. Takata, K. Domen, Oxysulfide photocatalyst for visible-light-driven overall water splitting, Nat. Mater. 18 (2019) 827−832.
[30] X. Wang, K. Maeda, A. Thomas, K. Takanabe, G. Xin, J.M. Carlsson, K. Domen, M. Antonietti, A metal-free polymeric photocatalyst for hydrogen production from water under visible light, Nat. Mater. 8 (2009) 76−80.
[31] G. Zhang, Z.-A. Lan, L. Lin, S. Lin, X. Wang, Overall water splitting by Pt/g-C_3N_4 photocatalysts without using sacrificial agents, Chem. Sci. 7 (2016) 3062−3066.
[32] Z. Pan, S. Wang, P. Niu, M. Liu, X. Wang, Photocatalytic overall water splitting by spatially-separated Rh and RhO_x cocatalysts on polymeric carbon nitride nanosheets, J. Catal. 379 (2019) 129−137.
[33] Z. Pan, Y. Zheng, F. Guo, P. Niu, X. Wang, Decorating CoP and Pt nanoparticles on graphitic carbon nitride nanosheets to promote overall water splitting by conjugated polymers, ChemSusChem 10 (2017) 87−90.
[34] W. Liu, L. Cao, W. Cheng, Y. Cao, X. Liu, W. Zhang, X. Mou, L. Jin, X. Zheng, W. Che, Q. Liu, T. Yao, S. Wei, Single-site active cobalt-based photocatalyst with a long carrier lifetime for spontaneous overall water splitting, Angew. Chem. Int. Ed. 56 (2017) 9312−9317.
[35] M.J. Bojdys, J.-O. Müller, M. Antonietti, A. Thomas, Ionothermal synthesis of crystalline, condensed, graphitic carbon nitride, Chem. Eur. J. 14 (2008) 8177−8182.
[36] E. Wirnhier, M. Döblinger, D. Gunzelmann, J. Senker, B.V. Lotsch, W. Schnick, Poly(triazine imide) with intercalation of lithium and chloride ions $[(C_3N_3)_2(NH_xLi_{1-x})_3 \cdot LiCl]$: a crystalline 2D carbon nitride network, Chem. Eur. J. 17 (2011) 3213−3221.
[37] L. Lin, C. Wang, W. Ren, H. Ou, Y. Zhang, X. Wang, Photocatalytic overall water splitting by conjugated semiconductors with crystalline poly(triazine imide) frameworks, Chem. Sci. 8 (2017) 5506−5511.
[38] L. Lin, Z. Lin, J. Zhang, X. Cai, W. Lin, Z. Yu, X. Wang, Molecular-level insights on the reactive facet of carbon nitride single crystals photocatalysing overall water splitting, Nat. Catal. 3 (2020) 649−655.
[39] L. Wang, Y. Wan, Y. Ding, S. Wu, Y. Zhang, X. Zhang, G. Zhang, Y. Xiong, X. Wu, J. Yang, H. Xu, Conjugated microporous polymer nanosheets for overall water splitting using visible light, Adv. Mater. 29 (2017) 1702428.
[40] L. Wang, X. Zheng, L. Chen, Y. Xiong, H. Xu, Van der Waals heterostructures comprised of ultrathin polymer nanosheets for efficient Z-scheme overall water splitting, Angew. Chem. Int. Ed. 57 (2018) 3454−3458.
[41] Y. Bai, K. Nakagawa, A.J. Cowan, C.M. Aitchison, Y. Yamaguchi, M.A. Zwijnenburg, A. Kudo, R.S. Sprick, A.I. Cooper, Photocatalyst Z-scheme system composed of a linear conjugated polymer and $BiVO_4$ for overall water splitting under visible light, J. Mater. Chem. 8 (2020) 16283−16290.
[42] Q. Wang, Y. Li, T. Hisatomi, M. Nakabayashi, N. Shibata, J. Kubota, K. Domen, Z-scheme water splitting using particulate semiconductors immobilized onto metal layers for efficient electron relay, J. Catal. 328 (2015) 308−315.
[43] Q. Wang, T. Hisatomi, M. Katayama, T. Takata, T. Minegishi, A. Kudo, T. Yamada, K. Domen, Particulate photocatalyst sheets for Z-scheme water splitting: advantages over powder suspension and photoelectrochemical systems and future challenges, Faraday Discuss. 197 (2017) 491−504.
[44] Q. Wang, T. Hisatomi, Q. Jia, H. Tokudome, et al., Scalable water splitting on particulate photocatalyst sheets with a solar-to-hydrogen energy conversion efficiency exceeding 1%, Nat. Mater. 15 (2016) 611−616.

[45] Q. Wang, T. Hisatomi, Y. Suzuki, Z. Pan, et al., Particulate photocatalyst sheets based on carbon conductor layer for efficient Z-scheme pure-water splitting at ambient pressure, J. Am. Chem. Soc. 139 (2017) 1675−1683.
[46] Z. Pan, T. Hisatomi, Q. Wang, et al., Photocatalyst sheets composed of particulate $LaMg_{1/3}Ta_{2/3}O_2N$ and Mo-doped $BiVO_4$ for Z-scheme water splitting under visible light, ACS Catal. 6 (2016) 7188−7196.
[47] Z. Pan, T. Hisatomi, Q. Wang, et al., Photoreduced graphene oxide as a conductive binder to improve the water splitting activity of photocatalyst sheets, Adv. Funct. Mater. 26 (2016) 7011−7019.
[48] Z. Pan, T. Hisatomi, Q. Wang, et al., Application of $LaMg_{1/3}Ta_{2/3}O_2N$ as a hydrogen evolution photocatalyst of a photocatalyst sheet for Z-scheme water splitting, Appl. Catal. Gen. 521 (2016) 26−33.
[49] V. Meignen, L. Cario, A. Lafond, Y. Moëlo, C. Guillot-Deudon, A. Meerschaut, Crystal structures of two new oxysulfides $La_5Ti_2MS_5O_7$ (M=Cu, Ag): evidence of anionic segregation, J. Solid State Chem. 177 (2004) 2810−2817.
[50] T. Suzuki, T. Hisatomi, K. Teramura, Y. Shimodaira, H. Kobayashi, K. Domen, A titanium-based oxysulfide photocatalyst: $La_5Ti_2MS_5O_7$ (M = Ag, Cu) for water reduction and oxidation, Phys. Chem. Chem. Phys. 14 (2012) 15475−15481.
[51] J. Liu, T. Hisatomi, G. Ma, A. Iwanaga, T. Minegishi, Y. Moriya, M. Katayama, J. Kubota, K. Domen, Improving the photoelectrochemical activity of $La_5Ti_2CuS_5O_7$ for hydrogen evolution by particle transfer and doping, Energy Environ. Sci. 7 (2014) 2239−2242.
[52] T. Higashi, Y. Shinohara, et al., Sunlight-driven overall water splitting by the combination of surface-modified $La_5Ti_2Cu_{0.9}Ag_{0.1}S_5O_7$ and $BaTaO_2N$ photoelectrodes, ChemPhotoChem 1 (2017) 167−172.
[53] T. Higashi, Y. Sasaki, Y. Kawase, H. Nishiyama, M. Katayama, K. Takanabe, K. Domen, Surface-modified Ta_3N_5 photoanodes for sunlight-driven overall water splitting by photoelectrochemical cells, Catalysts 11 (2021) 584.
[54] S. Sun, T. Hisatomi, Q. Wang, S. Chen, G. Ma, J. Liu, S. Nandy, T. Minegishi, M. Katayama, K. Domen, Efficient redox-mediator-free Z-scheme water splitting employing oxysulfide photocatalysts under visible light, ACS Catal. 8 (2018) 1690−1696.
[55] S. Nandy, Y. Goto, T. Hisatomi, Y. Moriya, T. Minegishi, M. Katayama, K. Domen, Synthesis and photocatalytic activity of $La_5Ti_2Cu(S_{1-x}Se_x)_5O_7$ solid solutions for H_2 production under visible light irradiation, ChemPhotoChem 1 (2017) 265−272.
[56] S. Nandy, T. Hisatomi, G. Ma, T. Minegishi, M. Katayama, K. Domen, Enhancement of the H_2 evolution activity of $La_5Ti_2Cu(S_{1-x}Se_x)_5O_7$ photocatalysts by coloading Pt and NiS cocatalysts, J. Mater. Chem. 5 (2017) 6106−6112.
[57] S. Nandy, T. Hisatomi, M. Katayama, T. Minegishi, Domen, Effects of calcination temperature on the physical properties and hydrogen evolution activities of $La_5Ti_2Cu(S_{1-x}Se_x)_5O_7$ photocatalysts, Part. Part. Syst. Char. 35 (2018) 1700275.
[58] S. Nandy, T. Hisatomi, S. Sun, M. Katayama, T. Minegishi, Domen, Effects of Se incorporation in $La_5Ti_2CuS_5O_7$ by annealing on physical properties and photocatalytic H_2 evolution activity, ACS Appl. Mater. Interfaces 11 (2019) 5595−5601.
[59] S. Chen, G. Ma, Q. Wang, et al., Metal selenide photocatalysts for visible-light-driven Z-scheme pure water splitting, J. Mater. Chem. 7 (2019) 7415−7422.
[60] S. Chen, J.J.M. Vequizo, T. Hisatomi, et al., Efficient photocatalytic hydrogen evolution on single-crystalline metal selenide particles with suitable cocatalysts, Chem. Sci. 11 (2020) 6436−6441.
[61] S. Chen, J.J.M. Vequizo, Z. Pan, et al., Surface modifications of $(ZnSe)_{0.5}(CuGa_{2.5}Se_{4.25})_{0.5}$ to promote photocatalytic Z-scheme overall water splitting, J. Am. Chem. Soc. 143 (2021) 10633−10641.
[62] M. Schröder, K. Kailasam, et al., Hydrogen evolution reaction in a large-scale reactor using a carbon nitride photocatalyst under natural sunlight irradiation, Energy Technol. 3 (2015) 1014−1017.
[63] Y. Goto, T. Hisatomi, Q. Wang, et al., A particulate photocatalyst water-splitting panel for large-scale solar hydrogen generation, Joule 2 (2018) 509−520.
[64] H. Nishiyama, T. Yamada, et al., Photocatalytic solar hydrogen production from water on a 100-m^2 scale, Nature 598 (2021) 304−307.

CHAPTER 8

Advanced carbon nanomaterial–based anodes for sodium-ion batteries

Ghulam Yasin[1,2], Shumaila Ibraheem[1,2], Sehrish Ibrahim[3], Anuj Kumar[4], Muhammad Asim Mushtaq[1], Rajesh Pathak[5]

[1]Institute for Advanced Study, Shenzhen University, Shenzhen, Guangdong, China; [2]College of Physics and Optoelectronic Engineering, Shenzhen University, Shenzhen, Guangdong, China; [3]College of Life Science and Technology, Beijing University of Chemical Technology, Beijing, China; [4]Nano-Technology Research Laboratory, Department of Chemistry, GLA University, Mathura, Uttar Pradesh, India; [5]Applied Materials Division, Argonne National Laboratory, Lemont, IL, United States

Abstract

Electrochemical storage technology of sodium ions is an intriguing approach because of its ease of establishment, low cost, and great efficiency compared to its counterparts. Sodium-ion batteries a viable alternative to lithium-ion batteries have recently gained much attention due to sodium's abundant supply, low cost, and remarkable physicochemical properties. Advances in anode materials have made SIBs technology much easier in recent years. Therefore, anodes made of carbonaceous materials are the most promising for SIBs due to their low cost, long-term stability, and excellent conductivity. In this chapter, we have highlighted the recent advancements on nanocarbon-based materials, for instance, carbon quantum dots, carbon nanofibers, carbon nanotubes, graphene, amorphous carbon, and graphite as potential anodes for the development of high-performance SIBs.

Keywords: Anodes; Carbon nanomaterials; Sodium-ion batteries; Sodium-ion storage.

1. Introduction

Energy, the environment, and water are three of the most important concerns society is dealing with right now [1,2]. These three big concerns are growing more significant as the world's population rises and fossil fuel consumption expands [3–8]. Transitioning to a renewable energy system is no longer an option for combating energy and natural resource depletion, global warming, and climate change challenges [9–13]. For this reason, next-

Advanced Nanomaterials and Their Applications in Renewable Energy. https://doi.org/10.1016/B978-0-323-99877-2.00008-4

generation electrochemical energy conversion and storage technologies are crucial in today's situation [14–19]. In this context, lithium-ion batteries (LIBs), a kind of secondary battery, have long been regarded as the most practical energy storage and conversion device because of their obvious advantages in energy and power density [20–27]. However, because of the limited supply and irregular distribution of Li in the Earth's crust, concerns about lithium's (Li) availability increase as the demand for LIB's rises [28,29].

In contrast, sodium (Na) is plentiful and serves the same duties; therefore, LIBs can be replaced as a viable option by sodium-ion battery (SIB) systems, although their electrochemical activity is often modest [30,31]. Because Na has a larger electrochemical potential than Li, it can operate at lower voltages and hence has lower energy densities. On the other hand, energy density is not a major issue in large-scale energy storage systems (ESSs). When cycling an SIB, Na^+ ions are heavier and bigger than Li^+ ions, resulting in slower diffusion inside a solid electrode during cycling and more electrode volume expansion than LIBs. In recent years, many cathode materials have been suggested for SIBs, but data on anode materials is few [32].

Nanocarbon-based anode materials for the development of electrochemical energy storage technologies have been intensively investigated, owing to their low cost, high conductivity, and surface area, as well as their high availability in nature. Even though some nanocarbon-based materials have inadequate rate capabilities and deliver deprived cycling performance [33]. However, customizing the size and structure of carbon nanostructures is a successful strategy for increasing its electron and ion transport capabilities. For instance, carbon materials with certain morphologies and nanodimensions exhibit excellent ion transport and electrical conductivity, as well as exceptional mechanical proficiencies. The shorter ion-diffusion distances are typically achieved by using carbon materials with nanodimensions to improve Na^+ diffusion and rapid electron/ion transportation. When it comes to improving the electrochemical characteristics of electrode materials, various nanostructures have a distinct impact on enabling enhanced storage capacity and rate performance.

In addition, there are various investigations on carbonaceous materials, including hard and soft carbons and graphite, for use as anode materials in SIBs. For SIBs, nongraphitizable hard carbon, the first carbon to be employed as anode materials, is the utmost auspicious anode material at the moment. Nanocarbons with a variety of sizes and degrees of graphitization (such as carbon quantum dots (CQD), carbon nanotubes (CNTs), carbon nanofibers (CNFs), graphene, and graphite) display a wide range of electrochemical properties due to the divergences in their microstructures. There has been a substantial increase in publications on nanostructured carbon-based materials for SIB since 2011. Therefore, this chapter briefly summarizes the advancement and use of nanocarbon as high-performance anode materials for next-generation SIBs.

2. Carbon nanomaterials for high-performance SIBs

Various carbon nanomaterials and nanoarchitectures and their modification approaches have been studied in terms of their size and graphitization level to develop SIB anodes. Fig. 8.1 summarizes some critical strategies, such as the introduction of heteroatoms to tailor their electronic structures, the control of pore structure to adapt their physical properties, the introduction of functional groups to change their chemical properties, and the design and construction of hybrid or hierarchical materials to change their chemical properties [33].

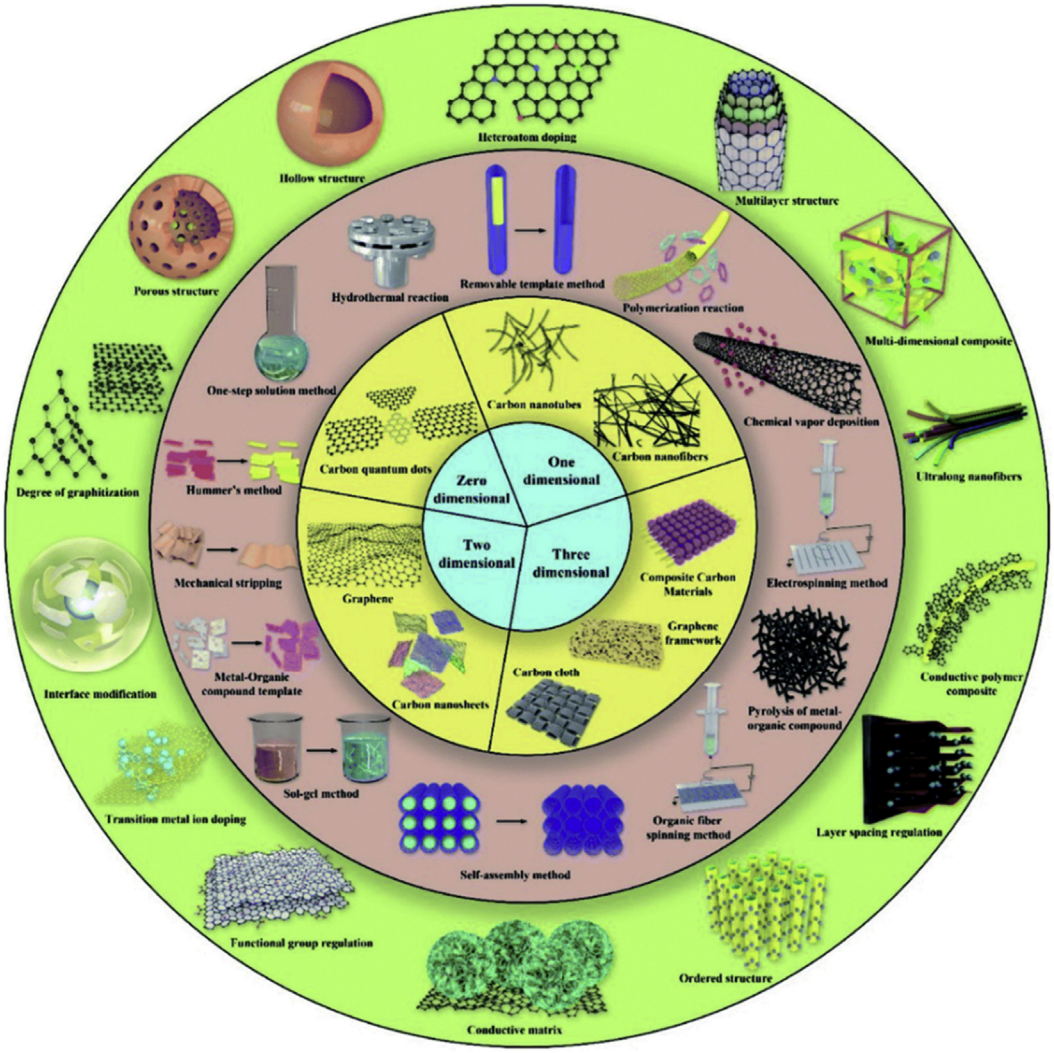

Figure 8.1
A variety of carbon nanostructures and the methods used to modify them [33].

2.1 Carbon quantum dots

Due to their nontoxicity, facile construction, wider excitation-dependent emission, and optical absorption behavior, a new generation of carbon-based nanomaterials have emerged and attracted considerable attention, making them particularly well suited for applications in photocatalysis, green energy production and storage, bioimaging, sensor technology, and other fields [34]. They were constructing CQDs from acetone in a single process with the help of sodium hydroxide (NaOH), which was recently characterized as a suitable anode material for SIBs. They worked well and enabled high electrochemical performance, with long cycle lifetimes and extremely high rates [35].

In addition to improving electrical conductivity and efficiency, lessening charge transfer resistance, and enhancing kinetics. It has been discovered that TiO_2 nanorods/CQD composites can be synthesized by using hydrothermal reactions of P and NaOH in the presence of CDs, which were followed by ion exchange and heating treatments, can significantly improve the electrical conductivity and charge transfer capacities of TiO_2 nanorods [36]. After 300 cycles at 5C, the composite retains 93.6% of its capacity, 166 mA h g^{-1} [36]. Rutile TiO_2 nanoparticles were transformed into needle-like by CQDs, which then self-organized into a 3D petal-like structure with amazing long-term cycles. It is possible to retain an overall rate of 94.4% after 4000 cycles, even when the current flow rate is as high as possible, such as 10C (3350 mAg^{-1}) [37].

2.2 Carbon nanotubes

For secondary batteries demanded to deliver high capacity and long-term stability, normal nanocarbon particles with an unstable surface morphology are inappropriate nanomaterials because they were easily aggregated and lost their benefits in terms of nanostructure and high surface-to-volume ratio. Nanocarbon materials with a higher surface area, such as CNTs and CNFs, which are one-dimensional (1D), have drawn much interest due to their unusual physical and chemical properties [38]. CNTs are the 1D allotrope of the carbon atom. They have many advantages over other carbon nanostructures, such as typical graphite and other carbon nanoparticles, because of their higher specific surface area (SSA), greater electrical conductivity, and hollow structure, which reduce volume expansion when storing Na^+ ions, compared to other carbon nanostructures, for instance, graphite and carbon nanoparticles.

As conductive additives and current collectors, CNTs are also commonly employed to enhance the performance and alter the existing electrode materials. CNT bundles and even individual and single CNT become current collectors when connected to active materials. Not only could they be used as a skeleton to hold the active material in place, but they also provided a significant amount of surface area, quick transport routes, and a significant

amount of flexibility and mechanical strength [39,40]. CNTs may be introduced to precursors at the early stages of the active material's synthetic process, allowing for higher penetration of CNTs into and through the active material. Functional groups like −COOH, $-NH_3$, or −OH are often added to CNTs to enhance the chemical bond between the prepared active materials and CNTs. Instead of being grown outside of the active material, CNTs may be grown directly inside it. A hybrid cathode and anode based on CNTs are possible, in which, the CNTs themselves could work as anodes.

2.3 Carbon nanofibers

Carbon nanofibers have gotten much attention lately because they are small. Various methods have been used to produce CNF, including chemical vapor deposition growth, template-based synthesis, electrospinning, and direct pyrolysis [41]. Their storage capacity is high, around 200−400 mA h g^{-1}, because of many defects and improved electronic and ionic conductivity. For 400 cycles, the hollow carbon nanowires (CNWs) synthesized from pyrolyzed hollow polyaniline precursors had remarkable cycling stability and a high reversible storage capacity over 251 mA h g^{-1} [42].

The performance of SIBs could be facilitated by the CNF network's enhanced electronic conductivity, ions transportation, and pore access for electrolytes [43]. An N, O-dual doped carbon (NOC) network has been devised and manufactured, making it ideal for Na^+ storage. Due to its high specific capacity and ultra-long cycling stability, it can supply 545 mA h g^{-1} at 100 mA g^{-1} after 100 cycles and maintain 240 mA h g^{-1} at 2 A g^{-1} after 2000 cycles. When combined with N, O-dual-doped active sites, the NOC composite increases Na^+ ions storage capacity by enhancing ions diffusion in 3D well-defined porous network. Due to its innovative 3D porous interconnected nanostructure and N, O-dual doping, the NOC composite has shown excellent electrochemical performance. For example, as illustrated in Fig. 8.2, the 3D-linked CNFs could be used as electron transport channels. In contrast, huge numbers of nanopores in NOC can be used as reservoirs for the additional storage of Na^+ ions [43].

2.4 Graphene

Because of its huge surface area and high electrical conductivity, graphene has shown to be an excellent electrode material for storing and transporting ions and electrons in metal-ion batteries. Furthermore, the high degree of elasticity of the graphene film prevents the active ingredients from being pulverized, resulting in good film stability [44−51]. NaCl has been shown to adhere to both sides of graphene layers, resulting in exceptional capacity over 300−550 mA h g^{-1}. When it deals with graphene sheets, it has been discovered that the strong π−π interactions between them can cause difficulties with dispersion, restacking, and multilayer thickness during the synthesis process. This avoids

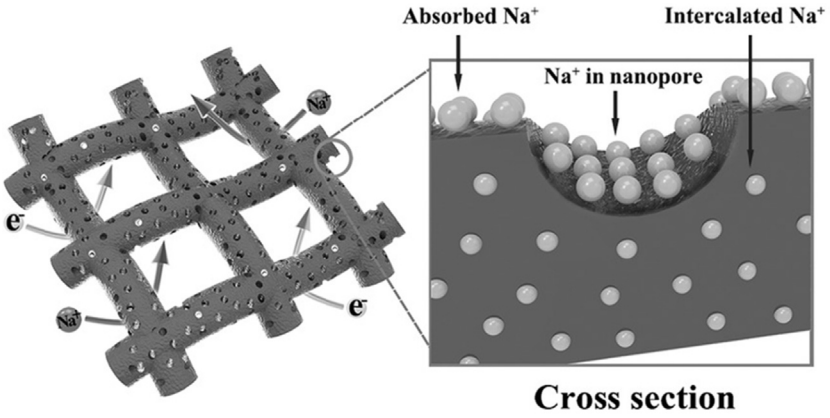

Figure 8.2
Schematic diagram depicting the flow of Na-ions and electrons in the nitrogen and oxygen dual-doped carbon composite network [43].

fully recognizing its large SS, outstanding electrical conductivity, and remarkable theoretical storage capacity, lowering its electrochemical performance toward SIBs.

The high surface area of graphene nanosheets and their resilience and electrical conductivity make them excellent electrode materials for electrochemical energy storage devices after being reduced in size. In recent years, such nanosheets have made their way into the field of SIB devices as electrode materials, although they have received little attention in the literature. When tested at a current density of 40 mA g^{-1}, thermally reduced graphene oxide (rGO) had a specific capacity of 174 mA h g^{-1} at d = 3.7 Å. At a current density of 20 mA cm^{-2}, increasing the interlayer spacing to 4.3 Å increased the capacity to 280 mA g^{-1} [33,52]. Yun [53], showed that thionyl chloride treatment of graphene oxide (GO) may significantly increase the storage capacity of graphene-based anodes in SIBs and that the crumpled structure of GO was responsible for this increase in the storage capacity (Fig. 8.3).

Graphene's interesting properties as a two-dimensional material are well-known by scientists. The restacking or agglomeration of graphene sheets dramatically lowers their key qualities, severely limiting their practical use. It is required to build a unique graphene structure, such as the 3D graphene architecture (3DG), which has many in-plane vacancies that enhance the cross-plane ion diffusion. Macropores in 3DG structures operate as ion buffers, reducing the distance between the electrolyte and device interior surface. These macropore-containing 3DG structures include graphene aerogels, foams, and network structures. The electrical conductivity, surface area, and mechanical properties of various 3D rGO materials are very high quality [54].

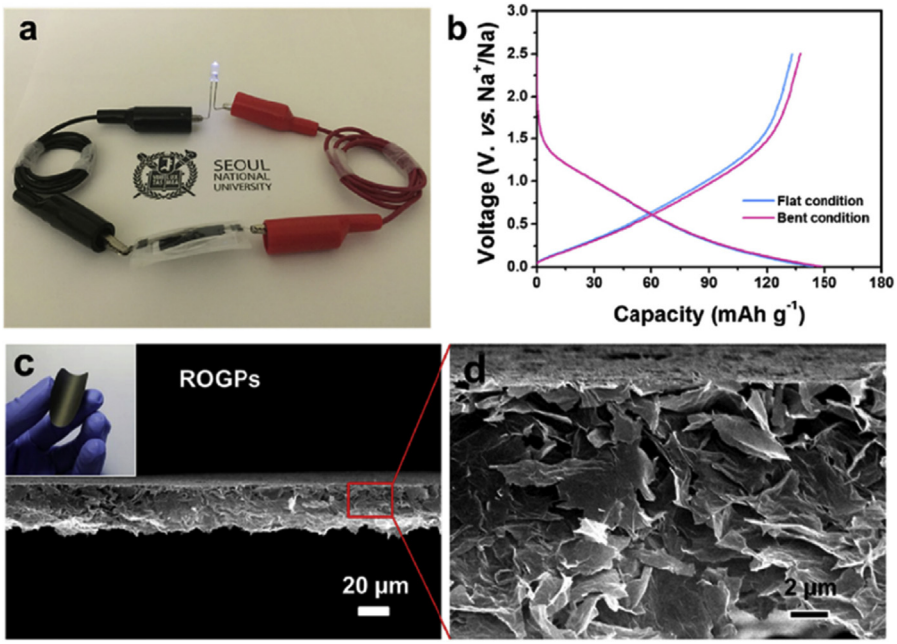

Figure 8.3

(A) Photograph of a homemade pouch cell and (B) galvanostatic discharge/charge profiles of the pouch cell at a current density of 200 mA g^{-1} under its flat and bent conditions. (C) and (D) Scanning electron microscopy (SEM) images of the cross-sectional morphology of ROGP in different magnifications. The inset of (C) shows an optical image of the randomly oriented graphene paper (ROGP) [53].

Depending on the most common preparation methods, 3DG may be made using a template-aided process, self-assembly, or 3D printing. The synthesis of 3DG can be performed more quickly and with more flexibility by utilizing GO-based chemical synthesis techniques than with previous procedures. An N-doped graphene nanoparticle solution was used by Xu J. et al. to synthesize a 3D free-standing graphene aerogel with an extraordinarily high initial reversible capacity of over 852.6 mA h g^{-1} [55]. For this reason, volumetric energy density is projected to be decreased as a result of the 3DG porosity structure. To produce high-density porous graphene macro-foam (HPGM), Zhang J. fabricated a HPGM via drying simply graphene hydrogels at around 80°C in a typical air-circulating oven. The achieved HPGM showed a notable density of 1.04 g cm^{-3}, considerably larger than another type of prepared porous graphene foam, denoted as PGM that had just 0.32 g cm^{-3}, which was synthesized through freeze-drying the graphene hydrogels, and HPGM anode provided an uppermost increased volumetric capacity of over 132 mA h cm^{-3} under the current rate of 0.05 A g^{-1} [56].

Recently, our group has reported designing a cost-effective and novel strategy for constructing hard carbon spheres enveloped with graphene networks as a high-

performance anode material for sodium-ion batteries (Fig. 8.4). The malleable and robust structure of the graphene wrapped hard carbon spheres (G-HCS) material-based anode can enable the quick sodium ions and electrons transport rate and tolerate rapid sodium storage with capacity retention of 122 mA h g^{-1} after a long cycling performance of 4000 cycles at an ultra-high current density of 10 A g^{-1}, due to the development of the conductive network of graphene nanosheets with remarkable electrical conductivity, which supports virtuous interaction between graphene sheets and hard carbon sphere particles [57].

2.5 Disordered carbon materials

In carbon materials, the expression "amorphous carbon" refers to carbon materials that have a disordered structure and a low degree of graphitization but which are nonetheless capable of supporting a significant extent of storage capacity. Amorphous carbon, also known as "soft carbon" or "hard carbon," is a type of carbon composed primarily of

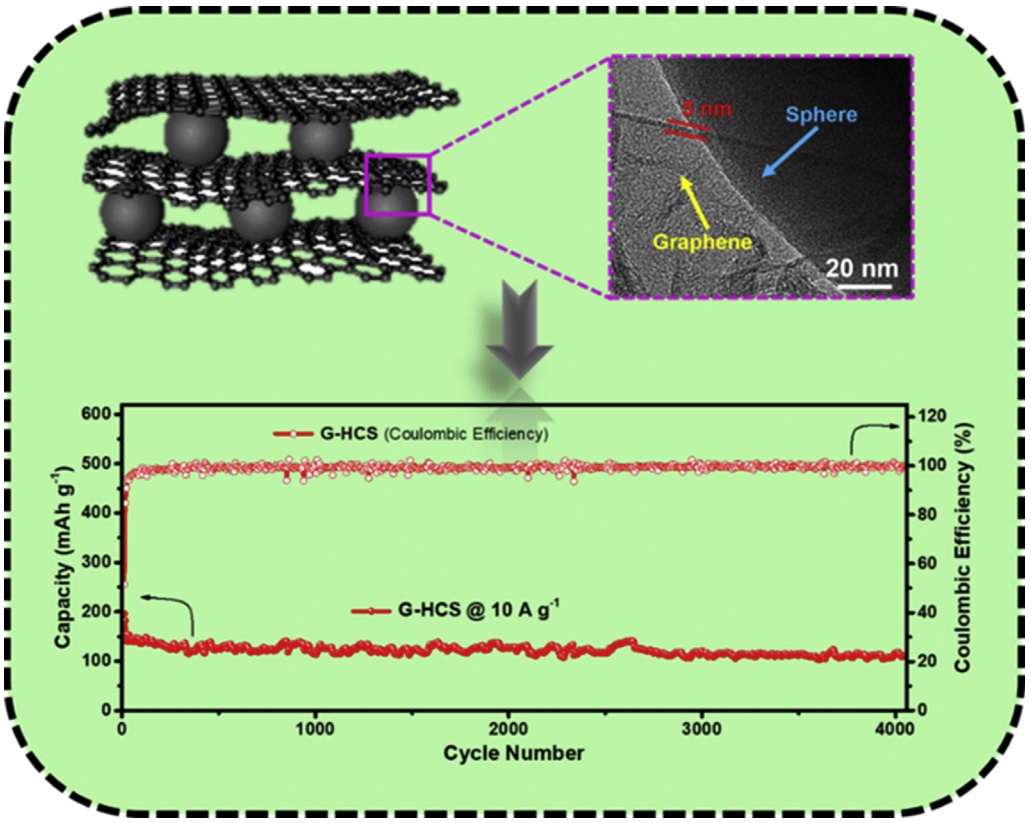

Figure 8.4
Hard carbon spheres enveloped with graphene networks as a high-performance anode material for sodium-ion batteries [57].

disordered graphene layers and randomly packed microdomains, with only a trace of crystalline carbon. For one thing, graphite can be created from soft carbon even at temperatures as high as 2500°C, but this is not true for the other. Its amorphous structure, which has nanopores and a large interlayer gap, allows it to keep many sodium ions, far more than graphite can hold on a single sheet [58,59].

Before high-temperature graphitization, soft carbon had a semi-graphitic structure with fewer flaws and a greater crystallinity than hard carbon. Soft carbon has both a high-strain and low-strain structure. Unorganized carbon makes up the high-strain zone, while high-crystallinity carbon makes up the low-strain region, resulting in highly electrically conductive carbon. In the range of 200–250 mA h g^{-1}, soft carbons have been observed the storage capacity to date, whereas the anode material for SIBs typically demonstrates outstanding rate performance. Mesophase pitch (MPP) was used as the carbon precursor in the preparation of mesoporous soft carbon (MSC) by Song's group [60] (Fig. 8.5). At the current rate of 30 mA g^{-1}, MSC has an initial reversible capacity of 331 mA h g^{-1}, and 53 mA h g^{-1} is maintained at 10 A g^{-1}. Even after 3000 cycles, MSC's capacity remains 103 mA h g^{-1} under 500 mA g^{-1}.

2.6 Na-ion storage mechanism in hard carbons

However, the normal low-voltage plateau of hard carbons also shows a sloping voltage zone that is remarkably similar to that of soft carbons [61,62]. This results in generally

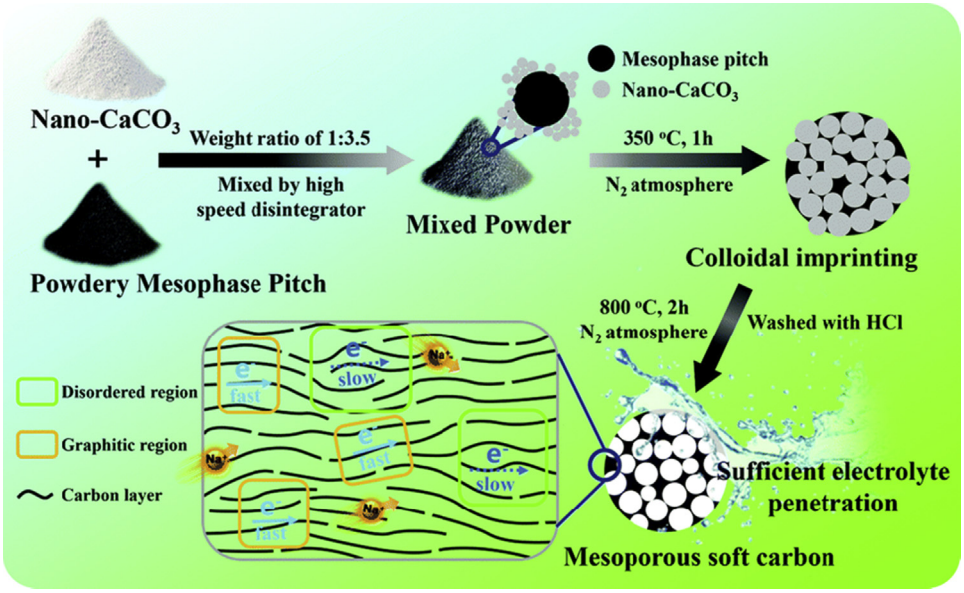

Figure 8.5
Schematic illustration of the preparation of mesoporous soft carbon (MSC) [60].

greater capacities and smaller average oxidation voltages than the soft carbons, resulting in much higher specific energy than those of the soft carbons. The majority of these carbons exhibited very high capacities, reaching from 250 to 350 mA h g^{-1} and typical oxidation voltages in the vicinity of 0.3 V on average. Hard carbon has been hampered by low initial coulombic efficiency (ICE), less than 75%, and poor rate performance throughout a wide range of cycling performance under higher rates. In order to improve hard carbon performance, it is necessary to have a thorough knowledge of the exact structure of hard carbon, ion-transfer process, and storage mechanism [63].

A plateau and a slope region characterize the usual discharge curve of hard carbon versus Na metal. There has been much dispute about categorizing these two areas (Fig. 8.6) [63]. Using in situ X-ray diffraction, Stevens and Dahn [64,65] postulated that the slope area is because of defect-aided interlayer intercalation that has been verified by an increase in interlayer distance and a drop in peak intensity when sodiation is carried out. Slope regions are thought to be linked to the good binding of Na at available local defects and heteroatoms doped on the surface of turbostratic crystallites, as derived from a theoretical calculation that defects improve sodiation potential and demonstrated by experimental studies on the defect effect on hard carbon performance [33,63].

According to SAXS experiments by Dahn and Stevens, the low-potential plateau's capacity may be accredited to nano-plating (adsorption) inside the "enclosed" micropores between the domains because of the findings from that research. Sodium filling the nanoporous area led to a drop in SAXS intensity, supporting their claims. For the first time, Grey et al. [66] published a comparison of ex-situ and operating ^{23}Na NMR spectroscopy that revealed the formation of Na clusters in nanopores after discharge. According to several additional investigations, the sodiation process should be re-evaluated. According to Bommier et al. the turbostratic nano-domains boosted the slope capacity while decreasing it in the plateau zone. Instead of the sloping zone, the Na-ion intercalation is connected to the plateau region [33,67].

2.7 Heteroatom-doped carbon nanomaterials

Heteroatom doping proved to be an effective method of increasing these materials' sodium storage capacity. Heteroatom doping in carbonaceous materials is an excellent approach to boost electrochemical performance. The addition of heteroatoms, that is, phosphorus (P), boron (B), sulfur (S), nitrogen (N), fluorine (F), and so on., fundamentally means to incorporate or chemically attach them into the backbone of the corresponding carbon matrix, could produce various extrinsic defects with modifying the carbon lattices, which eventually boost their reaction kinetics significantly and improve the electrochemical performance through adjusting the chemical and electronic properties [22,68,69].

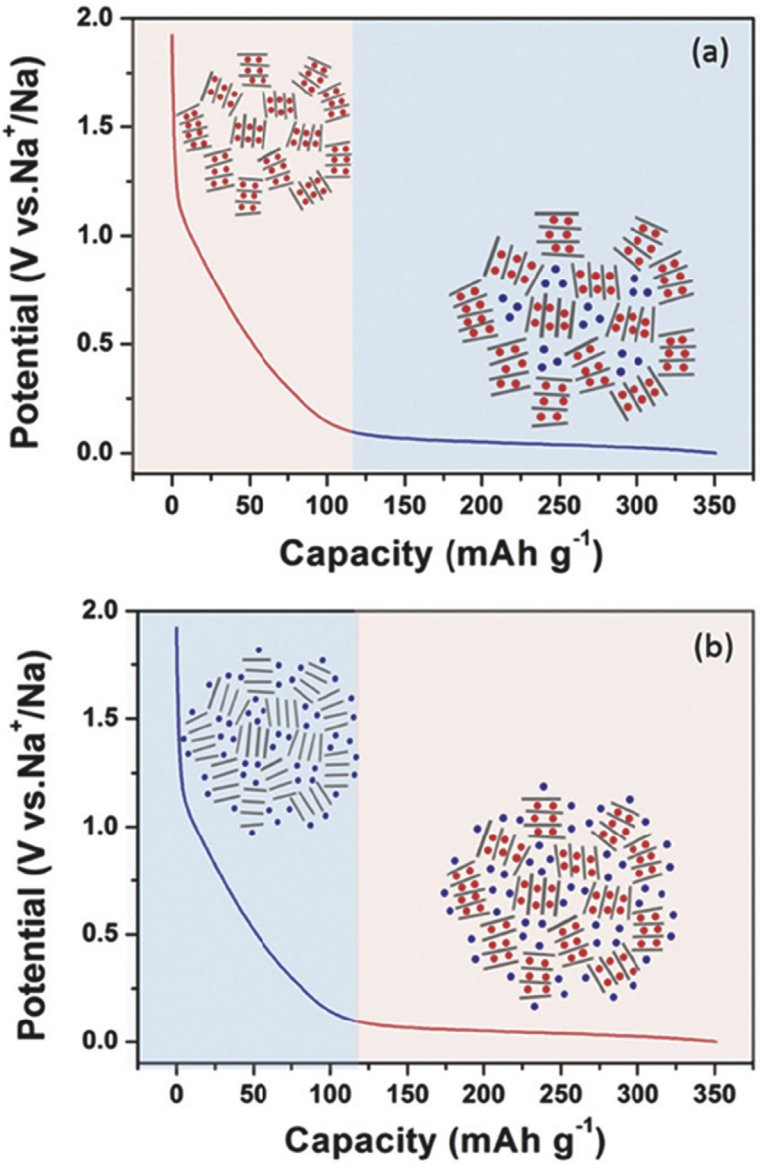

Figure 8.6
Schematic illustration of the mechanisms for Na-ion storage in hard carbon: (A) "intercalation–adsorption" mechanism and (B) "adsorption–intercalation" mechanism [63].

Nitrogen is the most often researched heteroatom for doping because of its proximity to carbon. This is because combining nitrogen with carbon is a rather straightforward chemical reaction. Aside from these attributes, nitrogen's excellent bonding with carbon is made possible by its high electronegativity, high electron affinity, and five valence

electrons. The heating of organic precursors such as melamine, aminated sugars, PAN, PANI, and polypyrrole (PPY) may directly integrate nitrogen atoms into carbon backbones.

Wang [70] used KOH activation to construct functionalized 3D porous nitrogen-doped carbon nanosheets. These materials' unique structural and compositional properties could allow quick ionic and electronic transportation, and outstanding supercapacitive and sodium-ion storage capacities are demonstrated. In-situ, Li [71] has effectively manufactured N-doped carbon nanosheets in situ using an in-situ polymerization method (G-NCs). The G-NCs were shown to have a reversible capacity of 110 mA h g^{-1} as an anode material for SIBs, even though the tested current reached 10,000 mA g^{-1}. At 5000 mA g^{-1}, the specific capacity of the cell was 154 mA h g^{-1} after 10,000 cycles. Liu [72] constructed N-doped three-dimensional graphene through an in situ PANI polymerization and subsequent pyrolysis process (Fig. 8.7). The graphene composition with an N-doped 3D structure results in a high reversible sodium storage capacity, remarkable cycle durability, and great rate capability. Consequently, a hybrid nanostructure of graphene and nitrogen-doped carbon is a viable anode material for next-generation SIBs [73,74].

For example, sulfur doping has been demonstrated to boost electrical conductivity and provide additional lithium and sodium ion reaction sites. Reversible electrochemical reactions between sulfur and lithium and sodium are also possible. Carbonaceous materials with wider interlayer distances and improved electrical characteristics may be achieved by doping S with bigger sizes and lower electronegativity than nitrogen. Poly(3,4-ethylene dioxythiophene) and other sulfur-containing precursors can be directly pyrolyzed, or sulfur can be mixed with an organic precursor [75], or phenol disulfide, sulfuric acid, or thiourea can be used as S-donors [76,77]. A sufficiently high-rate capability of 161.8 mA h g^{-1} at a

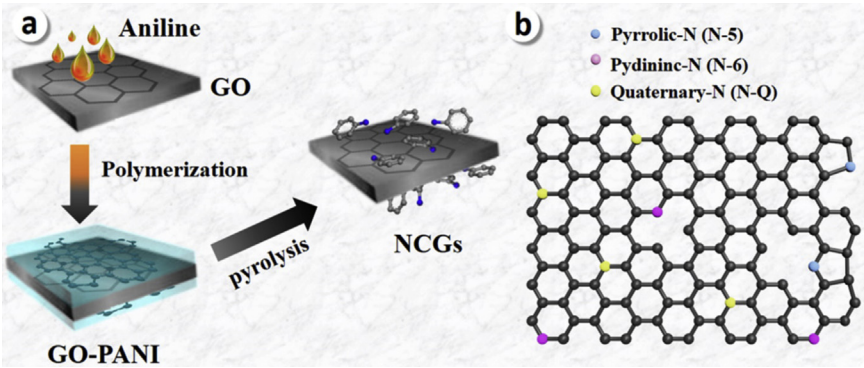

Figure 8.7

(A) Schematic diagram for the preparation of nitrogen-doped carbon/graphenes (NCGs); (B) the bonding configurations of nitrogen functionalities in NCGs [72].

current density of 5 A g^{-1} is maintained at 5000 cycles, which can be attributed to the fast surface-induced capacitive behavior derived from its high surface area, as demonstrated by the controllable interlayer spacing range of 0.38−0.41 nm and the ability to maintain a current density of 5 A g^{-1} for 5000 cycles [78].

It is possible to synthesize sulfur-doped graphene (SDG) from dimethyl sulfoxide (DMSO) in only one step using a one-pot solvothermal technique. The produced sulfur-doped graphene had a large interlayer distance and many active sites. A sulfur-doped graphene anode for SIBs showed the outstanding reversible capacity of 390 mA h g^{-1} at 100 mA g^{-1} and great rate performance of 217 mA h g^{-1} at an extremely high current density of 3200 mA g^{-1} after 300 cycles [79]. By incorporating S into the carbon matrix with varied defect configurations, Hong Z [80] adjusted the S doping sites and the interlayer distance of disordered carbon. Using sulfur and $Na_2S_2O_3$, a molten salt approach synthesized S-doped porous hard carbon (S-PHC-p) and S-doped hard carbon (S-HC-p). S likes to dope in the interlayer for the ideal structure, whereas S prefers to dope on the carbon layer with constructing the defective structure. Because of this, S-doped hard carbon with some defects has an interlayer distance (39.97 nm) higher than that of porous carbon (36.95 nm) with many defects, which is S-doped. Even after 4000 cycles at 1 A g^{-1}, the S-doped carbon with a higher interlayer spacing and some holes, delivered a capacity retention of around 200 mA h g^{-1} (Fig. 8.8).

When it comes to the electrochemical properties of phosphorus, the red polymorph, in particular, is well recognized as an active one [81,82]. Low-cost and facile constructed BP/rGO layered structure-based anodes with outstanding cycle stability and rate capability are shown by Zhou et al., using an 8-GPa pressure at room temperature [82]. Unfortunately, the carbon/red polymorph's cycle stability and ICE are still lacking. Carbon precursors may be used with P donor chemicals, for instance, phosphoric acid or bis(diphenylphosphino)methane to perform P-doping, and effective at low voltages, which simply could be attained through mixing the P donor precursors, for example, bis(diphenylphosphino)methane or phosphoric acid with carbon precursor [83,84], delivering the capacities in the range of 350−400 mA h g^{-1}.

Incorporating boron (B) into carbon-based materials is another method of altering their properties. Boric acid may also be added to the carbon precursor to create boron doping. Boron-functionalized rGO was produced in a single hydrothermal treatment of GO with H_3BO_4 (BF-rGO). After 5000 cycles at 1000 mA g^{-1} of current density, 89.4% of the capacity retention of the Na/BF-rGO half cells are still delivered, with the capacity remaining at 110 mA h g^{-1} (a capacity decline of only 0.002% for each cycle) [85].

Synergistic effects between heteroatoms doped into carbonaceous host materials have recently been discovered, increasing electrochemical performance. N/Pco-doping or N/Sco-doping have been studied to boost Na^+ storage capacity and cycling performance

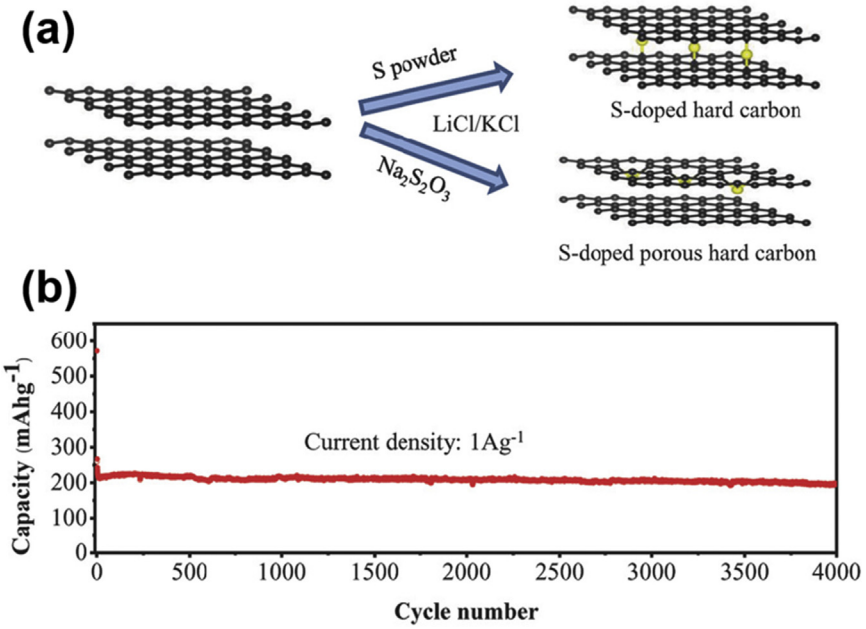

Figure 8.8
(A) Schematic illustration of the synthesis of S-HC-p and S-PHC-p, (B) Long cycling stability of S-HC-p electrode at a constant current density of 1 A g^{-1} [80].

by increasing the interlayer spacing between matrix layers [86,87]. It was possible to synthesize S, N-co-doped carbon nanosheets utilizing p-amino-benzene sulfonic acid as the S source and N source in a solvent-free one-pot process, with an adjustable interlayer spacing of 0.37–0.41 nm, using this method. The SN-C anode showed an improved storage capacity of 380 mA h g^{-1} under a current density of 100 mA g^{-1} for over 100 cycles. Moreover, an excellent high-rate capacity of over 178 mA h g^{-1} was maintained even under an ultra-high current rate of 5 A g^{-1} for over 5000 cycles [86].

2.8 Porous carbon

Several factors determine how quickly electron and ion transportation may occur, such as the material's form and the electrolyte's diffusion pathways [92]. Hollow, porous, ordered structures, ultra-long nanofibers, and multilayer structures are all examples of nanostructured carbon materials that may be utilized to increase the power density of the materials dramatically. As we know, porous structures may reduce sodium ion transport distances. Since for SIBs, the volume change during ion insertion and extraction is well buffered by their structure of are porous materials [88]. Template-based production of porous carbon is the most common approach [89]. A low-cost pitch and phenolic resin were used to create a 3D porous carbon material using a NaCl template approach. When

this 3D porous carbon employed an anode material for SIBs, it showed excellent electrochemical performance due to its high reversible capacity (280 mA h g^{-1} at a low current density of 0.03 A g^{-1}) and high-rate capability (66 mA h g^{-1} at 9.6 A g^{-1}) [90].

For the first time, Zhang K [91] has shown that nitrogen can be added to carbon materials at low temperatures (60−70°C) using HNO_3 as the N source, allowing for the construction of N-doped double-shelled hollow carbon sphere (N-DHCSs). A uniformly porous and interconnected DHCS was formed when the precursors were washed with H_2SO_4 or HCl (Fig. 8.9). It has been shown that N-DHCSs as high-performance anode materials in sodium half-cells have 120 mA h g^{-1} at a current of 0.2 A g^{-1} after 100 cycles of operation.

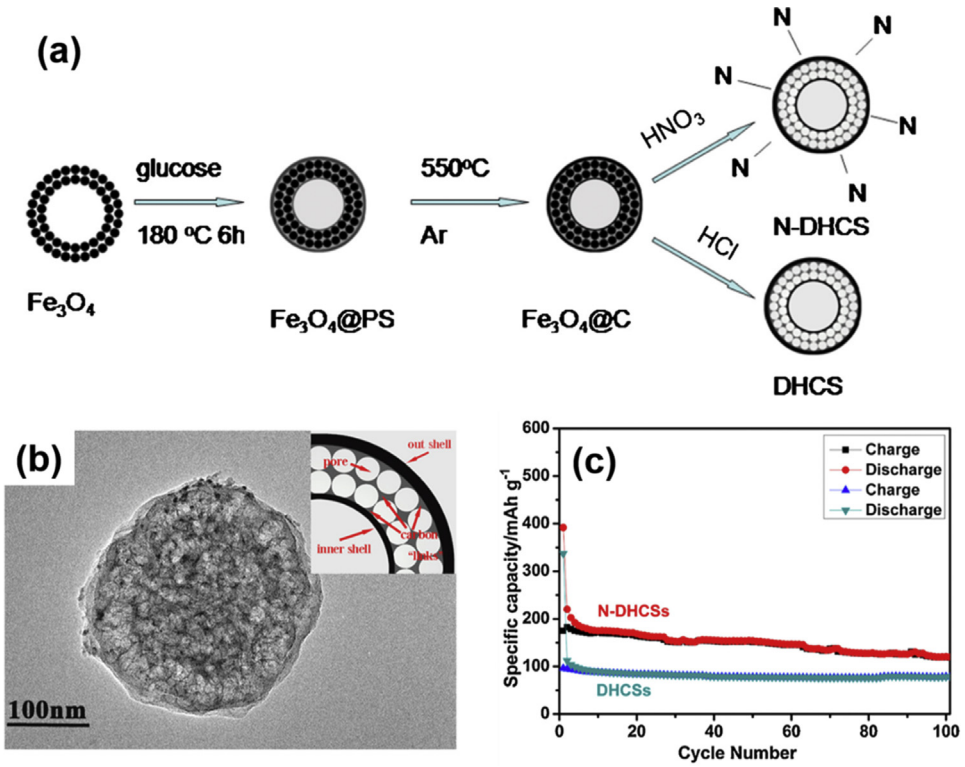

Figure 8.9

(A) A systematic synthesis scheme for the double-shelled hollow carbon sphere and N-doped double-shelled hollow carbon sphere, (B) the high-resolution (HR)-transmission electron microscopy (TEM) pictures of the as-obtained N-doped double-shelled hollow carbon sphere and simulated pattern inset, and (C) cycle performance in sodium-ion batteries (SIBs) of double-shelled hollow carbon sphere and N-doped double-shelled hollow carbon sphere at a current density of 0.2 A g^{-1} [91].

3. Conclusions and perspectives

Many different types of anode materials are available for SIBs, but carbon-based nanomaterials' utilization advances rapidly. These tailored carbon nanomaterials were discovered to have a high-rate capability and extended cycle life for SIB anodes because of their smaller ionic/electronic transport distance and good malleability. They may also be utilized as buffers of the volumetric variations for various alloy anodes during the insertion and extraction of Na ions upon long cycling. The impending growth of compact and wearable electronic devices has made the realization of thin and one-dimensional SIBs much imperative. The 0D (CQDs), 1D (CNFs and CNTs), 2D (graphene sheets), and 3D nanostructured carbon materials are predicted to be highly sought for the development of next-generation SIBs and other EESs. Because the nanoarchitecture could enable different synergistic effects, with each unit imposing its advantages and overcoming the deficiencies of the other units, more attention should be paid to carbon-based nanomaterials as efficient anodes in the SIB full cells, which may increase their energy and power density for practical use. Presently, this is an important and major aspect for SIBs to develop and advance the carbon-based nanostructured anode materials for successful commercialization and to meet the battery market demand.

Acknowledgements

The authors acknowledge the support from the Research Fund for International Scientists (RFIS-Grant number: 52150410410) National Natural Science Foundation of China. Rajesh Pathak is supported by Laboratory Directed Research and Development (LDRD) funding from Argonne National Laboratory, provided by the Director, Office of Science, of the U.S. DOE under Contract No. DE-AC02-06CH11357.

References

[1] J. Kim, M.S. Choi, K.H. Shin, M. Kota, Y. Kang, S. Lee, J.Y. Lee, H.S. Park, Rational design of carbon nanomaterials for electrochemical sodium storage and capture, Adv. Mater. 31 (34) (2019) 1803444, https://doi.org/10.1002/adma.201803444.

[2] G. Yasin, S. Ibraheem, S. Ali, M. Arif, S. Ibrahim, R. Iqbal, A. Kumar, M. Tabish, M.A. Mushtaq, A. Saad, H. Xu, W. Zhao, Defects-engineered tailoring of a tri-doped interlinked metal-free bifunctional catalyst with lower Gibbs free energy of OER/HER intermediates for overall water splitting, Mater. Today Chem. 23 (2022) 100634, https://doi.org/10.1016/j.mtchem.2021.100634.

[3] S. Ibraheem, S. Chen, J. Li, Q. Wang, Z. Wei, In situ growth of vertically aligned FeCoOOH-nanosheets/nanoflowers on Fe, N co-doped 3D-porous carbon as efficient bifunctional electrocatalysts for rechargeable zinc−O2 batteries, J. Mater. Chem. 7 (16) (2019) 9497−9502, https://doi.org/10.1039/C9TA01964B.

[4] S. Ibraheem, S. Chen, L. Peng, J. Li, L. Li, Q. Liao, M. Shao, Z. Wei, Strongly coupled iron selenides-nitrogen-bond as an electronic transport bridge for enhanced synergistic oxygen electrocatalysis in rechargeable zinc-O2 batteries, Appl. Catal. B Environ. 265 (2020) 118569, https://doi.org/10.1016/j.apcatb.2019.118569.

[5] S. Ibraheem, S. Chen, J. Li, W. Li, X. Gao, Q. Wang, Z. Wei, Three-dimensional Fe, N-decorated carbon-supported NiFeP nanoparticles as an efficient bifunctional catalyst for rechargeable zinc−O2 batteries, ACS Appl. Mater. Interfaces 11 (1) (2019) 699−705, https://doi.org/10.1021/acsami.8b16126.

[6] S. Ibraheem, X. Li, S.S.A. Shah, T. Najam, G. Yasin, R. Iqbal, S. Hussain, W. Ding, F. Shahzad, Tellurium triggered formation of Te/Fe-NiOOH nanocubes as an efficient bifunctional electrocatalyst for overall water splitting, ACS Appl. Mater. Interfaces 13 (9) (2021) 10972−10978, https://doi.org/10.1021/acsami.0c22573.

[7] S. Ibraheem, G. Yasin, R. Iqbal, A. Saleem, T.A. Nguyen, S. Ibrahim, 6 - silicon-based nanomaterials for energy storage, in: S. Thomas, T.A. Nguyen, M. Ahmadi, G. Yasin, N. Joshi (Eds.), Silicon-Based Hybrid Nanoparticles, Elsevier, 2022, pp. 103−124.

[8] T. Mehtab, G. Yasin, M. Arif, M. Shakeel, R.M. Korai, M. Nadeem, N. Muhammad, X. Lu, Metal-organic frameworks for energy storage devices: batteries and supercapacitors, J. Energy Storage 21 (2019) 632−646, https://doi.org/10.1016/j.est.2018.12.025.

[9] A. Kumar, S. Ibraheem, T. Anh Nguyen, R.K. Gupta, T. Maiyalagan, G. Yasin, Molecular-MN4 vs. atomically dispersed M−N4−C electrocatalysts for oxygen reduction reaction, Coord. Chem. Rev. 446 (2021) 214122, https://doi.org/10.1016/j.ccr.2021.214122.

[10] A. Kumar, G. Yasin, R.M. Korai, Y. Slimani, M.F. Ali, M. Tabish, M. Tariq Nazir, T.A. Nguyen, Boosting oxygen reduction reaction activity by incorporating the iron phthalocyanine nanoparticles on carbon nanotubes network, Inorg. Chem. Commun. 120 (2020) 108160, https://doi.org/10.1016/j.inoche.2020.108160.

[11] A. Kumar, G. Yasin, V.K. Vashistha, D.K. Das, M.U. Rehman, R. Iqbal, Z. Mo, T.A. Nguyen, Y. Slimani, M.T. Nazir, W. Zhao, Enhancing oxygen reduction reaction performance via CNTs/graphene supported iron protoporphyrin IX: a hybrid nanoarchitecture electrocatalyst, Diam. Relat. Mater. 113 (2021) 108272, https://doi.org/10.1016/j.diamond.2021.108272.

[12] S. Ibraheem, G. Yasin, A. Kumar, M.A. Mushtaq, S. Ibrahim, R. Iqbal, M. Tabish, S. Ali, A. Saad, Iron-cation-coordinated cobalt-bridged-selenides nanorods for highly efficient photo/electrochemical water splitting, Appl. Catal. B Environ. 304 (2022) 120987, https://doi.org/10.1016/j.apcatb.2021.120987.

[13] M.A. Mushtaq, M. Arif, X. Fang, G. Yasin, W. Ye, M. Basharat, B. Zhou, S. Yang, S. Ji, D. Yan, Photoelectrochemical reduction of N2 to NH3 under ambient conditions through hierarchical MoSe2@g-C3N4 heterojunctions, J. Mater. Chem. 9 (5) (2021) 2742−2753, https://doi.org/10.1039/D0TA10620H.

[14] A. Kumar, D.K. Das, V.K. Vashistha, S. Ibraheem, G. Yasin, S. Gautam, V. Sharma, A novel CoN4-driven self-assembled molecular engineering for oxygen reduction reaction, Int. J. Hydrog. Energy 46 (52) (2021) 26499−26506, https://doi.org/10.1016/j.ijhydene.2021.05.114.

[15] M. Nadeem, G. Yasin, M. Arif, M.H. Bhatti, K. Sayin, M. Mehmood, U. Yunus, S. Mehboob, I. Ahmed, U. Flörke, Pt-Ni@PC900 hybrid derived from layered-structure Cd-MOF for fuel cell ORR activity, ACS Omega 5 (5) (2020) 2123−2132, https://doi.org/10.1021/acsomega.9b02741.

[16] M. Nadeem, G. Yasin, M. Arif, H. Tabassum, M.H. Bhatti, M. Mehmood, U. Yunus, R. Iqbal, T.A. Nguyen, Y. Slimani, H. Song, W. Zhao, Highly active sites of Pt/Er dispersed N-doped hierarchical porous carbon for trifunctional electrocatalyst, Chem. Eng. J. 409 (2021) 128205, https://doi.org/10.1016/j.cej.2020.128205.

[17] M. Nadeem, G. Yasin, M.H. Bhatti, M. Mehmood, M. Arif, L. Dai, Pt-M bimetallic nanoparticles (M = Ni, Cu, Er) supported on metal-organic framework-derived N-doped nanostructured carbon for hydrogen evolution and oxygen evolution reaction, J. Power Sources 402 (2018) 34−42, https://doi.org/10.1016/j.jpowsour.2018.09.006.

[18] G. Yasin, S. Ibrahim, S. Ibraheem, S. Ali, R. Iqbal, A. Kumar, M. Tabish, Y. Slimani, T.A. Nguyen, H. Xu, W. Zhao, Defective/graphitic synergy in a heteroatom-interlinked-triggered metal-free electrocatalyst for high-performance rechargeable zinc-air batteries, J. Mater. Chem. 9 (34) (2021) 18222−18230, https://doi.org/10.1039/D1TA05812F.

[19] D. Yu, A. Kumar, T.A. Nguyen, M.T. Nazir, G. Yasin, High-voltage and ultrastable Aqueous zinc−iodine battery enabled by N-doped carbon materials: revealing the contributions of nitrogen configurations, ACS Sustain. Chem. Eng. 8 (36) (2020) 13769−13776, https://doi.org/10.1021/acssuschemeng.0c04571.
[20] G. Yasin, M. Arif, T. Mehtab, X. Lu, D. Yu, N. Muhammad, M.T. Nazir, H. Song, Understanding and suppression strategies toward stable Li metal anode for safe lithium batteries, Energy Storage Mater. 25 (2020) 644−678, https://doi.org/10.1016/j.ensm.2019.09.020.
[21] H. Wang, L. Sheng, G. Yasin, L. Wang, H. Xu, X. He, Reviewing the current status and development of polymer electrolytes for solid-state lithium batteries, Energy Storage Mater. 33 (2020) 188−215, https://doi.org/10.1016/j.ensm.2020.08.014.
[22] G. Yasin, M. Arif, J. Ma, S. Ibraheem, D. Yu, L. Zhang, D. Liu, L. Dai, Self-templating synthesis of heteroatom-doped large-scalable carbon anodes for high-performance lithium-ion batteries, Inorg. Chem. Front. (2022), https://doi.org/10.1039/D1QI01105G.
[23] S. Ullah, B.D.L. Campéon, S. Ibraheem, G. Yasin, R. Pathak, Y. Nishina, T. Anh Nguyen, Y. Slimani, Q. Yuan, Enabling the fast lithium storage of large-scalable γ-Fe2O3/Carbon nanoarchitecture anode material with an ultralong cycle life, J. Ind. Eng. Chem. 101 (2021) 379−386, https://doi.org/10.1016/j.jiec.2021.05.045.
[24] S. Ullah, G. Yasin, A. Ahmad, L. Qin, Q. Yuan, A.U. Khan, U.A. Khan, A.U. Rahman, Y. Slimani, Construction of well-designed 1D selenium−tellurium nanorods anchored on graphene sheets as a high storage capacity anode material for lithium-ion batteries, Inorg. Chem. Front. 7 (8) (2020) 1750−1761, https://doi.org/10.1039/C9QI01701A.
[25] N. Muhammad, G. Yasin, A. Li, Y. Chen, H.M. Saleem, R. Liu, D. Li, Y. Sun, S. Zheng, X. Chen, H. Song, Volumetric buffering of manganese dioxide nanotubes by employing 'as is' graphene oxide: an approach towards stable metal oxide anode material in lithium-ion batteries, J. Alloys Compd. 842 (2020) 155803, https://doi.org/10.1016/j.jallcom.2020.155803.
[26] G. Yasin, N. Muhammad, T.A. Nguyen, P. Nguyen-Tri, Chapter one-nano battery: an introduction, in: H. Song, R. Venkatachalam, T.A. Nguyen, H.B. Wu, P. Nguyen-Tri (Eds.), Nano Batteries and Nanogenerators, Elsevier, 2021, pp. 3−9.
[27] G. Yasin, N. Muhammad, T.A. Nguyen, P. Nguyen-Tri, Chapter five-battery-nanogenerator hybrid systems, in: H. Song, R. Venkatachalam, T.A. Nguyen, H.B. Wu, P. Nguyen-Tri (Eds.), Nano Batteries and Nanogenerators, Elsevier, 2021, pp. 61−68.
[28] G. Yasin, M. Arif, M.A. Mushtaq, M. Shakeel, N. Muhammad, M. Tabish, A. Kumar, T.A. Nguyen, Chapter nine-nanostructured anode materials in rechargeable batteries, in: H. Song, R. Venkatachalam, T.A. Nguyen, H.B. Wu, P. Nguyen-Tri (Eds.), Nano Batteries and Nanogenerators, Elsevier, 2021, pp. 187−219.
[29] G. Yasin, N. Muhammad, A. Kumar, M. Tabish, M.U. Malik, M.T. Nazir, D. Liu, T.A. Nguyen, Chapter eleven-nanostructured cathode materials in rechargeable batteries, in: H. Song, R. Venkatachalam, T.A. Nguyen, H.B. Wu, P. Nguyen-Tri (Eds.), Nano Batteries and Nanogenerators, Elsevier, 2021, pp. 293−319.
[30] G. Yasin, M.A. Khan, W.Q. Khan, T. Mehtab, R.M. Korai, X. Lu, M.T. Nazir, M.N. Zahid, Facile and large-scalable synthesis of low-cost hard carbon anode for sodium-ion batteries, Results Phys. 14 (2019) 102404, https://doi.org/10.1016/j.rinp.2019.102404.
[31] V. Palomares, M. Casas-Cabanas, E. Castillo-Martínez, M.H. Han, T. Rojo, Update on Na-based battery materials. A growing research path, Energy Environ. Sci. 6 (8) (2013) 2312−2337, https://doi.org/10.1039/C3EE41031E.
[32] N. Yabuuchi, K. Kubota, M. Dahbi, S. Komaba, Research development on sodium-ion batteries, Chem. Rev. 114 (23) (2014) 11636−11682, https://doi.org/10.1021/cr500192f.
[33] H. Zhang, Y. Huang, H. Ming, G. Cao, W. Zhang, J. Ming, R. Chen, Recent advances in nanostructured carbon for sodium-ion batteries, J. Mater. Chem. 8 (4) (2020) 1604−1630, https://doi.org/10.1039/C9TA09984K.

[34] S.Y. Lim, W. Shen, Z. Gao, Carbon quantum dots and their applications, Chem. Soc. Rev. 44 (1) (2015) 362−381, https://doi.org/10.1039/C4CS00269E.
[35] H. Hou, C.E. Banks, M. Jing, Y. Zhang, X. Ji, Carbon quantum dots and their derivative 3D porous carbon frameworks for sodium-ion batteries with ultralong cycle life, Adv. Mater. 27 (47) (2015) 7861−7866, https://doi.org/10.1002/adma.201503816.
[36] K.-X. Wang, X.-H. Li, J.-S. Chen, Surface and interface engineering of electrode materials for lithium-ion batteries, Adv. Mater. 27 (3) (2015) 527−545, https://doi.org/10.1002/adma.201402962.
[37] Y. Zhang, C.W. Foster, C.E. Banks, L. Shao, H. Hou, G. Zou, J. Chen, Z. Huang, X. Ji, Graphene-Rich wrapped petal-like rutile TiO2 tuned by carbon dots for high-performance sodium storage, Adv. Mater. 28 (42) (2016) 9391−9399, https://doi.org/10.1002/adma.201601621.
[38] Z. Yang, J. Ren, Z. Zhang, X. Chen, G. Guan, L. Qiu, Y. Zhang, H. Peng, Recent advancement of nanostructured carbon for energy applications, Chem. Rev. 115 (11) (2015) 5159−5223, https://doi.org/10.1021/cr5006217.
[39] Z. Wang, G. Chen, D. Xia, Coating of multi-walled carbon nanotube with SnO2 films of controlled thickness and its application for Li-ion battery, J. Power Sources 184 (2) (2008) 432−436, https://doi.org/10.1016/j.jpowsour.2008.03.028.
[40] H. Lin, W. Weng, J. Ren, L. Qiu, Z. Zhang, P. Chen, X. Chen, J. Deng, Y. Wang, H. Peng, Twisted aligned carbon nanotube/silicon composite fiber anode for flexible wire-shaped lithium-ion battery, Adv. Mater. 26 (8) (2014) 1217−1222, https://doi.org/10.1002/adma.201304319.
[41] W. Li, M. Li, K.R. Adair, X. Sun, Y. Yu, Carbon nanofiber-based nanostructures for lithium-ion and sodium-ion batteries, J. Mater. Chem. 5 (27) (2017) 13882−13906, https://doi.org/10.1039/C7TA02153D.
[42] Y. Cao, L. Xiao, M.L. Sushko, W. Wang, B. Schwenzer, J. Xiao, Z. Nie, L.V. Saraf, Z. Yang, J. Liu, Sodium ion insertion in hollow carbon nanowires for battery applications, Nano Lett. 12 (7) (2012) 3783−3787, https://doi.org/10.1021/nl3016957.
[43] M. Wang, Z. Yang, W. Li, L. Gu, Y. Yu, Superior sodium storage in 3D interconnected nitrogen and oxygen dual-doped carbon network, Small 12 (19) (2016) 2559−2566, https://doi.org/10.1002/smll.201600101.
[44] S. Stankovich, D.A. Dikin, G.H.B. Dommett, K.M. Kohlhaas, E.J. Zimney, E.A. Stach, R.D. Piner, S.T. Nguyen, R.S. Ruoff, Graphene-based composite materials, Nature 442 (7100) (2006) 282−286, https://doi.org/10.1038/nature04969.
[45] G. Yasin, M. Arif, M. Shakeel, Y. Dun, Y. Zuo, W.Q. Khan, Y. Tang, A. Khan, M. Nadeem, Exploring the nickel−graphene nanocomposite coatings for superior corrosion resistance: manipulating the effect of deposition current density on its morphology, mechanical properties, and erosion-corrosion performance, Adv. Energy Mater. 20 (7) (2018) 1701166, https://doi.org/10.1002/adem.201701166.
[46] A. Jabbar, G. Yasin, W.Q. Khan, M.Y. Anwar, R.M. Korai, M.N. Nizam, G. Muhyodin, Electrochemical deposition of nickel graphene composite coatings: effect of deposition temperature on its surface morphology and corrosion resistance, RSC Adv. 7 (49) (2017) 31100−31109, https://doi.org/10.1039/C6RA28755G.
[47] G. Yasin, M.A. Khan, M. Arif, M. Shakeel, T.M. Hassan, W.Q. Khan, R.M. Korai, Z. Abbas, Y. Zuo, Synthesis of spheres-like Ni/graphene nanocomposite as an efficient anti-corrosive coating; effect of graphene content on its morphology and mechanical properties, J. Alloys Compd. 755 (2018) 79−88, https://doi.org/10.1016/j.jallcom.2018.04.321.
[48] G. Yasin, M. Arif, M.N. Nizam, M. Shakeel, M.A. Khan, W.Q. Khan, T.M. Hassan, Z. Abbas, I. Farahbakhsh, Y. Zuo, Effect of surfactant concentration in the electrolyte on the fabrication and properties of nickel-graphene nanocomposite coating synthesized by electrochemical co-deposition, RSC Adv. 8 (36) (2018) 20039−20047, https://doi.org/10.1039/C7RA13651J.
[49] M. Tabish, M.U. Malik, M.A. Khan, G. Yasin, H.M. Asif, M.J. Anjum, W.Q. Khan, S. Ibraheem, T.A. Nguyen, Y. Slimani, M.T. Nazir, Construction of NiCo/graphene nanocomposite coating with bulges-like morphology for enhanced mechanical properties and corrosion resistance performance, J. Alloys Compd. 867 (2021) 159138, https://doi.org/10.1016/j.jallcom.2021.159138.

[50] G. Yasin, M. Arif, T. Mehtab, M. Shakeel, M.A. Khan, W.Q. Khan, Chapter 14—metallic nanocomposite coatings, in: S. Rajendran, T.A.N.H. Nguyen, S. Kakooei, M. Yeganeh, Y. Li (Eds.), Corrosion Protection at the Nanoscale, Elsevier, 2020, pp. 245—274.
[51] G. Yasin, M.J. Anjum, M.U. Malik, M.A. Khan, W.Q. Khan, M. Arif, T. Mehtab, T.A. Nguyen, Y. Slimani, M. Tabish, D. Ali, Y. Zuo, Revealing the erosion-corrosion performance of sphere-shaped morphology of nickel matrix nanocomposite strengthened with reduced graphene oxide nanoplatelets, Diam. Relat. Mater. 104 (2020) 107763, https://doi.org/10.1016/j.diamond.2020.107763.
[52] Y.-X. Wang, S.-L. Chou, H.-K. Liu, S.-X. Dou, Reduced graphene oxide with superior cycling stability and rate capability for sodium storage, Carbon 57 (2013) 202—208, https://doi.org/10.1016/j.carbon.2013.01.064.
[53] Y.S. Yun, Y.-U. Park, S.-J. Chang, B.H. Kim, J. Choi, J. Wang, D. Zhang, P.V. Braun, H.-J. Jin, K. Kang, Crumpled graphene paper for high power sodium battery anode, Carbon 99 (2016) 658—664, https://doi.org/10.1016/j.carbon.2015.12.047.
[54] N.A. Kumar, R.R. Gaddam, S.R. Varanasi, D. Yang, S.K. Bhatia, X.S. Zhao, Sodium-ion storage in reduced graphene oxide, Electrochim. Acta 214 (2016) 319—325, https://doi.org/10.1016/j.electacta.2016.08.058.
[55] J. Xu, M. Wang, N.P. Wickramaratne, M. Jaroniec, S. Dou, L. Dai, High-performance sodium-ion batteries based on a 3D anode from nitrogen-doped graphene foams, Adv. Mater. 27 (12) (2015) 2042—2048, https://doi.org/10.1002/adma.201405370.
[56] J. Zhang, W. Lv, Y. Tao, Y.-B. He, D.-W. Wang, C.-H. You, B. Li, F. Kang, Q.-H. Yang, Ultrafast high-volumetric sodium storage of folded-graphene electrodes through surface-induced redox reactions, Energy Storage Mater. 1 (2015) 112—118, https://doi.org/10.1016/j.ensm.2015.08.006.
[57] G. Yasin, M. Arif, T. Mehtab, M. Shakeel, M.A. Mushtaq, A. Kumar, T.A. Nguyen, Y. Slimani, M.T. Nazir, H. Song, A novel strategy for the synthesis of hard carbon spheres encapsulated with graphene networks as a low-cost and large-scalable anode material for fast sodium storage with an ultralong cycle life, Inorg. Chem. Front. 7 (2) (2020) 402—410, https://doi.org/10.1039/C9QI01105F.
[58] X. Zhong, Y. Wu, S. Zeng, Y. Yu, Carbon, and carbon hybrid materials as anodes for sodium-ion batteries, Chem. Asian J. 13 (10) (2018) 1248—1265, https://doi.org/10.1002/asia.201800132.
[59] M. Wahid, D. Puthusseri, Y. Gawli, N. Sharma, S. Ogale, Hard carbons for sodium-ion battery anodes: synthetic strategies, material properties, and storage mechanisms, ChemSusChem 11 (3) (2018) 506—526, https://doi.org/10.1002/cssc.201701664.
[60] B. Cao, H. Liu, B. Xu, Y. Lei, X. Chen, H. Song, Mesoporous soft carbon as an anode material for sodium-ion batteries with superior rate and cycling performance, J. Mater. Chem. 4 (17) (2016) 6472—6478, https://doi.org/10.1039/C6TA00950F.
[61] W. Luo, Z. Jian, Z. Xing, W. Wang, C. Bommier, M.M. Lerner, X. Ji, Electrochemically expandable soft carbon as anodes for Na-ion batteries, ACS Cent. Sci. 1 (9) (2015) 516—522, https://doi.org/10.1021/acscentsci.5b00329.
[62] C. Bommier, W. Luo, W.-Y. Gao, A. Greaney, S. Ma, X. Ji, Predicting the capacity of hard carbon anodes in sodium-ion batteries using porosity measurements, Carbon 76 (2014) 165—174, https://doi.org/10.1016/j.carbon.2014.04.064.
[63] S. Qiu, L. Xiao, M.L. Sushko, K.S. Han, Y. Shao, M. Yan, X. Liang, L. Mai, J. Feng, Y. Cao, X. Ai, H. Yang, J. Liu, Manipulating adsorption—insertion mechanisms in nanostructured carbon materials for high-efficiency sodium-ion storage, Adv. Energy Mater. 7 (17) (2017) 1700403, https://doi.org/10.1002/aenm.201700403.
[64] D.A. Stevens, J.R. Dahn, An in situ small-angle X-ray scattering study of sodium insertion into a nanoporous carbon anode material within an operating electrochemical cell, J. Electrochem. Soc. 147 (12) (2000) 4428, https://doi.org/10.1149/1.1394081.
[65] D.A. Stevens, J.R. Dahn, The mechanisms of lithium and sodium insertion in carbon materials, J. Electrochem. Soc. 148 (8) (2001) A803, https://doi.org/10.1149/1.1379565.

[66] J.M. Stratford, P.K. Allan, O. Pecher, P.A. Chater, C.P. Grey, Mechanistic insights into sodium storage in hard carbon anodes using local structure probes, Chem. Commun. 52 (84) (2016) 12430−12433, https://doi.org/10.1039/C6CC06990H.

[67] C. Bommier, T.W. Surta, M. Dolgos, X. Ji, New mechanistic insights on Na-ion storage in nongraphitizable carbon, Nano Lett. 15 (9) (2015) 5888−5892, https://doi.org/10.1021/acs.nanolett.5b01969.

[68] J. Yang, X. Zhou, D. Wu, X. Zhao, Z. Zhou, S-doped N-rich carbon nanosheets with expanded interlayer distance as anode materials for sodium-ion batteries, Adv. Mater. 29 (6) (2017) 1604108, https://doi.org/10.1002/adma.201604108.

[69] G. Ma, K. Huang, Q. Zhuang, Z. Ju, Superior cycle stability of nitrogen-doped graphene nanosheets for Na-ion batteries, Mater. Lett. 174 (2016) 221−225, https://doi.org/10.1016/j.matlet.2016.03.111.

[70] H. Wang, Y. Zhang, W. Sun, H.T. Tan, J.B. Franklin, Y. Guo, H. Fan, M. Ulaganathan, X.-L. Wu, Z.-Z. Luo, S. Madhavi, Q. Yan, Conversion of uniform graphene oxide/polypyrrole composites into functionalized 3D carbon nanosheet frameworks with superior supercapacitive and sodium-ion storage properties, J. Power Sources 307 (2016) 17−24, https://doi.org/10.1016/j.jpowsour.2015.12.104.

[71] D. Li, L. Zhang, H. Chen, J. Wang, L.-X. Ding, S. Wang, P.J. Ashman, H. Wang, Graphene-based nitrogen-doped carbon sandwich nanosheets: a new capacitive process controlled anode material for high-performance sodium-ion batteries, J. Mater. Chem. 4 (22) (2016) 8630−8635, https://doi.org/10.1039/C6TA02139E.

[72] H. Liu, M. Jia, B. Cao, R. Chen, X. Lv, R. Tang, F. Wu, B. Xu, Nitrogen-doped carbon/graphene hybrid anode material for sodium-ion batteries with excellent rate capability, J. Power Sources 319 (2016) 195−201, https://doi.org/10.1016/j.jpowsour.2016.04.040.

[73] H. An, Y. Li, Y. Gao, C. Cao, J. Han, Y. Feng, W. Feng, Free-standing fluorine and nitrogen co-doped graphene paper as a high-performance electrode for flexible sodium-ion batteries, Carbon 116 (2017) 338−346, https://doi.org/10.1016/j.carbon.2017.01.101.

[74] F. Yang, Z. Zhang, K. Du, X. Zhao, W. Chen, Y. Lai, J. Li, Dopamine derived nitrogen-doped carbon sheets as anode materials for high-performance sodium-ion batteries, Carbon 91 (2015) 88−95, https://doi.org/10.1016/j.carbon.2015.04.049.

[75] W. Li, M. Zhou, H. Li, K. Wang, S. Cheng, K. Jiang, A high-performance sulfur-doped disordered carbon anode for sodium-ion batteries, Energy Environ. Sci. 8 (10) (2015) 2916−2921, https://doi.org/10.1039/C5EE01985K.

[76] D. Xu, C. Chen, J. Xie, B. Zhang, L. Miao, J. Cai, Y. Huang, L. Zhang, A hierarchical N/S-codoped carbon anode fabricated facilely from cellulose/polyaniline microspheres for high-performance sodium-ion batteries, Adv. Energy Mater. 6 (6) (2016) 1501929, https://doi.org/10.1002/aenm.201501929.

[77] Z. Li, C. Bommier, Z.S. Chong, Z. Jian, T.W. Surta, X. Wang, Z. Xing, J.C. Neuefeind, W.F. Stickle, M. Dolgos, P.A. Greaney, X. Ji, Mechanism of Na-ion storage in hard carbon anodes revealed by heteroatom doping, Adv. Energy Mater. 7 (18) (2017) 1602894, https://doi.org/10.1002/aenm.201602894.

[78] G. Zou, C. Wang, H. Hou, C. Wang, X. Qiu, X. Ji, Controllable interlayer spacing of sulfur-doped graphitic carbon nanosheets for fast sodium-ion batteries, Small 13 (31) (2017) 1700762, https://doi.org/10.1002/smll.201700762.

[79] B. Quan, A. Jin, S.-H. Yu, S.M. Kang, J. Jeong, H.D. Abruña, L. Jin, Y. Piao, Y.-E. Sung, Solvothermal-derived S-doped graphene as an anode material for sodium-ion batteries, Adv. Sci. 5 (5) (2018) 1700880, https://doi.org/10.1002/advs.201700880.

[80] Z. Hong, Y. Zhen, Y. Ruan, M. Kang, K. Zhou, J.-M. Zhang, Z. Huang, M. Wei, Rational design and general synthesis of S-doped hard carbon with tunable doping sites toward excellent Na-ion storage performance, Adv. Mater. 30 (29) (2018) 1802035, https://doi.org/10.1002/adma.201802035.

[81] W. Liu, X. Yuan, X. Yu, A core-shell structure of polydopamine-coated phosphorus−carbon nanotube composite for high-performance sodium-ion batteries, Nanoscale 10 (35) (2018) 16675−16682, https://doi.org/10.1039/C8NR04290J.

[82] Y. Liu, Q. Liu, A. Zhang, J. Cai, X. Cao, Z. Li, P.D. Asimow, C. Zhou, Room-temperature pressure synthesis of layered black phosphorus−graphene composite for sodium-ion battery anodes, ACS Nano 12 (8) (2018) 8323−8329, https://doi.org/10.1021/acsnano.8b03615.

[83] Y. Yang, D.-M. Tang, C. Zhang, Y. Zhang, Q. Liang, S. Chen, Q. Weng, M. Zhou, Y. Xue, J. Liu, J. Wu, Q.H. Cui, C. Lian, G. Hou, F. Yuan, Y. Bando, D. Golberg, X. Wang, "Protrusions" or "holes" in graphene: which is the better choice for sodium-ion storage? Energy Environ. Sci. 10 (4) (2017) 979−986, https://doi.org/10.1039/C7EE00329C.

[84] Z. Li, L. Ma, T.W. Surta, C. Bommier, Z. Jian, Z. Xing, W.F. Stickle, M. Dolgos, K. Amine, J. Lu, T. Wu, X. Ji, High capacity of hard carbon anode in Na-ion batteries unlocked by POx doping, ACS Energy Lett. 1 (2) (2016) 395−401, https://doi.org/10.1021/acsenergylett.6b00172.

[85] Y. Wang, C. Wang, Y. Wang, H. Liu, Z. Huang, Boric acid assisted reduction of graphene oxide: a promising material for sodium-ion batteries, ACS Appl. Mater. Interfaces 8 (29) (2016) 18860−18866, https://doi.org/10.1021/acsami.6b04774.

[86] G. Zou, H. Hou, G. Zhao, Z. Huang, P. Ge, X. Ji, Preparation of S/N-codoped carbon nanosheets with tunable interlayer distance for high-rate sodium-ion batteries, Green Chem. 19 (19) (2017) 4622−4632, https://doi.org/10.1039/C7GC01942D.

[87] C. Li, Q. Fu, K. Zhao, Y. Wang, H. Tang, H. Li, H. Jiang, L. Chen, Nitrogen and phosphorous dual-doped graphene aerogel with the rapid capacitive response for sodium-ion batteries, Carbon 139 (2018) 1117−1125, https://doi.org/10.1016/j.carbon.2018.06.035.

[88] Z. Lyu, L. Yang, D. Xu, J. Zhao, H. Lai, Y. Jiang, Q. Wu, Y. Li, X. Wang, Z. Hu, Hierarchical carbon nanocages as high-rate anodes for Li- and Na-ion batteries, Nano Res. 8 (11) (2015) 3535−3543, https://doi.org/10.1007/s12274-015-0853-4.

[89] D. Zhou, L.-Z. Fan, Facile synthesis of three-dimensional porous carbon networks for highly stable sodium storage, Ionics 24 (10) (2018) 3065−3073, https://doi.org/10.1007/s11581-017-2434-x.

[90] P. Lu, Y. Sun, H. Xiang, X. Liang, Y. Yu, 3D amorphous carbon with controlled porous and disordered structures as a high-rate anode material for sodium-ion batteries, Adv. Energy Mater. 8 (8) (2018) 1702434, https://doi.org/10.1002/aenm.201702434.

[91] K. Zhang, X. Li, J. Liang, Y. Zhu, L. Hu, Q. Cheng, C. Guo, N. Lin, Y. Qian, Nitrogen-doped porous interconnected double-shelled hollow carbon spheres with high capacity for lithium-ion batteries and sodium-ion batteries, Electrochim. Acta 155 (2015) 174−182, https://doi.org/10.1016/j.electacta.2014.12.108.

[92] G. Yasin, M. Arif, J. Ma, S. Ibraheem, D. Yu, L. Zhang, D. Liu, L. Dai, Self-templating synthesis of heteroatom-doped large-scalable carbon anodes for high-performance lithium-ion batteries, Inorg. Chem. Front. 9 (6) (2022) 1058−1069, https://doi.org/10.1039/D1QI01105G.

CHAPTER 9

Recent advances in catalytic hydrogen generation from formic acid using carbon-based catalysts

David Salinas-Torres[1,2], Miriam Navlani-García[2], Kohsuke Mori[3,4], Yasutaka Kuwahara[5], Diego Cazorla-Amorós[2], Hiromi Yamashita[3,4]

[1]Department of Chemical and Environmental Engineering, Technical University of Cartagena, Cartagena, Spain; [2]University Materials Institute of Alicante (IUMA), University of Alicante, Alicante, Spain; [3]Japan Units of Elements Strategy Initiative for Catalysts and Batteries, Kyoto University, Kyoto, Japan; [4]Division of Materials and Manufacturing Science, Osaka University, Suita, Osaka, Japan; [5]School of Engineering, Osaka University Division of Materials and Manufacturing Science, Japan

Abstract

Hydrogen is a crucial actor in the future sustainable energy scenario. However, its implementation is held back by several considerations, mainly related to its production and storage. Chemical hydrogen storage in liquid organic hydrogen carriers (LOHCs) stands up as a great alternative to those conventional systems used for physical hydrogen storage. Among the LOHC available, formic acid, the simplest carboxylic acid, is considered one of the most auspicious options. Both homogeneous and heterogeneous systems can catalyze the dehydrogenation of formic acid, but heterogeneous catalysts are preferred practically. Finding active, selective, and stable catalysts able to produce hydrogen from formic acid is challenging. However, significant breakthroughs have recently been achieved by properly controlling and modulating the properties of both the active phase and support. Palladium is the most investigated active phase, which has been shown to display good performance when loaded onto adequate supports. Carbon materials are the most fruitfully investigated catalytic supports, which is due to their outstanding properties as well as tunable surface chemistry. The present chapter covers some representative breakthroughs recently achieved while exploring the performance of monometallic and bimetallic Pd-based catalysts supported on carbon materials.

Keywords: Bimetallic nanoparticles; Carbon materials; Formic acid; Hydrogen; Pd nanoparticles.

Advanced Nanomaterials and Their Applications in Renewable Energy. https://doi.org/10.1016/B978-0-323-99877-2.00013-8

1. Introduction

The energy crisis is one of the central issues we face nowadays, and it is continuously being aggravated by the increasingly growing world population and current living standards. The energy system has been dominated by the exploitation of large reservoirs of carbon-based fossil fuels, and, even today, they provide ~80% of the total energy need (31.2%, 27.1%, and 24.7% of the total energy share in 2020, for oil, coal, and natural gas, respectively) [1]. Such exploitation of fossil fuels has exacted a huge toll on humanity and the environment. Carbon dioxide (CO_2) is a key greenhouse gas (GHG) linked to the deployment of fossil fuels. It is the primary causative agent of climate change even though the global warming potential (GWP) of CO_2 is much lower than that of other gases (GWP of CO_2 is 1, while it is 28−36 and 265−298 times that of CO_2 for CH_4 and N_2O, respectively [2], the emissions of CO_2 are far more abundant.

As proof of the impact of anthropogenic activities in the emission of CO_2, its concentration in the atmosphere has increased greatly since the Industrial Revolution (270−275 ppm in 1750; 310 ppm in 1950; 408 ppm in 2018; 413 ppm in 2021) [3], with a total emission of 36 Gt CO_2 per year, 91% of it being generated by anthropogenic activities [4]. In such energy and environmental context, it is evident that a massive change in the current energy scenario is necessary to avoid further irreversible environmental impacts. Finding carbon-emission-free energy sources is mandatory. The gradual global energy transformation from a fossil fuel-based energy system to a low-carbon energy system is supported by several international policies. The Sustainable Development Goals (SDGs), adopted by the United Nations General Assembly (UNGA) in 2015, is a robust framework for international cooperation to achieve a sustainable future [5]. Goal number 7 aims at ensuring access to affordable, reliable, sustainable, and modern energy for all so that the gradual introduction of alternative energy sources to the detriment of fossil fuels is required to meet such a goal. Renewable energy sources (i.e., wind, biomass, sunlight, water, Earth's internal heat, etc.) play an important role in the energy scenario since they are inexhaustible and environmentally friendly. However, renewable resources are not always available where and when the energy is needed, causing a mismatch between energy demand and supply. This decoupling together with the challenges associated with the generation of large quantities of power achieved by renewable energy technology compared to fossil fuels−derived energy and the massive upfront capital outlay, overshadow the potential of the renewable energy sources [6].

Against such a context, hydrogen is an alternative carbon emission-free energy carrier (or secondary energy source) postulated as an auspicious candidate to transform the fossil fuel−dependent life and economy into a greener and environmentally friendly picture. Some of the advantages of hydrogen as an energy carrier were nicely summarized by Rosen and Koohi-Fayegh [7]:

- Hydrogen can be manufactured from hydrocarbon and nonhydrocarbon.
- Hydrogen can be deployed as a chemical fuel and as a chemical feedstock in many industrial processes and transportation.
- It is transportable.
- It is environmentally friendly since the combustion of hydrogen is a carbon-free reaction.
- Physical and chemical methods can store hydrogen.

As for hydrogen production, since hydrogen, like electricity, is a secondary energy source (or energy carrier), it has to be produced from primary energy sources (i.e., fossil, nuclear, or renewable). The vast majority of hydrogen is currently produced from fossil fuels without CO_2 capture (gray hydrogen), which is not a sustainable option because it does not eliminate carbon emission [8]. Hydrogen storage also has challenges. It has the highest energy per mass of any fuel. However, its low ambient temperature density results in a low energy per unit volume, so that developing advanced storage methods to achieve higher energy density is required. Hydrogen has some properties that make it safer to handle than other fuels. For instance, hydrogen is nontoxic and much lighter than air, so that it allows easy dispersion in case of a leak [9]. However, some other properties, such as the wide range of flammable concentrations in air and low ignition energy, require additional attention to design a safe hydrogen system, thus holding back the widespread adoption of hydrogen-based energy systems.

Conversely, chemical hydrogen storage stands as a safe and more convenient option than classical physical storage. Hydrogen carrier molecules can reversibly deliver hydrogen via chemical reactions. Of special interest are the liquid organic hydrogen carriers (LOHCs), since they provide great advantages in terms of availability, recharging, and safety [10–12]. LOHC systems are formed by a hydrogen-lean organic compound and a hydrogen-rich organic compound. Hydrogen is stored by converting the hydrogen-lean compound into the hydrogen-rich counterpart by a catalytic hydrogenation reaction. In contrast, hydrogen is released by the dehydrogenation of the hydrogen-rich compound. Bessarabov et al. recently summarized the main properties that LOHCs molecules should possess [11]:

- Low melting point and high boiling point.
- High hydrogen storage capacity.
- Ability to undergo selective hydrogenation and dehydrogenation for long life cycles of charging and discharging.
- Compatibility with the current infrastructure for fuels.
- Low production costs and good technical availability.
- Toxicological and eco-toxicological safety during transportation and use.

There are several LOHCs systems (i.e., cyclohexane-benzene, methylcyclohexane-toluene, decalin-naphthalene, perhydro-N-ethylcarbazole-N-ethyl carbazole, and perhydro dibenzyl

toluene-dibenzyl toluene, etc.), which have been recognized as suitable candidates [11,13]. Formic acid is a prominent example of LOHC, which has merited numerous studies in the last decade [14–19].

2. Formic acid

Formic acid (HCOOH, FA), systematically called methanoic acid, is the simplest carboxylic acid. FA was seen as potential hydrogen storage more than 4 decades ago [20], but it was not until the 2000s when its use as an LOHC was recognized in the independent investigations conducted by Laurenczy's and Beller's research groups [21,22]. Later, in the 2010s, FA started to gain more and more interest as a suitable hydrogen carrier, and it is nowadays considered one of the most promising LOHCs [15].

FA is a colorless, clear, and corrosive liquid with a pungent odor [23]. It has a volumetric capacity of 53 g_{H2} L^{-1}, low toxicity, nonflammability (flashpoint of 69°C, which is much higher than that of methanol (12°C) and gasoline (−40 °C)), and it is biodegradable [18]. FA has a boiling point of 100.8°C and a density of 1.22 g mL^{-1}.

FA is naturally present in most ants and some species of bees. The production of FA can be obtained by several processes, such as acidolysis of formate salts, oxidation of hydrocarbons, hydrolysis of formamide, mineral acid catalysis, and hydrolysis of lower alkyl formats [24]. Large-scale production of FA from renewable sources is highly desirable to emphasize its potential in a future green energy scenario. The production of FA from biomass-derived feedstock by several processes (i.e., hydrolysis, wet oxidation, and catalytic oxidation) was recently reviewed by Bulushev and Ross [25]. Interestingly, FA can also be obtained from hydrogenating carbon dioxide (CO_2) utilizing chemical, photochemical, and electrochemical routes and selecting a proper catalyst and reaction conditions [26]. FA and CO_2 are thus involved in an ideal carbon-neutral cycle, which is very appealing from a sustainable viewpoint [27].

FA is an essential chemical commercially deployed in several fields, such as in industry, grass silage, leather tanning, anti-icing, textile dyeing, food additives, natural rubber, drilling fluids, etc. [23,24].

Concerning the decomposition of FA, it can follow two different ways:

- Dehydrogenation: $HCOOH \leftrightarrow H_2 + CO_2$ ($\Delta G^\circ = -32.9$ kJmol^{-1})
- Dehydration: $HCOOH \leftrightarrow H_2O + CO$ ($\Delta G^\circ = -12.4$ kJmol^{-1})

The Gibbs free energy of the dehydrogenation of FA is low compared to other hydrogen storage chemicals [23]. It can occur at moderate temperatures, reinforcing its suitability as a hydrogen carrier. Also, as mentioned before, the CO_2 generated in the reaction can be

hydrogenated back to FA ($H_2 + CO_2 \leftrightarrow HCOOH$), so that FA is a reversible hydrogen storage molecule.

Upon proper selection of the catalysts, FA can be converted to hydrogen under mild conditions. Both homogeneous and heterogeneous catalysts with diverse compositions have already been explored in the literature. The studies of Laurenczy et al. and Beller et al. deserve special mention among those reporting on homogeneous catalytic systems [28–31], while those breakthroughs achieved by Xu et al. [32–35], Mori et al. [36–39] and Bulushev et al. [40–43] should be remarked among those studies dealing with the decomposition of FA with heterogeneous catalysts. Due to the advantages of heterogeneous catalysts, the present chapter is focused on the main recent insights achieved by representative heterogeneous systems.

The main factors considered while optimizing the catalytic systems able to boost the dehydrogenation of FA are the following [15]: (i) Selectivity toward the production of hydrogen via dehydrogenation reaction, (ii) catalytic activity, expressed in terms of turnover frequency (TOF) at a given reaction time temperature, (iii) catalytic stability or durability under reaction conditions, and (iv) cost of the catalysts. With all this in mind, several approaches have been covered in the literature. On the one hand, the properties of the active phase, which is frequently in the form of metal nanoparticles, have been fruitfully explored, with the composition being the most investigated aspect. In this respect, Pd-based catalysts have been claimed to be the most suitable due to their excellent activity and selectivity toward the desired dehydrogenation pathway, thus suppressing the formation of CO by the dehydration reaction. On the other hand, supports of very diverse composition (i.e., zeolites [44,45], silica [46,47], resins [37,48], metal-organic frameworks (MOFs) [49,50], etc.) have been used to develop heterogeneous catalysts for the present application. Among investigated, carbon materials are the more widely explored catalytic supports [51] due to their excellent properties and versatility [52]. Thus, the present chapter is devoted to summarizing some of the recent breakthroughs achieved by carbon material-based heterogeneous catalysts in the decomposition of FA.

3. Dehydrogenation of formic acid attained by carbon-based catalysts

As mentioned before, several factors control the catalytic dehydrogenation of FA, which, in a very simplified classification, can be divided into those related to the properties of the active metal phase and those related to the properties of the supports. Both aspects are interconnected so that analyzing the effect of either the active phase or support in the final catalytic performance while disregarding the effect of the other component is somehow challenging. For the sake of clarity, the following two sections summarize the most important findings achieved while exploring the effect of the properties of the active phase and support with both monometallic Pd catalysts (Section 3.1) and bimetallic catalysts

(Section 3.2). Unless indicated, the studies covered in the following sections are related to catalysts used in the dehydrogenation of FA in the liquid phase.

3.1 Monometallic Pd-based catalysts

Several factors should be considered when optimizing the features of the active metal phase. Among them, the composition of the metal nanoparticles has been the most explored aspect. Pd-based catalysts are the most active and selective toward the dehydrogenation of FA. Several factors have been considered to design efficient catalysts for this application. As previously mentioned, they are related to the features of the active metal phase and the properties of the support.

As for the properties of the monometallic Pd active sites, the size and electronic properties of the nanoparticles are the most widely investigated aspects of optimizing the performance of the catalysts for the dehydrogenation of FA. Some works anticipated the importance of controlling the size of Pd nanoparticles in attaining good catalytic performance [53−55], but our group was a pioneer in studying the effect of the nanoparticle size of Pd-based catalysts in the decomposition of FA [56,57] systematically. For that, colloidal Pd nanoparticles were synthesized using the reduction by solvent method (so-called polyol method), with ethylene glycol as the solvent, polyvinylpyrrolidone (PVP) as a stabilizing agent, and palladium (II) acetate as a Pd precursor. The size of the nanoparticles was controlled by adjusting the experimental conditions (i.e., PVP/Pd molar ratio, synthesis temperature, and time), and once the nanoparticles were formed, they were subsequently incorporated onto the carbon support (a commercial activated carbon (Shirasagi M)) by following a standard impregnation method. Catalysts with an average size of 2.7, 3.6, 3.9, 4.2, and 5.5 nm were achieved, and they were denoted as Pd/C(1)−(5), respectively. They all had Pd nanoparticles with a spherical shape, very narrow size distribution, and homogeneous dispersion. After the characterization of the catalysts by several physicochemical techniques, their performance in the dehydrogenation of FA was assessed by monitoring the reaction by gas chromatography using a reaction temperature of 30 °C. The results achieved are summarized in Fig. 9.1. Fig. 9.1(A) depicts the hydrogen production achieved after 3 h of reaction as a function of the average nanoparticle size of the catalysts. Among investigated, that catalyst with an average nanoparticle size of 3.9 nm showed the best activity under the experimental conditions used in that study. The volcano-type relationship established between the production of hydrogen and the size of Pd nanoparticles was explained by the relative proportion of low-coordinated atoms (LC) and high-coordinated atoms (HC) present in the catalysts concerning the total surface atoms [58]. The TOF values were calculated based on these specific atoms (Fig. 9.1B), and the results indicated that the reaction is structure-sensitive. The high-coordinated Pd atoms at terrace sites are the main active species in controlling the activity of the catalysts.

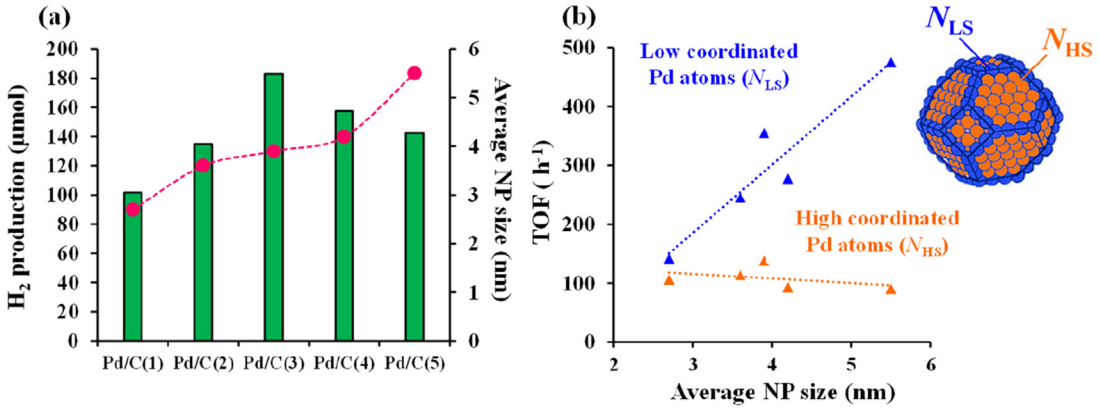

Figure 9.1

(A) Relationship between H_2 production after 3 h of reaction at 30°C and the average Pd nanoparticles (NPs) size; (B) normalized TOF values calculated based on high-coordinated (HC) and low-coordinated (LC) as a function of the average Pd NP size. *Adapted with permission from Ref. [57]. Copyright 2016, Wiley-VCH.*

Following that study, some other reports were published on the effect of Pd nanoparticles' size on the dehydrogenation of FA. However, the size-dependent Pd-catalyzed dehydrogenation of FA is still controversial, and different tendencies have been found in the recent literature.

For instance, Cai et al. explored the effect of the Pd nanoparticle size by synthesizing surfactant-free carbon (i.e., Vulcan XC-72) supported catalysts with nanoparticle size from 2.0 to 5.2 nm [59]. The control of the size of the nanoparticles was achieved by varying the pH from 7.0 to 9.5 by adding Na_2CO_3, $NH_3 \cdot H_2O$, or NaOH to the solution with the Pd precursor and with sodium borohydride ($NaBH_4$) as a reducing agent. The selection of those additives was made based on the changes of the redox potential of M^{n+}/M depending on the coordination of the metal ions and the pH dependence of the reducing strength of $NaBH_4$. The as-synthesized catalysts also showed a volcano-type relationship between the TOF value and the Pd nanoparticle size. The catalysts with an average size of 2.2 nm showed the best activity. As in our study [57], the volcano-type dependence of TOF on Pd nanoparticle size was attributed to the changing ratios of high-coordinated and low-coordinated sites on the surface of the nanoparticles, but other factors, such as the electronic properties of the Pd species, were also mentioned. Lu et al. also investigated the effect of the size of the nanoparticles by developing carbon-supported Pd catalysts, using sizes from 2.1 to 4.5 nm [60]. The size of the nanoparticle was controlled by setting different reduction temperatures and the addition of $NaBH_4$ (5, 25, or 60 °C) or sodium citrate to Pd precursor (ratio 8:1 or 2:1). The activity of the resulting catalysts at 25°C was evaluated by registering the volume of gas generated. It was seen that the sample with

nanoparticles of 2.1 nm had the best performance and that the performance, in terms of both reaction rate and conversion, progressively decayed with increasing nanoparticle size. Based on the calculation of the TOF values considering the high-coordinated surface atoms, the low-coordinated surface atoms, and the total number of surface atoms, it was claimed that all the Pd surface atoms act as active sites and are involved in the decomposition of FA.

Kim et al. also synthesized size-controlled Pd/C catalysts using $NaBH_4$ as a reducing agent, and the resulting catalysts had a Pd size ranging from 2.5 to 4.8 nm. In that study, the reaction was monitored at different temperatures (30−60 °C) to ascertain whether the Pd nanoparticle's size was thermodynamic. It was observed that the catalysts with the smallest nanoparticle size displayed the highest activity for all the reaction temperatures and that they declined with increasing particle size. In order to get further insights into that issue, TOF values were calculated based on the total number of Pd (TOF bulk, h^{-1}) and some surface Pd sites (TOF surface, h^{-1}). It was seen that TOF surface values presented different tendencies depending on the reaction temperatures. As in the case of TOF bulk, at low temperatures (i.e., 30 and 40 °C), the TOF surface values decreased with increasing particle size, suggesting that small Pd nanoparticles were more active for this reaction. However, it was observed that at higher temperatures (i.e., 50 and 60 °C), the TOF surface values were independent of the nanoparticle size. The authors of that study concluded that there is a thermodynamic effect of Pd nanoparticles size on the dehydrogenation of FA, which was demonstrated by the increase in activation energy with the increase in the size of the nanoparticles. More recently, following our study [57], Odriozola et al. checked the structure sensitivity of FA dehydrogenation reaction over Pd nanoparticles supported on activated carbon by extending the size range from 2.8 to 56.0 nm and avoiding the use of stabilizing agents [61]. The control of the size of the nanoparticles was achieved upon variation of the synthesis conditions such as the Pd precursor (i.e., palladium (II) trimer acetate, $Pd_3(OAc)_6$; palladium (II) nitrate, $Pd(NO_3)_2$, and palladium (II) chloride, $PdCl_2$) and solvent (water and acetone). It was observed that, within the range of 2−7 nm, a volcano-type relationship between the catalytic activity and the size of the nanoparticles existed, with the maximum TOF for those catalysts with an average size of 4−5 nm. As expected, the activity significantly decayed for larger nanoparticles. As we did in our study [57], the size-activity dependence was explained based on the relative proportion of low and high coordinated atoms.

The control of the size of the nanoparticles usually requires the use of a capping agent and certain pH conditions, thus involving quite complex synthetic protocols. Jiang et al. developed a simple strategy for synthesizing in situ formed Pd/C catalysts in the presence of citric acid and supported on Vulcan XC-72 carbon [54]. The reducing agent used was sodium formate, a common additive used in the dehydrogenation of FA. The resulting catalysts showed dispersed ultrafine Pd nanoparticles and displayed improved activity

compared to that observed in the absence of citric acid during the nucleation and growth of Pd nanoparticles. It was postulated that citric acid did not act as a co-catalyst, but it has an important role in forming the nanoparticles serving as an efficient dispersing agent. As explained in that publication, the carboxylate anions of citric acid strongly adsorb on the carbon support surface, and they attach Pd species, serving as nucleation sites. Then, once the reduction of the Pd species with sodium formate takes place, citric acid anchors the Pd nanoparticles, thus attaining a good control of the size and dispersion of the nanoparticles on the carbon surface.

Some other strategies have been applied to achieve well-dispersed metal species. For instance, Bulushev et al. reported for the first time on Pd single-site supported on nitrogen-doped carbon for the dehydrogenation of FA in the gas phase [41]. A detailed characterization of the samples by experimental and theoretical analysis revealed that those isolated Pd^{2+} cations stabilized on mesoporous carbon by a pair of pyridinic type nitrogen atoms on the edge of a graphene sheet showed excellent activity toward the dehydrogenation of FA in the gas phase. A similar strategy was also followed by using different carbon materials [62] and other metal species [63,64].

Wang et al. also checked the incorporation of nitrogen functional groups as a suitable strategy to achieve promising carbon-based catalysts for the dehydrogenation of FA [65]. Well-dispersed Pd nanoparticles with an average particle size of 2.5 nm were attained on amino-functionalized hierarchically porous carbon. The results of the catalytic tests indicated that the N-containing samples (Pd/NHPC−NH_2) had much superior performance than that of N-free catalysts, achieving a TOF value of 1265 h^{-1} at room temperature on total Pd atoms. Such an enhancement was attributed to the synergistic effect between Pd and amino groups. It was postulated that amino groups assisted the activation of the O−H bond of FA molecules, which is a key step in the reaction mechanism. The proposed mechanism is schematized in Fig. 9.2. As indicated, Pd/NHPC−NH_2 acted as proton scavengers creating a basic environment and promoting the dissociation of the O−H bond, producing H^+. After that, the positively charged Pd species promotes the adsorption of $HCOO^-$ and the formation of formate intermediates. Then, CO_2 is released, and H^- is produced. The last step is the generation of H_2 by the combination of H^+ and H^-.

Xing et al. prepared pyridinic-nitrogen-doped Pd catalysts via in situ polymerization reaction from a hyperbranched polyamide and with Vulcan XC-72 as support [66]. The approach followed afforded catalysts with very small Pd nanoparticles (2.2−2.3 nm), attributed to the quasi-spherical nanocage architecture of the hyperbranched polyamide serving as an effective template to obtain small Pd nanoparticles. As expected, the catalysts with nitrogen presented much better activity than those without nitrogen, and a linear correlation between the catalytic activity and the surface nitrogen content was found.

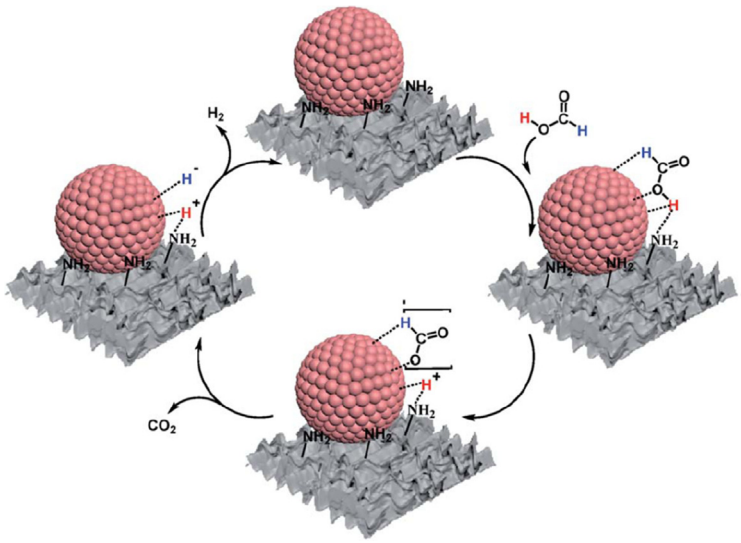

Figure 9.2
Reaction pathway for the dehydrogenation of formic acid (FA) over Pd/NHPC−NH_2. *Reprinted with permission from Ref. [65]. Copyright 2019, Royal Society of Chemistry.*

Our group has also addressed the incorporation of nitrogen functional groups as a promising strategy for enhancing the performance of carbon-supported catalysts. Such functionalities modify the local basicity of the catalysts and influence the metal species' electronic density. We evaluated the effect of the nitrogen doping level on the catalytic performance of Pd-based catalysts in the dehydrogenation of FA by using carbon xerogels as supports [67]. In those materials, the nitrogen content and the porous texture were modulated by controlling the experimental conditions used in the synthesis. To do this, N-doped carbon xerogels were synthesized by a polycondensation method of resorcinol and formaldehyde in the presence of melamine [68], and the resulting materials were impregnated with the Pd precursor. The characterization of the materials confirmed that the nitrogen doping level was a key aspect to attain small and well-dispersed Pd nanoparticles. Among investigated, the catalysts with a nitrogen content of ∼4 wt% were optimum to achieve well-dispersed nanoparticles. It was also observed that, for given nitrogen content, the catalyst with a well-defined micro-mesoporous texture presented better activity than that of the sample with micro-macro porosity, thus suggesting the importance of controlling the porosity development of the carbon support. In a more recent publication, we developed nitrogen-doped carbon-supported catalysts using support prepared from a biomass waste (hemp residue) by H_3PO_4-assisted hydrothermal carbonization [69]. In that case, we incorporated the nitrogen functional groups by an organic reaction in the presence of pyridine. N-free and N-containing catalysts were prepared by a standard impregnation method. It was observed that the incorporation of

nitrogen had a positive effect on the catalytic performance. The developed catalysts showed excellent stability even after 12 consecutive reaction cycles at 75°C, thus overcoming one of the main limitations of most of the catalysts used in this application. It was also seen that those catalysts with in situ reduced Pd nanoparticles showed better performance than those reduced with $NaBH_4$.

Podyacheva et al. recently reported on the catalytic performance of Pd catalysts supported on bamboo-like nitrogen-doped carbon nanotubes for the dehydrogenation of FA in the gas phase [70]. As Bulushev et al. had already reported in their study [41], single isolated Pd ions were detected in the catalysts, stabilized on the accessible pyridinic centers. In that study, carbon nanotubes were synthesized by the CVD method, and they were subsequently loaded with the Pd precursor to achieving catalysts with Pd contents between 0.2 and 2.0 wt%. The resulting catalysts had a very small Pd nanoparticle size (1.3−2.3 nm) and no detectable nanoparticles in those catalysts with the lowest Pd content. Among investigated, those catalysts with the lowest Pd content (0.2 wt%) achieved the highest TOF (324 h^{-1}) due to the presence of such isolated palladium species.

Xu et al. also reported the suitability of N-containing Pd catalysts for the dehydrogenation of FA [34]. In that study, catalysts based on Pd nanoparticles immobilized in nitrogen-doped hierarchically porous carbon were prepared from an Al-based MOF (Al-MIL-101-NH_2). The obtained catalyst had both micro- and mesoporosity and Pd nanoparticles of 1.1 nm, and it showed an excellent catalytic activity (TOF of 14,400 h^{-1}, at 60 °C). As we observed [67], the mesopores contributed to the suitable catalytic performance due to the efficient mass transport in the catalysts. Also, the synergistic effect between N and Pd was pointed out in that study. The same research group further explored the potential of incorporating heteroatoms in the carbon support to attain catalysts with good catalytic activity for the present application by synthesizing catalysts based on Pd nanoparticles supported on boron-oxygen-nitrogen-functionalized carbon nanospheres [71]. First, boron-oxygen (B−O)-functionalized carbon nanospheres (OB−C) were prepared from Vulcan XC-72R carbon and boric acid. Nitrogen functionalization was incorporated by introducing melamine in the synthesis. It was observed that the incorporation of N atoms favored the incorporation of more B atoms compared to the N-free sample, thus overcoming the difficulties faced sometimes in doping B into the carbon framework. Supports with various contents of both B and N were prepared, and the resulting carbons were loaded with Pd nanoparticles by wet impregnation and reduction with $NaBH_4$ assisted by NaOH. The functionalization of carbon with B and N was beneficial to achieve smaller nanoparticles of 1.4−1.7 nm compared to those detected in the catalysts based on the pristine carbon support (3.1 nm). The results of the catalytic tests evidenced the superiority of B−N-doped catalysts, which showed a TOF of 5354 h^{-1} at 50 °C, which

was about 3 and 10 times larger than those of the N-free catalysts and pristine catalysts, respectively.

Chang et al. recently explored the potential of a more complex system based on Cr_2O_3 co-doped MOF-derived porous carbon-supported Pd nanoparticles [72]. The porous carbon was prepared by carbonization of NH_2-MIL-101(Cr) at different temperatures (i.e., 550, 650, 750, 850, and 950 °C). The obtained support was loaded with the Pd precursor, which was reduced with $NaBH_4$. The resulting catalysts were denoted as Pd@Cr_2O_3-NPCB-T, being "T" the temperature used in the calcination step. It was observed that the catalyst obtained from the support prepared at 850 °C was the most active, with a TOF of 3473 h^{-1}. It was concluded that the good activity displayed by that material was due to the beneficial role of N and Cr_2O_3, which could modify the electronic properties of Pd species, giving rise to electron-rich Pd nanoparticles. That species facilitates the dissociation of the C−H bond in FA molecules. It was also claimed that the presence of N and Cr_2O_3 helps to achieve ultrafine Pd nanoparticles and prevents their agglomeration, which resulted in catalysts with excellent cycling stability during five consecutive reactions at 60 °C.

3.2 Bimetallic Pd-based catalysts

Great breakthroughs have recently been achieved using monometallic Pd-based catalysts. However, those catalysts frequently show some issues related to their deactivation due to the adsorption of poisoning intermediates and/or changes in the properties of the catalysts. Such an issue can be palliated by using bimetallic Pd-based catalysts or catalysts, which have Pd species with modified electronic structures than monometallic systems. Also, bimetallic catalysts may have weakened hydrogen adsorption on the surface of the nanoparticles, which eventually results in a favored production of molecular hydrogen from the combination of two hydrogen atoms [73]. The enhanced performance of bimetallic catalysts has also been attributed to controlling the size of alloy nanoparticles compared to monometallic catalysts [74].

Among the possible combinations, PdAg and PdAu are the most fruitfully investigated systems in bimetallic nanoparticles and multimetallic catalysts [75−77].

The high activity shown by PdAg-based catalysts in the dehydrogenation of FA is frequently related to the efficient electron density transfer from Ag to Pd and subsequent electron enrichment on the surface of the Pd species (the so-called "ligand effect") due to the net difference in electronegativity of both elements (1.9 and 2.2 in Pauling scale, for Ag and Pd, respectively) [51,74]. Tedsree et al. reported one of the first studies on FA decomposition catalyzed by PdAg systems [78]. In that study, core-shell bimetallic

nanoparticles were prepared with the aim of generating electronically modified Pd. Compared to the monometallic counterpart, the improvement observed for that system was related to the charge transfer from the Ag core to the Pd shell and the strengthened adsorption of formate intermediates. The interesting results achieved in that study paved the way for new investigations on PdAg catalysts for this application. From that study, many investigations have been conducted to elucidate the optimum composition and properties of bimetallic PdAg nanoparticles to achieve promising catalysts in the dehydrogenation of FA.

Sun et al. evaluated the activity of alloy AgPd catalysts with various compositions (i.e., $Ag_{25}Pd_{75}$, $Ag_{42}Pd_{58}$, $Ag_{52}Pd_{48}$, $Ag_{60}Pd_{40}$, and $Ag_{80}Pd_{20}$) and supported on Ketjen carbon. The better activity shown in the bimetallic system was attributed to the small size of the nanoparticles and the synergistic effect between Pd and Ag in the alloy. Such an effect inhibited the adsorption of CO on Pd active sites, thus resulting in enhanced performances. Among investigated, the samples with a composition of $Ag_{42}Pd_{58}$ were optimum.

Chen et al. checked the effect of the composition of AgPd catalysts supported on graphene [79]. The nanoparticles were prepared by co-reduction of the metal precursors (i.e., silver nitrate and palladium acetylacetonate) in 1-octadecene and oleic acid and with *tert*-butylamine borane as the reducing agent, and they were subsequently loaded onto graphene. Catalysts with alloy structure and various compositions of the nanoparticles were synthesized and evaluated in the dehydrogenation of FA at room temperature. It was observed that the bimetallic catalysts displayed better performance than the monometallic counterparts, and the most active sample ($Ag_{74}Pd_{26}$/graphene) had a TOF value of 572 h^{-1} at room temperature.

Aside from the composition of the bimetallic PdAg nanoparticles, the synthetic route followed in the preparation of bimetallic nanoparticles is crucial to determine the properties of the resulting catalysts. For instance, Li et al. explored the effect of the reducing agent by using sodium borohydride (SB), FA, ascorbic acid (AA), and hydrogen (catalysts denoted as PdAg/C-SB, PdAg/C-FA, and PdAg/C-AA, and PdAg/C−H, respectively) [80]. It was seen that those catalysts prepared by a wet reduction approach had an average nanoparticle size of ∼5 nm, while gas-chemical reduction gave rise to larger nanoparticles (7.5 nm). The surface composition of the nanoparticles was also determined in that study. It was observed that the Pd/Ag molar ratio also depended on the reducing agent (Pd/Ag of 2.97, 2.48, 2.34, and 0.81 for PdAg/C-AA, PdAg/C-FA, PdAg/C−H, and PdAg/C-SB, respectively, compared to the nominal Pd/Ag ratio of 1). Not only the particle size and the distribution of the atoms in the nanoparticles were affected by the reducing agent used in the synthesis but also the electronic state of the surface of the nanoparticles. Among studied, the sample reduced with FA showed the best activity, with an initial TOF of 90 h^{-1} at room temperature. We also checked the impact of the surface

composition of PdAg catalysts in the activity of carbon-supported catalysts by screening the performance of 12 catalysts formed by preformed nanoparticles supported on a commercial activated carbon [81]. In that case, the nanoparticles were prepared by the polyol method, and their composition was modified by varying the concentration of the metal precursors (Pd/Ag molar ratios of 1/0.5, 1/1, 1/2, and 1/4). Also, four different PVP/metal molar ratios were used in the synthesis. The characterization of the catalysts indicated that, for a given Pd/Ag molar ratio used in the synthesis of the nanoparticles, their surface composition depended on the amount of PVP used in the synthesis (i.e., lower PVP content favored the formation of Pd-rich surface nanoparticles). The performance of the developed catalysts was evaluated in the dehydrogenation of FA at 75°C, and the sample with molar ratios of Pd/Ag of 1/2 and metal/PVP of 1/1 was optimum among investigated.

As in the case of monometallic catalysts, they were incorporating nitrogen functional groups has been shown to enhance the activity of bimetallic PdAg catalysts. We recently explored the performance of catalysts formed by PdAg nanoparticles loaded onto mesoporous carbon functionalized with amino groups for reversible dehydrogenation of FA and CO_2 hydrogenation [82]. It was observed that the presence of phenylamine groups near the PdAg active sites affected the dissociation of the O—H bond in FA and also the CO_2 adsorption capacity in the catalyst. It was also seen that the presence of nitrogen functionalization resulted in electron-deficient Pd species. In contrast, the presence of Ag in the nanoparticles favored the presence of electron-rich Pd species in the catalysts. The developed materials showed excellent ability toward the interconversion of FA and CO_2, with a TOF as high as 21,686 h^{-1} (considering the surface on Pd atoms) for the dehydrogenation of FA at 75°C. Other nitrogen-containing carbon-based supports have also been utilized. For instance, Jia et al. explored the performance of AgPd alloy nanoparticles, with different molar ratios (Ag: Pd of 1:4, 1:1, 2:1, 1:0, and 0:1) supported on carbon nitride (C_3N_4) for the dehydrogenation of FA at 75°C [83]. As expected, the XPS analysis confirmed the formation of alloy nanoparticles and the electron transfer from Ag to Pd in the nanoparticles. It was also proved that the catalytic performance strongly depended on the composition of the nanoparticles, and it was optimum for that sample with an Ag/Pd ratio of 1/2, with a TOF of 621 h^{-1}.

Yang et al. also used C_3N_4-based PdAg catalysts to produce hydrogen from FA, but, in that study, their activity toward the visible-light-driven photocatalytic reaction was addressed [84]. In that case, two-dimensional *g*-C_3N_4 nanosheets (2D convolutional neural networks (CNNs)) were prepared from melamine and lithium chloride. They were subsequently loaded with the metal precursors, which were reduced with $NaBH_4$ to attain the AgPd/2D CNNs photocatalyst (see Fig. 9.3). Catalysts with the following composition of the nanoparticles were synthesized: Ag/2D CNNs, $Ag_{0.1}Pd_{0.9}$/2D CNNs, $Ag_{0.2}Pd_{0.8}$/2D CNNs, $Ag_{0.3}Pd_{0.7}$/2D CNNs, and Pd/2D CNNs. The photocatalytic performance of these

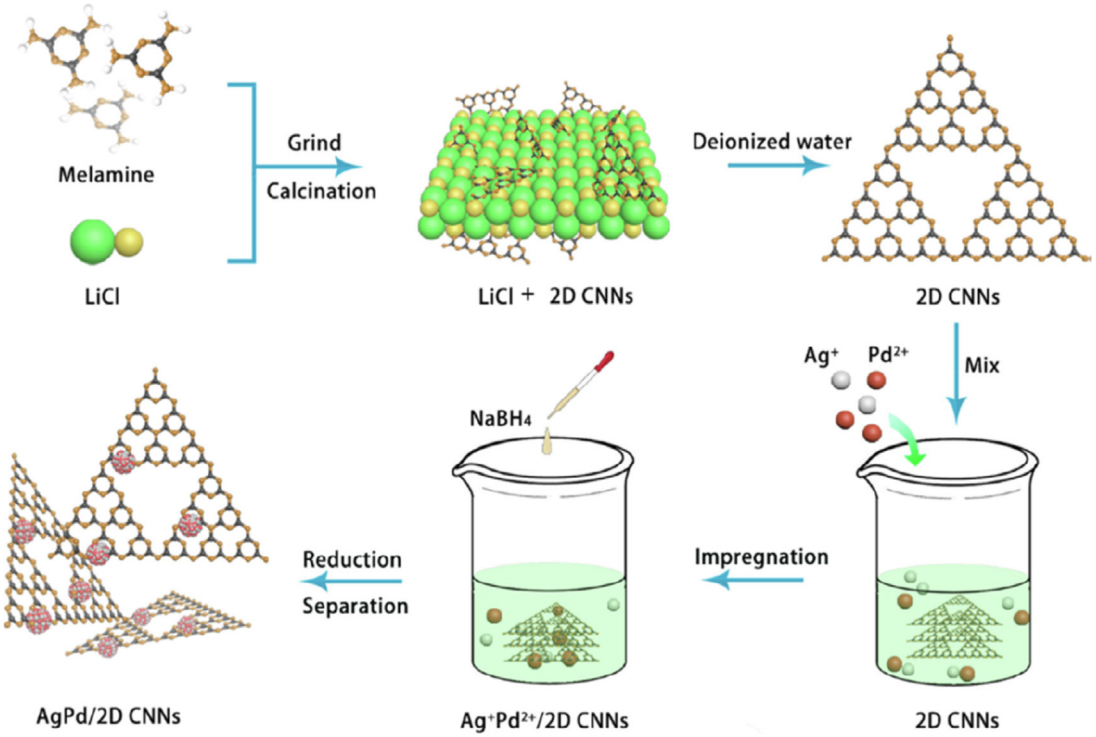

Figure 9.3
Schematic illustration of the synthesis of AgPd/2D convolutional neural networks (CNNs) photocatalyst. *Reprinted with permission from Ref. [84]. Copyright 2020, Elsevier.*

samples under visible light illumination ($\lambda > 400$ nm) revealed that $Ag_{0.1}Pd_{0.9}$/2D CNNs was the most active, generating 135 mL of gas ($H_2 + CO_2$) in only 1.3 min, and with a TOF of 2936.8 h^{-1}, which was much higher than that of Pd monometallic counterpart catalysts, (1185.7 h^{-1}) and that of $Ag_{0.1}Pd_{0.9}$/CN, which had *g*-C_3N_4 as support (837.2 h^{-1}). The superior photocatalytic behavior of $Ag_{0.1}Pd_{0.9}$/2D CNNs was attributed to the charge redistribution and strong Pd−Ag interactions and the interaction between nanoparticles and 2D CNNs support. Comparing the catalytic tests under dark and visible light irradiation made the authors determine that the contribution of the thermal effect and light irradiation was 54% and 46%, respectively. That catalyst also displayed excellent stability during 10 consecutive photocatalytic cycles.

Cheng et al. recently reported the applicability of N-deficient-ordered mesoporous graphitic carbon nitride coupled with AgPd nanoparticles (AgPd/N-ompg-C_3N_4) [85]. For that, N-ompg-C_3N_4 was synthesized using SBA-15 and cyanamide as the hard template and the precursor, respectively, and the properties of the support were modulated by using different etching agents (i.e., NaOH, hydrogen fluoride, and ammonium bifluoride;

supports denoted as N-ompg-C_3N_4, N_H-ompg-C_3N_4, and N_N-ompg-C_3N_4, respectively), during the template removal. After that, the supports were impregnated with the metal precursors, and they were reduced with $NaBH_4$. To explore the catalytic activity of the developed materials (see Fig. 9.4), the effect of the composition of the nanoparticles was studied, and it was found that $Ag_{0.1}Pd_{0.9}$/N-ompg-C_3N_4 was the optimum among investigated, with an initial TOF of 1588 h^{-1} (Fig. 9.4A and B). It was also observed that the performance varied depending on the etching agent used in the synthesis, and $Ag_{0.1}Pd_{0.9}$/N-ompg-C_3N_4 (prepared using NaOH) had the optimal performance, which is nearly 1.7 and 1.4 times higher than those of $Ag_{0.1}Pd_{0.9}/N_H$-ompg-C_3N_4 (929.7 h^{-1}) and $Ag_{0.1}Pd_{0.9}/N_N$-ompg-C_3N_4 (1157 h^{-1}), prepared with hydrogen fluoride and ammonium

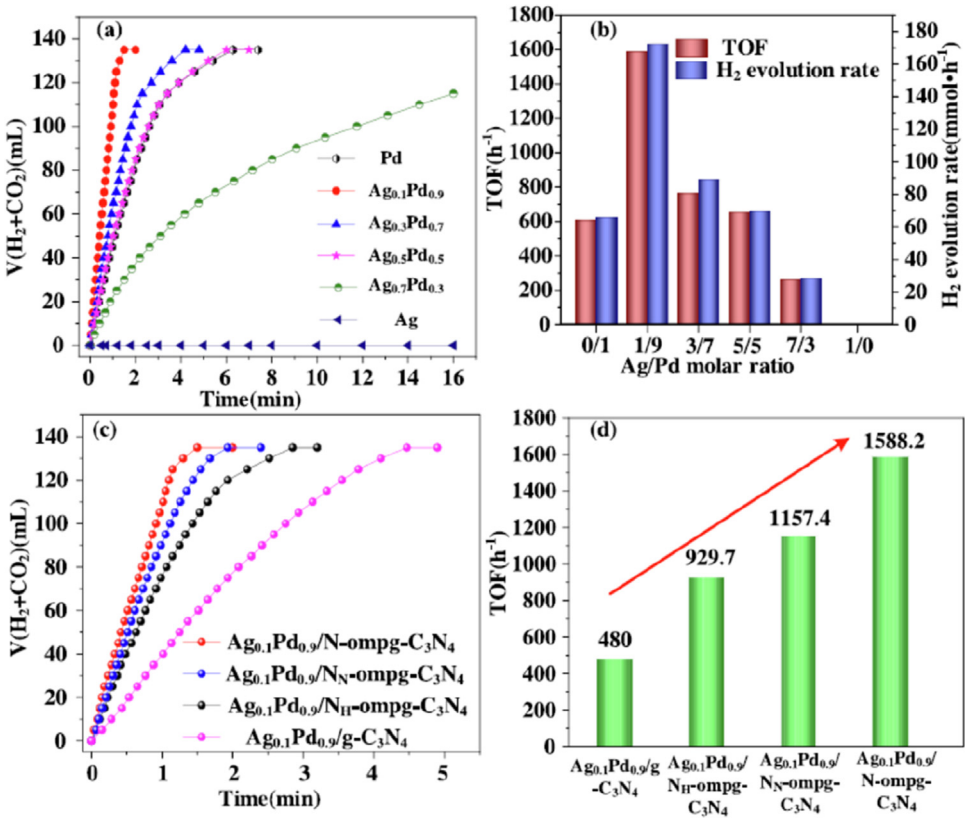

Figure 9.4

(A) The plots of generated gas (CO_2 + H_2) versus time and (B) the corresponding hydrogen evolution rate and initial turnover frequency (TOF) values of N-ompg-C_3N_4 different Ag/Pd molar ratio at 50°C (n_{FA} = 3 mmol, n_{SF} = 1 mmol). (C) The plots of generated gas (CO_2 + H_2) versus time and (D) the corresponding initial TOF values of $Ag_{0.1}Pd_{0.9}$/g-C_3N_4, $Ag_{0.1}Pd_{0.9}$/N-ompg-C_3N_4, $Ag_{0.1}Pd_{0.9}$/NH-ompg-C_3N_4, and $Ag_{0.1}Pd_{0.9}$/NN-ompg-C_3N_4. *Reprinted with permission from Ref. [85]. Copyright 2022, Elsevier.*

bifluoride, respectively (Fig. 9.4C and D). Such an effect was attributed to the smallest size of the nanoparticles present in $Ag_{0.1}Pd_{0.9}$/N-ompg-C_3N_4 catalysts. Also, the strong metal−support interaction between AgPd and N-ompg-C_3N_4 contributed to the enhanced activity observed in the catalysts with N-deficiency compared to that supported on *g*-C_3N_4 ($Ag_{0.1}Pd_{0.9}$/N-ompg-C_3N_4). It was concluded in that study that the hard template method was favorable for the formation of mesopores in the support and for the generation of many nitrogen vacancies that favored the distribution of the active species.

Li et al. also mentioned the importance of the metal−support interaction in attaining suitable performances [86]. In their study, catalysts based on PdAg nanoparticles supported on N-doped carbon/cerium oxide (PdAg/CeO_x-NPC) were prepared and evaluated in the dehydrogenation of FA at 30 °C. The N-doped carbon support, which derived from the pyrolysis of a zeolitic imidazolate framework (ZIF-8), was mixed with the precursors of Pd, Ag, and CeO_x. $NaBH_4$ was subsequently added to attain $Pd_{0.7}Ag_{0.3}$/CeO_x-NPC nanocatalyst. The same process was followed to prepare catalysts with the same Pd/Ag molar ratio and supported in other carbon materials (i.e., PdAg/CeO_x-rGO, PdAg/CeO_x-XC 72R, PdAg/CeO_x-multiwalled carbon nanotubes (MNCTs, PdAg/CeO_x-MNCTs) and PdAg/NPC) for comparison. Also, catalysts with different Pd/Ag molar ratios were synthesized, among which the sample $Pd_{0.7}Ag_{0.3}$/CeO_x-NPC displayed the best activity, with a TOF of 875 h^{-1}. The superior activity of that sample was also demonstrated when compared with those catalysts supported on other carbon materials. Since all these samples had similar nanoparticle sizes (∼2.5 nm), the effect of the size of the nanoparticles in ruling the activity of those samples was excluded. The evaluation of the CeO_x-free catalyst ($Pd_{0.7}Ag_{0.3}$/CeO_x-NPC) confirmed the positive role of CeO_x in attaining good activity in the dehydrogenation of FA. It was claimed that CeO_x promoted the electron transfer from the support to the PdAg nanoparticles, resulting in electron-rich species that are beneficial for activating the C−H bond of the PdAg−formate intermediates during the dehydrogenation of FA. The stability of $Pd_{0.7}Ag_{0.3}$/CeO_x-NPC was evaluated during five consecutive runs. It did not show significant degradation under reaction conditions, which was attributed to the good stabilization of the ultrafine (2.5 nm) nanoparticles on the support due to the strong metal−support interaction.

Similar aspects have been studied for PdAu-based catalysts. This composition of the nanoparticles started to gain interest for the catalysts used in the dehydrogenation of FA in 2008 since Xing et al. found that high-quality hydrogen was obtained from PdAu/C catalysts, which inhibited the adsorption of CO and the poisoning of the active sites [87]. The same research group also studied the effect of rare earth elements (Dy, Eu, and Ho) in promoting the activity of PdAu/C catalysts [88]. It was claimed that such rare-earth elements efficiently removed poisoning intermediates, such as adsorbed CO molecules. It was postulated that these elements provide oxygen groups that react with the

intermediates, thus dramatically improving the activity of the resulting material compared to rare earth-free counterparts.

As in PdAg catalysts, the composition of PdAu nanoparticles was one of the key aspects in controlling the catalytic performance. Sun et al. prepared monodisperse alloy AuPd nanoparticles supported on Ketjen carbon by co-reduction the metal precursors and with oleylamine acting as both solvent and surfactant [89]. The composition of the nanoparticles was varied (i.e., $Au_{67}Pd_{33}$, $Au_{59}Pd_{41}$, $Au_{41}Pd_{59,}$ and $Au_{32}Pd_{68}$), and the as-prepared nanoparticles were subsequently loaded onto the carbon support, and the oleylamine was removed by treating the samples with acetic acid at 70 °C. It was observed that $Au_{41}Pd_{59}$-based catalyst was the most active in that study, and it had an initial TOF of 230 h^{-1} at 50 °C, much higher than that of the monometallic Pd catalysts (TOF of 30 h^{-1}). Villa et al. also studied the effect of the composition of PdAu nanoparticles in the dehydrogenation of FA [90]. In that study, bimetallic Pd−Au with different Pd: Au atomic ratios (nominal molar ratio: 8−2, 6−4, 4−6, and 2−8) were supported on high temperature (3000 °C) heat-treated (HHT) carbon nanofibers and the activity of the resulting catalysts (Pd_xAu_y@HHT), together with that shown by the monometallic counterparts (Pd@HHT and Au@HHT), was checked by performing the reaction at room temperature. It was observed that all the catalysts had similar average nanoparticles sizes, ranging from 2.9 to 4.0 nm. Also, it was shown by XPS analysis that a charge transfer from Au to Pd occurred. The result of the catalytic activity proved that all the bimetallic catalysts showed better performance than those displayed by the monometallic counterparts. It was observed that the activity improved with the amount of Au in the nanoparticles until reaching a maximum in sample Pd_6Au_4@HHT with an initial TOF 3539 h^{-1}. The stability of the samples with the best performance (Pd_6Au_4@HHT and Pd_8Au_2@HHT) was compared to that of the Pd monometallic catalysts by doing six consecutive reaction cycles (results shown in Fig. 9.5). According to what it was found in that work, the poor stability displayed by monometallic catalyst was due to the

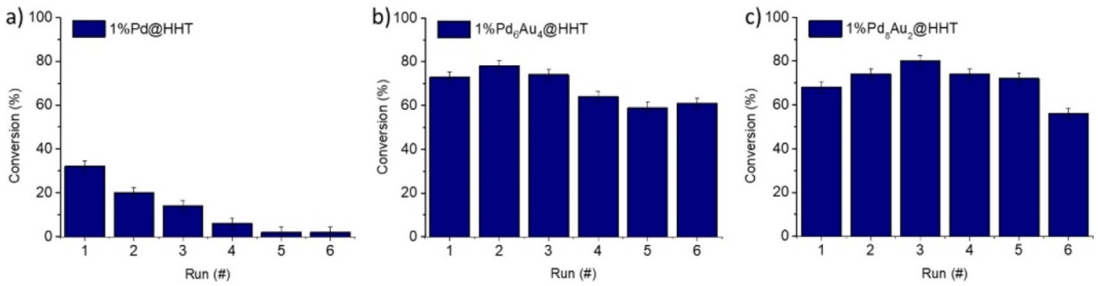

Figure 9.5

Recycling tests (A) monometallic 1%Pd@HHT (B) 1%Pd_6Au_4@HHT (C) 1%Pd_8Au_2@HHT.

Reprinted with permission from Ref. [90]. Copyright 2021, Wiley-VCH.

aggregation of Pd nanoparticles (from 3.0 nm in the fresh sample to 4.7 nm in the spent catalysts), while bimetallic nanoparticles showed better resistance against sintering. The authors of that study also performed Density Functional Theory (DFT) calculations to complete their work. It was postulated that monometallic Au species did not interact with FA molecules. However, Pd and PdAu nanoparticles had exothermic adsorption of FA, which was particularly favored in the case of the bimetallic catalysts. Also, it was proved that monometallic catalysts could follow the dehydration reaction ($CO + H_2O$). At the same time, the dehydrogenation pathway was preferred for the bimetallic PdAu system, thus confirming their superiority over the monometallic catalysts.

Albdiry et al. developed AuPd bimetallic nanoparticles supported on reduced graphene oxide nanosheets (Au_xPd_y/rGO, with x/y mole ratio Au/Pd of 3:1, 1:1, and 1:3) to check the effect of the composition of the nanoparticles in the dehydrogenation of FA at 50 °C [91]. It was observed that the catalytic activity was composition dependent for the Au_xPd_y-based catalysts, and the largest among of gas was generated by Au_1Pd_3/rGO, with a TOF of 1050 h^{-1}. The stability of that samples was evaluated in five consecutive runs, after which it partially lost its initial activity, a fact that the authors of that study attributed to the nanoparticles sintering (average nanoparticles size of 3.5 ± 0.3 nm, and 6.8 ± 0.3 nm, in the fresh and spent catalysts, respectively). Blanita et al. also prepared bimetallic PdAu nanoparticles (with a fixed composition of 7.5 wt% Pd and 2.5 wt% Au) supported on rGO for their application in the decomposition of FA using various experimental conditions (i.e., FA concentration, FA/sodium formate molar ratio, and reaction temperature) [92]. It was claimed that the presence of Au favored the formation of smaller nanoparticles compared to the monometallic Pd catalysts. It was also found that the bimetallic catalyst decreased the activation energy, which was calculated to be half from the activation energy for the monometallic catalyst.

The nanoparticles' composition and the distribution of Pd and Au in the nanoparticles have been reported to affect the catalytic performance. For instance, Wong et al. reported on the preparation of Au nanoparticles decorated with a controlled amount of Pd (Pd-on-Au nanoparticles) and immobilized on carbon support [93]. Depending on the Pd surface coverage (sc%), different Pd species were identified: single-atoms, two-dimensional Pd ensembles (Pd atoms in contact with Au), and three-dimensional Pd ensembles (a portion of Pd atoms is not in contact with Au). For the preparation of the catalysts, the amount of Pd was fixed to 1 wt%, and the Au content was varied to have different Pd surface coverage (i.e., 30, 60, 150, and 300 sc% Pd-on-Au). The nanoparticles, prepared in a sol phase, were loaded onto activated carbon, and the resulting catalysts were evaluated in the decomposition of FA at room temperature. Among investigated, 300 sc% Pd-on-Au/C catalyst was the most active and had a TOF value of 123 h^{-1}. The characterization and catalytic tests help the study's authors establish a relationship between the surface Pd surface coverage and the prevalent reaction mechanism (dehydrogenation or FA

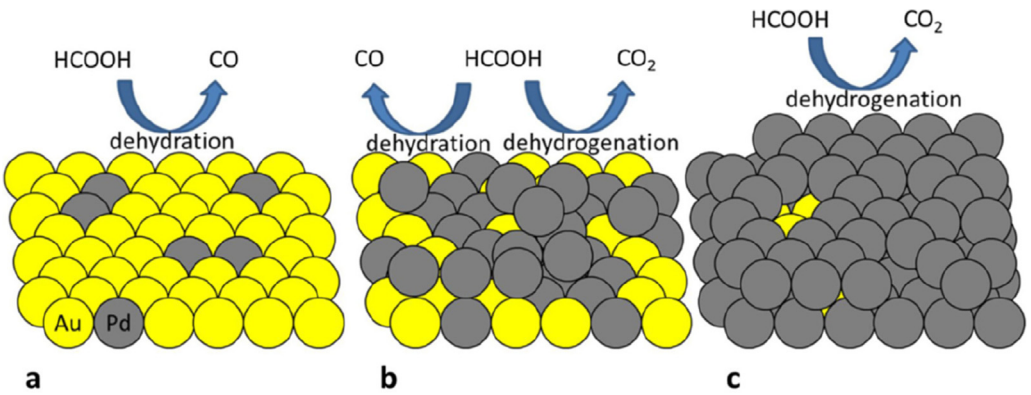

Figure 9.6
Proposed reaction pathways on (A) low sc% Pd-on-Au nanoparticle (NP) surface, (B) intermediate sc% Pd-on-Au NP surface, and (C) high sc% Pd-on-Au NP surface. *Reprinted with permission from Ref. [93]. Copyright 2019, Elsevier.*

dehydration). As schematized in Fig. 9.6, the selectivity of the catalysts was controlled by the Pd surface coverage in the nanoparticles: it was found that low sc% favored the dehydration of FA. In contrast, high sc% promoted the formation of H_2 via dehydrogenation reaction, and intermediate sc% led to both dehydration and dehydrogenation reactions.

Su et al. successfully prepared size-controlled PdAu nanoparticles using amino acids (lysine, serine, and glutamic acid) with different isoelectric points as structure-directing agents [94]. To prepare the catalysts, the metal precursors were dispersed in methanol, and then the carbon support (Vulcan XC-72) was added to the solution. After that, an aqueous solution of the amino acid was incorporated into the mixture, and, finally, the reducing agent ($NaBH_4$) was added. Catalysts with different Pd/Au ratios were prepared, characterized, and evaluated in the dehydrogenation of FA at 25°C. It was claimed that when lysine was used as the structure-directing agent, the NH_2 and COO^- groups interacted with $AuCl_4^-$ and Pd^{2+} via electrostatic interaction, which avoided the motion of reduced Pd and Au species resulting in catalysts with small nanoparticles (3.8 ± 0.5 nm). However, the use of glutamic acid (with protonated COOH groups) led to weak immobilization of the metal precursors, resulting in catalysts with larger nanoparticles (12.8 ± 0.5 nm). The sample prepared with serine had medium-size nanoparticles (7.2 ± 0.5). Among evaluated lysine-directed catalysts with small nanoparticles showed the most promising activity.

Odriozola et al. recently reported on the preparation of PdAu bimetallic nanoparticles supported on activated carbon Darco for their application in the dehydrogenation of FA

[95]. In that study, different Pd/Au compositions were used (Pd_xAu_{100-x}, where x = 25, 50, and 75), and their effect on alloy structure, size, and dispersion of the nanoparticles was checked. The monometallic counterpart catalysts were also prepared for comparison purposes. It was observed that the bimetallic nanoparticles had a smaller size than the monometallic, which suggested the synergistic effect between Pd and Au. The activity of PdAu samples was size-dependent, and higher TOF values were achieved with smaller nanoparticles. It was determined that, among studies, $Pd_{25}Au_{75}$/C catalysts showed better performance due to the important activity for lower Pd content in the nanoparticles.

Zhang et al. also explored the performance of PdAu catalysts [96]. In that case, the catalysts were prepared by a co-impregnation method followed by an atmospheric pressure cold plasma treatment, which was shown to be an efficient strategy to favor the redispersion of the nanoparticles on the surface of the support. The smaller nanoparticles achieved with that method than those attained by a conventional synthesis resulted in better performance. It was also reported that the strong electric field in the plasma promoted the electron transfer and enhanced the degree of alloying in the nanoparticles.

In order to explore the effect of the support, Wang et al. synthesized PdAu catalysts on a graphene nanosheets-carbon black composite support [97]. For that, Vulcan XC-72 carbon powder and graphene oxide were dispersed in water by sonication. After that, the metal precursors and the reducing agent were added. For comparison, catalysts supported on either graphene nanosheets or carbon black were also synthesized. It was observed that the catalysts based on the composite support displayed a better performance than those based on the individual components. It was postulated that the catalysts based on the composite support showed a much better anti-poisoning capability of CO compared to carbon black. It prevented the aggregation of the nanoparticles more efficiently than the graphene nanosheets. Thus, the enhanced performance observed for PdAu catalysts on a graphene nanosheets-carbon black composite support was attributed to those factors.

As observed for other compositions of the nanoparticles, the use of nitrogen-containing support was suitable to achieve well-dispersed PdAu nanoparticles. Jiang et al. developed Au@Pd core-shell nanoclusters growing on nitrogen-doped reduced graphene oxide (Au@Pd/N-mrGO) [98]. The GO, prepared by a modified Hummers' method, was mixed with an ammonia solution for 8 h at 80 °C. Once the support was prepared, it was mixed with the metal precursor in a two-step process to achieve a core-shell-based catalyst. They were characterized and tested in the dehydrogenation of FA at room temperature. The activity of the obtained Au@Pd/N-mrGO catalysts was compared with that of AuPd/N-mrGO, Pd/N-mrGO, and Au/N-mrGO counterparts. It was observed that Au@Pd/N-mrGO catalysts had superior activity than the other catalysts evaluated. It was concluded that the core-shell structure of the nanoparticles favored the charge transfer between Au core and

Pd shell due to the ligand effect, which, together with the small nanoparticles (1.8 nm), favored the dehydrogenation of FA.

As can be extracted from comparing the studies reporting on the dehydrogenation of FA found in the literature, there are no well-established benchmark experimental conditions to carry out the catalytic tests. The reaction temperature is one of the aspects that should be considered while comparing the catalytic performance of a certain system. Mild conditions are preferred because of the energy efficiency of the process, but the reaction does not always proceed successfully with a certain system. In an attempt to highlight the suitability of their developed catalysts, Chen et al. evaluated the activity of Au−Pd alloy catalysts supported on carbon black at nearly 0 °C [99]. It was reported that the samples developed in that study had a TOF of 1075 h^{-1} and 635 h^{-1}, at room temperature and 0 °C, respectively, which made the authors claim that that system development was potentially suitable for their application in proton exchange membrane fuel cell in cold areas.

The studies reviewed in this section demonstrate the potential of heterogeneous Pd-based catalysts supported on carbon materials for the present application. Many aspects make the assessment and comparison of the activity and stability of the catalysts a bit tricky since neither benchmark experimental conditions nor benchmark catalysts for the decomposition of FA are established so far in the literature so that determining the optimum properties of the catalysts and experimental conditions to perform the catalytic test would require a closer look.

4. Conclusion

The deployment of hydrogen offers a sustainable alternative to fossil fuels. However, creating an adequate and safe infrastructure for storing and transporting hydrogen is challenging and costly. Chemical hydrogen storage is a promising alternative to those traditionally used physical storage methods upon selecting a suitable hydrogen carrier molecule that decomposes, giving molecular hydrogen under mild conditions. Even though the potential of formic acid in hydrogen storage was firstly claimed several decades ago, its use as a convenient LOHC molecule has sparked great attention in the last years, which has been reflected in the increasing number of studies addressing the design of catalysts for the dehydrogenation of formic acid. Most studies explore the active phase features that result in good catalytic activity and selectivity toward the desired reaction pathway. Optimizing the properties of the active phase is usually the cornerstone of the successful preparation of highly performing catalysts. However, despite the support properties being frequently disregarded, several studies evidence their paramount importance in controlling the final catalytic performance. Due to the relevance of these catalysts in this field of

research, the present chapter is focused on revising some of the current strategies addressed for the preparation of catalysts based on active phases formed by monometallic Pd nanoparticles bimetallic PdAg and PdAu nanoparticles supported on carbon materials. Identifying the optimum heterogeneous catalysts under certain experimental conditions frequently lies in finding the optimum size and composition of the nanoparticles. However, as exemplified in the works cited in this chapter, the versatility of carbon materials provides numerous alternatives to achieve enhanced catalytic performances by modulating their surface chemistry, porous texture, and metal−support interaction, among other characteristics. Most of the studies reported so far are focused on attaining active and selective catalysts under mild conditions. Despite the vital importance of the stability and recyclability of the catalysts, only the most recent works address such an aspect. Nevertheless, long-term stability tests are not included, and, at best, only a few consecutive reaction cycles are performed. Significant breakthroughs have been made in the stability of the catalysts by exploring the potential of using functionalized carbon materials, but further efforts should be devoted to fully unveiling the deactivation mechanism and the most suitable options for the regeneration of heterogeneous catalysts able to operate under reaction conditions during long reaction cycles.

Acknowledgments

The authors would like to thank MICINN, FEDER (RTI2018-095291-B-I00) for the financial support. DST thanks Vicerrectorado de Investigación y Transferencia de Conocimiento de la Universidad de Alicante for the financial support (GRE19-16). MNG would like to thank the Plan GenT project (CDEIGENT/2018/027) from the Generalitat Valenciana and GRE20-19-A from Vicerrectorado de Investigación y Transferencia de Conocimiento de la Universidad de Alicante for the financial support.

Author contribution

The manuscript was written through the contributions of all authors. All authors have approved the final version of the manuscript. The authors further acknowledge that there is no financial relationship with the editors or publisher and have contributed original work in this chapter, other than what was acknowledged or appropriately cited with copyright permission.

References

[1] BP p.l.c. https://www.bp.com/en/global/corporate/energy-economics/statistical-review-of-world-energy/primary-energy.html. Accessed October 4, 2021.
[2] U.S. Environmental Protection Agency. https://www.epa.gov/ghgemissions/understanding-global-warming-potentials. Accessed October 6, 2021.
[3] Global Monitoring Laboratory, NOAA Research. https://gml.noaa.gov/ccgg/trends/. Accessed October 6, 2021.
[4] United Nations, Climate Change. https://unfccc.int/process-and-meetings/the-paris-agreement/the-paris-agreement. Accessed September 24, 2021.

[5] United Nations, Department and Economic Social Affairs. Sustainable Development, Sustainable Development Goal 7: Ensure Access to Affordable, Reliable, Sustainable and Modern Energy. https://sustainabledevelopment.un.org/sdg7. Accessed October 15, 2021.
[6] D. Gielen, F. Boshell, D. Saygin, M.D. Bazilian, N. Wagner, R. Gorini, The role of renewable energy in the global energy transformation, Energy Strategy. Rev. 24 (2019) 38−50, https://doi.org/10.1016/j.esr.2019.01.006.
[7] M.A. Rosen, S. Koohi-Fayegh, The prospects for hydrogen as an energy carrier: an overview of hydrogen energy and hydrogen energy systems, Energy Ecol. Environ. 1 (2016) 10−29, https://doi.org/10.1007/s40974-016-0005-z.
[8] International Renewable Energy Agency, IRENA, September 2019, Hydrogen: a renewable energy perspective. https://www.irena.org/publications/2019/Sep/Hydrogen-A-renewable-energy-perspective. Accessed October 11, 2021.
[9] U.S. Department of Energy, Office of Energy Efficiency and Renewable Energy. https://www.energy.gov/eere/fuelcells/safe-use-hydrogen. Accessed August 23, 2021.
[10] P.T. Aakko-Saksa, C. Cook, J. Kiviaho, T. Repo, Liquid organic hydrogen carriers for transportation and storing of renewable energy − review and discussion, J. Power Sources 396 (2018) 803−823, https://doi.org/10.1016/J.JPOWSOUR.2018.04.011.
[11] P.M. Modisha, C.N.M. Ouma, R. Garidzirai, P. Wasserscheid, D. Bessarabov, The prospect of hydrogen storage using liquid organic hydrogen carriers, Energy Fuels 33 (2019) 2778−2796, https://doi.org/10.1021/acs.energyfuels.9b00296.
[12] G. Sievi, D. Geburtig, T. Skeledzic, A. Bösmann, P. Preuster, O. Brummel, et al., Towards an efficient liquid organic hydrogen carrier fuel cell concept, Energy Environ. Sci. 12 (2019) 2305−2314, https://doi.org/10.1039/C9EE01324E.
[13] V. Meille, I. Pitault, Liquid organic hydrogen carriers or organic liquid hydrides: 40 Years of history, Reactions 2 (2021) 94−101, https://doi.org/10.3390/reactions2020008.
[14] D.A. Bulushev, Progress in catalytic hydrogen production from formic acid over supported metal complexes, Energies 14 (2021), https://doi.org/10.3390/en14051334.
[15] J. Eppinger, K.-W. Huang, Formic acid as a hydrogen energy carrier, ACS Energy Lett. 2 (2017) 188−195, https://doi.org/10.1021/acsenergylett.6b00574.
[16] J. Guo, C.K. Yin, D.L. Zhong, Y.L. Wang, T. Qi, G.H. Liu, et al., Formic acid as a potential on-board hydrogen storage method: development of homogeneous noble metal catalysts for dehydrogenation reactions, ChemSusChem 14 (2021) 2655−2681, https://doi.org/10.1002/cssc.202100602.
[17] K. Müller, K. Brooks, T. Autrey, Hydrogen storage in formic acid: a comparison of process options, Energy Fuels 31 (2017) 12603−12611, https://doi.org/10.1021/acs.energyfuels.7b02997.
[18] M. Navlani-García, K. Mori, D. Salinas-Torres, Y. Kuwahara, H. Yamashita, New approaches toward the hydrogen production from formic acid dehydrogenation over Pd-based heterogeneous catalysts, Front. Mater. 6 (2019) 44, https://doi.org/10.3389/fmats.2019.00044.
[19] A.K. Singh, S. Singh, A. Kumar, Hydrogen energy future with formic acid: a renewable chemical hydrogen storage system, Catal. Sci. Technol. 6 (2015) 12−40, https://doi.org/10.1039/c5cy01276g.
[20] R. Williams, R.S. Crandall, A. Bloom, Use of carbon dioxide in energy storage, Appl. Phys. Lett. 33 (1978) 381−383, https://doi.org/10.1063/1.90403.
[21] C. Fellay, P.J. Dyson, G. Laurenczy, A viable hydrogen-storage system based on selective formic acid decomposition with a ruthenium catalyst, Angew. Chemie Int. Ed. 47 (2008) 3966−3968, https://doi.org/10.1002/anie.200800320.
[22] B. Loges, A. Boddien, H. Junge, M. Beller, Controlled generation of hydrogen from formic acid amine adducts at room temperature and application in H_2/O_2 fuel cells, Angew. Chemie Int. Ed. 47 (2008) 3962−3965, https://doi.org/10.1002/anie.200705972.
[23] H. Kawanami, Y. Himeda, G. Laurenczy, Formic acid as a hydrogen carrier for fuel cells toward a sustainable energy system, Adv. Inorg. Chem. 70 (2017) 395−427, https://doi.org/10.1016/BS.ADIOCH.2017.04.002.

[24] D.S. Patle, A.P. Gadhamsetti, S. Sharma, V. Agrawal, G.P. Rangaiah, Plantwide control of the formic acid production process using an integrated framework of simulation and heuristics, Ind. Eng. Chem. Res. 57 (2018) 13478−13489, https://doi.org/10.1021/acs.iecr.8b02654.
[25] D.A. Bulushev, J.R.H. Ross, Towards sustainable production of formic acid, ChemSusChem 11 (2018) 821−836, https://doi.org/10.1002/cssc.201702075.
[26] X. Chen, Y. Liu, J. Wu, Sustainable production of formic acid from biomass and carbon dioxide, Mol. Catal. 483 (2020) 110716, https://doi.org/10.1016/J.MCAT.2019.110716.
[27] S. Enthaler, J. Von Langermann, T. Schmidt, Carbon dioxide and formic acid—the couple for environmental-friendly hydrogen storage? Energy Environ. Sci. 3 (2010) 1207−1217, https://doi.org/10.1039/b907569k.
[28] C. Fellay, N. Yan, P.J. Dyson, G. Laurenczy, Selective formic acid decomposition for high-pressure hydrogen generation: a mechanistic study, Chem. Eur. J. 15 (2009) 3752−3760, https://doi.org/10.1002/chem.200801824.
[29] D. Mellmann, P. Sponholz, H. Junge, M. Beller, Formic acid as a hydrogen storage material-development of homogeneous catalysts for selective hydrogen release, Chem. Soc. Rev. 45 (2016) 3954−3988, https://doi.org/10.1039/C5CS00618J.
[30] N. Onishi, G. Laurenczy, M. Beller, Y. Himeda, Recent progress for reversible homogeneous catalytic hydrogen storage in formic acid and in methanol, Coord. Chem. Rev. 373 (2018) 317−332, https://doi.org/10.1016/j.ccr.2017.11.021.
[31] K. Sordakis, C. Tang, L.K. Vogt, H. Junge, P.J. Dyson, M. Beller, et al., Homogeneous catalysis for sustainable hydrogen storage in formic acid and alcohols, Chem. Rev. 118 (2018) 372−433, https://doi.org/10.1021/acs.chemrev.7b00182.
[32] W. Hong, M. Kitta, N. Tsumori, Y. Himeda, T. Autrey, Q. Xu, Immobilization of highly active bimetallic PdAu nanoparticles onto nano carbon for dehydrogenation of formic acid, J. Mater. Chem. A 7 (2019) 18835−18839, https://doi.org/10.1039/C9TA06014F.
[33] F.Z. Song, Q.L. Zhu, X. Yang, W.W. Zhan, P. Pachfule, N. Tsumori, et al., Metal-organic framework templated porous carbon-metal oxide/reduced graphene oxide as superior support of bimetallic nanoparticles for efficient hydrogen generation from formic acid, Adv. Energy Mater. 8 (2018) 1−5, https://doi.org/10.1002/aenm.201701416.
[34] Q. Wang, N. Tsumori, M. Kitta, Q. Xu, Fast dehydrogenation of formic acid over palladium nanoparticles immobilized in nitrogen-doped hierarchically porous carbon, ACS Catal. 8 (2018) 12041−12045, https://doi.org/10.1021/acscatal.8b03444.
[35] Q. Wang, L. Chen, Z. Liu, N. Tsumori, M. Kitta, Q. Xu, Phosphate-mediated immobilization of high-performance AuPd nanoparticles for dehydrogenation of formic acid at room temperature, Adv. Funct. Mater. 29 (2019a) 1903341, https://doi.org/10.1002/adfm.201903341.
[36] M. Martis, K. Mori, K. Fujiwara, W.-S. Ahn, H. Yamashita, Amine-functionalized MIL-125 with imbedded palladium nanoparticles as an efficient catalyst for dehydrogenation of formic acid at ambient temperature, J. Phys. Chem. C 117 (2013), https://doi.org/10.1021/jp4069027.
[37] K. Mori, M. Dojo, H. Yamashita, Pd and Pd-Ag nanoparticles within a macro reticular basic resin: an efficient catalyst for hydrogen production from formic acid decomposition, ACS Catal. 3 (2013) 1114−1119, https://doi.org/10.1021/cs400148n.
[38] K. Mori, K. Naka, S. Masuda, K. Miyawaki, H. Yamashita, Palladium copper chromium ternary nanoparticles constructed *in situ* within a basic resin: enhanced activity in the dehydrogenation of formic acid, ChemCatChem 9 (2017) 3456−3462, https://doi.org/10.1002/cctc.201700595.
[39] K. Mori, Y. Futamura, S. Masuda, H. Kobayashi, H. Yamashita, Controlled release of hydrogen isotope compounds and tunneling effect in the heterogeneously-catalyzed formic acid dehydrogenation, Nat. Commun. 10 (2019) 4094, https://doi.org/10.1038/s41467-019-12018-7.
[40] D.A. Bulushev, S. Beloshapkin, J.R.H. Ross, Hydrogen from formic acid decomposition over Pd and Au catalysts, Catal. Today 154 (2010) 7−12, https://doi.org/10.1016/j.cattod.2010.03.050.

[41] D.A. Bulushev, M. Zacharska, E.V. Shlyakhova, A.L. Chuvilin, Y. Guo, S. Beloshapkin, et al., Single isolated Pd^{2+} cations supported on N-doped carbon as active sites for hydrogen production from formic acid decomposition, ACS Catal. 6 (2016b) 681−691, https://doi.org/10.1021/acscatal.5b02381.
[42] F.S. Golub, S. Beloshapkin, A.V. Gusel'nikov, V.A. Bolotov, V.N. Parmon, D.A. Bulushev, Boosting hydrogen production from formic acid over Pd catalysts by deposition of N-containing precursors on the carbon support, Energies 12 (2019) 3885, https://doi.org/10.3390/en12203885.
[43] M. Zacharska, A.L. Chuvilin, V.V. Kriventsov, S. Beloshapkin, M. Estrada, A. Simakov, et al., Support effect for nanosized Au catalysts in hydrogen production from formic acid decomposition, Catal. Sci. Technol. 6 (2016) 6853−6860, https://doi.org/10.1039/C6CY00552G.
[44] A. Gallas-Hulin, J. Mielby, S. Kegnæs, Efficient production of hydrogen from decomposition of formic acid over zeolite incorporated gold nanoparticles, ChemistrySelect 1 (2016) 3942−3945, https://doi.org/10.1002/slct.201600831.
[45] M. Navlani-García, M. Martis, D. Lozano-Castelló, D. Cazorla-Amorós, K. Mori, H. Yamashita, Investigation of Pd nanoparticles supported on zeolites for hydrogen production from formic acid dehydrogenation, Catal. Sci. Technol. 5 (2015) 364−371, https://doi.org/10.1039/c4cy00667d.
[46] J. García-Aguilar, M. Navlani-García, Á. Berenguer-Murcia, K. Mori, Y. Kuwahara, H. Yamashita, et al., Evolution of the PVP-Pd surface interaction in nanoparticles through the case study of formic acid decomposition, Langmuir 32 (2016) 12110−12118, https://doi.org/10.1021/acs.Langmuir.6b03149.
[47] M. Yadav, A.K. Singh, N. Tsumori, Q. Xu, Palladium silica nanosphere-catalyzed decomposition of formic acid for chemical hydrogen storage, J. Mater. Chem. 22 (2012) 19146−19150, https://doi.org/10.1039/c2jm32776g.
[48] K. Mori, H. Tanaka, M. Dojo, K. Yoshizawa, H. Yamashita, Synergic catalysis of PdCu alloy nanoparticles within a macroreticular basic resin for hydrogen production from formic acid, Chem. Eur. J. 21 (2015) 12085−12092, https://doi.org/10.1002/chem.201501760.
[49] M. Garai, C.T. Yavuz, Robust mesoporous Zr-MOF with Pd nanoparticles for formic-acid-based chemical hydrogen storage, Matter 4 (2021) 10−12, https://doi.org/10.1016/j.matt.2020.12.011.
[50] M. Wen, K. Mori, Y. Futamura, Y. Kuwahara, M. Navlani-García, T. An, et al., PdAg nanoparticles within core-shell structured zeolitic imidazolate framework as a dual catalyst for formic acid-based hydrogen storage/production, Sci. Rep. 9 (2019) 15675, https://doi.org/10.1038/s41598-019-52133-5.
[51] M. Navlani-García, K. Mori, Y. Kuwahara, H. Yamashita, Recent strategies are targeting efficient hydrogen production from chemical hydrogen storage materials over carbon-supported catalysts, NPG Asia Mater. 10 (2018) 1−16, https://doi.org/10.1038/s41427-018-0025-6.
[52] L.R. Radovic, T.J. Bandosz, Z. Zhu, F. Rodríguez-Reinoso, A. Sepúlveda-Escribano, J.H. Bitter, et al., Carbon Materials for Catalysis, 2009, pp. 9856−9858.
[53] F.-Z. Song, Q.-L. Zhu, N. Tsumori, Q. Xu, Diamine-alkalized reduced graphene oxide: immobilization of sub-2 nm palladium nanoparticles and optimization of catalytic activity for dehydrogenation of formic acid, ACS Catal. 5 (2015) 5141−5144, https://doi.org/10.1021/acscatal.5b01411.
[54] Z.-L. Wang, J.-M. Yan, H.-L. Wang, Y. Ping, Q. Jiang, Pd/C synthesized with citric acid: an efficient catalyst for hydrogen generation from formic acid/sodium formate, Sci. Rep. 2 (2012) 598, https://doi.org/10.1038/srep00598.
[55] Q.L. Zhu, N. Tsumori, Q. Xu, Sodium hydroxide-assisted growth of uniform Pd nanoparticles on nanoporous carbon MSC-30 for efficient and complete dehydrogenation of formic acid under ambient conditions, Chem. Sci. 5 (2014) 195−199, https://doi.org/10.1039/c3sc52448e.
[56] M. Navlani-García, K. Mori, M. Wen, Y. Kuwahara, H. Yamshita, Size effect of carbon-supported Pd nanoparticles in the hydrogen production from formic acid, Bull. Chem. Soc. Jpn. 1370 (2015b) 78−80, https://doi.org/10.1080/03758397.1955.10857269.
[57] M. Navlani-García, K. Mori, A. Nozaki, Y. Kuwahara, H. Yamashita, Investigation of size sensitivity in the hydrogen production from formic acid over carbon-supported Pd nanoparticles, ChemistrySelect 1 (2016a) 1879−1886, https://doi.org/10.1002/slct.201600559.

[58] K. Mori, T. Hara, T. Mizugaki, K. Ebitani, K. Kaneda, Hydroxyapatite-supported palladium nanoclusters: a highly active heterogeneous catalyst for selective oxidation of alcohols by use of molecular oxygen, J. Am. Chem. Soc. 126 (2004) 10657−10666, https://doi.org/10.1021/ja0488683.

[59] S. Zhang, B. Jiang, K. Jiang, W.B. Cai, Surfactant-free synthesis of carbon-supported palladium nanoparticles and size-dependent hydrogen production from formic acid-formate solution, ACS Appl. Mater. Interfaces 9 (2017) 24678−24687, https://doi.org/10.1021/acsami.7b08441.

[60] J. Li, W. Chen, H. Zhao, X. Zheng, L. Wu, H. Pan, et al., Size-dependent catalytic activity over carbon-supported palladium nanoparticles in the dehydrogenation of formic acid, J. Catal. 352 (2017) 371−381, https://doi.org/10.1016/j.jcat.2017.06.007.

[61] J.L. Santos, C. Megías-Sayago, S. Ivanova, M.Á. Centeno, J.A. Odriozola, Structure-sensitivity of formic acid dehydrogenation reaction over additive-free Pd NPs supported on activated carbon, Chem. Eng. J. 420 (2021) 127641, https://doi.org/10.1016/j.cej.2020.127641.

[62] O.Y. Podyacheva, D.A. Bulushev, A.N. Suboch, D.A. Svintsitskiy, A.S. Lisitsyn, E. Modin, et al., Highly stable single-atom catalyst with ionic Pd active sites supported on N-doped carbon nanotubes for formic acid decomposition, ChemSusChem 11 (2018) 3724−3727, https://doi.org/10.1002/cssc.201801679.

[63] D.A. Bulushev, M. Zacharska, A.S. Lisitsyn, O.Y. Podyacheva, F.S. Hage, Q.M. Ramasse, et al., Single atoms of Pt-group metals stabilized by N-doped carbon nanofibers for efficient hydrogen production from formic acid, ACS Catal. 6 (2016a) 3442−3451, https://doi.org/10.1021/acscatal.6b00476.

[64] D.A. Bulushev, A.L. Chuvilin, V.I. Sobolev, L.V. Pirutko, Y.V. Fedoseeva, E.V. Lobiak, et al., Single Au atoms on the surface of N-free and N-doped carbon: interaction with formic acid and methanol molecules, Top. Catal. 62 (2019) 508−517, https://doi.org/10.1007/s11244-019-01166-1.

[65] Z. Wang, C. Wang, S. Mao, Y. Gong, Y. Chen, Y. Wang, Pd nanoparticles anchored on amino-functionalized hierarchically porous carbon for efficient dehydrogenation of formic acid under ambient conditions, J. Mater. Chem. A 7 (2019b) 25791−25795, https://doi.org/10.1039/C9TA10196A.

[66] Y. Yu, X. Wang, C. Liu, F. Vladimir, J. Ge, W. Xing, Surface interaction between Pd and nitrogen derived from hyperbranched polyamide towards highly effective formic acid dehydrogenation, J. Energy Chem. 40 (2020) 212−216, https://doi.org/10.1016/j.jechem.2019.04.017.

[67] M. Navlani-García, D. Salinas-Torres, K. Mori, A.F. Léonard, Y. Kuwahara, N. Job, et al., Insights on palladium decorated nitrogen-doped carbon xerogels for the hydrogen production from formic acid, Catal. Today 324 (2019) 90−96, https://doi.org/10.1016/j.cattod.2018.06.013.

[68] D. Salinas-Torres, A.F. Léonard, V. Stergiopoulos, Y. Busby, J.J. Pireaux, N. Job, Effect of nitrogen doping on the pore texture of carbon xerogels based on resorcinol-melamine-formaldehyde precursors, Microporous Mesoporous Mater. 256 (2018) 190−198, https://doi.org/10.1016/j.micromeso.2017.08.004.

[69] J. Chaparro-Garnica, M. Navlani-García, D. Salinas-Torres, E. Morallón, D. Cazorla-Amorós, Highly stable N-doped carbon-supported Pd-based catalysts prepared from biomass waste for H_2 production from formic acid, ACS Sustain. Chem. Eng. 8 (2020) 15030−15043, https://doi.org/10.1021/acssuschemeng.0c05906.

[70] A.N. Suboch, O.Y. Podyacheva, Pd catalysts supported on bamboo-like nitrogen-doped carbon nanotubes for hydrogen production, Energies 14 (2021), https://doi.org/10.3390/en14051501.

[71] S. Zhong, N. Tsumori, M. Kitta, Q. Xu, Immobilizing palladium nanoparticles on boron-oxygen-functionalized carbon nanospheres towards efficient hydrogen generation from formic acid, Nano Res. 12 (2019) 2966−2970, https://doi.org/10.1007/s12274-019-2539-9.

[72] J. Duan, Q. Li, Y. Fu, J. Chang, In-situ nitrogen and Cr2O3 co-doped MOF-derived porous carbon-supported palladium nanoparticles: a highly effective catalyst towards formic acid dehydrogenation, Int. J. Hydrog. Energy (2021), https://doi.org/10.1016/j.ijhydene.2021.09.191.

[73] D. Liu, Z.Y. Gao, X.C. Wang, J. Zeng, Y.M. Li, DFT study of hydrogen production from formic acid decomposition on Pd-Au alloy nanoclusters, Appl. Surf. Sci. 426 (2017) 194−205, https://doi.org/10.1016/j.apsusc.2017.07.165.

[74] M. Navlani-García, D. Salinas-Torres, D. Cazorla-Amorós, Hydrogen production from formic acid attained by bimetallic heterogeneous PdAg catalytic systems, Energies 12 (2019b) 1−27, https://doi.org/10.3390/en12214027.
[75] Z. Khan, Trimetallic nanoparticles: synthesis, characterization, and catalytic degradation of formic acid for hydrogen generation, Int. J. Hydrog. Energy 44 (2019) 11503−11513, https://doi.org/10.1016/j.ijhydene.2019.03.122.
[76] X. Liu, C. Dai, D. Wu, A. Fisher, Z. Liu, D. Cheng, Facile synthesis of PdAgCo trimetallic nanoparticles for formic acid electrochemical oxidation, Chem. Lett. 45 (2016) 732−734, https://doi.org/10.1246/cl.160243.
[77] S.-L. Zhang, S.-J. Li, J.-Y. Wang, H.-N. Shang, Y.-X. Bai, J.-S. Liang, Amine-functionalized carbon nanotubes supported NiAuPd nanoparticles as an efficient in-situ prepared catalyst for formic acid dehydrogenation, Int. J. Hydrog. Energy 46 (2021) 34727−34736, https://doi.org/10.1016/j.ijhydene.2021.08.063.
[78] K. Tedsree, T. Li, S. Jones, C.W.A. Chan, K.M.K. Yu, P.A.J. Bagot, et al., Hydrogen production from formic acid decomposition at room temperature using an Ag-Pd core-shell nanocatalyst, Nat. Nanotechnol. 6 (2011) 302−307, https://doi.org/10.1038/nnano.2011.42.
[79] L. Yang, X. Hua, J. Su, W. Luo, S. Chen, G. Cheng, Highly efficient hydrogen generation from formic acid-sodium formate over monodisperse AgPd nanoparticles at room temperature, Appl. Catal. B Environ. 168−169 (2015) 423−428, https://doi.org/10.1016/j.apcatb.2015.01.003.
[80] Y. Huang, J. Xu, T. Long, Q. Shuai, Q. Li, Reducing agent-structure-activity relationship of PdAg/C catalysts in formic acid decomposition for hydrogen generation, J. Nanosci. Nanotechnol. 17 (2017) 3798−3802, https://doi.org/10.1166/jnn.2017.14009.
[81] M. Navlani-García, K. Mori, A. Nozaki, Y. Kuwahara, H. Yamashita, Screening of carbon-supported PdAg nanoparticles in the hydrogen production from formic acid, Ind. Eng. Chem. Res. 55 (2016) 7612−7620, https://doi.org/10.1021/acs.iecr.6b01635.
[82] S. Masuda, K. Mori, Y. Futamura, H. Yamashita, PdAg nanoparticles supported on functionalized mesoporous carbon: promotional effect of surface amine groups in reversible hydrogen delivery/storage mediated by formic acid/CO_2, ACS Catal. 8 (2018) 2277−2285, https://doi.org/10.1021/acscatal.7b04099.
[83] Q.-F. Deng, J.-J. Xin, S.-K. Ma, F.-J. Cui, Z.-L. Zhao, L.-H. Jia, Hydrogen production from the decomposition of formic acid over carbon nitride-supported AgPd alloy nanoparticles, Energy Technol. 6 (2018) 2374−2379, https://doi.org/10.1002/ente.201800402.
[84] C. Wan, L. Zhou, L. Sun, L. Xu, D. Cheng, F. Chen, et al., Boosting visible-light-driven hydrogen evolution from formic acid over AgPd/2D g-C_3N_4 nanosheets Mott-Schottky photocatalyst, Chem. Eng. J. 396 (2020) 125229, https://doi.org/10.1016/j.cej.2020.125229.
[85] C. Wan, L. Zhou, S. Xu, B. Jin, X. Ge, X. Qian, et al., Defect engineered mesoporous graphitic carbon nitride modified with AgPd nanoparticles for enhanced photocatalytic hydrogen evolution from formic acid, Chem. Eng. J. 429 (2022) 132388, https://doi.org/10.1016/j.cej.2021.132388.
[86] B. Yin, E. Zhao, X. Hua, K. Wang, W. Wang, G. Li, et al., Ultrafine PdAg nanoparticles immobilized on nitrogen-doped carbon/cerium oxide for superior dehydrogenation of formic acid, New J. Chem. 44 (2020) 2011−2015, https://doi.org/10.1039/C9NJ05661K.
[87] X. Zhou, Y. Huang, W. Xing, C. Liu, J. Liao, T. Lu, High-quality hydrogen from the catalyzed decomposition of formic acid by Pd-Au/C and Pd-Ag/C, Chem. Commun. (2008) 3540−3542, https://doi.org/10.1039/b803661f.
[88] X. Zhou, Y. Huang, C. Liu, J. Liao, T. Lu, W. Xing, Available hydrogen from formic acid decomposed by rare earth elements promoted Pd-Au/C catalysts at low temperatures, ChemSusChem 3 (2010) 1379−1382, https://doi.org/10.1002/cssc.201000199.
[89] Ö. Metin, X. Sun, S. Sun, Monodisperse gold-palladium alloy nanoparticles and their composition-controlled catalysis in formic acid dehydrogenation under mild conditions, Nanoscale 5 (2013) 910−912, https://doi.org/10.1039/C2NR33637E.

[90] I. Barlocco, S. Capelli, X. Lu, S. Bellomi, X. Huang, D. Wang, et al., Disclosing the role of gold on palladium−gold alloyed supported catalysts in formic acid decomposition, ChemCatChem 13 (2021) 4210−4222, https://doi.org/10.1002/cctc.202100886.

[91] A. Al-Nayili, M. Albdiry, Au-Pd bimetallic nanoparticles supported on reduced graphene oxide nanosheets as catalysts for hydrogen generation from formic acid under ambient temperature, New J. Chem. 45 (2021) 10040−10048, https://doi.org/10.1039/D1NJ01658J.

[92] O. Grad, M. Mihet, M. Coros, M. Dan, M.D. Lazar, G. Blanita, Reduced graphene oxide modified with noble metal nanoparticles for formic acid dehydrogenation, Catal. Today 366 (2021) 41−47, https://doi.org/10.1016/j.cattod.2020.08.009.

[93] Z. Zhao, K.N. Heck, P. Limpornpipat, H. Qian, J.T. Miller, M.S. Wong, Hydrogen-generating behavior of Pd-decorated gold nanoparticles *via* formic acid decomposition, Catal. Today 330 (2019) 24−31, https://doi.org/10.1016/j.cattod.2018.06.044.

[94] J. Cheng, X. Gu, X. Sheng, P. Liu, H. Su, Exceptional size-dependent catalytic activity enhancement in the room-temperature hydrogen generation from formic acid over bimetallic nanoparticles supported by porous carbon, J. Mater. Chem. A 4 (2016) 1887−1894, https://doi.org/10.1039/C5TA08534A.

[95] J.L. Santos, C. León, G. Monnier, S. Ivanova, M.Á. Centeno, J.A. Odriozola, Bimetallic PdAu catalysts for formic acid dehydrogenation, Int. J. Hydrog. Energy 45 (2020) 23056−23068, https://doi.org/10.1016/j.ijhydene.2020.06.076.

[96] J. Zhang, H. Wang, Q. Zhao, L. Di, X. Zhang, Facile synthesis of PdAu/C by cold plasma for efficient dehydrogenation of formic acid, Int. J. Hydrog. Energy 45 (2020) 9624−9634, https://doi.org/10.1016/j.ijhydene.2020.01.196.

[97] Y. Qin, J. Wang, Y. Wu, L. Wang, Improved hydrogen production from formic acid under ambient conditions using a PdAu catalyst on graphene nanosheets−carbon black support, RSC Adv. 4 (2014) 30068, https://doi.org/10.1039/C4RA05379F.

[98] Z.-L. Wang, J.-M. Yan, H.-L. Wang, Y. Ping, Q. Jiang, Au@Pd core-shell nanoclusters growing on nitrogen-doped mildly reduced graphene oxide with enhanced catalytic performance for hydrogen generation from formic acid, J. Mater. Chem. A 1 (2013) 12721−12725, https://doi.org/10.1039/C3TA12531A.

[99] S. Wu, F. Yang, P. Sun, T. Chen, Au−Pd alloy catalyst with high performance for hydrogen generation from formic acid-formate solution at nearly 0 °C, RSC Adv. 4 (2014) 44500−44503, https://doi.org/10.1039/C4RA08389J.

CHAPTER 10

Postface: a path to sustainable energy by 2030 and beyond. Role of new electrocatalysts in the development of a sustainability platform

Sajid Bashir[1], Sai Raghuveer Chava[4], Tian-Hao Yan[2], Jingbo Louise Liu[1,3]

[1]The Department of Chemistry, Texas A&M University, Kingsville, TX, United States; [2]Department of Chemistry, Hong-Cai Zhou Research Group, Texas A&M University, College Station, TX, United States; [3]Texas A&M Energy Institute, College Station, TX, United States; [4]Texas A&M University-Kingsville, TAMUK, The Department of Chemistry, Kingsville, TX, United States

This postface perspective provides insights on the nanomaterials design, evaluation, and applications focusing on the electrocatalyst study. Approximately, five different families of materials were discussed in the monograph with tunable structures and properties. The oxygen reduction reaction (ORR) is thermodynamically important in the fuel cells study to achieve high power density and meet current and future energy demand. The design and synthesis of nanoscale catalysts require careful coordination between the structural support and correct placement of the catalyst atoms for single-atom catalysis or a cluster of atoms at a specific face or location. Often this is accomplished by sol−gel, solvothermal, electrochemical deposition or sputtering of co-alloyed metals, metal insertion, metal-ion doping, or metal substitution to achieve the correct site-A or site-B stoichiometric or delta minus for nonstoichiometric incorporation. Doping or usage of a carbon scaffold transition metal incorporating reduced graphene oxide as the electrocatalysts. Often neglected, the transition from catalyst ink/powder to an actual electrode is a critical design element. Here, electrode thickness and geometry (2D planar-flat, 3D round, hexagonal) are important considerations for facile penetration of electrolyte supporting surface catalysis.

The synthesis of nanomaterials helps to lay the foundation for discovering novel nanomaterials. Even though numerous new nanomaterials have been discovered year over year, the synthetic approach can be summarized into several classic methods. The synthetic methods can be categorized into two major approaches, the top-down approach and the bottom-up approach.

Advanced Nanomaterials and Their Applications in Renewable Energy. https://doi.org/10.1016/B978-0-323-99877-2.00004-7

The top-down approach focuses on making bulky materials smaller, which can be done with multiple physical methods. Besides the ball milling method, which is purely mechanical, most top-down methods utilize the power of electron or electromagnetic waves to help break down, transport, and repile bulky materials into predesigned nano morphology. This chapter will introduce methods like ball milling, etching, machining, and other classic methods.

The bottom-up approach starts with small molecules (or even atoms and ions) to build up the nanostructures. This process usually highly relies on the precise tuning and engineering of chemical reactions. Different strategies, precursors, assistive agents, and reaction conditions will result in very different products for the same reactions. Based on the researcher's numerous works on that, several classic synthetic methods have been summarized, like sol-gel synthesis, emulsion synthesis, self-assembly, and so on. Besides the wet chemistry approaches, the submolecular methods like vapor deposition and molecular beam epitaxy can also help build up nanomaterials from ingredients like atoms or ions.

Besides the traditional nanomaterials, framework materials gain more and more attention as their properties have intrinsic ordered porosity and high tunability. As framework nodes' design and precise modification are greatly different from other nanomaterials, a chapter is prepared to introduce it exclusively. Besides that, as highly crystalline materials but built with metal clusters and organic ligands, the evolution, combination, and hierarchy of framework materials show its diversity.

Electrocatalysts for fuel cells are an attractive option where chemical fuels are converted to electrical energy with lower carbon emissions. The fuel (methanol or hydrogen) is oxidized at the anode, and electrons are released through an external circuit to the cathode, where oxygen is reduced. This ORR is thermodynamically the most challenging due to its large potential resulting in slow kinetics at a near applied potential. The most common electrocatalysts are platinum. Using nonplatinum catalysts such as nitrogen-doped carbon nanotubes in alkaline media have been applied to oxygen evolution reaction, nitrogen reduction reaction, and hydrogen evolution reaction to the same effect. These have resulted in faster kinetics with a pH dependence for the ORR reaction as the reaction is sensitive to how electrons are transferred. This is related to catalyst active sites in acidic electrolytes and how these electrocatalysts are used at the device level via membrane electrode assemblies. The goal is to fine-tune the carbon sp^2 microenvironment with an electron-rich heteroatom such as nitrogen or electron injections using transition metals as cathode materials. These materials may have been used as lower power devices and have inherited advantages over their metal electrode counterparts. This is because carbon is more inert under acid conditions and not prone to metal-ion contamination. While the addition of nitrogen appears straightforward, deeper analysis suggests the form and location of nitrogen concerning carbon is important in the different nitrogen forms exhibit different reactivities (pyrrolic vs. pyridinic vs. quaternary) and whether the scaffold

consists of mesoporous N-dropped or activated N-doped carbon will influence the ORR reaction as these environments to offer different gas diffusion channels and surface areas. Multidoping with electron-deficient heteroatoms such as boron or atoms from the nitrogen family such as sulfur or phosphorous may have advantages in acidic electrolyte over nitrogen-doped carbon. Much of the electrochemistry is evaluated using half-cells. However, it falls short when integrated into the fuel device. Here, electrode architecture and geometry are important considerations in designing reactive surfaces and sites to promote efficient mass transfer.

acidic electrolyte:

$$O_2 + 4H^+ + 4e^- \rightarrow 2H_2O \text{ or } O_2 + 2H^+ + 2e^- \rightarrow H_2O$$
$$H_2O_2 + 2H^+ + 2e- \rightarrow 2H_2O$$

basic electrolyte:

$$O_2 + 2H_2O + 4e^- \rightarrow 4OH- \text{ or } O_2 + H_2O + 2e^- \rightarrow HO_2- + OH^-$$
$$H_2O + HO_2^- + 2e- \rightarrow 3OH^-$$

In multidimensional geometries, multiple paths for the 3D substrate enable catalysis from all sides but limit the absolute load of the active catalyst within the electrode to the upper mg catalyst/cm^2 of the electrode. The purpose is to give the same catalytic performance as the ideal catalyst surface (e.g., Pt) without the actual bulk quantity of Pt. The inclusion of binders introduced a barrier to wettability and agglomeration but is required for efficient dopant separation for transition or noble metal catalysts, facilitating "single or clustered atom" catalysis. To promote electron transport within the electrode and interfacial layers, carbon nanotubes or graphene are often employed to decrease bulk resistance, open active sites, and enable the diffusion of ions. This electrode material may be in Ni forms or sponge close to carbon conducting polymers that bring strong electrical connections between a catalyst and current collector. Graphene sheets offer an ideal platform for the deposition of single or clustered atoms. However, much like gold deposition on a glass slide, they offer a low resistance path for electron flow to the external circuit. Graphene also enables high gas diffusion and penetration of electrolytes for higher photothermal energy conversion without cathode flooding (from the water reaction) due to its hydrophobicity.

The next generation of nonnoble catalysts has exhibited high discharge capacity and higher reversibility for LiO_2 batteries using Co_2S_4-based electrocatalysts, which employ unique 3D mesoporous stacked structures for the oxygen evolution reaction. By coupling the oxygen evolution reaction to the oxygen reduction reaction, the volumetric energy of the metal-air batteries can be lowered and energy capacity enhanced. This reaction is often accomplished using bi-functional materials tuned for one specific reaction. One possible approach uses a bimetallic V_2O_5/MnO_2 aligned nanoribbon for high supercapacitance by selecting transition metals with vacant orbitals for mixing, solvothermal/hydrothermal

synthesis, and sputtering for perovskite (LCrSF)-based electrocatalyst. The analysis underscores the difficulty of transitioning from catalyst powder/ink to electrode as electrode geometry and electrolyte and cell design greatly influence electrochemical device performance. The "end-game" is to transition to a sustainable energy platform at ambient temperature and pressure, like plants and microbes. While their conversion percent and actual synthesis rate are low, the aggregate biomass production is very large. This catalyst design requires an intimate understanding of the photosynthetic or redox proteins' intricate microbial/plant biochemistry and the synthesis of catalytic surfaces that imitate these centers in a photo- or redox chemistries. Lastly, yeast as biotic catalysts in microbial fuel cells can be grown on graphene as abiotic catalysts, resulting in a higher power and current densities is underappreciated in the fuel cell inventory and should be explored further. Comparing the power profile of the de novo versus graphene encapsulation also gave insight into the biotia electron transport mechanism, enabling the microbe to convert carbon to carbon dioxide using oxygen or weaker oxidizing agents and is an area where we envisage more potential for growth.

One subtle difference between microbial fuel cells and nonmetal catalyst fuel cells at the device level is the employment of thicker MEAs. This is because the kinetic efficiencies are lower relative to platinum necessitating greater catalyst loading. This thicker MEA will reduce transport efficiencies and needs more robust gaskets and seals than ultrathin Pt-based M.E.A.s. The device performance may also drop due to poorer oxygen flow and the porosity of the overall surface. Advanced X-ray tomography tools to reconstruct the 3D structure of the MEA is essential to understand the chemistries involved. Operando synchrotron X-ray spectroscopy or in situ neutron imaging are complementary tools that require more widespread access to further our knowledge of changes in material properties through prolonged usage. Three-dimensional high-precision printing of MEA, seals, and gaskets will enable the design and construction of seamless devices to prolonged endurance and reliability.

One area which is fasting becoming a tool kit for material scientists is the application of artificial intelligence (AI) in the design of inorganic catalyst or application of density functional theory (DFT) calculations to evaluate the feasibility and degree of modification of electrocatalysts by doping, co-alloying, substitution, or interstitial insertion. In some studies, it has been demonstrated based on AI/DFT that anionic mismatch between two transition metal ions could occur, such as Mn^{4+} and V^{5+}. These ionic radii between them are less than 12%. The resulting structure would exhibit twinned channels between Mn^{4+} and ribboned vanadium oxide to promote L^{i+} and charge carriers. The resulting electrochemistry supported the initial hypothesis where power densities of 9000 W kg^{-1} were determined. The future integration of AI with materials synthesis can identify potential metal oxides with oxidation states with the appropriate redox chemistries that have not been synthesized for catalyst fabrication either as electrodes or electrides.

Lastly, a sustainable energy portfolio must be broad to offset one commodity's market price increases and ensure countries have energy security without environmental stress. Hydrogen co-generation should be part of this energy mix. Currently, ammonia and hydrogen production are energy-intensive, requiring coal-derived energy, which generates carbon dioxide and lowers the carbon neutrality of the fuel. As stated earlier, microorganisms such as nitrogen reductases are capable of ammonia synthesis using pyruvate as a carbon source, protons using ferredoxins, molybdoferredoxin, and vanadium-ferredoxin as potential co-factors, and adenosine triphosphate as chemical energy to produce generate ammonia and hydrogen, adenosine diphosphate, and inorganic phosphate. The application of AI could allow the improved synthesis of $Mo^{3+} \rightarrow S-Fe^{3+}-C-S \rightarrow Fe^{2+}-$based FeMoS complexes, or quantum dots coupled MoFe proteins for "artificial synthesis" using similar architecture outside the fragility of the host plasma membrane/cell wall, which is sensitive to pH and temperature.

In summary, we have highlighted some challenges mainly related to the slower kinetics of the oxygen evolution reaction, which limits the performance of the electrocatalyst. The current approach is still rooted in the employment of noble metal-based catalysts in acidic media with high activity (<250 mV @ 12 $MA \cdot cm^{-2}$), but materials that can function under acidic and alkaline conditions are required. The design of electrocatalysts is often hindered by in situ mechanistic studies where the change of the catalytic surface in real-time and migration of ions is often not understood at the $t = 0$ and $t = 10$ h (end of study).

These advances will increase our capacity and ability to transition from carbon emissions to carbon-neutral and ultimately to carbon negative, where CO_2 is converted to useful byproducts lowering the potential for greenhouses gases and acid rain precursors. The future of energy generation, conversion, and storage is promising with a multifold of material science-based approaches, highlighted in this postface perspective.

Author contributions and acknowledgments

T. Y and the last section wrote the bulk of the preface SRC SB, and JLL edited the manuscript, and all authors agreed on the changes. This work is partially supported by the Welch Foundation (AC 0006).

Index

Note: Page numbers followed by "*f*" indicate figures and "*t*" indicate tables.

C

D

G

H

I

N

O

P

Q

R

S

T

Z